UNIVERSITÉ DU LUXEMBOURG

PhD-FSTM-2023-079
The Faculty of Science, Technology and Medicine

DISSERTATION

Defence held on 15/09/2023 in Esch-sur-Alzette
to obtain the degree of

DOCTEUR DE L'UNIVERSITÉ DU LUXEMBOURG

EN BIOLOGIE

by

Mohaned Abd Moh BENZARTI
Born on 17 March 1991 in Tripoli (LIBYA)

ELUCIDATING THE METABOLIC FLEXIBILITY AND PLASTICITY OF ONE-CARBON CYCLE IN CANCER CELLS WITHIN STRESSFUL METABOLIC ENVIRONMENTS

Dissertation defence committee

Dr. Johannes Meiser, dissertation supervisor
Department of Cancer Research, Luxembourg Institute of Health, Luxembourg.

Dr. Elisabeth Letellier, Chair
Assistant Professor, Department of Life Sciences and Medicine, University of Luxembourg, Luxembourg.

Dr Stephanie Kreis, Vice-Chair
Associate Professor, Department of Life Sciences and Medicine, University of Luxembourg, Luxembourg.

Dr. Vignir Helgason, External member
Professor, School of Cancer Sciences, University of Glasgow, UK.

Dr. Arnaud Blomme, External member
Faculty of Medicine, Liege University, Belgium.



The work presented in this dissertation was conducted at the:

Cancer Metabolism Group (CMG)

Department of Cancer Research (DoCR)

Luxembourg Institute of Health (LIH)



The work presented in this dissertation was sponsored by:

FNR-ATTRACT program (A18/BM/11809970)

Fonds National de la Recherche Luxembourg (FNR)



Doctoral Program in Systems and Molecular Biomedicine

Doctoral School in Science and Engineering (DSSE)

University of Luxembourg (uni.lu)



Fondation du Pélican de Mie et Pierre Hippert-Faber



Affidavit

I, Mohaned Benzarti, hereby confirm that the PhD dissertation entitled "Elucidating the metabolic flexibility and plasticity of one-carbon cycle in cancer cells within stressful metabolic environments" has been written independently and without any other sources than cited.

Luxembourg, Luxembourg 14th July, 2023

Mohaned Benzarti

Acknowledgements

Before I start, I would like to thank absolutely everyone who have helped throughout my PhD journey regardless of how little that help might have been.

My outmost gratitude will have to go to my supervisor Dr. Johannes Meiser. The support and patience you have shown me over the years of us working together was unmatched by anyone I have worked with before. Your enthusiasm for science and research is highly contagious and has spread throughout the entire CMG group from day one and I owe everything that I have learned about cancer metabolism to you. I sincerely thank you for giving me the opportunity to join your lab and the confidence you have shown in me throughout my PhD.

Special thanks goes to my CET committee members Prof. Dirk Brenner and Dr. Jochen Schneider for all of their scientific advice throughout the last 4 years, feedback and guidance. I would like to thank all of our collaborators for their technical and scientific support to make my project and this dissertation possible. Huge thanks to all the metabolomics platforms that I had the chance to work with throughout my project and especially the LIH and LCSB platforms and their respective members Dr. Antoine, Francois, Dr. Christian, Xiangyi and Floriane for their immense support and willingness to measure as many samples as I could generate. My project would not have been possible without the support of your platforms. Big thanks to Dr. Jerome Paggetti and Dr. Etienne Moussay for their continuous advice and putting trust in me to involve me in many of their projects. Thanks to all the members of the animal facility and especially Anais Oudin for their help and support with in vivo work. Huge thanks and gratitude to Dr. Elisabeth Letellier for her great support and guidance with my project and agreeing to chair my defense. I deeply thank Dr. Stephanie Kreis, Prof. Vignir Helgason and Dr. Arnaud Blomme for taken the time and effort to read my dissertation and agree to be members of my defense jury committee. I am grateful that you are part of my defense committee and I highly value all of your feedback and guidance.

I am extremely grateful to Luxembourg Institute of Health and the University of Luxembourg for giving me the opportunity to achieve this momentous step of my education at such a prestigious level. Big thanks to Fonds National de la Recherche and Fondation du Pélican de Mie et Pierre Hippert-Faber for providing the necessary funds to make my dissertation work feasible.

Next, I would like to thank the CMG members for their relentless support and creating such a positive and supportive working environment. I deeply enjoyed our time together and the stimulating discussions we had inside the lab but more importantly our social activities away from work. Nicole, thank you for all your guidance and scientific help. You were always happy to answer any questions I might have with a smile and were more than willing to provide constructive feedback on any issues I might face. I also have mention all

the lovely sweets and treats that you always happily prepared for all of us. Big thanks to my office neighbor Catherine for always giving me a hand with anything I needed in the lab and your positive attitude towards work and keeping everything we shared organized. I also really enjoyed all your baking treats. Lara, thank you for helping me figure out how to deal with my BMDMs frustrations at the beginning of my PhD and being more than willing to drive me home after very long lab days. Also all the memes and Nigel & Marmalade videos. Bjeorn, thank you for always being willing to have deep discussions about metabolism and tracing with me but always with a laugh. Our conversations continuously gave me new ideas and experiments to try out. Huge thanks to the best lab manager out there, Laura. Thank you for all the support and help you always gave with amazing enthusiasm. To the newer members of CMG Kim, Oleg and Christina thank you for your help with my project and support in the lab and especially the fun times we had together.

I would like to thank all the PIs, postdocs, PhDs and staff from DoCR at LIH, members of TSI group at LIH, Dr. Elisabeth Letellier's lab members and Prof. Dirk Brenner's lab members for all the good times we had together and their support for my work and engaging scientific discussions.

My biggest supporters my family and friends, thank you for always having my back and being there for me when times got tough. To my wonderful parents, thank you for always believing in me and your unconditional support towards me in every way you can. Your kind words and prayers meant the world to me and without your care; I wouldn't have been able to get through this challenge. To my brothers and sisters Mohammed, Mawada, Malek and Masarra, we joke around a lot and like to make fun of each other all the time but deep down I know that we share a great bond and genuinely care for each other, shokra for that. Abdo and Mohammed, you always have been my best and closest friends and you have giving me so much support over the years and especially during my PhD, thank you for always being there and ready to hear my complaints. Both my uncles Edawi and Ahmed thank you very much for always checking on me and making sure everything was going smoothly, I always appreciate our phone conversations. To the rest of my aunt, uncles and cousins thank you for your total and absolute support. Abdulhafid, Adam, Alaa, Aiyoup, Jehad, Majd, Monder, Mostafa, Nuri, Siraj and Zeyad we shared a lot of laughs and great memories together over the years, thank you for that and I'm grateful for all your help and friendship. Sarmini, thank you for being there through the difficult COVID times, we shared a lot of funny moments and (CTR) adventures. It was great to have someone I can speak in Arabic to and share my daily problems with throughout my PhD, even though, we did not agree on many Arabic words (7ot). To the foodies; Ernesto, Carina and Andrea, thank you for all the wonderful moments and nights in Luxembourg and joining me in trying different cuisines. Last but not least, Alice thank you for your unwavering and unconditional support through the last and most difficult part of my PhD, I will always be grateful for everything.

To everyone who have helped with this significant period of my career, you have my deepest and outmost gratitude.

Table of Contents

Affidavit iii

Acknowledgements iv

List of Illustrations x

List of Tables xi

List of Abbreviations xii

List of Publications xiv

SUMMARY xvi

..... 1

CHAPTER 1: SYNOPSIS 1

1.1. Cancer 2

1.1.1. Definition and epidemiology 2

1.1.2. Hallmarks and evolution 2

1.1.3. Metabolic reprogramming facilitates tumorigenesis 2

1.2. Cancer Metabolism 3

1.2.1. Flexibility and plasticity of cancer metabolism 4

1.2.2. Tumor microenvironment and nutrient availability 4

1.2.3. Metastatic organotropism 5

1.3. Aerobic glycolysis “fermentation” 5

1.3.1. PKM2 and aerobic glycolysis 7

1.3.2. Determinants of aerobic glycolysis 10

1.3.3. Unmasking metabolic flexibility and plasticity using galactose 11

1.4. Serine metabolism in cancer 13

1.4.1. Serine synthesis pathway 13

1.4.2. Folate cycle 15

1.5. One-carbon cycle 17

1.5.1. The canonical 1C cycle 18
1.5.2. Compartmentalization of 1C cycle 20
1.5.3. Flexibility and plasticity of 1C cycle 22
1.5.3.1. Bioenergetic potential in 1C cycle 23
1.5.3.2. Redox balance potential in 1C cycle 23
1.6. Clinical perspective of cancer metabolism 24
1.6.1. Targeting cancer metabolic pillars 24
1.6.2. Challenges of targeting cancer metabolism 25
1.7. Metabolomics 26
1.7.1. Isotope tracing in metabolic studies 26
1.7.2. Metabolic parameters 28
HYPOTHESIS AND AIMS 31
CHAPTER 2: Metabolic Potential of Cancer Cells in Context of the Metastatic Cascade 32
2.1. Preface: 33
2.2. Personal contribution 33
2.3. Manuscript 33
CHAPTER 3: PKM2 diverts glycolytic flux in dependence on mitochondrial one-carbon cycle 59
3.1. Preface 60
3.2. Personal contribution 60
3.3. Manuscript 61
Abstract 63
Introduction 64
Results 65
Discussion 73
Material and Methods 76
Figures 84
CHAPTER 4: Mitochondria preserve an autarkic one-carbon cycle to confer growth-independent cancer cell migration and metastasis 118

4.1. Preface 119

4.2. Personal contribution 119

4.3. Manuscript 119

CHAPTER 5: Discussion and Future Perspectives 153

REFERENCES of CHAPTER 1 and 5 168

APPENDICES 178

Appendix 1: Extended data related to chapter 3. 179

Appendix 2: PARK7/DJ-1 promotes pyruvate dehydrogenase activity and maintains Treg homeostasis during ageing 180

Appendix 3: Extracellular Vesicle Secretion by Leukemia Cells In Vivo Promotes CLL Progression by Hampering Antitumor T-cell Responses 216

Appendix 4: Inhibition of MYC translation through targeting of the newly identified PHB-eIF4F complex as therapeutic strategy in CLL 241

Appendix 5: Pyruvate dehydrogenase fuels a critical citrate pool that is essential for Th17 cell effector functions 260

List of Illustrations

Illustration 1. Hallmarks of cancer. 3
Illustration 2. Aerobic glycolysis mechanisms. 7
Illustration 3. Glycolysis and TCA cycle. 9
Illustration 4. Leloir pathway. 12
Illustration 5. Serine synthesis pathway and one-carbon cycle. 15
Illustration 6. Targeted metabolomics workflow. 29
Illustration 7. Comparison of glycolytic challenges. 155
Illustration 8. Metabolic rewiring in response to glycolytic stress in cancer cells. 156
Illustration 9. Pyruvate kinase flux. 157
Illustration 10. Cytoplasmic and mitochondrial route for phosphoenol pyruvate generation in gluconeogenesis. 161
Illustration 11. Summary of the metabolic rewiring in cancer cells under glycolytic stress. 164

List of Tables

TABLE 1. KM VALUE FOR HEXOKINASE AND LELOIR PATHWAY ENZYMES. 12
TABLE 2. BIOLOGICALLY RELEVANT FOLATE SPECIES. 16
TABLE 3. ONE-CARBON CYCLE STAGES AND THEIR CORRESPONDING ENZYMES. 18

List of Abbreviations

ΔG	Gibbs free energy
1C	One-carbon
3-PG	3-phosphoglycerate
3-PHP	3-phosphohydroxypyruvate
3-PS	3-phosphoserine
5-CH_3-THF	5-methyl-THF
5,10-CH^+-THF	5,10-methenyl-THF
5,10-CH_2-THF	5,10-methylene-THF
AK	Adenylate kinase
aKG	α-ketoglutarate
ALDH1L	10-CHO-THF dehydrogenase
ATP	Adenosine triphosphate
CORE	Consume/Release rates
DHF	Dihydrofolate
DHFR	Dihydrofolate reductase
dTMP	Deoxythymidine monophosphate
ETC	Electron transport chain
FPGS	Folylpolyglutamate synthetase
FTHFD	10-formyl-THF dehydrogenase
FTHFS	10-formyl-THF synthase
G6P	Glucose 6-phosphate
GC-MS	Gas chromatography-mass spectrometry
GCS	Glycine cleavage system
HCC	Hepatocellular carcinoma
LC-MS	Liquid chromatography-MS
MALDI	Matrix-assisted laser desorption/ionization
ME	Malic enzyme
MID	Mass isotopomer distribution
MS	Mass spectrometry
MSI	Mass spectrometry imaging

MTHFD	5,10-methylene-THF dehydrogenase/5,10-methenyl-THF cyclohydrolase
MTHFD1L	MTHFD1Like
MTHFR	5,10-CH_2-THF reductase
MTHFS	5,10-CH^+-THF synthetase
NMR	Nuclear magnetic resonance
OXPHOS	Oxidative phosphorylation
PDH	Pyruvate dehydrogenase
PEP	Phosphoenolpyruvate
PEPCK2	Phosphoenolpyruvate carboxykinase 2
PHGDH	Phosphoglycerate dehydrogenase
PK	Pyruvate kinase
PKM2	Pyruvate kinase isozyme M2
PPP	Pentose phosphate pathway
PSAT1	Phosphoserine aminotransferase1
PSPH	Phosphoserine phosphatase
ROS	Reactive oxygen species
SAM	s-adenosyl-methionine
SG	Serine/glycine
SHMT	Serine hydroxyl methyl-transferase
SSP	Serine synthesis pathway
TCA	Tricarboxylic acid
TIF	Tumor interstitial fluid
TME	Tumor microenvironment
TS	Thymidylate synthetase
UDP	Uridine diphosphate

List of Publications

The first 3 publications listed below are the core of my thesis:

1. **Review article (first co-authorship)**

BENZARTI, M., DELBROUCK, C., NEISES, L., KIWELER, N. & MEISER, J. 2020. Metabolic Potential of Cancer Cells in Context of the Metastatic Cascade. ***Cells***, 9. DOI: doi: 10.3390/cells9092035.

2. **Submitted research manuscript to Cell Reports (First authorship) available on BioRxiv**

BENZARTI, M., OUDIN, A., VIRY, E., GARGIULO, E., SCHMOETTEN, M., NEISES, L., PULIDO, C., LORENZ, N. I., RONELLENFITSCH, M. W., SUMPTON, D., WARMOES, M., JAEGER, C., LESUR, A., MOUSSAY, E., PAGGETTI, J., NICLOU, S.P., LETELLIER, E., MEISER, J. 2023. PKM2 diverts glycolytic flux in dependence on mitochondrial one-carbon cycle. BioRxiv https://www.biorxiv.org/content/10.1101/2023.01.23.525168v1.full.pdf.

3. **Research article (co-authorship)**

KIWELER, N., DELBROUCK, C., POZDEEV, V. I., NEISES, L., SORIANO-BAGUET, L., EIDEN, K., XIAN, F., **BENZARTI, M**., HAASE, L., KONCINA, E., SCHMOETTEN, M., JAEGER, C., NOMAN, M. Z., VAZQUEZ, A., JANJI, B., DITTMAR, G., BRENNER, D., LETELLIER, E. & MEISER, J. 2022. Mitochondria preserve an autarkic one-carbon cycle to confer growth-independent cancer cell migration and metastasis. ***Nature Communications***, 13, 2699. DOI: https://doi.org/10.1038/s41467-022-30363-y

The following four publications constitute part of my PhD work, however, they are out of the scope of my dissertation. Detailed personal contribution to these publications and the full manuscripts are listed in the appendices.

4. **Research article (co-authorship)**

DANILEVICIUTE, E., ZENG, N., CAPELLE, C. M., PACZIA, N., GILLESPIE, M. A., KURNIAWAN, H., **BENZARTI, M**., MERZ, M. P., COOWAR, D., FRITAH, S., VOGT WEISENHORN, D. M., GOMEZ GIRO, G., GRUSDAT, M., BARON, A., GUERIN, C., FRANCHINA, D. G., LÉONARD, C., DOMINGUES, O., DELHALLE, S., WURST, W., TURNER, J. D., SCHWAMBORN, J. C., MEISER, J., KRÜGER, R., RANISH, J., BRENNER, D., LINSTER, C. L., BALLING, R., OLLERT, M. & HEFENG, F. Q. 2022. PARK7/DJ-1 promotes pyruvate dehydrogenase activity and maintains Treg homeostasis during ageing. ***Nature Metabolism***, 4, 589-607. DOI: https://doi.org/10.1038/s42255-022-00576-y

5. **Research article (co-authorship)**

GARGIULO, E., VIRY, E., MORANDE, P. E., LARGEOT, A., GONDER, S., XIAN, F., IOANNOU, N., **BENZARTI, M**., KLEINE BORGMANN, F. B., MITTELBRONN, M., DITTMAR, G., NAZAROV, P. V., MEISER, J., STAMATOPOULOS, B., RAMSAY, A. G., MOUSSAY, E. & PAGGETTI, J. 2023. Extracellular Vesicle Secretion by Leukemia Cells In Vivo Promotes CLL Progression by Hampering Antitumor T-cell Responses. ***Blood Cancer Discovery***, 4, 54-77. DOI: https://doi.org/10.1158/2643-3230.BCD-22-0029

6. **Research article (co-authorship)**

LARGEOT, A., KLAPP, V., VIRY, E., GONDER, S., FERNANDEZ BOTANA, I., BLOMME, A., **BENZARTI, M**., PIERSON, S., DUCULTY, C., MARTTILA, P., WIERZ, M., GARGIULO, E., PAGANO, G., AN, N., EL HACHEM, N., PEREZ HERMANDEZ, D., CHAKRABORTY, S., YSEBAERT, L., FRANÇOIS, J. H., CORTEZ CLEMENTE, S. D., BERCHEM, G., EFREMOV, D. G., DITTMAR, G., SZPAKOWSKA, M., CHEVIGNE, A., NAZAROV, P. V., HELLEDAY, T., CLOSE, P., MEISER, J., STAMATOPOULOS, B., DÉSAUBRY, L., PAGGETTI, J. & MOUSSAY, E. 2023. Inhibition of MYC translation through targeting of the newly identified PHB-eIF4F complex as therapeutic strategy in CLL. ***Blood***. DOI: https://doi.org/10.1182/blood.2022017839

7. **Research article (co-authorship)**

SORIANO-BAGUET, L., GRUSDAT, M., KURNIAWAN, H., **BENZARTI, M**., BINSFELD, C., EWEN, A., LONGWORTH, J., BONETTI, L., GUERRA, L., FRANCHINA, D. G., KOBAYASHI, T., HORKOVA, V., VERSCHUEREN, C., HELGUETA, S., GÉRARD, D., MORE, T. H., HENNE, A., DOSTERT, C., FARINELLE, S., LESUR, A., GÉRARDY, J. J., JÄGER, C., MITTELBRONN, M., SINKKONEN, L., HILLER, K., MEISER, J. & BRENNER, D. 2023. Pyruvate dehydrogenase fuels a critical citrate pool that is essential for Th17 cell effector functions. ***Cell Reports***, 42, 112153. DOI: https://doi.org/10.1016/j.celrep.2023.112153

SUMMARY

Metabolism is an interlinked series of biochemical reactions that govern biomass and energy generation at a cellular and systemic level. Due to its critical role in generating biomass, rewiring metabolism is considered an enabling hallmark of cancer progression. A key biosynthetic pathway that is often upregulated in cancer cells is the one-carbon (1C) metabolism. 1C metabolism has been successfully targeted for its biosynthetic potential since the 1950s with chemotherapeutic agents like methotrexate. However, recent advances in the cancer metabolism field have hinted at possibilities that the 1C cycle can support energy generation and antioxidant defense. Recent work by our group has shown that the 1C cycle is running in excess of the anabolic need of the cell and that excess is excreted out of the cell as formate. Furthermore, we have shown that cancer cells often increase formate release rates under growth inhibitory perturbations. Such observations suggest that the 1C cycle serves additional metabolic functions in cancer cells. However, these functions are currently not well understood and the growth-independent potential of the 1C cycle remain unexplored.

In my dissertation, we studied cancer cells under glycolytic and growth stress conditions to identify growth-independent functions of the 1C cycle. We utilized galactose as a tool compound to mimic glucose limitation, a physiological relevant feature of the tumor microenvironment. Firstly, we corroborated previous findings regarding the rewiring of glutamine metabolism under glucose limitation towards serine synthesis pathway (SSP) and TCA cycle. Moreover, we were able to separate and stratify the two rewiring pathways with the identification of a glycolytic block. Using isotope tracers, we identified pyruvate kinase M2 isozyme (PKM2) as the rewiring point under glucose limitation as it is completely blocked under these conditions. This identified PKM2 block is novel and independent of serine levels. It rewired the limited glycolytic carbons towards SSP and the 1C cycle to support nucleotide synthesis and mitochondrial ATP and NADPH generation. Furthermore, using genetic ablation of 1C cycle enzymes we showed that the PKM2 block relied on active formate overflow.

To specifically identify growth-independent functions of the 1C cycle, we utilized methotrexate as a tool compound to fully inhibit the cytoplasmic 1C cycle, halting cancer cell proliferation. We identified that cancer cells are able to sustain their mitochondrial 1C flux independently of the cytoplasmic part. In addition, the independent mitochondrial 1C cycle was significantly important to support cancer cell motility and promote metastasis.

In conclusion, cancer cells are notorious to have a highly adaptable metabolic network that allow them to be metabolically resilient and to escape treatment. By utilizing nutrient stress tools *in vitro,* we are able to identify rewiring strategies that can uncover vulnerabilities of the most resilient cancer cell populations.

CHAPTER 1: SYNOPSIS

Synopsis

1.1. Cancer

1.1.1. Definition and epidemiology

Cancer represent a group of diseases that are characterized with uncontrollable growth and the ability to invade through neighboring tissues to seed into distant parts of the body. In people under the age of 70, cancer ranks as the leading cause of death in the majority of the western world and is either the first or the second cause of death in 112 different countries across the globe (Sung et al., 2021). According to the World Health Organization, roughly 20 million new cancer cases have been diagnosed in 2020 (Sung et al., 2021). Even though cancer treatments and interventions have dramatically improved over the last decades, it remains an undeniable fact that cancer is a major source of global mortality and morbidity (Sung et al., 2021). In fact, there were roughly 10 million cancer deaths in 2020 (Sung et al., 2021).

1.1.2. Hallmarks and evolution

Cancer is an umbrella term that describes many diseases with distinct molecular profiles; this poses tremendous challenges when it comes to therapy and research. However, efforts have been made to unify all human tumors under a set of cellular characteristics that governs the transition from normalcy into malignancy and these characteristics are referred to as hallmarks of cancer (Hanahan, 2022, Hanahan and Weinberg, 2000, Hanahan and Weinberg, 2011). The acquirement of these hallmarks (**Illustration 1**) is a gradual and multistep process that showcase the evolutionary nature of cancer (Hanahan and Weinberg, 2000). It is yet unclear which evolutionary dynamics cancer follows and it is arguably a mixture of branched and neutral mode of evolution (Vendramin et al., 2021). Nonetheless, what remains irrefutable is the presence of intratumor heterogeneity as characterized with the presence of distinct subclones within a tumor (Vendramin et al., 2021). This heterogeneity is what guarantees the progression and persistence of tumors when faced with selection pressures applied by harsh tumor microenvironments (TME). These selection pressures can be mechanical, biochemical, cellular and/or metabolic (Vendramin et al., 2021, Bergers and Fendt, 2021).

1.1.3. Metabolic reprogramming facilitates tumorigenesis

The deregulated growth and proliferation of cancer cells requires a reprogramming of the cellular biochemical network to accommodate for the new biosynthetic and bioenergetic demands (Hanahan and

Weinberg, 2011). Therefore, the metabolic changes that cancer cells undergo have been identified as an enabling characteristic of tumorigenesis (Hanahan and Weinberg, 2011).

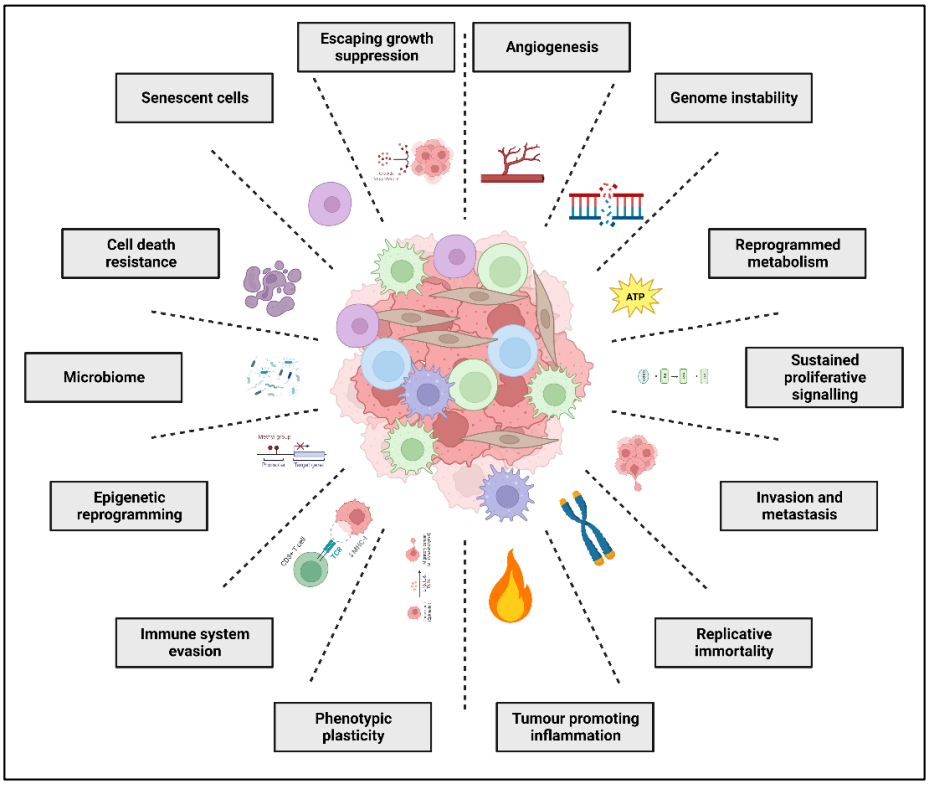


Illustration 1. Hallmarks of cancer.

In the transition from normalcy to tumorigenesis, cancer cells acquire multiple enabling hallmarks that are common across vast majority of human tumors. These characteristics are: prompting angiogenesis, genomic instability, reprogrammed metabolic network, sustained proliferative/oncogenic signaling, invasion and metastases formation, replicative immortality, inflammation, cellular plasticity, immune system evasion, epigenetic reprogramming, tumor-modulating microbiome, cell death resistance, senescent cell secretions and escaping from growth suppression. Figure adapted from (Hanahan, 2022) and created with Biorender.com.

1.2. Cancer Metabolism

Many of the cellular characteristics that differentiate cancer cells from their normal counterparts are regulated by the metabolic state of the cell or the metabolic composition of their environments (Finley, 2023). An example of the previous statement is the dependency of c-Myc expressing tumor cells on glutamine for uncontrolled proliferation (Edwards-Hicks et al., 2022, Wise et al., 2008). Moreover, studies have shown a direct link between oncogenic signaling and metabolic enzymes, for example, c-Myc was shown to activate Lactate dehydrogenase and this activation is essential for tumorigenesis (Shim et al., 1997). Therefore, it can be stated that cancer cells rely on their aberrant metabolic network for function and transformation (Finley, 2023). Yet it can be argued that the biggest advantage of the aberrant metabolic network for tumor cells is

its flexibility and plasticity, which permits for increased chances of survival and adaptability (Fendt et al., 2020, Bergers and Fendt, 2021). Meaning that the cancer metabolome plays a crucial role in cancer progression alongside oncogenic mutations. Below I will briefly address the concept of metabolic adaptability and nutrient availability in the context of cancer.

1.2.1. Flexibility and plasticity of cancer metabolism

As the primary tumor grows and across the metastatic cascade, cancer cells are faced with highly variable metabolic environments that challenges the survival of tumor cells. The encountered metabolic environments are usually harsh due to the poor vascularization of the primary tumor, increased biosynthetic demands leading to nutrient depletion and product accumulation, oxidative stress during metastasis and completely altered metabolic niche in metastatic sites (Benzarti et al., 2020, Bergers and Fendt, 2021, Fendt et al., 2020, Finley, 2023). Cancer cells are able to survive these hostile metabolic challenges due to their superior metabolic flexibility and plasticity. Metabolic flexibility is the ability to use different metabolites towards the same function, while plasticity is the ability to use the same metabolite for different purposes (Fendt et al., 2020). How cancer cells acquire these metabolic traits is currently not well understood. As highlighted previously in section 1.1.2., one theory is that during transformation and tumorigenesis cancer cells gain neutral characteristics that do not offer any growth advantage when conditions are favorable. However, when the metabolic niche becomes hostile, these neutral traits give rise to a metabolically-resilient sub-population that is capable of surviving and progressing through these challenges (Fendt et al., 2020, Vendramin et al., 2021). The relative ease of culturing tumor cells *in vitro* is a testimony to their metabolic flexibility (Eagle, 1955). Another demonstration of metabolic flexibility was shown in a study, where lung cancer cells adapted their metabolism differently to the *in vitro* metabolic environment when compared to the *in vivo* metabolic environment (Davidson et al., 2016). An example of metabolic plasticity was demonstrated when cancer cells were challenged with anchorage detachment. The detachment caused a rewiring of glutamine metabolism towards reductive carboxylation instead of the oxidative pathway, in order to combat the increased reactive oxygen species (ROS) (Jiang et al., 2016).

1.2.2. Tumor microenvironment and nutrient availability

Tumor interstitial fluid (TIF) metabolic profiling has demonstrated that tumor cells have to survive and proliferate in a metabolic niche that is significantly different from plasma and healthy tissues (Sullivan et al., 2019). Specifically, the TME is characterized to be depleted in several nutrients and at same time enriched in metabolic waste products (Faubert et al., 2020, Reinfeld et al., 2021, Sullivan et al., 2019). Oncogenic

mutations allow cancer cells to be in a state of anabolic growth facilitated by mechanisms of increased uptake of nutrients that out-compete stromal cells in the TME, hence overcoming the challenge of nutrient depletion (Faubert et al., 2020, Palm and Thompson, 2017). Moreover, cancer cells are able to take advantage of niche-specific nutrients to support their metabolism. These nutrients can be deposited by specific cells within the TME. For example, pancreatic ductal adenocarcinoma cells rely on alanine which is released by pancreatic stellate cells into the TME (Sousa et al., 2016). The metabolic cooperation within the TME is further discussed in the third section of chapter two.

1.2.3. Metastatic organotropism

Nutrient availability of the TME does not only impact the growth of the primary tumor, it can also dictate where specific tumor cells will be able to seed and form micro- and macrometastases. The propensity of primary tumors to form metastases at defined distant secondary sites is known as organotropism (Chen et al., 2018). Organotropism is driven by a multitude of factors including metabolic composition of the metastatic niche (Chen et al., 2018, Gao et al., 2019). Remarkably, tumors can even drive the deposition of specific metabolites into the pre-metastatic niche to prime it for tumor cells seeding and growth. This was recently shown in breast cancer, where tumor cells released soluble factors, which led to an increase in pulmonary palmitate levels. Such increased palmitate concentration facilitated pulmonary metastasis in breast cancer models (Altea-Manzano et al., 2023).

Overall, tumor cells must display superior metabolic flexibility and plasticity to successfully progress through the metastatic cascade. They do so by finely tuning many biochemical pathways in central carbon metabolism which are well-documented to be upregulated in cancer cells e.g. aerobic glycolysis, pentose phosphate pathway (PPP), one-carbon (1C) metabolism and glutamine anaplerosis (DeBerardinis and Chandel, 2016). The upregulation of these pathways is essential to supply the cell with building blocks for new cells (biosynthesis), energy for growth (bioenergetics) and to stabilize oxidative agents (redox balance). These aspects of cellular metabolism are often referred to as metabolic pillars (DeBerardinis and Chandel, 2016). I will focus the rest of the synopsis chapter on the key metabolic pathways addressed in my dissertation that support the above-mentioned pillars being aerobic glycolysis, serine synthesis and 1C metabolism.

1.3. Aerobic glycolysis “fermentation”

The beginning of cancer metabolism as a field can be traced back one century ago to the discoveries made by Otto Warburg on aerobic glycolysis in tumor tissue (Warburg, 1925). Aerobic glycolysis (also referred to

as Warburg effect) is the process observed in cancer cells when they metabolize glucose almost entirely into lactate even in normoxia. This was a unique observation for tumor cells because in normal tissues, when oxygen is available, glucose is usually mostly oxidized through the tricarboxylic acid (TCA) cycle and oxidative phosphorylation (OXPHOS) in the mitochondria, an observation that is referred to as the Pasteur effect (Finley, 2023). The term "Warburg effect" is used in the literature to imply reprogramming of the metabolic network to long-term fix cells to produce lactate (**Illustration 2**) even in the presence of oxygen (Diaz-Ruiz et al., 2011). However, recent sophisticated *in vivo* metabolic studies have revealed that cancer cells are able to revert back to using OXPHOS and reduce aerobic glycolysis (Bartman et al., 2023, Davidson et al., 2016). In fact, it was shown that in an orthotopic breast cancer model, lung metastasis had higher TCA cycle flux when compared with primary breast tumor (Bartman et al., 2023). The metabolic switch observed between primary tumor and metastases highlight two aspects: ① tumor cells with higher metabolic flexibility were able to form metastasis ② contrary to the Warburg effect, cancer cells are not fixed on a glycolytic phenotype and must be flexible to be able to give rise to metastasis. The reversibility nature of aerobic glycolysis is similar to another observed rewiring mechanism known as the "Crabtree effect" (Crabtree, 1929). The Crabtree effect is defined as a short-term and reversible aerobic glycolysis, which is mainly driven by the presence of abundant glucose that suppresses mitochondrial function (**Illustration 2**) (de Alteriis et al., 2018, Diaz-Ruiz et al., 2011).The two terms Warburg/Crabtree effect share a lot of similarities and are often used interchangeably in the literature. Therefore, to avoid confusion, I will not use these two terms from here onwards (**Illustration 2**). Technically glycolysis refers to the conversion of glucose to pyruvate and not lactate. Therefore, the absolute correct terminology to use here would be "aerobic fermentation" (Wang and Patti, 2023). However, for the sake of simplicity, familiarity and continuity, I will stick to the term "aerobic glycolysis" throughout this work.

Synopsis

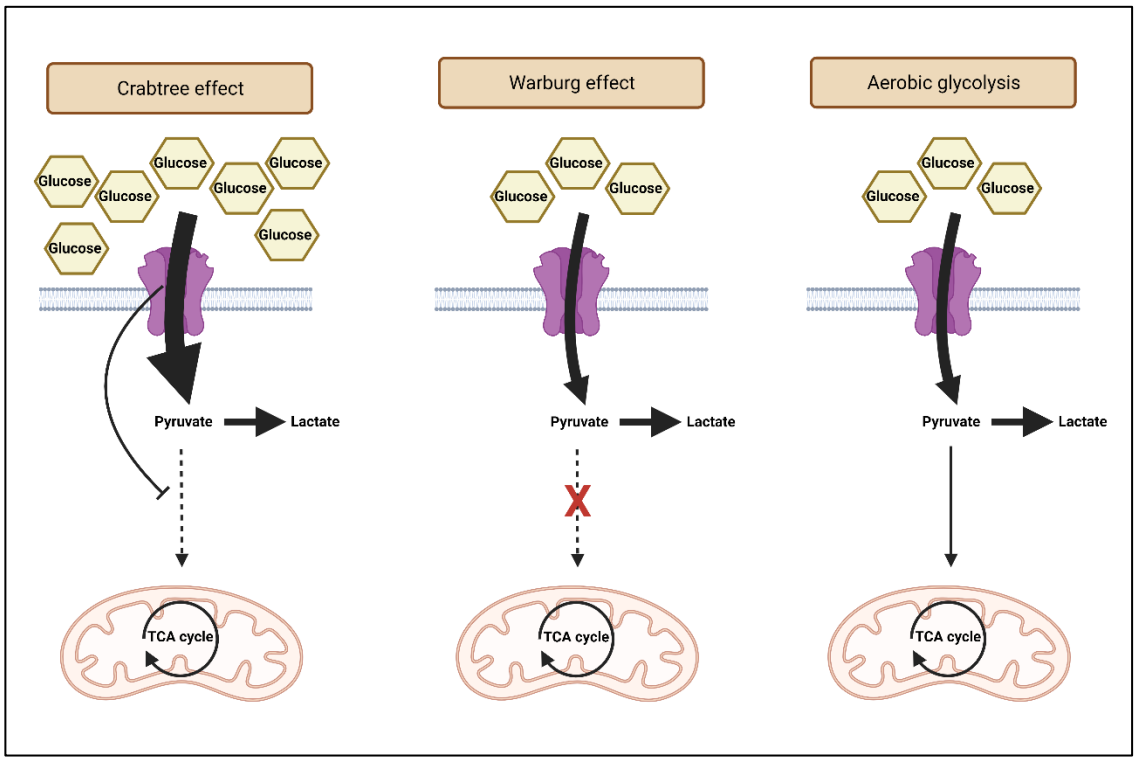


Illustration 2. Aerobic glycolysis mechanisms.

Aerobic glycolysis is characterized as the near-complete conversion of glucose to lactate in normoxia. Several effects have been described to explain this phenotype. Crabtree effect is explained as a short-term rewiring of glycolysis that is due to excess glucose repressing mitochondrial function (dotted line in the illustration indicates the reversibility of this phenotype). Warburg effect is a long-term rewiring of glycolysis as indicated with the red cross in the illustration. In cancer cells, aerobic glycolysis seems to be a reversible phenotype that can be adapted according to the tumor microenvironment as indicated in the illustration (Figure created with Biorender.com).

1.3.1. PKM2 and aerobic glycolysis

Glycolysis consists of ten biochemical reactions that start with the phosphorylation of glucose and end with the generation of pyruvate. Pyruvate is either reduced to lactate or oxidized to enter the TCA cycle (**Illustration 3**). Seven out of the 10 reactions in glycolysis are reversible and thermodynamically can go in both directions (depending on substrate/product balance) since their Gibbs free energy (ΔG) is close to zero (Nelson, 2017). The three remaining reactions (first, third and last reaction) have high negative ΔG values, meaning that they are irreversible and highly favorable in the forward direction (Chandel, 2021). These three reactions are often referred to as the regulatory nodes of glycolysis and they are catalyzed by hexokinase, phosphofructokinase and pyruvate kinase (Nelson, 2017). Nodes of glycolysis are regulated by several mechanisms including allosteric regulation, product inhibition, transcriptional changes and signaling pathways.

Synopsis

In the context of cancer metabolism, one of the most heavily studied nodes is pyruvate kinase (PK) that catalyzes the last step in glycolysis (**Illustration 3**). In mammals, PK exists as four isozymes from two different genes. The main isozyme in proliferating cells is pyruvate kinase isozyme M2 (PKM2), while the main isozyme in adult tissues is the M1 isozyme, PKM1 (Dayton et al., 2016). PKM1 exists as a high activity tetramer but PKM2 can exist as a tetramer or a lower activity dimer. The two states of PKM2 allow cancer cells the flexibility to rewire their metabolism and respond to different stimuli. The advantage of having a lower activity form is to be able to rewire the glycolytic flux towards biosynthetic branches of glycolysis like serine synthesis to facilitate proliferation (Dayton et al., 2016). Indeed, it was shown that upon the deletion of PKM2 and expression of PKM1, cancer cells had reduced ability to initiate tumors *in vivo* (Christofk et al., 2008). More importantly, the replacement of PKM2 with PKM1 led to the reversal of aerobic glycolysis, meaning that PKM2 and the metabolic flexibility it provides are essential for cancer cells to perform aerobic glycolysis. Wiese at al. (2021) went on to show that PKM1 (or activation of PKM2) represses aerobic glycolysis due to lactate dehydrogenase inhibition via elevated oxaloacetate (Wiese et al., 2021).

Synopsis

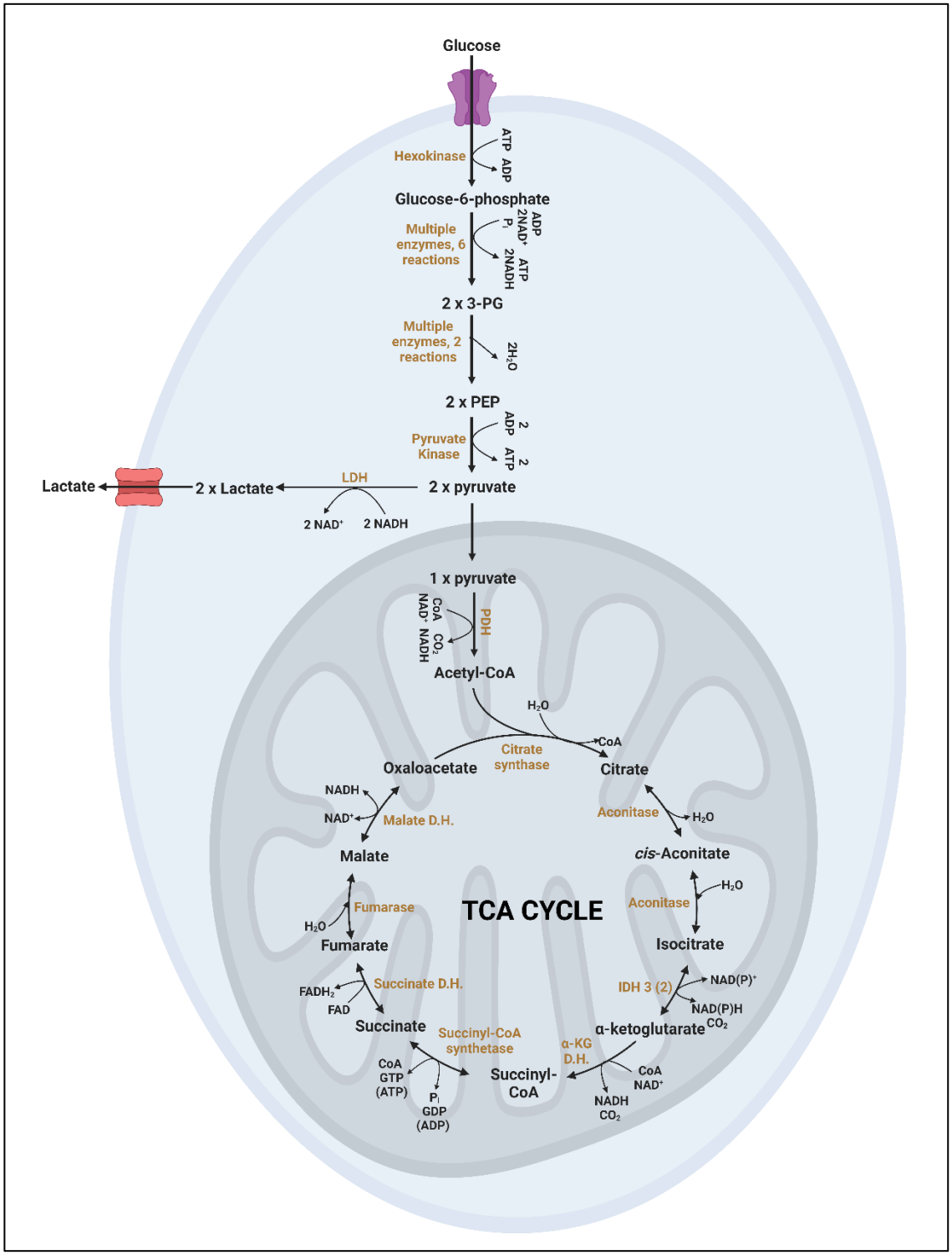


Illustration 3. Glycolysis and TCA cycle.

The biochemical reactions that take place in the pathways of glycolysis and the TCA cycle. 3-PG, 3-phosphoglycerate; PEP, phosphoenolpyruvate; ATP, adenosine triphosphate; ADP, adenosine diphosphate; NAD(H) nicotinamide adenine dinucleotide; NADP(H), nicotinamide adenine dinucleotide phosphate; GDP, guanosine diphosphate; GTP, guanosine triphosphate; FAD(H), Flavin adenine dinucleotide; α-KG, alpha-ketoglutarate; PDH, pyruvate dehydrogenase; LDH, lactate dehydrogenase; IDH, isocitrate dehydrogenase; D.H., dehydrogenase. Figure adapted from (Benzarti et al., 2020) and created with Biorender.com.

Synopsis

1.3.2. Determinants of aerobic glycolysis

Fermenting one glucose molecule through aerobic glycolysis yields a net of two ATP molecules with two lactate molecules released outside of the cell (**Illustration 3**). On the contrary, fully oxidizing one glucose molecule via the TCA cycle and OXPHOS yields a net of 30 or 32 ATP molecules (depending on the NADH shuttle system involved) (Benzarti et al., 2020). It is clear that aerobic glycolysis is far less energetically efficient when compared to OXPHOS and wasteful in terms of carbons for biomass as these are lost outside of the cell as lactate. The obvious question here is why do cancer cells adopt such an inefficient and wasteful biochemical process and this paradigm has never been entirely explained. However, recent publications have provided multiple models as reasoning for adopting aerobic glycolysis, meaning that the justification for using aerobic glycolysis is multifactorial and encompasses several determinants (Fernandez-de-Cossio-Diaz and Vazquez, 2017, Luengo et al., 2021, Niebel et al., 2019, Pfeiffer et al., 2001, Vazquez et al., 2010, Wang et al., 2022). Aerobic glycolysis determinants circulate around the inability of the mitochondria to handle the increased rate of glucose uptake and the early glycolytic reactions, which are upregulated due to oncogenic signaling (Amendola et al., 2019, Faubert et al., 2020, Osthus et al., 2000, Ying et al., 2012). These determinants include pathway kinetics, spatial arrangement, NAD^+ regeneration and ATP restoration (Fernandez-de-Cossio-Diaz and Vazquez, 2017, Luengo et al., 2021, Niebel et al., 2019, Pfeiffer et al., 2001, Vazquez et al., 2010, Wang et al., 2022).

Comparing the number of biochemical reactions involved in fermenting glucose to lactate as opposed to fully oxidizing it (**Illustration 3 and Table 1 in Chapter 2**), we can predict that aerobic glycolysis will have a faster rate (Benzarti et al., 2020). Moreover, since the yield of a reaction (ATP production in this case) is inversely proportional to its rate, it is only logical that aerobic glycolysis has faster kinetics (Pfeiffer et al., 2001). A further kinetic observation in favor of aerobic glycolysis is the fact that PDH highest turnover rate is 20-fold slower than the rate of glycolysis in some cells (Wang and Patti, 2023). PDH controls the rate at which pyruvate is oxidized into the TCA cycle (**Illustration 3**). Therefore, if glycolysis rate exceeds PDH activity, cells will have to reduce pyruvate into lactate (Wang and Patti, 2023). Another determinant of aerobic glycolysis is space availability as the cytoplasm has more solvent capacity than the mitochondria (Vazquez et al., 2010).

In early glycolytic reactions, NAD^+ is reduced to NADH in a redox reaction that converts glyceraldehyde 3-phosphate to 1,3-bisphosphoglycerate (Nelson, 2017). For glycolysis to continue, NAD^+ has to be continuously regenerated at the same pace as the early steps of glycolysis. The most efficient pathways to regenerate cytoplasmic NAD^+ is through either the malate-aspartate shuttle or glycerol 3-phosphate shuttle (Nelson, 2017). Wang et al have shown that in cancer cells, NADH shuttle systems are saturated and unable

to cope with the demand, therefore, the cell has to rely on an alternative NAD^+ generating reaction for glycolysis and proliferation to continue (Wang et al., 2022). In this study, the reaction was found to be the reduction of pyruvate into lactate i.e. aerobic glycolysis (**Illustration 3**). Another recent study has shown similar findings, where the rate of proliferation was reduced after forcing cells to oxidize glucose via the TCA cycle and OXPHOS (Luengo et al., 2021). According to the authors, this was caused by a reduction in the regeneration of NAD^+ (Luengo et al., 2021). ATP is also invested in the early steps of glycolysis and similarly to NAD^+, its restoration is required for the persistence of glycolysis and proliferation. It was proposed that cancer cells turn to aerobic glycolysis to restore ATP at a pace similar to its consumption to avoid an ATP depletion (de Alteriis et al., 2018). Aerobic glycolysis would be favored over OXPHOS in this scenario due the spatial and kinetic reasons highlighted above. This was verified when looking into the bioenergetics and biosynthetic demands for proliferation, where it was demonstrated that cancer cells must turn to aerobic glycolysis to achieve fast doubling times (Fernandez-de-Cossio-Diaz and Vazquez, 2017, Niebel et al., 2019).

Overall, the determinants discussed here highlight the idea of a mitochondrial bottleneck in cancer cells and why aerobic glycolysis is favored under conditions of nutrient abundance.

1.3.3. Unmasking metabolic flexibility and plasticity using galactose

Most of the current *in vitro* research is being carried out in media that were developed in the fifties (Dulbecco and Freeman, 1959, Eagle, 1955, Eagle, 1959, Moore et al., 1967). These media formulations were developed with the goal to provide proliferating cells with the ultimate nutrient composition for growth without the need to refeed them (Cantor, 2019). As a result, commonly used media contain supraphysiological concentrations of a multitude of metabolites including glucose. As discussed in section 1.5., excess glucose can force cells into aerobic glycolysis (de Alteriis et al., 2018, Diaz-Ruiz et al., 2011). Therefore, *in vitro* cancer cells appear fixed on aerobic glycolysis masking their metabolic flexibility. One method to circumvent this glycolysis addiction is to substitute glucose with galactose in media (Marroquin et al., 2007, Meiser et al., 2016).

Galactose can be metabolized to replace glucose via the Leloir pathway, which is depicted in **Illustration 4**. In brief, galactose is phosphorylated by galactokinase to produce galactose 1-phosphate. Galactose 1-phosphate then displaces glucose from uridine diphosphate (UDP)-glucose and the resultant glucose 1-phosphate is isomerized into glucose 6-phosphate (G6P) which is an intermediate of glycolysis (**Illustration 3**). UDP-glucose is replenished via the activity of UDP-glucose 4 epimerase enzyme in a reaction that has three intermediate steps (Nelson, 2017).

Synopsis

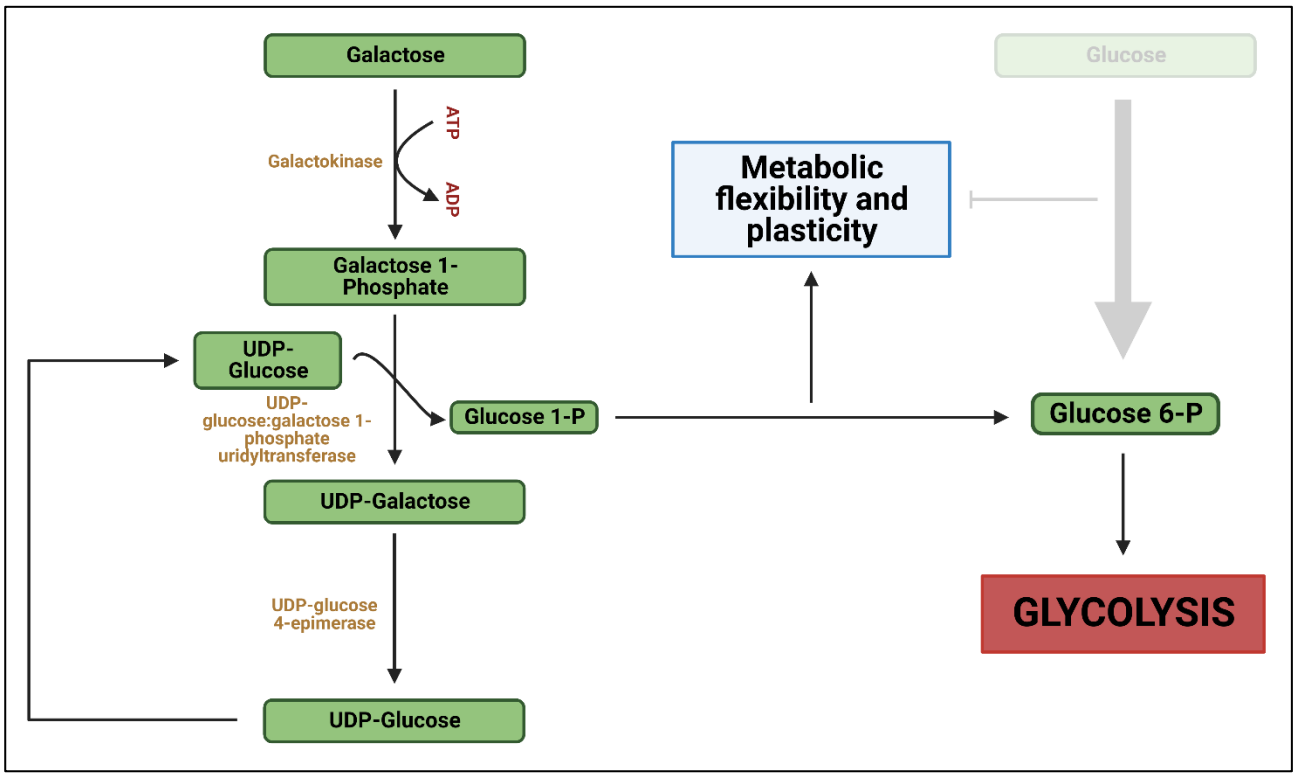


Illustration 4. Leloir pathway.

The biochemical steps that take place in Leloir pathway to metabolize galactose which supply the cell with a slower flux of glycolytic carbons compared to glucose (relative arrow size). ATP, adenosine triphosphate; ADP, adenosine diphosphate; UDP, uridine diphosphate (Figure created with Biorender.com).

The regeneration of UDP-glucose allows Leloir pathway to continue running as long as galactose molecules are available. If we compare galactose and glucose, in order to reach G6P and enter glycolysis, cells have to invest an ATP molecule in both cases (**Illustration 3 and 4**). However, reaching G6P involves one enzymatic step in the case of glucose, while for galactose four enzymatic reactions need to take place (Nelson, 2017). Moreover, the kinetics of the enzymes in the Leloir pathway are considerably slower in the case of galactokinase when compared to hexokinase (**Table 1**). Therefore, Leloir pathway is rate limiting for glycolysis and can provide a slower but constant supply of carbons to glycolysis, mimicking the glycolytic limitation that occur in the TME.

Table 1. Km value for hexokinase and Leloir pathway enzymes.

Enzyme	Km value	Reference
Hexokinase (2)	0.3 mM for glucose	(Wilson, 2003, Rempel et al., 1996)
Galactokinase	0.97 mM for galactose	(Timson and Reece, 2003)

Synopsis

Galactose 1-phosphate uridylyltransferase	0.12 mM for galactose 1-P	(Davit-Spraul et al., 1994)
UDP galactose 4 epimerase	50 µM for UDP-galactose	(McCorvie et al., 2011)
Phosphoglucomutase	80 µM for glucose 1-P	(Accorsi et al., 1989)

Recently, the composition of media used *in vitro* gained a lot of attention in the scientific community (Cantor, 2019). Efforts have resulted in the creation of media that resemble the polar metabolic composition of human plasma (Cantor et al., 2017, Vande Voorde et al., 2019). Thus, using these media can be an option to study metabolic rewiring *in vitro*. However, it was shown that TIF contain lower levels of glucose compared to plasma (Sullivan et al., 2019, Reinfeld et al., 2021). Moreover, these TIF measurements represent an average glucose level across the tumor and does not account for the fact that there are areas within the tumor with very limited glucose supply. The areas that are faced with limited glucose supply must be able to reduce their glycolytic rate in response. As discussed above metabolizing galactose is rate-limiting for glycolysis and thus can be used to study the metabolic changes undertaken by cancer cells with glucose limitation. Therefore, to mimic glycolytic limitation we opted to use galactose as a tool compound.

1.4. Serine metabolism in cancer

Serine is a non-essential amino acid that has gained a lot of attention recently in the cancer metabolism field. This focus stemmed from genetic studies that showed many key enzymes in serine metabolism to be amplified and have increased activity in several cancers (Mullarky et al., 2011, Nilsson et al., 2014, Possemato et al., 2011). Additionally, dietary studies showed the essentiality of serine (and glycine) for the growth of tumors *in vivo* (Maddocks et al., 2013, Maddocks et al., 2017). These studies rejuvenated interest into serine synthesis pathway (SSP), folate cycle and 1C cycle (**Illustration 5**) and their role in boosting the metabolism of cancer cells, thereby highlighting the success of antifolates as chemotherapeutic agents.

1.4.1. Serine synthesis pathway

Cells are able to maintain the intracellular pool of serine via serine *de novo* synthesis and the uptake of serine from extracellular surroundings (Meiser and Vazquez, 2016). In a branching reaction from glycolysis, phosphoglycerate dehydrogenase (PHGDH) will oxidize 3-phosphoglycerate (3-PG) to 3-phosphohydroxypyruvate (3-PHP), then 3-PHP is converted to 3-phosphoserine (3-PS) in an aminotransferase reaction catalyzed by phosphoserine aminotransferase1 (PSAT1), followed by dephosphorylation of 3-PS to

serine via phosphoserine phosphatase (PSPH) (Yang and Vousden, 2016). The rate-limiting step in SSP is the NAD^+ consuming reaction of PHGDH. PHGDH expression is amplified in several cancers including breast, lung and melanoma (Mullarky et al., 2011, Possemato et al., 2011, Zhang et al., 2017, Zhu et al., 2016). Cancer cell lines with genetic amplification of PHGDH exhibit, increased SSP activity and yet the same cells consume serine from their medium at higher rates than its *de novo* synthesis (Kiweler et al., 2022, Tedeschi et al., 2015). These observations indicate that obtaining serine may not be the sole advantage to cancer cells from SSP (Meiser and Vazquez, 2016). Indeed, SSP also generates NADH and α-ketoglutarate (aKG) (**Illustration 5**). Studies show that the level of aKG is relatively dependent on PHGDH expression and can impact epigenetic regulation due to its effect on histone demethylases (Gao and Locasale, 2016, Pan et al., 2016, Possemato et al., 2011). Moreover, it was recently shown that PHGDH protein itself displays non-enzymatic functions that promote metastasis and are independent of its role in SSP (Rossi et al., 2022).

One of the major sinks of serine is its contribution with 1C units towards the 1C cycle (Davis et al., 2004). The transfer and usage of 1C units is facilitated via several folate species (Tibbetts and Appling, 2010). Thus I will address the folate cycle first followed by the 1C cycle.

Synopsis

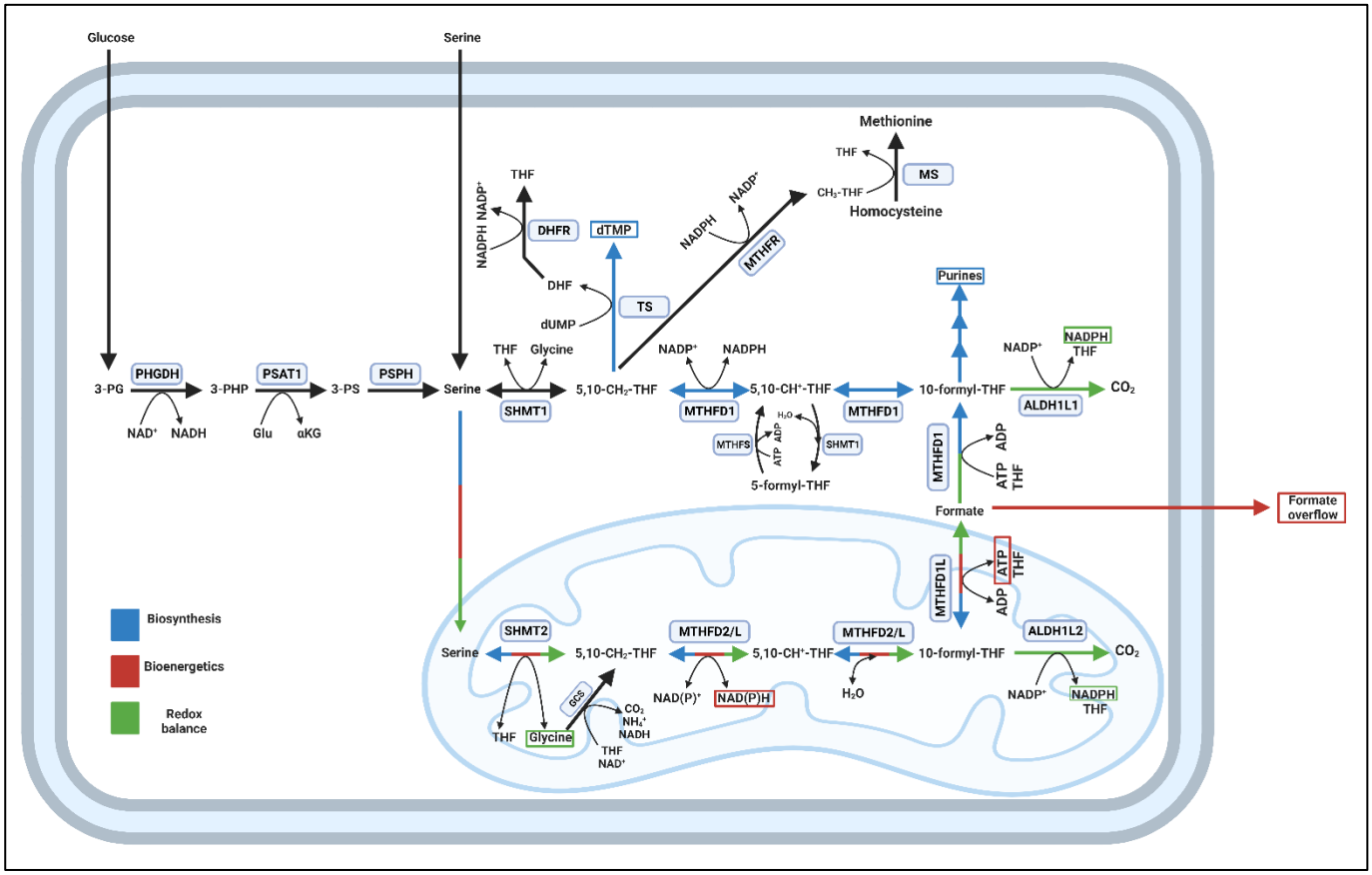


Illustration 5. Serine synthesis pathway and one-carbon cycle.

Serine is synthesized from a branched glycolysis pathway via three biochemical reactions. Afterwards serine donates its third carbon as a one-carbon unit (1C) to tetrahydrofolate, which enters the 1C cycle that is able to support biosynthetic reactions (in blue), bioenergetics (in red) and redox balance (in green). The colored arrows indicate whether a reaction is able to support one or multiple metabolic pillars. Glycine is also able to donate one-carbon unit via glycine cleavage system. 3-PG, 3-phosphoglycerate; PHGDH, phosphoglycerate dehydrogenase; 3-PHP, 3-phosphohydroxypyruvate; PSAT1, phosphoserine aminotransferase; 3-PS, 3-phosphoserine; PSPH, phosphoserine phosphotase; NADH, reduced nicotinamide adenine dinucleotide; Glu, glutamate; αKG, alpha-ketoglutarate; SHMT, serine hydroxyl methyl-transferase; MTHFD(L), 5,10-methylene-tetrahydrofolate dehydrogenase/5,10-methenyl-tetrahydrofolate cyclohydrolase (like); ALDH1L, 10-formyl-tetrahydrofolate dehydrogenase; THF, tetrahydrofolate; DHF, dihydrofolate; TS, thymidylate synthase; MS, methionine synthase; GCS, glycine cleavage system; 5,10-CH_2-THF, 5,10-methylene-tetrahydrofolate; 5,10-CH^+-THF, 5,10- methenyl-THF; CH_3-THF, 5-methyl-tetrahydrofolate; NADPH, nicotinamide adenine dinucleotide phosphate; ATP, adenosine triphosphate; MTHFS, methenyl tetrahydrofolate synthetase; MTHFR, methylene tetrahydrofolate reductase; DHFR, dihydrofolate reductase; dUMP, deoxyuridine monophosphate; dTMP, deoxythymidine monophosphate. Figure adapted from (Benzarti et al., 2020, Ducker and Rabinowitz, 2017, Meiser and Vazquez, 2016, Tibbetts and Appling, 2010, Yang and Vousden, 2016) and created with Biorender.com.

1.4.2. Folate cycle

Folic acid or folate (vitamin B9) is obtained through diet and upon its entry into cells, it is reduced to dihydrofolate (DHF) via dihydrofolate reductase (DHFR). Moreover, folate species are sequestered within specific subcellular compartments (cytoplasm/nucleus/mitochondria) due to having polyglutamate tails that prevent the folates from crossing membranes and increase their affinity to 1C cycle enzymes (Ducker and Rabinowitz, 2017, Tibbetts and Appling, 2010). DHF is further reduced to tetrahydrofolate (THF), the

biological active form of folates (Tibbetts and Appling, 2010). 1C units bind to THF covalently on nitrogen 5 and 10 (Ducker and Rabinowitz, 2017). Once bound to THF, the 1C unit can exist in three different oxidation states (**Table 2**), which are biologically active and can readily be interchanged across the 1C cycle (Ducker and Rabinowitz, 2017, Tibbetts and Appling, 2010).

A major biological function supported by these folate species is the *de novo* synthesis of nucleotides. Folate and 1C cycle support purine and thymidylate biosynthesis. THF is oxidized to DHF via thymidylate synthetase (TS), which in the same reaction catalyzes the conversion of deoxyuridine monophosphate to deoxythymidine monophosphate (dTMP) via the transfer of the 1C unit (Tibbetts and Appling, 2010). Subsequently, DHF is again reduced to THF via DHFR to complete the folate cycle (**Illustration 5**).

DHFR is the only enzyme that catalyzes the reduction of DHF to THF, which is essential for nucleotide synthesis (Tibbetts and Appling, 2010). Consequently, targeting DHFR is a vulnerability of proliferating cells like cancer cells. Indeed, chemotherapeutic antifolate agents like methotrexate target DHFR and lead to a complete block of proliferation in cancer cells (Farber and Diamond, 1948).

Table 2. Biologically relevant folate species.

The different species of cellular folates that are involved in the folate and 1C cycle. DHF, dihydrofolate; THF, tetrahydrofolate. Information in this table are summarized from (Ducker and Rabinowitz, 2017, Tibbetts and Appling, 2010).

Species	Symbol	Description	Function
DHF	DHF	Intermediary reduced form of folates prior to being reduced to THF.	
THF	THF	Most reduced form of folates.	Acceptor and donor of 1C units to supply different cellular functions.
5,10-methylene-THF	5,10-CH_2-THF	1C unit is covalently bound to the 5 and 10 position nitrogens on THF.	Donates 1C units for dTMP synthesis.
5,10-methenyl-THF	5,10-CH^+-THF	1C unit has a single covalent bond to the 10 position nitrogen and a double covalent bond to the 5 position nitrogen on THF.	No biological function. Intermediate folate form that can be converted to 5-formyl-THF.
5-formyl-THF	5-CHO-THF	1C unit bound to the 5 position nitrogen on THF.	No biological function. Regulates the function of 1C enzymes and acts as a reservoir for THF-bound 1C unit.
10-formyl-THF	10-CHO-THF	1C unit bound to the 10 position nitrogen on THF.	Donates 1C units for purine synthesis, formate release and oxidation to CO_2.

Synopsis

5-methyl-THF	5-CH_3-THF	1C unit is covalently bound to the 5 position nitrogen on THF.	Donation of 1C units to the methionine cycle.

Folate species cannot cross between mitochondria and cytoplasm, meaning that each compartment has a specific folate pool composition. Folate species are sequestered in different compartments when they have polyglutamate tails. These tails are added by folylpolyglutamate synthetase (FPGS) with the penta and hexa forms being the most prominent in cells (Tibbetts and Appling, 2010). The addition of the glutamate tails is essential for growth as knocking out FPGS completely halts the proliferation of cancer cells (Burgos-Barragan et al., 2017). In leukemia cells, 80% of total folate pool is found in the cytoplasm, with an extensive variation of the distribution of the different folate species between the cytoplasm and mitochondria (Trent et al., 1991). Most likely, the variation in the distribution of the different folate species is a result of directionality of the 1C cycle between the two compartments, which I will further address in section 1.4.

By using trimetrexate (a methotrexate derivative), Trent et al (1991) showed that THF cytoplasmic pool was almost halved while there was no effect of antifolate on the mitochondrial distribution. This signifies that trimetrexate and methotrexate are only able to target the cytosolic THF pool, while leaving the mitochondrial pool of THF unaffected. Therefore, methotrexate can be utilized as a tool compound to isolate and profile the mitochondrial 1C cycle as detailed in chapter four of this dissertation (Kiweler et al., 2022).

1.5. One-carbon cycle

1C cycle describes a series of biochemical reactions that involves the transfer of 1C units from donors like serine, glycine and formate to acceptors like nucleotides (**Illustration 5**). The 1C cycle can be divided into three stages (Tibbetts and Appling, 2010):

1. The donation of a 1C unit to THF.
2. Series of redox reactions that interconvert the THF-bound 1C units in different oxidation states to provide the different folate intermediates required for various functions (**Table 2**).
3. The release of the 1C unit from THF either as formate, CO_2 or into anabolic sinks.

The enzymes of the 1C cycle can be divided into having five different catalytic activities: methyl-transferase, 5,10-methylene-THF (5,10-CH_2-THF) dehydrogenase, 5,10-methenyl-THF (5,10-CH^+-THF) cyclohydrolase, 10-formyl-THF synthetase (FTHFS) and 10-formyl-THF- dehydrogenase (FTHFD), as summarized in **Table 3** (Meiser and Vazquez, 2016).

Synopsis

Table 3. One-carbon cycle stages and their corresponding enzymes.

SHMT, serine hydroxyl methyl-transferase; MTHFD(L), 5,10-methylene-tetrahydrofolate dehydrogenase/5,10-methenyl-tetrahydrofolate cyclohydrolase (like); ALDH1L, 10-formyl-tetrahydrofolate dehydrogenase; THF, tetrahydrofolate.

1C cycle stage	Enzyme(s) name	Catalytic activity
Donation and capture of 1C units	SHMT2 and SHMT1	Methyl transferase
Interconversion of THF-bound 1C unit	MTHFD2, MTHFD2L and MTHFD1	5,10-methylene-THF dehydrogenase
	MTHFD2, MTHFD2L and MTHFD1	5,10-methenyl-THF cyclohydrolase
Release of 1C units from THF	MTHFD1 and MTHFD1L	10-formyl-THF synthetase
	ALDH1L2 and ALDH1L1	10-formyl-THF- dehydrogenase

In terms of 1C donors, it has been established that under human physiological conditions, serine is the main substrate for the 1C cycle (Davis et al., 2004). In cancer cells, it was observed that serine deprivation leads to a p53-dependent cell cycle arrest. In p53-deleted cancer cells, serine starvation resulted in cell death (Maddocks et al., 2013). These observations confirm that serine is the main donor of 1C units in both physiological conditions and malignant neoplasia. Glycine can also act as a 1C donor via the activity of the glycine cleavage system (GCS), which is depicted briefly in **Illustration 5**. However, based on the evidence provided above and studies showcasing very little labeling in purines and dTMP when using isotopically labeled glycine, it appears that glycine has minimal contribution to the cycle in cancer cells (Fan et al., 2014, Meiser and Vazquez, 2016, Mukha et al., 2022). The only exception to that is hepatocellular carcinoma (HCC) cell lines, which show a modest enrichment into adenosine triphosphate (ATP) from glycine of about 10%, for comparison serine enriches the ATP pool at about 80% (Green et al., 2023, Mukha et al., 2022). Even though the glycine contribution through GCS is relatively small, it was shown that the deletion of GCS led to reduced tumor growth in HCC. However, this was explained by GCS promotion of mitochondrial metabolism through pyruvate dehydrogenase (PDH) lipoylation rather than GCS support for the 1C cycle (Mukha et al., 2022).

1.5.1. The canonical 1C cycle

The 1C cycle is depicted in detail in **Illustration 5**. Canonically, the cycle starts with mitochondrial serine hydroxyl methyl-transferase (SHMT2) transferring the third carbon of serine to a THF molecule, forming 5,10-CH_2-THF and releasing glycine to support heme, glutathione and protein synthesis (Yang and Vousden, 2016).

Synopsis

The bi-functional mitochondrial enzyme MTHFD2 is able to perform the functions 5,10-CH_2-THF dehydrogenase/5,10-CH^+-THF cyclohydrolase (MTHFD) in cancer cells (Mejia and MacKenzie, 1988). Subsequently, MTHFD2 oxidizes 5,10-CH_2-THF to 5,10-CH^+-THF, while reducing NAD^+ to NADH (Yang et al., 2020, Smith et al., 1990, Meiser et al., 2016, Bao et al., 2016). MTHFD2L is a homologous enzyme to MTHFD2 that exists in adult tissues, but is barely expressed in cancer cells so I will not cover it here (Bolusani et al., 2011). 5,10-CH^+-THF is an intermediary unstable form and is quickly hydrolyzed by MTHFD2 into 10-formyl-THF (10-CHO-THF). Biochemical assays have revealed that MTHFD2 is capable of using both NAD^+ and $NADP^+$ as cofactors (Shin et al., 2017, Smith et al., 1990). However, upon inhibition of electron transport chain (ETC), the mitochondrial 1C cycle is simultaneously inhibited (Bao et al., 2016, Meiser et al., 2016). When ETC is blocked, NADH accumulates and NAD^+ becomes limited, meaning that the simultaneous inhibition of MTHFD2 is NAD^+ dependent. Another recent study provided more evidence that MTHFD2 uses NAD^+ as a cofactor in intact proliferative cells (Yang et al., 2020). Yang et al. (2020) showed that the relative contribution of the 1C cycle towards NADH pool was significant both *in vitro* and *in vivo.*

Two mitochondrial enzymes are able to act on 10-CHO-THF: 10-CHO-THF dehydrogenase 2 (ALDH1L2) and MTHFD1Like (MTHFD1L). On the one hand, ALDH1L2 is able to fully oxidize the 1C unit to CO_2 and release THF in the process, while reducing $NADP^+$ to NADPH. Thus, ALDH1L2 contributes to the mitochondrial NADPH pool (Yang and Vousden, 2016). On the other hand, MTHFD1L is able to hydrolyze the 1C unit into a formate molecule alongside generating an ATP molecule (Prasannan et al., 2003, Tibbetts and Appling, 2010).

In the cytoplasm, formate is captured via MTHFD1 to form 10-CHO-THF in a non-reversible reaction (Zheng et al., 2018). MTHFD1 is a tri-functional enzyme capable of both MTHFD functions and FTHFS function (**Table 3**). Therefore, the cytoplasmic branch of the cycle is almost a mirror image of the mitochondrial section (difference in cofactors used) with the reactions catalyzed by MTHFD1 and SHMT1 (Ducker and Rabinowitz, 2017, Tibbetts and Appling, 2010, Yang and Vousden, 2016). The major two sinks for cytoplasmic THF-bound 1C units is the biosynthesis of purines and dTMP. For the synthesis of one purine molecule (ATP or guanosine triphosphate), two 1C units are required and these are obtained from 10-CHO-THF. dTMP is synthesized from 5,10-CH_2-THF via the action of TS (**Illustration 5**). The transfer of 1C units to purines or dTMP frees THF or DHF molecules, respectively. DHFR reduces the freed DHF to THF becoming available to accept more 1C units derived from mitochondrial serine catabolism. Alternatively, 10-CHO-THF can be oxidized to CO_2 via ALDH1L1 generating cytoplasmic NADPH and releasing THF in the process (Ducker and Rabinowitz, 2017, Tibbetts and Appling, 2010, Yang and Vousden, 2016). When serine is available and under proliferative conditions, SHMT1 is usually inactive in majority of cancer cell lines (Ducker et al., 2016). However, under physiological levels of

folates, some cancer cell lines appear to rely solely on the cytoplasmic branch of the cycle which will require the activity of SHMT1 (Lee et al., 2021). This study showcases the importance of performing metabolic studies under physiological levels of metabolites (Cantor et al., 2017, Lee et al., 2021, Vande Voorde et al., 2019).

Apart from biosynthesis, bioenergetics and redox balance, 1C cycle can support the methionine cycle with 1C units via the action of 5,10-CH_2-THF reductase (MTHFR). MTHFR reduces 5,10-CH_2-THF to the most reduced THF-bound 1C species 5-methyl-THF (5-CH_3-THF), which in turn methylates homocysteine to methionine via methionine synthetase (Tibbetts and Appling, 2010). The MTHFR reaction is irreversible but it is inhibited by s-adenosyl-methionine (SAM) levels. Therefore, under low levels of SAM, cells prioritize MTHFR reaction over nucleotide biosynthesis resulting in trapping majority of folates as 5-CH_3-THF (Scott and Weir, 1981, Zheng et al., 2018). However, tracing experiments have revealed that the methylation cycle is mainly supplied via extracellular methionine (Pike et al., 2010).

The last reaction not covered yet from **Illustration 5** is the futile cycle. In this cycle, 5-formyl-THF (5-CHO-THF) is formed via the irreversible action of SHMT1 on 5,10-CH^+-THF. The reversal of this reaction is catalyzed by 5,10-CH^+-THF synthetase (MTHFS), consuming ATP to form back 5,10-CH^+-THF (Ducker and Rabinowitz, 2017, Misselbeck et al., 2019, Tibbetts and Appling, 2010). 5-CHO-THF is not a biologically active folate species and its role is thought to be a reservoir of THF-bound 1C units and to regulate the activity of the 1C cycle via its inhibitory action on 1C cycle enzymes (Ducker and Rabinowitz, 2017, Misselbeck et al., 2019). The futile cycle, methionine cycle and GCS are not major sources or sinks for 1C units in cancer cells and accordingly I will not cover them further in my dissertation.

1.5.2. Compartmentalization of 1C cycle

The possibility of using methotrexate as a tool compound to isolate mitochondrial 1C cycle stems from the fact that it does not impact the mitochondrial pool of folates and the fact that these folate species do not diffuse between the mitochondria and cytoplasm (Kiweler et al., 2022, Trent et al., 1991).

The methotrexate observations suggest that compartmentalization of 1C cycle exists where reactions occur independently. Many advantages can be gained through compartmentalization of different reactions, including the ability to separate catabolic from anabolic pathways and oxidative from reductive pathways. This is important for the cell as these reactions often require a certain balance of oxidative:reductive cofactors and therefore these different cofactor ratios can coexist in the same cell but in different compartments (Ducker and Rabinowitz, 2017).

Synopsis

Since serine is the biggest source of 1C units in mammalian cells, deuterated serine (containing ^{2}H instead of ^{1}H) was used to determine the directionality of the 1C cycle (Ducker et al., 2016, Gregory et al., 2000, Herbig et al., 2002, Lewis et al., 2014). Specifically [2,3,3-$^{2}H_3$]-serine is a tracer which when taken up by cells and metabolized, the heavy-labeled atoms can be traced from serine to downstream metabolites of the 1C cycle by means of mass spectrometry (MS) analysis. The key metabolite detected in this case is dTMP.

The deuterium on the second carbon of serine will always remain on glycine via the action of either cytoplasmic or mitochondrial SHMT. On the one hand, if the 1C unit donated by serine follows the mitochondrial route then only one deuterium atom will reach dTMP (M+1). That is because one of the deuterium atoms on the third carbon of serine (1C unit) is lost via the oxidation reaction of MTHFD2, and end up on NADH (**Illustration 5**). The final deuterium atom will remain on formate as it is transported to the cytoplasm and transferred to dTMP. On the other hand, if the cytoplasmic fraction is the active part of the 1C cycle, then two deuterium atoms will be detected on dTMP (M+2). Therefore, by determining the fractional enrichment of M+1 and M+2 isotopologues in dTMP, it is possible to deduce the directionality of the 1C cycle in different conditions (Ducker et al., 2016, Gregory et al., 2000, Herbig et al., 2002, Lewis et al., 2014). When this strategy was applied to proliferative mammalian cells, it was shown that the 1C unit donated by serine first enters the mitochondria, then goes through the mitochondrial branch of the cycle before returning to the cytoplasm through formate. Formate is loaded into THF to form cytoplasmic 10-CHO-THF (Ducker et al., 2016, Gregory et al., 2000, Herbig et al., 2002, Meiser and Vazquez, 2016). This directionality is what I referred to as the canonical 1C cycle in section 1.4.1 and is what takes place in proliferating cells like cancer cells.

Closer inspection of the 1C cycle in **Illustration 5** reveals that the majority of the reactions in the cycle are reversible and can actually run in both directions. Indeed, this was shown to be the case through means of genetic manipulation of the mitochondrial enzyme MTHFD2, where the cells completely reversed the directionality of the cycle and relied on the cytoplasmic branch to deliver 1C units for nucleotide synthesis (Ducker et al., 2016). Having such flexibility in the directionality of the 1C cycle immediately poses two questions: what determines the canonical directionality and why is the mitochondrial branch required at all, if the cytoplasmic part is sufficient for proliferation (Ducker et al., 2016).

A potential answer to the first question goes back to advantages of compartmentalization. In the cytosol, $NADPH/NADP^{+}$ ratio is relatively high and this favors the MTHFD1 reaction to occur in the reductive direction, while in the mitochondria the $NADH/NAD^{+}$ ratio is low meaning that the MTHFD2 reaction happens in the oxidative direction supporting the canonical directionality (Ducker et al., 2016, Ducker and Rabinowitz, 2017,

Yang and Vousden, 2016). However, when MTHFD2 was genetically deleted in HEK293 cells and the 1C directionality was reversed as a result, no change was detected in the cytoplasmic cofactor balance. Yet the MTHFD1 reaction was running in the reverse direction to supply the folate pools, which were massively reduced with MTHFD2 ablation (Ducker et al., 2016). Therefore, it seems that the levels of the different folate species can affect the directionality of the different enzymes in the cycle, favoring the canonical directionality under proliferating conditions (Ducker et al., 2016). It should be noted here that the 1C units have sinks, subsequently they are required in stoichiometric amounts, while THF is needed in catalytic amounts and as such can influence the directionality of the cycle (Tibbetts and Appling, 2010). For the second question, no clear explanation have been reached in the literature, however, it has been proposed that perhaps serine catabolism is mostly secluded to the mitochondria to separate NAD^+-consuming reactions from the cytoplasm where glycolysis takes place and heavily relies on NAD^+/NADH balance (Ducker and Rabinowitz, 2017). Additional potential advantage of having the mitochondrial part of the 1C cycle is to support the ATP and NADPH mitochondrial pools.

1.5.3. Flexibility and plasticity of 1C cycle

As discussed in the previous section, the 1C cycle demonstrates a remarkable ability to mitigate metabolic challenges to continually support cancer cell survival as shown in many studies (Balsa et al., 2020, Ducker et al., 2016, Meiser et al., 2016). The flexibility of the 1C cycle was finely explored by using a novel inhibitor targeting exclusively the dehydrogenase activity of MTHFD. This lead to an accumulation of 10-CHO-THF (can support purines synthesis) and lack of supply of 1C units for dTMP synthesis. However, 1C cycle responded to this challenge by running the SHMT1 reaction in reverse and thus partially providing a supply for dTMP (Green et al., 2023).

The reversibility of the 1C cycle and its ability to adapt to genetic manipulations suggest the potential that the cycle is also able to adapt to metabolic needs of the cell. Therefore, the 1C cycle can be tailored towards supplying the cell with on demand products that can support any of the metabolic pillars being biosynthesis, bioenergetics and/or redox balance. In **Illustration 5**, I used color-coded arrows to indicate the path of the 1C unit if one of the metabolic pillars is prioritized. The role of the 1C cycle in biosynthesis (**Illustration 5**; blue arrows) has already been indicated in previous sections as I highlighted that the major sink for 1C units is the *de novo* synthesis of purine and dTMP. I will address the metabolic potential of the 1C cycle in bioenergetics and redox balance here and it is further discussed in the second chapter of my dissertation.

Synopsis

1.5.3.1. Bioenergetic potential in 1C cycle

The bioenergetic potential of the 1C cycle comes primarily from the mitochondrial fraction (**Illustration 5**; red arrows). MTHFD1L liberates the 1C unit from THF and it is transferred to the cytoplasm as a formate molecule. If formate is released outside of the cell, the chemical equation of the cycle is:

$$\text{Serine} + NAD^+ + ADP + H_2O \text{ ----------> } \text{Glycine} + ATP + NADH + \text{formate} \quad (1)$$

Meaning that the cell gains one ATP, glycine and NADH molecule if the end result of the 1C cycle was to release formate outside of the cell (Meiser et al., 2016). One mole of NADH can generate 2.5 moles of ATP and this is achieved via the ETC in the mitochondria (Nelson, 2017). Consequently, 3.5 moles of ATP are generated in the mitochondria alongside the release of one mole of formate. This means that by measuring the net release of formate, the bioenergetic output of the 1C cycle can be assayed (Meiser et al., 2016). Doing these formate measurements, it was shown that cancer cells are not only running the 1C cycle for biosynthetic purposes. On the contrary, the 1C cycle rate was running in excess of the anabolic needs indicating that the cycle supports other metabolic functions (Meiser et al., 2016). The phenomenon of running the mitochondrial branch of the 1C cycle to only generate formate was coined as 'formate overflow' (Meiser et al., 2016). It is important to note that formate overflow is wasteful in terms of biomass as the cell will lose the serine-derived carbon, further signifying the bioenergetic potential of formate overflow. Moreover, high $NADH/NAD^+$ ratio is observed under reduced respiration and this ratio inhibits all NADH-producing pathways with the exception of MTHFD2 in 1C cycle (Yang et al., 2020). Therefore, serine catabolism and formate overflow must provide bioenergetic advantage to the cell under energetic stress.

1.5.3.2. Redox balance potential in 1C cycle

NADPH is a crucial cofactor for ROS stabilization and redox balance. The 1C cycle in theory can support both cytoplasmic and mitochondrial generation of NADPH (**Illustration 5**; green arrows). Both ALDH1L1 and ALDH1L2 are able to produce NADPH when they oxidize 10-CHO-THF and as such, the 1C cycle can be tailored for redox balance with the following summary equation:

$$\text{Serine} + NAD^+ + NADP^+ \text{ ----------> } \text{Glycine} + NADH + NADPH + CO_2 \quad (2)$$

The role of the 1C cycle as a significant contributor to mitochondrial NADPH pool via ALDH1L2 has been shown in several studies (Balsa et al., 2020, Chen et al., 2019, Ducker et al., 2016, Fan et al., 2014, Hennequart et al., 2023, Piskounova et al., 2015). However, the role of ALDH1L2 as a promoter or an inhibitor of metastasis is not clearly understood as studies have shown opposing results (Hennequart et al., 2023, Piskounova et al., 2015). These conflicting data can be explained by the undisputed function of ALDH1L2 in

mitigating ROS via NADPH production (Balsa et al., 2020, Hennequart et al., 2023, Piskounova et al., 2015). Therefore, the relation between ALDH1L2 and metastasis is confounded by ROS, which has been shown to have drastically dynamic effects on cancer cells along the metastatic cascade (Cheung et al., 2020).

When it comes to cytoplasmic NADPH contribution, the role of the 1C cycle is more ambiguous than the mitochondrial one. Initially, it was shown that 1C cycle contributes significantly to the cytoplasmic NADPH pool via reversal action of MTHFD1 (Fan et al., 2014). However, this goes against the canonical directionality of the cycle (**Illustration 5**). The study reached its conclusions utilizing isotopically labeled glycine, however, as I have explained in section 1.4. glycine input into the 1C cycle is minimal and that led to misinterpreting the labeling data (Ducker et al., 2016, Fan et al., 2014). Indeed, the same lab was then able to show in follow-up studies that the 1C cycle does not contribute to cytoplasmic NADPH generation via MTHFD1 nor ALDH1L1 even when major cytoplasmic NADPH-generating pathways were blocked (Chen et al., 2019, Ducker et al., 2016).

Overall, 1C cycle displays exquisite metabolic flexibility and plasticity that can be tailored according to the metabolic need of the cell. However, *in vitro* (where majority of metabolic studies have been done) these metabolic capabilities are often masked by dominant metabolic phenotypes, like aerobic glycolysis as previously highlighted in section 1.3.

1.6. Clinical perspective of cancer metabolism

Targeting cancer metabolism has been the cornerstone of chemotherapy with the development of nucleotide synthesis inhibitors like aminopterin which was used since 1948 to target acute lymphocytic leukemia (Farber and Diamond, 1948). However, outside of targeting nucleotide synthesis, metabolic drugs has not been very successful so far due to a number of factors including the adaptability of cancer metabolism (Xiao et al., 2023).

Following on the three different pillars of metabolism explained in 1.2.3., I will categorize the different classes of cancer metabolism drugs being developed into targeting biosynthesis, bioenergetic and redox balance.

1.6.1. Targeting cancer metabolic pillars

The uncontrolled proliferative state of cancer cells imposes a biomass generation challenge on themselves, which leads to nucleotide synthesis pathways being a vulnerability. Indeed, as mentioned above targeting nucleotide synthesis has been a very successful strategy to target cancer cells. Providing 1C units is essential for the *de novo* synthesis of purines and pyrimidines and as such interfering with folate metabolism is one

way to halt nucleotide synthesis as seen with drugs like aminopterin and methotrexate (Farber and Diamond, 1948). Another strategy is using nucleotide analogs such as 5-fluorouracil which has reached the clinic since the sixties (Longley et al., 2003). Lastly, targeting specific synthetases in nucleotide synthesis like inhibiting ribonucleotide reductase with hydroxyurea has also been used to treat multiple cancers for more than 50 years (Huff et al., 2022).

Energy generating pathways are known to be increased in cancer, therefore, efforts were made to target such pathways to halt cancer growth. While such strategies were successful *in vitro* and in preclinical studies, the transition of energetic inhibitors, such as glycolysis inhibitors, into the clinic is still lacking (Xiao et al., 2023). One exception is the development and approval of using isocitrate dehydrogenase mutant inhibitors to treat acute myeloid leukemia and cholangiocarcinoma (Stine et al., 2022).

Targeting antioxidant defense systems in cancer cells have shown promise in some preclinical models but modest advances have been made clinically (Xiao et al., 2023). For example, the use of antioxidants to prevent cancer development have shown contradictory results which seem to rely on the type of tumor and timing of the intervention (Benzarti et al., 2020, Cheung et al., 2020).

Another emerging avenue for targeting cancer metabolism is dietary intervention (Xiao et al., 2023). Ketogenic and calorie restriction diets have been shown to suppress cancer progression in preclinical models (Pomatto-Watson et al., 2021, Zhu et al., 2022). Other promising preclinical findings is the restriction of serine/glycine and the resultant reduction of tumor growth (Maddocks et al., 2013, Maddocks et al., 2017).

1.6.2. Challenges of targeting cancer metabolism

Due to the fact that many upregulated metabolic pathways in cancer are also vital for normal cells, effectively targeting such pathways can lead to adverse effects. Indeed, it is well characterized that using chemotherapeutic agents can cause moderate to severe side effects that are mainly linked to normal proliferative cells e.g. hair follicles and cells along the digestive tract. Therefore, drugs affecting cancer metabolism typically have a slim therapeutic window as a challenge for their success (Xiao et al., 2023).

I have already outlined metabolic adaptability to be a superior aspect of cancer metabolism that allows them to survive stressful metabolic environments and at the same time, this aspect poses a challenge to target cancer metabolism. Metabolic flexibility and plasticity of cancer cells safeguards them against many metabolic interventions, as they are able to rewire their metabolism to overcome such inhibitions. Furthermore, the presence of subpopulations within the tumor that have different metabolic addictions can hinder the therapeutic potential of targeting metabolism (Xiao et al., 2023, Stine et al., 2022). Overall, apart

from targeting nucleotide synthesis, it has been challenging for metabolic drugs to enter the clinic for a variety of reasons. Yet, there are emerging strategies where metabolic interventions are combined with small molecule inhibitors to overcome the challenges I highlighted above (Xiao et al., 2023). For example, combining calorie restriction diet with PI3K inhibitors is currently being investigated in a Phase I clinical trial (NCT05300048).

Finally, identifying how cancer cells adapt metabolically to different stresses is key in overcoming the challenges present in cancer therapeutics. To do so, *in vitro* models that better reflect the metabolic composition of the TME are needed. Moreover, tools for visualizing and tracking cancer metabolism must be utilized to study the spatial distribution of metabolites *in vivo*.

1.7. Metabolomics

Many of the studies mentioned so far describe unique metabolic rewiring mechanisms in cancer cells under a wide variety of perturbations. However, assaying these metabolic adaptations require the use of many sophisticated techniques including metabolomics. Metabolomics is the inclusive analysis of metabolites and low-molecular weight molecules present in a biological sample (Clish, 2015). This field includes several techniques to detect and quantify single metabolites such as MS and nuclear magnetic resonance (NMR). Moreover, it can include techniques that measure the activity of certain metabolic pathways like the seahorse bioanalyser which assays glycolysis and OXPHOS (Nascentes Melo et al., 2022). Throughout this chapter, I have mentioned the use of stable isotopic tracers in several previous metabolic studies without going into detail about what these tracers are and how they can be used to analyze cellular metabolism. Thus, in the next section I will explore the field of metabolomics and isotopic tracers, focusing mainly on techniques that I have utilized in this dissertation.

1.7.1. Isotope tracing in metabolic studies

Cellular metabolic activities can be inferred through the simple measurements of metabolites present intracellularly. These levels can then be presented as relative or absolute values. To determine absolute levels of metabolites that would require the use of separate calibration curves for every single metabolite (Buescher et al., 2015). However, conclusions cannot be made solely relying on these levels. That is because an accumulation of a certain metabolite can be the result of a downregulation of an enzyme that consumes it, an upregulation of the enzyme that produces it or both. These conclusions are very different from each

other and therefore metabolic levels alone are not sufficient to assay the metabolic state of a cell (Nascentes Melo et al., 2022, Buescher et al., 2015).

Stable isotope tracers have been utilized to assay the metabolic activity of biological systems for decades. Stable isotopes are heavy labeled elements e.g. ^{13}C, ^{2}H and ^{15}N and stable isotope tracers are metabolites which contain these labeled elements. The heavy labeled elements can be separated from their unlabeled counterparts based on their masses using MS. Thus, once administered into the biological system being studied, the heavy labeled atoms can be traced into downstream metabolite pools. Therefore, using these tracers gives information on substrate (tracer) usage, metabolic rewiring and pathway activities (Dong et al., 2022). To use isotopic tracers for quantitative interpretations, two main conditions must be met: the biological system must be at a metabolic and isotopic steady state (Nascentes Melo et al., 2022).

Metabolic steady state describes a system where biomass and nutrients remain unchanged. *In vitro* this is not easily achieved and as such, experiments are usually performed at what is referred to as pseudo-steady state. In simpler terms, pseudo-steady state is the exponential growth phase of cells because at this stage the uptake/release rates of metabolites are constant over time and space is available for cells to continue doubling. For example, we aim to perform our metabolic studies at time-points where metabolites in the medium remain in excess and do not become depleted; usually this is the case up to 24 hours. If the experimental setup dictates going over 24 hours then the culture medium might need to be refreshed every 24 hours to ascertain the metabolic pseudo-steady state (Buescher et al., 2015, Nascentes Melo et al., 2022).

Isotopic steady state concerns the stable enrichment of a heavy labeled atom into a biological system over time. In the case of [U-^{13}C] glucose, once added and metabolized by the cell, the ^{13}C atoms will enrich different metabolites downstream of glucose at different rates but eventually the ^{13}C enrichment will become constant i.e. steady state. Therefore, isotopic steady state depends on the tracer used but also on the metabolite(s) of interest. For example, when using a glucose tracer, intermediates in glycolysis will reach the steady state in minutes, while downstream pathways like the TCA cycle can take hours (depending on the cell line) (Buescher et al., 2015, Nascentes Melo et al., 2022). Thereby, our 24 hour time point fits in this situation as we see that the metabolic network of cancer cells reach the isotopic and metabolic steady state. At the steady state, the ^{13}C enrichment into a specific metabolite refers to the intracellular metabolic turnover (relative flux) i.e. how much of that metabolite is synthesized by carbons from the tracer.

If metabolites were to be extracted prior to reaching the isotopic steady state, this would be referred to as dynamic labeling. Dynamic labeling can be considered as a snapshot of the enrichment status at the time-point of metabolite extraction. Since the steady-state is not reached yet, dynamic labeling gives information

of the rate (speed) of pathway utilization of the tracer and not the relative flux. However, it should be noted that to perform dynamic labeling experiments, several time points are needed to infer the pattern of isotope enrichment (Buescher et al., 2015, Nascentes Melo et al., 2022).

1.7.2. Metabolic parameters

In our experimental setup (**Illustration 6**), we are able to measure the following metabolic parameters: relative intracellular metabolite levels, isotope enrichment and the uptake and release rates of metabolites. When the experimental medium is collected and compared to control medium, we are able to calculate the absolute amount of metabolites (in moles by using calibration curves) that a single cell consume/release (CORE) per hour. Extracting intracellular metabolites allows us to determine their relative levels between the conditions tested. As stated before it is possible to determine the absolute amounts using calibration curves which I have not done in my dissertation, instead we used standard addition method to determine the absolute concentration of glucose in plasma samples (Chapter 3; figure 8).

Another reading from measuring the intracellular metabolites is the mass isotopomer distribution (MID). MID describes the enrichment pattern of a metabolite from a tracer. In the example shown in **Illustration 6,** when [U-^{13}C] serine is used and metabolites are extracted, the serine intracellular pool will be heavily enriched by the uptake of the labelled serine. However, some of the intracellular serine will be synthesized by the SSP i.e. the carbon backbone will be coming from glucose. Serine synthesized by SSP has no labeled carbons and as such is denoted as M+0 (no mass shift). Serine coming from the culture medium has three ^{13}C in its backbone and is denoted as M+3 (3 mass unit shift). Finally, due to the activity of SHMT1/2 a serine mixture of labeled and unlabeled carbons will exist containing either one or two ^{13}C and denoted as M+1 and M+2, respectively. M+0, M+1, M+2 and M+3 are referred to as isotopologues and their collective pattern is known as MID. Isotopologues are presented as a fraction or a percentage of the total intracellular pool, meaning that the sum of all isotopologues is equal to one or 100%. It is important to note that the position of the ^{13}C is not taken into consideration in isotopologues. When the position of ^{13}C is considered, the different fractions are referred to as isotopomers and in **Illustration 6,** we can see that serine can have up to eight different isotopomers in this specific scenario. However, identification of these isotopomers requires tandem MS methods which we did not use in our studies (Buescher et al., 2015, Dong et al., 2022).

Synopsis

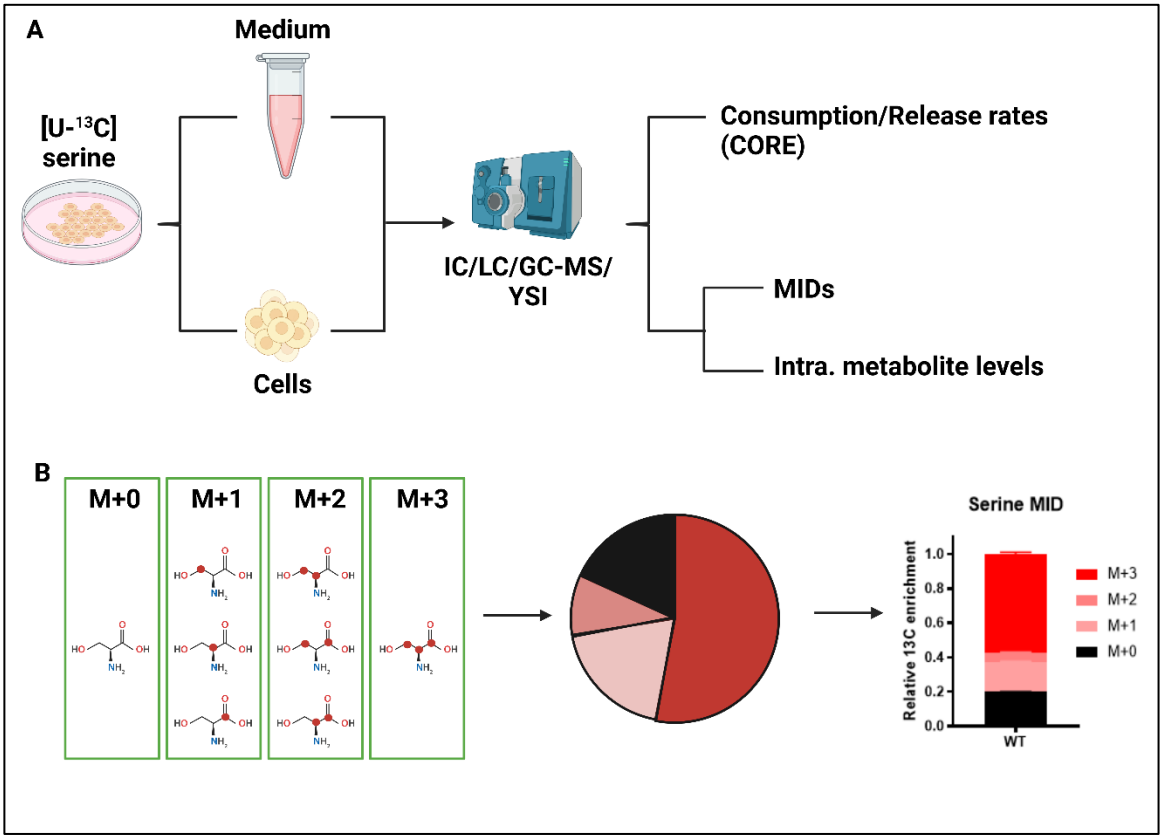


Illustration 6. Targeted metabolomics workflow.

A. Our experimental workflow starting from monolayer cell culture, followed by sample collection, measurements performed mostly with MS and finally data analysis and interpretation. B. The eight different possible isotopomers for serine which can be presented as four isotopologues in stacked bar blots. MID, mass isotopomer distribution; IC, ion chromatography; LC, liquid chromatography; GC, gas chromatography; MS, mass spectrometry (figure created with Biorender.com).

Stable isotopes exist in nature at a low percentage e.g. ^{13}C abundance in nature is 1.07%. The probability that the labeling we measure is due to natural abundance of isotopes must be taken into account and removed. We account for this by using in-house scripts previously described or freely available software (Hiller et al., 2009, Meiser et al., 2016). After subtracting the natural isotope abundance, labeling data can be plotted (**Illustration 6**) and analyzed in different ways. The MID can be plotted as is and interpreted according to the tracer used and metabolite in question. Alternatively, two other methods of data presentation can be used to infer on the totality of enrichment into a specific metabolite. First method is to use the total labeled fraction [1-(M+0)] which can be plotted and compared between conditions to simply assay the relative flux and pathway utilization of the tracer. The [1-(M+0)] method gives the percentage of the molecules which contain at least one ^{13}C (in the case of ^{13}C tracing). Second method is often referred to as carbon contribution in the literature and it provides information on the percentage of carbons which are ^{13}C out of the total carbon pool of a single metabolite. In the case of ^{13}C tracing, both methods give very similar results when

looking at low-carbon metabolites like serine or citrate. However, carbon contribution becomes far more accurate representation when looking at larger metabolites like fatty acids (Buescher et al., 2015).

Caution must be applied when using more complex tracing protocols. For example, when using the deuterium tracer [2,3,3-$^{2}H_3$] serine, kinetic isotopic effects must be taken into account. Kinetic isotopic effect describes the effects of isotopes on different enzymes leading to slower kinetics in the case ^{2}H compared to ^{1}H (Chen et al., 2019).

Synopsis

HYPOTHESIS AND AIMS

1C cycle is a metabolic pathway that extends across the cytoplasm and mitochondria and therefore allows for the translocation of 1C units across the aforementioned cellular compartments (Meiser and Vazquez, 2016). 1C units are essential for nucleotide biosynthesis, thus this pathway has been historically always linked with proliferation (Meiser and Vazquez, 2016). However, it was shown that 1C units were excreted out of the cell at rates that exceeded the anabolic needs of cancer cells, a phenotype termed as formate overflow and this phenotype provided a readout for the metabolic activity of mitochondrial 1C cycle (Meiser et al., 2016).

Under nutrient stress and reduced anabolic demands, one would expect that the activity of the 1C cycle is downregulated if it served mainly to support proliferation. On the contrary, when cancer cells were challenged with glycolytic limitation using galactose, serine catabolism and formate overflow were significantly increased (Meiser et al., 2016). These observations highlight the potential that the 1C cycle serves a growth-independent role in cancer cells under nutrient stress. Based on these findings, the hypothesis of my dissertation is as follows: **under nutrient stress and reduced anabolic demand, 1C cycle can serve a growth-independent function in cancer cells**. The specific aims to test my hypothesis are listed below:

- Establish that cancer cells are able to metabolize galactose and that galactose can be used as a tool to study glycolytic limitation.

- Investigate how central carbon metabolism is affected with the challenge of glycolytic limitation in cancer cells.

- Establish the metabolic potential of cancer cells when different metabolic pillars are prioritized.

- Investigate how 1C cycle can support the different metabolic pillars under glycolytic limitation.

- Investigate whether 1C cycle can support other cellular functions apart from proliferation

CHAPTER 2: Metabolic Potential of Cancer Cells in Context of the Metastatic Cascade

BENZARTI, M*., DELBROUCK, C*., NEISES, L., KIWELER, N. & MEISER, J.

2020*.* *Cells*, 9.

DOI: doi: 10.3390/cells9092035

2.1. Preface:

In the cancer metabolism field, majority of the research conducted have been on primary tumors with little focus on cancer cells throughout the metastatic cascade. In this review article, we tackled the topic of metabolism in the context of the metastatic cascade. Firstly, we addressed how metabolic constraints regulate the progression of primary tumors and metastases by looking specifically into oxidative stress and nutrient abundance. Specifically, we highlighted how the variability of the metabolic niche across the metastatic cascade aids in the selection of the most metabolically resilient cancer cell population.

Next, we quantitatively looked into the flexibility of cancer cells biochemical pathways when different constraints are applied. By focusing on one of the metabolic pillars at a time (biosynthesis, bioenergetics or redox balance) we explored the potential of the main pathways in central carbon metabolism. Finally, we put the 1C cycle in the spotlight and thoroughly dissected its potential to support the different metabolic pillars with evidence from recent elegant publications.

Overall, here we dived into the concept of metabolic flexibility and the potential of the metabolic network in cancer cells when different metabolic sinks are taken into consideration (third aim of the dissertation)

2.2. Personal contribution

My contribution to this review article involved the conceptualization of the manuscript and its structure, literature mining and the writing of the fourth section and section 3.2, designing and preparing figures 1 and 2, calculating the values for all the tables presented in the review and finally the revision of the article prior to submission and after receiving the reviewers comments.

2.3. Manuscript

cells

MDPI

Review

Metabolic Potential of Cancer Cells in Context of the Metastatic Cascade

Mohaned Benzarti [1,2,†], Catherine Delbrouck [1,2,†], Laura Neises [1], Nicole Kiweler [1,†] and Johannes Meiser [1,*,†,‡]

[1] Cancer Metabolism Group, Department of Oncology, Luxembourg Institute of Health, L-1526 Luxembourg, Luxembourg; Mohaned.Benzarti@lih.lu (M.B.); Catherine.Delbrouck@lih.lu (C.D.); Laura.Neises@lih.lu (L.N.); Nicole.Kiweler@lih.lu (N.K.)

[2] Faculty of Science, Technology and Medicine, University of Luxembourg, 2 Avenue de l'Université, L-4365 Esch-sur-Alzette, Luxembourg

* Correspondence: Johannes.Meiser@lih.lu

† These authors have contributed equally to this work.

‡ Lead contact.

Received: 7 August 2020; Accepted: 2 September 2020; Published: 5 September 2020



Abstract: The metastatic cascade is a highly plastic and dynamic process dominated by cellular heterogeneity and varying metabolic requirements. During this cascade, the three major metabolic pillars, namely biosynthesis, RedOx balance, and bioenergetics, have variable importance. Biosynthesis has superior significance during the proliferation-dominated steps of primary tumour growth and secondary macrometastasis formation and only minor relevance during the growth-independent processes of invasion and dissemination. Consequently, RedOx homeostasis and bioenergetics emerge as conceivable metabolic key determinants in cancer cells that disseminate from the primary tumour. Within this review, we summarise our current understanding on how cancer cells adjust their metabolism in the context of different microenvironments along the metastatic cascade. With the example of one-carbon metabolism, we establish a conceptual view on how the same metabolic pathway can be exploited in different ways depending on the current cellular needs during metastatic progression.

Keywords: metastasis; cancer metabolism; one-carbon metabolism; tumour microenvironment; ROS; hypoxia; biosynthesis; bioenergetics; RedOx balance; metabolic plasticity

1. Introduction

The term metastasis originates from the Greek words meta, meaning next, and stasis, meaning placement [1] and describes fittingly the metastatic process in which a primary tumour spreads to a secondary organ site. The clinical onset of metastasis formation is the result of a complex multi-step process whereby a specific subpopulation of cancer cells within a primary tumour detaches and disseminates into a non-native environment. Such a progression to metastatic disease is the most common cause of cancer related death. While current five-year survival rates of local disease for most cancer types are above 80%, metastatic disease is generally associated with five-year survival rates below 30% [2].

To date, most traditional anti-neoplastic chemotherapeutics have been specifically designed to target rapidly dividing cells [3]. To illustrate, approved drug classes in classical cancer therapy include alkylating agents, antimetabolites, taxanes, alkaloids, anthracyclines, and camptothecin derivatives, all of which interfere with DNA synthesis and thus restrict cell proliferation [4,5]. Such drugs are not especially adopted to slow or non-proliferating, yet potentially malignant cells that can give rise to

metastasis. Of note, cancer cell invasion was shown to be negatively correlated with proliferation [6]. This indicates that the invasive, metastatic cell subpopulation might persist when the primary tumour is eliminated by standard antiproliferative cancer therapy. Indeed, primary cancer cells acquire distinct and potentially targetable genetic and phenotypic alterations that favour metastatic progression to distant organs [7]. Prospectively, the enhanced understanding of such specific phenotypic changes in invasive cancer cells could lead to the expansion of current chemotherapeutic regimens and the design of new therapeutic combination schemes. This could include components that do not only target tumour cell proliferation, but also hinder metastatic progression early on. It is thus somewhat surprising that only a minor fraction (**<**4%) of publications on cancer therapy in general discusses metastatic prevention therapy [8].

In chapter 2 of this review, we briefly revisit the general concept of metastatic progression and metabolic adaptation. In chapter 3, this concept is exemplified with a specific emphasis on the effects of oxygen and nutrient availability in respect of varying tumour microenvironments (TMEs). In chapter 4, we provide a comprehensive insight on the biochemical potential of metabolic pathways that capacitate tumour cells to coordinate their available carbon units for biosynthesis, RedOx balance, and energy production. The potential of metabolic pathways is explored in detail within the context of one-carbon (1C) metabolism.

2. Cancer Cells Acquire Specific Traits That Govern Metastatic Progression

During their journey, metastatic cancer cells are described to acquire four specific hallmarks which signify a cell that traverses the metastatic cascade and are indicative of eventual effective secondary tumour formation. Such specific traits include motility and invasion, the ability to modulate the secondary site or local microenvironments, plasticity and the ability to colonise secondary tissues [9].

Cancer cell invasion is a complex sequential and interrelated process, which is initiated by the migration and local invasion of cells from the primary tumour into the surrounding extracellular matrix (ECM). Subsequently, cells that detached from the primary tumour and invaded through the tissue of origin have to intravasate into the vascular system, survive within the bloodstream, extravasate into a distant organ, adapt to the new microenvironment, and multiply to form macrometastases [9,10]. Throughout the metastatic cascade, cancer cells must respond to continuously changing TME conditions, e.g., oxygen partial pressure (pO_2), nutrients, and mechanical stress [9]. Only cells that successfully adapt to such varying microenvironments between the tissue of origin, the blood or lymph vessels, and the non-native environment in secondary tissues can effectively metastasise. Hereby, cancer cell plasticity provides a selective advantage to allow effective metastatic dissemination to one or several organs. Congruently, a loss of plasticity has been shown to block the ability to metastasise [11]. Mammalian metabolism is one important mechanism that enables such plasticity.

Metabolic plasticity is not only characteristic to cancer cells but is also a common phenomenon in non-malignant cells. For example, both macrophages and lymphocytes strongly rewire their metabolism upon activation. The way this rewiring takes place depends however on the activating stimulus and cell type and can be directed towards an anabolic or catabolic program [12]. In a similar way, cancer cells are capable of adapting their metabolic phenotype towards their specific needs (Figure 1) [13]. Within a proliferating primary tumour, this rewiring is directed towards an anabolic program to synthesise proteins, lipids, and nucleotides [14]. Throughout the metastatic cascade, the metabolic phenotype can adjust according to current cellular demands during the proliferation-independent dissemination process [6,15].

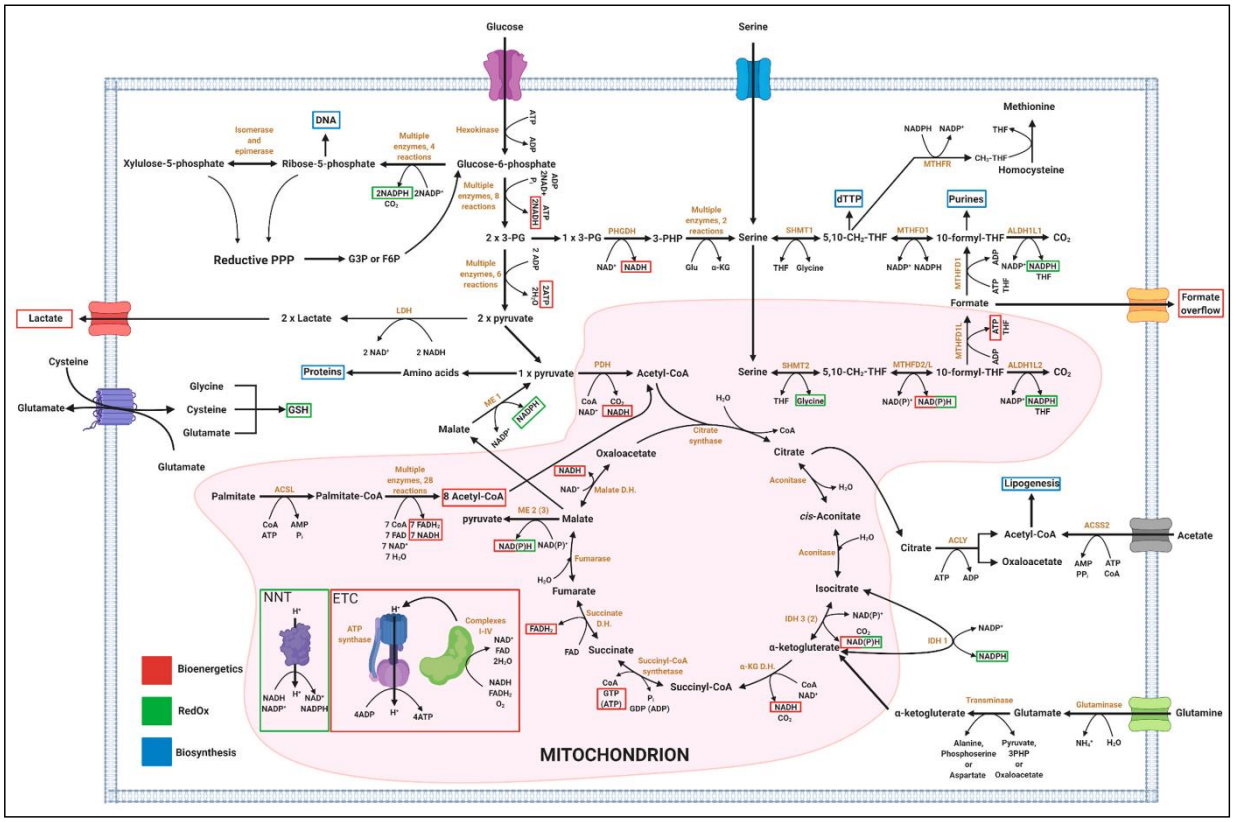


Figure 1. The fate of available carbon sources within cancer cells according to different metabolic sinks. Glucose, serine, glutamine and palmitate are utilised in different pathways to generate co-factors and intermediates that the cell then utilises for biosynthesis (blue), bioenergetics (red) or RedOx balance (green). 3PG, 3-phosphoglycerate; G3P, glyceraldehyde-3-phosphate; F6P, fructose-6-phosphate; PHGDH, phosphoglycerate dehydrogenase; 3-PHP, 3-phosphohydroxypyruvate; Glu, glutamate; α-KG, alpha-ketoglutarate; THF, tetrahydrofolate; SHMT1**/**2, cytosolic**/**mitochondrial serine hydroxyl methyl-transferase; MTHFD, 5,10-methylene-tetrahydrofolate dehydrogenase**/**5,10-methylene-tetrahydrofolate cyclohydrolase; MTHFR, methylene tetrahydrofolate reductase; ALDH1L1**/**2, cytosolic**/**mitochondrial 10-formyltetrahydrofolate dehydrogenase; 5,10-CH_2-THF, 5,10-methylene-THF; CH_3-THF, 5-methyl-THF; PDH, pyruvate dehydrogenase; LDH, lactate dehydrogenase; ME, malic enzyme; ACLY, ATP-citrate lyase; ACSS2, Acetyl-CoA synthetase 2; ACSL, acyl-CoA synthetase; IDH, isocitrate dehydrogenase; D.H., dehydrogenase; GSH, glutathione.

3. Constraints in the Tumour Microenvironment Determine Metabolic Adaptations and Tumour Progression along the Metastatic Cascade

As cells traverse the metastatic cascade, key microenvironmental conditions are constantly altering and may change drastically from solid primary tumour to final macrometastasis establishment in a different organ. In the confined local primary tumour, poor vascularisation has been shown to promote hypoxic regions [16], reactive oxygen species (ROS) stress [17], and altered nutrient availability [18–20]. In contrast, disseminated cancer cells may face oxygen-rich environments upon entering the bloodstream or drastically altered nutrient conditions upon seeding in secondary organs [9]. Successful adaptation to these varying conditions can be decisive in the failure or success of metastatic tumour dissemination.

3.1. Changing Oxygen and ROS Levels Shape the Cancer Phenotype Along the Metastatic Cascade

Although median oxygen levels in most primary tumours are **<**2% O_2, there is significant heterogeneity reported between individual primary tumours in different tissues of origin [21]. Hereby, the highest decrease in pO_2 in comparison to normal tissue was reported for human pancreatic (19.1–22.7-fold), prostate (2.8–12.5-fold), breast (5.2-fold) and liver cancer (5.0-fold) [21]. Such variability in oxygen saturation between tumour tissues is most probably due to differences in individual tumour vascularisation and the maximal inherent hypoxia tolerance of each tissue of origin [22]. However, somewhat surprisingly, pO_2 is independent of clinical size, histology and grade for many tumour types [21]. The pO_2 within tumour tissue can herein be either chronically reduced due to locally prolonged diffusion distances for oxygen within the tissue upon tumour growth (chronic hypoxia) or acutely reduced due to ischemic perfusion limitation in intratumoural blood vessels (acute hypoxia) [21,23]. Signalling of this hypoxic state is hereafter mainly conveyed intracellularly through the accumulation of the hypoxia-inducible factor (HIF)-α subunits HIF-1**/**2α [24]. Upon hypoxia, HIF-1**/**2α subunits are stabilised and translocated to the nucleus to form an active transcription factor complex with the constitutively expressed HIF-1β subunit [24]. The subsequent expression of a multitude of HIF target genes in cancer cells has wide-spread promoting effects on angiogenesis, invasion, extravasation, motility, epithelial-mesenchymal transition (EMT) signalling, ECM remodelling, cancer stem cell maintenance, and immune evasion [16,22–39]. For example, hypoxia within the primary tumour and the resulting induction of an intra-tumoural hypoxic gene signature were explicitly shown to foster in vivo metastasis formation by promoting a ROS-resistant cancer cell sub-population [40]. Therefore, hypoxic signalling has not only been shown to be characteristic for most established primary tumours, but is also important for their transition to a metastatic phenotype.

Furthermore, HIF-dependent signalling in hypoxic regions of primary tumours is well known to reprogram tumour metabolism. HIF induces glucose metabolism via upregulation of glucose transporters and glycolytic enzymes [41–46], increases reductive glutamine metabolism and lipid synthesis [47–49] and promotes pentose phosphate pathway (PPP) [50–52] to sustain the anabolic phenotype of proliferating tumour cells. One prominent side effect in such highly proliferative, metabolically active cancer cells is the enhanced generation of ROS from increased mitochondrial activity [18,53,54]. On first view, it might be puzzling how hypoxic tumour areas with activated HIF are able to run oxidative phosphorylation (OXPHOS) as this is an oxygen-dependent process. However, it should be noted that oxygen tension usually follows a gradient with a transition zone from oxygen-repleted to oxygen-deprived conditions. Moreover, and maybe even more importantly, OXPHOS can still be active at oxygen concentration of ~1% [55]. Hence, it might be possible that there are transition zones where concomitant HIF activation and active OXPHOS are co-existing. Additionally, there are other factors, which can stabilise HIF, e.g., high ROS level [56]. Interestingly, mitochondrial respiration and ROS derived thereof are important for the adaptation to changing oxygen levels [57]. Enhanced OXPHOS activity has been shown for multiple types of cancers even in the presence of high glycolytic rates [58,59]. This is in contrast to the historic observation of Warburg that led many scientists to assume that upregulated glycolysis in cancer cells would necessarily entail

electron transport chain (ETC) downregulation [58]. Rather, cancer cells sustain or even increase their mitochondrial activity and at the same time strongly increase their glycolytic rate. This represents a "full blown" metabolism that works towards its capacity limits to allow fast proliferation [60]. One explanation for increased glycolytic rates is that cells reach their mitochondrial capacity limit. In the case of such limitation, NADH cannot be oxidised anymore via the ETC to regenerate NAD^+. This can limit the catabolism of nutrients as it requires NAD^+. Therefore, a way to increase the ATP production rate is to increase glycolysis at the cost of lactate (carbon) overflow. In the case of glucose fermentation, no net production of NADH occurs and the only product that remains in the cell is ATP. When speed and cellular space are the constraints, glycolysis seems to outperform OXPHOS [60–62]. This might be pronounced in oxygen transition zones where oxygen availability becomes limiting for OXPHOS.

Upon escape from the primary site and intravasation to blood or lymph vessels, cells are challenged with enhanced oxygen concentrations, which increase from **<**2% in hypoxic tumour regions to concentrations as high as 4.5% in the lymphatic system and 14% in the blood vasculature [18]. Prominent secondary metastasis sites, such as the lungs, bones, brain, and liver, exhibit oxygen concentrations of up to 4%, 6%, 8%, and 14%, respectively [18]. Thus, progression along the metastatic cascade forces cells to cope with in part drastic increases in oxygen availability and in consequence the enhanced presence of intracellular ROS. Additional sources for ROS in cancer cells encompass the action of oncogenes such as mutant *Ras* and *BCR*\|*ABL* [63–66], loss-of-function mutations in tumour suppressor genes such as *FH* and *FOXO3a* [67,68], mitochondrial dysfunctions due to mitochondrial DNA mutations of ETC coding genes such as *ND5* [69], inflammatory bursts, and genotoxic stresses upon chemotherapy [53,68–70]. The resulting sustained high levels of ROS are termed oxidative stress and are known to exert tumourigenic, cytotoxic, and inflammatory responses as a result of physical damage to lipids, proteins, and DNA. Therefore, effective ROS detoxification is important to prevent cellular damage and emerges as a need for effective metastatic progression [40,51,71]. Indeed, cancer cells often have increased concentrations of glutathione (GSH) and antioxidant defence systems, such as superoxide dismutases, catalases, and glutathione peroxidases, to prevent ROS-induced cell damage [53,72–74]. The successful execution of these defence systems depends on increased metabolic activity to supply sufficient GSH to cells and provide sufficient RedOx co-factors in the form of NADPH. NADPH is needed for anabolic processes (i.e., fatty acid synthesis) and concurrently required to provide reducing power to the antioxidant defence system. In the given setting of increased oxidative insults, the available cellular NADPH is mainly required to support ROS detoxification.

The gatekeeper to control cellular ROS homeostasis is the transcription factor NRF2 [74]. Upon ROS-dependent activation, NRF2 induces the transcription of different defence systems including metabolic pathways that support the antioxidant defence [74–76]. One important downstream target of NRF2 is the transcription factor ATF4, which activates serine de novo synthesis and 1C metabolism [77]. In the context of ROS defence, serine metabolism is especially required to provide glycine for GSH de novo synthesis. In contrast to excessive ROS levels that are detrimental to cells, it has been shown that low to moderate levels of ROS can trigger pro-migratory and invasive signalling pathways [78–81]. Thus, being at the right dose, enhanced ROS exposure upon high proliferation rates or in oxygen-rich microenvironments can successfully drive metastatic progression. Exemplary findings include the ROS-dependent induction of cell migration and invasion through the upregulation of ECM-degrading matrix metalloproteases (MMPs) [82], stimulation of MAPK, ERK, and JNK signalling [83], promotion of Rac-dependent actin remodelling [84], and the expression of EMT-associated miRNAs and EMT regulators and marker proteins [85,86]. As such, it is of no surprise that antioxidant treatment has been considered in cancer prevention studies [87,88]. However, recent works by two independent groups have demonstrated that pharmacological and genetic interventions that promote antioxidant programs both resulted in increased metastasis in lung cancer [89,90]. Non-existent beneficial or even adverse effects of such approaches could be explained by the recent finding that ROS effects along the metastatic cascade are highly dynamic. Cheung et al. demonstrated that enhanced ROS levels

promote invasion and EMT transition, and, in contrast, reduced survival of secondary metastases in pancreatic ductal adenocarcinoma (PDAC) models [91].

In summary, the shortage of oxygen within hypoxic regions of the primary tumour as well as the enhanced availability of oxygen in lymph and blood vessels and secondary organ sites, have the potential to support cancer progression towards a more malignant phenotype. However, as these oxygen-dependent pro-malignant effects are also on the edge of cell survival, they might be one factor that explains the overall inefficient process of metastasis formation.

3.2. The Availability of Nutrients Selects for the Most Metabolically Resilient Cancer Cells

In addition to adaptation to variable oxygen saturation within the different TMEs, the extracellular nutrient availability influences the phenotypic characteristics of cancer cells undergoing metastasis. The TME is thought to be scarce in the availability of nutrients due to the high proliferative activity of the primary tumour and inefficient vascularisation. In a very recent, elegant study, it was demonstrated that in PDAC, nutrient availability in the TME does not reflect what is usually observed from in vitro studies [19]. Even glucose was not fully depleted, however, it was still measured at concentrations lower than those of the plasma [19]. Nevertheless, following on these novel insights, there is common sense that the metabolic signature of the TME is different to healthy tissue and plasma metabolite levels. Yet, the specific metabolic composition is most likely tumour-specific and needs to be considered as context dependent. Given the specific TME, cancer cells will adapt to the local metabolic constraints they are exposed to. For example, disseminating cells, that in contrast to proliferating, biosynthesis-driven cancer cells, do not rely on the de novo synthesis of macromolecules, can engage autophagy to counteract nutrient scarce conditions to better survive the dissemination process [14,92]. Furthermore, it is appreciated that cancer cells often adapt to increased anabolic demands by upregulating nutrient acquisition mechanisms [14]. One example is mutations in molecular switches downstream of growth factor signalling, e.g., PI3K/AKT, resulting in the upregulation of mTOR and the anabolic phenotype [93,94]. Other common mutations are found in the AMPK-activating kinase LKB1 [95], which downregulates the tumour suppressive effects of AMPK. This convergence of different metabolic sensors allows cancer cells to be phenotypically anabolic with no reliance on growth signals [96].

Another advantage gained by tumours in response to stressful nutrient-poor conditions is the selection of clones within the tumour that harbour genetic mutations that offer them survival advantage over other cells in the TME. One example is the selection for cells overexpressing GLUT1 in glucose-reduced conditions [97]. Furthermore, increased expression of pyruvate kinase 2 (PKM2) was shown to promote invasion through regulating MMP2 in lung cancer [98]. Besides glucose, further precursors for lipid, protein and nucleotide synthesis can become exhausted in the TME [99]. For instance, all cells within the TME require lipids in order to synthesise membranes. Breast cancer cells are able to overcome this limitation through acetate uptake and the upregulation of Acetyl-CoA synthetase 2 (ACSS2), which ligates acetate to a CoA group to synthesise acetyl-CoA and hence provides the key precursor for lipogenesis [100]. Another example is seen in about half of melanoma, breast, and lung cancers where tumour cells upregulate PHGDH, the rate-limiting and NAD^+-dependent enzyme in serine de novo synthesis. Thereby, the cells circumvent a potential dismal depletion of serine in the TME, an amino acid that is essential for protein, lipid and nucleotide synthesis [101–104]. Interestingly, nutritional intervention to limit serine availability showed anti-tumourigenic effects when PHGDH levels are low [105]. Additional advances in nutritional aspects and cancer metabolism are highlighted in three in-depth recent reviews [106–108]. Finally, metabolic waste accumulation can trigger the escape of cancer cells from the primary tumour to metastasise to distal organs in multiple ways. The release of lactate, ammonia, formate, and CO_2 into the TME from metabolically active cancer cells impacts the pH. This can in turn prompt invasion, e.g., via NFκB, leading to the release of MMP9 and the degradation of the ECM [109,110].

In addition, the TME itself can also support cancer progression. A key aspect of that is sustenance, by which different cell types deposit metabolites that cancer cells use for their proliferation and

growth [14]. Glutamate is abundant in the brain as a neurotransmitter and can act as a source for glutamine in cells that harbour the enzyme glutamine synthetase (GS). Glioblastoma cells lacking GS rely on astrocytes to provide them with glutamine, which they require for purine synthesis and hence proliferation [111]. Bone marrow stromal cells support the ability of chronic lymphocytic leukaemia cells to survive elevated levels of ROS through supplying them with the GSH precursor cysteine [112]. PDAC cells are able to circumvent their nutrient-poor TME by relying on alanine deposited by pancreatic stellate cells to fuel their central carbon metabolism [113]. Furthermore, in breast cancer, cancer-associated fibroblasts (CAFs) were shown to be highly glycolytic and can deposit lactate and pyruvate into the TME to support tumour growth [114]. In case lipid supply becomes limited within the adipose tissue in the abdomen, metastatic ovarian cancer cells reprogram CAFs to release cytokines, which in turn enable the cancer cell to metabolise glycogen for energy and biosynthesis [115]. Not only stromal cells of the TME, but also the ECM of the TME impacts tumour development. It was recently shown that the ECM can interact mechanically with cells and inhibit glycolysis. Lung cancer cells are able to bypass such mechanical inhibition through adapting their cytoskeleton and hence maintain high glycolytic rates while other cells in the TME cannot [116]. In general, the composition of the ECM has an impact on the cell's metabolic phenotype and also impacts the adhesion and migration efficiency of cells [117–122].

In order to enter the bloodstream, metastasising cells show traits of EMT, allowing them to escape from the primary tumour and to intravasate [18]. The EMT transcription factor Snail was shown to redirect glycolytic flux towards the PPP to increase NADPH synthesis to balance cancer cell survival during dissemination from the primary tumour [123]. In lung cancer, the depletion of UDP-glucose activates signalling via EGFR and stabilises Snail expression [124]. NFκB signalling in consequence of increased glycolytic activity can upregulate the EMT transcription factors ZEB1/2 [125]. Extracellular lactate was also shown to promote EMT and trigger invasion in renal cell carcinoma through the inhibition of histone deacetylation [126]. The conditionally essential amino acid asparagine was shown to be necessary for EMT gene expression and invasion of breast cancer cells. Knockdown of asparagine synthetase and asparagine starvation both resulted in the inhibition of metastasis without affecting primary lump growth [127]. Very recently, it was also shown that the microbiome impacts the EMT signature and invasive progression of colorectal cancer cells [128] as well as the function of p53 as a tumour suppressor [129].

As detailed in Section 3.1, cancer cells that circulate throughout the body in the bloodstream are exposed to increased ROS levels. However, in contrast to the TME of the primary tumour, glucose is abundant in the bloodstream and thus, these circulating cells are able to utilise this carbon source to balance ROS [123]. A recent study also revealed that the presence of the lactate transporter MCT1 and concomitant lactate consumption positively impacts the metastatic potential of melanoma cells [18,130]. Silencing MCT1 resulted in reduced PPP activity, elevated ROS levels and reduced metastasis formation. This study highlights the high degree of metabolic flexibility of metastasising tumour cells and the need to properly balance ROS during the dissemination stage to reach distant organs [130].

Organotropic metastasis describes the tendency of defined primary tumours to form metastasis in specific secondary organs [131]. While the metabolic niche is not the only factor dictating such relationship, it is indeed an important one. Nutrient availability in the metastatic niche imposes a selection pressure on invading cancer cells and thereby leads to clonal selection of subclones that harbour beneficial metabolic adaptations. The specific nutrient milieu within these metastatic niches and the respective, necessary metabolic adaptations within migrating tumour cells can herein differ significantly depending on the organ primary tumour cells disseminate to. For example, whereas secondary TME conditions in the lungs are dominated by constant oxygen exposure, the liver and brain harbour enhanced concentrations of alternative carbon sources such as acetate, branched chain amino acids and glutamine, that are suited to facilitate high proliferation of specialised metastatic cells [18]. Consequently, primary tumours, which show specific, beneficial metabolic adaptations in heterogeneous cellular subpopulations, are able to form metastases in different secondary organs [18,96]. Evidences

of such intricate metabolic patterns of organotropic metastasis have been extensively summarised in specific reviews [18,131–134]. Targeting OXPHOS in melanoma patients led to a decreased number of brain but not lung metastases [135]. This indicates the existence of at least two clonal subpopulations within melanoma cells that preferentially survive in two distinct metastatic niches and hence indicates a greater chance for cancer progression and therapy resistance [135]. Taken this concept even further, it was recently discovered that in collectively invasive cells, leader cells rely more on mitochondrial activity and PDH activity, while follower cells depend on glucose uptake, confirming that even within one cluster of invasive cells metabolically heterogeneous phenotypes exist [136]. While in Section 2, individual tumour cell plasticity was delineated as an essential trait for successful dissemination throughout the metastatic cascade, these findings additionally highlight the heterogeneity of the tumour and selection of the fittest cell subpopulations as another cornerstone of effective metastatic progression.

In addition to acting as substrates within specific metabolic pathways, metabolites can also have roles beyond their metabolic function. One example for this dual role is the usage of abundant pulmonary pyruvate by metastasising breast cancer cells. On the one hand, pyruvate can anaplerotically re-fill the tricarboxylic acid (TCA) cycle via the activity of pyruvate carboxylase [137,138]. On the other hand, pyruvate can dictate the modification of collagen in the ECM of the lungs to facilitate metastatic growth [139]. Moreover, metabolites can also function as allosteric regulators that impact metabolic fluxes [140] or reshape the epigenetic methylation and acetylation landscape. Impacting epigenetics is feasible as intracellular substrate concentrations to convey such modifications are achievable within the range of the K_m values of the respective modifying enzymes [141].

In conclusion, pathways in central carbon metabolism can be dynamically altered to adjust to metabolic constraints during the metastatic cascade. Hereby, engagement of the same central pathways can lead to distinctively different metabolic outputs. For example, cancer cells can utilise glucose as carbon-source for bioenergetics, biosynthesis or RedOx balance generating in the process different and proportionally variable amounts of co-factors, building blocks and ATP. Hereby, cancer cells in the primary tumour are for instance able to adapt their metabolism to proliferation rates that exceed the capacity limit of the ETC [60]. Metastatic tumour cells, on the other hand, have to withstand harsher metabolic environments that require a different re-wiring of their central carbon metabolism to counteract oxidative stress, allow cell survival and effective outgrowth at metastatic sites. The following section of the review will thus explore the metabolic potential of the pathways of central carbon metabolism by looking at their energy and co-factor balances exemplifying how each pathway can be exploited.

4. Metabolic Flexibility Permits Adaptation to Changing Microenvironments

In Tables 1–3, examples are provided on how substrate utilisation can vary if bioenergetics, biosynthesis, or RedOx demand is predominant. The focus is hereby set on the major cellular carbon substrates glucose, serine, fatty acids (FA; with palmitate as an example) and glutamine [99].

Table 1 summarises how these main energy metabolites can be oxidised to maximise ATP generation and thereby cellular energy production. Glucose molecules traverse glycolysis in the cytoplasm generating two pyruvate, two ATP, and two NADH molecules. One pyruvate molecule can either be reduced to lactate (consuming one NADH molecule in the process) or be fully oxidised in the mitochondrion to generate three CO_2, one ATP, four NADH, and one $FADH_2$ [142]. Serine can be catabolised to produce glycine and formate, which both can be secreted from cells in significant amounts [143]. This catabolism generates one ATP and one NAD(P)H per serine molecule [144]. Of note, using stable-isotope tracing to follow the fate of serine, serine catabolism to pyruvate via serine dehydratase was not observed. Instead, all serine was catabolised to glycine and formate via 1C metabolism [143]. Complete oxidation of FA stoichiometrically yields a number of acetyl-CoA molecules that equates half the number of carbons that the FA contained. Hereby, the generation of each acetyl-CoA molecule is accompanied by the production of one NADH and one $FADH_2$ molecule. Subsequently, each acetyl-CoA enters the TCA cycle to be fully oxidised producing two

CO_2, three NADH, one $FADH_2$, and one ATP [142]. Glutamine is readily converted to α-ketoglutarate, which passes through the TCA cycle up to malate. Malate is then oxidised to pyruvate through the action of malic enzyme 1, 2, or 3 (ME) producing cytosolic NADPH, mitochondrial NADH or mitochondrial NADPH, respectively [145–147]. Subsequently, lactate or acetyl-CoA can be produced from pyruvate. Alternatively, pyruvate can be oxidised by PDH and fed back into the TCA cycle. If 50% of glutamine-derived malate is converted to oxaloacetate, while the other 50% are converted to pyruvate via ME, glutamine can be fully oxidised via the TCA cycle without the need of any other carbon sources. If palmitate and glutamine are both catabolised, glutamine-derived oxaloacetate and palmitate-derived acetyl-coA can be oxidised jointly.

Table 1. ATP and co-factors produced from glucose, palmitate, serine and glutamine when bioenergetics are the main metabolic constraint. Glucose can either be oxidised to 2 lactate or to 6 CO_2 molecules. One carbon (1C) metabolism can generate 1 ATP if only the mitochondrial 1C cycle is run and the end-product formate is not recycled. MTHFD2/L has two separate enzyme activities, a dehydrogenase and a hydrolase activity. Complete oxidation of a fatty acid e.g., palmitate yields 16 CO_2 and generates energy in the form of 6 ATP, 31 NADH and 15 $FADH_2$ molecules. Breakdown of glutamine in the TCA cycle and subsequent conversion of malate to pyruvate through the action of malic enzyme 2 (ME2) generates 1 ATP, 1 NADH and 1 $FADH_2$ molecule. Total ATP for each reaction is calculated based on ATP molecules generated, each NADH molecule producing 2.5 ATP molecules and $FADH_2$ producing 1.5 molecules of ATP molecules upon OXPHOS. * Depending on the shuttle system used to transport cytosolic NADH to the mitochondrion, 2.5 or 1.5 ATP molecules can be produced per molecule cytosolic NADH in this case [142]. Gly, glycine; $HCOO^-$, formate; FAO, fatty acid oxidation; TCA, tricarboxylic acid; ME, malic enzyme; RXN, reaction; C, carbons per substrate molecule.

Substrate	Pathway	C	RXNs	Products	ATP	NADH	$FADH_2$	Total ATP	ATP/RXN
Glucose	Glycolysis	6	17	2 Lactate	2	0	0	2	0.12
Glucose	Glycolysis TCA cycle	6	35	6 CO_2	4	10	2	30 or 32 *	0.86 or 0.91
Serine	Mitochondri 1C Cycle	3	4	1 Gly, 1 $HCOO^-$	1	1	0	3.5	0.88
Palmitate	FAO TCA cycle	16	101	16 CO_2	6	31	15	106	1.05
Glutamine	TCA Cycle ME2	5	7	Pyruvate, 2 CO_2	1	2	1	7.5	1.1

Table 2. ATP and co-factors produced from glucose, serine, and glutamine when biosynthesis is the main metabolic constraint. Metabolism of glucose can downstream contribute to the synthesis of nucleotides, fatty acids, amino acids and ribose-5-phosphate through the utilisation of its carbon atoms within specific pathways. One-carbon cycle is utilised to free one-carbon units from serine to generate purines and dTTP. Glutamine can anaplerotically support the TCA cycle and generate cytosolic citrate through reductive carboxylation which subsequently feeds into fatty acid synthesis. NADH generated per product is shown here to indicate the burden of NADH during anabolic state [60]. 3PG, 3-phosphoglycerate; Gly, glycine; FA, fatty acids; THF, tetrahydrofolate; 5,10-CH_2-THF, 5,10-methylene-tetrahydrofolate; dTTP, deoxythymdine triphosphate; RXN, reaction; C, carbons per substrate molecule.

Substrate	Macromolecule	C	RXNs	Products	ATP	NADH	NADPH	Total ATP	NADH/ Product
Glucose	Nucleotides	6	15	2 serine	−1	4	0	9	2
Glucose (via ACLY)	FA	6	21	2 Acetyl-CoA 2 CO_2	0	4	0	10	2
Glucose	Amino Acids	6	17	2 Alanine	2	2	0	7	1
Glucose	Ribose Sugar	6	5	Ribose 5-phosphate, CO_2	−1	0	2	−1	0
2 Serine	Purines	6	10	2 10-formyl-THF, 2 Gly	0	2	0	5	1
Serine	dTTP	3	7	5,10-CH_2-THF, Gly	0	1	−1	2.5	1
Glutamine (reductive route)	FA	5	6	Acetyl-CoA, Oxaloacetate	−1	0	−1	−1	0

Table 3. ATP and co-factors produced from glucose, palmitate, serine, and glutamine when RedOx balance is the main metabolic constraint. Glucose contributes to the generation of NADPH through the oxidative and reductive cycles of pentose phosphate pathway (PPP). The number of reactions is calculated assuming the smallest number needed to generate the most amount of NADPH. Serine catabolism through mitochondrial one carbon cycle can generate NADPH as a side product of the enzymatic activity of MTHFD2/L and ALDH1L2. Palmitate oxidation is shown here as an example for the potential of generating reducing power in the form of NADPH via NNT activity. Moreover, all mitochondrial NADH molecules generated in the other examples are assumed to be converted to NADPH. Conversion of malate to pyruvate via ME1 can generate NADPH instead of NADH during glutamine catabolism [145–147]. 1C, one-carbon; NNT, nicotinamide nucleotide transhydrogenase; ME, malic enzyme; RXN, reaction; C, carbons per substrate molecule.

Substrate	Pathway	C	RXNs	Products	ATP	NADPH	$FADH_2$	Total ATP	NADPH/RXN
Glucose	Oxidative & Reductive PPP	6	49	6 CO_2	−1	12	0	0	0.24
Serine	1C Cycle	3	4	Gly, CO_2	0	2	0	0	0.5
Palmitate	Potential Action of NNT	16	101	16 CO_2	6	31	15	28.5	0.31
Glutamine	TCA Cycle, ME1	5	8	Lactate, 2 CO_2	1	2	1	2.5	0.25

Table 2 summarises the potential metabolic products generated from the above-discussed main metabolic substrates if biosynthesis is the primary demand. As seen in Figure 1, glucose can provide carbon units for every major building block (nucleotides, lipids, and proteins) by supporting glycolysis (glycerol for lipids, 3PG for serine and hence nucleotides, pyruvate for alanine), PPP (riboses for nucleotides) or TCA cycle (acetyl-CoA for FA and different non-essential amino acids for proteins). The cytosolic acetyl-CoA pool is the main source for FA synthesis. This pool is mostly filled through the activity of ACLY (Figure 1), which cleaves cytosolic citrate into acetyl-CoA and oxaloacetate [142]. Moreover, a recent study found that pyruvate can be oxidised to CO_2 and acetyl-CoA in a ROS-dependent manner [148]. This alternate mechanism could be of relevance during invasion, a process that has been shown to be propagated by ROS as detailed in Section 2 of this review [78–80]. Cytosolic citrate levels are mainly sustained via glucose through glycolysis and the TCA cycle or glutamine depending on the cell's state and TME [47,49,149,150]. However, it is important to keep in mind that biosynthesis is also an energy expensive process that requires significant amounts of ATP to build up macromolecules. This ATP needs to be generated by the cells in parallel to the consumption of available carbons for macromolecule synthesis. As the cell dry mass composition is well defined for mammalian cells [151] and costs for protein translation, lipogenesis and nucleotide synthesis are also known [142], the energy demand for the duplication of the cell's content can be estimated. Such estimation revealed that the duplication of 1 litre cell volume costs ~6 moles of ATP, which is a high demand of ATP molecules if set into context with e.g., a blood glucose concentration of 5 mmol per litre [60]. In addition to ATP, NADPH is needed for de novo FA synthesis. Such extensive carbon demand for biosynthesis makes it conceivable that the absolute intracellular carbon demand is highest in proliferating cells. This further underlines the concept of a "full blown" metabolism described in chapter 2.

Table 3 provides an overview of metabolic routes when maintenance of ROS balance (RedOx homeostasis) is the predominant cellular constraint. PPP is divided into two parts, namely oxidative and reductive, providing ribose-5-phosphate for nucleotide synthesis and cytosolic NADPH for RedOx balance [142]. Depending on the intracellular and TME conditions, a cancer cell determines whether to run both, the oxidative and reductive part of the PPP or only the oxidative part. During anabolic state and biomass generation, glucose carbons are metabolised exclusively by the oxidative PPP to generate ribose units for biosynthesis. This oxidative path yields 2 mol NADPH per mol glucose. However, if maintenance of RedOx balance is the main interest, carbons are cycled through the oxidative and reductive PPP in parallel to generate the maximum possible number of NADPH from one glucose molecule [142]. Per cycle through the oxidative PPP, the cell loses one carbon atom in form of CO_2.

NADPH is used by cells as a reducing power to reduce the oxidised form of GSH, which is then in turn utilised to reduce ROS and maintain RedOx balance [152]. In consequence, NADPH production will be the major sink of glucose carbons when the cell faces a RedOx imbalance. A recent report nicely demonstrated by non-stationary flux analysis that cells can quickly adjust their glycolytic metabolism towards PPP to maximise NADPH production. Upon oxidative insult, GAPDH was oxidised, which blocked glucose carbons from entering lower glycolysis and redirected these carbons through G6PDH for full oxidation via PPP [153]. Apart from PPP, the other two main sources of cytosolic NADPH are the enzymes ME1 and IDH1 (Figure 1, Table 3) [154,155]. RedOx cycling between cytosolic IDH1 and mitochondrial IDH2 can be used to specifically counteract mitochondrial ROS to support anchorage-independent growth [149,156]. Additionally, mitochondrial NADPH can be potentially generated through the activity of nicotinamide nucleotide transhydrogenase (NNT), which is capable to convert NADH to NADPH [157,158]. This pathway is represented in Table 3 as part of the oxidation of palmitate, which is a major source for mitochondrial NADH.

It should be noted that the purpose of these tables is to illustrate how one pathway can be potentially maximised towards a certain constraint. In reality, different intermediate combinations will exist depending on the cellular and microenvironmental context. This concept of metabolic flexibility and adaptation occurs in the cell as one complex system. For the sake of simplicity, it is possible to zoom into one metabolic pathway and dissect its potential with respect to different metabolic sinks. Chapter 4 of this review will take an in-depth look into 1C metabolism and exemplarily highlight its potential in supporting each of the above-discussed constraints.

4.1. One-Carbon Metabolism has Implication in Biosynthesis, Bioenergetics and RedOx Control

Folate-mediated 1C metabolism describes a series of biochemical reactions that governs the transfer of 1C units from donor metabolites to different acceptors (Figures 1 and 2) [144,159,160]. Herby, the main donor metabolite is the non-essential amino acid serine. In contrast to the TCA cycle, which is exclusively located to the mitochondrion, the 1C cycle spreads across mitochondrion and cytoplasm. In the first, mitochondrial part of the cycle, serine is catabolised to glycine and a 1C unit (either formate or CO_2) under production of reducing equivalents and ATP. In the second cytoplasmic part of the cycle, both glycine and formate can subsequently serve as precursors for anabolic reactions or serine can be re-synthesised which then closes the 1C cycle. Thus, 1C metabolism is an example of a pathway in which catabolic and anabolic reactions are separated from each other by cellular compartmentalisation.

Of note, serine catabolism via the 1C cycle is also connected to the methionine cycle by donating CH_3-THF for the remethylation of homocysteine to methionine (Figure 1) [144]. However, the quantitative contribution of 1C units to the methionine cycle is in most cases rather low and environmental methionine seems to be critical in most tissues [159,161]. Therefore, we do not include the methionine cycle in our discussions in this section.

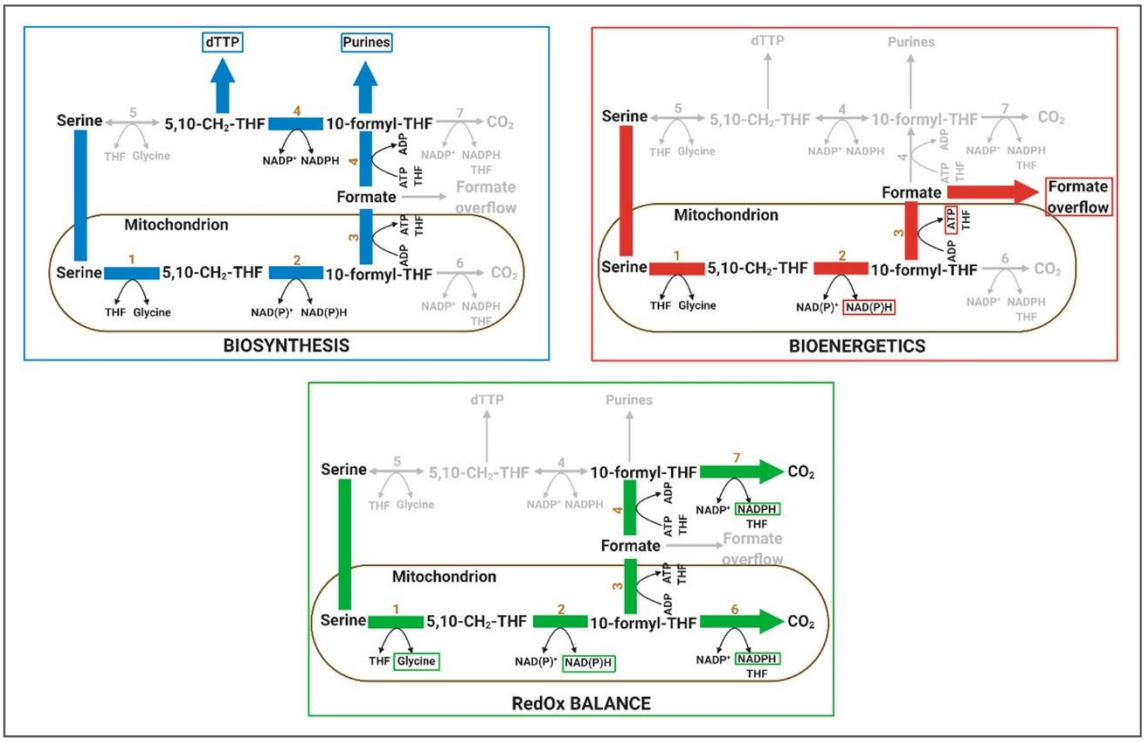


Figure 2. One-carbon cycle and its theoretical potential in supporting biosynthesis, bioenergetics and RedOx balance. One-carbon (1C) cycle can support biosynthesis through the generation of 10-formyl-THF and 5,10-CH_2-THF. When formate is released from the 1C cycle, this yields one NADH and one ATP molecule per serine supporting energy balance. Alternatively, the 1C unit can be released as CO_2 generating NADPH in the process through the action of ALDH1L1**/**2. NADPH can also be generated from the action of MTHFD2**/**L. In addition, serine-derived glycine can be used for purine synthesis (biosynthesis) or GSH synthesis (RedOx). Enzymes are abbreviated with numbers as following: 1: SHMT2; 2: MTHFD2**/**L; 3: MTHFD1L; 4: MTHFD1; 5: SHMT1; 6: ALDH1L2; 7: ALDH1L1. 5,10-CH_2-THF, 5,10-methylene-THF; THF, tetrahydrofolate; SHMT, serine hydroxyl methyl-transferase; MTHFD, 5,10-methylene-tetrahydrofolate dehydrogenase**/**5,10-methylene- tetrahydrofolate cyclohydrolase; ALDH1L, 10-formyltetrahydrofolate dehydrogenase.

4.1.1. Relevance of 1C Metabolism in Biosynthesis

1C metabolism became a hotspot in cancer research due to its essential role in the de novo synthesis of nucleotides, which renders it crucial for biosynthesis in proliferating cells [162]. To synthesise a purine molecule, one glycine and two 1C units are required. For the synthesis of one dTMP, one 1C unit is required. As purine demand in mammalian cells strongly exceeds pyrimidine demand, the absolute purine flux is higher than the 1C flux for dTMP synthesis. dTMP is only required for DNA synthesis and the cellular ratio of RNA to DNA is roughly 3:1 [163]. The highest demand is posed by the synthesis of adenine, as this purine is not only needed as a building block for DNA and RNA, but also for cellular ATP, which is present in millimolar concentrations. Inhibition of serine catabolism can inhibit proliferation by blocking nucleotide synthesis. However, when only mitochondrial serine catabolism via SHMT2 is inhibited, a cytosolic analogue of the enzyme, SHMT1, can compensate to a certain extend and sustain growth [164]. In addition to nucleotide synthesis, glycine is required for haem and GSH biosynthesis. Besides ATP, GSH is one of the few other metabolites that are concentrated within the millimolar range. Therefore, GSH represents a major sink for glycine. Targeting GSH de novo synthesis via the rate-limiting enzyme glutamate cysteine ligase has been shown to have detrimental effects in cancer cells as well as in immune cells [74,165]. Finally, serine is a proteinogenic amino acid that is also consumed for protein biosynthesis.

4.1.2. Relevance of 1C Metabolism in Bioenergetics

To generate formate, the 1C unit CH_2-THF is oxidised via MTHFD2 which in turn reduces $NAD(P)^+$ to NAD(P)H, a RedOx-relevant reaction. As oxidation of CH_2-THF is located in the mitochondrion, the generated NADH can readily be oxidised at complex I of the ETC, which generates 2.5 mol ATP per mol NADH. It is under debate if the oxidation of CH_2-THF in cancer cells is coupled to NAD^+ or $NADP^+$. Early in vitro results pointed towards NAD^+ [166], while later the Appling lab provided evidence by biochemical in vitro assays that MTHFD2 shows similar kinetics for both co-factors to oxidise polyglutamated CH_2-THF [167]. Yet, a study investigating this question in intact cells remains to be undertaken. However, the different concentrations of the co-factors in the mitochondrion and the experimental evidence that inhibition of the ETC, which is required to oxidise NADH, inhibits mitochondrial 1C unit oxidation [143,168] indicate that, in intact cells, the oxidation of CH_2-THF depends on NAD^+ and active respiration. This is supported by a recent study showing that MTHFD2 can still oxidise 1C units at decreasing NAD^+/NADH levels at which enzymes of the TCA cycle are already inhibited [169]. In such case, a larger fraction of OXPHOS-derived ATP could originate from serine catabolism. It therefore implies that mitochondrial 1C metabolism might have a meaningful role in bioenergetics under specific TME settings. Yet, it is important to note that even if MTHFD2 is less sensitive to feedback inhibition by NADH, the absolute flux of 1C unit oxidation is strongly inhibited when the ETC is strongly inhibited (e.g., by severe hypoxia or complex I inhibition) [143,168–170]. Thus, even if the relative flux might not change, the absolute flux clearly decreases when the respiration is inhibited. This is best illustrated by the observation that serine consumption rates and formate release rates strongly decrease when the ETC is blocked [135,161]. Hence, the quantitative analysis of serine consumption and formate release rates provides a robust tool to measure the rate of serine catabolism.

Once formyl-THF (CHO-THF) has been generated from CH_2-THF by the activity of MTHFD2, formate can either be further oxidised by ALDH1L2 to CO_2 under production of NADPH or released from THF under production of ATP. Hence, depending on the environmental condition, the fate of 1C units can differ and the catabolism of serine can support RedOx and/or bioenergetics. Under standard cell culture conditions, it was observed that in proliferating cells the largest fraction of generated 1C units are excreted in the form of formate in a process designated as formate overflow despite the cell's high demand of 1C units for nucleotide synthesis [143]. In a subsequent study, this phenomenon was also observed in different oxidative tumours in vivo [170]. Release of every formate molecule indicates a net production of ATP at the price of carbon loss that could otherwise be used for biomass production. Formate overflow has therefore some parallels to lactate overflow. In both cases, all carbon is lost and ATP is gained. However, the difference is that lactate overflow is cytoplasmic and formate overflow depends on the mitochondrial activity. Using different cancer models, it was observed that under nutrient stress conditions, when glycolysis is limited and cell growth is arrested, serine catabolism and formate overflow increases [143]. Whether or not this is mediated via AMPK, which was also activated under these nutrient stress conditions, remains to be elucidated. Although the detailed physiological relevance still needs to be unravelled, these observations suggest an additional catabolic role for serine metabolism via the 1C cycle. First results demonstrated that serine catabolism and its product formate can promote invasion of glioblastoma cells, a growth-independent process that could promote metastatic progression [170].

In summary, the overall balance of mitochondrial serine catabolism is:

$$1\ \text{serine} + 1NAD^+ + 1ADP \rightarrow 1\ \text{glycine} + 1\ \text{formate} + 1ATP + 1\ NADH \quad (1)$$

In the case of NADH oxidation via the ETC and formate excretion, the catabolism of serine generates 3.5 ATP with only four enzymatic reactions, which equals 0.88 mol ATP per reaction (Table 1). This is a similar efficiency as full oxidation of glucose to CO_2 via glycolysis and TCA cycle. Compared to glutamine oxidation, serine catabolism has also a reduced NADH burden, which could be of advantage in cancer cells that are likely to struggle to regenerate sufficient NAD^+. Thus, in growth-independent

conditions or glucose-deprived TME, catabolism of serine could be an attractive pathway to exploit serine as an energy substrate. Alternatively, if, e.g., the level of oxidative stress and therefore the demand for reducing equivalents rises, formate could instead be directed to ALDH1L2 for full oxidation and concomitant NADPH production [51,154].

4.1.3. Relevance of 1C Metabolism in RedOx

If formate is not excreted from the cytoplasm, it can be bound again to THF under consumption of 1 ATP, which renders the ATP balance of the 1C cycle zero. Cytosolic CHO-THF can then be used for purine synthesis or alternatively be reduced to CH_2-THF by cytosolic MTHFD1. CH_2-THF is required for the synthesis of the pyrimidine thymine and it has been shown that most CH_2-THF for dTMP synthesis is derived from the mitochondrion [171]. Interestingly, MTHFD1 is strictly $NADP^+$-dependent [144]. Thus, regeneration of CH_2-THF in the cytoplasm results in net consumption of NADPH. Experimental evidence showing that a significant fraction of serine-derived 1C units are resynthesized to serine in the cytoplasm indicates that 1C cycle consumes NADPH [164]. Following this logic, it appears more rational to fully oxidise formate to CO_2 by ALDH1L2 or ALDH1L1, if maintenance of the RedOx balance is the major cellular constraint (Figures 1 and 2) as in that case, there will be net production of NADPH by 1C cycle. In fact, a role for ALDH1L2 in RedOx control has recently been reported. When cells were put under nutrient stress, and hence exposed to increased ROS, ALDH1L2 activity increased to produce NADPH [154].

Given these biochemical relations, it nevertheless remains debatable if 1C metabolism represents a general major source for cellular NADPH. At first, in a pioneering study, 1C metabolism got into the spotlight for being a major contributor to cellular NADPH metabolism [172]. However, by showing that the co-deletion of ME1, IDH1, and G6PDH was detrimental to cancer cells and that no other pathway could compensate for the resulting lack of NADPH, the same lab was able to demonstrate in an elegant way that 1C metabolism has no major role for cytosolic NADPH production [155].

Even if not critical for the cytosolic NADPH pool, 1C metabolism could be of relevance for NADPH homeostasis in the mitochondrion under certain environmental conditions as has been shown previously [154]. However, in that case, NADPH is most likely derived from the activity of ALDH1L2 rather than MTHFD2 [164]. Yet, a quantitative comparison of NADPH production from ALDH1L2 compared to mitochondrial IDH2 and ME3 to elucidate the respective fractional contributions to the mitochondrial NADPH pool still needs to be conducted.

4.1.4. Systemic and Organ-Specific Aspects of 1C Metabolism

1C metabolism has also a significance on a systemic level. In a nutshell, most oxidative organs show glycine and formate overflow, while the kidney and especially the liver are thought to be glycine and formate sinks and to re-synthesise serine [160,170,173]. This whole-body cycle is important to keep the plasma levels of the 1C metabolism-related metabolites constant. To allow efficient recycling, liver and kidney express higher levels of MTHFD1 than most other organs. Therefore, using kidney or liver cell lines can lead to organ specific results that might not fully reflect other tissue-derived cancer cell lines [164]. In the landmark paper of Fan et al., quantitative analysis of 1C metabolism contribution to the cellular NADPH pool has been performed in immortalized baby mouse kidney cells (iBMK cells) [172]. In a follow-up publication of the same lab it was also demonstrated by using deuterated serine tracers that iBMKs show an unusual high activity of cytosolic serine catabolism via SHMT1 [164]. Here, it was concluded that mitochondrial 1C cycle-derived NADPH is mainly produced from the activity of ALDH1L2 [164]. Despite initial confusion around the role of 1C metabolism in cellular NADPH homeostasis, several excellent follow-up studies of the same lab as well as many other labs, advanced our understanding of 1C metabolism tremendously over the last five years.

By in-depth discussion of the example of 1C metabolism flexibility, it was illustrated how a single metabolic pathway can play different roles in bioenergetics, biosynthesis and RedOx homeostasis. It highlights thereby that cellular metabolism has the potential to adapt to different constraints

within the TME. The observation that nutrient availability can crucially alter the directionality and output of a plethora of metabolic pathways shows how vital the microenvironment is in dictating metabolic rewiring.

5. Concluding Remarks: D*iff*erential Carbon Distribution Allows Cells to Survive the Metastatic Cascade

It appears that, during dissemination, nutrient catabolism is not used for proliferation but instead can be exploited for survival and motility. During metastasis, cells are in cell cycle phase G0/G1 [6] and consequently, the energy demand to synthesise macromolecules is low. Under such growth-independent conditions, the suitable cellular adaptation by targeted rewiring of metabolic pathways can support cells with spare carbon units to be used for maintenance of RedOx balance and the generation of energy. Both of these carbon sinks are imperative to establish and support a motile invasive phenotype (Figure 3) [119]. Such spare energy and residual RedOx potential might be used during metastasis for "mechanical work" and the counteraction of oxidative stress (Figure 3).

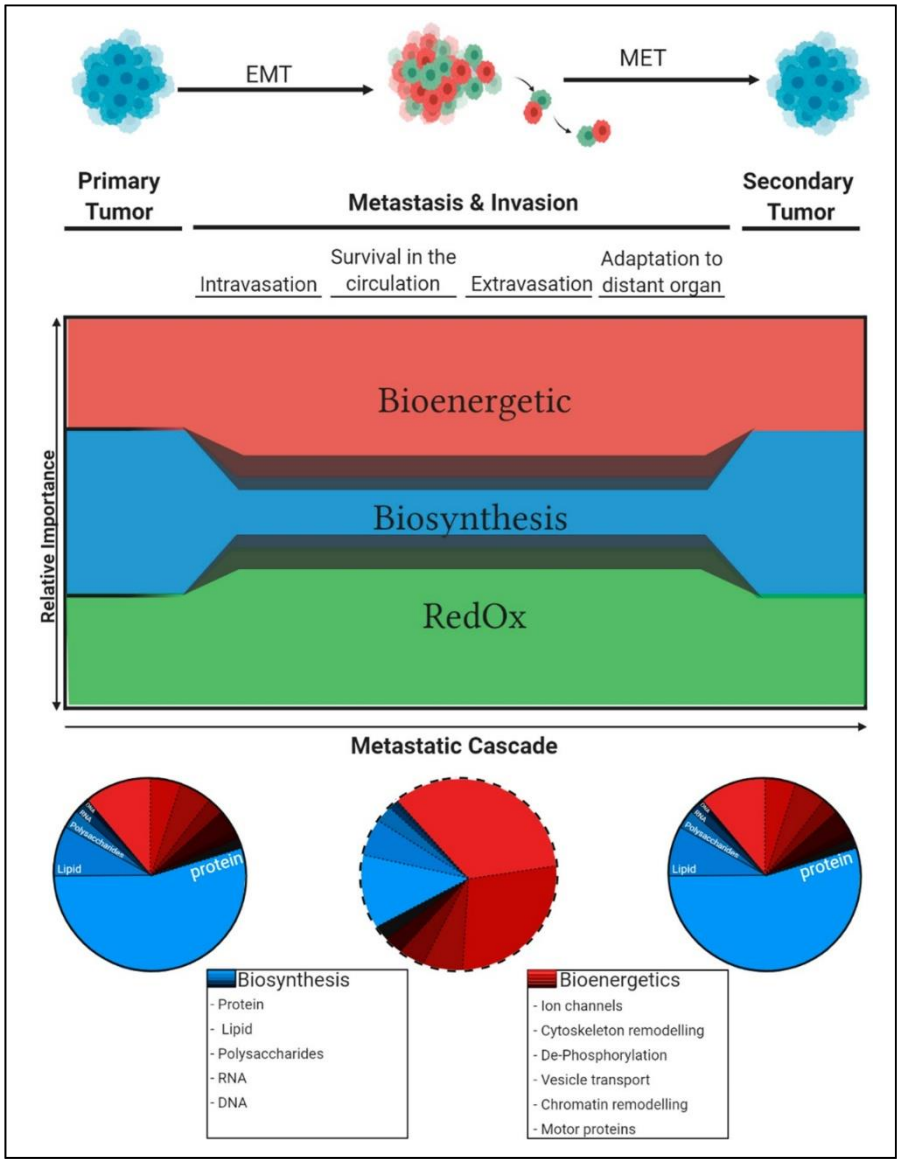


Figure 3. Flexible metabolic conversion of available carbon sources allows cancer cells to adapt to changing metabolic needs along the metastatic cascade. According to the cellular needs, the available

carbon atoms from nutrients are distributed between the three main metabolic sinks. The relative amount of carbon atoms that is invested for proliferation in primary tumour cells prohibits extensive energy allocation for invasion and metastasis. However, under growth-arrested conditions, cells spend less nutrients on biosynthesis and can reallocate the gained spare carbons to promote an invasive phenotype by investing in enhanced cellular energy production and/or improved anti-oxidant defence. Thus, upon proliferation within the primary tumour and in the developed metastasis (left and right pie chart), the cells invest most energy for building block production (protein, lipid, DNA/RNA synthesis). However, during the metastatic process (middle pie chart), the metastatic cells switch from anabolic to catabolic metabolism and energy might be redistributed to support cell invasion.

We are just now starting to understand how the detailed metabolic adaptations towards these metastatic constraints and demands look like. However, we currently lack sufficient in-depth knowledge and quantitative insight on these adaptation processes. Being able to comprehensively understand the dimensionality of metabolic adaptations and the intricate ways they manifest will allow for the design of tailored intervention strategies directed specifically against more dormant, metastasis-prone tumour cells. As potential interventions can vary from patient to patient, precision medicine and appendant patient-specific analysis of cancer metabolism may open new possibilities to define individual treatment regimens, even though there is still a long way to go to attain this final goal.

Author Contributions: Conceptualization, J.M. and N.K.; writing—original draft preparation, M.B., C.D., L.N., N.K., and J.M.; visualization, M.B., C.D., and L.N.; writing—review and editing M.B., N.K., and J.M.; supervision N.K. and J.M. All authors have read and agreed to the published version of the manuscript.

Funding: J.M. is supported by FNR-ATTRACT (A18/BM/11809970) and INTER-BMBF grant (18/13399110). M.B., C.D. and N.K. are funded via the by FNR-ATTRACT grant (A18/BM/11809970).

Acknowledgments: We thank all group members of the Meiser lab and Elisabeth Letellier (University of Luxembourg) for fruitful discussions and critical feedback. All figures were created with BioRender.com.

Conflicts of Interest: The authors declare no conflict of interest.

References

1. Retsas, S. Cancer and the arts: Metastasis-as perceived through the ages. *Esmo Open* **2017**, *2*, e000226. [CrossRef] [PubMed]
2. Siegel, R.L.; Miller, K.D.; Jemal, A. Cancer statistics, 2020. *CA Cancer J. Clin.* **2020**, *70*, 7–30. [CrossRef] [PubMed]
3. Yoo, B.; Fuchs, B.C.; Medarova, Z. New Directions in the Study and Treatment of Metastatic Cancer. *Front. Oncol.* **2018**, *8*, 258. [CrossRef] [PubMed]
4. Falzone, L.; Salomone, S.; Libra, M. Evolution of Cancer Pharmacological Treatments at the Turn of the Third Millennium. *Front. Pharmacol.* **2018**, *9*, 1300. [CrossRef] [PubMed]
5. Frei, E., 3rd; Jaffe, N.; Tattersall, M.H.; Pitman, S.; Parker, L. New approaches to cancer chemotherapy with methotrexate. *N. Engl. J. Med.* **1975**, *292*, 846–851. [PubMed]
6. Kohrman, A.Q.; Matus, D.Q. Divide or Conquer: Cell Cycle Regulation of Invasive Behavior. *Trends Cell Biol.* **2017**, *27*, 12–25. [CrossRef]
7. Steeg, P.S.; Theodorescu, D. Metastasis: A therapeutic target for cancer. *Nat. Clin. Pract. Oncol.* **2008**, *5*, 206–219. [CrossRef]
8. Meirson, T.; Gil-Henn, H.; Samson, A.O. Invasion and metastasis: The elusive hallmark of cancer. *Oncogene* **2020**, *39*, 2024–2026. [CrossRef]
9. Welch, D.R.; Hurst, D.R. Defining the Hallmarks of Metastasis. *Cancer Res.* **2019**, *79*, 3011–3027. [CrossRef]
10. Van Zijl, F.; Krupitza, G.; Mikulits, W. Initial steps of metastasis: Cell invasion and endothelial transmigration. *Mutat. Res.* **2011**, *728*, 23–34. [CrossRef]
11. Ishay-Ronen, D.; Diepenbruck, M.; Kalathur, R.K.R.; Sugiyama, N.; Tiede, S.; Ivanek, R.; Bantug, G.; Morini, M.F.; Wang, J.; Hess, C.; et al. Gain Fat-Lose Metastasis: Converting Invasive Breast Cancer Cells into Adipocytes Inhibits Cancer Metastasis. *Cancer Cell* **2019**, *35*, 17–32.e6. [CrossRef] [PubMed]

12. Leone, R.D.; Powell, J.D. Metabolism of immune cells in cancer. *Nat. Rev. Cancer* **2020**, *20*, 516–531. [CrossRef] [PubMed]
13. Ward, P.S.; Thompson, C.B. Metabolic reprogramming: A cancer hallmark even warburg did not anticipate. *Cancer Cell* **2012**, *21*, 297–308. [CrossRef] [PubMed]
14. Palm, W.; Thompson, C.B. Nutrient acquisition strategies of mammalian cells. *Nature* **2017**, *546*, 234–242. [CrossRef] [PubMed]
15. Fendt, S.M. Metabolic vulnerabilities of metastasizing cancer cells. *BMC Biol.* **2019**, *17*, 54. [CrossRef]
16. Schito, L.; Semenza, G.L. Hypoxia-Inducible Factors: Master Regulators of Cancer Progression. *Trends Cancer* **2016**, *2*, 758–770. [CrossRef]
17. Trachootham, D.; Alexandre, J.; Huang, P. Targeting cancer cells by ROS-mediated mechanisms: A radical therapeutic approach? *Nat. Rev. Drug Discov.* **2009**, *8*, 579–591. [CrossRef]
18. Kreuzaler, P.; Panina, Y.; Segal, J.; Yuneva, M. Adapt and conquer: Metabolic flexibility in cancer growth, invasion and evasion. *Mol. Metab.* **2020**, *33*, 83–101. [CrossRef]
19. Sullivan, M.R.; Danai, L.V.; Lewis, C.A.; Chan, S.H.; Gui, D.Y.; Kunchok, T.; Dennstedt, E.A.; Vander Heiden, M.G.; Muir, A. Quantification of microenvironmental metabolites in murine cancers reveals determinants of tumor nutrient availability. *Elife* **2019**, *8*, e44235. [CrossRef]
20. Dilillo, M.; Ait-Belkacem, R.; Esteve, C.; Pellegrini, D.; Nicolardi, S.; Costa, M.; Vannini, E.; de Graaf, E.L.; Caleo, M.; McDonnell, L.A. Ultra-High Mass Resolution MALDI Imaging Mass Spectrometry of Proteins and Metabolites in a Mouse Model of Glioblastoma. *Sci. Rep.* **2017**, *7*, 603. [CrossRef]
21. Vaupel, P.; Höckel, M.; Mayer, A. Detection and characterization of tumor hypoxia using pO_2 histography. *Antioxid. Redox Signal.* **2007**, *9*, 1221–1235. [CrossRef] [PubMed]
22. McKeown, S.R. Defining normoxia, physoxia and hypoxia in tumours-implications for treatment response. *Br. J. Radiol.* **2014**, *87*. [CrossRef] [PubMed]
23. Luo, W.; Wang, Y. Hypoxia Mediates Tumor Malignancy and Therapy Resistance. In *Hypoxia and Cancer Metastasis*; Gilkes, D.M., Ed.; Springer International Publishing: Cham, Switzerland, 2019; pp. 1–18.
24. Lee, J.W.; Ko, J.; Ju, C.; Eltzschig, H.K. Hypoxia signaling in human diseases and therapeutic targets. *Exp. Mol. Med.* **2019**, *51*, 68. [CrossRef] [PubMed]
25. Bertout, J.A.; Patel, S.A.; Simon, M.C. The impact of O_2 availability on human cancer. *Nat. Rev. Cancer* **2008**, *8*, 967–975. [CrossRef] [PubMed]
26. Cairns, R.A.; Kalliomaki, T.; Hill, R.P. Acute (cyclic) hypoxia enhances spontaneous metastasis of KHT murine tumors. *Cancer Res.* **2001**, *61*, 8903–8908. [PubMed]
27. Hajizadeh, F.; Okoye, I.; Esmaily, M.; Ghasemi Chaleshtari, M.; Masjedi, A.; Azizi, G.; Irandoust, M.; Ghalamfarsa, G.; Jadidi-Niaragh, F. Hypoxia inducible factors in the tumor microenvironment as therapeutic targets of cancer stem cells. *Life Sci.* **2019**, *237*, 116952. [CrossRef]
28. Jiang, J.; Tang, Y.L.; Liang, X.H. EMT: A new vision of hypoxia promoting cancer progression. *Cancer Biol. Ther.* **2011**, *11*, 714–723. [CrossRef]
29. Kidd, M.E.; Shumaker, D.K.; Ridge, K.M. The role of vimentin intermediate filaments in the progression of lung cancer. *Am. J. Respir. Cell Mol. Biol.* **2014**, *50*, 1–6. [CrossRef]
30. Kirschmann, D.A.; Seftor, E.A.; Fong, S.F.T.; Nieva, D.R.C.; Sullivan, C.M.; Edwards, E.M.; Sommer, P.; Csiszar, K.; Hendrix, M.J.C. A Molecular Role for Lysyl Oxidase in Breast Cancer Invasion. *Cancer Res.* **2002**, *62*, 4478–4483.
31. Krishnamachary, B.; Berg-Dixon, S.; Kelly, B.; Agani, F.; Feldser, D.; Ferreira, G.; Iyer, N.; LaRusch, J.; Pak, B.; Taghavi, P.; et al. Regulation of colon carcinoma cell invasion by hypoxia-inducible factor 1. *Cancer Res.* **2003**, *63*, 1138–1143.
32. LeBleu, V.S.; O'Connell, J.T.; Gonzalez Herrera, K.N.; Wikman, H.; Pantel, K.; Haigis, M.C.; de Carvalho, F.M.; Damascena, A.; Domingos Chinen, L.T.; Rocha, R.M.; et al. PGC-1α mediates mitochondrial biogenesis and oxidative phosphorylation in cancer cells to promote metastasis. *Nat. Cell Biol.* **2014**, *16*, 992–1003. [CrossRef] [PubMed]
33. Mao, Q.; Zhang, Y.; Fu, X.; Xue, J.; Guo, W.; Meng, M.; Zhou, Z.; Mo, X.; Lu, Y. A tumor hypoxic niche protects human colon cancer stem cells from chemotherapy. *J. Cancer Res. Clin. Oncol.* **2013**, *139*, 211–222. [CrossRef] [PubMed]
34. Rankin, E.B.; Giaccia, A.J. The role of hypoxia-inducible factors in tumorigenesis. *Cell Death Differ.* **2008**, *15*, 678–685. [CrossRef] [PubMed]

35. Tam, S.Y.; Wu, V.W.C.; Law, H.K.W. Hypoxia-Induced Epithelial-Mesenchymal Transition in Cancers: HIF-1α and Beyond. *Front. Oncol.* **2020**, *10*, 486. [CrossRef]
36. Vaapil, M.; Helczynska, K.; Villadsen, R.; Petersen, O.W.; Johansson, E.; Beckman, S.; Larsson, C.; Påhlman, S.; Jögi, A. Hypoxic conditions induce a cancer-like phenotype in human breast epithelial cells. *PLoS ONE* **2012**, *7*, e46543. [CrossRef]
37. Yang, M.-H.; Wu, M.-Z.; Chiou, S.-H.; Chen, P.-M.; Chang, S.-Y.; Liu, C.-J.; Teng, S.-C.; Wu, K.-J. Direct regulation of TWIST by HIF-1α promotes metastasis. *Nat. Cell Biol.* **2008**, *10*, 295–305. [CrossRef]
38. Zhu, L.L.; Wu, L.Y.; Yew, D.T.; Fan, M. Effects of hypoxia on the proliferation and differentiation of NSCs. *Mol. Neurobiol.* **2005**, *31*, 231–242. [CrossRef]
39. Qureshi-Baig, K.; Kuhn, D.; Viry, E.; Pozdeev, V.I.; Schmitz, M.; Rodriguez, F.; Ullmann, P.; Koncina, E.; Nurmik, M.; Frasquilho, S.; et al. Hypoxia-induced autophagy drives colorectal cancer initiation and progression by activating the PRKC/PKC-EZR (ezrin) pathway. *Autophagy* **2020**, *16*, 1436–1452. [CrossRef]
40. Godet, I.; Shin, Y.J.; Ju, J.A.; Ye, I.C.; Wang, G.; Gilkes, D.M. Fate-mapping post-hypoxic tumor cells reveals a ROS-resistant phenotype that promotes metastasis. *Nat. Commun.* **2019**, *10*, 4862. [CrossRef]
41. Chen, C.; Pore, N.; Behrooz, A.; Ismail-Beigi, F.; Maity, A. Regulation of glut1 mRNA by hypoxia-inducible factor-1. Interaction between H-ras and hypoxia. *J. Biol. Chem.* **2001**, *276*, 9519–9525. [CrossRef]
42. Firth, J.D.; Ebert, B.L.; Ratcliffe, P.J. Hypoxic regulation of lactate dehydrogenase A. Interaction between hypoxia-inducible factor 1 and cAMP response elements. *J. Biol. Chem.* **1995**, *270*, 21021–21027. [CrossRef] [PubMed]
43. Iyer, N.V.; Kotch, L.E.; Agani, F.; Leung, S.W.; Laughner, E.; Wenger, R.H.; Gassmann, M.; Gearhart, J.D.; Lawler, A.M.; Yu, A.Y.; et al. Cellular and developmental control of O_2 homeostasis by hypoxia-inducible factor 1 alpha. *Genes Dev.* **1998**, *12*, 149–162. [CrossRef] [PubMed]
44. Mathupala, S.P.; Rempel, A.; Pedersen, P.L. Glucose catabolism in cancer cells: Identification and characterization of a marked activation response of the type II hexokinase gene to hypoxic conditions. *J. Biol. Chem.* **2001**, *276*, 43407–43412. [CrossRef] [PubMed]
45. Maxwell, P.H.; Dachs, G.U.; Gleadle, J.M.; Nicholls, L.G.; Harris, A.L.; Stratford, I.J.; Hankinson, O.; Pugh, C.W.; Ratcliffe, P.J. Hypoxia-inducible factor-1 modulates gene expression in solid tumors and influences both angiogenesis and tumor growth. *Proc. Natl. Acad. Sci. USA* **1997**, *94*, 8104–8109. [CrossRef] [PubMed]
46. Semenza, G.L.; Roth, P.H.; Fang, H.M.; Wang, G.L. Transcriptional regulation of genes encoding glycolytic enzymes by hypoxia-inducible factor 1. *J. Biol. Chem.* **1994**, *269*, 23757–23763.
47. Metallo, C.M.; Gameiro, P.A.; Bell, E.L.; Mattaini, K.R.; Yang, J.; Hiller, K.; Jewell, C.M.; Johnson, Z.R.; Irvine, D.J.; Guarente, L.; et al. Reductive glutamine metabolism by IDH1 mediates lipogenesis under hypoxia. *Nature* **2012**, *481*, 380–384. [CrossRef]
48. Furuta, E.; Pai, S.K.; Zhan, R.; Bandyopadhyay, S.; Watabe, M.; Mo, Y.Y.; Hirota, S.; Hosobe, S.; Tsukada, T.; Miura, K.; et al. Fatty acid synthase gene is up-regulated by hypoxia via activation of Akt and sterol regulatory element binding protein-1. *Cancer Res.* **2008**, *68*, 1003–1011. [CrossRef]
49. Wise, D.R.; Ward, P.S.; Shay, J.E.; Cross, J.R.; Gruber, J.J.; Sachdeva, U.M.; Platt, J.M.; DeMatteo, R.G.; Simon, M.C.; Thompson, C.B. Hypoxia promotes isocitrate dehydrogenase-dependent carboxylation of α-ketoglutarate to citrate to support cell growth and viability. *Proc. Natl. Acad. Sci. USA* **2011**, *108*, 19611–19616. [CrossRef]
50. Frezza, C.; Zheng, L.; Tennant, D.A.; Papkovsky, D.B.; Hedley, B.A.; Kalna, G.; Watson, D.G.; Gottlieb, E. Metabolic profiling of hypoxic cells revealed a catabolic signature required for cell survival. *PLoS ONE* **2011**, *6*, e24411. [CrossRef]
51. Piskounova, E.; Agathocleous, M.; Murphy, M.M.; Hu, Z.; Huddlestun, S.E.; Zhao, Z.; Leitch, A.M.; Johnson, T.M.; DeBerardinis, R.J.; Morrison, S.J. Oxidative stress inhibits distant metastasis by human melanoma cells. *Nature* **2015**, *527*, 186–191. [CrossRef]
52. Yi, W.; Clark, P.M.; Mason, D.E.; Keenan, M.C.; Hill, C.; Goddard, W.A., 3rd; Peters, E.C.; Driggers, E.M.; Hsieh-Wilson, L.C. Phosphofructokinase 1 glycosylation regulates cell growth and metabolism. *Science* **2012**, *337*, 975–980. [CrossRef] [PubMed]
53. Panieri, E.; Santoro, M.M. ROS homeostasis and metabolism: A dangerous liason in cancer cells. *Cell Death Dis.* **2016**, *7*, e2253. [CrossRef] [PubMed]

54. Young, A.; Gardiner, D.; Brosnan, M.E.; Brosnan, J.T.; Mailloux, R.J. Physiological levels of formate activate mitochondrial superoxide/hydrogen peroxide release from mouse liver mitochondria. *FEBS Lett.* **2017**, *591*, 2426–2438. [CrossRef] [PubMed]
55. Palacios-Callender, M.; Quintero, M.; Hollis, V.S.; Springett, R.J.; Moncada, S. Endogenous NO regulates superoxide production at low oxygen concentrations by modifying the redox state of cytochrome c oxidase. *Proc. Natl. Acad. Sci. USA* **2004**, *101*, 7630–7635. [CrossRef]
56. Jung, S.N.; Yang, W.K.; Kim, J.; Kim, H.S.; Kim, E.J.; Yun, H.; Park, H.; Kim, S.S.; Choe, W.; Kang, I.; et al. Reactive oxygen species stabilize hypoxia-inducible factor-1 alpha protein and stimulate transcriptional activity via AMP-activated protein kinase in DU145 human prostate cancer cells. *Carcinogenesis* **2008**, *29*, 713–721. [CrossRef]
57. Hamanaka, R.B.; Weinberg, S.E.; Reczek, C.R.; Chandel, N.S. The Mitochondrial Respiratory Chain Is Required for Organismal Adaptation to Hypoxia. *Cell Rep.* **2016**, *15*, 451–459. [CrossRef]
58. Ashton, T.M.; McKenna, W.G.; Kunz-Schughart, L.A.; Higgins, G.S. Oxidative Phosphorylation as an Emerging Target in Cancer Therapy. *Clin. Cancer Res. Off. J. Am. Assoc. Cancer Res.* **2018**, *24*, 2482–2490. [CrossRef]
59. DeBerardinis, R.J.; Chandel, N.S. We need to talk about the Warburg effect. *Nat. Metab.* **2020**, *2*, 127–129. [CrossRef]
60. Fernandez-de-Cossio-Diaz, J.; Vazquez, A. Limits of aerobic metabolism in cancer cells. *Sci. Rep.* **2017**, *7*, 13488. [CrossRef]
61. Niebel, B.; Leupold, S.; Heinemann, M. An upper limit on Gibbs energy dissipation governs cellular metabolism. *Nat. Metab.* **2019**, *1*, 125–132. [CrossRef]
62. Park, J.O.; Tanner, L.B.; Wei, M.H.; Khana, D.B.; Jacobson, T.B.; Zhang, Z.; Rubin, S.A.; Li, S.H.-J.; Higgins, M.B.; Stevenson, D.M.; et al. Near-equilibrium glycolysis supports metabolic homeostasis and energy yield. *Nat. Chem. Biol.* **2019**, *15*, 1001–1008. [CrossRef] [PubMed]
63. Zamkova, M.; Khromova, N.; Kopnin, B.P.; Kopnin, P. Ras-induced ROS upregulation affecting cell proliferation is connected with cell type-specific alterations of HSF1/SESN3/p21Cip1/WAF1 pathways. *Cell Cycle* **2013**, *12*, 826–836. [CrossRef] [PubMed]
64. Ogrunc, M.; Di Micco, R.; Liontos, M.; Bombardelli, L.; Mione, M.; Fumagalli, M.; Gorgoulis, V.G.; d'Adda di Fagagna, F. Oncogene-induced reactive oxygen species fuel hyperproliferation and DNA damage response activation. *Cell Death Differ.* **2014**, *21*, 998–1012. [CrossRef] [PubMed]
65. Koptyra, M.; Falinski, R.; Nowicki, M.O.; Stoklosa, T.; Majsterek, I.; Nieborowska-Skorska, M.; Blasiak, J.; Skorski, T. BCR/ABL kinase induces self-mutagenesis via reactive oxygen species to encode imatinib resistance. *Blood* **2006**, *108*, 319–327. [CrossRef] [PubMed]
66. Liou, G.Y.; Storz, P. Reactive oxygen species in cancer. *Free Radic. Res.* **2010**, *44*, 479–496. [CrossRef]
67. Ferber, E.C.; Peck, B.; Delpuech, O.; Bell, G.P.; East, P.; Schulze, A. FOXO3a regulates reactive oxygen metabolism by inhibiting mitochondrial gene expression. *Cell Death Differ.* **2012**, *19*, 968–979. [CrossRef]
68. Zheng, L.; Cardaci, S.; Jerby, L.; MacKenzie, E.D.; Sciacovelli, M.; Johnson, T.I.; Gaude, E.; King, A.; Leach, J.D.G.; Edrada-Ebel, R.; et al. Fumarate induces redox-dependent senescence by modifying glutathione metabolism. *Nat. Commun.* **2015**, *6*, 6001. [CrossRef]
69. Park, J.S.; Sharma, L.K.; Li, H.; Xiang, R.; Holstein, D.; Wu, J.; Lechleiter, J.; Naylor, S.L.; Deng, J.J.; Lu, J.; et al. A heteroplasmic, not homoplasmic, mitochondrial DNA mutation promotes tumorigenesis via alteration in reactive oxygen species generation and apoptosis. *Hum. Mol. Genet.* **2009**, *18*, 1578–1589. [CrossRef]
70. Gaude, E.; Schmidt, C.; Gammage, P.A.; Dugourd, A.; Blacker, T.; Chew, S.P.; Saez-Rodriguez, J.; O'Neill, J.S.; Szabadkai, G.; Minczuk, M.; et al. NADH Shuttling Couples Cytosolic Reductive Carboxylation of Glutamine with Glycolysis in Cells with Mitochondrial Dysfunction. *Mol. Cell* **2018**, *69*, 581–593.e7. [CrossRef]
71. Redza-Dutordoir, M.; Averill-Bates, D.A. Activation of apoptosis signalling pathways by reactive oxygen species. *Biochim. Et Biophys. Acta (BBA) Mol. Cell Res.* **2016**, *1863*, 2977–2992. [CrossRef]
72. Feig, D.I.; Reid, T.M.; Loeb, L.A. Reactive oxygen species in tumorigenesis. *Cancer Res.* **1994**, *54*, 1890s–1894s. [PubMed]
73. Tafani, M.; Sansone, L.; Limana, F.; Arcangeli, T.; De Santis, E.; Polese, M.; Fini, M.; Russo, M.A. The Interplay of Reactive Oxygen Species, Hypoxia, Inflammation, and Sirtuins in Cancer Initiation and Progression. *Oxidative Med. Cell. Longev.* **2016**, *2016*, 3907147. [CrossRef] [PubMed]

74. Harris, I.S.; DeNicola, G.M. The Complex Interplay between Antioxidants and ROS in Cancer. *Trends Cell Biol.* **2020**, *30*, 440–451. [CrossRef] [PubMed]
75. Takahashi, N.; Chen, H.Y.; Harris, I.S.; Stover, D.G.; Selfors, L.M.; Bronson, R.T.; Deraedt, T.; Cichowski, K.; Welm, A.L.; Mori, Y.; et al. Cancer Cells Co-opt the Neuronal Redox-Sensing Channel TRPA1 to Promote Oxidative-Stress Tolerance. *Cancer Cell* **2018**, *33*, 985–1003.e7. [CrossRef]
76. Harris, I.S.; Treloar, A.E.; Inoue, S.; Sasaki, M.; Gorrini, C.; Lee, K.C.; Yung, K.Y.; Brenner, D.; Knobbe-Thomsen, C.B.; Cox, M.A.; et al. Glutathione and thioredoxin antioxidant pathways synergize to drive cancer initiation and progression. *Cancer Cell* **2015**, *27*, 211–222. [CrossRef]
77. DeNicola, G.M.; Chen, P.H.; Mullarky, E.; Sudderth, J.A.; Hu, Z.; Wu, D.; Tang, H.; Xie, Y.; Asara, J.M.; Huffman, K.E.; et al. NRF2 regulates serine biosynthesis in non-small cell lung cancer. *Nat. Genet.* **2015**, *47*, 1475–1481. [CrossRef]
78. Reczek, C.R.; Chandel, N.S. ROS-dependent signal transduction. *Curr. Opin. Cell Biol.* **2015**, *33*, 8–13. [CrossRef]
79. Lee, J.J.; van de Ven, R.A.H.; Zaganjor, E.; Ng, M.R.; Barakat, A.; Demmers, J.; Finley, L.W.S.; Gonzalez Herrera, K.N.; Hung, Y.P.; Harris, I.S.; et al. Inhibition of epithelial cell migration and Src/FAK signaling by SIRT3. *Proc. Natl. Acad. Sci. USA* **2018**, *115*, 7057–7062. [CrossRef]
80. Porporato, P.E.; Payen, V.L.; Pérez-Escuredo, J.; De Saedeleer, C.J.; Danhier, P.; Copetti, T.; Dhup, S.; Tardy, M.; Vazeille, T.; Bouzin, C.; et al. A mitochondrial switch promotes tumor metastasis. *Cell Rep.* **2014**, *8*, 754–766. [CrossRef]
81. Hunter, M.V.; Willoughby, P.M.; Bruce, A.E.E.; Fernandez-Gonzalez, R. Oxidative Stress Orchestrates Cell Polarity to Promote Embryonic Wound Healing. *Dev. Cell* **2018**, *47*, 377–387.e4. [CrossRef]
82. Nguyen, H.L.; Zucker, S.; Zarrabi, K.; Kadam, P.; Schmidt, C.; Cao, J. Oxidative stress and prostate cancer progression are elicited by membrane-type 1 matrix metalloproteinase. *Mol. Cancer Res. MCR* **2011**, *9*, 1305–1318. [CrossRef] [PubMed]
83. Gorrini, C.; Baniasadi, P.S.; Harris, I.S.; Silvester, J.; Inoue, S.; Snow, B.; Joshi, P.A.; Wakeham, A.; Molyneux, S.D.; Martin, B.; et al. BRCA1 interacts with Nrf2 to regulate antioxidant signaling and cell survival. *J. Exp. Med.* **2013**, *210*, 1529–1544. [CrossRef] [PubMed]
84. Jiang, H.; Sha, S.-H.; Schacht, J. Rac/Rho pathway regulates actin depolymerization induced by aminoglycoside antibiotics. *J. Neurosci. Res.* **2006**, *83*, 1544–1551. [CrossRef] [PubMed]
85. Chen, D.; Dang, B.L.; Huang, J.Z.; Chen, M.; Wu, D.; Xu, M.L.; Li, R.; Yan, G.R. MiR-373 drives the epithelial-to-mesenchymal transition and metastasis via the miR-373-TXNIP-HIF1α-TWIST signaling axis in breast cancer. *Oncotarget* **2015**, *6*, 32701–32712. [CrossRef]
86. Rhyu, D.Y.; Yang, Y.; Ha, H.; Lee, G.T.; Song, J.S.; Uh, S.T.; Lee, H.B. Role of reactive oxygen species in TGF-beta1-induced mitogen-activated protein kinase activation and epithelial-mesenchymal transition in renal tubular epithelial cells. *J. Am. Soc. Nephrol. JASN* **2005**, *16*, 667–675. [CrossRef]
87. The ATBC Cancer Prevention Study Group. The alpha-tocopherol, beta-carotene lung cancer prevention study: Design, methods, participant characteristics, and compliance. *Ann. Epidemiol.* **1994**, *4*, 1–10. [CrossRef]
88. Klein, E.A.; Thompson, I.M., Jr.; Tangen, C.M.; Crowley, J.J.; Lucia, M.S.; Goodman, P.J.; Minasian, L.M.; Ford, L.G.; Parnes, H.L.; Gaziano, J.M.; et al. Vitamin E and the risk of prostate cancer: The Selenium and Vitamin E Cancer Prevention Trial (SELECT). *JAMA* **2011**, *306*, 1549–1556. [CrossRef]
89. Wiel, C.; Le Gal, K.; Ibrahim, M.X.; Jahangir, C.A.; Kashif, M.; Yao, H.; Ziegler, D.V.; Xu, X.; Ghosh, T.; Mondal, T.; et al. BACH1 Stabilization by Antioxidants Stimulates Lung Cancer Metastasis. *Cell* **2019**, *178*, 330–345.e22. [CrossRef]
90. Lignitto, L.; LeBoeuf, S.E.; Homer, H.; Jiang, S.; Askenazi, M.; Karakousi, T.R.; Pass, H.I.; Bhutkar, A.J.; Tsirigos, A.; Ueberheide, B.; et al. Nrf2 Activation Promotes Lung Cancer Metastasis by Inhibiting the Degradation of Bach1. *Cell* **2019**, *178*, 316–329.e18. [CrossRef]
91. Cheung, E.C.; DeNicola, G.M.; Nixon, C.; Blyth, K.; Labuschagne, C.F.; Tuveson, D.A.; Vousden, K.H. Dynamic ROS Control by TIGAR Regulates the Initiation and Progression of Pancreatic Cancer. *Cancer Cell* **2020**, *37*, 168–182.e4. [CrossRef]
92. Kimmelman, A.C.; White, E. Autophagy and Tumor Metabolism. *Cell Metab.* **2017**, *25*, 1037–1043. [CrossRef]
93. Saxton, R.A.; Sabatini, D.M. mTOR Signaling in Growth, Metabolism, and Disease. *Cell* **2017**, *168*, 960–976. [CrossRef] [PubMed]

94. Goncalves, M.D.; Hopkins, B.D.; Cantley, L.C. Phosphatidylinositol 3-Kinase, Growth Disorders, and Cancer. *N. Engl. J. Med.* **2018**, *379*, 2052–2062. [CrossRef] [PubMed]
95. Ji, H.; Ramsey, M.R.; Hayes, D.N.; Fan, C.; McNamara, K.; Kozlowski, P.; Torrice, C.; Wu, M.C.; Shimamura, T.; Perera, S.A.; et al. LKB1 modulates lung cancer differentiation and metastasis. *Nature* **2007**, *448*, 807–810. [CrossRef] [PubMed]
96. Faubert, B.; Solmonson, A.; DeBerardinis, R.J. Metabolic reprogramming and cancer progression. *Sci.* **2020**, *368*, eaaw5473. [CrossRef] [PubMed]
97. Yun, J.; Rago, C.; Cheong, I.; Pagliarini, R.; Angenendt, P.; Rajagopalan, H.; Schmidt, K.; Willson, J.K.V.; Markowitz, S.; Zhou, S.; et al. Glucose Deprivation Contributes to the Development of KRAS Pathway Mutations in Tumor Cells. *Science* **2009**, *325*, 1555–1559. [CrossRef] [PubMed]
98. Sun, H.; Zhu, A.; Zhang, L.; Zhang, J.; Zhong, Z.; Wang, F. Knockdown of PKM2 Suppresses Tumor Growth and Invasion in Lung Adenocarcinoma. *Int. J. Mol. Sci.* **2015**, *16*, 24574–24587. [CrossRef] [PubMed]
99. Pavlova, N.N.; Thompson, C.B. The Emerging Hallmarks of Cancer Metabolism. *Cell Metab.* **2016**, *23*, 27–47. [CrossRef]
100. Schug, Z.T.; Peck, B.; Jones, D.T.; Zhang, Q.; Grosskurth, S.; Alam, I.S.; Goodwin, L.M.; Smethurst, E.; Mason, S.; Blyth, K.; et al. Acetyl-CoA Synthetase 2 Promotes Acetate Utilization and Maintains Cancer Cell Growth under Metabolic Stress. *Cancer Cell* **2015**, *27*, 57–71. [CrossRef]
101. Zhang, B.; Zheng, A.; Hydbring, P.; Ambroise, G.; Ouchida, A.T.; Goiny, M.; Vakifahmetoglu-Norberg, H.; Norberg, E. PHGDH Defines a Metabolic Subtype in Lung Adenocarcinomas with Poor Prognosis. *Cell Rep.* **2017**, *19*, 2289–2303. [CrossRef]
102. Zhu, J.; Ma, J.; Wang, X.; Ma, T.; Zhang, S.; Wang, W.; Zhou, X.; Shi, J. High Expression of PHGDH Predicts Poor Prognosis in Non–Small Cell Lung Cancer. *Transl. Oncol.* **2016**, *9*, 592–599. [CrossRef]
103. Possemato, R.; Marks, K.M.; Shaul, Y.D.; Pacold, M.E.; Kim, D.; Birsoy, K.; Sethumadhavan, S.; Woo, H.-K.; Jang, H.G.; Jha, A.K.; et al. Functional genomics reveal that the serine synthesis pathway is essential in breast cancer. *Nature* **2011**, *476*, 346–350. [CrossRef] [PubMed]
104. Mullarky, E.; Mattaini, K.R.; Vander Heiden, M.G.; Cantley, L.C.; Locasale, J.W. PHGDH amplification and altered glucose metabolism in human melanoma. *Pigment Cell Melanoma Res.* **2011**, *24*, 1112–1115. [CrossRef] [PubMed]
105. Maddocks, O.D.K.; Athineos, D.; Cheung, E.C.; Lee, P.; Zhang, T.; van den Broek, N.J.F.; Mackay, G.M.; Labuschagne, C.F.; Gay, D.; Kruiswijk, F.; et al. Modulating the therapeutic response of tumours to dietary serine and glycine starvation. *Nature* **2017**, *544*, 372–376. [CrossRef] [PubMed]
106. Kanarek, N.; Petrova, B.; Sabatini, D.M. Dietary modifications for enhanced cancer therapy. *Nature* **2020**, *579*, 507–517. [CrossRef] [PubMed]
107. Bose, S.; Allen, A.E.; Locasale, J.W. The Molecular Link from Diet to Cancer Cell Metabolism. *Mol. Cell* **2020**, *78*, 1034–1044. [CrossRef] [PubMed]
108. Tajan, M.; Vousden, K.H. Dietary Approaches to Cancer Therapy. *Cancer Cell* **2020**, *37*, 767–785. [CrossRef] [PubMed]
109. Kato, Y.; Lambert, C.A.; Colige, A.C.; Mineur, P.; Noël, A.; Frankenne, F.; Foidart, J.M.; Baba, M.; Hata, R.; Miyazaki, K.; et al. Acidic extracellular pH induces matrix metalloproteinase-9 expression in mouse metastatic melanoma cells through the phospholipase D-mitogen-activated protein kinase signaling. *J. Biol. Chem.* **2005**, *280*, 10938–10944. [CrossRef]
110. Estrella, V.; Chen, T.; Lloyd, M.; Wojtkowiak, J.; Cornnell, H.H.; Ibrahim-Hashim, A.; Bailey, K.; Balagurunathan, Y.; Rothberg, J.M.; Sloane, B.F.; et al. Acidity Generated by the Tumor Microenvironment Drives Local Invasion. *Cancer Res.* **2013**, *73*, 1524–1535. [CrossRef]
111. Tardito, S.; Oudin, A.; Ahmed, S.U.; Fack, F.; Keunen, O.; Zheng, L.; Miletic, H.; Sakariassen, P.Ø.; Weinstock, A.; Wagner, A.; et al. Glutamine synthetase activity fuels nucleotide biosynthesis and supports growth of glutamine-restricted glioblastoma. *Nat. Cell Biol.* **2015**, *17*, 1556–1568. [CrossRef]
112. Zhang, W.; Trachootham, D.; Liu, J.; Chen, G.; Pelicano, H.; Garcia-Prieto, C.; Lu, W.; Burger, J.A.; Croce, C.M.; Plunkett, W.; et al. Stromal control of cystine metabolism promotes cancer cell survival in chronic lymphocytic leukaemia. *Nat. Cell Biol.* **2012**, *14*, 276–286. [CrossRef] [PubMed]
113. Sousa, C.M.; Biancur, D.E.; Wang, X.; Halbrook, C.J.; Sherman, M.H.; Zhang, L.; Kremer, D.; Hwang, R.F.; Witkiewicz, A.K.; Ying, H.; et al. Pancreatic stellate cells support tumour metabolism through autophagic alanine secretion. *Nature* **2016**, *536*, 479–483. [CrossRef] [PubMed]

114. Becker, L.M.; O'Connell, J.T.; Vo, A.P.; Cain, M.P.; Tampe, D.; Bizarro, L.; Sugimoto, H.; McGow, A.K.; Asara, J.M.; Lovisa, S.; et al. Epigenetic Reprogramming of Cancer-Associated Fibroblasts Deregulates Glucose Metabolism and Facilitates Progression of Breast Cancer. *Cell Rep.* **2020**, *31*, 107701. [CrossRef] [PubMed]
115. Curtis, M.; Kenny, H.A.; Ashcroft, B.; Mukherjee, A.; Johnson, A.; Zhang, Y.; Helou, Y.; Batlle, R.; Liu, X.; Gutierrez, N.; et al. Fibroblasts Mobilize Tumor Cell Glycogen to Promote Proliferation and Metastasis. *Cell Metab.* **2019**, *29*, 141–155.e9. [CrossRef]
116. Park, J.S.; Burckhardt, C.J.; Lazcano, R.; Solis, L.M.; Isogai, T.; Li, L.; Chen, C.S.; Gao, B.; Minna, J.D.; Bachoo, R.; et al. Mechanical regulation of glycolysis via cytoskeleton architecture. *Nature* **2020**, *578*, 621–626. [CrossRef]
117. Rudzka, D.A.; Spennati, G.; McGarry, D.J.; Chim, Y.-H.; Neilson, M.; Ptak, A.; Munro, J.; Kalna, G.; Hedley, A.; Moralli, D.; et al. Migration through physical constraints is enabled by MAPK-induced cell softening via actin cytoskeleton re-organization. *J. Cell Sci.* **2019**, *132*, jcs224071. [CrossRef]
118. Bayer, S.V.; Grither, W.R.; Brenot, A.; Hwang, P.Y.; Barcus, C.E.; Ernst, M.; Pence, P.; Walter, C.; Pathak, A.; Longmore, G.D. DDR2 controls breast tumor stiffness and metastasis by regulating integrin mediated mechanotransduction in CAFs. *Elife* **2019**, *8*, e45508. [CrossRef]
119. Zanotelli, M.R.; Rahman-Zaman, A.; VanderBurgh, J.A.; Taufalele, P.V.; Jain, A.; Erickson, D.; Bordeleau, F.; Reinhart-King, C.A. Energetic costs regulated by cell mechanics and confinement are predictive of migration path during decision-making. *Nat. Commun.* **2019**, *10*, 4185. [CrossRef]
120. Nikolaou, S.; Machesky, L.M. The stressful tumour environment drives plasticity of cell migration programmes, contributing to metastasis. *J. Pathol.* **2020**, *250*, 612–623. [CrossRef]
121. Velez, D.O.; Ranamukhaarachchi, S.K.; Kumar, A.; Modi, R.N.; Lim, E.W.; Engler, A.J.; Metallo, C.M.; Fraley, S.I. 3D collagen architecture regulates cell adhesion through degradability, thereby controlling metabolic and oxidative stress. *Integr. Biol. Quant. Biosci. Nano Macro* **2019**, *11*, 221–234. [CrossRef]
122. Sullivan, W.J.; Mullen, P.J.; Schmid, E.W.; Flores, A.; Momcilovic, M.; Sharpley, M.S.; Jelinek, D.; Whiteley, A.E.; Maxwell, M.B.; Wilde, B.R.; et al. Extracellular Matrix Remodeling Regulates Glucose Metabolism through TXNIP Destabilization. *Cell* **2018**, *175*, 117–132.e21. [CrossRef] [PubMed]
123. Kim, N.H.; Cha, Y.H.; Lee, J.; Lee, S.-H.; Yang, J.H.; Yun, J.S.; Cho, E.S.; Zhang, X.; Nam, M.; Kim, N.; et al. Snail reprograms glucose metabolism by repressing phosphofructokinase PFKP allowing cancer cell survival under metabolic stress. *Nat. Commun.* **2017**, *8*, 14374. [CrossRef] [PubMed]
124. Wang, X.; Liu, R.; Zhu, W.; Chu, H.; Yu, H.; Wei, P.; Wu, X.; Zhu, H.; Gao, H.; Liang, J.; et al. UDP-glucose accelerates SNAI1 mRNA decay and impairs lung cancer metastasis. *Nature* **2019**, *571*, 127–131. [CrossRef] [PubMed]
125. Ahmad, A.; Aboukameel, A.; Kong, D.; Wang, Z.; Sethi, S.; Chen, W.; Sarkar, F.H.; Raz, A. Phosphoglucose Isomerase/Autocrine Motility Factor Mediates Epithelial-Mesenchymal Transition Regulated by miR-200 in Breast Cancer Cells. *Cancer Res.* **2011**, *71*, 3400–3409. [CrossRef] [PubMed]
126. Miranda-Gonçalves, V.; Lameirinhas, A.; Macedo-Silva, C.; Lobo, J.; Paula, C.D.; Ferreira, V.; Henrique, R.; Jerónimo, C. Lactate Increases Renal Cell Carcinoma Aggressiveness through Sirtuin 1-Dependent Epithelial Mesenchymal Transition Axis Regulation. *Cells* **2020**, *9*, 1053. [CrossRef] [PubMed]
127. Knott, S.R.V.; Wagenblast, E.; Khan, S.; Kim, S.Y.; Soto, M.; Wagner, M.; Turgeon, M.-O.; Fish, L.; Erard, N.; Gable, A.L.; et al. Asparagine bioavailability governs metastasis in a model of breast cancer. *Nature* **2018**, *554*, 378–381. [CrossRef] [PubMed]
128. Slowicka, K.; Petta, I.; Blancke, G.; Hoste, E.; Dumas, E.; Sze, M.; Vikkula, H.; Radaelli, E.; Haigh, J.J.; Jonckheere, S.; et al. Zeb2 drives invasive and microbiota-dependent colon carcinoma. *Nat. Cancer* **2020**, *1*, 620–634. [CrossRef]
129. Kadosh, E.; Snir-Alkalay, I.; Venkatachalam, A.; May, S.; Lasry, A.; Elyada, E.; Zinger, A.; Shaham, M.; Vaalani, G.; Mernberger, M.; et al. The gut microbiome switches mutant p53 from tumour-suppressive to oncogenic. *Nature* **2020**. [CrossRef]
130. Tasdogan, A.; Faubert, B.; Ramesh, V.; Ubellacker, J.M.; Shen, B.; Solmonson, A.; Murphy, M.M.; Gu, Z.; Gu, W.; Martin, M.; et al. Metabolic heterogeneity confers differences in melanoma metastatic potential. *Nature* **2020**, *577*, 115–120. [CrossRef]
131. Chen, W.; Hoffmann, A.D.; Liu, H.; Liu, X. Organotropism: New insights into molecular mechanisms of breast cancer metastasis. *npj Precis. Oncol.* **2018**, *2*, 4. [CrossRef]

132. Schild, T.; Low, V.; Blenis, J.; Gomes, A.P. Unique Metabolic Adaptations Dictate Distal Organ-Specific Metastatic Colonization. *Cancer Cell* **2018**, *33*, 347–354. [CrossRef] [PubMed]
133. Smith, H.A.; Kang, Y. Determinants of Organotropic Metastasis. *Annu. Rev. Cancer Biol.* **2017**, *1*, 403–423. [CrossRef]
134. Gao, Y.; Bado, I.; Wang, H.; Zhang, W.; Rosen, J.M.; Zhang, X.H.F. Metastasis Organotropism: Redefining the Congenial Soil. *Dev. Cell* **2019**, *49*, 375–391. [CrossRef]
135. Fischer, G.M.; Jalali, A.; Kircher, D.A.; Lee, W.-C.; McQuade, J.L.; Haydu, L.E.; Joon, A.Y.; Reuben, A.; de Macedo, M.P.; Carapeto, F.C.L.; et al. Molecular Profiling Reveals Unique Immune and Metabolic Features of Melanoma Brain Metastases. *Cancer Discov.* **2019**, *9*, 628–645. [CrossRef]
136. Commander, R.; Wei, C.; Sharma, A.; Mouw, J.K.; Burton, L.J.; Summerbell, E.; Mahboubi, D.; Peterson, R.J.; Konen, J.; Zhou, W.; et al. Subpopulation targeting of pyruvate dehydrogenase and GLUT1 decouples metabolic heterogeneity during collective cancer cell invasion. *Nat. Commun.* **2020**, *11*, 1533. [CrossRef] [PubMed]
137. Christen, S.; Lorendeau, D.; Schmieder, R.; Broekaert, D.; Metzger, K.; Veys, K.; Elia, I.; Buescher, J.M.; Orth, M.F.; Davidson, S.M.; et al. Breast Cancer-Derived Lung Metastases Show Increased Pyruvate Carboxylase-Dependent Anaplerosis. *Cell Rep.* **2016**, *17*, 837–848. [CrossRef] [PubMed]
138. Lao-On, U.; Rojvirat, P.; Chansongkrow, P.; Phannasil, P.; Siritutsoontorn, S.; Charoensawan, V.; Jitrapakdee, S. c-Myc directly targets an over-expression of pyruvate carboxylase in highly invasive breast cancer. *Biochim. Et Biophys. Acta (BBA) Mol. Basis Dis.* **2020**, *1866*, 165656. [CrossRef]
139. Elia, I.; Rossi, M.; Stegen, S.; Broekaert, D.; Doglioni, G.; van Gorsel, M.; Boon, R.; Escalona-Noguero, C.; Torrekens, S.; Verfaillie, C.; et al. Breast cancer cells rely on environmental pyruvate to shape the metastatic niche. *Nature* **2019**, *568*, 117–121. [CrossRef] [PubMed]
140. Chaneton, B.; Hillmann, P.; Zheng, L.; Martin, A.C.L.; Maddocks, O.D.K.; Chokkathukalam, A.; Coyle, J.E.; Jankevics, A.; Holding, F.P.; Vousden, K.H.; et al. Serine is a natural ligand and allosteric activator of pyruvate kinase M2. *Nature* **2012**, *491*, 458–462. [CrossRef]
141. Reid, M.A.; Dai, Z.; Locasale, J.W. The impact of cellular metabolism on chromatin dynamics and epigenetics. *Nat. Cell Biol.* **2017**, *19*, 1298–1306. [CrossRef]
142. Nelson, D.L.; Cox, M.M. *Lehninger Principles of Biochemistry*, 7th ed.; W.H. Freeman and Company: New York, NY, USA, 2017.
143. Meiser, J.; Tumanov, S.; Maddocks, O.; Labuschagne, C.F.; Athineos, D.; Van Den Broek, N.; Mackay, G.M.; Gottlieb, E.; Blyth, K.; Vousden, K.; et al. Serine one-carbon catabolism with formate overflow. *Sci. Adv.* **2016**, *2*, e1601273. [CrossRef] [PubMed]
144. Tibbetts, A.S.; Appling, D.R. Compartmentalization of Mammalian folate-mediated one-carbon metabolism. *Annu. Rev. Nutr.* **2010**, *30*, 57–81. [CrossRef] [PubMed]
145. Mandella, R.D.; Sauer, L.A. The mitochondrial malic enzymes. I. Submitochondrial localization and purification and properties of the NAD(P)+-dependent enzyme from adrenal cortex. *J. Biol. Chem.* **1975**, *250*, 5877–5884. [PubMed]
146. Jiang, P.; Du, W.; Mancuso, A.; Wellen, K.E.; Yang, X. Reciprocal regulation of p53 and malic enzymes modulates metabolism and senescence. *Nature* **2013**, *493*, 689–693. [CrossRef]
147. Pongratz, R.L.; Kibbey, R.G.; Shulman, G.I.; Cline, G.W. Cytosolic and mitochondrial malic enzyme isoforms differentially control insulin secretion. *J. Biol. Chem.* **2007**, *282*, 200–207. [CrossRef]
148. Liu, X.; Cooper, D.E.; Cluntun, A.A.; Warmoes, M.O.; Zhao, S.; Reid, M.A.; Liu, J.; Lund, P.J.; Lopes, M.; Garcia, B.A.; et al. Acetate Production from Glucose and Coupling to Mitochondrial Metabolism in Mammals. *Cell* **2018**, *175*, 502–513.e13. [CrossRef]
149. Jiang, L.; Shestov, A.A.; Swain, P.; Yang, C.; Parker, S.J.; Wang, Q.A.; Terada, L.S.; Adams, N.D.; McCabe, M.T.; Pietrak, B.; et al. Reductive carboxylation supports redox homeostasis during anchorage-independent growth. *Nature* **2016**, *532*, 255–258. [CrossRef]
150. Fan, J.; Kamphorst, J.J.; Mathew, R.; Chung, M.K.; White, E.; Shlomi, T.; Rabinowitz, J.D. Glutamine-driven oxidative phosphorylation is a major ATP source in transformed mammalian cells in both normoxia and hypoxia. *Mol. Syst. Biol.* **2013**, *9*, 712. [CrossRef]
151. Alberts, B.; Johnson, A.; Lewis, J.; Morgan, D.; Raff, M.; Roberts, K.; Walter, P. *Molecular Biology of the Cell*, 6th ed.; Garland Science: New York, NY, USA, 2015.

152. Traverso, N.; Ricciarelli, R.; Nitti, M.; Marengo, B.; Furfaro, A.L.; Pronzato, M.A.; Marinari, U.M.; Domenicotti, C. Role of glutathione in cancer progression and chemoresistance. *Oxidative Med. Cell. Longev.* **2013**, *2013*, 972913. [CrossRef]
153. Van der Reest, J.; Lilla, S.; Zheng, L.; Zanivan, S.; Gottlieb, E. Proteome-wide analysis of cysteine oxidation reveals metabolic sensitivity to redox stress. *Nat. Commun.* **2018**, *9*, 1581. [CrossRef]
154. Balsa, E.; Perry, E.A.; Bennett, C.F.; Jedrychowski, M.; Gygi, S.P.; Doench, J.G.; Puigserver, P. Defective NADPH production in mitochondrial disease complex I causes inflammation and cell death. *Nat. Commun.* **2020**, *11*, 2714. [CrossRef]
155. Chen, L.; Zhang, Z.; Hoshino, A.; Zheng, H.D.; Morley, M.; Arany, Z.; Rabinowitz, J.D. NADPH production by the oxidative pentose-phosphate pathway supports folate metabolism. *Nat. Metab.* **2019**, *1*, 404–415. [CrossRef]
156. Labuschagne, C.F.; Cheung, E.C.; Blagih, J.; Domart, M.C.; Vousden, K.H. Cell Clustering Promotes a Metabolic Switch that Supports Metastatic Colonization. *Cell Metab.* **2019**, *30*, 720–734.e5. [CrossRef]
157. Gameiro, P.A.; Laviolette, L.A.; Kelleher, J.K.; Iliopoulos, O.; Stephanopoulos, G. Cofactor Balance by Nicotinamide Nucleotide Transhydrogenase (NNT) Coordinates Reductive Carboxylation and Glucose Catabolism in the Tricarboxylic Acid (TCA) Cycle. *J. Biol. Chem.* **2013**, *288*, 12967–12977. [CrossRef]
158. Ward, N.P.; Kang, Y.P.; Falzone, A.; Boyle, T.A.; DeNicola, G.M. Nicotinamide nucleotide transhydrogenase regulates mitochondrial metabolism in NSCLC through maintenance of Fe-S protein function. *J. Exp. Med.* **2020**, *217*, e20191698. [CrossRef]
159. Meiser, J.; Vazquez, A. Give it or take it: The flux of one-carbon in cancer cells. *FEBS J.* **2016**, *283*, 3695–3704. [CrossRef]
160. Brosnan, M.E.; Brosnan, J.T. Formate: The Neglected Member of One-Carbon Metabolism. *Annu. Rev. Nutr.* **2016**, *36*, 369–388. [CrossRef]
161. Sanderson, S.M.; Gao, X.; Dai, Z.; Locasale, J.W. Methionine metabolism in health and cancer: A nexus of diet and precision medicine. *Nat. Rev. Cancer* **2019**, *19*, 625–637. [CrossRef]
162. Locasale, J.W. Serine, glycine and one-carbon units: Cancer metabolism in full circle. *Nat. Rev. Cancer* **2013**, *13*, 572–583. [CrossRef]
163. Milo, R.; Phillips, R. *Cell Biology by the Numbers*; Garland Science: New York, NY, USA, 2015.
164. Ducker, G.S.; Chen, L.; Morscher, R.J.; Ghergurovich, J.M.; Esposito, M.; Teng, X.; Kang, Y.; Rabinowitz, J.D. Reversal of Cytosolic One-Carbon Flux Compensates for Loss of the Mitochondrial Folate Pathway. *Cell Metab.* **2016**, *23*, 1140–1153. [CrossRef]
165. Mak, T.W.; Grusdat, M.; Duncan, G.S.; Dostert, C.; Nonnenmacher, Y.; Cox, M.; Binsfeld, C.; Hao, Z.; Brüstle, A.; Itsumi, M.; et al. Glutathione Primes T Cell Metabolism for Inflammation. *Immunity* **2017**, *46*, 675–689. [CrossRef]
166. Smith, G.K.; Banks, S.D.; Monaco, T.J.; Rigual, R.; Duch, D.S.; Mullin, R.J.; Huber, B.E. Activity of an NAD-dependent 5,10-methylenetetrahydrofolate dehydrogenase in normal tissue, neoplastic cells, and oncogene-transformed cells. *Arch. Biochem. Biophys.* **1990**, *283*, 367–371. [CrossRef]
167. Shin, M.; Momb, J.; Appling, D.R. Human mitochondrial MTHFD2 is a dual redox cofactor-specific methylenetetrahydrofolate dehydrogenase/methenyltetrahydrofolate cyclohydrolase. *Cancer Metab.* **2017**, *5*, 11. [CrossRef]
168. Bao, X.R.; Ong, S.E.; Goldberger, O.; Peng, J.; Sharma, R.; Thompson, D.A.; Vafai, S.B.; Cox, A.G.; Marutani, E.; Ichinose, F.; et al. Mitochondrial dysfunction remodels one-carbon metabolism in human cells. *Elife* **2016**, *5*, e10575. [CrossRef]
169. Yang, L.; Garcia Canaveras, J.C.; Chen, Z.; Wang, L.; Liang, L.; Jang, C.; Mayr, J.A.; Zhang, Z.; Ghergurovich, J.M.; Zhan, L.; et al. Serine Catabolism Feeds NADH when Respiration Is Impaired. *Cell Metab.* **2020**, *31*, 809–821.e6. [CrossRef]
170. Meiser, J.; Schuster, A.; Pietzke, M.; Vande Voorde, J.; Athineos, D.; Oizel, K.; Burgos-Barragan, G.; Wit, N.; Dhayade, S.; Morton, J.P.; et al. Increased formate overflow is a hallmark of oxidative cancer. *Nat. Commun.* **2018**, *9*, 1368. [CrossRef]
171. Lewis, C.A.; Parker, S.J.; Fiske, B.P.; McCloskey, D.; Gui, D.Y.; Green, C.R.; Vokes, N.I.; Feist, A.M.; Vander Heiden, M.G.; Metallo, C.M. Tracing compartmentalized NADPH metabolism in the cytosol and mitochondria of mammalian cells. *Mol. Cell* **2014**, *55*, 253–263. [CrossRef]

172. Fan, J.; Ye, J.; Kamphorst, J.J.; Shlomi, T.; Thompson, C.B.; Rabinowitz, J.D. Quantitative flux analysis reveals folate-dependent NADPH production. *Nature* **2014**, *510*, 298–302. [CrossRef]
173. Pietzke, M.; Meiser, J.; Vazquez, A. Formate metabolism in health and disease. *Mol. Metab.* **2020**, *33*, 23–37. [CrossRef]



© 2020 by the authors. Licensee MDPI, Basel, Switzerland. This article is an open access article distributed under the terms and conditions of the Creative Commons Attribution (CC BY) license (http://creativecommons.org/licenses/by/4.0/).

CHAPTER 3: PKM2 diverts glycolytic flux in dependence on mitochondrial one-carbon cycle

BENZARTI, M., OUDIN, A., VIRY, E., GARGIULO, E., SCHMOETTEN, M., NEISES, L., PULIDO, C., LORENZ, N. I., RONELLENFITSCH, M. W., SUMPTON, D., WARMOES, M., JAEGER, C., LESUR, A., MOUSSAY, E., PAGGETTI, J., NICLOU, S.P., LETELLIER, E., MEISER, J.

2023. Submitted to Cell Reports and is currently available on BioRxiv:

https://www.biorxiv.org/content/10.1101/2023.01.23.525168v1.full.pdf

3.1. Preface

The TME is known to be depleted in nutrients due to increased biosynthetic demands and poor vascularization. However, cancer cells are able to withstand such hostile metabolic environment due to their superior metabolic flexibility and plasticity. *In vitro* studies are conducted in media which contain supraphysiological concentrations of multiple metabolites including glucose. This forces the cells into aerobic glycolysis and limit the ability to study their metabolic flexibility. In this manuscript we aimed to uncover the metabolic potential of cancer cells under glycolytic limitation and in doing so addressing aim one, two, four and five of my thesis. Previous studies of glycolytic stress have used media that did not contain glucose i.e. complete glucose starvation. However, when we look at the *in vivo* situation, the disorganized vasculature means that certain areas of the tumor will experience limited glucose supply rather than full starvation. This means that these areas will rapidly consume the available glucose, which will then be replenished via the circulation. *In vitro*, we are able to mimic this glycolytic limitation by substituting glucose with galactose in the media, as galactose is metabolized with slower kinetics as highlighted in chapter one.

Firstly, we confirmed that cancer cells are able to metabolize galactose and use it to support early glycolysis (aim one). Subsequently, we showed that cancer cells rewire their limited carbon supply towards 1C cycle (aim 2) and this rewiring supports proliferation and viability of cancer cells alongside the metabolic functions of the 1C cycle (aim four and five).

3.2. Personal contribution

This manuscript represents the majority of my PhD work. For the *in vitro* part, I performed all the experiments, analyzed the data generated and created the corresponding figures. For the genetically modified cell lines, MDA-MB-468 cells harboring a genetic deletion of either MTHFD1L, MTHFD2 or ALDH1L2 were available in our lab. AMPK double knockout in LN-229 cells were kindly provided by our collaborators. I generated the phosphoenolpyruvate carboxykinase 2 (PEPCK2) knockout and knockdown cell lines used in this manuscript. The metabolomics samples were generated by me, their measurement was conducted across three different metabolomics platforms and data analysis and interpretation was done by me. For the *in vivo* part (Figure 8), I helped in the take down process and sample collection, I then processed the samples and analyzed the generated data. I created all the figures and wrote the draft of the manuscript that was then reviewed by all the co-authors prior to the submission.

3.3. Manuscript

PKM2 diverts glycolytic flux in dependence on mitochondrial one-carbon cycle

Mohaned Benzarti[1,2], Anais Oudin[3], Elodie Viry[4], Ernesto Gargiulo[4], Maryse Schmoetten[5], Laura Neises[1], Coralie Pulido[6], Nadia I. Lorenz[7-10], Michael W. Ronellenfitsch[7-10], David Sumpton[11], Marc Warmoes[12], Christian Jaeger[12], Antoine Lesur[1], Etienne Moussay[4], Jerome Paggetti[4], Simone P. Niclou[2,3], Elisabeth Letellier[5], Johannes Meiser[1]*

[1]Cancer Metabolism Group, Department of Cancer Research, Luxembourg Institute of Health, Luxembourg, Luxembourg.

[2]Faculty of Science, Technology and Medicine, University of Luxembourg, 2 avenue de Université, Esch-sur-Alzette, Luxembourg.

[3]NORLUX Neuro-Oncology Laboratory, Department of Cancer Research, Luxembourg Institute of Health, Luxembourg, Luxembourg.

[4]Tumor Stroma Interactions, Department of Cancer Research, Luxembourg Institute of Health, Luxembourg, Luxembourg.

[5]Molecular Disease Mechanisms Group, Faculty of Science, Technology and Medicine, Department of Life Sciences and Medicine, University of Luxembourg, Esch-sur-Alzette, Luxembourg.

[6]Animal Facility, Department of Cancer Research, Luxembourg Institute of Health, Luxembourg, Luxembourg

[7]Dr. Senckenberg Institute of Neurooncology, University Hospital Frankfurt, Goethe University, Frankfurt am Main, Germany.

[8]German Cancer Consortium, Partner Site Frankfurt/Mainz, Frankfurt am Main, Germany;

[9]Frankfurt Cancer Institute (FCI), University Hospital Frankfurt, Goethe University, Frankfurt am Main, Germany.

[10]University Cancer Center Frankfurt (UCT), University Hospital Frankfurt, Goethe University, Frankfurt am Main, Germany.

[11]Cancer Research U.K. Beatson Institute, Switchback Rd, Bearsden, Glasgow G61 1BD, UK.

[12]Luxembourg Centre for Systems Biomedicine, University of Luxembourg, 6 Avenue du Swing, 4367 Esch-sur-Alzette, Luxembourg.

*Correspondence:

Email: johannes.meiser@lih.lu

Twitter: @JohannesMeiser

Abstract

Throughout the metastatic cascade, cancer cells are faced with harsh metabolic environments and nutritional stresses which apply selection pressure leaving only the most metabolically resilient cells to survive and form metastases. Metabolic characterisation of such cell populations *in vitro* is currently challenging. Using galactose as a tool compound to mimic glycolytic limitation within the tumour microenvironment of primary and secondary neoplastic sites, we were able to uncover metabolic flexibility and plasticity of cancer cells *in vitro*. In contrast to the established idea that high glycolytic flux and expression of dimeric PKM2 redirects carbons towards anabolic routes such as the pentose phosphate pathway and serine synthesis pathway (SSP), we have discovered by using stable-isotope tracing that also glycolytic limitation results in metabolic rewiring. Surprisingly, despite limited carbon availability and energetic stress, cells induce a near complete block of pyruvate kinase isozyme M2 (PKM2) to divert carbons towards SSP. Simultaneously, TCA cycle flux is sustained and oxygen consumption is increased, both supported by glutamine. Glutamine not only supports TCA cycle flux but also SSP via distinct mechanisms. Due to PKM2 block, malic enzyme exclusively supports TCA cycle flux while mitochondrial phosphoenolpyruvate carboxykinase supports SSP. Moreover, by using genetic modifications of different one-carbon (1C) cycle enzymes, we are able to reverse the PKM2 block suggesting a link between mitochondrial 1C cycle and pyruvate kinase. Thus we show that PKM2 inhibition acts as a branching point to direct glycolytic and glutamine carbons into distinct routes, overall supporting the metabolic plasticity and flexibility of cancer cells.

Introduction

Increased aerobic glycolysis has been identified as a characteristic of cancer cells almost 100 years ago and subsequently highlighted as a hallmark of cancer (*1-3*). This is the phenomenon whereby cancer cells increase the fermentation of glucose to lactate even in the presence of oxygen, at the cost of releasing and thereby losing carbons as lactate (*4*). Many theories have been suggested as to why cancer cells adopt such a biomass-wasteful and energy-inefficient phenotype with the majority of these theories circulating around the idea that mitochondria are unable to cope with very high rates of early glycolytic reactions that are driven by oncogenic signalling (*5-10*). In these early steps of glycolysis, NAD^+ and ATP are consumed and need to be regenerated for glycolysis to continue. This regeneration of NAD^+ and ATP seems to be the decisive bottleneck where the cancer cell has to decide whether to ferment glucose or oxidise it fully in the TCA cycle (*9, 11-13*). Indeed, two recent publications highlighted how aerobic glycolysis rates are decided based on NADH shuttle capacity and the regeneration of NAD^+ (*12, 13*). Moreover, it was proposed that cells downregulate mitochondrial respiration to avoid ATP depletion when the mitochondria are unable to replenish ATP used in the early steps of glycolysis fast enough. Therefore, cells turn to ATP generation via lactate overflow to avoid an ATP crisis (*4, 9, 11*).

While it has been suggested that aerobic glycolysis is not the main driver of high proliferation rates (*13*), it remains undeniable that cancer cells engage high proliferative rates in favourable metabolic environments with ampleness of glucose being an example of such environments. Therefore, *in vitro* it might seem that cancer cells are fixed on aerobic glycolysis, while *in vivo* they actually display metabolic flexibility and plasticity (*14*). This is to survive nutrient depleted and hostile metabolic environments within the local tumour microenvironment (TME) and along the metastatic cascade (*15*). However, such metabolic flexibility is usually masked within *in vitro* studies due to the usage of synthetic media containing supraphysiological concentrations of various metabolites (*16*). Aerobic glycolysis can be caused *in vitro* as cancer cells become reversibly addicted to glycolysis and repress their mitochondrial respiration in response to high glucose concentration in their respective media i.e. the Crabtree effect (*11, 17*).

One method to circumvent this glycolytic addiction and to unmask cancer cells metabolic flexibility *in vitro* is to substitute glucose for galactose. Galactose is metabolised via the Leloir pathway to produce glucose 6-phosphate (G6P), meaning that it can support glycolysis (*18*). While glucose is converted into G6P in a one-step reaction by hexokinase (Km ~ 0.3 mM) (*19, 20*), galactose requires four biochemical reactions to continuously supply the cell with G6P with the initial reaction catalysed by galactosekinase having a Km value three times higher than hexokinase (galactokinase Km ~ 1 mM) (*21*). This results in galactose providing a slow, yet continuous, supply of carbons, mimicking the TME where glucose is rapidly consumed but continuously being replenished via circulation (*22, 23*). Therefore, we used galactose as an *in vitro* tool compound to mimic glycolytic limitation that occurs within the TME.

We have previously shown that cancer cells increase serine catabolism and formate overflow under glycolytic limitation even though biosynthetic demands were decreased (*24*), indicating a role for one-carbon (1C) cycle in bioenergetics and redox balance (*25*). However, the functional advantage and the exact source of carbons for the increased serine catabolism and formate overflow under glycolytic limitation remains unknown. Moreover, it was previously highlighted that glutamine flux is rewired towards serine synthesis pathway (SSP) under glucose starvation via phosphoenolpyruvate carboxykinase 2 (PEPCK2) (*26-29*). Both observations indicate that metabolic rewiring takes place towards SSP under glycolytic limitation, yet the exact mechanisms and metabolic advantages of this rewiring remain unclear. Building on these observations, we used stable-isotopic tracers and targeted metabolomics to study the metabolic fluxes of central carbon metabolism and the rewiring that takes place under glycolytic limitation. By using galactose to model glycolytic limitation, we observed a continued but decreased flux through glycolysis while oxygen consumption rates (OCR) were increased (*24*). We were able to corroborate previous findings on the rewiring of glutamine metabolism towards SSP via PEPCK2. Surprisingly and despite increased OCR, galactose derived carbons did not enter the TCA cycle for mitochondrial oxidation, suggesting glutamine is the main substrate to support the TCA cycle in these conditions. This block on glycolytic carbons toward mitochondrial metabolism is facilitated by a strong pyruvate kinase isozyme M2 (PKM2) block, pinpointing PKM2 as the rewiring point in glycolysis under glycolytic limitation. Furthermore, we observed that the PKM2 block redirects the limited glycolytic carbons toward SSP to support the survival and proliferation of cancer cells. Finally, we observed an upregulation of the mitochondrial enzymes of 1C cycle where they cooperate to support biosynthesis, bioenergetics and redox balance under glycolytic limitation. These findings reveal that 1C cycle is needed for the proliferation of cancer cells when faced with limited glycolytic supply, and blocking lower glycolysis at PKM2 contributes to keeping the 1C cycle running in these conditions.

Results

Cancer cells metabolize galactose and utilize it to support early glycolysis

To ascertain that cancer cells are able to metabolize galactose (Gal), we used a fully labelled [U-^{13}C] Gal tracer and compared the relative flux through the Leloir pathway (Fig. 1A) and early glycolysis to the fluxes measured when a [U-^{13}C] glucose (Glc) tracer is used (Fig. 1B). The relative flux to UDP-glucose and UDP-galactose was comparable between Glc and Gal tracing and even higher in the case of glucose 1-phosphate in Gal (Fig. 1C-E). When looking at the glycolytic intermediate fructose 1,6-bisphosphate (F 1,6-BP), the ^{13}C enrichment was comparable between both tracers suggesting a similar flux of Glc and Gal (Fig. 1F). Pentose phosphate pathway (PPP) is usually highly enriched with ^{13}C within the first minutes of [U-^{13}C] Glc tracing (*30*). Consequently, we saw high enrichments using [U-^{13}C] Gal tracing in early PPP intermediate 6-phosphogluconate M+6 (Fig. 1G). However, the ^{13}C enrichment in ribose 5-phosphate (R5P) and sedoheptulose 7-phosphate (S7P) showed multiple labelled isotopologues

indicating higher shunting of carbons between PPP, early glycolysis and gluconeogenesis in Gal conditions (Fig. 1H, I). Overall, these data demonstrate that cancer cells are able to utilise Gal to fuel early glycolysis and PPP intermediates through the Leloir pathway.

Glutamine and lactate maintain an upregulated oxidative TCA cycle function under glycolytic limitation

To test the validity of using Gal as a tool compound to mimic glycolytic limitation, we sought to first measure the contribution of other carbon sources to the TCA cycle that might support the elevated mitochondrial metabolism under Gal as characterized by increased oxygen consumption rates (OCR) (*24*) (Fig. S1A). It was previously shown that glutamine anaplerosis into the TCA cycle is increased under full glucose starvation (*29, 31*). To test if this is also the case upon limited glycolytic flux (compared to full starvation), we first measured glutamine consumption and observed generally no striking change in the consumption in multiple cancer cell lines under glycolytic limitation (Fig. 2A). Subsequently, we performed [U-^{13}C] glutamine tracing in MDA-MB-468, 4T1 and B16-F10 cell lines in Glc and Gal. Upon Gal, we noted an increased relative flux from glutamine into the TCA cycle metabolites in all three cell lines (Fig. 2B-D), indicating that while the absolute consumption was not changed, the usage of glutamine flux is altered. Under Glc, we observed that glutamine enrichment in the TCA cycle metabolites decreased as we move away from glutamine. In contrast, the enrichment remains unchanged under Gal (Fig. 2B-D), indicating that the TCA cycle is running with strongly reduced carbon input from glycolysis. Yet, acetyl-CoA input is required to sustain glutamine oxidation through the TCA cycle, hinting towards malic enzyme (ME) activity to sustain pyruvate levels under glycolytic limitation. ME decarboxylates malate into pyruvate and indeed, we observed a substantial M+3 labelling of pyruvate and lactate from [U-^{13}C] glutamine under glycolytic limitation (Fig. 2E and S1B). ME involvement is further supported by an increase in citrate M+6 isotopologue enrichment from glutamine under Gal which suggests increased usage of glutamine derived acetyl-CoA for citrate (Fig. 2F-H). Additionally, when looking at the ratio of M+3 pyruvate/M+4 malate (ME flux), we observe a significant increase under glycolytic limitation (Fig. 2I) (*31*). These findings display the metabolic plasticity of cancer cells, as they are able to rewire their metabolism to run the TCA cycle mainly on glutamine. However, we are still able to detect an unlabelled fraction in citrate (Fig. 2F-H) which most likely results from fatty acid oxidation.

An additional carbon source that we might neglect with our *in vitro* setup is lactate whose build up is a prominent feature of most solid tumours (*32*). In fact, recent evidence from *in vivo* studies suggest that lactate can be a major carbon source to the TCA cycle of cancer cells (*33, 34*). To test if this feature can be recapitulated in our *in vitro* model, we performed [U-^{13}C] lactate tracing at a concentration of 5 mM as this was indicated as a physiological relevant concentration within the TME (*22, 35*). Supported by the increase in NAD^+/NADH ratio (Fig. 2J), we measured increased ^{13}C contribution to pyruvate and the TCA cycle under glycolytic limitation from [U-^{13}C] lactate (Fig. 2K, 2L and S1C, S1D). Of note, the lactate derived carbon contribution to the TCA cycle was mainly via PDH and not via pyruvate carboxylase (Fig S1E, S1F). In summary, we conclude that glutamine and lactate can substitute

for glucose to support and run lower glycolysis and the TCA cycle. In the case of lactate, this is facilitated by the increased NAD^+/NADH ratio favouring lactate oxidation. Other carbon sources might also contribute towards the TCA cycle, however, these contributions are expected to be smaller in comparison to the sources highlighted in this study (*33*). Finally, the sustained PDH flux (Fig. S1E) under Gal suggests that a block upstream of PDH prevents glycolysis derived entry into the TCA cycle.

Glutamine metabolism is redirected towards SSP under glycolytic limitation via PEPCK2

It has previously been shown that under full glucose starvation, gluconeogenesis enzyme PEPCK2 becomes active and supports the biosynthesis of glycolytic intermediates (*26-29, 36*). To test if this is also the case in Gal and not only upon full hexose starvation, we monitored glutamine derived carbon contribution to phosphoenolpyruvate (PEP) and 3-PG (Fig. S2A-B) and observed an active PEPCK flux also upon low glycolytic flux. Furthermore, we observed that the ^{13}C enrichment was similar under serine/glycine (SG) starvation conditions. Overall, we were able to confirm PEPCK activity in three different cancer cell lines with up to 30% of the measured serine being fully labelled under SG starvation (Fig. 3A). Even with SG in the medium, the glutamine flux to serine under Gal was comparable to the one from Glc (Fig. 3B). As serine is the major substrate for 1C metabolism, we measured the flux from glutamine into vital downstream metabolites of 1C metabolism. We observed ^{13}C enrichment in ATP (Fig. 3C), glutathione (GSH) (Fig. 3D) and formate (Fig. S2C). Of note, the labelled fraction of ATP reached an astonishing 40-50% under SG starvation in all three cell lines (Fig. 3C).

PEPCK catalyses the decarboxylation of oxaloacetate into PEP, therefore, we can measure its metabolic flux by using aspartate as a surrogate for oxaloacetate as the tracer medium contains no aspartate (*37*). Doing so, we observed a clear increase in PEPCK flux under glycolytic limitation with and without SG (Fig. 3E). Mitochondrial PEPCK (PEPCK2) has been identified as the major isoform present in most tumour tissues (*26*). Here we observed that PEPCK2 protein expression was markedly increased under glycolytic limitation in all the cell lines tested (Fig. S2D). Subsequently, we used two different genetic approaches to target PEPCK2; we knocked down PEPCK2 in MDA-MB-468 cells using shRNA and knocked it out using CRISPR/Cas9 system in 4T1 and B16-F10 cells (Fig. S2E, F). Overall, we were able to confirm PEPCK2 as the culprit for the ^{13}C enrichment into serine from glutamine (Fig. 3F). More importantly, serine intracellular levels significantly dropped in MDA-MB-468 and 4T1 but not in B16-F10, signifying the importance of the glutamine flux for the serine pool while also highlighting varying cell line specific dependencies on PEPCK2 (Fig. 3G). Furthermore, the labelling into ATP and GSH was significantly reduced in PEPCK2 KD and eliminated in the KOs (Fig. 3H, I), while formate overflow was unchanged in the PEPCK2 KOs (Fig. S2G). Moreover, we observed a trend of a mild increase in the flux towards malate and pyruvate from glutamine in PEPCK2 KD/KOs which most likely is a result of the elimination of the flux through PEPCK (Fig. S2H, I). Despite the significance of the glutamine flux into SSP, we noted no difference in proliferation of 4T1 PEPCK2KO under glycolytic limitation (Fig. 3J). This indicates that 4T1 cells are able to compensate for the missing contribution

into serine by either increasing uptake of serine from the medium or increasing the flux from Gal under SG starvation (Fig. S2J). Overall, by using Gal as a tool compound, we were able to see that glutamine metabolism is rewired in cancer cells to run the TCA cycle independently and to support SSP via enhanced activity of PEPCK2 (Fig. 3K). However, it remains unclear how PEPCK2 and ME fluxes are coordinated as these fluxes cannot be disentangled by using [U-^{13}C] glutamine. Therefore, we opted to use [U-^{13}C] Gal as a tracer to clearly follow the glycolytic flux into lower glycolysis and TCA cycle under glycolytic limitation.

Cancer cells sustain carbon flux towards SSP under glycolytic limitation

To study the relative fluxes of lower glycolysis under glycolytic limitation in more detail we used [U-^{13}C] Gal. Across a panel of nine different cancer cell lines representing four different tumours (breast, colorectal, glioblastoma and melanoma) we observed robust Gal metabolization through glycolysis and SSP (Fig. 4A-C). Despite similar enrichment in F 1,6-BP (Fig. 1F), the relative flux of ^{13}C in Gal decreased towards late glycolytic intermediates with especially pyruvate showing only about 10% of the ^{13}C enrichment observed under Glc, which could be explained partly by the increased flux from [U-^{13}C] glutamine under Gal (Fig. 4B). In comparison, cells appeared to keep about 25 – 50% of their relative flux towards serine under Gal (Fig. 4C). To exclude that this effect is due to differences in the time needed to reach isotopic steady state (*37*), we performed a time course experiment. We observed isotopic steady state conditions with both tracers at around 24h and longer incubation times did not result in higher ^{13}C enrichment of pyruvate, suggesting that the different labelling pattern in pyruvate is not a result of different flux rates but of an alteration of central carbon metabolism upon Gal (Fig. S3A). Furthermore, different Gal concentrations also did not affect how much [U-^{13}C] Gal enriched the pyruvate pool (Fig. S3A) nor did the usage of RPMI-1640 (Fig. S3B). Using dialysed or normal FBS did not affect pyruvate enrichment as well (Fig. S3C). To test the [U-^{13}C] Gal enrichment in a more physiological setting, we repeated the ^{13}C tracing in Plasmax medium (*38*) and observed similar reduction in M+3 pyruvate isotopologue between Gal and Glc (Fig. S3D). To eliminate the possibility of an inhibitory action of Gal, we mixed Glc and Gal in a 1:1 mix where the Glc added was ^{13}C. If Gal had a direct inhibitory action on glycolysis we would expect to see a clear reduction of ^{13}C flux towards pyruvate, however, we observed no difference in ^{13}C enrichment in glycolysis under such conditions (Fig. S3E). These observations indicate that the reduced glycolytic ^{13}C flux is a result of the cells' response to the limited availability of carbons under Gal.

To better visualise the differences between the relative flux towards lower glycolysis and SSP, we used 3-PG (divergent point between SSP and lower glycolysis) M+3 isotopologue as a common denominator to normalise the main labelled isotopologue of different metabolites (e.g. M+3 serine/M+3 3PG, M+3 pyruvate/M+3 3PG, M+2 citrate/M+3 3PG etc). The resulting ratios are presented as a fold change of the same ratios under Glc (Fig. 4D, E). We found that in some cell lines the ratio for serine under Gal was comparable to the same ratio under Glc, which indicates maintained flux to SSP under glycolytic limitation. In contrast, the ratio of M+3 pyruvate / M+3 3PG was

strikingly lower under Gal than under Glc, which indicates significantly less carbon flux towards pyruvate under Gal. Thus, we observed that cancer cells re-wire their limited ^{13}C supply under Gal towards SSP resulting in SSP as the significantly favoured destination compared to lower glycolysis. This phenotype was predominant in cell lines which doubled under 24h (fast-growing) (Fig. 4D, E). One exception was the murine breast cancer cell line 4T1, which is extremely glycolytic and is very sensitive to Gal, indicating that this cell line may not be able to adapt to such an environment (Fig. 4E). Furthermore, we took note of a similar observation of the rewiring when looking at the intracellular levels of serine and pyruvate (Fig. 4F, G). Subsequently, we validated the re-wiring phenotype when MDA-MB-468 were cultured in the physiological medium Plasmax (Fig. 4H). When ^{13}C-Glc was mixed 1:1 with ^{12}C-Gal, we saw that there was no change in the ^{13}C flux ratios, showing again that Gal is not inhibitory of glycolysis (Fig. 4I). However, when ^{13}C-Gal was mixed with ^{12}C-Glc we saw that the flux was heavily favoured towards pyruvate and lactate and not to SSP (Fig. 4I). This indicates that under ample supply of glycolytic carbons, ^{13}C flux from Gal is not rewired towards SSP.

Based on the observed rewiring, we checked the expression of SSP enzymes and observed a modest increase in the protein expression of phosphoserine aminotransferase 1 (PSAT1) and phosphoserine phosphatase (PSPH), while phosphoglycerate dehydrogenase (PHGDH) expression was mostly not elevated (Fig. S3F, S3G). This indicates that the sustained flux through SSP is not a result of altered gene expression but rather a more direct metabolic adaptation of enzyme activity. In summary, under glycolytic limitation, fast-growing cancer cells (cell lines with doubling times <24 hours) re-wire their metabolism upon limited glycolytic flux towards SSP at the cost of pyruvate oxidation.

Glycolytic limitation inhibits glycolysis at PKM2

Having identified a block at lower glycolysis and re-routing of glycolytic carbons towards SSP, we looked to determine how cancer cells mechanistically undergo the proposed re-wiring. Since the re-wiring occurs somewhere between 3-PG and pyruvate, we hypothesised that this might occur at pyruvate kinase which is a known regulatory node of glycolysis (*39*) (Fig. 5A). This hypothesis is supported by the observation that under Gal cancer cells excrete almost no lactate (Fig. S4A) and its intracellular levels drop significantly (Fig. 4F). This finding also explains why cancer cells are very vulnerable to adenine nucleotide translocator (ANT) inhibition under glucose starvation (*40*) as in the absence of lactate production they would be highly relying on mitochondrial ATP. Specifically, we have observed that PEP accumulates under Gal while pyruvate levels drop dramatically (Fig. 5B-E), further supporting the hypothesis that the metabolic block occurs at the level of pyruvate kinase. This is further substantiated by the observation that ^{13}C labelling in pyruvate is nearly absent across all cell lines analyzed, while PEP remains significantly labelled (Fig. 5B-E). To confirm the glycolytic block at PKM2, we used the PKM2 activator TEPP-46 (*41*) and repeated stable isotope tracing with [U-^{13}C] Gal. The activation of PKM2 increased the ^{13}C flux towards citrate at the cost of serine synthesis (Fig. 5F). Furthermore, we observed a significant reduction of the

labelling into serine from [U-^{13}C] glutamine solidifying our model that the rewiring into SSP is supported by PKM2 inhibition (Fig. S4B). Finally, the activation of PKM2 and subsequent prevention of the rewiring towards SSP lead to a significant decrease in proliferation of MDA-MB-468 (Fig. 5G) and reduction in 3D growth using anchorage-independent conditions (Fig. S4C), concluding that maybe not the PEPCK2 flux but the inhibition of the PKM2 flux is important for survival, at least in our experimental setup (Fig. 3J, 5G). F 1,6-BP binds to PKM2 and induces the formation of the active tetramer form (*42, 43*). Under Gal we saw that the intracellular levels of F 1,6-BP drop (Fig. S4D) which is known to lead to a reduction in PKM2 activity (*42, 43*). However, what we observe with Gal is a complete block of the glycolytic flux at PKM2, indicating that factors other than the low levels of F 1,6-BP are contributing to this rewiring.

In summary, we provide so far evidence that when hexose availability for glycolysis is limited, the residual glycolytic carbon remains in upper glycolysis to support SSP. Meanwhile, glutamine and lactate compensate for carbon demand of the TCA cycle to support increased mitochondrial respiration. Moreover, we are able to increase the mechanistic granularity of the glutamine rewiring through ME and PEPCK by identifying the PKM2 block which means that ME flux (Gln --> Pyruvate) is exclusive to supporting the TCA cycle while PEPCK flux (Gln --> PEP) is exclusive to support SSP (Fig. 5H).

SSP is needed for proliferation and viability under glycolytic limitation

Next, we sought to investigate the functional advantage of the observed metabolic re-wiring towards SSP. We noted a weak correlation between the growth rate of cancer cells under Glc and to what extent Gal inhibited their proliferation (Fig. 6A). Based on that observation we studied the proliferative capacity of the MDA-MB-468 cell line upon treatment with a competitive inhibitor of PHGDH (the rate-limiting enzyme of SSP) BI-4916 (*44*) while under glycolytic limitation. We observed the lowest proliferative capacity of MDA-MB-468 cells when SSP was inhibited under glycolytic limitation (Fig. 6B). MDA-MB-468 cells grown in 3D using anchorage independent conditions with both normal and dialysed FBS also showed the significant growth reduction upon SSP inhibition and glycolytic limitation (Fig. 6C, D and S5A). We further confirmed these results in different cancer cell lines with similar results for two out of three cell lines tested (Fig. 6E). Lastly, we also analyzed the viability of different cancer cell lines in Gal treated with BI-4916 and compared the fold-change apoptosis induction to Glc cultivation in different cell lines. We found an increased percentage of apoptotic (Ann V^{+}) cells when PHGDH flux was blocked under glycolytic limitation (Fig. 6F). The exception is here again the 4T1 cell line, a finding that matches the fact this was the only cell line not showcasing the observed rewiring towards SSP under glycolytic limitation (Fig. 4E). Overall, it is evident that sustained SSP exerts a pro-proliferative and anti-apoptotic role under glycolytic limitation.

SSP flux is crucial to sustain mitochondrial formate production and to support all three metabolic pillars

In addition to serine synthesis, we were interested to understand the functional relevance of sustained serine availability. We sought to uncover the metabolic purpose of such rewiring, especially since 1C metabolism is able to support all of the three metabolic pillars; biosynthesis, bioenergetics and redox balance (*25*) (Fig. 7A).

We analyzed the expression of the different enzymes of the 1C cycle and found that the mitochondrial enzymes SHMT2 and MTHFD2 displayed increased mRNA expression under glycolytic limitation while the expression of their cytoplasmic versions were mostly kept unchanged with MTHFD2 expression also increased at the protein level (Fig. 7B-C). The product of the mitochondrial 1C cycle branch is the release of the 1C unit as formate and we have previously shown that serine catabolism and formate overflow increase upon Gal (*24*). In corroboration, we performed formate measurements in a panel of cancer cell lines and observed increased formate release under glycolytic limitation across the cell lines tested (Fig. 7D). Similar to lactate overflow, formate overflow produces one ATP molecule per MTHFD1L reaction. In addition to ATP production, formate overflow yields one NADH molecule via MTHFD2 (*45*). The coupling of MTHFD2-derived NADH to the electron transport chain (ETC) thereby contribute to mitochondrial ATP production and the observed increase in OCR upon Gal (Fig. S1A) (*24*). Meaning that the increased formate release can serve as a crucial bioenergetic function by supporting mitochondrial ATP production under glycolytic limitation (*24*). Furthermore, we have previously shown that under glycolytic limitation, AMPK is activated alongside the increased formate release (*24*) which is an observation we could confirm in the glioblastoma cell line LN-229 (Fig. S6A). To test whether AMPK is responsible for the rewiring towards SSP and 1C cycle, we utilized LN-229 cells harbouring a genetic deletion of both alpha subunits of AMPK (Fig. S6B) (*46*). We observed no difference in the AMPKKO cells in terms of formate release (Fig. S6C) and ^{13}C flux rewiring (Fig. S6D), indicating that AMPK activation and increased formate overflow are not in causal relation. Furthermore, knocking-out MTHFD1L, the enzyme catalysing formate release, led to only a subtle decrease in growth of MDA-MB-468 cells in 3D anchorage-independent conditions under glycolytic limitation (Fig. S6E-G).

Having observed that the bioenergetic aspect of ATP production upon formate overflow might only partially contribute to the functional implications during glycolytic restriction, we investigated potential additional metabolic aspects of the 1C cycle that support redox balance and biosynthesis. The 1C unit donated by serine can either be used for de novo purine and pyrimidine synthesis or can be oxidised to CO_2 via ALDH1L2 or ALDH1L1 while generating NADPH in the latter reaction (Fig. 7A). NADPH provides the cell with reducing equivalents required to counter reactive oxygen species (ROS). We explored both biosynthesis and redox balance as potential sinks for the rewired ^{13}C flux. ALDH1L2 expression was markedly increased under glycolytic limitations in different cancer cell lines while the expression of ALDH1L1 was unchanged at mRNA level (Fig. 7B, 7E). This indicates that 1C metabolism is mostly involved in maintaining mitochondrial rather than cytosolic redox state under glycolytic limitation. Moreover, when we cultivated the highly glycolytic breast cancer cell line 4T1 (Fig. S4A) for 72h in Glc without medium change, we saw that the expression of ALDH1L2 increased as Glc concentration became limited supporting the ALDH1L2 data we obtained using Gal (Fig. 7F). Knocking out ALDH1L2 in MDA-MB-468 cells (Fig.

S6H) resulted in mildly reduced proliferation under glycolytic limitation in both 2D and 3D assays (Fig. 7G, H). Concurrent increased expression of ALDH1L2 and increased formate overflow would together highlight the extent of increased carbon flux through SSP and 1C cycle as despite the release of 1C as CO_2, formate overflow is still significantly increased.

PPP is a key regulator of biosynthesis and redox balance as it supplies the cells with R5P and NADPH (*47*). The cycling of carbons we observed (Fig. 1H, I) suggests that PPP is shifted towards maximising the production of NADPH and R5P from the limited carbon supply under Gal. Due to this carbon cycling in PPP and subsequent labelling of R5P, it is not possible to determine the contribution of 1C metabolism to nucleotide biosynthesis by using [U-^{13}C] Glc and Gal tracers (Fig 7I and S6I-M). Therefore, we utilised [U-^{13}C] serine tracer and observed that the flux from serine towards nucleotide biosynthesis is sustained under glycolytic limitation (Fig. 7J). Overall, it can be concluded that the metabolic functions of the 1C metabolism are individually only partially contributing to the functionality of cells under glycolytic limitation. Conclusively, this suggests the idea that the flux through the mitochondrial 1C cycle might serve multiple metabolic purposes.

To test if mitochondrial 1C metabolism plays a combined role in controlling metabolic adaptation to glycolytic limitation, we performed [U-^{13}C] Gal tracing in MTHFD1L and MTHFD2 KO cells (Fig. S6G) and found that the we can detect an increase in labelling into TCA cycle upon loss of mitochondrial 1C cycle activity (Fig. 7K, L). This can be seen in the decrease in ^{13}C flux to serine and glycine with concomitant increase of ^{13}C flux to citrate (Fig. S6N, O). This effect was clearest in MTHFD1LKO and was similar to what we observed with PKM2 activation (Fig. 5F). These observations indicate that the mitochondrial 1C pathway contributes to the rewiring of lower glycolysis.

Put together, it is apparent that the rewiring towards SSP and the plasticity of 1C metabolism under glycolytic limitation serves all three metabolic pillars with sustained carbon flux from serine to purines and increased ATP and NADPH generation. In particular, mitochondrial formate production needs to be increased, as an increased fraction of formate is likely to be oxidized due to increased protein levels of ALDH1L2 while at the same time formate overflow is also increased. Additionally, cytosolic formate is needed to support purine and pyrimidine biosynthesis to sustain proliferation. Finally, we observed that loss of mitochondrial 1C pathway activity results in ^{13}C carbon re-entry through PKM2 towards the TCA cycle.

In vivo relevance of Gal to model glycolytic limitation

The *in vitro* modelling of the metabolic environment that cancer cells face *in vivo* is extremely challenging due to the heterogeneity of the tumour tissue and the varying metabolite composition of the TME. Using Gal as a tool, we aimed to mimic glucose limitation as one important variable of the *in vivo* TME. To test the physiological relevance of using Gal as a tool compound to study glycolytic limitation, we subcutaneously injected B16-F10 cells into the flanks of C57BL/6 mice. We then allowed the tumours to grow for 16 and 9 days, thereby generating larger and smaller tumours, respectively, (Fig. 8A, B) and then we infused the mice under anaesthesia with [U-^{13}C]

Glc tracer for 2 hours. Next, we performed targeted metabolomics on pieces of dissected tumour and compared the small tumours to the inside and the outside of the big tumours to measure the gradient of metabolite levels between the outer layer and the core of the relatively big tumours. We observed that glucose levels strikingly drop in the core of the big tumour compared to its outer layer (Fig. 8C). Meanwhile, other metabolites that can act as secondary carbon sources for tumours (lactate, glutamine and serine) were all present at similar levels between core and the outer layer (Fig. 8C). Moreover, when looking at the MIDs of 3-PG we can see that the ^{13}C enrichment is slightly higher on the outer layer than in the core (Fig. 8D). In tumours, when the ^{13}C fraction of pyruvate is normalised to the ^{13}C fraction of 3-PG, the ratio is equal to one when newly synthesised pyruvate is entirely generated by glycolysis (*34*). The ratio is in contrast >1 when other ^{13}C sources outside of glycolysis, that are labelled elsewhere by [U-^{13}C] Glc and then supply the tumour from circulation, contribute to the pyruvate pool (*34*). Comparing these ratios between the outer and inner layers of the B16-F10 tumours, we can see that the ratio is ~ 2.3 in the inner core and 1.5 in the outer layer (Fig. 8E). This indicates that the core is depleted of glucose in bigger tumours and cells within this core are relying more on other carbon sources due to altering their glycolytic usage i.e. metabolic flexibility. In contrast, serine ratios remain rather constant suggesting a switch of the glycolytic flux towards serine (Fig. 8E). Even though these data are not definitive proof, they hint towards similar rewiring as observed *in vitro* when culturing cells in Gal.

In a second *in vivo* model we performed the adoptive transfer of TCL1-355 into C57BL/6 mice as a model of chronic lymphocytic leukaemia (CLL) (*48, 49*). In this model, leukemic B cells proliferate rapidly within the spleen which in theory should create areas depleted of glucose as within solid tumours which is what we are mimicking *in vitro* using Gal. Indeed, we have observed decreased glucose concentration in the spleens of CLL mice compared to healthy mice (Fig. 8F). Therefore, the CLL model can be employed as an *in vivo* model for glycolytic limitation. After the disease developed, mice were continuously infused via the tail vein with [U-^{13}C] Glc tracer for 2 hours. When comparing B cells from healthy spleens against CLL B cells from diseased spleens, we observed that CLL cells significantly increased their relative flux from glucose towards serine and glycine while showing a reduced flux towards citrate, indicating low pyruvate oxidation (Fig. 8G). This altered metabolic phenotype between normal and leukemic B cells *in vivo* is partly recapitulated *in vitro* by switching cancer cells from Glc to Gal. In summary, by using Gal we are able to capture relevant metabolic features of tumour cells that occur in glucose depleted TME, specifically, the glycolytic rewiring towards serine to support cancer cell metabolism.

Discussion

In the present study, we discover a novel rewiring of glycolytic flux towards SSP via a PKM2 block when the supply of glycolytic carbons is inadequate as modelled with Gal as a tool compound to mimic glycolytic limitation within the TME. In addition, we were able to corroborate previously described rewiring of glutamine metabolism towards SSP under glucose starvation. However, by identifying the block of lower glycolysis at PKM2, we were able to add

another mechanistic layer that differentiates the glutamine flux under glycolytic limitation to either exclusively support SSP via PEPCK2 or TCA cycle via ME (Fig. 5H). We observed that both fluxes contribute to the survival and proliferation of several cancer cell lines and to supply the 1C cycle with the necessary carbons to perform biosynthetic, bioenergetic and redox balance functions.

Cancer cells *in vitro* usually engage in aerobic glycolysis due to the ample availability of glucose. This does not reflect glucose levels and cancer cell metabolism within the TME. A key metabolite that drives the metabolic phenotype of cancer cells is glucose and its availability, which has been shown to be decreased in the tumour interstitial fluid (TIF) when compared to plasma (*22, 23*). TIF measurements represent the average level of glucose across the area of the whole tumour. However, inside the tumour, areas do exist where cells are even more deprived of glucose (Fig. 8C) and those cells withstanding such severe metabolic stress (alongside other niche stresses) are the plastic cells that are capable of surviving the metastatic cascade (*15*). Uncovering the metabolic rewiring in these deprived cells hold therapeutic promise to target cancer growth and metastasis (*25*).

By culturing cancer cells under glycolytic stress conditions, we were able to see their ability to use the same carbon source for different functions (metabolic plasticity) upon the PKM2 block and rewiring of carbons towards SSP. On the other hand, cancer cells also re-direct the glutamine flux towards SSP showcasing an example of metabolic flexibility (*14*). PEPCK2 is the main instigator of glutamine flux rewiring towards SSP. It is intriguing that the mitochondrial isoform of PEPCK is involved under glycolytic limitations, as usually this isoform is only involved when cytoplasmic NADH levels are not depleted (*50*). However, under glycolytic limitations, NAD/NADH ratio is increased and yet the cells still preferably engage PEPCK2 over cytoplasmic PEPCK1 whose involvement would transfer mitochondrial NADH to the cytoplasm via malate oxidation (*50*). This finding can be explained by the possibility that the gluconeogenesis pathway is activated mainly to support SSP and therefore, cytoplasmic NADH is not required to reduce 1,3-bisphosphoglycerate into glyceraldehyde 3-phosphate as per the conventional gluconeogenesis pathway. Furthermore, in our system we did not observe a proliferative advantage in activating PEPCK2 under glycolytic limitation contrary to what has previously been published on PEPCK2. One major difference in our setup compared to earlier studies that could explain this observation is the usage of cell lines which have PHGDH amplification and are capable of increasing their serine synthesis flux independent of PEPCK2.

The diversion of the glycolytic flux away from lower glycolysis and towards SSP offers many metabolic advantages for the cell. For bioenergetics, SSP and subsequent 1C cycle generate two NADH and one ATP per 3-PG molecule, while lower glycolysis generates one ATP and consumes one NADH. Meaning if energy is the main constraint for the cell under glycolytic limitation, it will benefit more from running SSP and the subsequent serine catabolism and formate overflow (*24*). Furthermore, the additional advantage of sustaining the flux towards serine catabolism lies in its pathway flexibility. The fate of the 1C can be tailored for the cell's need; full oxidisation of 1C via ALDH1L2 will generate NADPH, the MTHFD1L reaction will generate ATP, or it can be incorporated in purines and dTMP in the cytosol (*25*). Here we show that under glycolytic limitation, the rewiring towards SSP and 1C cycle supports all

the three different pillars of metabolism, specifically the mitochondrial part of the 1C cycle (Fig. 7). In fact, we observe that even though the cells increase the expression of ALDH1L2 and subsequently lose more carbon as CO_2, formate overflow is still increased, highlighting the non-biosynthetic benefit of running the mitochondrial branch of the 1C cycle under glycolytic limitation.

Cancer cells preferentially express PKM2 over other isozymes of pyruvate kinase as it provides them with the metabolic flexibility to regulate the glycolytic flux, as PKM2 can be regulated via allosteric signals that shifts its form between a high activity tetramer and a low activity dimer (*42*). This allows cancer cells to rewire their glycolytic flux towards biosynthetic pathways when needed by expressing the dimer form of PKM2 to accommodate higher proliferative rates under high glycolytic flux (*42*). In the present study, we observed a complete block PKM2 metabolic activity when the glycolytic flux is limited to rewire the limited carbon input towards SSP. Previous work has shown that serine acts as an allosteric activator of PKM2, while the lack of extracellular serine lead to an inhibition of PKM2 activity (*51, 52*). Here we observed that when glucose is limited, even with serine/glycine available in the media, PKM2 glycolytic flux was inhibited. Indicating that even when serine was available for the cells, the lack of glycolytic carbons inhibited pyruvate kinase activity to rewire the glycolytic flux towards SSP. This observation highlights an intriguing difference between de novo serine synthesis flux and extracellular serine consumption and potentially could be explained by recent work that has shown that PHGDH functions beyond its catalytic activity within tumour cells and can allosterically regulate the function of phosphofructokinase (*53*). Moreover, here we presented evidence that the removal of MTHFD2 or MTHFD1L was sufficient to partially re-establish PKM2 activity, meaning that mitochondrial 1C cycle is able to directly regulate PKM2 function alongside other regulators like F 1,6-BP. This would hint at a possible link between the PKM2 block and the increased formate overflow under glycolytic limitation. Entangling the direct cause of PKM2 block and the link with 1C cycle is the subject of ongoing work in our lab.

The findings presented here highlight the flexibility and plasticity of the biochemical network in tumour cells. These adaptive traits present a challenge in developing precision-medicine drugs that target the cells' metabolism. For such therapeutic strategies to be successful, context dependent understanding of environmental conditions and nutrient availability of the TME need to be considered alongside specific oncogenic driver mutations (*54*).

Acknowledgements

We are grateful to Stephanie Kreis (University of Luxembourg) for providing us with B16-F10, A375, SKMeL28 cells, Clement Thomas (LIH, Luxembourg) for providing 4T1 and BT-20 cells and Lewis Cantley (Harvard Medical School) for providing MDA-MB-468 WT and MTHFD1LKO cells. We are grateful for all the technical and analytical support from the different metabolomics platforms towards the work presented here and in specific: Francois Bernardin from the metabolomics platform at LIH, Xiangyi Dong, Floriane Gavotto and Lucia Gallucci from the LCSB metabolomics platform, Luxembourg. We are thankful for the support of the National Cytometry Platform

(Quantitative Biology Unit, LIH) for support with flow cytometry measurements and analysis. Figures 1A, 1B, 3K, 5A, 5H, 7A and 8A were created with biorender.com.
M.B. is supported by the Fondation du Pélican de Mie et Pierre Hippert-Faber, under the aegis of the Fondation de Luxembourg. M.B. and J.M. are supported by the Luxembourg National Research Fund (FNR) ATTRACT program (A18/BM/11809970). J.M. is supported by FNR-PRIDE NEXTIMMUNE (PRIDE/11012546), FNR-PRIDE i2Tron (PRIDE19/14254520). E.L. is supported by the FNR-CORE program (C16/BM/11282028 and C20/BM/14591557), by a Proof of Concept FNR grant (PoC/18/12554295), a PRIDE17/11823097 and by i2Tron (PRIDE19/14254520). E.G., J.P., and E.M. are supported by grants from the FNR and Fondation Cancer (PRIDE15/10675146/CANBIO, C20/BM/14582635, and C20/BM/14592342). E.V. is supported by FNRS-Télévie (7.4509.20 and 7.4572.22).

Author's contribution

M.B. and J.M. conceptualised and designed the study. M.B. performed all of the experiments. A.O., E.V., E.G., M.S., C.P., J.P., E.M., S.P.N. and E.L., assisted for the design and performing of the *in vivo* work. L.N., N.I.L. and M.W.R. aided in the generation of different KO cell lines used. D.S., M.W., C.J. and A.L. performed YSI, LC-MS, GC-MS and IC-MS measurements while M.B. performed the corresponding data analysis according to D.S., M.W., C.J., A.L., J.M., instructions. Original draft written by M.B. and J.M. Review and editing done by all authors.

Competing interest

Authors of the presented study declare no competing interests.

Material and Methods

Chemicals

Galactose, glucose, serine, glutamine and glycine were purchased from Sigma Aldrich and stock solutions were prepared in ^{MQ}water. BI-4916 and TEPP-46 were purchased from MedChemExpress and stocks were prepared in DMSO. BI-4916 was always used at a final concentration of 15µM while TEPP-46 was used at 100µM.

Cell culture

MDA-MB468, 4T1, MDA-MB-231, HCT116, LN-229 and B16-F10 were cultured in DMEM (Thermo Fisher Scientific, 1443001) supplemented with 17.5 mM glucose, 2mM glutamine and 10% FBS. BT20 were cultured in advanced DMEM/F12 (Thermo Fisher Scientific, 12634010) supplemented with 2 mM glutamine and 10% FBS. A375 and SKMeL28 were cultured in RPMI 1640 (Thermo Fisher Scientific, 61870010) supplemented with 10% FBS. All cells were maintained at 37°C and 5% CO_2 and routinely tested for mycoplasma contamination. Serine/glycine starvation experiments were carried out using customised DMEM (Thermo Fisher Scientific, lot No. GME11933004) without phenol red, glucose, serine, glycine, tryptophan, pyruvate and glutamine with the missing

ingredients added according to the concentrations present in full DMEM and experimental setup. All experiments (except anchorage independent growth assays, see below) were seeded on D-1 and cells were allowed to adhere and attach overnight. Medium was aspirated and experimental medium plus treatment was added for the indicated time points in figures.

MDA-MB-468 WT and MTHFD1L-KO were received from Lewis Cantley lab, Weill Cornell Medical College, USA (*55*). STR profiling in our lab in 2021 authenticated MDA-MB-468. LN-229 WT and AMPK-dKO cells were obtained from Michael Ronellenfitsch, Dr Senckenberg Institute of Neurooncology, University Hospital Frankfurt, Goethe University and have been previously described in (*46*), B16-F10, A375 and SKMeL28 cells were received from Stephanie Kreis lab, University of Luxembourg, Luxembourg. 4T1 and BT20 were received from Clement Thomas lab, Luxembourg institute of Health, Luxembourg. MDA-MB-231 were obtained from Alexei Vasquez lab, Beatson Institute of Cancer Research, UK. All cell lines were originally purchased from ATCC.

Lentiviral mediated knockdown of *PCK2*

The procedure followed was described in detail in (*56*). For silencing *PCK2* gene in MDA-MB-468 cells, pGIPZ shPCK2-2: ATTATTGGACAGTCTTTGT (V3LHS_410309) vector plasmid purchased from Horizon Discovery was used.

CRISPR/Cas9 KO of *Pck2, MTHFD2, ALDH1L2*

MDA-MB-468 cells harbouring deletion of MTHFD2 have been previously generated in (*56*). To KO *Pck2* in 4T1 and B16-F10, we used the same procedure described in (*56*); two different gRNAs were used: 1. TATGCGTATTATGACCCGCC (Vector ID: VB211125-1122kdb, gRNA #654) to generate 4T1 clone A9 and B16-F10 clone A5. 2. GCGGGTCATAATACGCATAC (Vector ID: VB211125-1123gfv, gRNA #653) to generate 4T1 clone B7 and B16-F10 clone A9. For *ALDH1L2* deletion in MDA-MB-468 cells the same procedure in (*56*) was utilised with two different gRNAs: 1. GCAGAAGCCTACAGATCCGT (Vector ID: VB190719-1044jbf, gRNA #1529) to generate MDA-MB-468 clone F11. 2. GCGCTCCGGCGCTTCTCCAC (Vector ID: VB190719-1054khg, gRNA #1st Exon) to generate MDA-MB-468 clone D1.

Animal experiments

All experiments involving laboratory animals were conducted in a specific pathogen-free animal facility with the approval of the animal welfare structure of LIH and the Luxembourg Ministry for Agriculture, Viticulture and rural development under the references LUPA 2021/08 and LUPA 2021/22. Mice were treated in accordance with the European Directive 2010/63/EU. C57BL/6 mice were purchased from Janviers Labs (France).

TCL1-355 adoptive transfer

The TCL1-355 murine cell line was kindly provided by Dr Efremov (*49*). A total of 2,000 TCL1-355 cells resuspended in DMEM without phenol red were injected intravenously (iv; 100 µL) in the tail vein of C57BL/6 mice. CLL progression was monitored by determining the percentage of $CD5^{+}CD19^{+}$ circulating CLL cells in the peripheral blood using flow cytometry. 14 days after iv injection, leukemic mice and age matched control mice were anaesthetised with 2.0 – 2.5% of isoflurane and continuously infused with [U-^{13}C] glucose (50% solution in 0.9%

NaCl) for 2h at a constant rate of 1.8g/Kg/h via the tail vein. At the end of the infusion, mice were euthanized via cervical dislocation and blood, organs and cells collection was rapidly performed.

Blood sampling was performed before and after infusion. Plasma was collected after two successive centrifugations at 1000 RCF for 10 min. B cells were isolated from the spleen. Briefly, suspension of splenocytes was prepared using gentleMACS™ Dissociator (Miltenyi). Then, B cells isolation (negative sorting) was performed using MojoSort™ Mouse Pan B Cell Isolation Kit II (Miltenyi), according to manufacturer's instructions. Cells were counted prior to pelleting and snap freezing. Pieces of spleen were also snap frozen in liquid nitrogen for metabolomics.

B16-F10 subcutaneous model

A total of 250,000 B16-F10 cells resuspended in PBS were injected subcutaneously (100 µL) into the flank of C57BL/6 mice and tumours were allowed to grow for 16 days for one group and 9 days for the second group. At endpoint, both groups were infused with [U-^{13}C] glucose as described above. After infusion, mice were euthanized with cervical dislocation and blood was collected into heparin tubes to separate plasma. Plasma and tumour tissue were snap frozen in liquid nitrogen.

Western blot

KOs and KDs cell pellets were directly obtained from cell culture by pelleting cells at 350 RCF for 5 min followed by a PBS wash and then freezing at -20°C awaiting cell lysis. Probing protein expression after treatments: cells were cultured at 150,000 cells/well density in a 6-well plate on D-1. At time point of extraction, the plate was placed on ice, medium was aspirated and cells were washed in ice-cold PBS. Cell lysis buffer (150 mM NaCl, 1 mM EDTA, 50 mM Tris-HCl, 1% NP-40 with proteases and phosphatases inhibitors (Roche)) was added directly to the wells and cells were scraped and collected in pre-cooled Eppendorf tubes followed by sonification for 10 min. Lysates were spun at 16,000 RCF, 4°C for 10 minutes, the supernatant was collected in new tubes and the concentration of protein was determined with a Bradford assay. 20 – 40 µg of total protein was loaded into 15-well or 12-well RunBlue 4-12% Bis-Tris gels (Westburg) with the addition of 10mM DTT (Sigma Aldrich) and 4x NuPage LDS Sample buffer (Thermo Fisher Scientific) and gels were run for 90 minutes at 120V. Protein bands were blotted onto nitrocellulose membrane for 2h at 30 V. Membranes were blocked using 5% milk powder in TBS-0.1% Tween solution for 1h at RT. Membranes were incubated in the corresponding primary antibody overnight at 4°C and for 1h at RT in secondary antibodies. Detection of protein bands was done using Odyssey CLx Infrared Imaging system (LI-COR). Image StudioLite software Vers.5.2 (LI-COR) was used for quantifications and analysis. Primary antibodies used in this paper: AMPKα (Cell Signalling Technology, 5831S), p-AMPK^{Thr172} (Cell Signalling Technology, 72335S), ACC (Cell Signalling Technology, 3676S), p-ACC^{Ser79} (Cell Signalling Technology, 11818S) MTHFD2 (Cell Signalling Technology, ab151447), ALHD1L2 (Sigma Aldrich, HPA020549 and Proteintech, 21391-1-AP), β-Actin (Cell Signalling Technology, 3700), PSAT1 (Sigma Aldrich, HPA042924), PSPH (Sigma Aldrich, HPA020376), PHGDH (Sigma Aldrich, HPA021241), PEPCK2 (Cell Signalling Technology, 6924S) and MTHFD1L

(Proteintech, 16113-1-AP). All antibodies were used at 1:1000 dilution unless stated otherwise. Secondary antibodies: IRDye 680RD Goat Anti-Mouse IgG (H + L) (926-68070) and IRDye 800CW Donkey Anti-Rabbit IgG (H + L) (926-32213) from LI-COR (used in a 1:10,000 dilution)..

Flow cytometry analysis of Apoptosis

250,000 cells (MDA-MB-468, B16-F10 and A375) or 200,000 cells (4T1) were seeded in 6-well plate, allowed to attach overnight and treated as indicated for 48h. At endpoint, medium was collected, cells were washed with PBS and PBS was collected followed by cell trypsinisation. Cells were pelleted and washed with ice-cold PBS. Each sample was stained for 15 min on ice and in the dark with 50 µL AnnexinV staining solution (5% AnnexinV-FITC antibody in AnnexinV binding buffer (10 mM HEPES pH 7.4, 140 mM NaCl, 2.5 mM $CaCl_2$, 0.1% BSA in ^{MQ}water)). Directly prior to measurements, 450 µL of propidium iodide (PI) staining solution was added (11.1 µg/ml in AnnexinV binding buffer). Measurements were done using NovoCyte Quanteon (Agilent) and software NovoExpress (version 1.5.0). FlowJo version 10.6.2 was used for analysis.

Proliferation assays

Cells were seeded at a concentration of 25,000 cells/well in a 12-well plate or 12,500 cells/well in a 24-well plate in triplicates. Separate triplicate wells were counted when treatment was added to set 0h count for fold change calculations. Medium and treatment were replaced at 48h and 72h. At endpoint, cells were trypsinised and viable cell count was obtained using Countess™ automated counter (Thermo Fisher). Growth rate in Fig. 6A was calculated using the equation: [*ln*(final cell count/initial cell count)]/duration.

Anchorage Independent 3D growth assays

Cells were cultured in ultra-low attachment flask (Greiner) for a minimum of five days. Cells were collected and spun at 100 RCF for 5 min and afterwards resuspended in Ca^{+2} and Mg^{+2} free PBS. 5,000 cells were seeded in 96-well ultra-low attachment plates (S-Bio or facellitate) already in the experimental medium and the plates were spun at 100 RCF for 10 minutes. 3D growth was determined using IncuCyte® S3 Live-Cell Analysis system (Sartorius) over the indicated time periods.

RNA extraction, cDNA synthesis and RT-qPCR

300,000 cells were seeded in 6-well plate and treated for 24h as indictaed in the figures. RNA was extracted directly from the plates using RNeasy Mini Kit (Qiagen, 74104). 2µg of RNA were used for cDNA synthesis using High Capacity cDNA Reverse Transcription Kit (Thermo Fischer Scientific, 4368814). For qPCR, we used Fast SYBR™ Green Master Mix (Thermo Fischer Scientific, 4368814) with 20 ng cDNA/sample in triplicates or duplicates and the reaction was conducted at 95°C for 20 s followed with 40 cycles of 95°C for 1 s and 60°C for 20 s. The QuantStudio 5 Real-Time PCR System was used (Applied Biosciences, ThermoFisher Scientific). CT values were determined by QuantStudio Design and Analysis v1.5.1 software (Applied Biosciences, ThermoFisher Scientific). Fold change of mRNA expression was determined using ddCt algorithm. Primers used in this study are listed in Table S1.

Targeted gene	Species	Forward primer sequence	Reverse primer sequence
Psph	Mouse	AGATTTCCCAGGGATCCGGC	CAGTCCTCACTCAAGGCTCG
Psat1	Mouse	CCCAGCTGTGCGGAATGAGA	GAGCACACTGATGCCGAGTC
Phgdh	Mouse	CAGTGCAAGAAAGGTGTGCG	TTCTCGTGGTCCACTAAGGC
Shmt1	Mouse	TGCCCTCCCCATTTGAACAC	ATCTCTTTGCCAGTCTTGGGAT
Shmt2	Mouse	CTGCACAGTGGGGAGTCAAT	GTCAGTGCCAGGTTGAGCTT
Mthfd2	Mouse	CTGCGTTGGCTGTGCGGTT	CTGAGGTGTGGCCGCTTGT
Mthfd1	Mouse	CGTGGGTGGCAGACTAGCAA	TACCTGCTCCTGCATCCGAG
Aldh1l1	Mouse	TAGCAGGTGCCTTCCAACCT	CTTAAACACGGGCACGCCAT
Aldh1l2	Mouse	TTGACAGCCCAAAGCATGGC	CTGCCCAGAAAACAGAAAACCCA
Mthfd1l	Mouse	CTTTGGTGGGAACGATGAGCA	CCAGCCTTGACCGCATCTT
Gapdh	Mouse	CATCACTGCCACCCAGAAGACTG	ATGCCAGTGAGCTTCCCGTTCAG
Sdha	Mouse	CTTCGCTGGTGTGGATGTCA	GTGGGAATCCCACCCATGT
PSPH	Human	GACAGCACGGTCATCAGAGAAG	CGCTCTGTGAGAGCAGCTTTGA
PSAT1	Human	GGCTTGGTTCTGGAGTGGAT	ATGCCTCCCACAGACACGTA
PHGDH	Human	CTTACCAGTGCCTTCTCTCCAC	GCTTAGGCAGTTCCCAGCATTC
SHM1	Human	GAAGAAAATCTCTGCCACGTCC	GATCAGCTTCGGGTGGAAGAG
SHMT2	Human	GCCTCATTGACTACAACCAGCTG	ATGTCTGCCAGCAGGTGTGCTT
MTHFD1	Human	TTGGACAGGCTCCAACGGAGAA	AGAAGTGGTGAGAGCCAGGACA
MTHFD2	Human	CTCCTTGTTCAGTTGCCTCTTCC	CTGATCCAAACACATTCGTCCTAC
MTHFD1L	Human	CGCACACCTGAATGTCAACTCC	CGTGGATGTCTCCAGTCAAGTG
ALDH1L2	Human	CTTCTCCACTGGCCGGGTTTAT	CTGGAACTGTGAACACCCCT
GAPDH	Human	CATGAGAAGTATGACAACAGCCT	AGTCCTTCCACGATACCAAAGT
ACTINβ	Human	CACCCTGAAGTACCCCATCG	GCTGGGGTGTTGAAGGTCTC

Supplementary Table 1. List of primers used in this study and their sequences.

Metabolomics

Stable Isotope Tracing and Metabolite Extraction

- ***In vitro* tracing and metabolite extraction:**

Stable isotope tracing experiments with [U-^{13}C] glucose, [U-^{13}C] galactose, [U-^{13}C] glutamine, [U-^{13}C] serine (Cambridge Isotope Laboratories, CLM-1396, CLM-1570, CLM-1822 and CLM-1574 respectively) and [U-^{13}C] lactate (Sigma Aldrich, 485926) were performed in DMEM (Thermo Fisher Scientific, 1443001), RPMI 1640 for SILAC (Thermo Fisher Scientific, 88365), Advanced DMEM/F12 for SILAC (Thermo Fisher Scientific, A2494301) or

customised DMEM (Thermo Fisher Scientific, lot No. GME11933004) depending on the cell lines used. These tracer mediums were supplemented with the missing metabolites according to the experimental setup to mimic the original formula of DMEM, RPMI 1640 or advanced DMEM/F12. For sodium [U-^{13}C] lactate 5 mM final concentration was used. For glucose and galactose tracing 10% normal FBS was used while for the rest we used 10% dialysed FBS. Experimental set-up and extraction of metabolites for GC-MS analysis was done as described in (*56*). Metabolite extraction for LC-MS was done as described in (*24*). Metabolite extraction for IC-MS was identical to LC-MS.

- ***In vivo*** **metabolite extraction**

Metabolite extraction from tumours, spleen and plasma was performed as detailed in (*24*). The absolute quantification of glucose in plasma and spleen was performed using standard addition method. In brief, known concentrations of glucose were added serially to metabolite extracts of each sample. After measurements, a calibration curve was used to determine the concentration of glucose in the original samples by determining the x-axis intercept.

For B cells separated from the spleen, cells were washed with ice-cold PBS and subsequently 40 µL/one million cells extraction buffer [acetonitrile/$^{MQ}H_2O$/methanol (ratio, 3:2:5); liquid chromatography–MS (LC-MS) grade solvents)] was added to each cell pellet. Cells were mixed for 10 min on a thermomixer at 4°C at maximum speed, and then the tubes were centrifuged for 10 min at 16,100 RCF at 4°C. 50 µL of the supernatant was collected and transferred to an already-cooled LC-MS glass vial with inserts and stored at -80°C until measurement.

YSI measurements and medium exchange rates:

Medium samples were filtered (PVDF, 0.22 µm) prior measurement to remove particulates.

Absolute quantitative values for lactic acid and glutamine were acquired using a YSI 2950D Biochemistry Analyzer (Kreienbaum KWM). The instrument was calibrated and prepared according to the manufacturers' instruction. For a precise and reliable quantification, external concentration curves of each target compound were prepared and measured in triplicates. Absolute uptake and release rates were calculated as described in (*24*).

GC-MS measurements

- <u>Formate measurements</u>

Formate was derivatized to benzyl formate from the collected medium samples using the MCF protocol described in (*24*). GC-MS analysis was performed using an Agilent 7890 A GC coupled to an Agilent 5975 C inert XL Mass Selective Detector (Agilent Technologies). A sample volume of 1 µL was injected into a Split/Splitless inlet, operating in split mode (20:1) at 280 °C. The gas chromatograph was equipped with a 30 m (I.D. 250 µm, film 0.25 µm) ZB-5MSplus capillary column (Phenomenex, 7HG-G030-11-GGA) plus 5 m GUARDIAN in front of the analytical column. Helium was used as carrier gas with a constant flow rate of 1.4 ml/min. GC oven temperature was held at 90 °C for 1 min and increased to 115 °C at 10 °C/min followed by 20 °C/min to 160 °C and a post run time of 4.25 min at 325 °C. Total run time was 10 min. Transfer line temperature was set to 280 °C. Mass selective detector

(MSD) was operating under electron ionization at 70 eV. MS source was held at 230 °C and the quadrupole at 150 °C. For precise quantification, measurements were performed in selected ion monitoring mode. Target ions (m/z) and dwell times are listed below in Table S2. GC-MS chromatograms were processed using Agilent MassHunter Quantitative Analysis for GC-MS, Version B.08.00. Natural isotope correction and analysis of formate release rates was done as previously described in (*24*).

Derivative (Metabolite)	Quant-Ion (m/z)	Dwell Time (ms)
Benzyl Formate M_0	136.1	40
Benzyl Formate M_1	137.1	40
IS-Benzyl Formate (^{13}C,D) M_0	138.1	40
IS-Benzyl Formate (^{13}C,D) M_1	139.1	40
IS-Benzyl Formate(^{13}C,D) M_2	140.1	40

Supplementary Table 2. Dwell times and quantification ions for the derivatized formate.

- Intracellular metabolites measurements (Fig. S3A, C)

First, dried polar extracts were derivatized for 90 min at 55 °C with 20 µl of methoxyamine (c = 20 mg/ml) in pyridine under continuous shaking and subsequently for 60 min at 55 °C with additional 20 µl of MTBSTFA w/ 1% TBDMCS. GC-MS analysis was performed using an Agilent 7890B GC coupled to an Agilent 5977 A Mass Selective Detector (Agilent Technologies). A sample volume of 1 µl was injected into a Split/Splitless inlet, operating in splitless mode at 270 °C. Gas chromatograph was equipped with a 30 m (I.D. 250 µm, film 0.25 µm) ZB-35MS capillary column with 5 m guard column (Phenomenex). Helium was used as carrier gas with a constant flow rate of 1.2 ml/min. GC oven temperature was held at 100°C for 2 min and increased to 300°C at 10°C/min and held for 4 min. Total run time was 26 min. Transfer line temperature was set to 280°C. Mass selective detector (MSD) was operating under electron ionization at 70 eV. MS source was held at 230°C and the quadrupole at 150 °C. For precise quantification of the MID, measurements were performed in selected ion monitoring mode. The derivative measured here was pyruvic acid 1MeOX 1TBDMS with target ions 174.0 – 180.1 [M-57 fragment] and dwell times of 15 ms. The MetaboliteDetector software package (Version 3.220180913) was used for mass spectrometric data post processing, quantification, MID calculations, correction of natural isotope abundance, and determinations of fractional carbon contributions (*57*).

IC-MS measurements (Fig. 1C-I, Fig. S4D and S6I-K)

For the IC-MS measurements, polar extracts were analyzed as previously described (*58*) with the following adjustments. 50-75% of the total polar extract was dried overnight under vacuum. Dried polar metabolite pellets were reconstituted in 25 µl of water (Milli-Q Advantage A10) of which 20 µl was injected. For the ICMS system, we interfaced a Dionex ICS-6000+ ion chromatograph coupled with a QExactive high resolution mass spectrometer (Thermo Fisher Scientific). The guard, column, gradient settings, and suppressor type remained unchanged (*58*). The electrospray ionization (ESI) was set as follows: spray voltage of 2.500 kV, auxiliary gas temperature of 420 °C,

seep gas flow rate of 0, auxiliary gas flow rate of 15 units, and sheath gas flow rate of 50 units. The settings for acquisition of MS1 data were: m/z scan range of 80-750, resolution of 17500 at 200 m/z, automatic gain control (AGC) target of 1e6, and maximum injection time of 100 milliseconds. Data were acquired using two micro-scans.

LC-MS Measurements

Metabolite analyses were performed using a Vanquish Flex LC coupled to a Q Exactive HF mass spectrometer (Thermo Scientific). Chromatography was carried out with a SeQuant ZIC-pHILIC 5 µm particles column (150 x 2.1 mm) protected by SeQuant ZIC-pHILIC Guard (20 x 2.1 mm) pre-column. Column temperature was maintained at 45°C. The flow rate was set to 0.2 ml/min and the mobile phases consisted of 20 mmol/L ammonium carbonate in water, pH 9.2 (Eluent A) and Acetonitrile (Eluent B). The gradient was: 0 min, 80% B; 2 min, 80% B; 17 min, 20% B; 18 min 20% B; 19 min 80% B; 20 min 80% B (0.4ml/min); 24 min 80% B (0.4ml/min); 24.5 min 80% B. The injection volume was 5 µL. All MS experiments were performed using electrospray ionization with polarity switching enabled . The source parameters were applied as follows: sheath gas flow rate, 25; aux gas flow rate, 15; sweep gas flow rate, 0; spray voltage, 4.5 kV (+) / 3.5 kV (-); capillary temperature, 325°C; S-lense RF level, 50; aux gas heater temperature, 50°C. The Orbitrap mass analyzer was operated at a resolving power of 30,000 at 200 m/z in full-scan mode (scan range: *m/z* 75…1000; automatic gain control target: 1e6; maximum injection time: 250 ms).

Data from IC-MS and LC-MS measurements were acquired with Thermo Xcalibur software (Version 4.3.73.11) and analyzed with TraceFinder (Version 4.1). Natural isotope subtraction and subsequent analysis were performed as previously described using in-house scripts (*24*).

Oxygen consumption rate measurements

10,000 cells (MDA-MB-468, 4T1 and MDA-MB-231) or 20,000 cells (HCT116) were seeded into 96-seahorse microplate (Agilent) on D-1. After attachment, glucose and galactose medium were added and cells were incubated for 24h. Basal OCR was measured using XF96 Extracellular Flux Analyzer (Seahorse bioscience, Agilent) following the manufacturer's protocol, Wave 2.6.0 software was used for analysis. OCR was normalised by the protein concentration of the corresponding wells following the protocol described in (*59*) and using a Bradford assay.

Statistics

Unless stated otherwise, unpaired two-tailed student's t-test with Welch's correction was used throughout the presented study as statistical tests were always performed between two groups. GraphPad PRISM (9.5.0) was used to calculate the *p* value. In the present study, *in vitro n* is defined as one independent experiment with at least two replicate wells (except for protein lysates and RNA samples where single wells were used). For *in vivo* experiments, *n* is defined as a sample from one mouse.

Figures

Figure 1

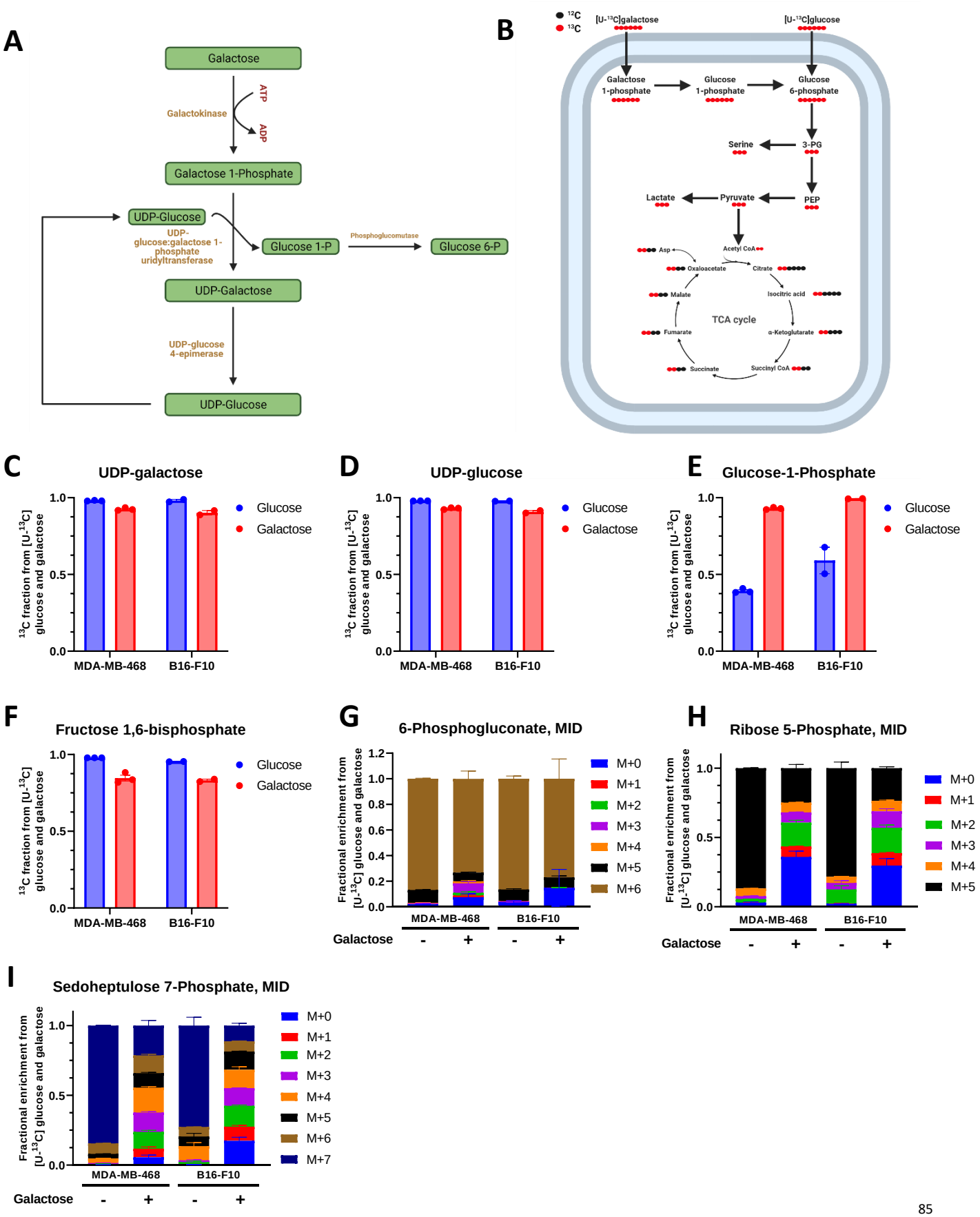

A
Galactose
Galactokinase
ATP
ADP
Galactose 1-Phosphate
UDP-Glucose
UDP-glucose:galactose 1-phosphate uridyltransferase
Glucose 1-P
Phosphoglucomutase
Glucose 6-P
UDP-Galactose
UDP-glucose 4-epimerase
UDP-Glucose
B
12C
13C
[U-13C]galactose
[U-13C]glucose
Galactose 1-phosphate
Glucose 1-phosphate
Glucose 6-phosphate
Serine
3-PG
Lactate
Pyruvate
PEP
Acetyl CoA
Asp
Oxaloacetate
Citrate
Malate
Isocitric acid
TCA cycle
Fumarate
α-Ketoglutarate
Succinate
Succinyl CoA
C
UDP-galactose
D
UDP-glucose
E
Glucose-1-Phosphate
13C fraction from [U-13C] glucose and galactose
Glucose
Galactose
MDA-MB-468
B16-F10
F
Fructose 1,6-bisphosphate
G
6-Phosphogluconate, MID
H
Ribose 5-Phosphate, MID
Fractional enrichment from [U-13C] glucose and galactose
M+0
M+1
M+2
M+3
M+4
M+5
M+6
Galactose
I
Sedoheptulose 7-Phosphate, MID
M+7

Figure 1. Cancer cells metabolize galactose and utilize it to support early glycolysis. A Schematic representation of Leloir pathway for galactose metabolism. **B** Schematic representation of the expected labelling pattern of simplified central carbon metabolism when using [U-^{13}C] glucose and [U-^{13}C] galactose tracer. **C-F** ^{13}C fraction from [U-^{13}C] glucose and [U-^{13}C] galactose into UDP-galactose **(C)**, UDP-glucose **(D)**, glucose 1-phosphate **(E)** and fructose 1,6-bisphosphate **(F)** after 24h incubation. (**C-F**) Each dot represents an independent experiment averaged from 3 different replicate wells. **G-I** Fractional enrichment in 6-phosphogluconate **(G)**, ribose 5-phosphate **(H)** and sedoheptulose 7-phosphate **(I)** from [U-^{13}C] glucose and [U-^{13}C] galactose after 24h incubation. Data shown is mean±SEM of 3 (MDA-MB-468) or 2 (B16-F10) independent experiments each being the average of 3 different replicate wells.

Figure 2

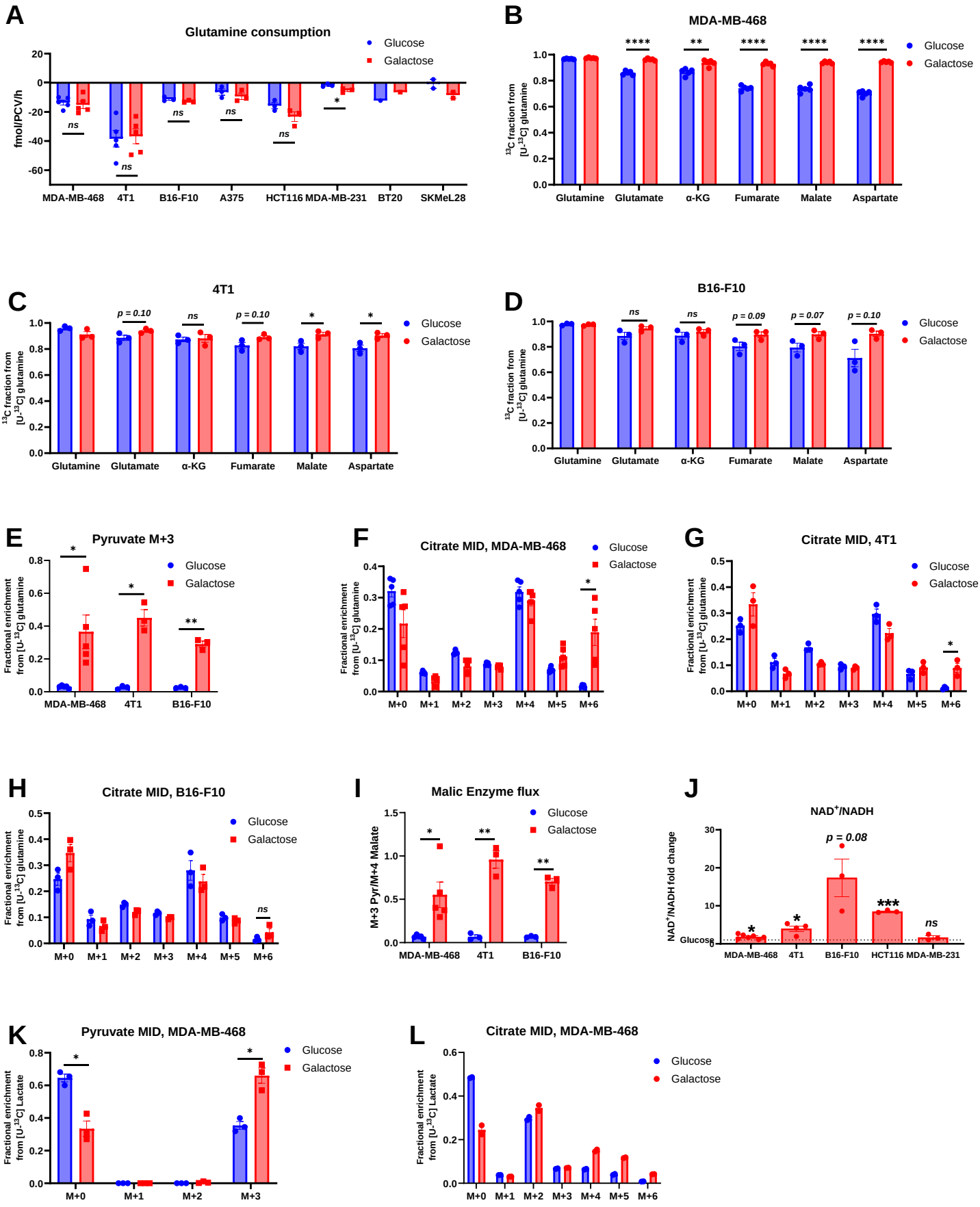

A
Glutamine consumption
Glucose
Galactose
fmol/PCV/h
MDA-MB-468
4T1
B16-F10
A375
HCT116
MDA-MB-231
BT20
SKMeL28
B
MDA-MB-468
Glucose
Galactose
Glutamine
Glutamate
α-KG
Fumarate
Malate
Aspartate
C
4T1
D
B16-F10
E
Pyruvate M+3
Fractional enrichment from [U-13C] glutamine
F
Citrate MID, MDA-MB-468
G
Citrate MID, 4T1
H
Citrate MID, B16-F10
I
Malic Enzyme flux
M+3 Pyr/M+4 Malate
J
NAD+/NADH
p = 0.08
NAD+/NADH fold change
K
Pyruvate MID, MDA-MB-468
Fractional enrichment from [U-13C] Lactate
L
Citrate MID, MDA-MB-468

Figure 2. Glutamine and lactate maintain upregulated oxidative TCA cycle function in reliance on malic enzyme (ME). **A** Absolute quantification of glutamine consumption from multiple cancer cell lines after 24h incubation with either glucose or galactose medium. **B-D** ^{13}C fraction in TCA cycle metabolites from [U-^{13}C] glutamine after 24h incubation with either glucose or galactose medium in MDA-MB-468 **(B)**, 4T1 **(C)** and B16-F10 **(D)**. **E** Fractional enrichment in M+3 pyruvate from [U-^{13}C] glutamine after 24h incubation with either glucose or galactose medium in MDA-MB-468, 4T1 and B16-F10. **F-H** Fractional enrichment in citrate from [U-^{13}C] glutamine after 24h incubation with either glucose or galactose medium in MDA-MB-468 **(F)**, 4T1 **(G)** and B16-F10 **(H)**. **I** Malic enzyme flux ratio calculated as M+3 pyruvate/M+4 malate isotopologues from [U-^{13}C] glutamine after 24h incubation with either glucose or galactose medium in MDA-MB-468, 4T1 and B16-F10. **J** NAD^+/NADH ratio measured with LC-MS in the indicated cancer cell lines after 24h incubation with galactose and normalised to the same ratio with 24h incubation with glucose medium. **K-L** Fractional enrichment in pyruvate **(K)** and citrate **(L)** from 5mM [U-^{13}C] sodium lactate after 24h incubation with either glucose or galactose medium in MDA-MB-468. (**A-L**) Each dot represents an independent experiment averaged from 3 different replicate wells unless stated otherwise. (**A-L**) Mean±SEM, * p<0.05, ** p<0.01, *** p<0.001, **** p<0.0001, ns p>0.1. *P* value is calculated by Student's t-test, two-tailed, unpaired with Welch's correction unless stated otherwise.

Figure 3

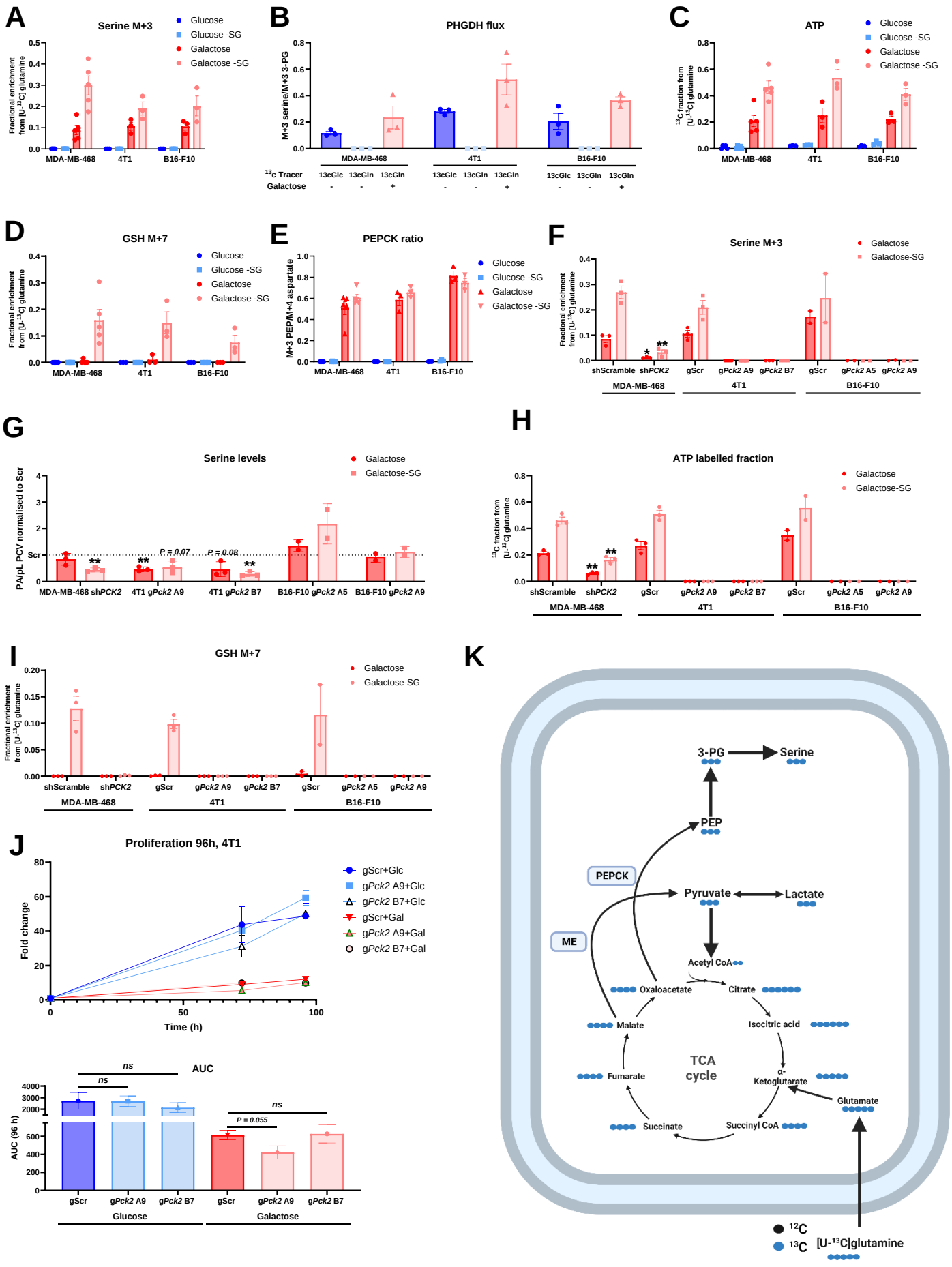

A
Serine M+3
Glucose
Glucose -SG
Galactose
Galactose -SG
Fractional enrichment from [U-13C] glutamine
MDA-MB-468
4T1
B16-F10
B
PHGDH flux
M+3 serine/M+3 3-PG
13C Tracer
Galactose
13cGlc
13cGln
C
ATP
13C fraction from [U-13C] glutamine
D
GSH M+7
E
PEPCK ratio
M+3 PEP/M+4 aspartate
F
Serine M+3
Galactose
Galactose-SG
shScramble
shPCK2
gScr
gPck2 A9
gPck2 B7
gPck2 A5
G
Serine levels
PA/pL PCV normalised to Scr
P = 0.07
P = 0.08
H
ATP labelled fraction
I
GSH M+7
J
Proliferation 96h, 4T1
Fold change
Time (h)
gScr+Glc
gPck2 A9+Glc
gPck2 B7+Glc
gScr+Gal
gPck2 A9+Gal
gPck2 B7+Gal
AUC
AUC (96 h)
ns
P = 0.055
Glucose
Galactose
K
3-PG
Serine
PEP
PEPCK
Pyruvate
Lactate
ME
Acetyl CoA
Oxaloacetate
Citrate
Malate
Isocitric acid
TCA cycle
Fumarate
α-Ketoglutarate
Glutamate
Succinate
Succinyl CoA
12C
13C
[U-13C]glutamine

Figure 3. Glutamine metabolism is redirected towards SSP under glycolytic limitation via PEPCK. A Fractional enrichment in M+3 serine from [U-^{13}C] glutamine after 24h incubation with either glucose ± serine and glycine (SG) or galactose ± SG medium in MDA-MB-468, 4T1 and B16-F10. **B** Phosphoglycerate dehydrogenase (PHGDH) enzyme flux ratio calculated as M+3 serine/M+3 3-PG isotopologues from [U-^{13}C] glucose or glutamine (either with glucose or galactose medium) after 24h incubation in MDA-MB-468, 4T1 and B16-F10. **C** ^{13}C fraction in ATP from [U-^{13}C] glutamine after 24h incubation with either glucose ± SG or galactose ± SG medium in MDA-MB-468, 4T1 and B16-F10. **D** Fractional enrichment in M+7 glutathione (GSH) from [U-^{13}C] glutamine after 24h incubation with either glucose ± SG or galactose ± SG medium in MDA-MB-468, 4T1 and B16-F10. **E** Phosphoenolpyruvate carboxykinase (PEPCK) enzyme flux ratio calculated as M+3 PEP/M+4 aspartate isotopologues from [U-^{13}C] glutamine after 24h incubation with either glucose ± SG or galactose ± SG medium in MDA-MB-468, 4T1 and B16-F10. **F** Fractional enrichment in M+3 serine from [U-^{13}C] glutamine after 24h incubation with either glucose ± SG or galactose ± SG medium in MDA-MB-468 shScramble and sh*PCK2* cells, 4T1 and B16-F10 gScramble and g*Pck2* cells. **G** Peak areas (PA) of intracellular serine in PEPCK2 KD/KOs normalised to packed cell volume (PCV) in picolitres (pL) and presented as fold change to the levels in scramble cells. Data shown is for the levels measured in galactose ± SG medium. **H** ^{13}C fraction in ATP from [U-^{13}C] glutamine after 24h incubation with galactose ± SG medium and the comparison between scramble and PEPCK2 KD/KOs cells. **I** Fractional enrichment in M+7 glutathione (GSH) from [U-^{13}C] glutamine after 24h incubation with galactose ± SG medium and the comparison between scramble and PEPCK2 KD/KOs cells. **J** 2D proliferation curve of 4T1 gScramble and g*Pck2* cells with either glucose or galactose, with the corresponding area under the curve (AUC). 72h timepoint includes 3 independent experiments while 96h includes 4 independent experiments (from at least 3 different replicate wells for each independent experiment). (**A-J**) Each dot represents an independent experiment averaged from 3 different replicate wells unless stated otherwise. (**A-J**) Mean±SEM, * p<0.05, ** p<0.01, *** p<0.001, **** p<0.0001, ns p>0.1. *P* value is calculated by Student's t-test, two-tailed, unpaired with Welch's correction unless stated otherwise. **K** Schematic representation of the rewiring of glutamine metabolism that take place under glycolytic limitation.

Figure 4

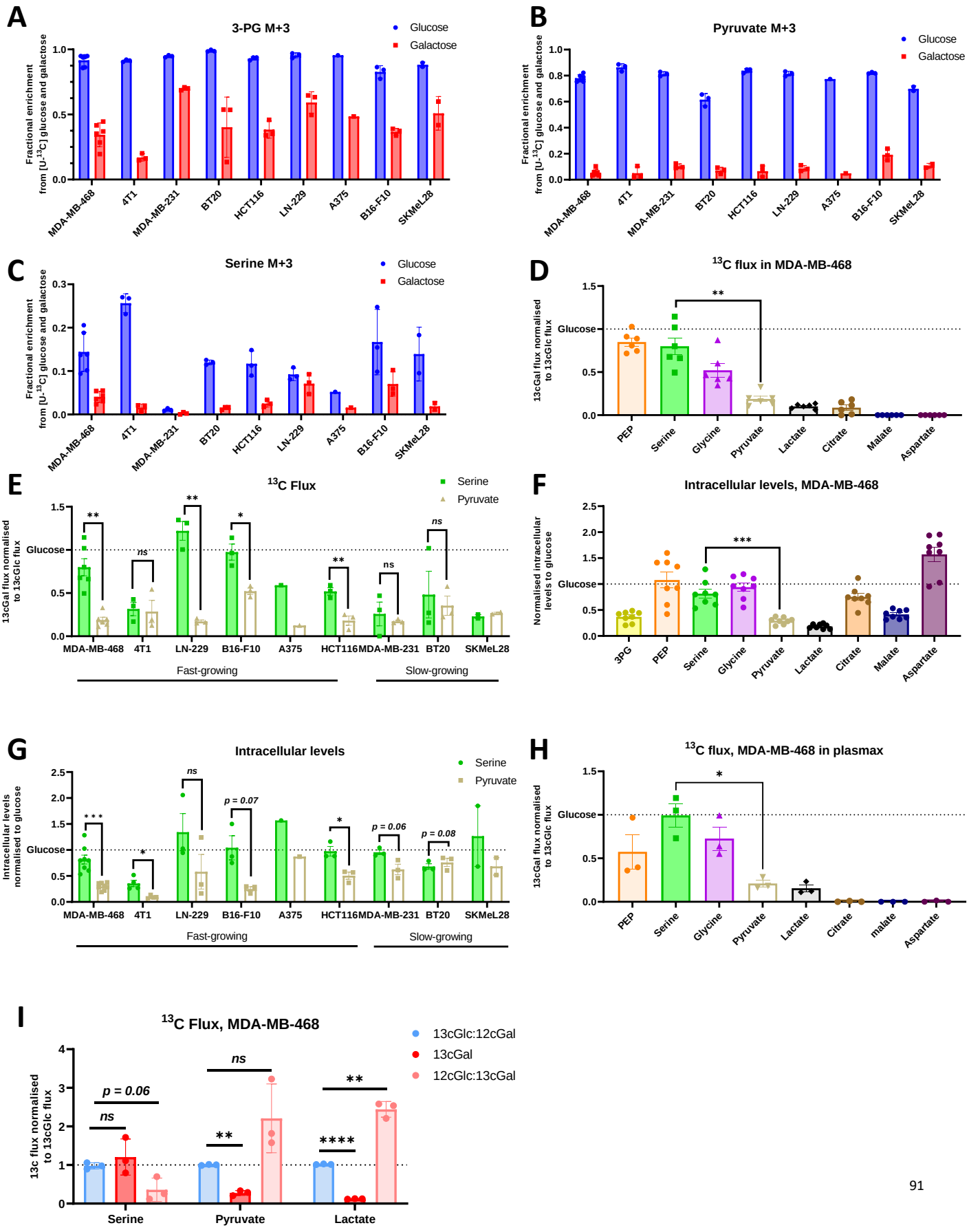

A
3-PG M+3
Glucose
Galactose
Fractional enrichment from [U-13C] glucose and galactose
MDA-MB-468
4T1
MDA-MB-231
BT20
HCT116
LN-229
A375
B16-F10
SKMeL28
B
Pyruvate M+3
C
Serine M+3
D
13C flux in MDA-MB-468
13cGal flux normalised to 13cGlc flux
PEP
Serine
Glycine
Pyruvate
Lactate
Citrate
Malate
Aspartate
E
13C Flux
Fast-growing
Slow-growing
F
Intracellular levels, MDA-MB-468
Normalised intracellular levels to glucose
3PG
G
Intracellular levels
H
13C flux, MDA-MB-468 in plasmax
I
13C Flux, MDA-MB-468
13cGlc:12cGal
13cGal
12cGlc:13cGal
13c flux normalised to 13cGlc flux

Figure 4. Cancer cells sustain carbon flux towards serine synthesis pathway (SSP) under glycolytic limitation. A-C Fractional enrichment from 17.5 mM [U-^{13}C] glucose and galactose into M+3 3PG (**A**), M+3 pyruvate (**B**) and M+3 serine (**C**) after 24h incubation measured with LC-MS. **D-E** The normalised relative ^{13}C flux under galactose towards multiple metabolites represented as a fold change of the same ratio under glucose in MDA-MB-468 (**D**) and a panel of 9 cancer cell lines (**E**). Fast-growing cells are those with doubling time <24h. **F-G** Intracellular levels of multiple metabolites under galactose represented as a fold change of the levels under glucose in MDA-MB-468 (**F**) and a panel of 9 cancer cell lines (**G**). **H** The normalised relative ^{13}C flux under galactose towards multiple metabolites represented as a fold change of the same ratio under glucose in MDA-MB-468 when cultured in physiological medium Plasmax. **I** The normalised relative ^{13}C flux under galactose and glucose:galactose mixes towards multiple metabolites represented as a fold change of the same ratio under glucose in MDA-MB-468. (**A**-**I**) Each dot represent an independent experiment (from 3 different replicate wells). (**A-I**) Mean±SEM, * p<0.05, ** p<0.01, *** p<0.001, **** p<0.0001, ns p>0.1. *P* value is calculated by Student's t-test, two-tailed, unpaired with Welch's correction.

Figure 5

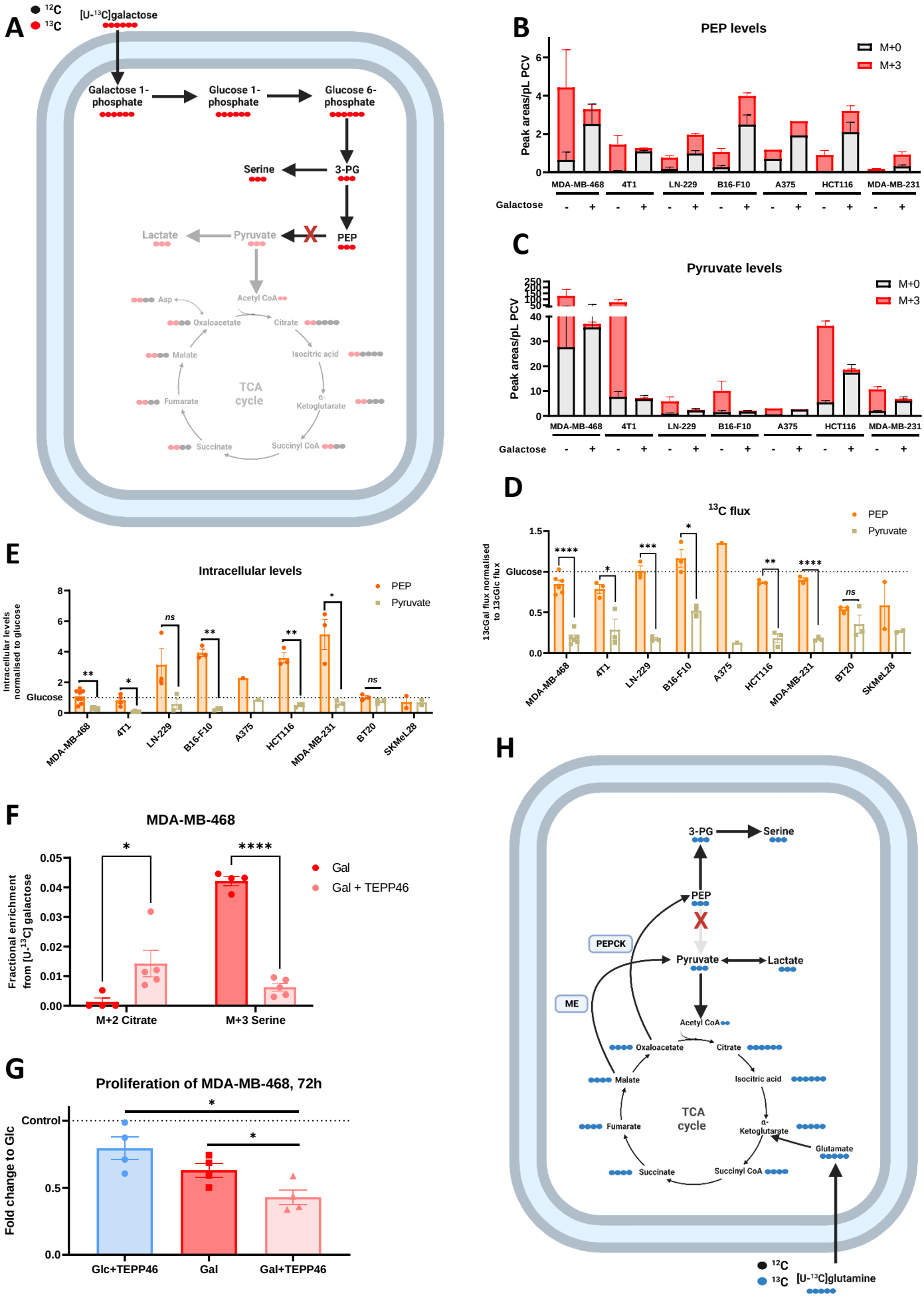

A
12C
13C
[U-13C]galactose
Galactose 1-phosphate
Glucose 1-phosphate
Glucose 6-phosphate
Serine
3-PG
Lactate
Pyruvate
PEP
Acetyl CoA
Asp
Oxaloacetate
Citrate
Isocitric acid
Malate
TCA cycle
Fumarate
α-Ketoglutarate
Succinate
Succinyl CoA
B
PEP levels
M+0
M+3
Peak areas/pL PCV
MDA-MB-468
4T1
LN-229
B16-F10
A375
HCT116
MDA-MB-231
Galactose
C
Pyruvate levels
D
13C flux
PEP
Pyruvate
13cGal flux normalised to 13cGlc flux
Glucose
BT20
SKMeL28
E
Intracellular levels
Intracellular levels normalised to glucose
F
MDA-MB-468
Fractional enrichment from [U-13C] galactose
Gal
Gal + TEPP46
M+2 Citrate
M+3 Serine
G
Proliferation of MDA-MB-468, 72h
Fold change to Glc
Control
Glc+TEPP46
Gal
Gal+TEPP46
H
3-PG
Serine
PEP
PEPCK
Pyruvate
Lactate
ME
Acetyl CoA
Oxaloacetate
Citrate
Malate
Isocitric acid
TCA cycle
Fumarate
α-Ketoglutarate
Glutamate
Succinate
Succinyl CoA
12C
13C
[U-13C]glutamine

Figure 5. Glycolytic limitation inhibits glycolytic flux at pyruvate kinase isozyme M2 (PKM2). A Schematic representation of glycolysis and TCA cycle upon isotopologue labelling with [U-^{13}C] glucose and galactose with the proposed block at PKM2. **B-C** Peak areas of M+0 and M+3 isotopologues of PEP (**B**) and pyruvate (**C**) after 24h incubation with [U-^{13}C] glucose and galactose and normalisation to packed cell volume (PCV). **D** The normalised relative ^{13}C flux under galactose towards PEP and pyruvate represented as a fold change of the same ratio under glucose in a panel of 9 cancer cell lines. **E** Intracellular levels of PEP and pyruvate under galactose represented as a fold change of the levels under glucose in a panel of 9 cancer cell lines. **F** Fractional enrichment from [U-^{13}C] galactose into M+2 citrate and M+3 serine after 24h incubation (Gal+TEPP-46) as measured with LC-MS. **G** 2D proliferation of MDA-MB-468 treated with 100 μM of TEPP-46 with either glucose or galactose and measured as cell counts at 72h relative to proliferation under glucose. (**B**-**G**) Each dot represents an independent experiment (from at least 3 different replicate wells). (**B**-**G**) Mean±SEM, * p<0.05, ** p<0.01, *** p<0.001, **** p<0.0001, ns p>0.1. *P* value is calculated by Student's t-test, two-tailed, unpaired with Welch's correction. **H** Schematic representation of the rewiring of glutamine metabolism that take place under glycolytic limitation and the differentiation between ME and PEPCK2 fluxes.

Figure 6

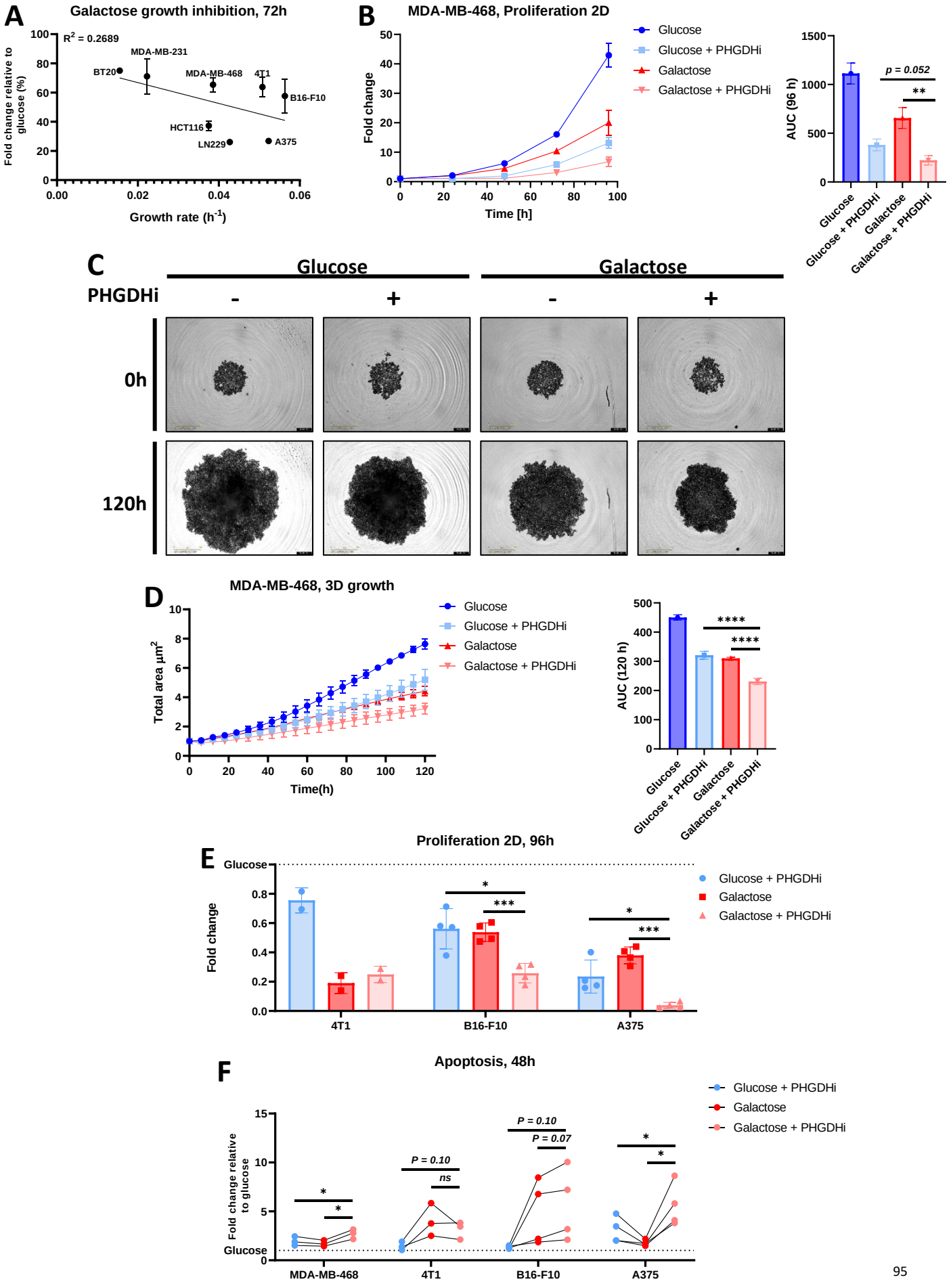

A
Galactose growth inhibition, 72h
R² = 0.2689
MDA-MB-231
BT20
MDA-MB-468
4T1
B16-F10
HCT116
LN229
A375
Fold change relative to glucose (%)
Growth rate (h-1)
B
MDA-MB-468, Proliferation 2D
Glucose
Glucose + PHGDHi
Galactose
Galactose + PHGDHi
Fold change
Time [h]
AUC (96 h)
p = 0.052
**
C
Glucose
Galactose
PHGDHi
0h
120h
D
MDA-MB-468, 3D growth
Total area µm²
Time(h)
AUC (120 h)
****
E
Proliferation 2D, 96h
Fold change
4T1
B16-F10
A375
F
Apoptosis, 48h
Fold change relative to glucose
MDA-MB-468
P = 0.10
ns
P = 0.07

Figure 6. SSP is needed for proliferation and viability under glycolytic limitation. A The correlation between the growth rate of different cancer cell lines and the extent to which galactose inhibits their proliferation (represented as a percentage of growth under glucose). MDA-MB-468 n=5, 4T1 n=2, HCT116 n=2, MDA-MB-231 n=2, B16-F10 n=3, A375 n=3, BT20 n=1 and LN-229 n=1. R^2 measured for the line of best-fit using simple linear regression. **B** 2D proliferation of MDA-MB-468 when treated with 15 μM of the PHGDH inhibitor BI-4916 (PHGDHi) with either glucose or galactose, with the corresponding area under the curve (AUC). 24h and 96h timepoints include 4 independent replicates while 48h and 72h include 5 independent replicates (from at least 3 different replicate wells for each independent experiment). **C** Bright field images are representative of 3 independent experiments of MDA-MB-468 aggregates growing in anchorage-independent conditions. Scale bar represent 800 μm. **D** 3D growth of MDA-MB-468 aggregates using anchorage-independent conditions when treated with 15 μM of PHGDHi with either glucose or galactose, with the corresponding AUC. 3 independent experiments are represented each with at least 6 different replicate wells. **E** 2D proliferation of multiple cancer cell lines when treated with 15 μM of PHGDHi with either glucose or galactose as measured with cell counts at 96h relative to proliferation under glucose. Each dot represent an independent experiment from at least 3 different replicate wells. (**B**, **D, E**) Mean±SEM, * p<0.05, ** p<0.01, *** p<0.001, **** p<0.0001, n.s. p>0.1. *P* value is calculated by Student's t-test, two-tailed, unpaired with Welch's correction. **F** Viability of different cancer cell lines when treated with 15 μM of PHGDHi with either glucose or galactose for 48h as measured as annexin V^+ cells after excluding necrotic cells (PI). MDA-MB-468 and 4T1 n=3, B16-F10 and A375 n=4. Data shown is the mean, * p<0.05, ns p>0.1. *P* value is calculated by Student's t-test, two-tailed, paired.

Figure 7

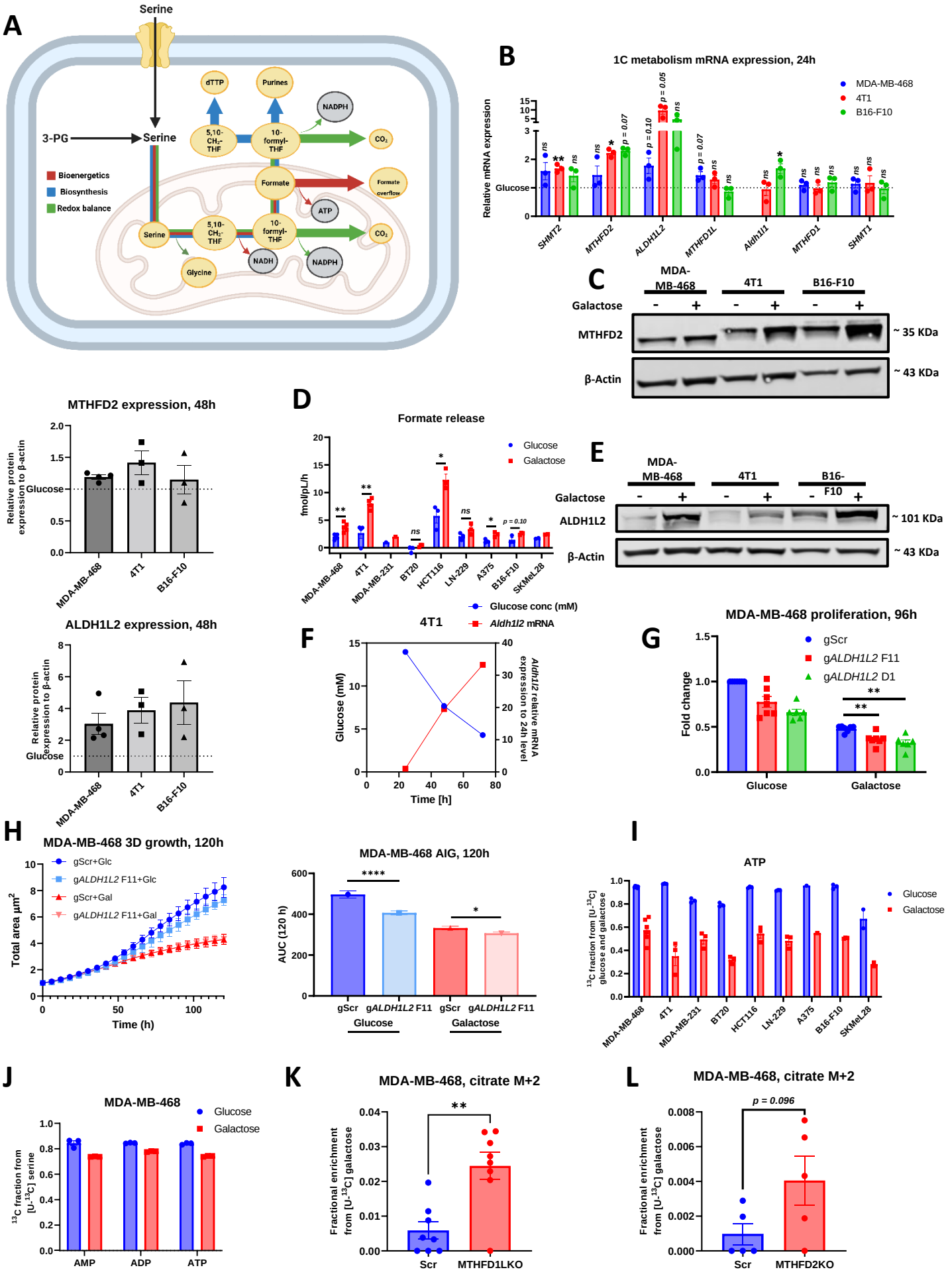
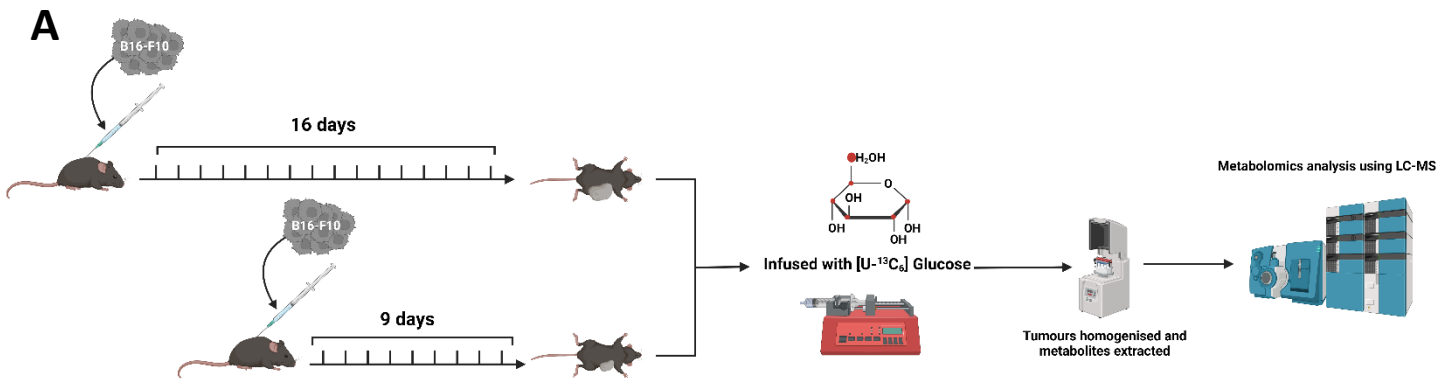
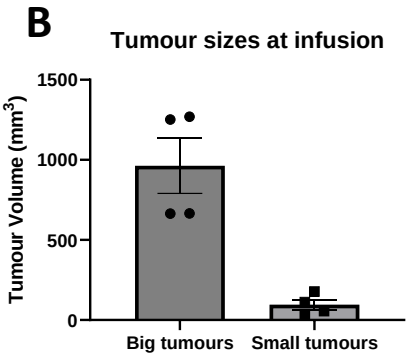
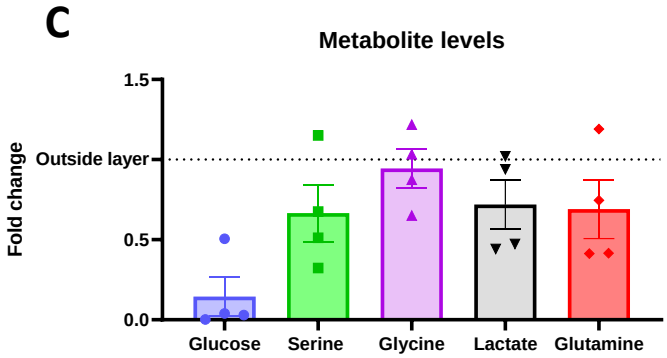

A
Serine
3-PG
Serine
dTTP
Purines
NADPH
5,10-CH2-THF
10-formyl-THF
CO2
Formate
Formate overflow
ATP
Bioenergetics
Biosynthesis
Redox balance
Serine
5,10-CH2-THF
10-formyl-THF
CO2
NADH
NADPH
Glycine
B
1C metabolism mRNA expression, 24h
MDA-MB-468
4T1
B16-F10
Relative mRNA expression
Glucose
SHMT2
MTHFD2
ALDH1L2
MTHFD1L
Aldh1l1
MTHFD1
SHMT1
C
MDA-MB-468
4T1
B16-F10
Galactose
MTHFD2
~ 35 KDa
β-Actin
~ 43 KDa
MTHFD2 expression, 48h
Relative protein expression to β-actin
Glucose
MDA-MB-468
4T1
B16-F10
D
Formate release
Glucose
Galactose
fmol/pL/h
MDA-MB-468
4T1
MDA-MB-231
BT20
HCT116
LN-229
A375
B16-F10
SKMeL28
E
MDA-MB-468
4T1
B16-F10
Galactose
ALDH1L2
~ 101 KDa
β-Actin
~ 43 KDa
ALDH1L2 expression, 48h
Relative protein expression to β-actin
Glucose
MDA-MB-468
4T1
B16-F10
F
4T1
Glucose conc (mM)
Aldh1l2 mRNA
Glucose (mM)
Aldh1l2 relative mRNA expression to 24h level
Time [h]
G
MDA-MB-468 proliferation, 96h
gScr
gALDH1L2 F11
gALDH1L2 D1
Fold change
Glucose
Galactose
H
MDA-MB-468 3D growth, 120h
gScr+Glc
gALDH1L2 F11+Glc
gScr+Gal
gALDH1L2 F11+Gal
Total area µm2
Time (h)
MDA-MB-468 AIG, 120h
AUC (120 h)
gScr
gALDH1L2 F11
gScr
gALDH1L2 F11
Glucose
Galactose
I
ATP
Glucose
Galactose
13C fraction from [U-13C] glucose and galactose
MDA-MB-468
4T1
MDA-MB-231
BT20
HCT116
LN-229
A375
B16-F10
SKMeL28
J
MDA-MB-468
Glucose
Galactose
13C fraction from [U-13C] serine
AMP
ADP
ATP
K
MDA-MB-468, citrate M+2
Fractional enrichment from [U-13C] galactose
Scr
MTHFD1LKO
L
MDA-MB-468, citrate M+2
p = 0.096
Fractional enrichment from [U-13C] galactose
Scr
MTHFD2KO

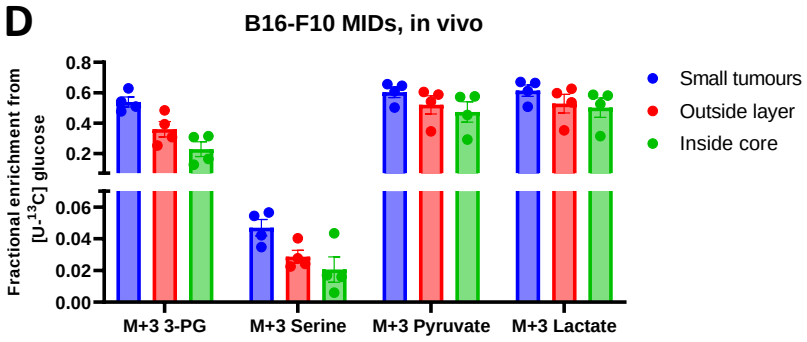
Figure 7. SSP flux is crucial to sustain mitochondrial formate production to support all three metabolic pillars. A Schematic representation of the one-carbon cycle with the different pillars and how it can contribute to biosynthesis, bioenergetic and redox balance. **B** mRNA expression of *SHMT2*, *MTHFD2*, *AALDH1L2*, *MTHFD1L*, *Aldh1l1, MTHFD1* and *SHMT1* genes relative to *GAPDH* and *ACTINβ* or *Gapdh and Sdha* after 24h incubation with either glucose or galactose measured with RT-qPCR. Data presented as fold change to the mRNA expression in cells cultured with glucose. **C** Protein expression of MTHFD2 after 48h incubation with either glucose or galactose, with the quantification of these signals relative to β-actin as a loading control and presented as a fold change of expression under galactose to that of glucose. **D** Absolute quantification of formate release from the indicated cancer cell lines after 24h incubation with either glucose or galactose. **E** Protein expression of ALDH1L2 after 48h incubation with either glucose or galactose, with the quantification of these signals relative to β-actin as a loading control and presented as a fold change of expression under galactose to that of glucose. **F** Concentration of glucose as measured in media in which 4T1 cells were cultured for 72h, compared to A*ldh1l2* mRNA expression relative to *Gapdh* and presented as fold change for expression at 24h. Data presented in **F** is from one independent experiment, mRNA was extracted from single wells while medium measurement are mean±SEM of 3 different replicate wells. **G** 2D proliferation of MDA-MB-468 Scramble and ALDH1L2KO cells cultured in either glucose or galactose as measured with cell counts at 96h relative to proliferation of scramble cells under glucose. **H** 3D growth of MDA-MB-468 control and ALDH1L2KO aggregates using anchorage-independent conditions in either glucose or galactose, with the corresponding AUC. 3 independent experiments are represented each with at least 6 different replicate wells. **I** ^{13}C fraction in ATP from [U-^{13}C] glucose and galactose after 24h incubation in multiple cell lines. **J** ^{13}C fraction in AMP/ADP/ATP from [U-^{13}C] serine after 24h incubation in MDA-MB-468. **K-L** Fractional enrichment from [U-^{13}C] galactose into M+2 citrate after 24h incubation in MDA-MB-468 Scramble compared to MTHFD1LKO (**K**) and MTHFD2KO (**L**) as measured with LC-MS. (**B-L**) Each dot represent an independent experiment averaged from 3 different replicate wells unless stated otherwise. (**B**-**L**) Mean±SEM, * p<0.05, ** p<0.01, *** p<0.001, **** p<0.0001, ns p>0.1. *P* value is calculated by Student's t-test, two-tailed, unpaired with Welch's correction unless stated otherwise.

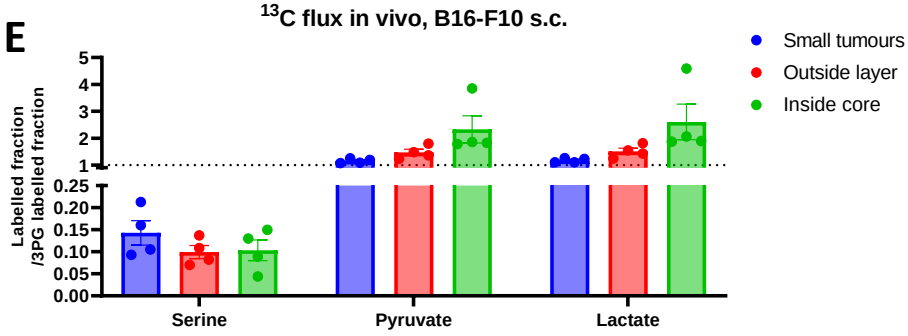
Figure 8

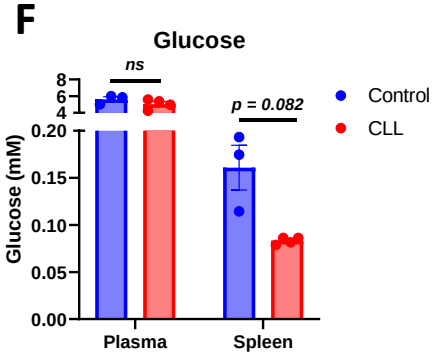

A
B16-F10
16 days
B16-F10
9 days
Infused with [U-13C6] Glucose
Tumours homogenised and metabolites extracted
Metabolomics analysis using LC-MS


B
Tumour sizes at infusion
Tumour Volume (mm3)
1500
1000
500
0
Big tumours
Small tumours


C
Metabolite levels
Fold change
1.5
Outside layer
0.5
0.0
Glucose
Serine
Glycine
Lactate
Glutamine


D
B16-F10 MIDs, in vivo
Fractional enrichment from [U-13C] glucose
0.8
0.6
0.4
0.2
0.06
0.04
0.02
0.00
M+3 3-PG
M+3 Serine
M+3 Pyruvate
M+3 Lactate
Small tumours
Outside layer
Inside core


E
13C flux in vivo, B16-F10 s.c.
Labelled fraction /3PG labelled fraction
5
4
3
2
1
0.25
0.20
0.15
0.10
0.05
0.00
Serine
Pyruvate
Lactate
Small tumours
Outside layer
Inside core


F
Glucose
ns
p = 0.082
Glucose (mM)
8
6
4
0.20
0.15
0.10
0.05
0.00
Plasma
Spleen
Control
CLL

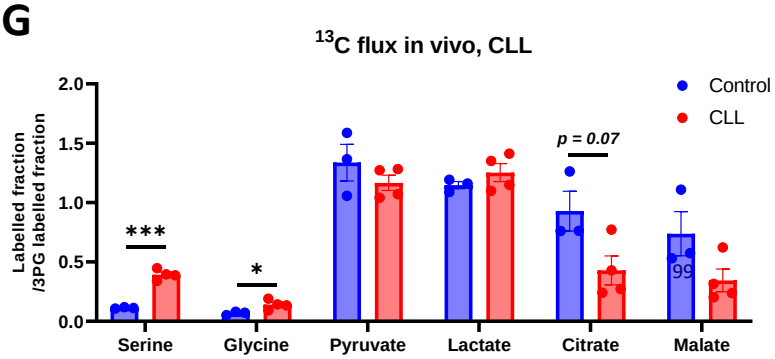
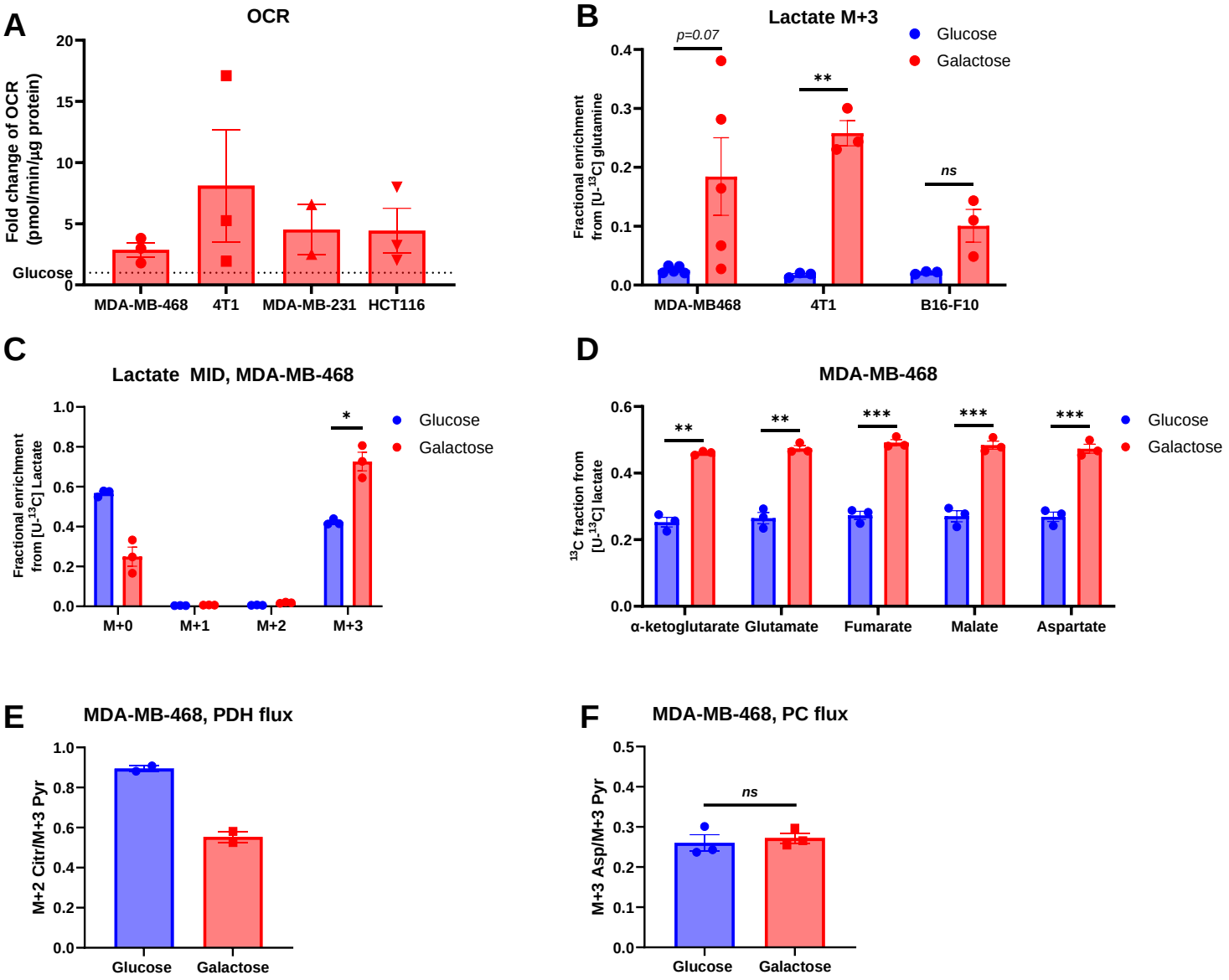

G
13C flux in vivo, CLL
Labelled fraction /3PG labelled fraction
2.0
1.5
1.0
0.5
0.0
***
*
p = 0.07
Serine
Glycine
Pyruvate
Lactate
Citrate
Malate
Control
CLL

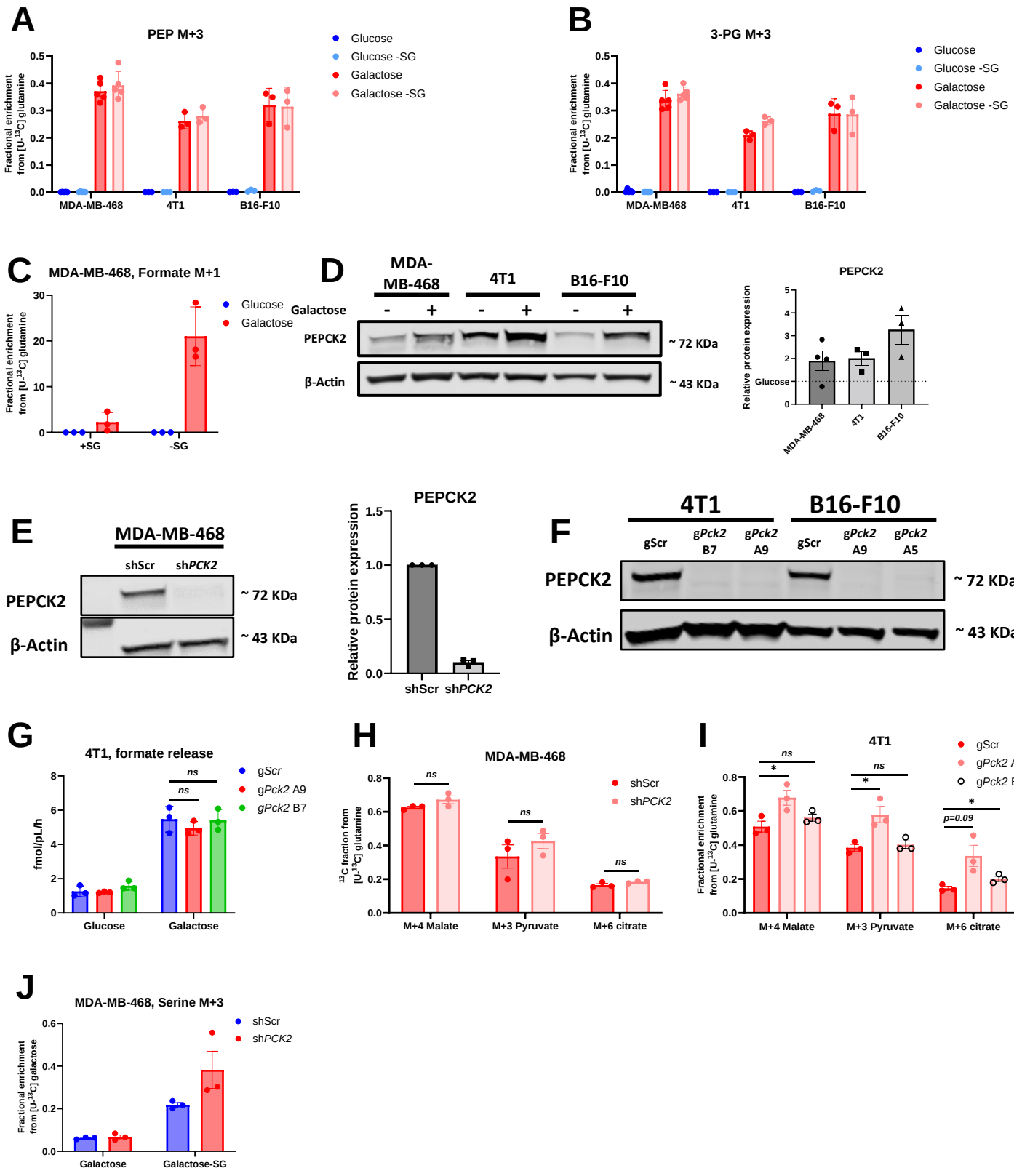
Figure 8. *In vivo* relevance of using Gal to model glycolytic limitation. **A** Schematic representation of the *in vivo* setup for B16-F10 subcutaneous tumours. **B** Tumour volume of B16-F10 tumours grown subcutaneously on the flanks of C57BL/6 mice (n=4/group). **C** Metabolite levels measured from the inside core of B16-F10 tumours and presented as fold change of the level of those metabolites in the outside layer of the same tumours. **D** Fractional enrichment in tumour piece of the presented metabolites after 2h infusion with [U-^{13}C] glucose via the tail vain. **E** The ^{13}C flux from 3-PG towards multiple metabolites measured in B16-F10 tumours. **F** Glucose concentration as measured in the plasma and in grinded spleen tissue from control and CLL mice after 2h continuous infusion with [U-^{13}C] glucose. The concentration was determined using standard addition method. **G** The ^{13}C flux from 3-PG towards multiple metabolites measured in CLL cells collected from the spleen of CLL mice. (**B-G**) Each dot represent a biological replicate. (**A-F**) Mean±SEM, * p<0.05, ** p<0.01, *** p<0.001, **** p<0.0001, ns p>0.1. *P* value is calculated by Student's t-test, two-tailed, unpaired with Welch's correction unless stated otherwise.

Figure S1


A
OCR
Fold change of OCR (pmol/min/µg protein)
Glucose
MDA-MB-468
4T1
MDA-MB-231
HCT116
B
Lactate M+3
p=0.07
**
ns
Glucose
Galactose
Fractional enrichment from [U-13C] glutamine
MDA-MB468
4T1
B16-F10
C
Lactate MID, MDA-MB-468
*
Glucose
Galactose
Fractional enrichment from [U-13C] Lactate
M+0
M+1
M+2
M+3
D
MDA-MB-468
**
**
***
***
***
Glucose
Galactose
13C fraction from [U-13C] lactate
α-ketoglutarate
Glutamate
Fumarate
Malate
Aspartate
E
MDA-MB-468, PDH flux
M+2 Citr/M+3 Pyr
Glucose
Galactose
F
MDA-MB-468, PC flux
ns
M+3 Asp/M+3 Pyr
Glucose
Galactose

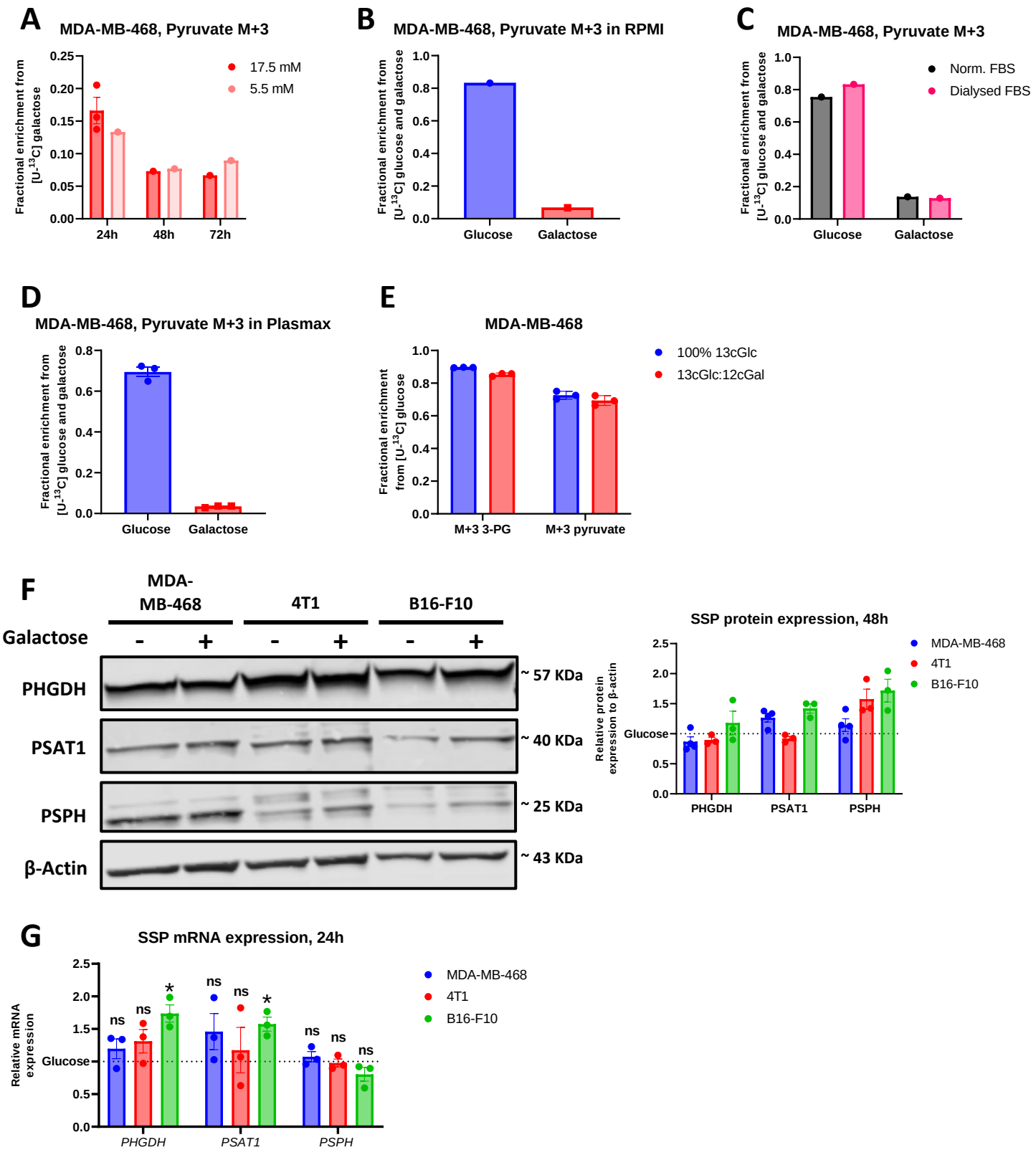
Supplementary Figure 1. A Basal oxygen consumption rate (OCR) measured by seahorse in 4 different cancer cell lines after 24h incubation with galactose and presented as fold change to the same measurements with glucose. **B** Fractional enrichment in M+3 lactate from [U-^{13}C] glutamine after 24h incubation with either glucose or galactose medium in MDA-MB-468, 4T1 and B16-F10. **C** Fractional enrichment in lactate from [U-^{13}C] sodium lactate after 24h incubation with either glucose or galactose medium in MDA-MB-468. **D** ^{13}C fraction in TCA cycle metabolites from [U-^{13}C] sodium lactate after 24h incubation with either glucose or galactose medium in MDA-MB-468. **E** Pyruvate dehydrogenase (PDH) enzyme flux ratio calculated as M+2 citrate/M+3 pyruvate isotopologues from [U-^{13}C] sodium lactate after 24h incubation with either glucose or galactose medium in MDA-MB-468. **F** Pyruvate carboxylase (PC) enzyme flux ratio calculated as M+3 aspartate/M+3 pyruvate isotopologues from [U-^{13}C] sodium lactate after 24h incubation with either glucose or galactose medium in MDA-MB-468. (**A-F**) Each dot represents an independent experiment averaged from 3 different replicate wells. (**A-F**) Mean±SEM, * p<0.05, ** p<0.01, *** p<0.001, **** p<0.0001, ns p>0.1. *P* value is calculated by Student's t-test, two-tailed, unpaired with Welch's correction.

Figure S2


A
PEP M+3
Fractional enrichment from [U-13C] glutamine
MDA-MB-468
4T1
B16-F10
Glucose
Glucose -SG
Galactose
Galactose -SG
B
3-PG M+3
MDA-MB468
C
MDA-MB-468, Formate M+1
+SG
-SG
D
MDA-MB-468
4T1
B16-F10
Galactose
PEPCK2
β-Actin
~ 72 KDa
~ 43 KDa
PEPCK2
Relative protein expression
Glucose
E
MDA-MB-468
shScr
shPCK2
F
4T1
B16-F10
gScr
gPck2 B7
gPck2 A9
gPck2 A5
G
4T1, formate release
fmol/pL/h
gScr
gPck2 A9
gPck2 B7
H
MDA-MB-468
13C fraction from [U-13C] glutamine
M+4 Malate
M+3 Pyruvate
M+6 citrate
I
4T1
p=0.09
J
MDA-MB-468, Serine M+3
Fractional enrichment from [U-13C] galactose
Galactose
Galactose-SG

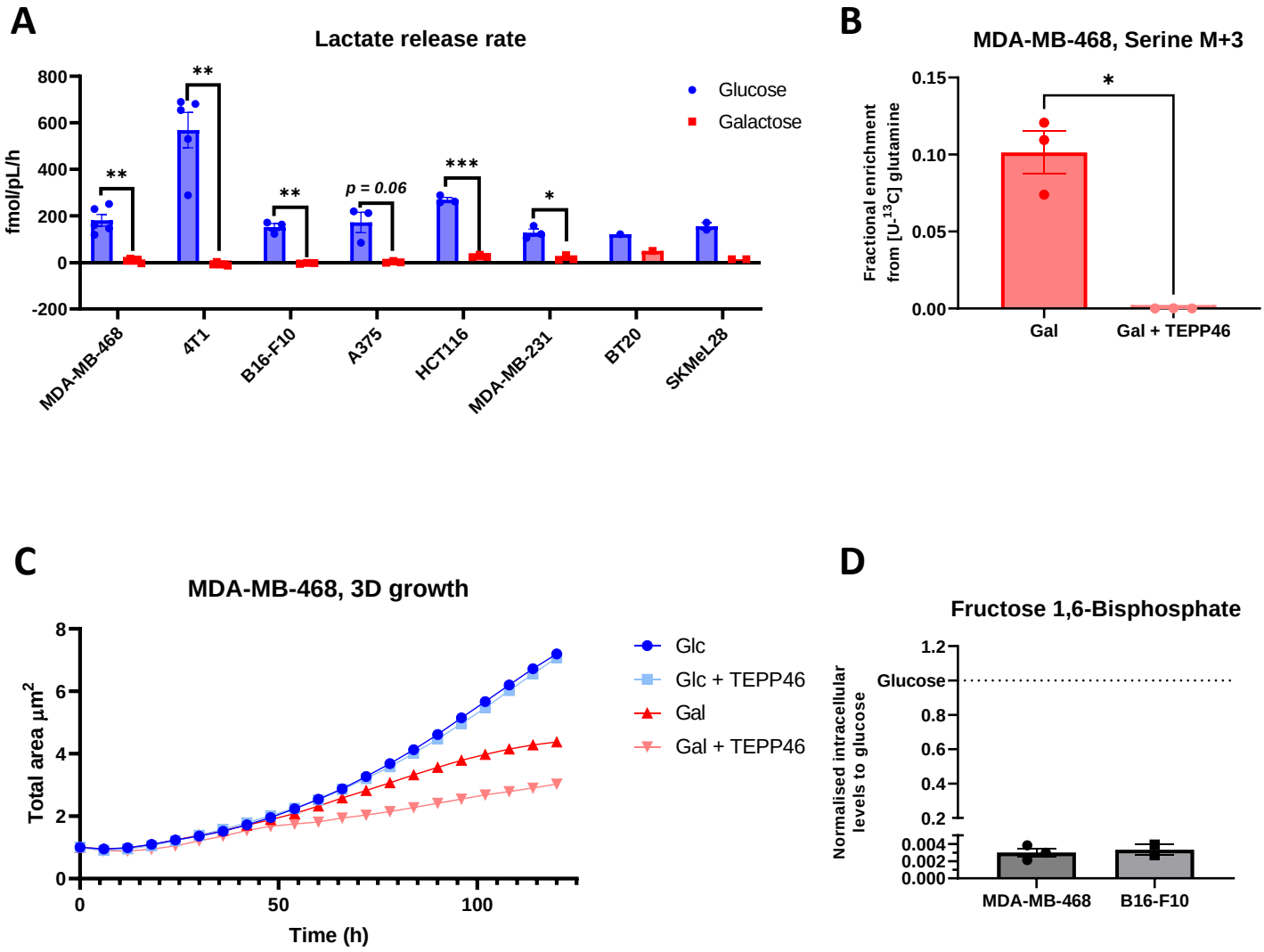
Supplementary Figure 2. A-B Fractional enrichment in M+3 PEP **(A)** and M+3 3-PG **(B)** from [U-^{13}C] glutamine after 24h incubation with either glucose ± serine and glycine (SG) or galactose ± SG medium in MDA-MB-468, 4T1 and B16-F10. **C** Fractional enrichment in M+1 formate from [U-^{13}C] glutamine after 24h incubation with either glucose ± serine and glycine (SG) or galactose ± SG medium in MDA-MB-468. **D** Protein expression of PEPCK2 after 48h incubation with either glucose or galactose, with the corresponding quantification of signal intensities relative to β-actin as a loading control and presented as a fold change of expression under galactose to that of glucose. **E-F** Protein expression of PEPCK2 comparing scramble to PEPCK2 KD/KOs, with the corresponding quantification of these signals relative to β-actin as a loading control. **G** Absolute quantification of formate release from 4T1 after 24h incubation with either glucose or galactose. **H-I** Fractional enrichment in M+4 malate, M+3 pyruvate and M+6 citrate from [U-^{13}C] glutamine after 24h incubation with galactose + SG medium and comparison between control and MDA-MB-468 PEPCK2 KD **(H)** and 4T1 PEPCK2 KOs **(I)**. **J** Fractional enrichment in M+3 serine from [U-^{13}C] galactose after 24h incubation with galactose ± SG medium in MDA-MB-468 shScramble and sh*PCK2*. (**A-J**) Each dot represents an independent experiment averaged from 3 different replicate wells replicate unless stated otherwise. (**A-J**) Mean±SEM, * p<0.05, ** p<0.01, *** p<0.001, **** p<0.0001, ns p>0.1. *P* value is calculated by Student's t-test, two-tailed, unpaired with Welch's correction unless stated otherwise.

Figure S3


A
MDA-MB-468, Pyruvate M+3
Fractional enrichment from [U-13C] galactose
17.5 mM
5.5 mM
24h
48h
72h
B
MDA-MB-468, Pyruvate M+3 in RPMI
Fractional enrichment from [U-13C] glucose and galactose
Glucose
Galactose
C
MDA-MB-468, Pyruvate M+3
Fractional enrichment from [U-13C] glucose and galactose
Norm. FBS
Dialysed FBS
Glucose
Galactose
D
MDA-MB-468, Pyruvate M+3 in Plasmax
Fractional enrichment from [U-13C] glucose and galactose
Glucose
Galactose
E
MDA-MB-468
Fractional enrichment from [U-13C] glucose
100% 13cGlc
13cGlc:12cGal
M+3 3-PG
M+3 pyruvate
F
MDA-MB-468
4T1
B16-F10
Galactose
PHGDH
PSAT1
PSPH
β-Actin
~ 57 KDa
~ 40 KDa
~ 25 KDa
~ 43 KDa
SSP protein expression, 48h
Relative protein expression to β-actin
Glucose
MDA-MB-468
4T1
B16-F10
PHGDH
PSAT1
PSPH
G
SSP mRNA expression, 24h
Relative mRNA expression
Glucose
ns
*
MDA-MB-468
4T1
B16-F10
PHGDH
PSAT1
PSPH

Supplementary Figure 3. A Fractional enrichment into M+3 pyruvate using [U-^{13}C] galactose after 24, 48, and 72 hour incubation and using 17.5 or 5.5 mM of the tracer in MDA-MB-468. **B** Fractional enrichment into M+3 pyruvate using [U-^{13}C] glucose and galactose in RPMI1640 in MDA-MB-468 with 10% dialysed FBS. **C** Fractional enrichment into M+3 pyruvate using [U-^{13}C] glucose and galactose after 24 hour incubation and using 17.5 mM of the tracer in MDA-MB-468 with 10% FBS or 10% dialysed FBS. **D** Fractional enrichment into M+3 pyruvate using [U-^{13}C] glucose and galactose in physiological medium Plasmax in MDA-MB-468. **E** Fractional enrichment from 17.5 mM [U-^{13}C] glucose into M+3 3PG and M+3 pyruvate after 24h incubation measured with LC-MS. **F** Protein expression of PHGDH, PSAT and PSPH after 48h incubation with either glucose or galactose, with the quantification of signal intensities relative to β-actin as a loading control and shown as a fold change of expression under galactose to that of glucose. **G** mRNA expression of *PHGDH*, *PSAT1*, *PSPH* relative to *GAPDH* and *ACTINβ* or *Gapdh and Sdha* after 24h incubation with either glucose or galactose measured with RT-qPCR. Data presented as fold change to the mRNA expression in cells cultured with glucose. (**A**-**G**) Each dot represent an independent experiment (**A-E** each independent experiment is from at least 3 different replicate wells). (**A**-**G**) Mean±SEM, * p<0.05, ** p<0.01, *** p<0.001, **** p<0.0001, ns p>0.1. *P* value is calculated by Student's t-test, two-tailed, unpaired with Welch's correction.

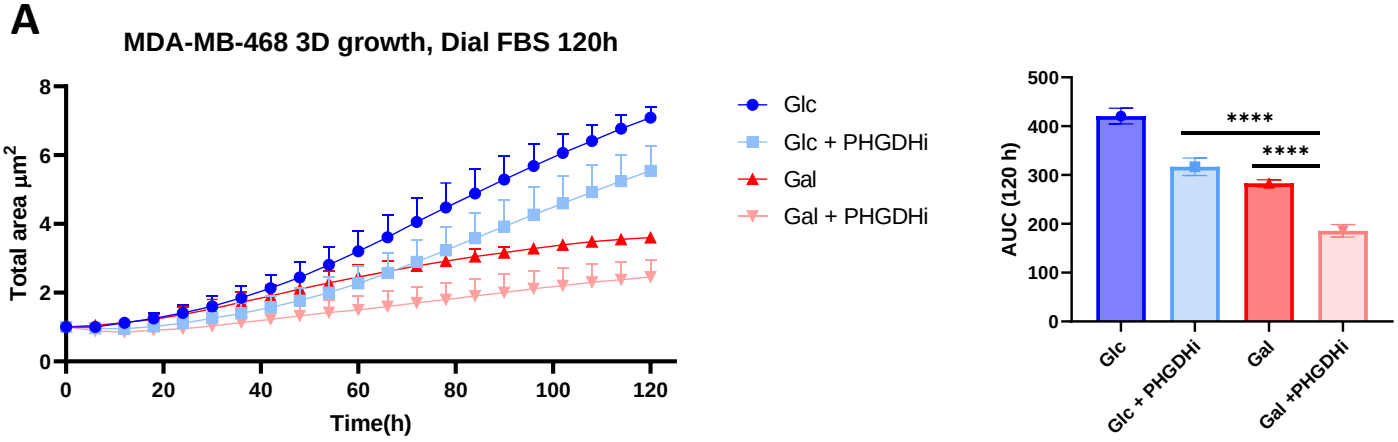
Figure S4


A
Lactate release rate
fmol/pL/h
800
600
400
200
0
-200
**
**
**
p = 0.06
***
*
Glucose
Galactose
MDA-MB-468
4T1
B16-F10
A375
HCT116
MDA-MB-231
BT20
SKMeL28
B
MDA-MB-468, Serine M+3
Fractional enrichment from [U-13C] glutamine
0.15
0.10
0.05
0.00
*
Gal
Gal + TEPP46
C
MDA-MB-468, 3D growth
Total area µm2
8
6
4
2
0
0
50
100
Time (h)
Glc
Glc + TEPP46
Gal
Gal + TEPP46
D
Fructose 1,6-Bisphosphate
Normalised intracellular levels to glucose
1.2
Glucose
0.8
0.6
0.4
0.2
0.004
0.002
0.000
MDA-MB-468
B16-F10

Supplementary Figure 4. A Absolute quantification of lactate released into the medium per hour of incubation with normalisation to packed cell volume per condition in either glucose or galactose in multiple cancer cell lines. **B** Fractional enrichment from [U-^{13}C] glutamine into M+3 serine after 24h incubation measured with LC-MS. **C** 3D growth of MDA-MB-468 aggregates using anchorage-independent conditions when treated with 100 µM of TEPP-46 with either glucose or galactose. 1 independent experiment is represented with at least 6 different replicate wells. **D** Intracellular levels of fructose 1,6-BP under galactose represented as a fold change of the levels under glucose in MDA-MB-468 and B16-F10. (**A**, **B** and **D**) Each dot represent an independent experiment (from 3 different replicate wells). (**A**-**C**) Mean±SEM, * p<0.05, ** p<0.01, *** p<0.001, **** p<0.0001, ns p>0.1. *P* value is calculated by Student's t-test, two-tailed, unpaired with Welch's correction.

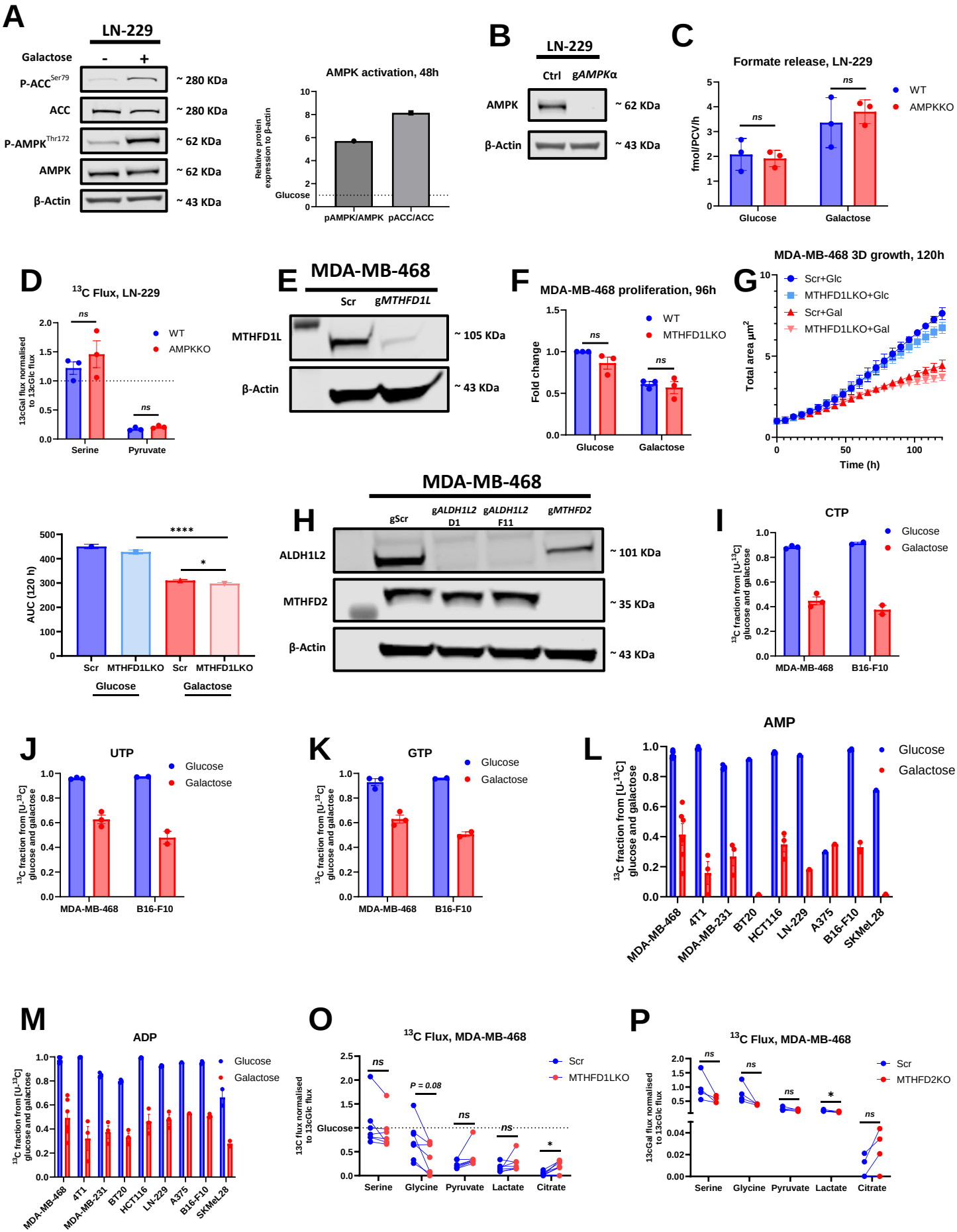
Figure S5

A


MDA-MB-468 3D growth, Dial FBS 120h
Total area µm²
Time(h)
0
2
4
6
8
0
20
40
60
80
100
120
Glc
Glc + PHGDHi
Gal
Gal + PHGDHi
AUC (120 h)
0
100
200
300
400
500
****
****
Glc
Glc + PHGDHi
Gal
Gal +PHGDHi

Supplementary Figure 5. A 3D growth of MDA-MB-468 aggregates using anchorage-independent conditions when treated with 15 μM of PHGDHi with either glucose or galactose with 10% dialysed FBS, with the corresponding AUC. 3 independent experiments are represented each with at least 6 replicate wells. Mean±SEM, * p<0.05, ** p<0.01, *** p<0.001, **** p<0.0001, ns p>0.1. *P* value is calculated by Student's t-test, two-tailed, unpaired with Welch's correction.

Figure S6


A
LN-229
Galactose
-
+
P-ACC Ser79
ACC
P-AMPK Thr172
AMPK
β-Actin
~ 280 KDa
~ 280 KDa
~ 62 KDa
~ 62 KDa
~ 43 KDa
AMPK activation, 48h
Relative protein expression to β-actin
Glucose
pAMPK/AMPK
pACC/ACC
B
LN-229
Ctrl
gAMPKα
AMPK
β-Actin
~ 62 KDa
~ 43 KDa
C
Formate release, LN-229
fmol/PCV/h
ns
WT
AMPKKO
Glucose
Galactose
D
13C Flux, LN-229
13cGal flux normalised to 13cGlc flux
WT
AMPKKO
Serine
Pyruvate
E
MDA-MB-468
Scr
gMTHFD1L
MTHFD1L
β-Actin
~ 105 KDa
~ 43 KDa
F
MDA-MB-468 proliferation, 96h
Fold change
WT
MTHFD1LKO
Glucose
Galactose
G
MDA-MB-468 3D growth, 120h
Scr+Glc
MTHFD1LKO+Glc
Scr+Gal
MTHFD1LKO+Gal
Total area µm2
Time (h)
AUC (120 h)
Scr
MTHFD1LKO
Glucose
Galactose
MDA-MB-468
gScr
gALDH1L2 D1
gALDH1L2 F11
gMTHFD2
ALDH1L2
MTHFD2
β-Actin
~ 101 KDa
~ 35 KDa
~ 43 KDa
I
CTP
13C fraction from [U-13C] glucose and galactose
Glucose
Galactose
MDA-MB-468
B16-F10
J
UTP
K
GTP
L
AMP
MDA-MB-468
4T1
MDA-MB-231
BT20
HCT116
LN-229
A375
B16-F10
SKMeL28
M
ADP
O
13C Flux, MDA-MB-468
13C flux normalised to 13cGlc flux
Scr
MTHFD1LKO
P = 0.08
Serine
Glycine
Pyruvate
Lactate
Citrate
P
13C Flux, MDA-MB-468
13cGal flux normalised to 13cGlc flux
Scr
MTHFD2KO

Supplementary Figure 6. A Protein expression of p-AMPK, AMPK, p-ACC and ACC in LN-229 after 48h incubation with either glucose or galactose, with the quantification of signal intensities relative to β-actin as a loading control and shown as a fold change of expression under galactose to that of glucose. **B** Protein expression of AMPK comparing control to the corresponding KO with β-actin as a loading control. **C** Absolute quantification of formate release from LN-229 control and AMPKKO after 24h incubation with either glucose or galactose. **D** The normalised relative ^{13}C flux under galactose towards serine and pyruvate is represented as a fold change of the same ratio under glucose in LN-229 control and AMPKKO. **E** Protein expression of MTHFD1L comparing scramble to the corresponding KO with β-actin as a loading control. **F** 2D proliferation of MDA-MB-468 Scramble and MTHFD1LKO cells cultured in either glucose or galactose as measured with cell counts at 96h relative to proliferation of scramble cells under glucose. **G** 3D growth of MDA-MB-468 control and MTHFD1LKO cell aggregates using anchorage-independent conditions in either glucose or galactose, with the corresponding AUC. 3 independent experiments are represented each with at least 6 different replicate wells. **H** Protein expression of MTHFD2 and ALDH1L2 comparing scramble to the corresponding KOs with β-actin as a loading control. **I-K** Fractional enrichment in CTP **(I)**, UTP **(J)** and GTP **(K)** from [U-^{13}C] glucose and galactose after 24h incubation. Data shown is the mean±SEM of 3 (MDA-MB-468) or 2 (B16-F10) independent experiments each being the average of 3 different replicate wells. **L-M** ^{13}C fraction in AMP **(L)** and ADP **(M)** from [U-^{13}C] glucose and galactose after 24h incubation in multiple cell lines. **N**-**O** The normalised relative ^{13}C flux under galactose towards multiple metabolites represented as a fold change of the same ratio under glucose in MDA-MB-468 scramble compared to MTHFD1LKO (**N**) and MTHFD2KO (**O**). (**A, C-D, F and I-O**) each dot represent an independent experiment averaged from 3 different replicate wells unless stated otherwise. (**A-O**) Mean±SEM, * $p<0.05$, ** $p<0.01$, *** $p<0.001$, **** $p<0.0001$, ns $p>0.1$. *P* value is calculated by Student's t-test, two-tailed, unpaired with Welch's correction unless stated otherwise.

References:

1. H. G. Crabtree, Observations on the carbohydrate metabolism of tumours. *Biochem J* **23**, 536-545 (1929).

2. D. Hanahan, R. A. Weinberg, Hallmarks of cancer: the next generation. *Cell* **144**, 646-674 (2011).

3. O. Warburg, The Metabolism of Carcinoma Cells1. *The Journal of Cancer Research* **9**, 148-163 (1925).

4. M. G. Vander Heiden, L. C. Cantley, C. B. Thompson, Understanding the Warburg effect: the metabolic requirements of cell proliferation. *Science* **324**, 1029-1033 (2009).

5. C. R. Amendola, J. P. Mahaffey, S. J. Parker, I. M. Ahearn, W. C. Chen, M. Zhou, H. Court, J. Shi, S. L. Mendoza, M. J. Morten, E. Rothenberg, E. Gottlieb, Y. Z. Wadghiri, R. Possemato, S. R. Hubbard, A. Balmain, A. C. Kimmelman, M. R. Philips, KRAS4A directly regulates hexokinase 1. *Nature* **576**, 482-486 (2019).

6. J. Fernandez-de-Cossio-Diaz, A. Vazquez, Limits of aerobic metabolism in cancer cells. *Sci Rep* **7**, 13488 (2017).

7. J. W. Locasale, A. R. Grassian, T. Melman, C. A. Lyssiotis, K. R. Mattaini, A. J. Bass, G. Heffron, C. M. Metallo, T. Muranen, H. Sharfi, A. T. Sasaki, D. Anastasiou, E. Mullarky, N. I. Vokes, M. Sasaki, R. Beroukhim, G. Stephanopoulos, A. H. Ligon, M. Meyerson, A. L. Richardson, L. Chin, G. Wagner, J. M. Asara, J. S. Brugge, L. C. Cantley, M. G. Vander Heiden, Phosphoglycerate dehydrogenase diverts glycolytic flux and contributes to oncogenesis. *Nat Genet* **43**, 869-874 (2011).

8. R. C. Osthus, H. Shim, S. Kim, Q. Li, R. Reddy, M. Mukherjee, Y. Xu, D. Wonsey, L. A. Lee, C. V. Dang, Deregulation of glucose transporter 1 and glycolytic gene expression by c-Myc. *J Biol Chem* **275**, 21797-21800 (2000).

9. A. Vazquez, J. Liu, Y. Zhou, Z. N. Oltvai, Catabolic efficiency of aerobic glycolysis: The Warburg effect revisited. *BMC Systems Biology* **4**, 58 (2010).

10. H. Ying, A. C. Kimmelman, C. A. Lyssiotis, S. Hua, G. C. Chu, E. Fletcher-Sananikone, J. W. Locasale, J. Son, H. Zhang, J. L. Coloff, H. Yan, W. Wang, S. Chen, A. Viale, H. Zheng, J. H. Paik, C. Lim, A. R. Guimaraes, E. S. Martin, J. Chang, A. F. Hezel, S. R. Perry, J. Hu, B. Gan, Y. Xiao, J. M. Asara, R. Weissleder, Y. A. Wang, L. Chin, L. C. Cantley, R. A. DePinho, Oncogenic Kras maintains pancreatic tumors through regulation of anabolic glucose metabolism. *Cell* **149**, 656-670 (2012).

11. E. de Alteriis, F. Cartenì, P. Parascandola, J. Serpa, S. Mazzoleni, Revisiting the Crabtree/Warburg effect in a dynamic perspective: a fitness advantage against sugar-induced cell death. *Cell Cycle* **17**, 688-701 (2018).

12. A. Luengo, Z. Li, D. Y. Gui, L. B. Sullivan, M. Zagorulya, B. T. Do, R. Ferreira, A. Naamati, A. Ali, C. A. Lewis, C. J. Thomas, S. Spranger, N. J. Matheson, M. G. Vander Heiden, Increased demand for NAD(+) relative to ATP drives aerobic glycolysis. *Mol Cell* **81**, 691-707.e696 (2021).

13. Y. Wang, E. Stancliffe, R. Fowle-Grider, R. Wang, C. Wang, M. Schwaiger-Haber, L. P. Shriver, G. J. Patti, Saturation of the mitochondrial NADH shuttles drives aerobic glycolysis in proliferating cells. *Molecular Cell* **82**, 3270-3283.e3279 (2022).

14. G. Bergers, S. M. Fendt, The metabolism of cancer cells during metastasis. *Nat Rev Cancer* **21**, 162-180 (2021).

15. S.-M. Fendt, C. Frezza, A. Erez, Targeting Metabolic Plasticity and Flexibility Dynamics for Cancer Therapy. *Cancer Discovery* **10**, 1797-1807 (2020).

16. J. R. Cantor, The Rise of Physiologic Media. *Trends in Cell Biology* **29**, 854-861 (2019).

17. R. Díaz-Ruiz, N. Avéret, D. Araiza, B. Pinson, S. Uribe-Carvajal, A. Devin, M. Rigoulet, Mitochondrial oxidative phosphorylation is regulated by fructose 1,6-bisphosphate. A possible role in Crabtree effect induction? *J Biol Chem* **283**, 26948-26955 (2008).

18. H. M. Holden, I. Rayment, J. B. Thoden, Structure and function of enzymes of the Leloir pathway for galactose metabolism. *J Biol Chem* **278**, 43885-43888 (2003).

19. A. Rempel, S. P. Mathupala, C. A. Griffin, A. L. Hawkins, P. L. Pedersen, Glucose catabolism in cancer cells: amplification of the gene encoding type II hexokinase. *Cancer Res* **56**, 2468-2471 (1996).

20. J. E. Wilson, Isozymes of mammalian hexokinase: structure, subcellular localization and metabolic function. *Journal of Experimental Biology* **206**, 2049-2057 (2003).

21. D. J. Timson, R. J. Reece, Functional analysis of disease-causing mutations in human galactokinase. *European Journal of Biochemistry* **270**, 1767-1774 (2003).

22. M. R. Sullivan, L. V. Danai, C. A. Lewis, S. H. Chan, D. Y. Gui, T. Kunchok, E. A. Dennstedt, M. G. Vander Heiden, A. Muir, Quantification of microenvironmental metabolites in murine cancers reveals determinants of tumor nutrient availability. *eLife* **8**, e44235 (2019).

23. B. I. Reinfeld, M. Z. Madden, M. M. Wolf, A. Chytil, J. E. Bader, A. R. Patterson, A. Sugiura, A. S. Cohen, A. Ali, B. T. Do, A. Muir, C. A. Lewis, R. A. Hongo, K. L. Young, R. E. Brown, V. M. Todd, T. Huffstater, A. Abraham, R. T. O'Neil, M. H. Wilson, F. Xin, M. N. Tantawy, W. D. Merryman, R. W. Johnson, C. S. Williams, E. F. Mason, F. M. Mason, K. E. Beckermann, M. G. Vander Heiden, H. C. Manning, J. C. Rathmell, W. K. Rathmell, Cell-programmed nutrient partitioning in the tumour microenvironment. *Nature* **593**, 282-288 (2021).

24. J. Meiser, S. Tumanov, O. Maddocks, C. F. Labuschagne, D. Athineos, N. Van Den Broek, G. M. Mackay, E. Gottlieb, K. Blyth, K. Vousden, J. J. Kamphorst, A. Vazquez, Serine one-carbon catabolism with formate overflow. *Sci Adv* **2**, e1601273 (2016).

25. M. Benzarti, C. Delbrouck, L. Neises, N. Kiweler, J. Meiser, Metabolic Potential of Cancer Cells in Context of the Metastatic Cascade. *Cells* **9**, (2020).

26. P. Hyroššová, M. Aragó, J. Moreno-Felici, X. Fu, A. Mendez-Lucas, P. M. García-Rovés, S. Burgess, A. Figueras, F. Viñals, J. C. Perales, PEPCK-M recoups tumor cell anabolic potential in a PKC-ζ-dependent manner. *Cancer Metab* **9**, 1 (2021).

27. R. Keshet, J. S. Lee, L. Adler, M. Iraqi, Y. Ariav, L. Q. J. Lim, S. Lerner, S. Rabinovich, R. Oren, R. Katzir, H. Weiss Tishler, N. Stettner, O. Goldman, H. Landesman, S. Galai, Y. Kuperman, Y. Kuznetsov, A. Brandis, T. Mehlman, S. Malitsky, M. Itkin, S. E. Koehler, Y. Zhao, K. Talsania, T.-w. Shen, N. Peled, I. Ulitsky, A. Porgador, E. Ruppin, A. Erez, Targeting purine synthesis in ASS1-expressing tumors enhances the response to immune checkpoint inhibitors. *Nature Cancer* **1**, 894-908 (2020).

28. K. Leithner, A. Hrzenjak, M. Trötzmüller, T. Moustafa, H. C. Köfeler, C. Wohlkoenig, E. Stacher, J. Lindenmann, A. L. Harris, A. Olschewski, H. Olschewski, PCK2 activation mediates an adaptive response to glucose depletion in lung cancer. *Oncogene* **34**, 1044-1050 (2015).

29. E. E. Vincent, A. Sergushichev, T. Griss, M. C. Gingras, B. Samborska, T. Ntimbane, P. P. Coelho, J. Blagih, T. C. Raissi, L. Choinière, G. Bridon, E. Loginicheva, B. R. Flynn, E. C. Thomas, J. M. Tavaré, D. Avizonis, A. Pause, D. J. Elder, M. N. Artyomov, R. G. Jones, Mitochondrial Phosphoenolpyruvate Carboxykinase Regulates Metabolic Adaptation and Enables Glucose-Independent Tumor Growth. *Mol Cell* **60**, 195-207 (2015).

30. J. van der Reest, S. Lilla, L. Zheng, S. Zanivan, E. Gottlieb, Proteome-wide analysis of cysteine oxidation reveals metabolic sensitivity to redox stress. *Nature Communications* **9**, 1581 (2018).

31. C. Yang, B. Ko, C. T. Hensley, L. Jiang, A. T. Wasti, J. Kim, J. Sudderth, M. A. Calvaruso, L. Lumata, M. Mitsche, J. Rutter, M. E. Merritt, R. J. DeBerardinis, Glutamine oxidation maintains the TCA cycle and cell survival during impaired mitochondrial pyruvate transport. *Mol Cell* **56**, 414-424 (2014).

32. C. A. Lyssiotis, A. C. Kimmelman, Metabolic Interactions in the Tumor Microenvironment. *Trends in Cell Biology* **27**, 863-875 (2017).

33. S. Hui, J. M. Ghergurovich, R. J. Morscher, C. Jang, X. Teng, W. Lu, L. A. Esparza, T. Reya, Z. Le, J. Yanxiang Guo, E. White, J. D. Rabinowitz, Glucose feeds the TCA cycle via circulating lactate. *Nature* **551**, 115-118 (2017).

34. B. Faubert, K. Y. Li, L. Cai, C. T. Hensley, J. Kim, L. G. Zacharias, C. Yang, Q. N. Do, S. Doucette, D. Burguete, H. Li, G. Huet, Q. Yuan, T. Wigal, Y. Butt, M. Ni, J. Torrealba, D. Oliver, R. E. Lenkinski, C. R. Malloy, J. W. Wachsmann, J. D. Young, K. Kernstine, R. J. DeBerardinis, Lactate Metabolism in Human Lung Tumors. *Cell* **171**, 358-371.e359 (2017).

35. S. M. Cheung, E. Husain, Y. Masannat, I. D. Miller, K. Wahle, S. D. Heys, J. He, Lactate concentration in breast cancer using advanced magnetic resonance spectroscopy. *British Journal of Cancer* **123**, 261-267 (2020).

36. K. Leithner, A. Triebl, M. Trötzmüller, B. Hinteregger, P. Leko, B. I. Wieser, G. Grasmann, A. L. Bertsch, T. Züllig, E. Stacher, A. Valli, R. Prassl, A. Olschewski, A. L. Harris, H. C. Köfeler, H. Olschewski, A. Hrzenjak, The glycerol backbone of phospholipids derives from noncarbohydrate precursors in starved lung cancer cells. *Proceedings of the National Academy of Sciences* **115**, 6225-6230 (2018).

37. J. M. Buescher, M. R. Antoniewicz, L. G. Boros, S. C. Burgess, H. Brunengraber, C. B. Clish, R. J. DeBerardinis, O. Feron, C. Frezza, B. Ghesquiere, E. Gottlieb, K. Hiller, R. G. Jones, J. J. Kamphorst, R. G. Kibbey, A. C. Kimmelman, J. W. Locasale, S. Y. Lunt, O. D. Maddocks, C. Malloy, C. M. Metallo, E. J. Meuillet, J. Munger, K. Nöh, J. D. Rabinowitz, M. Ralser, U. Sauer, G. Stephanopoulos, J. St-Pierre, D. A. Tennant, C. Wittmann, M. G. Vander Heiden, A. Vazquez, K. Vousden, J. D. Young, N. Zamboni, S. M. Fendt, A roadmap for interpreting (13)C metabolite labeling patterns from cells. *Curr Opin Biotechnol* **34**, 189-201 (2015).

38. J. Vande Voorde, T. Ackermann, N. Pfetzer, D. Sumpton, G. Mackay, G. Kalna, C. Nixon, K. Blyth, E. Gottlieb, S. Tardito, Improving the metabolic fidelity of cancer models with a physiological cell culture medium. *Sci Adv* **5**, eaau7314 (2019).

39. F. P. Lemaigre, G. G. Rousseau, Transcriptional control of genes that regulate glycolysis and gluconeogenesis in adult liver. *Biochem J* **303 (Pt 1)**, 1-14 (1994).

40. A. Kano, T. Iwasaki, M. Shindo, Bongkrekic acid facilitates glycolysis in cultured cells and induces cell death under low glucose conditions. *Biochemistry and Biophysics Reports* **20**, 100683 (2019).

41. D. Anastasiou, Y. Yu, W. J. Israelsen, J. K. Jiang, M. B. Boxer, B. S. Hong, W. Tempel, S. Dimov, M. Shen, A. Jha, H. Yang, K. R. Mattaini, C. M. Metallo, B. P. Fiske, K. D. Courtney, S. Malstrom, T. M. Khan, C. Kung, A. P. Skoumbourdis, H. Veith, N. Southall, M. J. Walsh, K. R. Brimacombe, W. Leister, S. Y. Lunt, Z. R. Johnson, K. E. Yen, K. Kunii, S. M. Davidson, H. R. Christofk, C. P. Austin, J. Inglese, M. H. Harris, J. M. Asara, G. Stephanopoulos, F. G. Salituro, S. Jin, L. Dang, D. S. Auld, H. W. Park, L. C. Cantley, C. J. Thomas, M. G. Vander Heiden, Pyruvate kinase M2 activators promote tetramer formation and suppress tumorigenesis. *Nat Chem Biol* **8**, 839-847 (2012).

42. T. L. Dayton, T. Jacks, M. G. Vander Heiden, PKM2, cancer metabolism, and the road ahead. *EMBO Rep* **17**, 1721-1730 (2016).

43. J. D. Dombrauckas, B. D. Santarsiero, A. D. Mesecar, Structural basis for tumor pyruvate kinase M2 allosteric regulation and catalysis. *Biochemistry* **44**, 9417-9429 (2005).

44. H. Weinstabl, M. Treu, J. Rinnenthal, S. K. Zahn, P. Ettmayer, G. Bader, G. Dahmann, D. Kessler, K. Rumpel, N. Mischerikow, F. Savarese, T. Gerstberger, M. Mayer, A. Zoephel, R. Schnitzer, W. Sommergruber, P. Martinelli, H. Arnhof, B. Peric-Simov, K. S. Hofbauer, G. Garavel, Y. Scherbantin, S. Mitzner, T. N. Fett, G. Scholz, J. Bruchhaus, M. Burkard, R. Kousek, T. Ciftci, B. Sharps, A. Schrenk, C. Harrer, D. Haering, B. Wolkerstorfer, X. Zhang, X. Lv, A. Du, D. Li, Y. Li, J. Quant, M. Pearson, D. B. McConnell, Intracellular Trapping of the Selective Phosphoglycerate Dehydrogenase (PHGDH) Inhibitor BI-4924 Disrupts Serine Biosynthesis. *J Med Chem* **62**, 7976-7997 (2019).

45. G. K. Smith, S. D. Banks, T. J. Monaco, R. Rigual, D. S. Duch, R. J. Mullin, B. E. Huber, Activity of an NAD-dependent 5,10-methylenetetrahydrofolate dehydrogenase in normal tissue, neoplastic cells, and oncogene-transformed cells. *Arch Biochem Biophys* **283**, 367-371 (1990).

46. N. I. Lorenz, B. Sauer, P. S. Zeiner, M. I. Strecker, A.-L. Luger, D. Schulte, M. Mittelbronn, T. Alekseeva, L. Sevenich, P. N. Harter, C. Münch, J. P. Steinbach, M. W. Ronellenfitsch, AMP-kinase mediates adaptation of glioblastoma cells to conditions of the tumour microenvironment. *bioRxiv*, 2022.2003.2025.485624 (2022).

47. J. Fan, J. Ye, J. J. Kamphorst, T. Shlomi, C. B. Thompson, J. D. Rabinowitz, Quantitative flux analysis reveals folate-dependent NADPH production. *Nature* **510**, 298-302 (2014).

48. R. Bichi, S. A. Shinton, E. S. Martin, A. Koval, G. A. Calin, R. Cesari, G. Russo, R. R. Hardy, C. M. Croce, Human chronic lymphocytic leukemia modeled in mouse by targeted TCL1 expression. *Proc Natl Acad Sci U S A* **99**, 6955-6960 (2002).

49. S. Chakraborty, C. Martines, F. Porro, I. Fortunati, A. Bonato, M. Dimishkovska, S. Piazza, B. S. Yadav, I. Innocenti, R. Fazio, T. Vaisitti, S. Deaglio, A. Zamò, A. J. Dimovski, L. Laurenti, D. G. Efremov, B-cell receptor signaling and genetic lesions in TP53 and CDKN2A/CDKN2B cooperate in Richter transformation. *Blood* **138**, 1053-1066 (2021).

50. D. L. a. Nelson, *Lehninger principles of biochemistry*. (W.H. Freeman and Company ; Houndmills, Basingstoke : Macmillan Higher Education, New York, NY, USA, 2017).

51. B. Chaneton, P. Hillmann, L. Zheng, A. C. L. Martin, O. D. K. Maddocks, A. Chokkathukalam, J. E. Coyle, A. Jankevics, F. P. Holding, K. H. Vousden, C. Frezza, M. O'Reilly, E. Gottlieb, Serine is a natural ligand and allosteric activator of pyruvate kinase M2. *Nature* **491**, 458-462 (2012).

52. J. Ye, A. Mancuso, X. Tong, P. S. Ward, J. Fan, J. D. Rabinowitz, C. B. Thompson, Pyruvate kinase M2 promotes de novo serine synthesis to sustain mTORC1 activity and cell proliferation. *Proceedings of the National Academy of Sciences* **109**, 6904-6909 (2012).

53. M. Rossi, P. Altea-Manzano, M. Demicco, G. Doglioni, L. Bornes, M. Fukano, A. Vandekeere, A. M. Cuadros, J. Fernández-García, C. Riera-Domingo, C. Jauset, M. Planque, H. F. Alkan, D. Nittner, D. Zuo, L. A. Broadfield, S. Parik, A. A. Pane, F. Rizzollo, G. Rinaldi, T. Zhang, S. T. Teoh, A. B. Aurora, P. Karras, I. Vermeire, D. Broekaert, J. V. Elsen, M. M. L. Knott, M. F. Orth, S. Demeyer, G. Eelen, L. E. Dobrolecki, A. Bassez, T. V. Brussel, K. Sotlar, M. T. Lewis, H. Bartsch, M. Wuhrer, P. v. Veelen, P. Carmeliet, J. Cools, S. J. Morrison, J.-C. Marine, D. Lambrechts, M. Mazzone, G. J. Hannon, S. Y. Lunt, T. G. P. Grünewald, M. Park, J. v. Rheenen, S.-M. Fendt, PHGDH heterogeneity potentiates cancer cell dissemination and metastasis. *Nature* **605**, 747-753 (2022).

54. A. Muir, M. G. Vander Heiden, The nutrient environment affects therapy. *Science* **360**, 962-963 (2018).

55. Y. Zheng, T. Y. Lin, G. Lee, M. N. Paddock, J. Momb, Z. Cheng, Q. Li, D. L. Fei, B. D. Stein, S. Ramsamooj, G. Zhang, J. Blenis, L. C. Cantley, Mitochondrial One-Carbon Pathway Supports Cytosolic Folate Integrity in Cancer Cells. *Cell* **175**, 1546-1560.e1517 (2018).

56. N. Kiweler, C. Delbrouck, V. I. Pozdeev, L. Neises, L. Soriano-Baguet, K. Eiden, F. Xian, M. Benzarti, L. Haase, E. Koncina, M. Schmoetten, C. Jaeger, M. Z. Noman, A. Vazquez, B. Janji, G. Dittmar, D. Brenner, E. Letellier, J. Meiser, Mitochondria preserve an autarkic one-carbon cycle to confer growth-independent cancer cell migration and metastasis. *Nat Commun* **13**, 2699 (2022).

57. K. Hiller, J. Hangebrauk, C. Jäger, J. Spura, K. Schreiber, D. Schomburg, MetaboliteDetector: comprehensive analysis tool for targeted and nontargeted GC/MS based metabolome analysis. *Anal Chem* **81**, 3429-3439 (2009).

58. T. Wang, J. N. R. Gnanaprakasam, X. Chen, S. Kang, X. Xu, H. Sun, L. Liu, H. Rodgers, E. Miller, T. A. Cassel, Q. Sun, S. Vicente-Muñoz, M. O. Warmoes, P. Lin, Z. L. Piedra-Quintero, M. Guerau-de-Arellano, K. A. Cassady, S. G. Zheng, J. Yang, A. N. Lane, X. Song, T. W. Fan, R. Wang, Inosine is an alternative carbon source for CD8(+)-T-cell function under glucose restriction. *Nat Metab* **2**, 635-647 (2020).

59. B. P. Dranka, G. A. Benavides, A. R. Diers, S. Giordano, B. R. Zelickson, C. Reily, L. Zou, J. C. Chatham, B. G. Hill, J. Zhang, A. Landar, V. M. Darley-Usmar, Assessing bioenergetic function in response to oxidative stress by metabolic profiling. *Free Radic Biol Med* **51**, 1621-1635 (2011).

CHAPTER 4: Mitochondria preserve an autarkic one-carbon cycle to confer growth-independent cancer cell migration and metastasis

KIWELER, N., DELBROUCK, C., POZDEEV, V. I., NEISES, L., SORIANO-BAGUET, L., EIDEN, K., XIAN, F., **BENZARTI, M**., HAASE, L., KONCINA, E., SCHMOETTEN, M., JAEGER, C., NOMAN, M. Z., VAZQUEZ, A., JANJI, B., DITTMAR, G., BRENNER, D., LETELLIER, E. & MEISER, J.

2022. ***Nature Communications***, 13, 2699.

DOI: https://doi.org/10.1038/s41467-022-30363-y

4.1. Preface

1C and folate cycles are essential for nucleotide synthesis as they provide cells with 1C units that are incorporated into newly synthesized purines and thymidine. Consequently, antifolates have been widely used as chemotherapeutics to target primary tumors as they induce metabolic stress. Typically these antifolates target the cytosolic fraction of the 1C cycle, leading to full inhibition of nucleotide synthesis and proliferation. In this manuscript, we aimed to study the effect of antifolates (methotrexate) on the mitochondrial fraction of the 1C cycle and whether proliferation-independent functions are supported by mitochondrial 1C cycle.

We show that the inhibition of the cytosolic 1C cycle via methotrexate does indeed inhibit proliferation but counterintuitively it did not affect migration of cancer cells. Through our metabolic profiling we were able to see that mitochondrial 1C cycle activity was enhanced under methotrexate treatment and proving that the mitochondrial fraction of the 1C cycle can run independently of the cytoplasmic part. By genetically targeting the mitochondrial 1C cycle, we were able to prove that under growth inhibiting conditions the cells rely on the mitochondrial 1C cycle to promote invasion and migration (aim five).

4.2. Personal contribution

I contributed to this manuscript by assisting in the laboratory work to metabolically profile methotrexate treated cells. This involved derivatizing formate in medium samples, processing polar metabolic extracts prior to gas chromatography-mass spectrometry (GC-MS) measurements and setting-up an analysis method to quantify the consumption/release rates of different metabolites between cells and their culturing medium. Moreover, I performed extracellular flux analysis of oxygen consumption rate using seahorse analyzer and analyzed the generated data. These contributions translated to data used in the following figure panels: 3b, 3c, 3e, 3f, 3g, 3h, 3j, 4b, 4i, 5a, 5b, 5c and S3c. I read and reviewed the manuscript prior to submission.

4.3. Manuscript

nature COMMUNICATIONS

ARTICLE

https://doi.org/10.1038/s41467-022-30363-y OPEN

Mitochondria preserve an autarkic one-carbon cycle to confer growth-independent cancer cell migration and metastasis

Nicole Kiweler[1], Catherine Delbrouck[1,2], Vitaly I. Pozdeev[3], Laura Neises[1], Leticia Soriano-Baguet[2,4,5], Kim Eiden[1,2], Feng Xian[6], Mohaned Benzarti[1,2], Lara Haase[1,2,7], Eric Koncina[3], Maryse Schmoetten[3], Christian Jaeger[7], Muhammad Zaeem Noman[8], Alexei Vazquez[9], Bassam Janji[8], Gunnar Dittmar[2,6], Dirk Brenner[4,5,10], Elisabeth Letellier[3] & Johannes Meiser[1]✉

Metastasis is the most common cause of death in cancer patients. Canonical drugs target mainly the proliferative capacity of cancer cells, which leaves slow-proliferating, persistent cancer cells unaffected. Metabolic determinants that contribute to growth-independent functions are still poorly understood. Here we show that antifolate treatment results in an uncoupled and autarkic mitochondrial one-carbon (1C) metabolism during cytosolic 1C metabolism impairment. Interestingly, antifolate dependent growth-arrest does not correlate with decreased migration capacity. Therefore, using methotrexate as a tool compound allows us to disentangle proliferation and migration to profile the metabolic phenotype of migrating cells. We observe that increased serine de novo synthesis (SSP) supports mitochondrial serine catabolism and inhibition of SSP using the competitive PHGDH-inhibitor BI-4916 reduces cancer cell migration. Furthermore, we show that sole inhibition of mitochondrial serine catabolism does not affect primary breast tumor growth but strongly inhibits pulmonary metastasis. We conclude that mitochondrial 1C metabolism, despite being dispensable for proliferative capacities, confers an advantage to cancer cells by supporting their motility potential.

[1] Cancer Metabolism Group, Department of Cancer Research, Luxembourg Institute of Health, Luxembourg, Luxembourg. [2] Faculty of Science, Technology and Medicine, University of Luxembourg, 2 avenue de Université, Esch-sur-Alzette, Luxembourg. [3] Faculty of Science, Technology and Medicine, Department of Life Sciences and Medicine, Molecular Disease Mechanisms Group, University of Luxembourg, Esch-sur-Alzette, Luxembourg. [4] Experimental & Molecular Immunology, Department of Infection and Immunity, Luxembourg Institute of Health, 29 Rue Henri Koch, Esch-sur-Alzette, Luxembourg. [5] Immunology & Genetics, Luxembourg Centre for Systems Biomedicine, University of Luxembourg, 7 Avenue des Hauts Fourneaux, Esch-sur-Alzette, Luxembourg. [6] Proteomics of cellular signaling, Department of Infection and Immunity, Luxembourg Institute of Health,1a Rue Thomas Edison, Strassen, Luxembourg. [7] Luxembourg Centre for Systems Biomedicine, University of Luxembourg, Esch-sur-Alzette, Luxembourg. [8] Tumor Immunotherapy and Microenvironment (TIME) Group, Department of Cancer Research, Luxembourg Institute of Health, Luxembourg, Luxembourg. [9] Institute of Cancer Sciences, University of Glasgow, Glasgow, UK. [10] Odense Research Center for Anaphylaxis (ORCA), Department of Dermatology and Allergy Center, Odense University Hospital, University of Southern Denmark, Odense, Denmark. ✉email: johannes.meiser@lih.lu

The survival rates of patients harboring primary tumors steadily increase due to targeted treatment schemes. However, in case of tumor relapse and metastatic disease, effective therapies are mostly lacking with the consequence that secondary tumors account for the majority of cancer deaths[1]. Classical chemotherapeutic approaches to counteract cancer growth aim to target biomass production by interfering with the synthesis of proteins, lipids, and nucleotides and thereby directly interfere with central pathways of cancer cell metabolism[2,3]. Prospectively, therapeutic approaches targeting metabolic pathways that also support the invasive and migratory properties of cancer cells would help to prevent metastatic progression of the initial disease. However, profound knowledge of specific metabolic dependencies that support growth-independent processes during the metastatic cascade, are only starting to be understood[4].

Nucleotide synthesis is an essential requirement for cancer cell proliferation. Consequently, antifolates such as Methotrexate (MTX) and related compounds have been proven as successful chemotherapeutics for several decades. Although differences between the various antifolates exist, a shared mode of action is the inhibition of one-carbon (1C) metabolism which provides essential building blocks for thymidylate and purine synthesis. Additionally, 1C metabolism has implications in supporting methylation reactions, glutathione, heme, sphingolipid and protein synthesis[5]. 1C metabolism describes a metabolic cycle that is spread across mitochondrion and cytoplasm and it is mainly fueled by the non-essential amino acid serine. De-novo serine synthesis is catalyzed by the rate limiting enzyme phosphoglycerate dehydrogenase (PHGDH) which is amplified in different tumors[6–8]. Hence, targeting serine synthesis, serine catabolism or serine availability by starvation or inhibition of PHDGH has been proven successful to inhibit cancer progression[9–17]. To support the various anabolic programs, cytosolic 1C metabolism is of particular importance, while mitochondrial 1C metabolism is dispensable due to the reversibility of the cytosolic 1C metabolism[16]. In fact, depending on intracellular folate levels, cytosolic 1C metabolism can be the dominant route to provide one-carbon units for nucleotide synthesis[17]. In that light, reasons for conserved mitochondrial 1C metabolism are still not fully understood. Previous evidence suggests implications of mitochondrial 1C metabolism for mitochondrial translation[18,19]. One additional explanation resides in the observation that mitochondrial derived formate lowers the pool of free cytosolic folates by increasing the 10-CHO-THF pool thereby protecting it from degradation. Upon MTX, degradation is facilitated as folates accumulate in the oxidized DHF form, impeding the 10-CHO-THF synthetase activity of MTHFD1[20]. However, if mitochondrial folate-dependent 1C metabolism and formate production remains functional under conditions of cytosolic 1C metabolism impairment and whether mitochondrial 1C metabolism itself confers additional functions that contribute to tumorigenesis remains unknown.

We have previously shown that a reduction of biomass demand can result in increased formate release from cancer cells to their surrounding microenvironment[21] and that the rate of serine catabolism to formate is significantly increased in adenomas of the small intestine and breast tumors compared to normal tissue[22]. Importantly, enhanced formate release rates and increased extracellular formate concentrations have been shown to increase the invasiveness of glioblastoma cells in vitro[22].

Apart from our previous findings on formate overflow and its potential implications for cancer cell invasion[21,22], other reports substantiate a role of serine metabolism in the context of metastasis[7,14,23–25]. However, such studies were so far focused on the relevance of serine de novo synthesis via PHGDH or extracellular serine availability for metastatic outgrowth (proliferative aspect) in the secondary tissue[7,14,23–25]. In contrast, whether mitochondrial serine catabolism also has a growth-independent role in promoting cancer cell motility that potentially increases the rate of cancer cell escape from the primary tumor has not been addressed so far. Being able to identify and target metabolic programs that promote the early steps of the metastatic cascade would help to contain the tumor, a clinical phenotype with more favorable therapeutic outcome compared to advanced metastatic stages.

In the present study, we observed that antifolates, albeit being strongly cytostatic, did not decrease the cell's motility potential. Using MTX as a tool compound to selectively inhibit cytosolic 1C metabolism, we show that mitochondrial 1C metabolism runs as an autarkic, compartmentalized pathway that is important to drive cancer cell motility. In contrast, the cytosolic part of 1C metabolism, which is essential for nucleotide synthesis during proliferation, is dispensable for the cellular motility potential. Hence, we provide mechanistic evidence that one selective advantage of mitochondrial 1C metabolism is to support cell motility. We corroborate this hypothesis in an orthotopic breast cancer model. Here, we demonstrate that ablating mitochondrial 1C metabolism effectively blocks mitochondrial serine catabolism but does not affect primary tumor growth. Yet, it strongly inhibits pulmonary metastasis formation.

Results

Inhibition of anabolic synthesis routes differentially impacts the motility potential of cancer cells. To assess the relative importance of different anabolic pathways for cancer cell migration, we employed a panel of metabolic perturbations targeting glycolysis, mitochondrial electron transport chain (ETC) as well as lipid, protein, and nucleotide synthesis (Fig. 1a). As expected, the chosen metabolic interventions inhibited proliferation and affected cell cycle progression of MDA-MB-468 breast cancer cells with no to mild toxic effects after 48 h treatment (Fig. 1b–c, S1A). Inhibition of glycolysis, ETC, lipid, and protein synthesis significantly reduced migration of MDA-MB-468 cells (Fig. 1d). Surprisingly and in contrast to all other growth-inhibiting conditions, inhibition of nucleotide synthesis with various drugs did not diminish migration of MDA-MB-468 cells (Fig. 1e). Calculation of the area under curve (AUC) allowed us to quantitatively compare wound closure over time (Fig. 1d, e) and confirmed that wound closure was significantly reduced upon treatment with rotenone (Rot), galactose (Gal), simvastatin (SIM) and sirolimus (rapamycin, SIR). However, treatment with the antifolates methotrexate (MTX) and pemetrexed (PEM), as well as with hydroxyurea (HU) and clofarabine (CLO) did not affect or did even significantly increase wound closure in scratch assays in comparison to fully proliferative, untreated control cells. While cell migration correlates with reduced cell growth for all other metabolic perturbations, nucleotide synthesis inhibition does not reduce cell migration in correlation to growth inhibition (Fig. 1f, g). Sustained migration in response to nucleotide synthesis inhibition was verified in LN229 glioblastoma and 4T1 breast cancer cells (Fig. S1B–D). Of note, using dialyzed or normal FBS did not change the result (Fig. S1E). This observation was also confirmed in trans-well migration assays using Boyden chambers (Fig. 1h, S1F, G). Furthermore, using ECM-collagen coating in trans-well assay, we found that nucleotide synthesis inhibition also had no impact on the invasive capacity of MDA-MB-468 cells (Fig. 1h), LN229 and 4T1 cells (Fig. S1F, G). To validate if MTX resistance results in a pro-migratory effect, we generated MTX-resistant MDA-MB-468 cells by long-term cultivation in 50 nM MTX for 2 months. The resulting MTX-resistant MDA-MB-468 cells proliferate in the presence of increasing

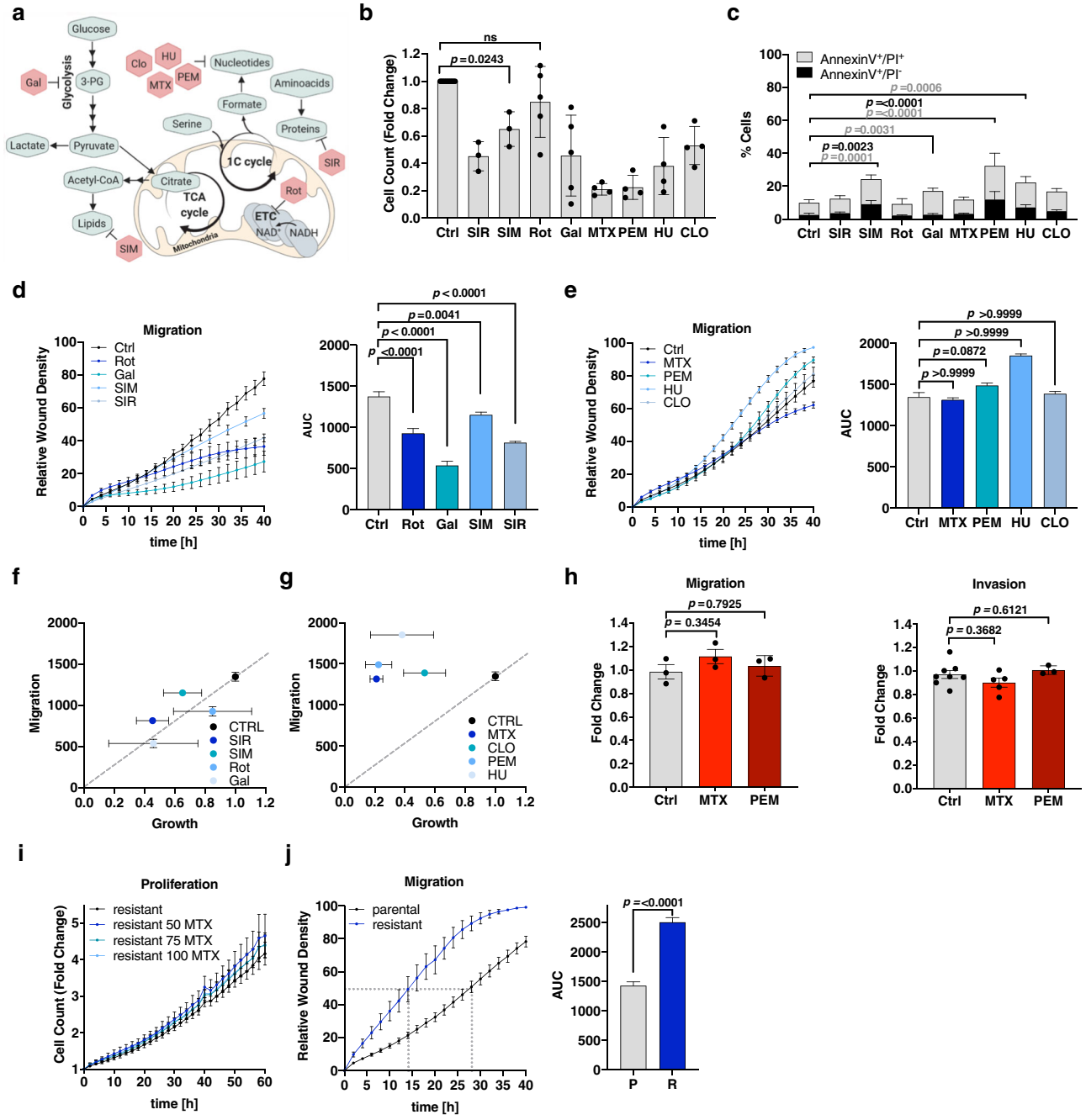


Fig. 1 Inhibition of major anabolic synthesis routes differentially impacts the motility potential of cancer cells. a Synthesis routes of metabolic building blocks (lipids, nucleotides, and proteins) and pharmacologic intervention points of the selected drug panel. **b** MDA-MB-468 cells were counted after 48 h treatment with 100 nM Sirolimus (SIR) ($n = 3$), 1 µM Simvastatin (SIM) ($n = 3$), 50 nM Rotenone (Rot) ($n = 5$), galactose (Gal) ($n = 5$) supplementation, 50 nM Methotrexate (MTX) ($n = 4$), 1 µM Pemetrexed (PEM) ($n = 4$), 0.5 mM hydroxyurea (HU) ($n = 4$), and 100 nM Clofarabine (CLO) ($n = 4$). Mean ± SD; ordinary one-way ANOVA with Dunnett's multiple comparisons test. Unlabeled comparisons to Ctrl are all significant with $p < 0.0001$. **c** MDA-MB-468 cells were treated as in (**b**). Cell death was assessed by flow cytometry and AnnexinV-FITC/PI-staining; mean ± SD of independent experiments ($n = 8$ (Ctrl), $n = 4$ (SIR, SIM, PEM, CLO), $n = 3$ (Rot, Gal, MTX, HU)). Two-way ANOVA with Dunnett's multiple comparisons test. **d**, **e** Migration of MDA-MB-468 cells upon (**d**) 50 nM Rot ($n = 5$), Gal ($n = 5$), 1 µM SIM ($n = 3$), and 100 nM SIR ($n = 4$) or (**e**) 50 nM MTX ($n = 7$), 1 µM PEM ($n = 3$), 0.5 mM HU ($n = 4$), and 100 nM CLO (n = 4) and respective area under curve (AUC); mean ± SEM of independent experiments; Brown-Forsythe and Welch one-way ANOVA with Dunnett's multiple comparisons test. **f**, **g** Correlation of cell migration (AUC over 40 h, mean ± SEM, ($n =$ as in (**d**, **e**)) and proliferation (fold cell growth after 48 h, mean ± SD ($n =$ as in (**b**)). MDA-MB-468 cells were treated as in (**b**) and (**d**, **e**). **h** Migration and invasion of MDA-MB-468 cells treated for 24 h with 50 nM MTX using non-coated (migration) or ECM-Collagen-coated (invasion) Boyden chambers. Mean ± SEM (Migration: $n = 3$, Invasion: $n = 7$ (Ctrl), 5 (MTX, 3 (Pem)); Brown-Forsythe and Welch one-way ANOVA with Dunnett's multiple comparisons test. **i** Proliferation of MTX-resistant MDA-MB-468 cells upon the indicated concentrations of MTX [nM]; mean ± SEM of independent experiments ($n = 4$). **j** Migration of parental and MTX-resistant MDA-MB-468 cells and respective AUC; mean ± SEM of independent experiments (parental $n = 15$, resistant $n = 6$); unpaired, two-tailed *t*-test with Welch's correction. Time point of 50% wound closure is indicated. Source data are provided as a Source Data file.

concentrations of MTX (Fig. 1i) and display enhanced migratory capacity compared to the parental MDA-MB-468 cell line (Fig. 1j).

In conclusion, the perturbation of any major anabolic route results in growth repression. However, the impact on cell migration highly depends on the targeted metabolic pathway, with nucleotide synthesis being an ineffective target to abrogate cell motility. Furthermore, prolonged nucleotide synthesis inhibition in drug-resistant cells acts as a selection pressure for more motile cancer subpopulations.

Sustained motility upon MTX is supported by a ROS-driven EMT phenotype. As MTX induced the strongest growth repression without increasing cell death (Fig. 1b, c), we used it as a tool compound to disentangle proliferation from migration to investigate the metabolic processes that support cancer cell migration. After testing multiple concentrations (Fig. S2A), we chose a concentration of 50 nM MTX for subsequent experiments. 50 nM MTX is significantly growth- and cell cycle-arresting in MDA-MB-468 cells (Fig. 1b, S1A) and has also been shown to be within the therapeutic window[26–29]. As this concentration of 50 nM is significantly lower compared to earlier in vitro studies[20,30–33], we first set out to validate known drug effects of MTX in our system. We observed that 48 h MTX treatment of MDA-MB-468 cells resulted in altered cellular morphology with individual cells visibly increasing in cell size and exhibiting an outstretched cell shape with protruding edges (Fig. 2a). MTX-resistant MDA-MB-468 cells showed comparable morphologic alterations (Fig. S2B). While the observed cell cycle and proliferation arrest upon MTX treatment was rapidly reversible (Fig. S2C, D) upon MTX removal, [U-^{13}C]serine tracing and metabolic flux analysis confirmed that 50 nM MTX did strongly inhibit nucleotide synthesis (Fig. 2b). Of note, nucleotide synthesis was partially restored in MTX-resistant MDA-MB-468 cells (Fig. S2E). Stable isotope labeling by amino acids in cell culture (SILAC) and quantitative proteomics analysis further confirmed the efficacy of the selected MTX dose as mechanistic targets of MTX such as dihydrofolate reductase (DHFR), thymidylate synthase (TYMS), and thymidine kinase (TK1) were upregulated by treatment as expected (Fig. S2F). DHFR expression was also increased in MTX resistant cells, while FolRa expression was slightly decreased (Fig. S2G). Moreover, superoxide dismutase (SOD) was one of the most significantly upregulated proteins in response to treatment (Fig. S2F), which corresponds to prior reports that depict MTX as a potent inducer of oxidative stress[30,34,35]. We validated these prior findings with our low dose of MTX by measuring a moderate but significant increase of mitochondrial and cytosolic reactive oxidant species (ROS) upon acute MTX treatment and in the MTX resistant cells (Fig. S2H, I, J). In line with increased ROS levels we observed NRF2 stabilization, however, this did not result in activation of the BACH1 axis, as reported earlier for metastatic lung cancer[36,37] (Fig. S2K, I). Increased ROS levels upon MTX correspond to earlier reports that highlight the potential of oxidative stress as a driver of cancer cell transformation via epithelial-mesenchymal transition (EMT)[38–44]. EMT is also a known general mechanism to escape chemotherapy induced effects.

In line with previous reports, we found that *ZEB1* and *ZEB2* expression as well as *VIM* expression was upregulated in a time-dependent manner in response to acute MTX treatment and in the MTX-resistant cell line (Fig. 2c, d, S2F, M, N). MTX-treatment also induced the expression of the collagenase *MMP9* (Fig. S2O), an enzyme which is involved in the degradation of the extracellular matrix during cancer cell invasion[45]. Treatment of cells with the antioxidant N-acetylcysteine (NAC) reduced ROS levels in MTX-treated MDA-MB-468 cells (Fig. S2P) and resulted in a significant reduction of MTX-induced cell migration (Fig. 2e) and EMT phenotype induction (Fig. 2f). These findings confirm that the chosen low dose of MTX is sufficient to promote EMT in a ROS dependent manner, supporting earlier reports suggesting EMT onset in context of pulmonary fibrosis using high doses of MTX[46,47]. Such moderate increase in cellular ROS levels after MTX might contribute to a pro-migratory stimulus that subsequently results in the observed sustained migration.

MTX-treated cells sustain high metabolic rates and enhance de novo serine synthesis. In addition to the here reported MTX-specific effects on ROS and EMT, we wanted to take advantage of the MTX effect (sustained migration) to identify growth-independent metabolic liabilities that support cell migration.

To that end, we profiled central carbon metabolism using [U-^{13}C]glutamine and [U-^{13}C]glucose tracing to monitor glycolytic activity and glutamine- or glucose-derived carbon oxidation through the TCA cycle (Fig. 3a, d). Absolute consumption and release (CORE) rates of glutamine and glutamate were sustained in response to MTX treatment (Fig. 3b), while the relative TCA-cycle flux of [U-^{13}C]glutamine was significantly increased in response to MTX (Fig. 3c). Absolute quantification of CORE rates of glucose and lactate also revealed sustained high glycolytic rates upon MTX treatment (Fig. 3e). This came as a surprise, as lactate release rates were previously shown to correlate with cell growth rates[48]. In MDA-MB-468 cells, the maintained glycolytic rate and the associated lactate release at constant high levels (Fig. 3e) indicate a constant generation of glycolysis-derived ATP even in the presence of reduced energetic demand for anabolic reactions in growth-arresting MTX conditions. Consequently, [U-^{13}C] glucose distribution within the TCA-cycle was sustained by MTX treatment in MDA-MB-468 cells (Fig. 3f) as well as in 4T1 and LN229 cells (Fig. S3A, B). It has previously been shown that MTX inhibits oxygen consumption rates (OCR) in HCT116 cells[18]. We could replicate this finding and observed a ~30 % reduction of OCR in HCT116 cells upon MTX (Fig, S3C), while OCR in MDA-MB-468, LN229, and 4T1 cells was sustained (Fig. 3g). This indicates cell line specific effects of MTX on OCR. Furthermore, MTX treatment significantly increased the relative flux of glucose to serine despite decreased anabolic demands for nucleotide synthesis (Fig. 3h, S3D). Protein levels of PHGDH, PSPH, and PSAT1 that catalyze the serine de novo synthesis pathway from glucose were unaltered in response to MTX treatment in multiple cell lines (Fig. S3E–H). In agreement with Diehl et al[49]. who showed that changes in NAD^+/NADH ratio can increase PHGDH activity and in consequence serine de novo synthesis rates, we observed an increased NAD^+/NADH ratio upon MTX (Fig. 3i). As MTX is well characterized as an inhibitor of DHFR and thus 1C metabolism, it came to our surprise that MTX treatment did also increase the abundance of extracellular formate M + 1 isotopologues derived from [U-^{13}C]glucose through serine and the mitochondrial 1C metabolism (Fig. 3j, S3I).

In summary, the metabolic profiling demonstrates that, despite decreased metabolic demand for biomass production, MTX-treated cells sustain high metabolic rates that are comparable to fully proliferating cells. Additionally, and in contrast to general assumptions, cytosolic DHFR inhibition results in increased rates of serine synthesis and downstream mitochondrial formate excretion suggesting an uncoupling of mitochondrial 1C metabolism from cytosolic 1C metabolism.

Mitochondria protect 1C metabolism-dependent serine catabolism upon cytosolic 1C pathway inhibition. Our finding of

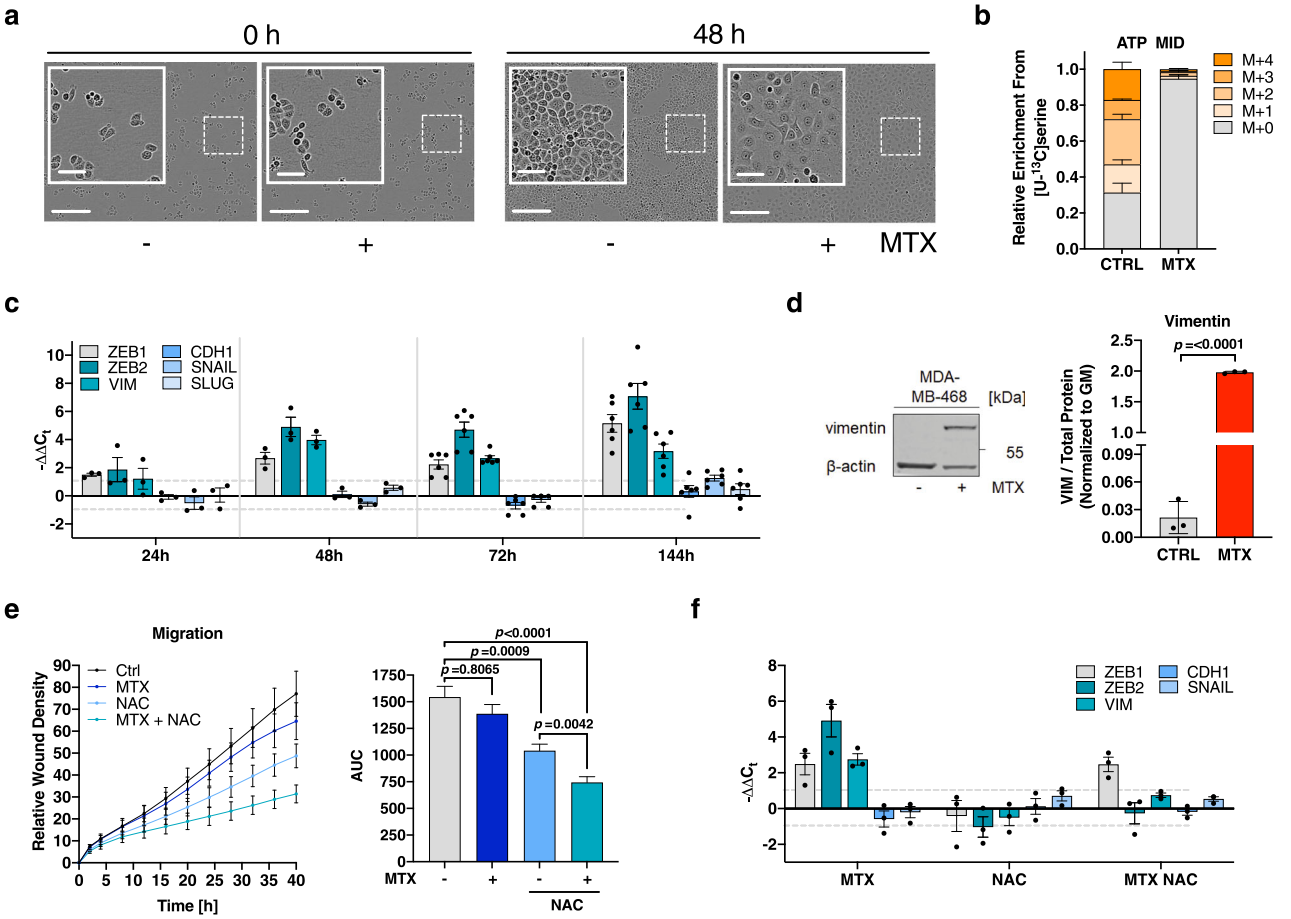


Fig. 2 Enhanced motility under MTX is supported by a ROS-driven EMT phenotype. a Morphology of MDA-MB-468 cells after 48 h 50 nM MTX. Bright-field images are representative of 3 independent experiments. Scale bars correspond to 60 and 300 µm. **b** Mass isotopomere distribution (MID) of intracellular ATP upon [U-^{13}C]serine tracer in response to 24 h 50 nM MTX in MDA-MB-468 cells. Mean ± SEM of 5 independent experiments each measured in triplicate wells. **c** mRNA expression from the indicated target genes in MDA-MB-468 cells upon 50 nM MTX at the indicated time points measured by real-time RT-qPCR. Mean ± SEM ($n = 3$ (24 h, 48 h), 6 (72 h, 144 h)). No data measured for SLUG expression at 72 h. **d** Protein levels of vimentin in MDA-MB-468 cells after 240 h 50 nM MTX; β-actin as loading control. Quantification of vimentin signal relative to total protein stain. Mean ± SD ($n = 3$); unpaired, two-tailed *t*-test with Welch's correction. **e** Migratory potential of MDA-MB-468 cells in response to 10 mM N-acetylcysteine (NAC) and 50 nM MTX as quantification of relative wound density in IncuCyte and respective AUC. Graph shows mean ± SEM of independent experiments ($n = 3$); Brown-Forsythe and Welch ANOVA test with Games-Howell's multiple comparisons test. **f** mRNA expression from the indicated target genes in MDA-MB-468 cells upon 10 mM NAC and 50 nM MTX at 72 h measured by real-time RT-qPCR. Mean ± SEM ($n = 3$). Source data are provided as a Source Data file.

increased [U-^{13}C]glucose-derived M + 1 formate excretion under MTX (Fig. 3j, S3I), allows the hypothesis that mitochondrial 1C metabolism can function in an autarkic manner when cytosolic 1C metabolism is inactivated (Fig. 4a). To corroborate this hypothesis, we employed [U-^{13}C]serine tracing to monitor serine flux through 1C metabolism. We observed that cytosolic block of 1C metabolism via MTX did not reduce the exchange rates of serine, glycine and formate in MDA-MB-468 or LN229 cells (Fig. 4b, C, S4A, C). In contrast, the formate release rate was significantly increased and the increased fraction of labeled formate proved that most of the released formate is derived from [U-^{13}C]serine and not from other carbon sources that could alternatively generate formate in presence of MTX. Of note, sustained serine consumption and formate overflow via 1C metabolism upon DHFR inhibition could also be confirmed in Plasmax medium[50], which is a culture medium closer to human physiology (Fig. S4D). Since cell dry mass composition is constituted by around 60% of proteins[51], growth arresting conditions generally result in decreased consumption rates of proteinogenic amino acids. In fact, a general trend for decreased consumption of essential amino acids was observed (Fig. S4b). Hence, sustained serine consumption rates upon growth arrest suggest that spared serine that is otherwise used for anabolic processes such as nucleotide synthesis, is used for alternative metabolic pathways that support cell motility and survival.

Mechanistically, 1C metabolism follows a cycle in which serine can be resynthesized in the cytoplasm and mitochondrion from glycine via serine hydroxymethyltransferase 1 and 2 (SHMT1, SHMT2) (Fig. 4a). As the SHMT reaction is highly reversible, the serine labeling pattern from [U-^{13}C]serine is composed of a mix of M + 1, M + 2 and M + 3 isotopologues, which represents the different recombination events with labeled and unlabeled glycine and formate[16,21,52]. Consequently, M + 1 and M + 2 serine isotopologues are expected to be absent upon complete 1C metabolism inhibition. Intriguingly, cytosolic DHFR inhibition with MTX neither completely abrogated serine M + 1 and M + 2 isotopologues upon [U-^{13}C]serine nor did it significantly affect the serine to glycine level ratio in MDA-MB-468 or LN229 cells (Fig. 4d, e, S4E, F), further supporting our hypothesis of a persistent mitochondrial 1C metabolism upon DHFR inhibition.

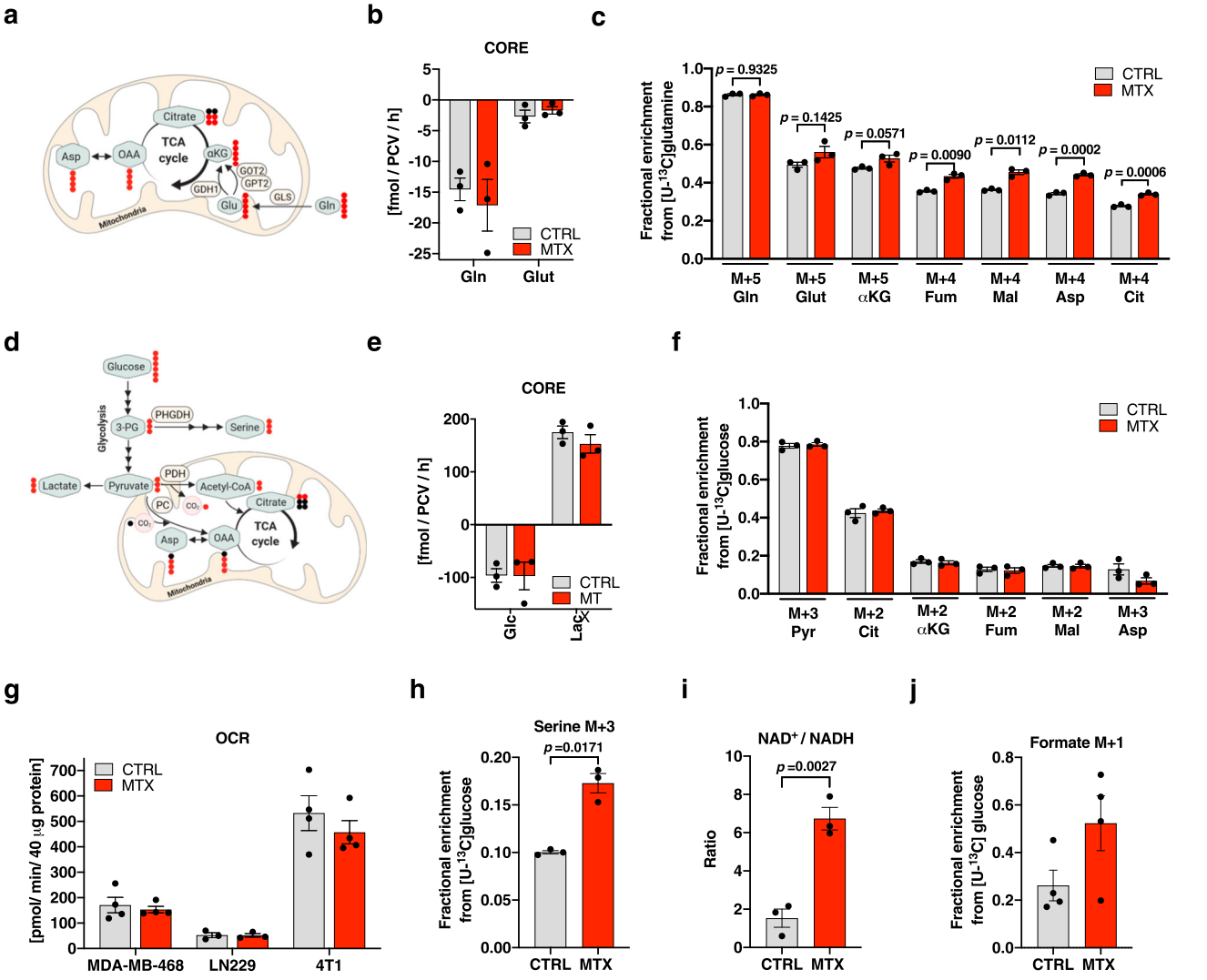


Fig. 3 MTX-treated cells sustain high metabolic rates and enhance de novo serine synthesis. a Interdependence of glycolysis and tricarboxylic acid (TCA) cycle and metabolic ^{13}C label pattern from [U-^{13}C]glutamine. **b** Absolute consumption and release (CORE) rates of glutamine (Gln) and glutamate (Glut) in the culture medium of MDA-MB-468 cells after 24 h 50 nM MTX. Dots represent the mean of an individual experiments composed of triplicate wells; mean ± SEM ($n = 3$). **c** Enrichment of selected isotopologues of Gln, Glut, α-ketoglutarate (αKG), fumarate (Fum), malate (Mal), aspartate (Asp), and citrate (Cit) upon [U-^{13}C]glutamine tracer in response to 24 h 50 nM MTX in MDA-MB-468 cells. Dots represent the mean of an independent experiments in triplicate wells; mean ± SEM; unpaired, two-tailed *t*-test with Welch's correction ($n = 3$). **d** Interdependence of glycolysis and TCA cycle and metabolic ^{13}C label pattern from [U-^{13}C]glucose. **e** Absolute CORE rates of lactate and glucose in the culture medium of MDA-MB-468 cells after 24 h 50 nM MTX. Dots represent the mean of an individual experiments composed of triplicate wells; mean ± SEM ($n = 3$). **f** Enrichment of selcted isotopologues of pyruvate (Pyr), Cit, αKG, Fum, Mal, and Asp upon [U-^{13}C]glucose tracer in response to 24 h 50 nM MTX in MDA-MB-468 cells. Dots represent the mean of an individual experiments composed of triplicate wells; mean ± SEM; unpaired *t*-test with Welch's correction ($n = 3$). **g** Basal cellular respiration upon 24 h 50 nM MTX in MDA-MB-468, LN229, and 4T1 cells as quantification of mitochondrial oxygen consumption rate (OCR). Dots represent the mean of an individual experiments composed of six technical replicates; mean ± SEM ($n = 3$ (LN229), 4 (MDA-MB-468, 4T1)). **h** Enrichment of M + 3 isotopologue of serine upon [U-^{13}C]glucose upon 24 h 50 nM MTX in MDA-MB-468 cells. Dots represent the mean of an independent experiments in triplicate wells; mean ± SEM; unpaired, two-tailed *t*-test with Welch's correction ($n = 3$). **i** Ratio of absolute intracellular NAD^+ to NADH in MDA-MB-468 cells upon 24 h 50 nM MTX. Dots represents the mean of an individual experiments composed of triplicate wells; mean ± SEM; unpaired *t*-test with Welch's correction ($n = 3$). **j** M + 1 isotopologue of extracellular formate in MDA-MB-468 cells from [U-^{13}C]glucose upon 24 h 50 nM MTX. Dots indicate the mean of an independent experiments measured in triplicate wells; mean ± SEM ($n = 4$). Source data are provided as a Source Data file.

To mechanistically disentangle cytosolic from mitochondrial 1C metabolism, we analyzed a panel of CRISPR knockouts in HAP1 cells in which either the cytosolic (SHMT1), the mitochondrial (MFT, SHMT2), or both compartments (FPGS, MFT + SHMT1) of 1C metabolism were abrogated[53]. Here, cytosolic *SHMT1* KO did not eliminate intermediary M + 1 and M + 2 serine isotopologues from [U-^{13}C]serine comparable to MTX treatment, whereas mitochondrial or combined cytosolic and mitochondrial inhibition of 1C metabolism upon *MFT* KO, *SHMT2* KO, *FPGS* KO and *MFT* + *SHMT1* KO resulted in a complete loss of M + 1 and M + 2 serine isotopologues (Fig. 4f). In mutants harboring a full inhibition of 1C metabolism or mitochondrial 1C metabolism alone, we additionally observed an increase in the ratio of serine to glycine levels, whereas MTX treatment and *SHMT1* KO did not substantially increase serine to glycine ratio (Fig. 4g).

Of note the protein abundance of mitochondrial serine catabolism enzymes was not increased upon MTX. MTHFD2

abundance even decreased upon MTX, however, this did apparently not affect the rate of serine catabolism (Fig. S4G, H).

To test if knock-out of mitochondrial serine catabolism stops formate overflow, we monitored formate release flux upon MTX in HAP1 cells deficient for SHMT1 or SHMT2. As expected, loss of SHMT2 completely abolished formate overflow, while SHMT1 KO increased formate overflow (Fig. 4h). This experiment was then validated in MDA-MB-468 cells harboring *MTHFD1L* KO[20]

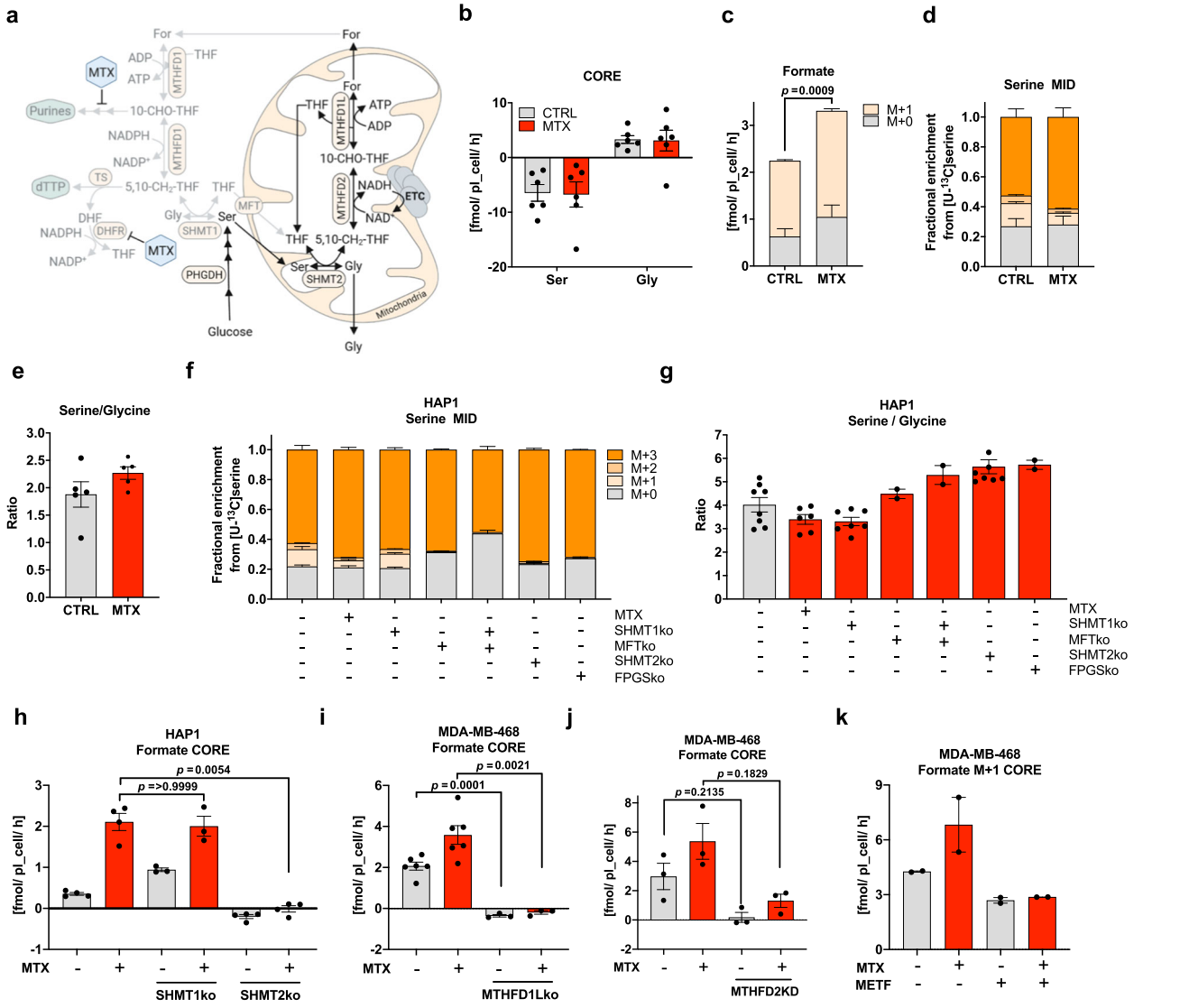


Fig. 4 Mitochondria protect 1C metabolism-dependent serine catabolism upon cytosolic 1C pathway inhibition. a Cytosolic and mitochondrial 1C metabolism and the pharmacologic intervention points of MTX. **b** Absolute consumption and release (CORE) rates of serine (Ser) and glycine (Gly) from MDA-MB-468 cells upon 24 h 50 nM MTX. Dots represent the mean of an individual experiment each measured in triplicate wells; mean ± SEM ($n = 6$). **c** Formate release rate upon [U-^{13}C]serine in MDA-MB-468 cells after 24 h 50 nM MTX; mean ± SEM of three independent experiments each measured in triplicate wells; unpaired *t*-test with Welch's correction for M + 1 isotopologue ($n = 3$). **d** MID of intracellular serine upon [U-^{13}C]serine in MDA-MB-468 cells upon 24 h 50 nM MTX; mean ± SEM of four independent experiments each measured in triplicate wells. **e** Ratio of absolute intracellular serine and glycine after 24 h 50 nM MTX in MDA-MB-468 cells. Dots represent the mean of an independent experiment in triplicate wells; mean ± SEM ($n = 5$). **f** MID of intracellular serine upon [U-^{13}C]serine in SHMT1, MFT, SHMT2, and FPGS-depleted HAP1 cells; mean ± SEM of independent experiments each measured in triplicate wells ($n = 8$ for CTRL, SHMT1ko, and SHMT2ko; $n = 5$ for MTX; $n = 2$ for FPGSko, MFTko and MFT/SHMT1ko). **g** Ratio of absolute intracellular serine and glycine levels in SHMT1, MFT, SHMT2, and FPGS depleted HAP1 cells. Dots represent the mean of an independent experiment in triplicate wells; mean ± SEM ($n = 8$ for CTRL and SHMT2ko, $n = 7$ for SHMT1ko, $n = 6$ for MTX, $n = 2$ for FPGSko, MFTko and MFT/SHMT1ko). **h** Absolute CORE rates of formate from WT and SHMT1- or SHMT2-depleted HAP1 cells upon 24 h 50 nM MTX. Each dot indicates the mean of an individual experiment measured in triplicate wells; Brown-Forsythe and Welch ANOVA test with Dunnetts multiple comparisons test. Mean ± SEM ($n = 4$ for CTRL, MTX, SHMT2ko, SHMT2ko MTX; $n = 3$ for SHMT1ko and SHMT1ko MTX) **i** Absolute CORE rates of formate from WT and MTHFD1L-depleted MDA-MB-468 cells upon 24 h 50 nM MTX. Mean ± SEM ($n = 6$ for CTRL and MTX; $n = 3$ for MTHFD1Lko + /- MTX) of an individual experiment measured in triplicate wells; Brown-Forsythe and Welch ANOVA test with Dunnetts multiple comparisons test. **j** Absolute CORE rates of formate from SCR and MTHFD2 KD MDA-MB-468 cells upon 24 h 50 nM MTX. Dots represent mean of an individual experiment measured in triplicate wells; mean ± SEM; ($n = 3$) Brown-Forsythe and Welch ANOVA test with Dunnetts multiple comparisons test. **k** Absolute CORE rates of formate from MDA-MB-468 cells upon 24 h treatment with 2.5 mM Metformin and 50 nM MTX. Dots represent mean of an individual experiment measured in triplicate wells; mean ± SEM ($n = 2$). Source data are provided as a Source Data file.

or shRNA mediated *MTHFD2* knock-down and *MTHFD2* KO (Fig. 4i, j, S4I-M). All genetic interventions resulted in a strong suppression of formate overflow during MTX treatment, further suggesting that increased formate overflow upon MTX depends on mitochondrial serine catabolism via the folate pathway (Fig. 4i, j, S4J, M).

As an alternative approach to genetic silencing we used Metformin to target complex 1 of the electron transport chain (ETC). We have previously shown that mitochondrial formate production depends on active ETC[21,22]. Here, we demonstrate that targeting of complex 1 with Metformin strongly suppresses mitochondrial formate production both at baseline and in presence of MTX, further supporting our finding that formate production in presence of MTX depends on mitochondrial 1C metabolism (Fig. 4k). To proof that Metformin indeed inhibits respiration under the applied conditions, we performed Seahorse experiments to measure the expected drop in oxygen consumption rate (Fig. S4N). We also monitored a reduction in proliferation (Fig. S4O) and we performed [U-^{13}C]glutamine tracing to monitor the expected strong increase in reductive carboxylation (Fig. S4P, Q), a well-known phenomenon upon ETC inhibition[54,55].

In summary, these results show that mitochondria provide a protected cellular environment that permits autarkic folate-mediated serine catabolism independent of the cytosolic folate metabolism.

Limiting serine availability decreases formate overflow and cancer cell migration. As we observed increased glucose derived serine synthesis and subsequent downstream catabolism of serine via mitochondrial 1C metabolism, we investigated if interfering with serine synthesis is effective to reduce sustained cell migration upon pharmacologic inhibition of cytosolic 1C metabolism. First, to identify an effective inhibitor of serine de novo synthesis, we tested multiple available allosteric and one competitive inhibitor of PHGDH. Indicated by the strong abrogation of labeled serine, we observed that the competitive inhibitor BI-4916 (BI)[12] had superior efficacy compared to the allosteric inhibitors WQ-2101 (WQ)[11], NCT-502 (NCT)[9], and CBR-5884 (CBR)[15] (Fig. 5a). Released M + 1 formate from [U-^{13}C]glucose was also effectively inhibited after BI treatment alone or in combination with MTX (Fig. 5b). Additionally, routine screening for metabolic side effects revealed that treatment with the allosteric inhibitors WQ, NCT, and CBR did result in a significant reduction of mitochondrial OCR (Fig. 5c), which was not observed with the competitive inhibitor BI (Fig. 5c). WQ and NCT also negatively affected TCA cycle activity as characterized by a reduction of M + 2 isotopologue abundance of TCA cycle associated metabolites (Fig. 5d). In contrast to the other inhibitors, BI had no adverse effect on TCA cycle activity and proliferation rate and thus emerged as the preferred PHGDH inhibitor in all subsequent experiments (Fig. 5d, S5A–D). Combined treatment with the specific PHGDH inhibitor BI significantly reduced MTX-mediated cell migration (Fig. 5e). This inhibitory effect was further enhanced upon combined PHGDH inhibition and serine and glycine (S/G) starvation (Fig. 5f). While S/G starvation alone resulted only in moderate inhibitory effects on migration of MTX-treated cells, combined treatment with PHGDH inhibition fully blunted cell migration (Fig. 5f). Similar results were observed in 4T1 cells (Fig. S5F). As all MTX conditions resulted in full growth arrest (Fig. S5E), this finding indicates a role for mitochondrial 1C metabolism in cell motility that is independent of serine's anabolic function to support biosynthetic processes.

While neither BI treatment alone nor S/G starvation alone were sufficient to prevent the induction of the observed EMT-phenotype, combined inhibition and starvation did minimize *ZEB1*, *ZEB2*, and *VIM* upregulation upon DHFR inhibition (Fig. 5g). This indicates that serine represents an underlying requirement for EMT onset upon DHFR inhibition. Importantly, S/G starvation did not further increase cell death after combined MTX and BI treatment (Fig. 5h). Of note, we also found that BI treatment was effective to reduce the migratory capacity of MTX-resistant, pro-migratory MDA-MB-468 cells (Fig. 5i). In summary, using MTX as a tool compound to study cell migration in absence of proliferation revealed that serine is essential to sustain full cancer cell migratory capacity (Fig. 5j).

Mitochondrial 1C metabolism supports cell motility and depends on mitochondrial THF availability. As withdrawal of serine can affect different aspects of cell physiology, we aimed to investigate more specifically the role of mitochondrial 1C metabolism in promoting cell migration. Analogue to the interventions presented in Fig. 4i–k, we used Metformin to target the ETC and genetic interventions to target *MTHFD2* or *MTHFD1L* both in MDA-MB-468 and 4T1 cells.

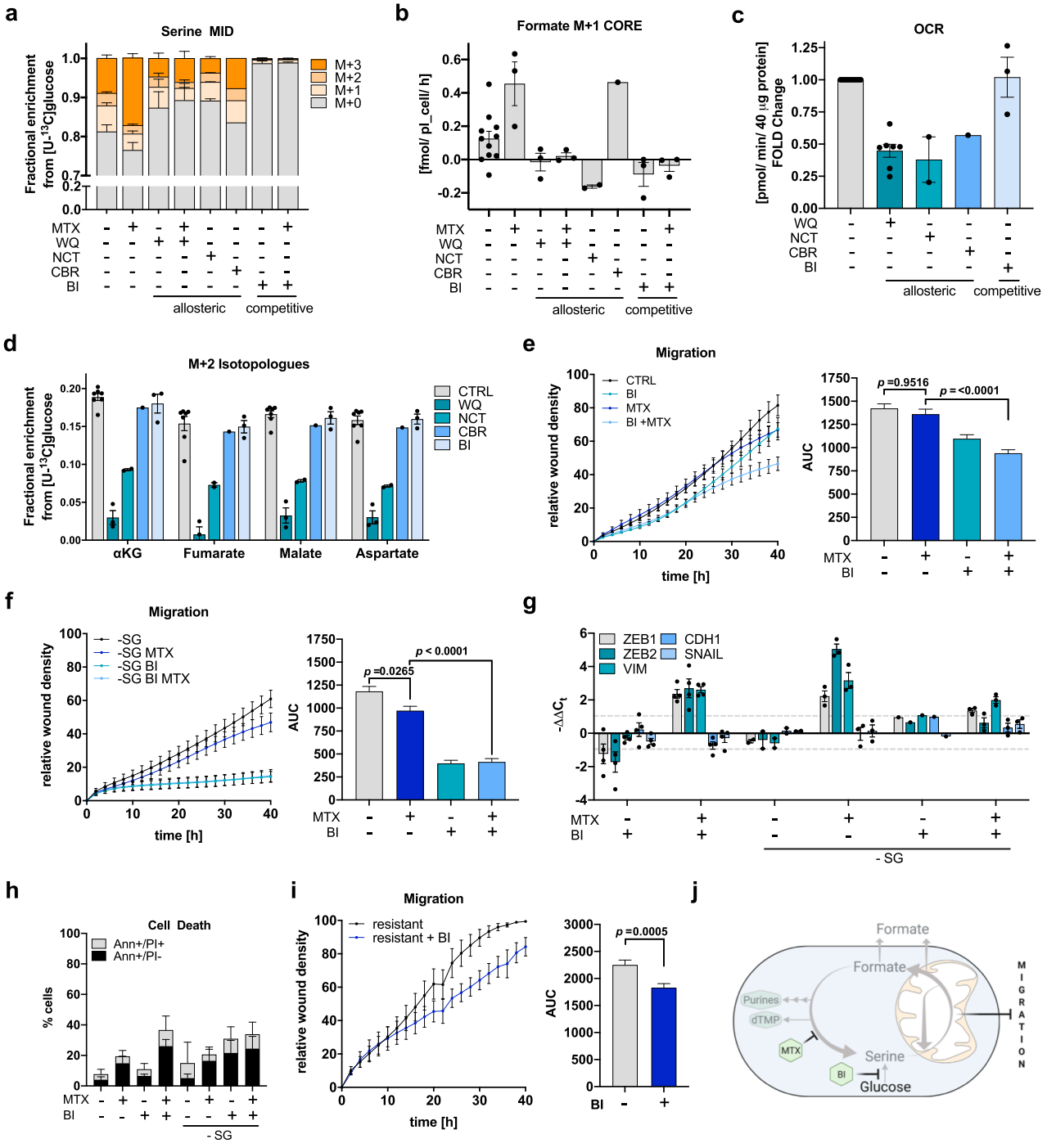
Metformin treatment of MTX exposed (growth arrested) cells reduced the migration of MDA-MB-468 cells (Fig. 6A), suggesting that one function of the ETC is to support cell migration.

Next, we investigated the role of mitochondrial serine catabolism in context of migration directly, by monitoring the migration of MTX treated *MTHFD2* or *MTHFD1L* silenced MDA-MB-468 and 4T1 cells. Of note, neither *MTHFD2* nor *MTHFD1L* silencing reduced cell proliferation or sensitivity to the growth-arresting effects of MTX (Fig. S6A–D). Also, cell death rates upon MTX were not affected by *MTHFD2* or *MTHFD1L* silencing (Fig. S6E–H). Scratch assay analysis showed that *MTHFD2* silencing markedly reduced MTX-mediated cell motility both in MDA-MB-468 and 4T1 cells (Fig. 6b, c). As shRNA used to silence human and murine *MTHFD2* were different, we do not expect shRNA specific off-target effects. Nevertheless, we confirmed the shMTHFD2 KD results in MDA-MB-468 cells with *MTHFD2* knock-out cells (Fig. S6I).

Mthfd1l silencing of MTX treated 4T1 cells also resulted in decreased migration (Fig. 6d). Somewhat surprisingly, loss of *MTHFD1L* in MDA-MB-468 cells had no negative effect on the migration of MTX treated cells (Fig. 6e). By following different hypotheses and various experiments, we realized that there is a striking difference in ALDH1L2 expression in 4T1 versus MDA-MB-468 cells, while MTHFD1L expression was comparable between these two cell lines (Fig. 6f, g).

This observation reminded us that in MDA-MB-468 cells, ALDH1L2 can act as an alternative outlet to oxidize formyl-THF to CO_2 thereby regenerating mitochondrial THF (in contrast to 4T1). That said, in MTHFD1L deficient cells, the ALDH1L2 status can be decisive whether THF can be regenerated or if THF will be trapped as 10-CHO-THF in the mitochondrion. Loss of free THF will potentially inhibit the autarkic mitochondrial cycle that can otherwise act in presence of MTX (Fig. 6h). In support of this hypothesis, we also measured increased formate release flux in 4T1 cells compared to MDA-MB468 (Fig. S6J), suggesting that in 4T1 cells less 10-CHO-THF is oxidized via Aldh1l2 and instead catabolized through Mthfd1l.

To test this hypothesis, we targeted *ALDH1L2* in MTHFD1L KO cells and monitored migration. We found that combinatorial depletion of *MTHFD1L* and *ALDH1L2* in MDA-MB-468 cells resulted at least in a reduction of migration upon MTX compared to single depletion of *MTHFD1L* alone. This was observed both for shRNA as well as for siRNA mediated knockdown of *ALDH1L2* (Fig. 6i, S6K).



In conclusion, these results reveal a growth-independent role of mitochondrial 1C metabolism for cancer cell motility. Interestingly, the pool of free THF might be relevant for the functionality of the autarkic mitochondrial 1C cycle and ALDH1L2 can serve as an alternative outlet to regenerate THF when MTHFD1L is missing (summarized in Fig. 6J).

Genetic targeting of mitochondrial 1C metabolism reduces metastasis formation in vivo. According to our model, we predict that sole inhibition of mitochondrial 1C metabolism might be sufficient and effective to reduce cancer cell escape from the primary tumor and subsequent metastasis formation. To test this hypothesis, we employed the 4T1 cells with *Mthfd1l* KD to study the metastatic cascade in orthotopic tumors in vivo.

To evaluate first if Mthfd1l KD cells are more prone to oxidative stress, which could impact metastatic dissemination in vivo[56], we measured ROS levels in MTHFD1L silenced MDA-MB-468 and 4T1 cells at baseline and after MTX treatment. At baseline, ROS levels between MTHDF1L silenced and control cells were unchanged. MTX treatment induced ROS levels to comparable extends and 500 µM of H_2O_2 treatment did induce cell death rate comparable to Ctrl cells (Fig. S7A–C). In summary, these experiments do not indicate that loss of MTHFD1L results in increased cellular ROS levels or increased susceptibility to oxidative insults.

We then injected 4T1 cells with or without silenced *Mthfd1l* into the mammary fat pad of immunocompetent BALB/c mice to form orthotopic tumors (Fig. 7a). Primary tumor growth was

Fig. 5 Limiting serine availability decreases formate overflow and cancer cell migration. a MID of intracellular serine in MDA-MB-468 cells upon [U-^{13}C]glucose and 24 h 10 μM WQ-2101, 10 μM NCT-502, 30 μM CBR-5884, 15 μM BI-4916, and 50 nM MTX; mean ± SEM ($n = 10$ for CTRL; $n = 3$ for WQ, MTX, WQ MTX, BI, BI MTX; $n = 2$ for NCT; $n = 1$ for CBR) of independent experiments each measured in triplicate wells. **b** Formate M + 1 isotopologue exchange rate in MDA-MB-468 cells using [U-^{13}C]glucose and treatment as in (**a**). Dots indicate independent experiments measured in triplicate wells; mean ± SEM ($n = 10$ for CTRL; $n = 3$ for WQ, MTX, WQ MTX, BI, BI MTX; $n = 2$ for NCT; $n = 1$ for CBR). **c** Basal cellular respiration upon 24 h 10 μM WQ-2101, 10 μM NCT-502, 30 μM CBR-5884, and 15 μM BI-4916 in MDA-MB-468 cells as fold mitochondrial OCR compared to control. Dots represent individual experiments composed of six technical replicates; mean ± SEM ($n = 10$ for CTRL, $n = 7$ for WQ, $n = 3$ for BI, $n = 2$ for NCT, $n = 1$ for CBR). **d** M + 2 isotopologues of selected TCA-metabolites in MDA-MB-468 cells upon [U-^{13}C]glucose and treatment as in (**b**). Dots indicate independent experiments measured in triplicate wells; mean ± SEM ($n = 7$ for CTRL, $n = 3$ for WQ, BI, $n = 2$ for NCT, $n = 1$ for CBR). **e** Migration of MDA-MB-468 cells upon 50 nM MTX, 15 μM BI-4916 and **f** serine- and glycine starvation and respective AUC; mean ± SEM of independent experiments ($n = 5$ for (**e**), $n = 4$ for (**f**)); Brown-Forsythe and Welch one-way ANOVA with Dunnett's multiple comparisons test. **g** mRNA expression from indicated genes in MDA-MB-468 cells upon 72 h 50 nM MTX, 15 μM BI-4916, and serine- and glycine starvation measured by real-time RT-qPCR. Mean ± SEM ($n = 4$ for BI, BI + MTX, $n = 3$ for MTX-SG, MTX-SG + BI, $n = 2$ for -SG, $n = 1$ for BI-SG). **h** Cell death induction in MDA-MB-468 cells upon 48 h 50 nM MTX, 15 μM BI-4916 and serine- and glycine starvation was assessed by flow cytometry and AnnexinV-FITC/PI-staining; mean ± SD of independent experiments ($n = 3$). Two-way ANOVA with Dunnett's multiple comparisons test. **i** Migration of MTX-resistant MDA-MB-468 cells upon 50 nM MTX and 15 μM BI-4916 and respective AUC; mean ± SEM of independent experiments ($n = 4$); Brown-Forsythe and Welch one-way ANOVA with Dunnett's multiple comparisons test. **j** Cytosolic and mitochondrial compartments of 1C metabolism and the pharmacologic intervention points of MTX and inhibitors of PHGDH. Source data are provided as a Source Data file.

monitored over 6 weeks. In concordance with the in vitro data, primary tumor growth was not affected and tumor weight at endpoint was not different compared to Ctrl conditions (Fig. 7b, c). Knock-down of Mthfd1l in the primary tumors was confirmed by Western Blot (Fig. 7d, S7D–F). In line with our hypothesis, the number of macroscopic lung metastases was significantly reduced in mice that were carrying tumors deficient in Mthfd1l (Fig. 7e). While all mice that were injected with Mthfd1l-expressing 4T1 cells exhibited lung metastases, over 50% of mice injected with *Mthfd1l* KD cells did not show macroscopic metastatic lesions. Of note, expression of EMT related genes in the primary tumor was unchanged between the two groups (Fig. S7G). H&E staining of lungs and quantification of the metastatic area per lung confirmed reduced metastasis in Mthfd1l deficient tumors (Fig. 7f, g).

These in vivo findings further strengthen the key relevance of mitochondrial 1C metabolism as a cornerstone to support cancer cell migration independent of primary tumor growth and cancer cell proliferation rates.

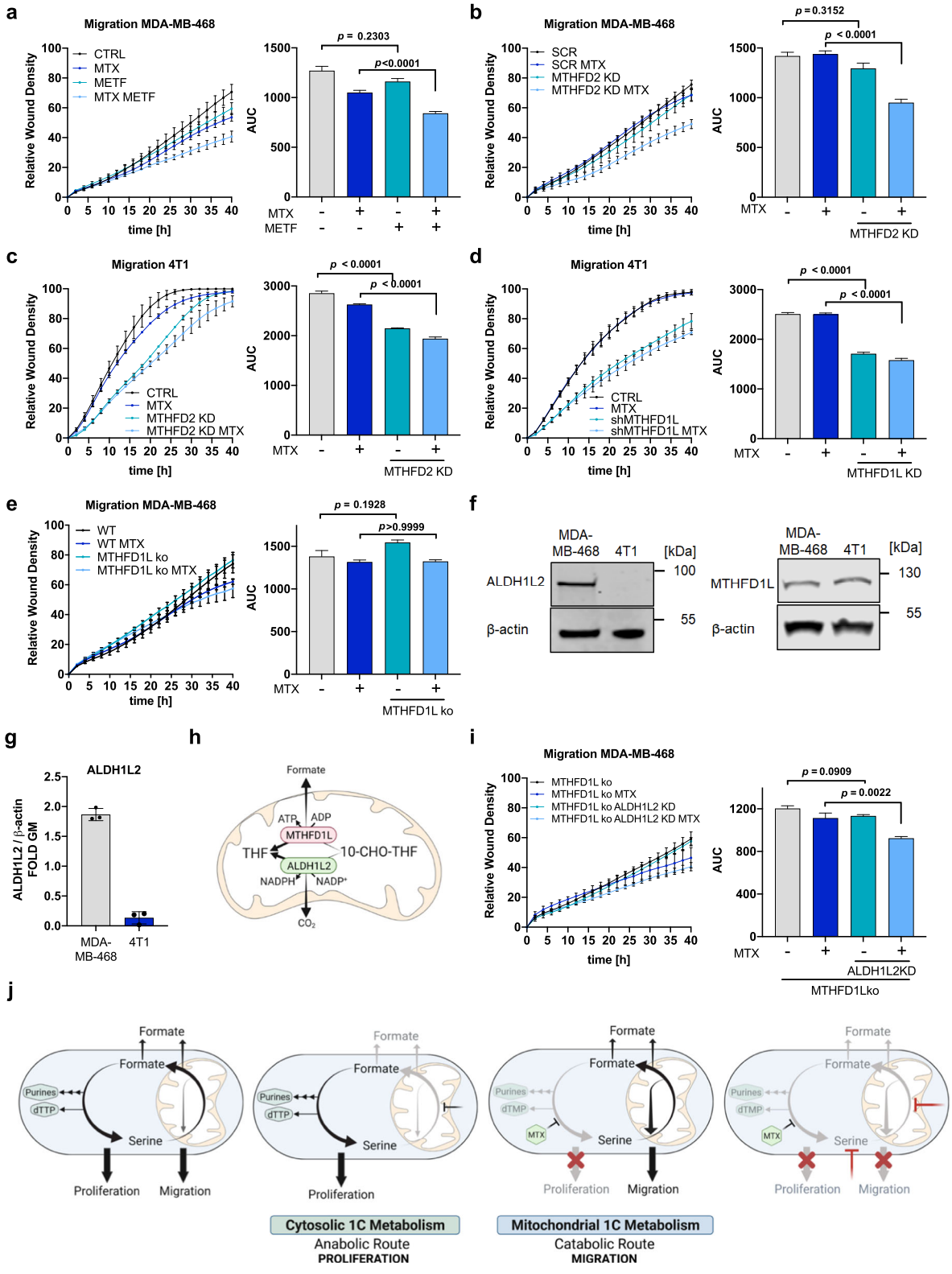
Discussion

In this study, we uncover a growth-independent function of mitochondrial serine catabolism to drive cancer cell motility. Importantly, by using MTX as a tool compound to study migration independent of proliferation, we observed that upon inhibition of cytosolic 1C metabolism, mitochondria sustain an autarkic 1C metabolism that is sufficient to sustain full migratory capacity.

Such compartmentalization of 1C metabolism during MTX treatment is feasible because release of the 1C unit from THF in the mitochondrial MTHFD1L reaction is, in contrast to cytosolic thymidylate synthetase reaction, not oxidizing THF to DHF. Therefore, the mitochondrial THF pool is sustained to allow SHMT2-dependent mitochondrial serine catabolism, while cytosolic 1C metabolism enzymes are inhibited due to accumulating DHF species. Our finding that ALDH1L2 can serve as an alternative source for THF regeneration in MTHFD1L deficient cells, supports the notion that mitochondria can maintain an independent THF pool that is required for an autarkic mitochondrial 1C metabolism as long as there is THF available that can accept the hydroxymethyl group in the first (SHMT2 dependent) step of serine catabolism.

An autarkic mitochondrial 1C metabolism is further supported by a chemical modification of folate species that alters their transport activities across the mitochondrial membrane. For maximal biologic activity, folate species need to be polyglutamated by folylpolyglutamate synthase (FPGS) and the resulting polyglutamate species were shown to be only poorly transported across the mitochondrial membrane[57,58]. Consequently, polyglutamated folate species can be chemically trapped within the mitochondria to sustain the mitochondrial 1C cycle. Especially, upon growth arrest when cells can retain their mitochondrial content and don't need to amplify their content as it is required during proliferation. Additionally, there is evidence that transport activity of the mitochondrial folate transporter is limited to reduced folates[59]. This indicates a limited transport of MTX and folic acid itself across the mitochondrial membrane. Taken together, such compartmentalization of 1C metabolism and autarkic function of mitochondrial 1C metabolism emerges as a selective advantage in cells upon perturbation of cytosolic 1C metabolism and indicates a function of the mitochondrial 1C metabolism pathway to support cell motility.

While our data demonstrate that mitochondrial serine catabolism is needed to allow full migratory capacity, the specific biochemical output conferring this function still needs to be determined in more detail. Mitochondrial serine catabolism can generate NADH, NADPH, ATP, glycine, CO_2, methylene- and formyl-THF and formate. The plasticity of this pathway allows tailoring the catabolism towards current cellular needs[38]. Therefore, it can be possible that serine is differentially catabolized along the metastatic cascade in a context dependent manner. We have previously shown that exogenous formate promotes cancer cell invasion[22] and various cellular stress situations such as energy stress[21] or MTX treatment (this study) can increase the rate of formate overflow which results in increased extracellular formate concentrations. It is therefore tempting to speculate that increasing formate concentrations in the tumor microenvironment promote a more invasive phenotype of stressed cancer cells. In more general terms, it could be possible that mitochondrial serine catabolism can selectively promote cell motility in response to extrinsic or intrinsic stress stimuli such as growth inhibition or nutrient deprivation. On the other hand, MDA-MB-468 MTHFD1L KO cells are also formate overflow negative but do not show reduced migration. As ROS levels are neither increased in MDA-MB-468 nor in 4T1 MTHFD1L deficient cells, we do not think that the observed migration effects in this study are ROS dependent. Given previous work[22] and the current study, there might also be differences when comparing migration with invasion.



Ongoing work in our lab will help clarifying these questions in the future. To do so, it will be of particular importance to further disentangle effects arising from exogenous formate from effects depending on endogenous serine catabolism. Independent of these yet unknown details, we remain with the conclusion that mitochondrial serine catabolism contributes to cancer cell migration and metastasis independent of its known anabolic functions.

Finally, we would like to note that although we mainly use MTX as a tool compound to separate proliferative from migratory processes and to inhibit cytosolic 1C metabolism, our results have also some implications in regard to MTX as an anchor drug in chronic treatment of autoimmune diseases. Intracellular erythrocyte and mean plasma concentration of MTX were reported to be in a comparable, even slightly higher, nM range to our chosen drug concentration[60,61]. Finally, we also

Fig. 6 Mitochondrial 1C metabolism supports cell motility and depends on mitochondrial THF availability. a Migration of MDA-MB-468 cells upon 2.5 mM Metformin and 50 nM MTX and respective AUC; mean ± SEM of independent experiments ($n = 3$); Brown-Forsythe and Welch one-way ANOVA with Dunnett's multiple comparisons test. **b** Migration of MDA-MB-468 cells upon MTHFD2 knockdown and 50 nM MTX and respective AUC; mean ± SEM of independent experiments ($n = 4$); Brown-Forsythe and Welch one-way ANOVA with Dunnett's multiple comparisons test. **c** Migration of 4T1 cells upon Mthfd2 knockdown and 75 nM MTX and respective AUC; mean ± SEM of independent experiments ($n = 3$); Brown-Forsythe and Welch one-way ANOVA with Dunnett's multiple comparisons test. **d** Migration of 4T1 cells upon Mthfd1l knockdown and 75 nM MTX and respective AUC; mean ± SEM of independent experiments ($n = 3$); Brown-Forsythe and Welch one-way ANOVA with Dunnett's multiple comparisons test. **e** Migration of MDA-MB-468 cells upon MTHFD1L knockout and 50 nM MTX and respective AUC; mean ± SEM of independent experiments ($n = 3$); Brown-Forsythe and Welch one-way ANOVA with Dunnett's multiple comparisons test. **f** ALDH1L2 and MTHFD1L protein expression in MDA-MB-468 and 4T1 cells. **g** Signal intensity of ALDH1L2 on Western Blot was quantified relative to β-actin as loading control. Mean ± SEM ($n = 3$); unpaired *t*-test with Welch's correction. **h** MTHFD1L- and ALDH1L2-dependent reactions in mitochondrial 1C metabolism. **i** Migration of MDA-MB-468 cells upon MTHFD1L knockout, ALDH1L2 knockdown and 50 nM MTX and respective AUC; mean ± SEM of independent experiments ($n = 3$); Brown-Forsythe and Welch one-way ANOVA with Dunnett's multiple comparisons test. **j** Model summarizing the autarkic activity of mitochondrial and cytosolic 1C metabolism and their respective relevance for cell migration and cell proliferation. Source data are provided as a Source Data file.

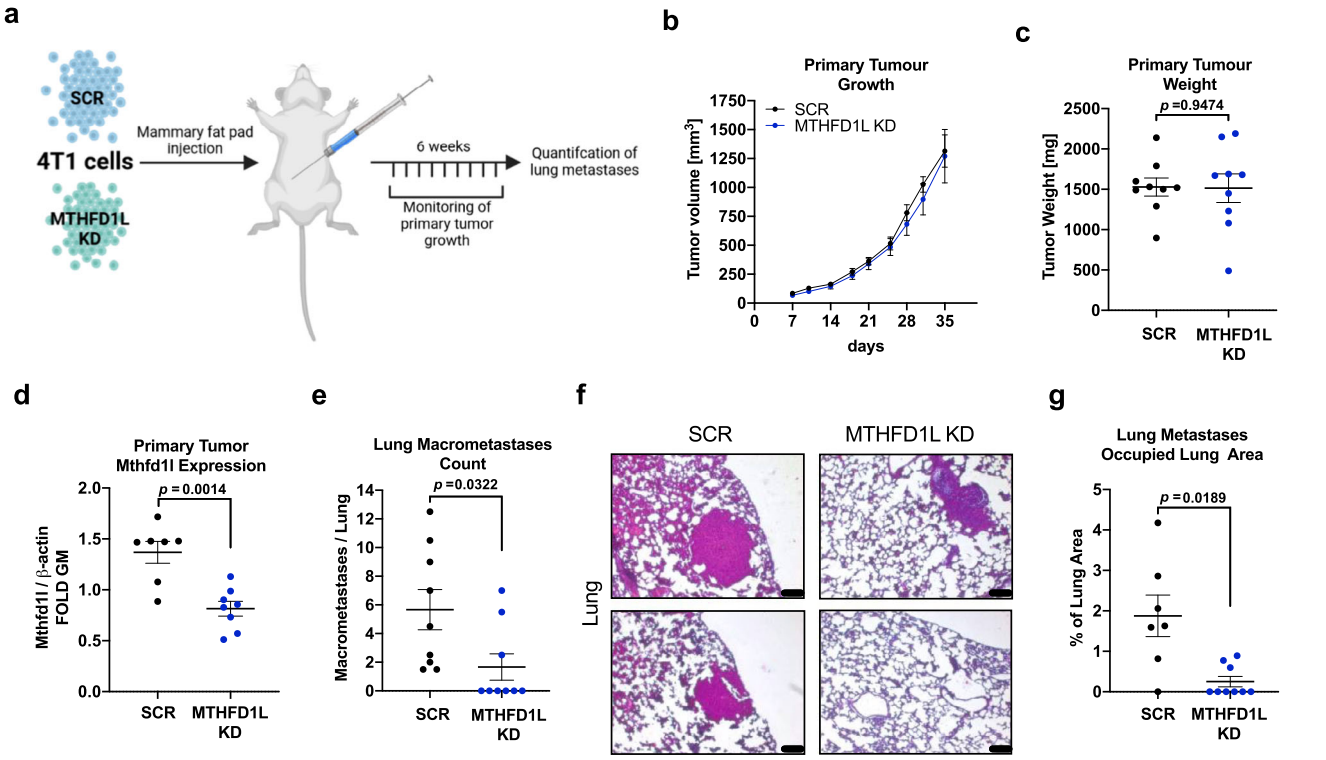


Fig. 7 Genetic targeting of mitochondrial 1C metabolism reduces metastasis formation in vivo. a 4T1 breast cancer cells transfected with non-targeting control (SCR, $n = 9$) and 4T1 cells with KD of *Mthfd1l* ($n = 9$) were injected into the mammary fat pads of immunocompetent female Balb/c mice. Primary tumor growth was monitored and lung metastasis formation was evaluated at end-point. **b** Primary tumor size was measured and mean tumor volume for each group was calculated; mean ± SEM ($n = 8$ (Scr) and 9 (Mthfd1l KD)). **c** Primary tumor weight was measured at the end-point. Dots indicate individual animals; mean ± SEM ($n = 9$); unpaired, two-tailed *t*-test with Welch's correction. **d** Primary tumor tissue was analyzed for Mthfd1l protein expression by Western Blot and quantified relative to β-actin as loading control. Dots indicate individual animals; mean ± SEM ($n = 7$ (Scr) and 8 (Mthfd1l KD)); unpaired, two-tailed *t*-test with Welch's correction. Protein lysates from tumors with significantly low Mthfd1l and β-actin expression relative to total protein were judged to be not pure tumor lysate and discarded from analysis (see Figure S7D–F for details). **e** Macroscopic lung metastases were counted and are depicted as number of metastases per lung. Dots indicate individual animals; mean ± SEM ($n = 9$); unpaired, two-tailed t-test with Welch's correction. **f** Lung tissue was embedded in paraffin and stained with H&E. 2 representative images per group are presented to show microscopic lung metastasis; scale bar corresponds to 100 µm. **g** Metastatic area per lung was quantified and is expressed as % area of lung tissue. Dots indicate individual animals; mean ± SEM ($n = 7$ (Scr) and 9 (Mthf1l KD)); unpaired, two-tailed *t*-test with Welch's correction. Source data are provided as a Source Data file.

would like to refer to a parallel and independent (back-to-back) publication that provides additional evidence that purine depletion promotes serine de novo synthesis and cell migration[62]. Interestingly, in this parallel work, the authors provide data that MTX also promotes the metastatic potential of melanoma cells in vivo. Hence, our findings on mitochondrial 1C metabolism might justify future investigations in cancer patients and patients that undergo chronic MTX therapy for an arthritic comorbidity.

Methods

Chemicals. Methotrexate, rotenone, PKUMDL-WQ-2101, galactose, hydroxyurea, NAC, metformin and fluorouracil were purchased from Sigma Aldrich. Clofarabine, pemetrexed disodium hydrate, sirolimus were purchased from Bio Connect. Simvastatin was purchased from Sanbio. CBR-5884 and BI-4916 were purchased from MedChemExpress. NCT-502 was purchased from ApeXBio.

Cell culture. All cell lines (except HAP1 cells) were cultured in Dulbecco's modified Eagle's medium (DMEM) without phenol red, glucose, and glutamine (Thermo Fisher Scientific) and supplemented with 2 mM glutamine, 17 mM

glucose, and 10% fetal bovine serum (FBS) at 37 °C and 5% CO_2. HAP1 cells were cultured in IMDM medium supplemented with 10% FBS. For galactose treatment, supplemented glucose was replaced by 17 mM galactose at the beginning of the experiment. For serine/glycine starvation experiments cells were kept in MEM (Thermo Fisher Scientific) supplemented with or without 400 µM glycine and serine, 2 mM glutamine, 17 mM glucose and 10% dialyzed FBS.

MDA-MB-468 and MTHFD1L CRISPR/Cas9 KO cells were obtained from Lewis Cantley lab, Weill Cornell Medical College, USA[20]. MDA-MB-468 were authenticated by STR profiling in our lab in 2021 (originally from ATCC); LN229 cells obtained from Alexei Vazquez lab Beatson Institute for Cancer Research (authenticated by STR profiling in our lab in 2021) (originally from ATCC); 4T1 cells from Luxembourg Institute of Health, Clement Thomas lab (authenticated by Clement lab in 2018) (originally from ATCC). HCT-116 cells from University of Luxembourg, Elisabeth Letellier lab (originally from ATCC), HEK293T: NorLux Lab, Luxembourg Institute of Health (originally from ATCC). HAP1 cells were obtained from Patel's laboratory[53] (originally from Horizon Discovery). MTX-resistant MDA-MB-468 cells were generated through prolonged culturing of MDA-MB-468 cells with 50 nM MTX for 2 months until cells started to regrowth under MTX. All cell lines were routinely tested for mycoplasma contamination.

Metabolic characterization. For metabolic characterization of cell lines, previously established protocols for absolute quantification of exchange fluxes and intracellular fluxes of one-carbon metabolism were applied[21].

Stable isotope tracing and metabolite extraction. Stable isotope tracing experiments with [U-^{13}C]-glucose tracer or [U-^{13}C]-glutamine tracer (Cambridge Isotope Laboratories, CLM-1396) were performed in DMEM supplemented with 2 mM glutamine, 17 mM glucose, and 10 % FBS. Stable isotope tracing experiments with [U-^{13}C]-serine tracer (Cambridge Isotope Laboratories) were performed in MEM (Thermo Fisher Scientific) supplemented with 400 µM glycine, 2 mM glutamine, 17 mM glucose, 400 µM serine tracer, and 10% FBS. To allow for adaptation, cells were cultivated in MEM for at least one passage prior to [U-^{13}C]-serine tracer experiments. 150,000 to 200,000 cells were seeded in 12-well plates in triplicates for each experimental condition. Identical triplicate wells were seeded to allow for cell count and cell volume determination (to calculate the packed cell volume (PCV)) at the start and end of each tracing experiment. The day after seeding, growth medium was replaced by tracer medium and cells were cultured for 24 h. In parallel, 3 wells per condition were counted to assess starting PCV. After 24 h, triplicate wells were counted to assess PCV at the end of the experiment and one set of triplicates was used for subsequent metabolite extraction. Medium of these triplicates were collected and analyzed for exchange rates. To determine the basal medium composition for the subsequent calculation of exchange rates, identical medium was incubated in triplicates in empty 12 wells throughout the experiment and analyzed in parallel to the medium samples. Collected medium samples were centrifuged at 300 g for 5 min. Supernatant was collected and stored at −20°C until extraction of metabolites. Formate extraction, derivatization, and quantification as well as metabolite extraction for LC-MS analysis was performed as described in[21]. For metabolite extraction for GC-MS analysis after [U-^{13}C]-glucose tracing and [U-^{13}C]-glutamine tracing, cells were washed with cold 0.9% NaCl solution. 400 µl ice-cold MeOH/H_2O_{MQ} [(ratio, 1:1) containing the internal standards pentanedioc-d6 acid and [U-^{13}C]-ribitol at a final concentration of 1 µg/ml and Tridecanoid-d25 acid at a final concentration of 5 µg/ml] was added to each well. Plates were incubated for 5 min at 4°C on a rocking shaker. Supernatant was collected, mixed with 200 µl $CHCl_3$, and centrifuged for 5 min at 13,000 g at 4°C. Upper polar phase was collected and stored at −20°C for subsequent MS analysis of polar metabolites.

GC-MS measurements

Analysis of formate release rates. Formate derivatization in the culture medium was performed using MCF derivatization as described in[21]. GC-MS analysis was performed using an Agilent 7890 A GC coupled to an Agilent 5975 C inert XL Mass Selective Detector (Agilent Technologies). A sample volume of 1 µl was injected into a Split/Splitless inlet, operating in split mode (20:1) at 270 °C. The gas chromatograph was equipped with a 30 m (I.D. 250 µm, film 0.25 µm) DB-5MS capillary column (Agilent J&W GC Column, 122-5532 G). Helium was used as carrier gas with a constant flow rate of 1.4 ml/min. GC oven temperature was held at 80 °C for 1 min and increased to 130 °C at 10 °C/min followed by a post run time of 4 min at 280 °C. Total run time was 15 min. Transfer line temperature was set to 280 °C. Mass selective detector (MSD) was operating under electron ionization at 70 eV. MS source was held at 230 °C and the quadrupole at 150 °C. For precise quantification, measurements were performed in selected ion monitoring mode. Target ions (*m/z*) and dwell times are shown in Table S1. GC-MS chromatograms were processed using Agilent MassHunter Quantitative Analysis for GC-MS, Version B.08.00. Final determination of release rates was performed as described in[21].

Determination of mass isotopomere distribution (MID) of Intracellular TCA Cycle Metabolites following Stable Isotope Tracing. First, polar metabolites were derivatized for 90 min at 55 °C with 20 µl of methoxyamine (c = 20 mg/ml) in pyridine under continuous shaking and subsequently for 60 min at 55 °C with additional 20 µl of MTBSTFA w/ 1% TBDMCS. GC-MS analysis was performed using an Agilent 7890B GC coupled to an Agilent 5977 A Mass Selective Detector (Agilent Technologies). A sample volume of 1 µl was injected into a Split/Splitless inlet, operating in splitless mode at 270 °C. Gas chromatograph was equipped with a 30 m (I.D. 250 µm, film 0.25 µm) ZB-35MS capillary column with 5 m guard column (Phenomenex). Helium was used as carrier gas with a constant flow rate of 1.2 ml/min. GC oven temperature was held at 100°C for 2 min and increased to 300°C at 10°C/min and held for 4 min. Total run time was 26 min. Transfer line temperature was set to 280°C. Mass selective detector (MSD) was operating under electron ionization at 70 eV. MS source was held at 230°C and the quadrupole at 150 °C. For precise quantification of the MID, measurements were performed in selected ion monitoring mode. Target ions (*m/z*) and dwell times are shown in Table S2.

The MetaboliteDetector software package (Version 3.220180913) was used for mass spectrometric data post processing, quantification, MID calculations, correction of natural isotope abundance, and determinations of fractional carbon contributions[63].

Analysis of medium exchange rates. Polar metabolites of the culture medium were derivatized for 90 min at 45°C with 20 µl of methoxyamine (c = 20 mg/ml) in pyridine under continuous shaking and subsequently for 30 min at 45 °C with 20 µl of MSTFA. GC-MS analysis was performed using an Agilent 7890B GC coupled to an Agilent 5977 A Mass Selective Detector (Agilent Technologies). A sample volume of 1 µl was injected into a Split/Splitless inlet, operating in split mode (10:1) at 270°C. Gas chromatograph was equipped with a 30 m (I.D. 250 µm, film 0.25 µm) ZB-35MS capillary column with 5 m guard column (Phenomenex). Helium was used as carrier gas with a constant flow rate of 1.2 ml/min. GC oven temperature program: 90°C for 1 min, 9°C/min to 270°C, 25°C/min to 320°C and held for 7 min. Total run time was 30 min. Transfer line temperature was set to 280°C. MSD was operated under electron ionization at 70 eV. MS source was held at 230°C and the quadrupole at 150°C. Full scan mass spectra were acquired between m/z 70 and 700.

The MetaboliteDetector software package (Version 3.220180913) was used for quantification. Briefly, peak areas of all isotopologues of defined quantification ions were summed up and divided by the peak area of the internal standard for normalization. In addition, a calibration curve was prepared to calculate absolute concentrations. Absolute uptake and release rates were calculated as described in[21]

LC-MS measurements. Untargeted LC-MS analysis was carried out as previously described in[21].

Nucleotide and NAD/NADH analysis. The following analytical conditions are based on a protocol from[21]. Metabolite analyses were performed using a Thermo Vanquish Flex Quaternary LC coupled to a Thermo Q Exactive HF mass spectrometer. Chromatography was carried out with a SeQuant ZIC-pHILIC 5 µm polymer (150 × 2.1 mm) column connected to the corresponding SeQuant ZIC-pHILIC Guard (20 × 2.1 mm) pre-column. Column temperature was maintained at 45 °C. The flow rate was set to 0.2 mL/min and the mobile phases consisted of 20 mmol/L ammonium carbonate in water, pH 9.2 (Eluent A) and Acetonitrile (Eluent B). The gradient was: 0 min, 80% B; 2 min, 80% B; 17 min, 20% B; 18 min 20% B; 19 min 80 % B; 20 min 80% B (0.4 mL/min); 24 min 80% B (0.4 mL/min); 24.5 min 80% B. The injection volume was 5 µL. All MS experiments were performed using electrospray ionization with polarity switching enabled (+ESI/-ESI). The source parameters were applied as follows: sheath gas flow rate, 25; aux gas flow rate, 15; sweep gas flow rate, 0; spray voltage, 4.5 kV (+) / 3.5 kV (–); capillary temperature, 325°C; S-lense RF level, 50; aux gas heater temperature, 50°C. The Orbitrap mass analyzer was operated at a resolving power of 30,000 in full-scan mode (scan range: *m/z* 75…1000; automatic gain control target: 1e6; maximum injection time: 250 ms). Data were acquired with Thermo Xcalibur software (Version 4.3.73.11) and analyzed with TraceFinder (Version 4.1). Subsequent data analysis for normalization and natural isotope subtraction were performed using in house scripts as in[21].

Western blot. Total cell lysates from cells cultured in vitro were prepared by 30 min incubation of cell pellets on ice in cell lysis buffer (150 mM NaCl, 1 mM EDTA, 50 mM Tris-HCl, 1% NP-40). Protein lysates from tumor tissue were obtained by lysing 10 mg tumor tissue pieces in 150 µl cell lysis buffer. Homogenization of tumor tissue lysates was achieved with TissueLyser II (Quiagen) using 5 mm metal beads. Lysis efficiency was maximized by sonification. Lysis solution was centrifuged at 13,000 g for 15 min at 4°C and supernatant was collected and stored at −80°C. Protein concentration was determined by Bradford assay. 15 – 30 µg of total protein were loaded on NuPAGE 4–12% Bis-Tris gels (Life Technologies) or RunBlue 4–12% Bis-Tris gels (Westburg) using 4x NuPage LDS Sample buffer (Thermo Fisher Scientific) supplemented with 10 mM DTT (Sigma Aldrich) and blotted on nitrocellulose membrane according to standard protocols. Membranes were stained with REVERT staining solution (LI-COR) and analyzed for total protein abundance. Subsequently, membranes were blocked with Odyssey TBS blocking buffer (LI-COR) or 5% milk-powder in TBST and incubated with the

indicated primary antibodies over night at 4°C. Incubation with secondary antibody occurred for 2 h at RT. Detection was performed with the Odyssey CLx Infrared Imaging System (LI-COR). ImageStudioLite Software Vers.5.2 (LI-COR) was used for image analysis. All uncropped and unprocessed scans are available in the source data file. Antibodies used for Western blot analysis in this study:

MTHFD1L (16113-1-AP, LOT: 00024322, RRID: AB_2250974) from Proteintech; Vimentin (3390, clone 5G3F10, LOT:2, RRID: AB_2216128), β-actin (3700, clone 8H10D10, LOT: 18, RRID: AB_2242334), NRF2 XP(R) (12721, clone D179C, LOT: 8, RRID: AB_2715528) and MTHFD2 (41377, D8W9U, LOT: 1, RRID: AB_2799200) from Cell Signaling Technology (CST); PHGDH (HPA021241, LOT: B115626, RRID: AB_1855299), PSAT1 (HPA042924, LOT: R40839, RRID: AB_2678223), PSPH (HPA020376, LOT: B115600, RRID: AB_1855867), SHMT1 (HPA023314, LOT: A78402, RRID: AB_1856830), and SHMT2 (HPA020549, LOT: A96534, RRID: AB_1856834) from Sigma Aldrich; LaminB (ab16048, LOT: GR32836742, RRID: AB_443298) from Abcam; IRDye 680RD Goat Anti-Mouse IgG (H + L) (926-68070, LOT: C90910-21, RRID: RRID AB_10956588) and IRDye 800CW Donkey Anti-Rabbit IgG (H + L) (926-32213, LOT: 926-32213, RRID: RRID AB_621848) from LI-COR (used in a 1:10,000 dilution). All antibodies were used in a 1:1,000 dilution unless stated otherwise.

Poly-L-Lysine coating. Poly-L-lysine (P1274) was purchased from Sigma-Aldrich and reconstituted at 500 µg/ml in H_2O_{MQ}. Wells were coated with PLL prior to Seahorse measurement and Scratch assay. To this end, PLL solution was diluted 1:20 in H_2O_{MQ} and added to the plates at least 1 h prior to seeding. Following incubation with PLL at 37°C and prior to cell seeding, plates were washed twice with H_2O_{MQ} and allowed to air-dry.

Seahorse measurements. The day prior to measurement, 40,000 cells were seeded on poly-L-lysine coated plates and treated the subsequent day as indicated. XF96 Extracellular Flux Analyzer (Seahorse Bioscience) was used to measure basal OCR following manufacturer's instructions using WAVE software. OCR was normalized to the protein concentration or cell number in the wells following the protocol described in[64] using Bradford assay.

Flow cytometric analysis of cell cycle distribution and cell death. 200,000 cells were seeded in 2 ml DMEM and treated the subsequent day as indicated. After incubation, medium was collected and cells were washed with PBS. PBS fraction was collected and cells were detached with trypsin. Detached cells were collected in DMEM. The combined, collected solutions were centrifuged and pellet was washed with PBS.

Cell cycle distribution. Centrifugation yielded a pellet that was resuspended in 100 µl PBS and fixed with ice-cold 80% EtOH. Fixed cells were stored at −20°C for at least 1 h and maximum 5 days prior to measurement. Cells were centrifuged, pellet was incubated for 1 h in 200 µl RNAse A in PBS (30 µg/ml) at RT. Immediately prior to measurement, 98 µl propidium iodide (PI) in PBS (50 µg/ml) was added. Flow cytometric analysis was performed using BD FACSCanto and BD FACSDiva software (version 8.0.1). Analysis was performed in FlowJo Version 10.6.2.

Cell death analysis. Pellet following centrifugation was resuspended in 50 µl AnnexinV-FITC staining solution (5% AnnexinV-FITC in AnnexinV binding buffer (10 mM HEPES pH 7.4, 140 mM NaCl, 2.5 mM $CaCl_2$, 0.1% BSA in $_{dd}H_2O$)) and incubated for 15 min on ice in the dark. 450 µl PI-staining solution (1.1 µg/ml PI in AnnexinV binding buffer) was added immediately prior to measurement using BD FACSCanto and BD FACSDiva software (version 8.0.1) (for wild-type cells) or NovoCyte Quanteon and software NovoExpress (version 1.5.0) (for GFP-positive transfected cells). Analysis was performed in FlowJo Version 10.6.2.

Flow cytometric analysis of ROS levels. 250,000 MDA-MB-468 cells were seeded in 2 ml medium and treated the subsequent day as indicated. Following incubation, cells were detached with trypsin, centrifuged at 350 *g* for 5 min and washed with warm DMEM. Cells were stained in 100 µl DMEM supplemented with 1:2,000 DAPI and 1:500 DCFDA for 30 min at 37°C. Following incubation, samples were centrifuged at 350 *g* for 5 min and washed with PBS. Following centrifugation at 350 *g* for 5 min, cells were resuspended in 100 µl PBS and measured using the BD LSRFortessa™ system and BD FACSDiva software (version 8.0.1). Data analysis was performed using FlowJo software Version 10.6.2.

Cell proliferation. Cell proliferation was determined using the IncuCyte® Live-Cell Analysis system (Essen Bioscience). Cell proliferation was either determined as measurement of cell density (confluence) or by quantification of red nuclei using the IncuCyte® NucLight Rapid Red Reagent (Essen Bioscience). Staining was performed according to manufacturer's instructions. Alternatively, viable cell number was determined by trypan blue staining and automatic counting using a Countess™ Cell Counting Chamber Slide (Thermo Fisher).

Migration assay (wound closure). Cell migration was determined using the IncuCyte® Scratch Wound Assay system for 96 well plates (Essen Bioscience). 96 well image lock plates (Essen Bioscience) were PLL coated prior to seeding of 40,000 cells per well. Wound application was performed 24 h post seeding using the 96-pin IncuCyte WoundMaker tool (Essen Bioscience) and indicated treatments were applied simultaneously. Measurement was performed in technical replicates ($n = 4–8$) and repeated as independent, biological experiments as stated for the respective experiment in figure legends.

Invasion and migration assay (transwell assay). Invasion and migration was analyzed by Boyden chamber assay as described in Meiser et al., 2018[22]. Transwells were coated with ECM-Collagen for invasion assays and left un-coated for migration assay. Treatment and migration/invasion was carried out for 18 h to 24 h.

RNA extraction, cDNA synthesis, and qPCR analysis. Total RNA was extracted from cell culture dishes following manufacturer instructions of RNeasy Mini Kit (Qiagen, 74104) or NucleoSpin RNA Kit (Machery&Nagel, 740955). For RNA extracts from tumor tissue, 10 mg tissue were homogenized in 350 µL RNA using 5 mm metal beads in TissueLyser II (Quiagen). RNA was transcribed to cDNA with High-capacity cDNA Reverse Transcription Kit (ThermoFisher, 4368814). qPCR was performed from 20 ng cDNA per sample using Fast SYBR™ Green Master Mix (ThermoFisher, 4385612). All samples were analyzed in technical duplicates or triplicates. qPCR using Fast SYBR Green was conducted at 95°C for 20 s, 40 cycles of 95°C for 1 s and 60°C for 20 s using the QuantStudio 5 Real-Time PCR System (Applied Biosciences, ThermoFisher Scientific). Specificity was verified by melt curve analysis. Relative quantification of each mRNA was done by QuantStudio Design&Analysis v1.5.1 software (Applied Biosciences, ThermoFisher Scientific) and comparative Ct method. All expression data was normalized to two housekeeping genes (*GAPDH* and *CycloA*). All primers used in this study are listed in Table S3.

shRNA-mediated gene silencing. Knockdown with shRNA was performed in MDA-MB-468 and 4T1 cells using lentiviral particles expressing two different shRNAs targeting the gene of interest and one non-silencing control vector (pGIPZ-shSCR: TTACTCTCGCCCAAGCGAG (Code: RHS4346). For silencing of the *MTHFD2* gene in MDA-MB-468 cells, pGIPZ shMTHFD2-2: ATTG-CATTTCTATTGGCCT (V2LHS_90968) purchased from Horizon Discovery was used. For silencing of the *ALDH1L2* gene in MDA-MB-468 cells, pGIPZ shALDH1L2: ACTGCTTTATCAACATCCG (Code: V3LHS_385780) purchased from Horizon Discovery was used. For silencing of the *Mthfd1l* gene in 4T1 cells, pGIPZ shMTHFD1L-2: TAGATTTCAATTTCATCTG (Code: V2LHS_96542) purchased from Horizon Discovery was used. For silencing Mthfd2 gene in 4T1 cells, pGIPZ shMthfd2-2: ATGACAACGGCTTCATTTC (Code: V2LMM_23800) purchased from Horizon Discovery was used. Plasmids used for generation of lentivirus were amplified from glycerol stocks, isolated (Machery&Nagel plasmid isolation kit), and used for transfection of HEK293T cells. Lentivirus was produced for 24 h in HEK293T cells co-transfected with the viral core packaging construct pCMVR8.74, the VSV-G envelope protein vector pMD2.G and the respective pGIPZ-shRNA-target plasmid using lipofectamine 3000 (Invitrogen #L3000008). Filtered virus supernatant was used to transduce MDA-MB-468 and 4T1 cells in DMEM supplemented with 2% FBS. After 24 h incubation at 37 °C, virus was removed and cells were cultured in DMEM supplemented with 10 % FBS for 48 h. 96 h post transduction, cells were cultured in selection media containing 2 µg/mL of puromycin (Sigma #P8833) for five passages to obtain stably transduced GFP-positive cells.

Generation of KO cells. Gene knock-out (KO) using the CRISPR-Cas9 system was performed in MDA-MB-468 using a vector expressing hCas9 and the respective guideRNA to target the gene of interest. For silencing of the *MTHFD2* gene in MDA-MB-468 cells, two different gRNA sequences (gRNA#918: CGCCAAC-CAGGATCACACTC (Vector ID: VB190718-1104ncn); gRNA1.Ex: GCTCGCGGCAGTTCGGTAAGA (Vector ID: VB190719-1026vzh) purchased from VectorBuilder were used. A control vector was used scramble_gRNA (GTGTAGTTCGACCATTCGTG (Vector ID: VB190718-1103vja) together with both constructs. To generate a *MTHFD2*-KO cell line, 300.000 cells were seeded the day prior to transfection into a 6 well plate in DMEM supplemented with 10% FBS. 24 h later, the culture medium was replaced with 2 mL of DMEM-F12 (LONZA #12-719 F) supplemented with 10 % FBS, Glucose (17 mM final concentration), Glutamine (2 mM final concentration), and 1 mM Sodium Formate and the cells were transfected using Opti-MEM, Lipofectamine, P3000 and 2 µg of plasmid DNA. Post incubation for 24 h, the transfection mix was removed and cells were replaced with fresh DMEM-F12. 72 h post transfection, cells were sorted into single cells by FACS based on their GFP fluorescence. Single cells were grown in DMEM-F12 supplemented with 1% Pen-Strep (Sigma, # P4333) until the formation of single colonies. These were further expanded and characterised by means of Western Blot.

siRNA-mediated gene silencing. 500.000 MDA-MB-468 cells were transfected with 40 pmol siRNA upon seeding in 6 well-plates using Lipofectamine 3000 (ThermoFisher) according to the manufacturer's instructions. Non-silencing control siRNA (siRNA ON-TARGETplus Human non-targeting (1810-10-05) siRNA SMARTpool) and siRNA directed against human *ALDH1L2* mRNA (siRNA ON-TARGETplus Human ALDH1L2 (160428; 26918-01-0005) siRNA SMARTpool) were purchased from Dharmacon.

Animal model. Animal experiments were performed according to all applicable laws and regulations, after receiving approval by the institution's Animal Experimentation Ethics Committee at UL (AEEC) and the veterinarian service of the Ministry of Agriculture, Viniculture & Rural Development (TumorMetab LUPA 2020/01). They ensure that care and use of animals for research purposes was conducted according to the EU Directive 2010/63/EU, as well as the Grand-Ducal Regulation of January 11, 2013 on the protection of animals used for scientific purposes. These included the justification of the use of animals, their welfare and the incorporation of the principles of the 3 R's (Replacement, Reduction and Refinement). A biostatistician reviewed all animal protocols. Mice were housed in a specific pathogen free (SPF) facility at a relative humidity of 40–70%, at 22 °C, and in 12 h dark/light cycles. Syngeneic 4T1 mammary carcinoma cells were orthotopically implanted into the left mammary fat pads (1 injection/mouse) of immune competent female Balb/c mice (8-10 month old) according to established protocols[65]. Briefly, each injection contained 2000 cells in a mixture of 25 µL PBS and 25 µL matrigel. 9 mice per group were injected with either 4T1 SCR or 4T1 *Mthfd1l* KD cells. Primary tumor growth was monitored between day 7 and day 35 of the experiment. Weight was monitored and no weight loss was observed. Experiment was terminated after 6 weeks and lung and liver were prepared for examination of metastatic outgrowth. No metastases were found in the liver. Macroscopic lung metastases were blindly counted under a microscope and microscopic lung metastases were visualized by H&E staining.

H&E staining. H&E staining was performed on 10 µm sections of paraffin embedded lung tissue. Staining was performed according to established protocols. Briefly, selected sections were dehydrated with MeOH and stained with Gill 2 hematoxylin. Sections were neutralized with successive washes of tap water, hard water (10 g $MgSO_4$ and 0.7 g $NaHCO_3$ per L), and distilled water. Subsequently, sections were stained with Eosin-solution and dehydrated through successive washes with 80%, 95%, 100% EtOH and Xylol prior to mounting. Images for quantification were acquired using BioTek Cytation 5 Cell Imaging Multimode Reader. Area of lung and metastasis were measured in ImageJ. Representative images for publication were acquired using Olympus IX83 microscope. Collapsed lungs were excluded from quantitative analysis.

Proteomics. SILAC (Stable Isotope Labeling with Amino acids in Cell culture) strategy was used for proteomic analysis. In general, MDA-MB-468 cells were cultivated in DMEM-F12 SILAC medium supplemented either with Lys^0 and Arg^0 (light channel) or Lys^8 and Arg^{10} (heavy channel). After 6 passages, labeling efficiency of heavy channel was confirmed using LC-MS/MS. Cells in light channel were treated with 50 nM MTX for 24 h and 72 h, while heavy channel was used as control. Cell pellets of biological duplicates were collected. Proteins were extracted in lysis buffer (50 mM ammonium bicarbonate, 6 M Urea, 2 M Thio-urea, pH 8) following a 30 min incubation at 4°C in the presence of protease inhibitors (cOmplete™ EDTA-free Protease Inhibitor Cocktail, Roche). Following centrifugation at 16,000 *g* for 10 min, supernatants were taken for protein quantification. Samples from light channel (50 µg protein) were mixed with control heavy channel (50 µg protein) for protein reduction (5 mM DTT, 1 h incubation at 37°C) and alkylation (10 mM IAA, 45 min in dark at room temperature). Protein digestion was performed with Lys-C (FUJIFILM Wako, 125-05061) at 1:30 ratio (enzyme/protein substances) for 4 h at 37 °C, then samples were diluted 4 times with 50 mM ammonium bicarbonate and digested overnight with 1 µg of trypsin at 37°C. Digestion was terminated through addition of formic acid (1% final concentration). Digested peptides were cleaned up with reverse phase Sep-Pak C18 1 cc Vac Cartridge (Waters, WAT054955) and eluted with 1 mL 50% ACN. Eluted peptides were dried by Speedvac (Thermo Fisher Scientific) and re-suspended in 0.1% formic acid. Peptide concentration was measured with Nanodrop. Peptides were measured by LC-MS/MS on Q-Exactive HF mass spectrometer (Thermo Fisher) connected to a Dionex Ultimate 3000 (Thermo Fisher). 500 ng of peptides were loaded onto a trap column (Acclaim PepMap 75 µm x 2 cm, C18, 3 µm) and separated on a 25 cm Acclaim pepmap RSLC column (75 µm x 25 cm, C18, 2 µm) using a 150 min gradient (2% to 90% acetonitrile) with a flow rate of 0.3 µL/min. MS data were acquired in data-dependent mode. Survey scans of peptide precursors from 375 to 1500 m/z were performed at 70,000 resolution with a 3×10^6 ion count target and the top 12 abundant peaks from survey scan were selected for fragmentation. Tandem MS was performed by isolation at 1.4 m/z with the quadrupole, HCD fragmentation with a normalized collision energy of 28. The MS2 ion count target was set to 1×10^5 and the max injection time was 45 ms. Only precursors with a charge state of 2–7 were sampled for MS2. The dynamic exclusion duration was set to 20 s with a 10 ppm mass tolerance around the selected precursor and its isotopes. Each sample was analyzed twice as technical replicates. All raw data was analyzed with MaxQuant (version 1.6.7.0) and searched with Andromeda against the Homo sapiens database from Uniprot. The minimal peptide length was set to 7 amino acids and the maximum of 3 missed cleavages were allowed. The search included variable modifications of methionine oxidation and N-terminal acetylation, deamidation (N and Q) and fixed modification of carbamidomethyl cysteine. The "Match between run" was checked within 1 min retention time window. Mass tolerance for peptide precursor and fragments were set as 10 ppm and 20 ppm, respectively. The FDR was set to 0.01 for peptide and protein identifications. SILAC based protein quantification (MaxQuant built-in) was used for quantitative evaluation of identified proteins. ProTIGY (https://github.com/broadinstitute/protigy), an R based tool, was used for differential analysis of MaxQuant output.

Statistics. Unpaired *t*-test with Welch's correction was applied for pairwise comparison (two-sided) using GraphPad Software Vers.8. For comparison of multiple groups ordinary Brown Forsythe & Welch one-way or two-way ANOVA with Dunnett's multiple comparison or Games-Howell's multiple comparisons test was performed using GraphPad Software Vers.8. Resulting *p*-values for comparisons of interest are given as numerical values within the respective graphs. For normalization, data points of one experiment were either normalized to the untreated control or divided by the global mean of the individual experiment. We define one *n* as one independent biological experiment (in some cases further consisting of several wells, e.g. triplicate wells for all stable isotope tracing experiments). The technical mean of one biological experiment was considered as one *n*. The mean values of several independent, biological experiments (as indicated in figure legends) were plotted and used for statistical analysis as indicated.

Reporting summary. Further information on research design is available in the Nature Research Reporting Summary linked to this article.

Data availability

Source data are provided with this paper. Proteomics data is available at the proteomics identification database (PRIDE) under the id: PXD027175 (INSERT URL here, once available). The remaining metabolomics data from targeted analysis are available within the article and the supplementary information files (source data file). Source data are provided with this paper.

Received: 24 January 2022; Accepted: 22 April 2022;
Published online: 16 May 2022

References

1. Siegel, R. L., Miller, K. D. & Jemal, A. Cancer statistics, 2019. *CA Cancer J. Clin.* **69**, 7–34 (2019).
2. Luengo, A., Gui, D. Y. & Vander, M. G. Heiden, targeting metabolism for cancer therapy. *Cell Chem. Biol.* **24**, 1161–1180 (2017).
3. Counihan, J. L., Grossman, E. A. & Nomura, D. K. Cancer metabolism: current understanding and therapies. *Chem. Rev.* **118**, 6893–6923 (2018).
4. Bergers, G. and S. M. Fendt, The metabolism of cancer cells during metastasis. *Nat. Rev. Cancer* **21**(3),162–180 (2021).
5. Locasale, J. W. Serine, glycine and one-carbon units: cancer metabolism in full circle. *Nat. Rev. Cancer* **13**, 572–583 (2013).
6. Locasale, J. W. et al. Phosphoglycerate dehydrogenase diverts glycolytic flux and contributes to oncogenesis. *Nat. Genet* **43**, 869–874 (2011).
7. Pollari, S. et al. Enhanced serine production by bone metastatic breast cancer cells stimulates osteoclastogenesis. *Breast Cancer Res Treat.* **125**, 421–430 (2011).
8. Possemato, R. et al. Functional genomics reveal that the serine synthesis pathway is essential in breast cancer. *Nature* **476**, 346–350 (2011).
9. Pacold, M. E. et al. A PHGDH inhibitor reveals coordination of serine synthesis and one-carbon unit fate. *Nat. Chem. Biol.* **12**, 452–458 (2016).
10. Tajan, M. et al. Serine synthesis pathway inhibition cooperates with dietary serine and glycine limitation for cancer therapy. *Nat. Commun.* **12**, 366 (2021).
11. Wang, Q. et al. Rational design of selective allosteric inhibitors of PHGDH and serine synthesis with anti-tumor activity. *Cell Chem. Biol.* **24**, 55–65 (2017).
12. Weinstabl, H. et al. Intracellular trapping of the selective phosphoglycerate dehydrogenase (PHGDH) inhibitor bi-4924 disrupts serine biosynthesis. *J. Med Chem.* **62**, 7976–7997 (2019).
13. Maddocks, O. D. K. et al. Modulating the therapeutic response of tumours to dietary serine and glycine starvation. *Nature* **544**, 372–376 (2017).
14. Ngo, B. et al. Limited environmental serine and glycine confer brain metastasis sensitivity to PHGDH inhibition. *Cancer Disco.* **10**, 1352–1373 (2020).

15. Mullarky, E. et al. Identification of a small molecule inhibitor of 3-phosphoglycerate dehydrogenase to target serine biosynthesis in cancers. *Proc. Natl Acad. Sci. USA* **113**, 1778–1783 (2016).
16. Ducker, G. S. et al. Reversal of cytosolic one-carbon flux compensates for loss of the mitochondrial folate pathway. *Cell Metab.* **24**, 640–641 (2016).
17. Lee, W. D. et al. Tumor reliance on cytosolic versus mitochondrial one-carbon flux depends on folate availability. *Cell Metab.* **33**, 190–198.e6 (2021).
18. Morscher, R. J. et al. Mitochondrial translation requires folate-dependent tRNA methylation. *Nature* **554**, 128–132 (2018).
19. Minton, D. R. et al. Serine catabolism by SHMT2 is required for proper mitochondrial translation initiation and maintenance of formylmethionyl-tRNAs. *Mol. Cell* **69**(4), 610–621.e5 (2018).
20. Zheng, Y. et al. Mitochondrial one-carbon pathway supports cytosolic folate integrity in cancer cells. *Cell* **175**(6), 1546–1560.e17 (2018).
21. Meiser, J. et al. Serine one-carbon catabolism with formate overflow. *Sci. Adv.* **2**(10), e1601273 (2016).
22. Meiser, J. et al. Increased formate overflow is a hallmark of oxidative cancer. *Nat. Commun.* **9**(1), 1368 (2018).
23. Rossi, M., et al., Heterogeneity in PHGDH protein expression potentiates cancer cell dissemination and metastasis. https://doi.org/10.1101/2021.01.24.427949 (2021).
24. Samanta, D. et al. PHGDH expression is required for mitochondrial redox homeostasis, breast cancer stem cell maintenance, and lung metastasis. *Cancer Res* **76**, 4430–4442 (2016).
25. Rinaldi, G. et al. In vivo evidence for serine biosynthesis-defined sensitivity of lung metastasis, but not of primary breast tumors, to mTORC1 inhibition. *Mol. Cell* **81**, 386–397.e7 (2021).
26. Stoller, R. G. et al. Use of plasma pharmacokinetics to predict and prevent methotrexate toxicity. *N. Engl. J. Med* **297**, 630–634 (1977).
27. Chabner, B. A. & Young, R. C. Threshold methotrexate concentration for in vivo inhibition of DNA synthesis in normal and tumorous target tissues. *J. Clin. Invest* **52**, 1804–1811 (1973).
28. Huang, S. et al. Study on relationships of tumor status and gene polymorphism with blood concentration of MTX and toxicities in 63 pediatric mature B cell lymphoma in chinese population. *Technol. Cancer Res Treat.* **20**, 1533033821995288 (2021).
29. Kawakatsu, S. et al. Population pharmacokinetic analysis of high-dose methotrexate in pediatric and adult oncology patients. *Cancer Chemother. Pharm.* **84**, 1339–1348 (2019).
30. Phillips, D. C., Woollard, K. J. & Griffiths, H. R. *T*he anti-inflammatory actions of methotrexate are critically dependent upon the production of reactive oxygen species. *Br. J. Pharm.* **138**, 501–511 (2003).
31. Soula, M. et al. Metabolic determinants of cancer cell sensitivity to canonical ferroptosis inducers. *Nat. Chem. Biol.* **16**, 1351–1360 (2020).
32. Wu, S. et al. Activation of RSK2 upregulates SOX8 to promote methotrexate resistance in gestational trophoblastic neoplasia. Lab Invest. 2021.
33. AlBasher, G. et al. Methotrexate-induced apoptosis in human ovarian adenocarcinoma SKOV-3 cells via ROS-mediated bax/bcl-2-cyt-c release cascading. *Onco Targets Ther.* **12**, 21–30 (2019).
34. Garcia-Sanchez, A., Miranda-Diaz, A. G. & Cardona-Munoz, E. G. The role of oxidative stress in physiopathology and pharmacological treatment with pro- and antioxidant properties in chronic diseases. *Oxid. Med Cell Longev.* **2020**, 2082145 (2020).
35. Babiak, R. M. et al. Methotrexate: pentose cycle and oxidative stress. *Cell Biochem Funct.* **16**, 283–293 (1998).
36. Lignitto, L. et al. Nrf2 activation promotes lung cancer metastasis by inhibiting the degradation of Bach1. *Cell* **178**, 316–329 e18 (2019).
37. Wiel, C. et al. BACH1 stabilization by antioxidants stimulates lung cancer metastasis. *Cell* **178**, 330–345 e22 (2019).
38. Benzarti, M. et al. Metabolic potential of cancer cells in context of the metastatic cascade. *Cells* **9**, 2035 (2020)
39. Nguyen, H. L. et al. Oxidative stress and prostate cancer progression are elicited by membrane-type 1 matrix metalloproteinase. *Mol. Cancer Res* **9**, 1305–1318 (2011).
40. Rhyu, D. Y. et al. Role of reactive oxygen species in TGF-beta1-induced mitogen-activated protein kinase activation and epithelial-mesenchymal transition in renal tubular epithelial cells. *J. Am. Soc. Nephrol.* **16**, 667–675 (2005).
41. Chen, D. et al. MiR-373 drives the epithelial-to-mesenchymal transition and metastasis via the miR-373-TXNIP-HIF1alpha-TWIST signaling axis in breast cancer. *Oncotarget* **6**, 32701–32712 (2015).
42. Reczek, C. R. & Chandel, N. S. ROS-dependent signal transduction. *Curr. Opin. Cell Biol.* **33**, 8–13 (2015).
43. Hunter, M. V. et al. Oxidative stress orchestrates cell polarity to promote embryonic wound healing. *Dev. Cell* **47**, 377–387 e4 (2018).
44. Porporato, P. E. et al. A mitochondrial switch promotes tumor metastasis. *Cell Rep.* **8**, 754–766 (2014).
45. Piperigkou, Z. et al. Key matrix remodeling enzymes: functions and targeting in cancer. *Cancers (Basel)*, **13**(6):1441 (2021)
46. Kawami, M. et al. Methotrexate-induced epithelial-mesenchymal transition in the alveolar epithelial cell line A549. *Lung* **194**, 923–930 (2016).
47. Ohbayashi, M. et al. Involvement of epithelial-mesenchymal transition in methotrexate-induced pulmonary fibrosis. *J. Toxicol. Sci.* **39**, 319–330 (2014).
48. Vazquez, A. et al. Catabolic efficiency of aerobic glycolysis: The Warburg effect revisited. *BMC Syst. Biol.* **4**, 58 (2010).
49. Diehl, F. F. et al. Cellular redox state constrains serine synthesis and nucleotide production to impact cell proliferation. *Nat. Metab.* **1**, 861–867 (2019).
50. Vande Voorde, J. et al. Improving the metabolic fidelity of cancer models with a physiological cell culture medium. *Sci. Adv.* **5**, eaau7314 (2019).
51. Palm, W. & Thompson, C. B. Nutrient acquisition strategies of mammalian cells. *Nature* **546**, 234–242 (2017).
52. Tibbetts, A. S. & Appling, D. R. Compartmentalization of Mammalian folate-mediated one-carbon metabolism. *Annu Rev. Nutr.* **30**, 57–81 (2010).
53. Burgos-Barragan, G. et al. Mammals divert endogenous genotoxic formaldehyde into one-carbon metabolism. *Nature* **548**, 549–554 (2017).
54. Mullen, A. R. et al. Reductive carboxylation supports growth in tumour cells with defective mitochondria. *Nature* **481**, 385–U171 (2012).
55. Metallo, C. M. et al. *Reductive glutamine metabolism by IDH1 mediates lipogenesis under hypoxia*. *Nature* **481**(7381), 380–384 (2011).
56. Piskounova, E. et al. Oxidative stress inhibits distant metastasis by human melanoma cells. *Nature* **527**, 186–191 (2015).
57. Lawrence, S. A. et al. Mammalian mitochondrial and cytosolic folylpolyglutamate synthetase maintain the subcellular compartmentalization of folates. *J. Biol. Chem.* **289**, 29386–29396 (2014).
58. Lowe, K. E. et al. Regulation of folate and one-carbon metabolism in mammalian cells. II. Effect of folylpoly-gamma-glutamate synthetase substrate specificity and level on folate metabolism and folylpoly-gamma-glutamate specificity of metabolic cycles of one-carbon metabolism. *J. Biol. Chem.* **268**, 21665–21673 (1993).
59. Horne, D. W., Holloway, R. S. & Said, H. M. Uptake of 5-formyltetrahydrofolate in isolated rat liver mitochondria is carrier-mediated. *J. Nutr.* **122**, 2204–2209 (1992).
60. den Boer, E. et al. Determinants of erythrocyte methotrexate polyglutamate levels in rheumatoid arthritis. *J. Rheumatol.* **41**, 2167–2178 (2014).
61. Zhu, T. et al. Investigation of potential drug-drug interactions between peficitinib (ASP015K) and methotrexate in patients with rheumatoid arthritis. *Clin. Drug Investig.* **40**, 827–838 (2020).
62. Soflaee, M. H. et al. Purine nucleotide depletion prompts cell migration by stimulating the serine synthesis pathway. *Nat. Commun.* https://doi.org/10.1038/s41467-022-30362-z (2022).
63. Hiller, K. et al. MetaboliteDetector: comprehensive analysis tool for targeted and nontargeted GC/MS based metabolome analysis. *Anal. Chem.* **81**, 3429–3439 (2009).
64. Dranka, B. P. et al. Assessing bioenergetic function in response to oxidative stress by metabolic profiling. *Free Radic. Biol. Med* **51**, 1621–1635 (2011).
65. Kocaturk, B. & Versteeg, H. H. Orthotopic injection of breast cancer cells into the mammary fat pad of mice to study tumor growth. *J. Vis. Exp.* 8(96), 51967 (2015).

Acknowledgements

We thank Fabien Rodriguez (Letellier lab) for technical support during the tissue analysis of the in vivo experiment. We are grateful to Lewis Cantley (Weill Cornell Medical College) for providing MDA-MB-468 cells with MTHFD1L KO[20] and to Patel's laboratory (Cambridge, UK) for providing various HAP1 KO cells[53] We thank Clément Thomas (LIH, Luxembourg) for providing 4T1 cells and Saverio Tardito (Cancer Research UK Beatson Institute, Glasgow, UK) for providing Plasmax medium.

We would like to thank: the LCSB Metabolomics Platform, especially Xiangyi Dong and Floriane Vanhalle, for providing technical and analytical support; the National Cytometry Platform (Quantitative Biology Unit, LIH) and especially Thomas Cerutti for support with flow cytometric analyses; Magretta Adiamah for her diligent proofreading of the manuscript; all our collaboration partners for fruitful discussions and constructive feedback. All graphical figures were produced with BioRender.com (Agreement Number *OJ23O9J9QD).*

J.M. is supported by the FNR-ATTRACT program (A18/BM/11809970), J.M. and L.H. are supported by the FNR-PRIDE NEXTIMMUNE (PRIDE/11012546) and J.M. and K.E. by the FNR-PRIDE i2Tron (PRIDE19/14254520) program. N.K. is supported by the LIH Career Launchpad program (Legs Baertz) and by a DFG fellowship (KI 2508/1-1). D.B. is supported by the FNR-ATTRACT program (A14/BM/7632103), the FNR-CORE program (C18/BM/12691266 and C21/BM/15796788) and the i2Tron (PRIDE19/14254520) grant. D.B. and L.S.B. are funded by the FNR-PRIDE (PRIDE/11012546/NEXTIMMUNE) scheme. E.L. is supported by the FNR-CORE program (C16/BM/11282028 and C20/BM/14591557), by a Proof of Concept FNR grant (PoC/18/12554295), a PRIDE17/11823097 and by i2Tron (PRIDE19/14254520). G.D. and F.X. are supported by FNR-

CORE (C17/BM/11642138). B.J. and M.Z.N. are supported by Luxembourg National Research Fund (C18/BM/12670304/COMBATIC) and FNRS Televie grant (7.4579.20).

Author contributions

Conceptualization, J.M., N.K.; Methodology, J.M., N.K., C.J., M.Z.N., B.J., E.L., D.B., G.D., V.I.P.; Software, A.V., F.X.; Validation, N.K., J.M., L.N., C.D., K.E., L.H.; Formal Analysis, N.K., C.D., L.N., M.B., L.S.B., F.X., V.I.P., M.S., C.J., K.E., E.K., L.H.; Investigation, N.K., C.D., L.N., M.B., L.S.B., F.X., V.I.P., M.S., E.L., K.E., L.H.; Resources, C.J., A.V., J.M., E.L.; Data Curation, N.K., J.M., F.X., A.V.; Writing – Original Draft, N.K., J.M.; Writing – Review & Editing, All Authors; Visualization, N.K., J.M., L.S.B., F.X., V.I.P.; Supervision, J.M., D.B., A.V., E.L., G.D.; Project Administration, J.M., Funding Acquisition, J.M., D.B., E.L., A.V., G.D.

Competing interests

The authors declare no competing interests.

Additional information

Supplementary information The online version contains supplementary material available at https://doi.org/10.1038/s41467-022-30363-y.

Correspondence and requests for materials should be addressed to Johannes Meiser.

Peer review information *Nature Communications* thanks the anonymous reviewer(s) for their contribution to the peer review of this work.

Reprints and permission information is available at http://www.nature.com/reprints

Publisher's note Springer Nature remains neutral with regard to jurisdictional claims in published maps and institutional affiliations.

Open Access This article is licensed under a Creative Commons Attribution 4.0 International License, which permits use, sharing, adaptation, distribution and reproduction in any medium or format, as long as you give appropriate credit to the original author(s) and the source, provide a link to the Creative Commons license, and indicate if changes were made. The images or other third party material in this article are included in the article's Creative Commons license, unless indicated otherwise in a credit line to the material. If material is not included in the article's Creative Commons license and your intended use is not permitted by statutory regulation or exceeds the permitted use, you will need to obtain permission directly from the copyright holder. To view a copy of this license, visit http://creativecommons.org/licenses/by/4.0/.

© The Author(s) 2022

SUPPLEMENTARY INFORMATION Kiweler et al.

Mitochondria preserve an autarkic one-carbon cycle to confer growth-independent cancer cell migration and metastasis

Nicole Kiweler[1], Catherine Delbrouck[1,2], Vitaly I. Pozdeev[3], Laura Neises[1], Leticia Soriano-Baguet[2,4,5], Kim Eiden[1,2], Feng Xian[6], Mohaned Benzarti[1,2], Lara Haase[1,2,7], Eric Koncina[3], Maryse Schmoetten[3], Christian Jaeger[7], Muhammad Zaeem Noman[8], Alexei Vazquez[9], Bassam Janji[8], Gunnar Dittmar[2,6], Dirk Brenner[4,5,10], Elisabeth Letellier[3], Johannes Meiser[1]*

[1] Cancer Metabolism Group, Department of Cancer Research, Luxembourg Institute of Health, Luxembourg, Luxembourg;

[2] Faculty of Science, Technology and Medicine, University of Luxembourg, 2 avenue de Université, Esch-sur-Alzette, Luxembourg;

[3] Faculty of Science, Technology and Medicine, Department of Life Sciences and Medicine, Molecular Disease Mechanisms Group, University of Luxembourg, Esch-sur-Alzette, Luxembourg;

[4] Experimental & Molecular Immunology, Department of Infection and Immunity, Luxembourg Institute of Health, 29 Rue Henri Koch, Esch-sur-Alzette, Luxembourg

[5] Immunology & Genetics, Luxembourg Centre for Systems Biomedicine, University of Luxembourg, 7 Avenue des Hauts Fourneaux, Esch-sur-Alzette, Luxembourg

[6] Proteomics of cellular signaling, Department of Infection and Immunity, Luxembourg Institute of Health,1a Rue Thomas Edison, Strassen, Luxembourg

[7] Luxembourg Centre for Systems Biomedicine, University of Luxembourg, Esch-sur-Alzette, Luxembourg;

[8] Tumor Immunotherapy and Microenvironment (TIME) Group, Department of Cancer Research, Luxembourg Institute of Health, Luxembourg, Luxembourg

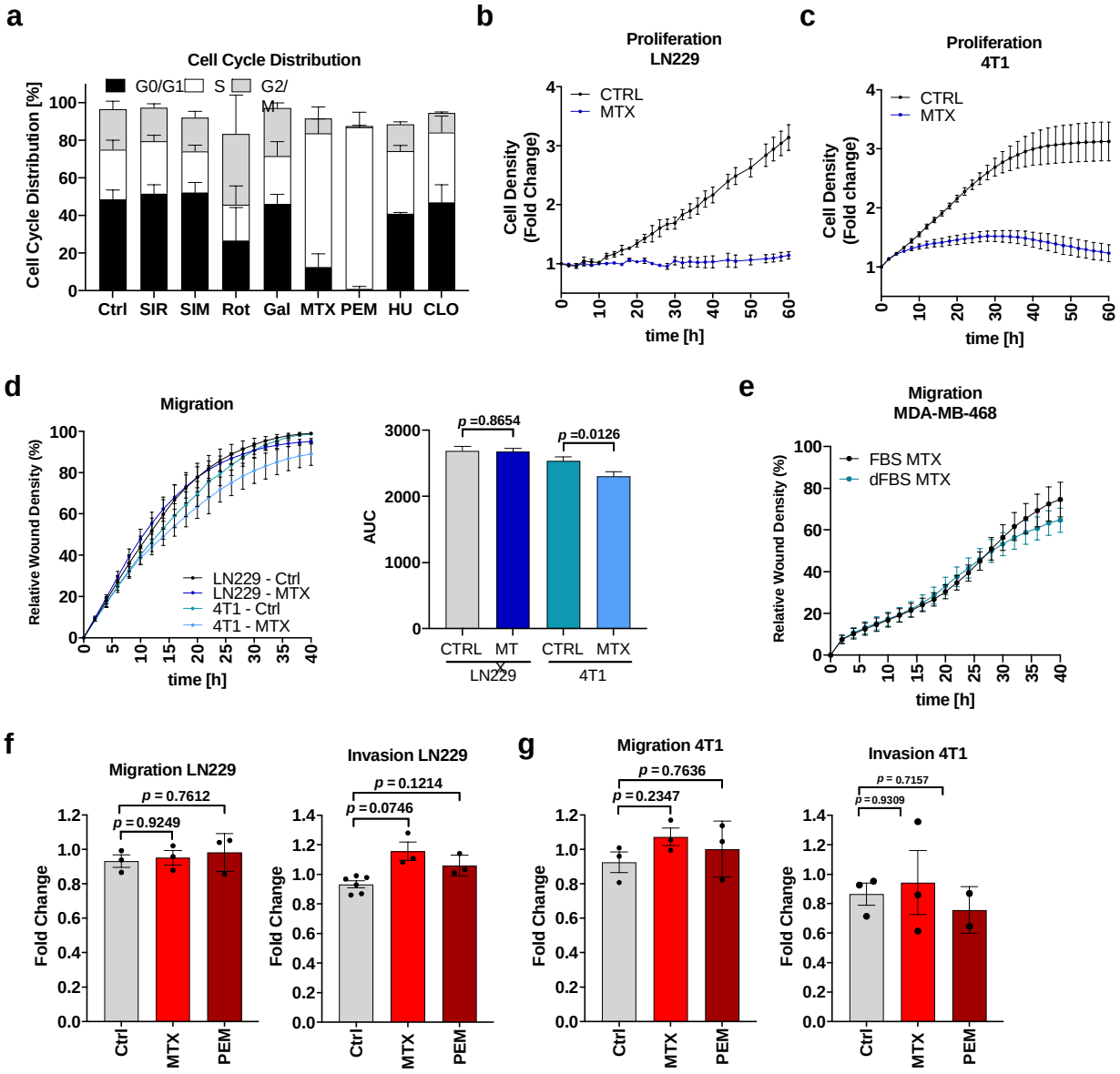
[9] Institute of Cancer Sciences, University of Glasgow, Glasgow, United Kingdom

[10] Odense Research Center for Anaphylaxis (ORCA), Department of Dermatology and Allergy Center, Odense University Hospital, University of Southern Denmark, Odense, Denmark;

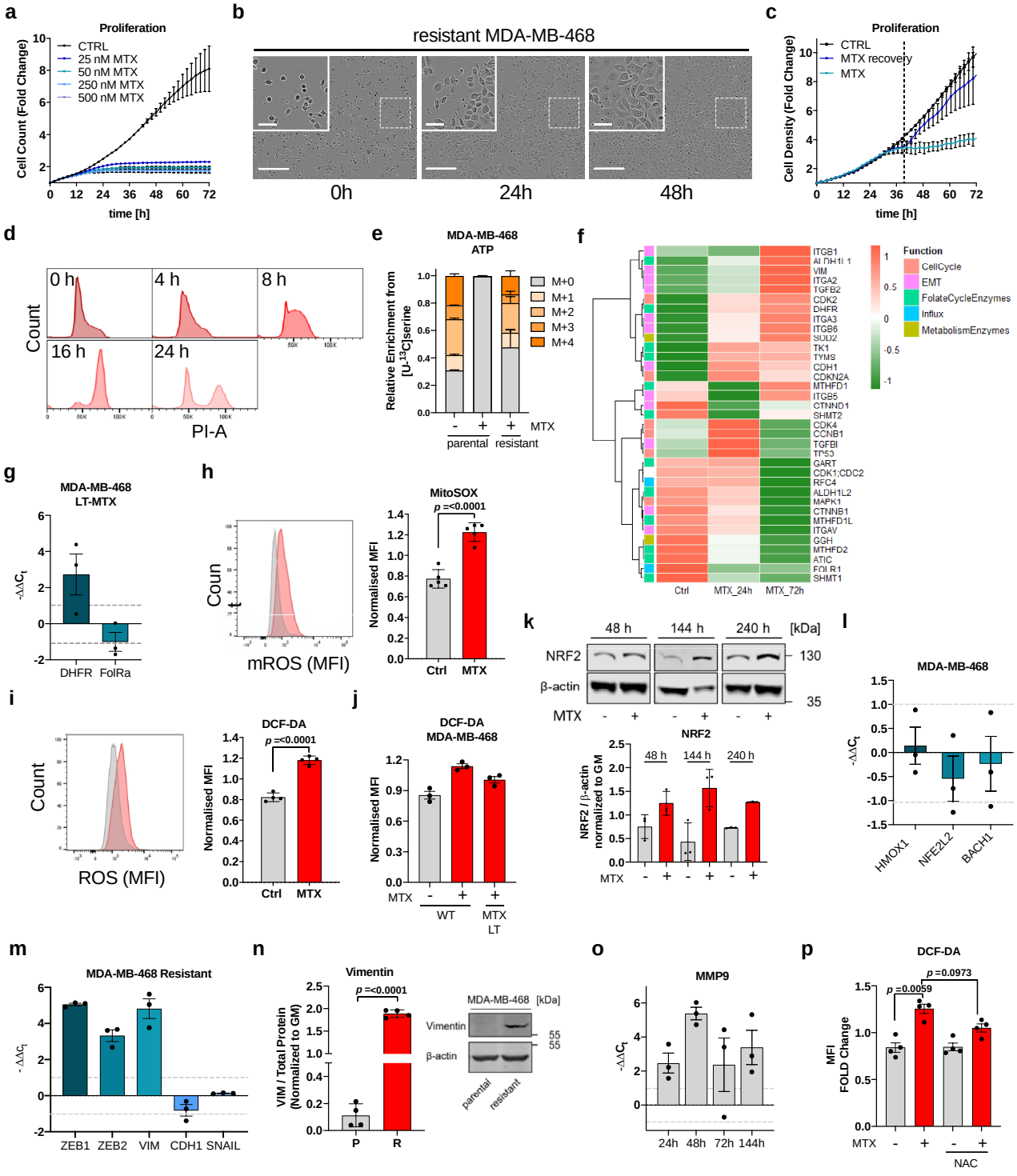
*Correspondence:

Email: johannes.meiser@lih.lu

Twitter: @JohannesMeiser

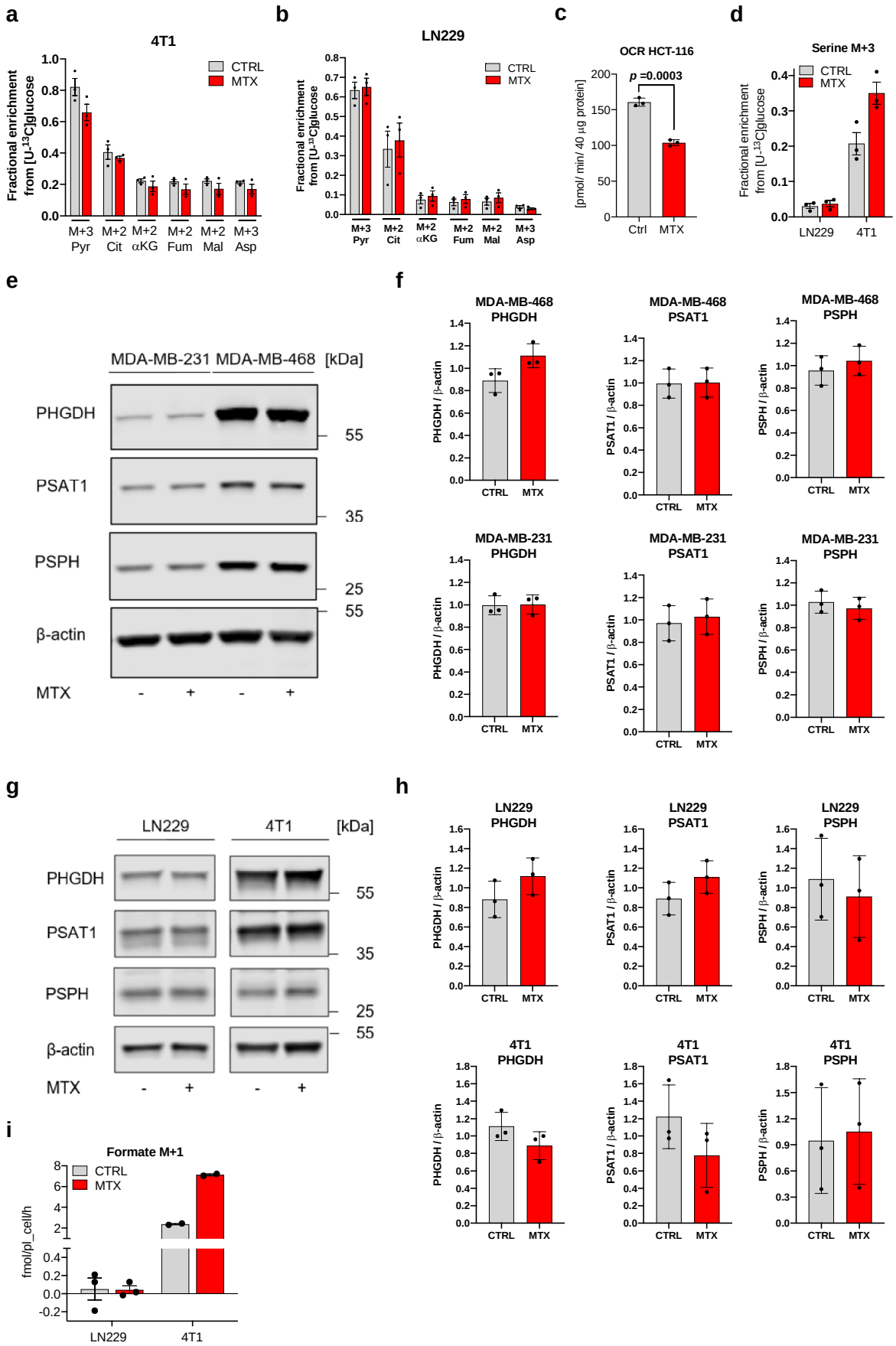


Supplementary Figure 1: (A) MDA-MB-468 cells were treated for 48 h with 100 nM Sirolimus (SIR), 1 µM Simvastatin (SIM), 50 nM Rotenone (Rot), galactose (Gal) supplementation, 50 nM Methotrexate (MTX), 1 µM Pemetrexed (PEM), 0.5 mM hydroxyurea (HU), and 100 nM Clofarabine (CLO). Cells were analyzed for cell cycle distribution by flow cytometry of PI-stained cells; mean ± SD of independent experiments (n = 11 for CTRL; n = 4 for SIR, MTX, PEM; n = 3 for SIM, Rot, Gal, HU, CLO). (B) Proliferation of LN229 cells in response to 50 nM MTX; mean ± SEM of independent experiments (n = 3). (C) Proliferation of 4T1 cells in response to 75 nM MTX; mean ± SEM of independent experiments (n = 4). (D) Migration of LN229 and 4T1 cells in response to 50 (LN229) or 75 (4T1) nM MTX and respective AUC; mean ± SEM of independent experiments (n = 5); unpaired, two-tailed t-test with Welch's correction. (E) Migration of MDA-MB-468 cells after 24 h treatment with 50 nM MTX in medium supplemented with normal or dialyzed FBS; graph shows mean ± SEM of four independent experiments. (F), (G) Migration and invasion of LN229 (F) and 4T1 (G) cells after 24h treatment with 50 nM (F), 75 nM (G) MTX was assessed using ECM-Collagen-coated or non-coated Boyden chambers. Each dot represents an independent experiment; mean ± SEM (n = 3); Brown-Forsythe and Welch one-way ANOVA with Dunnett's multiple comparisons test. Source data are provided as a Source Data file.



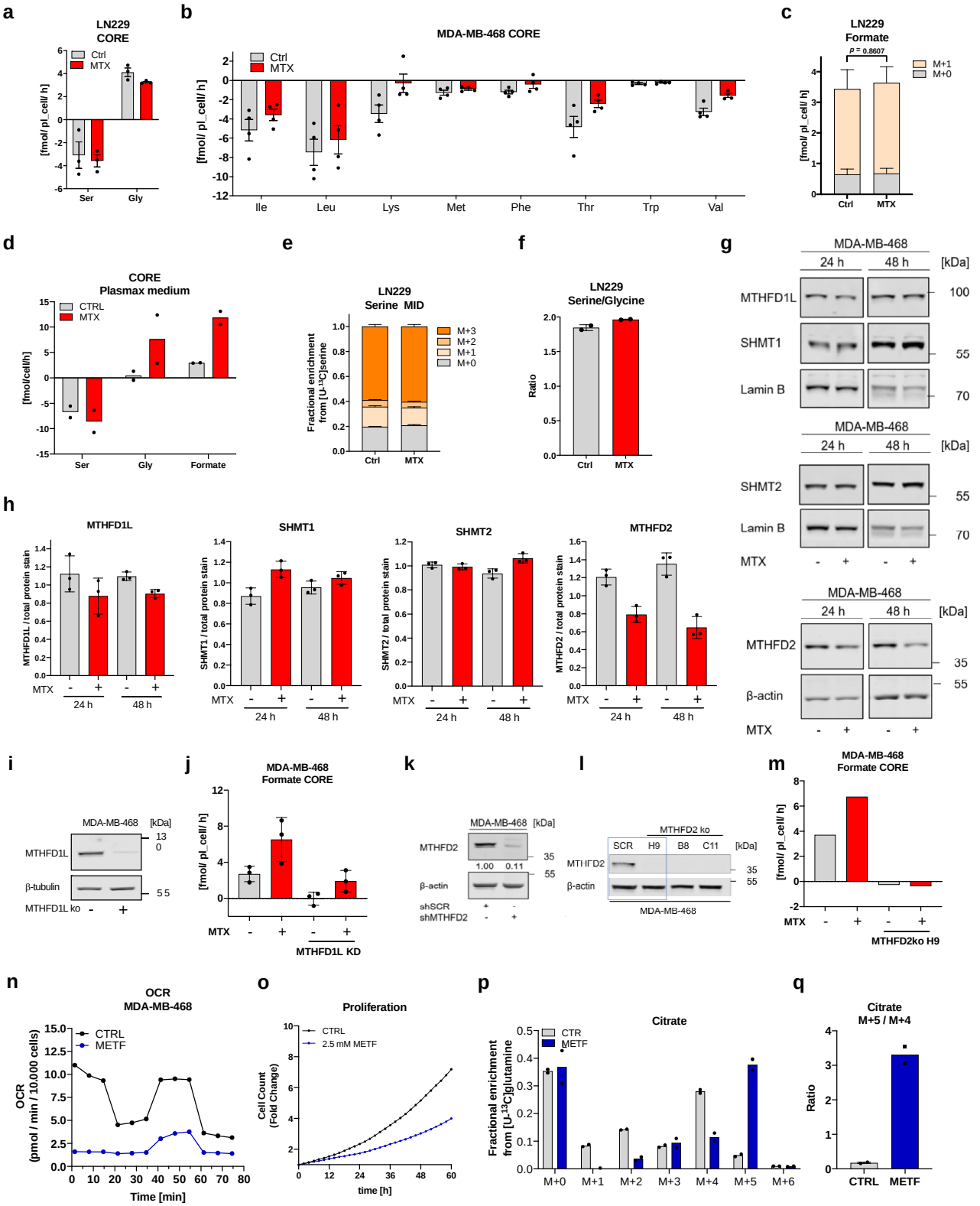
Supplementary Figure 2: (A) Proliferation of NucLight Rapid Red stained MDA-MB-468 cells upon the indicated concentrations of MTX; mean ± SEM of independent experiments (n = 3). **(B)** Morphology of proliferating MTX-resistant MDA-MB-468 cells. Bright-field images are representative of independent experiments. Scale bars correspond to 60 and 300 µm. **(C)** Growth of MDA-MB-468 cells in response to 50 nM MTX and growth recovery upon removal of MTX after 38 h assessed as fold change of cell density; mean ± SEM of independent experiments (n = 3). **(D)** Recovery of cell cycle profile at the indicated time points after MTX removal as in (C). Histograms are representative of three independent experiments. **(E)** MID of intracellular ATP upon [U-^{13}C]serine tracer in response to 24 h 50 nM MTX in parental MDA-MB-468 cells and MTX-resistant MDA-MB-468 cells. Graph shows mean ± SEM of two independent experiments each measured in triplicate wells. **(F)** Heatmap of selected protein expressions from SILAC quantitative proteomics measurement with different MTX

treatment durations. The log2 fold changes of each protein were standardized by row. Molecular function of proteins are indicated with colors. **(G)** mRNA expression from the indicated genes was quantified by real-time RT-qPCR in resistant long-term (LT) MTX treated MDA-MB-468 cells relative to MDA-MB-468 WT cells. Each dot represents one independent experiment; mean ± SD (n = 3). (**H**) Mitochondrial ROS levels in response to 24 h 50 nM MTX measured by flow cytometric quantification of MitoSOX mean fluorescence intensity. Each dot represents an independent experiment; mean ± SD (n = 5); unpaired, two-tailed t-test with Welch's correction. **(I)** Intracellular ROS levels in response to 24 h 50 nM MTX measured by flow cytometric quantification of DCF-DA mean fluorescence intensity. Each dot represents an independent experiment; mean ± SD (n = 4); unpaired, two-tailed t-test with Welch's correction. **(J)** Intracellular ROS levels in response to 24 h MTX treatment in MDA-MB-468 WT cells and in LT MTX treated MTX_resistant MDA-MB-468 cells measured by flow cytometric quantification of DCF-DA mean fluorescence intensity. Each dot represents one independent experiment; mean ± SD (n = 3). (**K**) NRF2 expression in MDA-MB-468 cells after treatment with 50 nM MTX for the indicated time was quantified by Western Blot. Normalized signal intensity was quantified relative to β-actin signal. Each dot represents an independent experiment; mean ± SD (n = 3). (**L**) mRNA expression from the indicated target genes in MDA-MB-468 cells was measured after 144 h 50 nM MTX and quantified relative to untreated cells using real-time RT-qPCR. Each dot represents one independent experiment; mean ± SD (n = 3). (**M**) mRNA expression from the indicated target genes in MTX-resistant MDA-MB-468 cells relative to parental MDA-MB-468 cells as measured using real-time RT-qPCR. Each dot represents an independent experiment; mean ± SEM (n = 3). **(N)** Expression of vimentin in parental and MTX-resistant MDA-MB-468 cells; β-actin serves as loading control. Quantification of vimentin signal intensity relative to total protein stain. Each dot represents an independent experiment; mean ± SD (n = 4); unpaired, two-tailed t-test with Welch's correction. (**O**) mRNA expression of MMP9 was quantified in MDA-MB-468 cells after 50 nM MTX at the indicated time points using real-time RT-qPCR. Each dot represents an independent experiment; mean ± SEM (n = 3). **(P)** Intracellular ROS levels in MDA-MB-468 cells in response to 24 h 50 nM MTX and 10 mM NAC as measured by flow cytometric quantification of DCF-DA mean fluorescence intensity. Each dot represents an independent experiment. Graph shows mean ± SD (n = 4); Brown-Forsythe and Welch ANOVA test with Games-Howell's multiple comparisons test. Source data are provided as a Source Data file.



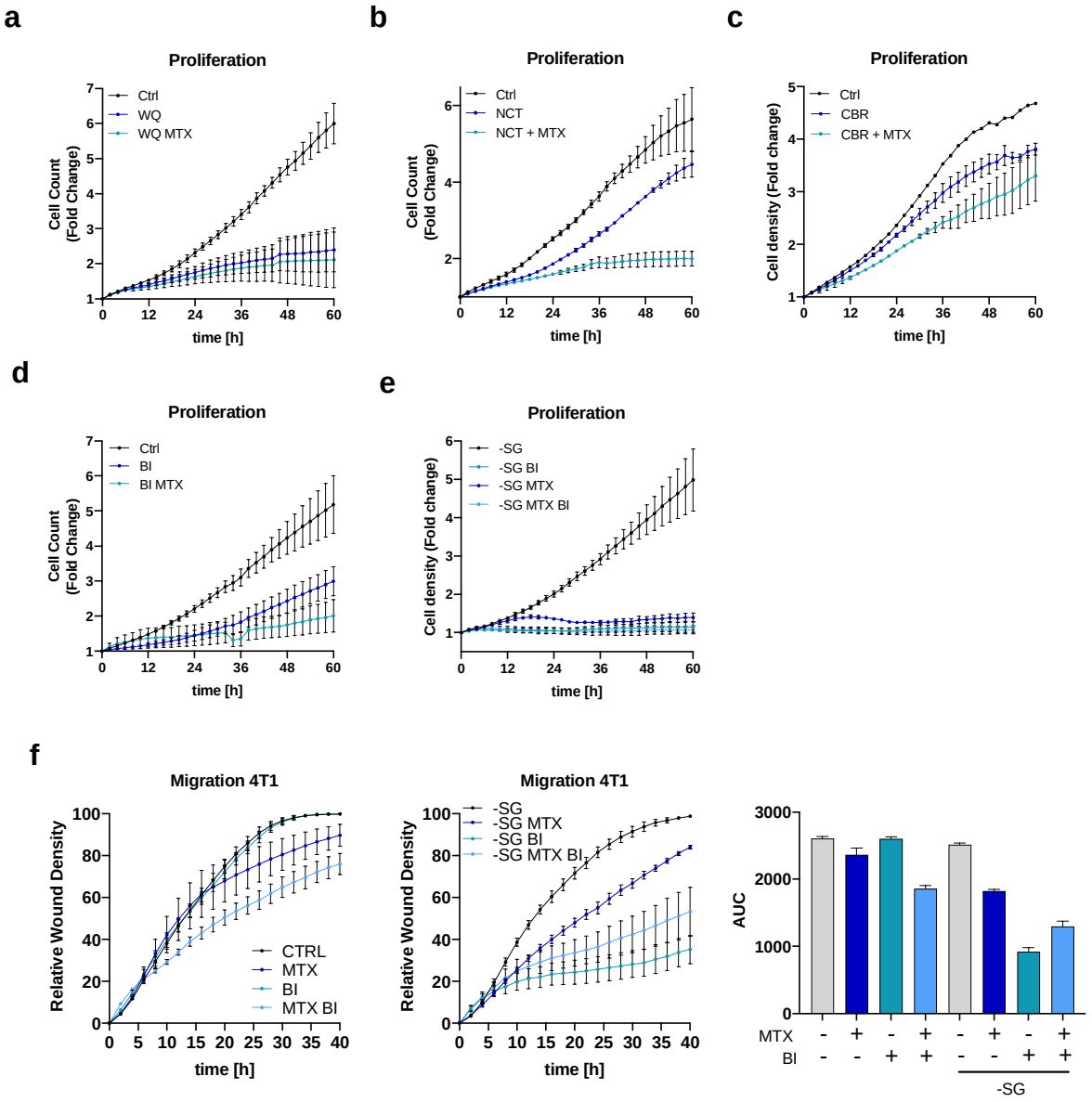
Supplementary Figure 3: (A), (B) Relative isotopologue abundance following [U-^{13}C]glucose tracing in 4T1 (A) and LN229 (B) cells in response to 24 h 75 nM MTX (A) and 50 nM MTX (B). Each dot represents an individual experiment composed

of triplicate wells; mean ± SEM (n = 3). **(C)** Basal cellular respiration in response to 24 h 50 nM MTX treatment was determined in HCT-116 cells as quantification of mitochondrial OCR. Each dot represents an individual experiment composed of six technical replicates; mean ± SEM (n = 3); unpaired, two-tailed t-test with Welch's correction. **(D)** M+3 isotopologue abundance of serine upon [U-^{13}C]glucose tracing in response to 24 h 50 nM MTX in LN229 and 24 h 75 nM MTX in 4T1 cells. Each dot represents an independent experiment in triplicate wells; mean ± SEM (n = 3). **(E)** Expression of PHGDH, PSAT1, and PSPH in MDA-MB231 and MDA-MB-468 cells upon 24 h 50 nM MTX treatment; β-actin serves as loading control. **(F)** Treatment as in (E). Quantification of PHGDH, PSAT1, and PSPH Western blot signal intensity relative to β-actin normalized to global mean in MDA-MB231 and MDA-MB-468 cells. Each dot represents an independent experiment; mean ± SD (n = 3). **(G)** Expression of PHGDH, PSAT1, and PSPH in LN229 and 4T1 cells upon 24 h 50 nM MTX (LN229) and 75 nM MTX (4T1) treatment; β-actin serves as loading control. **(H)** Treatment as in (G). Quantification of PHGDH, PSAT1, and PSPH Western blot signal intensity relative to β-actin and normalized to global mean in LN229 and 4T1 cells. Each dot represents an independent experiment; mean ± SD (n = 3). **(I)** M+1 formate release rate in LN229 and 4T1 cells after 24 h [U-^{13}C]glucose tracing and treatment with 50 nM (LN229) and 75 nM (4T1) MTX. Each dot indicates an independent experiment measured in triplicate wells; mean ± SEM (n = 3 (LN229), n = 2 (4T1)). Source data are provided as a Source Data file.

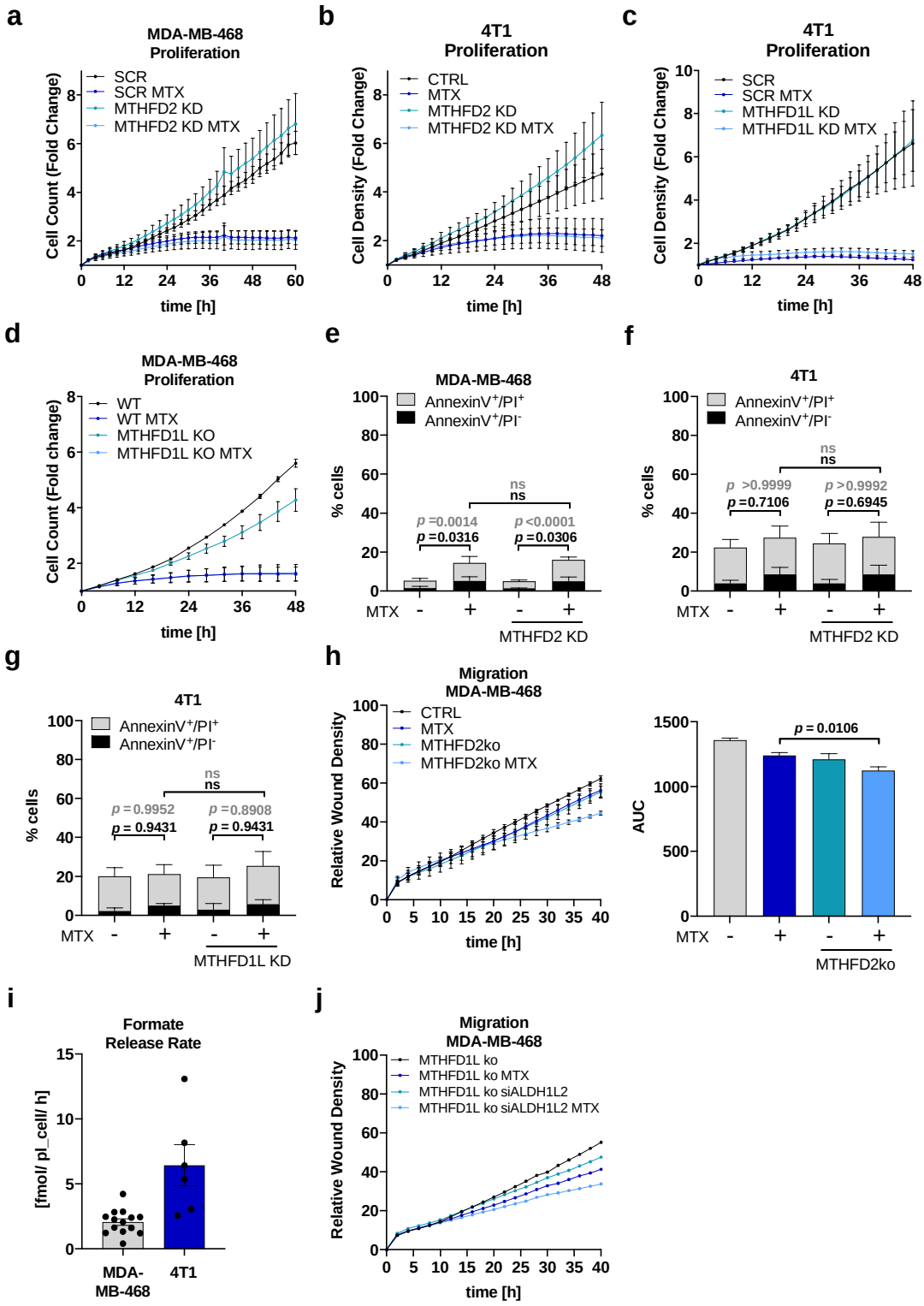


Supplementary Figure 4: (A) Absolute CORE rates of serine and glycine of LN229 cells in response to 24 h 50 nM MTX. Each dot represents the mean of an individual experiment each measured in triplicate wells; mean ± SEM. **(B)** Absolute CORE rates of essential amino acids as indicated in response to 24 h 50 nM MTX. Each dot represents an independent experiment in triplicate wells; mean ± SEM (n = 3). **(C)** Formate release rates of M+0 and M+1 formate isotopologues upon [U-^{13}C]serine tracing in LN229 cells in response to 24 h 50 nM MTX. Graph shows mean ± SEM of three independent experiments each measured in triplicate wells; unpaired, two-tailed t-test with Welch's correction. **(D)** Absolute CORE rates of serine, glycine, and formate in MDA-MB-468 cells in response to 24 h 50 nM MTX in Plasmax medium. Mean of two independent experiments in triplicate wells. **(E)** MID of intracellular serine upon [U-^{13}C]serine tracing in LN229 cells in response to 24 h 50 nM MTX; mean ± SEM of two independent experiments each measured in triplicate wells. **(F)** Ratio

of intracellular serine and glycine levels in response to 24 h 50 nM MTX in LN229 cells. Mean ± SEM of independent experiments in triplicate wells (n = 2). **(G)** Expression of MTHFD1L, SHMT1, SHMT2, and MTHFD2 in MDA-MB-468 cells 24 h and 48 h 50 nM MTX; β-actin serves as loading control. **(H)** Treatment as in (G). Quantification of MTHFD1L, SHMT1, SHMT2, and MTHFD2 Western blot signal intensity relative to total protein stain normalized to GM in MDA-MB-468 cells. Each dot represents an independent experiment; mean ± SD (n = 3). **(I)** Residual MTHFD1L protein expression in MDA-MB-468 MTHFD1L CRISPR KO cells was determined on Western Blot. β-tubulin serves as loading control. **(J)** Absolute CORE rates of formate from mock or shMTHFD1L-transfected MDA-MB-468 cells upon 24 h 50 nM MTX. Dots represent technical replicates of a representative experiment; mean ± SD (n = 3). **(K)** Residual MTHFD2 protein expression in mock or shMTHFD2-transfected MDA-MB-468 cells was determined on Western Blot. β-actin serves as loading control. **(L)** Residual MTHFD2 protein expression in three MDA-MB-468 MTHFD2 CRISPR KO clones was determined on Western Blot. β-actin serves as loading control. **(M)** Absolute CORE rates of formate from MDA-MB-468 cells upon depletion of MTHFD2 (CRISPR clone H9) and 24 h 50 nM MTX. Plot shows the median of one experiment done in triplicate wells. **(N)** Oxygen consumption rate (OCR) in MDA-MB-468 cells after 24h treatment with 2.5 mM Metformin. Graph shows mean of six technical replicates. **(O)** Proliferation of MDA-MB-468 cells in response to treatment with 2.5 mM Metformin. Graph shows mean of two independent experiments. **(P)** Citrate MID from [U-^{13}C]glutamine tracing in MDA-MB-468 cells after 24 h treatment with 2.5 mM Metformin. Graph shows mean of two independent experiments. Dots indicate the mean of each independent experiment performed in triplicate wells. **(Q)** Ratio of M+5/M+4 istotopologues of citrate after 24 h treatment with 2.5 mM Metformin and tracing with [U-^{13}C]glutamine tracing. Graph shows mean of two independent experiments. Dots indicate the mean of each independent experiment performed in triplicate wells. Source data are provided as a Source Data file.

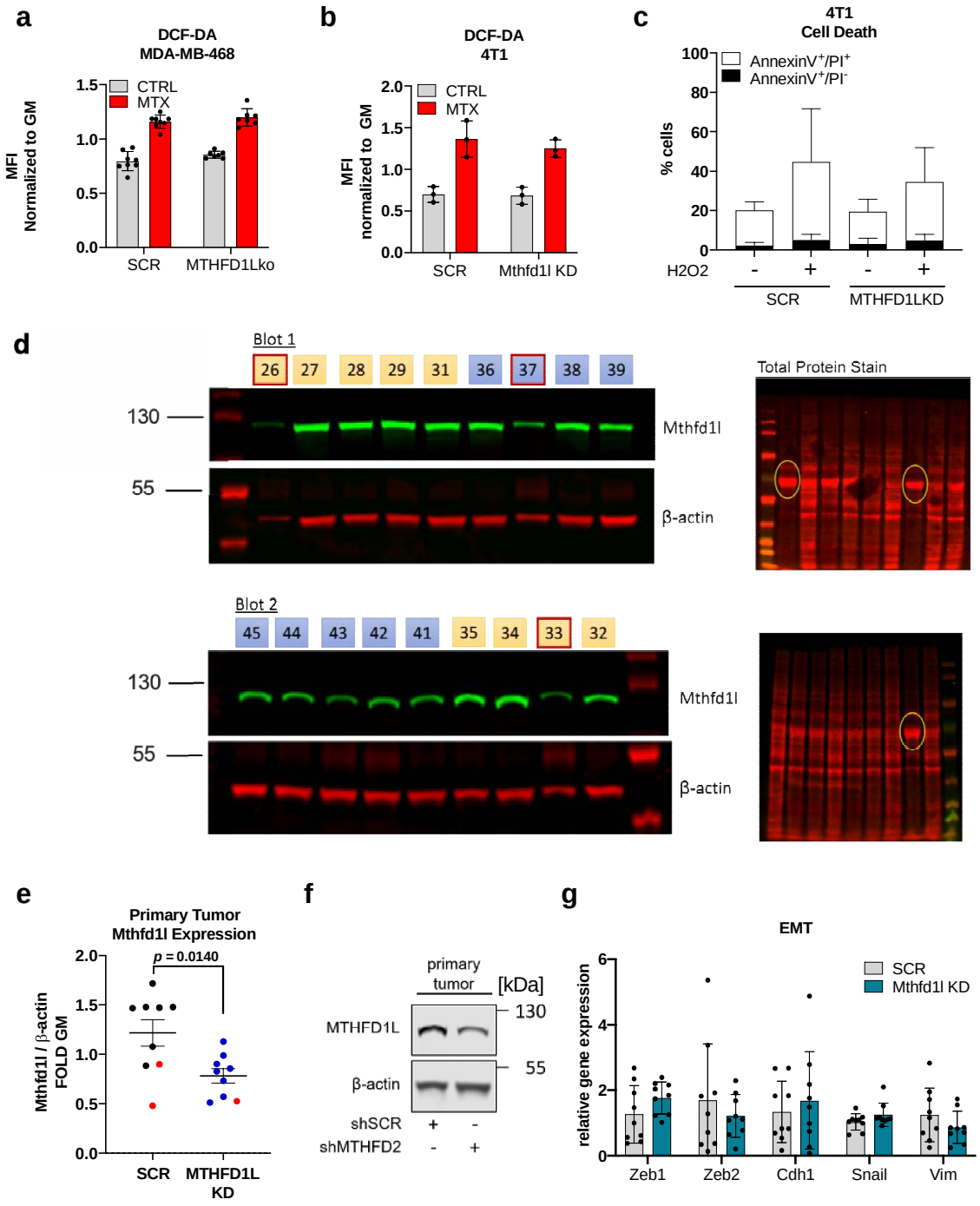


Supplementary Figure 5: (A) Proliferation of NucLight Rapid Red stained MDA-MB-468 cells upon treatment with 10 µM WQ-2101 and 50 nM MTX as indicated; mean ± SEM of independent experiments (n = 6). **(B)** Proliferation of NucLight Rapid Red stained MDA-MB-468 cells upon treatment with 10 µM NCT-502 and 50 nM MTX as indicated; mean ± SEM of independent experiments (n = 4). **(C)** Proliferation of MDA-MB-468 cells measured as fold cell density upon treatment with 30 µM CBR-5884 and 50 nM MTX as indicated; mean ± SEM of independent experiments (n = 1 (CTRL), n = 2 (CBR, CBR+MTX)). **(D)** Proliferation of NucLight Rapid Red stained MDA-MB-468 cells upon treatment with 15 µM BI-4916 and 50 nM MTX as indicated; mean ± SEM of independent experiments (n = 7). **(E)** Proliferation of serine- and glycine-starved MDA-MB-468 cells measured as fold cell density upon treatment with 15 µM BI-4916 and 50 nM MTX as indicated; mean ± SEM of independent experiments (n = 3). (**F**) Migration of 4T1 cells upon treatment with 75 nM MTX and 15 µM BI in the presence or absence of serine and glycine in culture medium and respective AUC over 40 h. Graph shows mean ± SD of one representative experiment performed in technical replicates (n = 3 for all –SG conditions, n = 4 for all others). Source data are provided as a Source Data file.



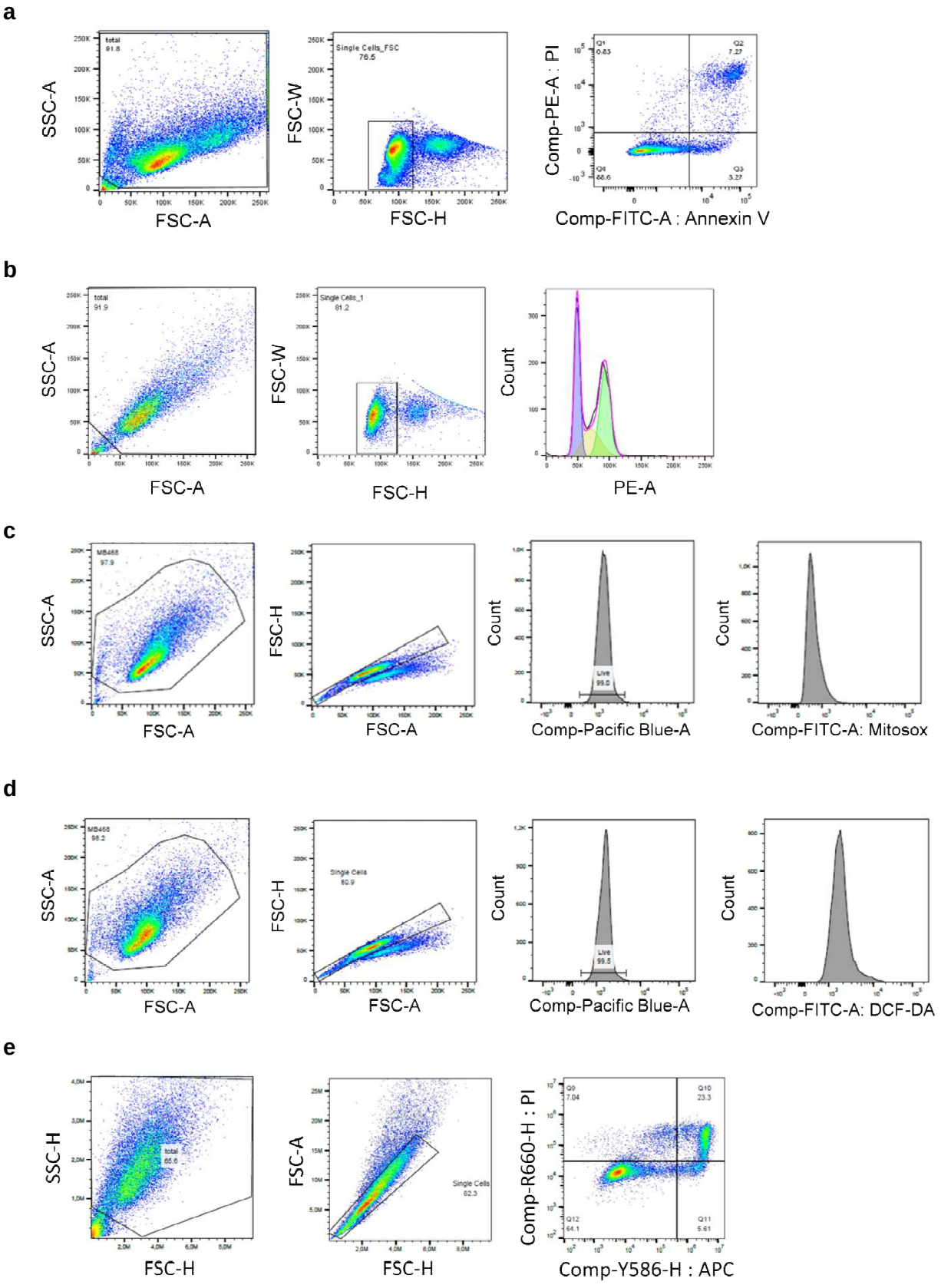
Supplementary Figure 6: (A-D) Proliferation of MDA-MB-468 (A,D) and 4T1 (B,C) cells upon MTHFD1L and MTHFD2 depletion as indicated after treatment with 50 nM MTX (A,D) or 75 nM MTX (B,C). Graph shows mean ± SEM of independent experiments (n = 6 (A); 3 (B); 1 (SCR MTX), 3 (SCR, MTHFD1LKD MTX) or 4 (MTHFD1LKD) (C); 4 (D)). (**E-G**) MDA-MB-468 (E) and 4T1 (F,G) cells depleted for MTHFD2 or MTHFD1L were treated with 50 nM (E) or 75 nM (F, G) MTX for 48h. Cell death was assessed by flow cytometry and AnnexinV-FITC/PI-staining; mean ± SD of independent experiments (n = 4). 2-way ANOVA with Dunnett's multiple comparisons test. **(H)** Migration of MDA-MB-468 cells (clone H9) in response to MTHFD2 knockout and 50 nM MTX treatment. Graph shows mean ± SEM (n = 3); Brown-Forsythe and Welch one-way ANOVA with Dunnett's multiple comparisons test. **(I)** Absolute formate release from MDA-MB-468 and 4T1

cells. Graph shows mean ±SEM of independent experiments, each performed in triplicate wells (n = 14 (MDA-MB-468), n = 6 (4T1)). **(J)** Migration of MDA-MB-468 MTHFD1L knockout cells in response to siRNA-mediated knockdown of ALDH1L2 and 50 nM MTX treatment. Graph shows mean of technical replicates (n = 7 (MTHFD1Lko, MTHFD1lko MTX) – 8 (MTHFD1Lko siALDH1L2, MTHFD1Lko siALDH1L2 MTX) wells). Source data are provided as a Source Data file.



Supplementary Figure 7: (A, B) Intracellular ROS levels in MDA-MB-468 and 4T1 cells in response to 24 h 50 nM MTX (A) or 75 nM MTX (B) measured by flow cytometric quantification of DCF-DA mean fluorescence intensity. Each dot represents one independent experiment; mean ± SD (n = 7 (MTHFD1Lko) – 8 (SC) (A) or n = 3 (B)). **(C)** 4T1 cells depleted or not for Mthfd1l were treated with 500 µM H_2O_2 for 24 h. Cell death was assessed by flow cytometry and AnnexinV-FITC/PI-staining; mean ± SD of independent experiments (n = 4). **(D)** Western blot images of protein lysates from primary tumor tissue. Indicated replicates (red frame around box) were excluded from analysis in Figure 7D, due to the here presented finding that total protein in these samples was mainly composed of a single protein (see Total Stain). This indicates unreliability of the sample. (E) Mthfd1l expression in primary tumor tissue obtained by orthotopic implantation of 4T1 SCR and Mthfd1lKD breast cancer cells. Red dots indicate data points that were excluded as explained in (D); mean ± SD (n = 9) unpaired, two-tailed t-test with Welch's correction.(**F)** Representative Western Blot image of Mthfd1l protein expression in primary tumor tissue in mice after orthotopic implantation of 4T1 scramble or Mthfd1l shRNA transfected breast cancer cells. β-actin serves as loading control. (**G**) mRNA expression from indicated target genes in primary tumor

tissue in mice after orthotopic implantation of 4T1 scramble or Mthfd1l shRNA transfected breast cancer cells measured by real-time RT qPCR. Each dot indicates one individual animal; mean ± SD (n = 9). Source data are provided as a Source Data file.



Supplementary Figure 8: (A) Exemplary gating for Annexin-PI measurement using Annexin-V-FITC and PI. **(B)** Exemplary gating for cell cycle analysis using automatic cell cycle analysis tool in FlowJo. **(C)** Exemplary gating for

mitochondrial ROS measurement using Mitosox dye. **(D)** Exemplary gating for cytosolic ROS measurement using DCF-DA dye. (**E**) Exemplary gating for Annexin-PI measurement using Annexin-V-APC and PI in GFP-positive cells.

Supplementary Table 1. Dwell times as well as quantification ions (m/z) for formate compounds.

Derivative (Metabolite)	Quant-Ion (m/z)	Dwell Time (ms)
Benzyl formate (Formic acid) – M_0	136.1	40
Benzyl formate (Formic acid) – M_1	137.1	40
IS Benzyl formate (Formic acid 13C, D) – M_0	138.1	40
IS Benzyl formate (Formic acid 13C, D) – M_1	139.1	40
IS Benzyl formate (Formic acid 13C, D) – M_2	140.1	40

Supplementary Table 2. Dwell times as well as quantification ions (m/z) for the measured compounds.

Derivative (m/z of selected fragment)	Quant-Ions (m/z)	Dwell Time (ms)	Sum Formula (Fragment)	MID size
Pyruvic Acid 1MeOX 1TBDMS (174)	174.0 – 180.1	15	C6H12O3NSi	4
Lactic Acid 2TBDMS (261)	261.1 – 267.1	15	C11H25O3Si2	4
Alanine 2TBDMS (260)	260.1 – 266.1	15	C11H26NO2Si2	4
Glycine 2TBDMS (246)	246.1 – 252.1	15	C10H24NO2Si2	3
Succinic Acid 2TBDMS (289)	289.1 – 296.1	15	C12H25O4Si2	5
Fumaric Acid 2TBDMS (287)	287.1 – 294.1	15	C12H23O4Si2	5
(Internal Standard) Pentanedioic-D6 Acid	235.2, 309.2, 351.3	30		
Serine 3TBDMS (390)	390.2 – 396.2	15	C17H40NO3Si3	4
a-Ketoglutaric Acid 1MeOX 2TBDMS (346)	346.2 – 354.2	10	C14H28NO5Si2	6
Malic Acid 2TBDMS (419)	419.2 – 426.2	15	C18H39O5Si3	5
Aspartic Acid 3TBDMS (418)	418.2 – 425.2	15	C18H40NO4Si3	5
Glutamic Acid 3TBDMS (432)	432.3 – 440.3	10	C19H42NO4Si3	6
Glutamine 3TBDMS (431)	431.3 – 439.3	10	C19H43N2O3Si3	6
Citric Acid 4TBDMS (591)	591.3 – 600.3	10	C26H55O7Si4	7
3-Phosphoglyceric Acid 4TBDMS (585)	585.4 – 592.4	15	C27H63O7PSi4	4

Supplementary Table 3: Realtime RT-qPCR primers used in this study for selcted human and murine genes of interest.

Gene Name	Species	Sequence Fwd (5' – 3')	Sequence Rev (5' – 3')
CDH1	human	AGTGCCAACTGGACCATTCA	TCTTTGACCACCGCTCTCCT
CycloA	human	CAGACAAGGTCCCAAAGACA	CCATTATGGCGTGTGAAGTC
GAPDH	human	CATGAGAAGTATGACAACAGCCT	AGTCCTTCCACGATACCAAAGT
MMP9	human	CGCGCTGGGCTTAGATCATT	GGTTCAGGGCGAGGACCATA
SLUG	human	CTACAGCGAACTGGACACACA	TGGAATGGAGCAGCGGTAGT
SNAIL	human	CGAAAGGCCTTCAACTGCAAA	TGACATCTGAGTGGGTCTGGA
VIM	human	CCTTGAACGCAAAGTGGAATC	GACATGCTGTTCCTGAATCTGAG
ZEB1	human	AAGAACTGCTGGGAGGATGACA	CCTCTTCAGGTGCCTCAGGAAAA
ZEB2	human	GCAAGAGGCGCAAACAAGC	GGGTTGGCAATACCGTCATCC
HMOX1	human	CTGCTCAACATCCAGCTCTTTG	ATCTTGCACTTTGTTGCTGGC
NFE2L2	human	AACTACTCCCAGGTTGCCCA	CAAGTGACTGAAACGTAGCCG
BACH1	human	GCCTCGCACAATATGGTTGAT	TGACATCGCACAGCACATCT
DHFR	human	AATCGGCTCAAAACCGCTTG	TCTGAATTCATTCCTGAGCGG
FolRa	human	TGGAACTGGACTTCAGGGTT	CACTCCCTCGGCTGTAGTTG
Zeb1	mouse	GGGAAATAGCACAGACAGTTGTT	TCACCTCTCCACAATGACGC
Zeb2	mouse	GTCGCTGTGTTTGGTTGCTAGA	CGTTGTCATAGTTCACCACGTT
Cdh1	mouse	TCATCAAATGGGGAAGCGGT	TTCATCACGGAGGTTCCTGG
Snail	mouse	GCTGCTTCGAGCCATAGAACTAAA	TTGAGGGAGGTAGGGAAGTGG
Vim	mouse	AGACCAGAGATGGACAGGTGA	CTGGTACTGCACTGTTGCAC
Gapdh	mouse	CATCACTGCCACCCAGAAGACTG	ATGCCAGTGAGCTTCCCGTTCAG
Sdha	mouse	CTTCGCTGGTGTGGATGTCA	GTGGGAATCCCACCCATGT

CHAPTER 5: Discussion and Future Perspectives

Historically, 1C metabolism was thought to be mainly involved with proliferation and biomass generation (Locasale, 2013). Accordingly, targeting the 1C cycle in cancer cells proved to be a successful strategy since the 1950s with the discovery of antifolates (Farber and Diamond, 1948). However, with the emergence of the field of cancer metabolism and technological advances in metabolomics over the last decade, it is now recognized that the 1C cycle can serve multiple metabolic functions in cancer apart from biosynthesis (Balsa et al., 2020, Ducker et al., 2016, Meiser et al., 2016, Yang et al., 2020). Consequently, the main goal of my dissertation work was to disentangle the 1C cycle from proliferation and study the potential of its growth-independent functions.

In my dissertation, we focused on the relevance of the 1C cycle under nutrient stress conditions. We achieved such metabolic stress using two different strategies. Firstly, we aimed to study the metabolic rewiring of cancer cells that face limited glucose supply in tumors; we used galactose as a tool compound to mimic this glucose limitation (**Chapter 3**). Secondly, we aimed to investigate growth-independent functions of the 1C cycle. To achieve that, we uncoupled the 1C cycle from proliferation by using methotrexate (**Chapter 4**). Using these two strategies, we were able to highlight the adaptability of the 1C cycle to accommodate metabolic challenges. These metabolic adaptations were key in the survival and progression of cancer cells under metabolic stress.

Galactose as a tool compound to study glycolytic limitation:

Researchers have utilized galactose containing-media to identify cell lines with OXPHOS deficiencies for decades (Robinson et al., 1992, Soderberg et al., 1980). This is due to the lower kinetics involved in metabolizing galactose into glycolysis (**Chapter 1: Table 3**), forcing cells to rely heavily on mitochondrial ATP for energy (Robinson et al., 1992, Kano et al., 2019). In addition to identifying OXPHOS deficiencies, the slow rate of galactose entry into glycolysis can be used to study glucose limitation. Several studies have looked into the metabolism of cancer cells under glucose starvation, where the media used contained either no glucose or very low glucose levels (Leithner et al., 2015, Li et al., 2018, Yang et al., 2014). However, such studies fail to imitate the limited glucose spatial distribution in the TME. Reason being that these studies profile the metabolic rewiring in response to complete lack of glucose rather than slow and constant supply of glucose that we hypothesize occur in certain areas of tumors *in vivo*. Another disadvantage of using glucose starvation is the inability to use stable isotopic tracers to study glycolytic rewiring (**Illustration 7**). Indeed, majority of studies using glucose starvation investigate glutamine metabolism and its rewiring rather than what happens to PPP, glycolysis and the 1C cycle (Leithner et al., 2015, Li et al., 2018, Yang et al., 2014). By using [U-^{13}C] galactose, we were able to prove that cancer cells are able to metabolize galactose and use it

to support PPP, upper glycolysis and 1C cycle. Furthermore, the use of labeled galactose made it possible to study the metabolic rewiring that occurs in cancer cells in response to slow glycolytic flux.

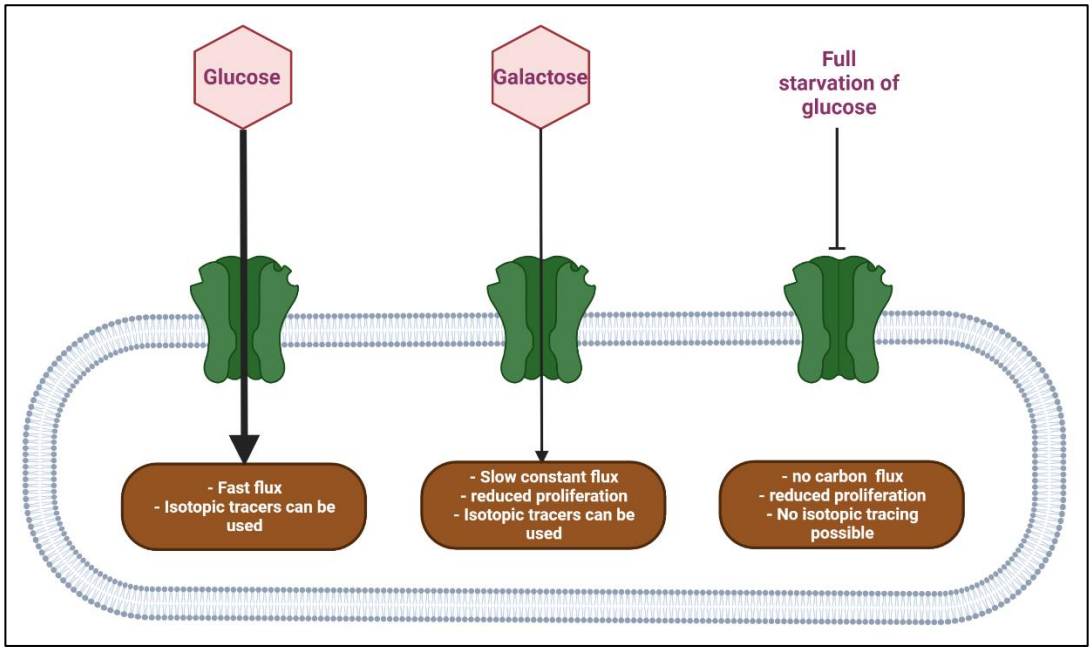


Illustration 7. Comparison of glycolytic challenges.

When cancer cells are cultured with glucose, they can run their glycolysis on full speed. When glucose is replaced with galactose, cells can still run glycolysis but at a much slower rate due to the slower kinetics of the Leloir pathway. However, it is still possible to use isotopically labeled galactose to study the glycolytic flux under glucose limitation. Whereas with full glucose starvation, it is not feasible to use stable isotope tracers to study glycolytic flux (Figure created with Biorender.com).

Glycolytic limitation using galactose reproduced the same rewiring of glutamine metabolism that occurs under full glucose starvation in cancer cells (Leithner et al., 2015, Yang et al., 2014). Moreover, when using a one:one mixture of glucose and galactose (labeled:unlabeled and vice versa) we saw no inhibitory action of galactose on glycolysis. Implying that the rewiring that we observed with media containing only galactose is a cellular response to the limited supply of glycolytic carbons. These observations validate the use of galactose to mimic glycolytic limitation.

Cancer cells display metabolic flexibility and plasticity in response to glycolytic stress:

The cellular metabolic response to glycolytic stress was to rewire different carbon sources towards SSP. Cancer cells rewired their limited carbon supply from galactose towards SSP and away from pyruvate in an example of metabolic plasticity (**Illustration 8**). We have identified the rewiring of glycolysis towards SSP to be present in variety of cancer cell lines representing four different types of tumors. These cell lines differ in their mutational status and driver mutations e.g. B16-F10 is BRAF wildtype while A375 carry a BRAF mutation, MDA-MB-468 have EGFR amplification while HCT-116 is KRAS mutant (Ahmed et al., 2013, Al Hashmi et al.,

2020, Chavez et al., 2010). Moreover, the panel of cell lines tested included a mixture of human and murine cancer cell lines. All of these differences showcase the robustness of the observed rewiring and its independence from any specific mutation. Glutamine carbons were also rewired towards SSP via the action of phosphoenolpyruvate carboxykinase 2 (PEPCK2), showcasing metabolic flexibility. Thereby, applying glycolytic stress to cancer cells uncovered their metabolic adaptability (Bergers and Fendt, 2021). Consequently, it can be assumed that within the TME, specifically in areas with limited glucose supply, cancer cells perform similar rewiring strategies that we observed with our models.

The ability to unmask the metabolic potential of cancer cells by using galactose unveiled metabolic escape rewiring that is needed for viability and thus can be targeted to limit metabolic adaptability of cancer. Therefore, modelling glycolytic limitation *in vitro* hold therapeutic potential by providing a tool to identify how cancer cells evade stressful metabolic environment through rewiring their metabolism.

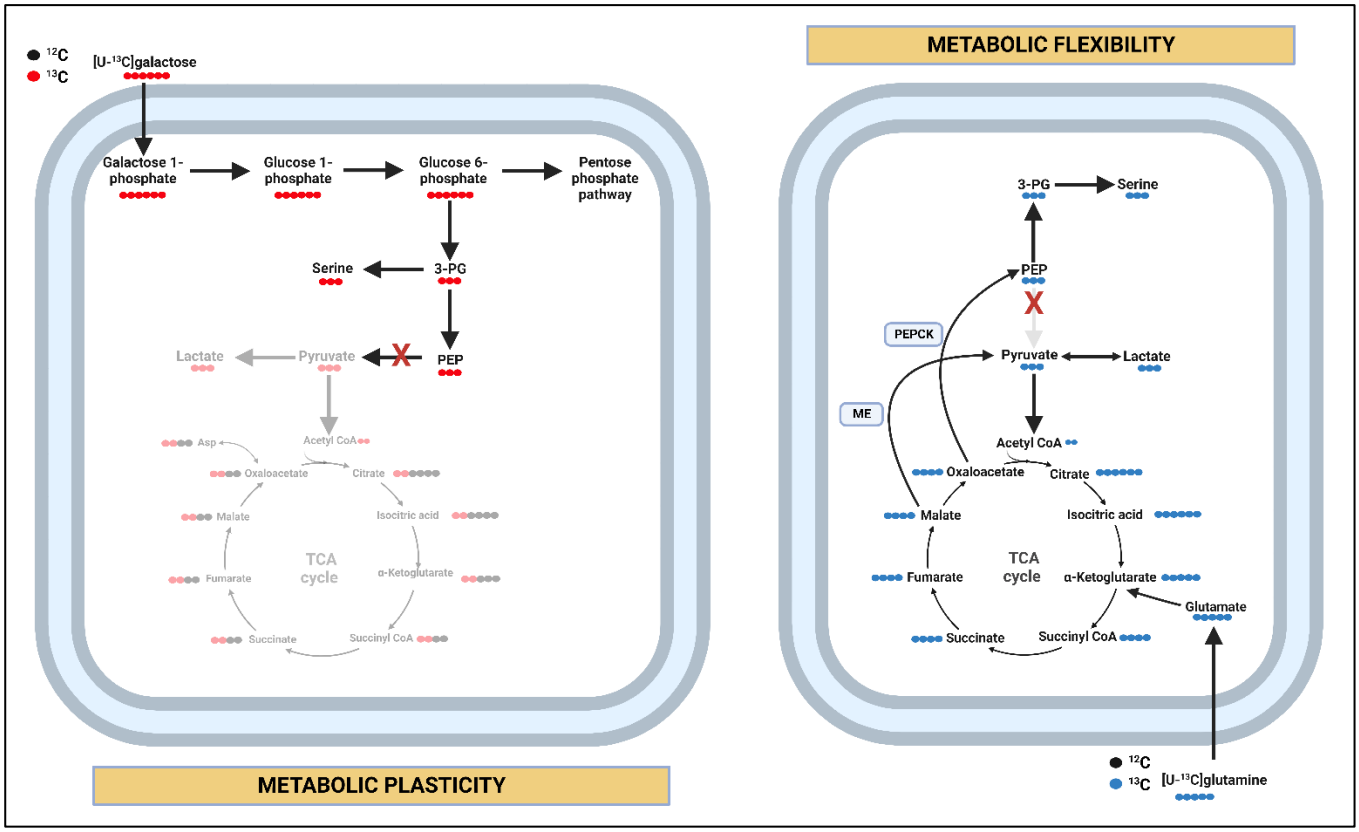


Illustration 8. Metabolic rewiring in response to glycolytic stress in cancer cells.

Cancer cells rewire their metabolism towards serine synthesis pathway from two carbon sources. Firstly, cancer cells rewire their limited glycolytic flux towards serine synthesis and pentose phosphate pathway in an example of metabolic plasticity. Secondly, glutamine flux is rewired towards serine synthesis in an example of metabolic flexibility. 3-PG, 3-phosphoglycerate; PEP, phosphoenolpyruvate. Adapted from chapter 3 of this dissertation (Figure created with Biorender.com).

PKM2 as the main rewiring point for glycolysis and glutamine metabolism under glycolytic limitation:

As outlined in 1.5.1., PKM2 is able to rewire glycolytic flux towards biosynthetic pathways depending on the cellular need as it is heavily regulated by several mechanisms (Chandel, 2021). This rewiring is a result of PKM2 existing in two different forms: high activity tetramer and lower activity dimer (Dayton et al., 2016). However, it needs to be stated that the dimer form of PKM2 still possess a relatively high activity as demonstrated with using isotopically labeled glucose (Chaneton et al., 2012). Remarkably, we show that when cancer cells were exposed to low glycolytic flux (galactose), PKM2 was inhibited (**Illustration 9**). Our findings are complementary to the observation that PKM2 expression is downregulated with glucose starvation (Li et al., 2018). We demonstrate a strong inhibition of PKM2 under glucose limitation that safeguards the limited glycolytic carbons available to the cell and rewires them towards PPP and 1C cycle (**Illustration 8**). Moreover, we show that this rewiring is needed for survival and growth under these nutritional stresses. Altogether, our findings highlight the different mechanisms by which cancer cells engage abundant nutritional status as opposed to optimizing the available carbons when nutrients are scarce.

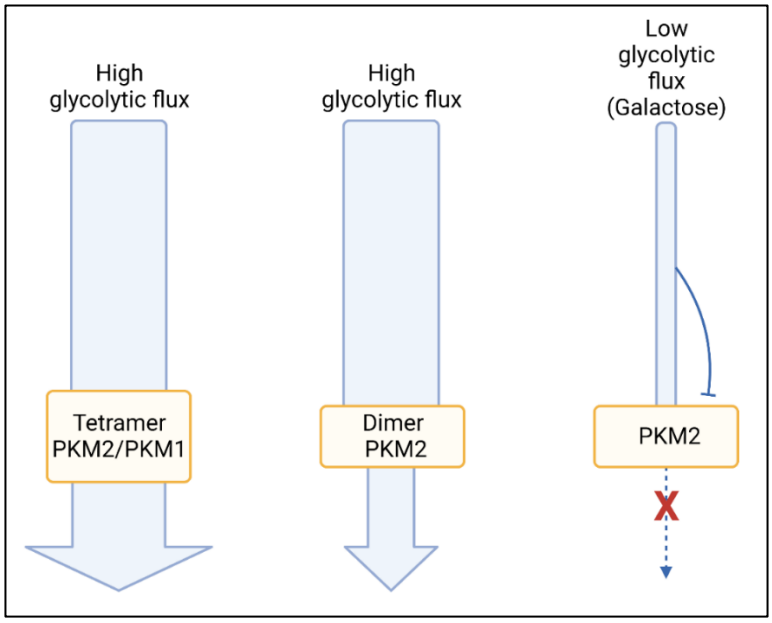


Illustration 9. Pyruvate kinase flux.

When ample glucose is available, the glycolytic flux is high and PKM2 can exist as either a tetramer or a dimer. When PKM2 is in the dimer form, some of the glycolytic flux is rewired away from pyruvate as indicated with the size of the arrows. However, if cells face low glycolytic flux then PKM2 activity is inhibited (Figure created with Biorender.com).

Serine is a known allosteric activator of PKM2 and cells cultured under serine/glycine (SG) starvation reduce the flux of PKM2 towards pyruvate (Chaneton et al., 2012). Therefore, PKM2 acts as a rheostat that controls how much of the glycolytic flux is rewired towards SSP and this is controlled by serine levels. The novelty of our work is in demonstrating that the PKM2 block and resultant rewiring towards SSP are ***independent*** of serine levels. Firstly, we showed that the levels of serine remain constant in the experimental conditions

where we observed the PKM2 block, meaning that the reported rewiring is not a result of a drop in the levels of serine. Secondly, the inhibition of PKM2 occur in media that contain ample supply of SG, indicating that cells can freely consume these amino acids. In fact, we have shown previously that under glucose limitation cancer cells increase their uptake of serine (Meiser et al., 2016). Thirdly, as expected intracellular serine levels dropped massively under SG starvation, however, in those conditions, the PKM2 flux was unchanged (as demonstrated by the citrate isotopologue M+2 in appendix 1, Supplementary fig 1). Finally, cells treated with an inhibitor of PHGDH under SG starvation had no detectable serine by LC-MS, suggesting that PKM2 cannot be activated by serine in these conditions (Appendix 1, Supplementary fig 1B). Yet, these cells displayed an increased PKM2 flux (Appendix 1, Supplementary fig 1A). A possible explanation as to why we observed an increased PKM2 flux with very limited serine is the lack of mitochondrial 1C cycle activity. This reasoning is based on the observation that we had an increased PKM2 flux when MTHFD1L or MTHFD2 are deleted. Therefore, we propose that under glycolytic limitation, cancer cells block PKM2 activity to rewire their glycolytic flux towards SSP independently of serine levels and in response to mitochondrial 1C cycle.

Previous reports have shown that under glucose starvation, glutamine flux is rewired towards SSP and to continually run the TCA cycle (Leithner et al., 2015, Vincent et al., 2015, Yang et al., 2014). However, it remained unknown why malic enzyme (ME) involvement is necessary to run the TCA cycle, since PEPCK2 can yield phosphoenolpyruvate (PEP), which in turn can feed into the TCA cycle. Our work identifying the PKM2 block answers this question. With the inhibition of PKM2, PEP cannot be converted to pyruvate and as such, PEPCK2 alone is not able to support the TCA cycle. This is important because under glucose limitation glutamine-derived acetyl-CoA is required to synthesize citrate and continue the TCA cycle. To circumvent the PKM2 block, cancer cells rely on ME activity to generate pyruvate which is then converted to acetyl-CoA via PDH, which we show, is active under glycolytic limitation. The fact that PDH is active under glucose limitation further confirms that the glycolytic bottleneck is PKM2.

There are three different isoforms of ME; all three decarboxylate malate to generate pyruvate, the difference between the isoforms is the subcellular localization and cofactor used (Chapter 2, Fig 1). ME1 is cytoplasmic and can generate NADPH, while ME2 and ME3 are mitochondrial and generate NADH and NADPH respectively (Benzarti et al., 2020). All three isoforms can be responsible for generating glutamine-derived pyruvate as both pyruvate and malate can be transported across the mitochondrial membrane (Nelson, 2017). ME2 was reported to be responsible for the rewiring of glutamine flux under glucose starvation (Yang et al., 2014). However, this study performed [U-^{13}C] glutamine tracing on isolated mitochondria and consequently could not have accounted for the cytoplasmic ME1. Indeed, recent study showed the involvement of ME1 under glucose starvation (Ying et al., 2021). Therefore, it is quite likely that multiple ME

isoforms are involved in our setup to rewire glutamine metabolism. This remains the subject of ongoing work in our lab.

Cell lines with *PHGDH* amplification overcome PEPCK2 deletion:

Apart from the rewiring of glutamine carbons via ME, we also corroborated previous findings regarding the involvement of PEPCK2 (Leithner et al., 2015, Vincent et al., 2015). Extraordinarily, under glucose limitation we observed a glutamine-derived flux into serine via PEPCK2 that was comparable to the glucose-derived flux. In previous studies, deletion of PEPCK2 reduced the growth of cancer cells both *in vitro* (under glucose starvation) and *in vivo*, thus we expected similar results with our system (Hyroššová et al., 2021, Vincent et al., 2015). Surprisingly, there was no definitive growth reduction under glucose limitation in cells with PEPCK2 ablation. While this is contradictory to what has been published on PEPCK2, there are few possible explanations. First of all, we tested the PEPCK2 deletion in melanoma cell line B16-F10 and triple-negative breast cancer cell lines MDA-MB-468 and 4T1, while previous studies have shown the importance of PEPCK2 in colorectal, lung and cervical cancer cell lines (Hyroššová et al., 2021, Leithner et al., 2015, Vincent et al., 2015). Second of all, the uniqueness of our set up in using galactose instead of full glucose starvation. This provides the cell with some glycolytic flux that can perhaps compensate for the lack of glutamine-derived serine. Indeed, all of the cell lines we used harbored an amplification of *PHGDH*, which means they are capable of increasing the SSP flux, an observation we showed to be the case in MDA-MB-468 cells (Chapter 3, Fig. S3J). Overall, PEPCK2 relevance to SSP under nutrients stress can be bypassed with increased PHGDH activity.

Another possibility to bypass PEPCK2 deletion is to increase the consumption of SG from the media. Consequently, we performed our proliferation assays in media lacking SG and we observed no difference between scramble cells and PEPCK2 KD/KO cells (data not shown). This would indicate that cells lacking PEPCK2 activity are preferentially increasing PHGDH flux over simply consuming more serine from the media. Such an observation would raise the question: is there a difference between obtaining serine via synthesis or consumption. In our experimental setup with glucose limitation, we observed an increased NAD^+/NADH ratio. The increased availability of NAD^+ pushes the PHGDH reaction towards synthesizing serine. This could explain why cancer cell lines are able to increase their PHGDH flux under glucose limitation easily. Indeed, it was reported that the NAD^+ is limiting for serine synthesis (Diehl et al., 2019), therefore, its increased availability under glycolytic limitation favors *de novo* serine synthesis. Moreover, as discussed in 1.3.1., increasing SSP activity offers increased amounts of aKG which could play an important epigenetic role (Possemato et al., 2011).

A cytoplasmic isozyme of PEPCK exists and is denoted as PEPCK1 which is part of the gluconeogenesis pathway alongside PEPCK2 (Nelson, 2017). Yet, in our experimental setup since the knockout of the mitochondrial PEPCK2 was sufficient to eliminate the glutamine-derived serine, it can be concluded that PEPCK1 is not active. On the one hand, PEPCK1 is involved following a series of reactions that transfer reducing equivalents in the form of NADH from the mitochondria to the cytoplasm. The aforementioned reactions being the reduction/oxidation of malate by malate dehydrogenase. This transfer of NADH is required to balance the NADH consumed in the cytoplasm downstream in gluconeogenesis pathway. On the other hand, PEPCK2 involvement does not transfer any reducing equivalents to the cytoplasm. However, under glycolytic limitation the NAD^+/NADH ratio is significantly increased, meaning that NADH is depleted relatively to its oxidized form in the cell. Logically, PEPCK1 would be the most suitable path to generate PEP since its NADH neutral. One explanation as to why PEPCK2 is the active form in this case is that NADH is not consumed in gluconeogenesis because the cell activate only the first part of the pathway to generate serine (**Illustration 10**). This explanation gives another evidence to the importance of serine synthesis in glycolysis stressed cells.

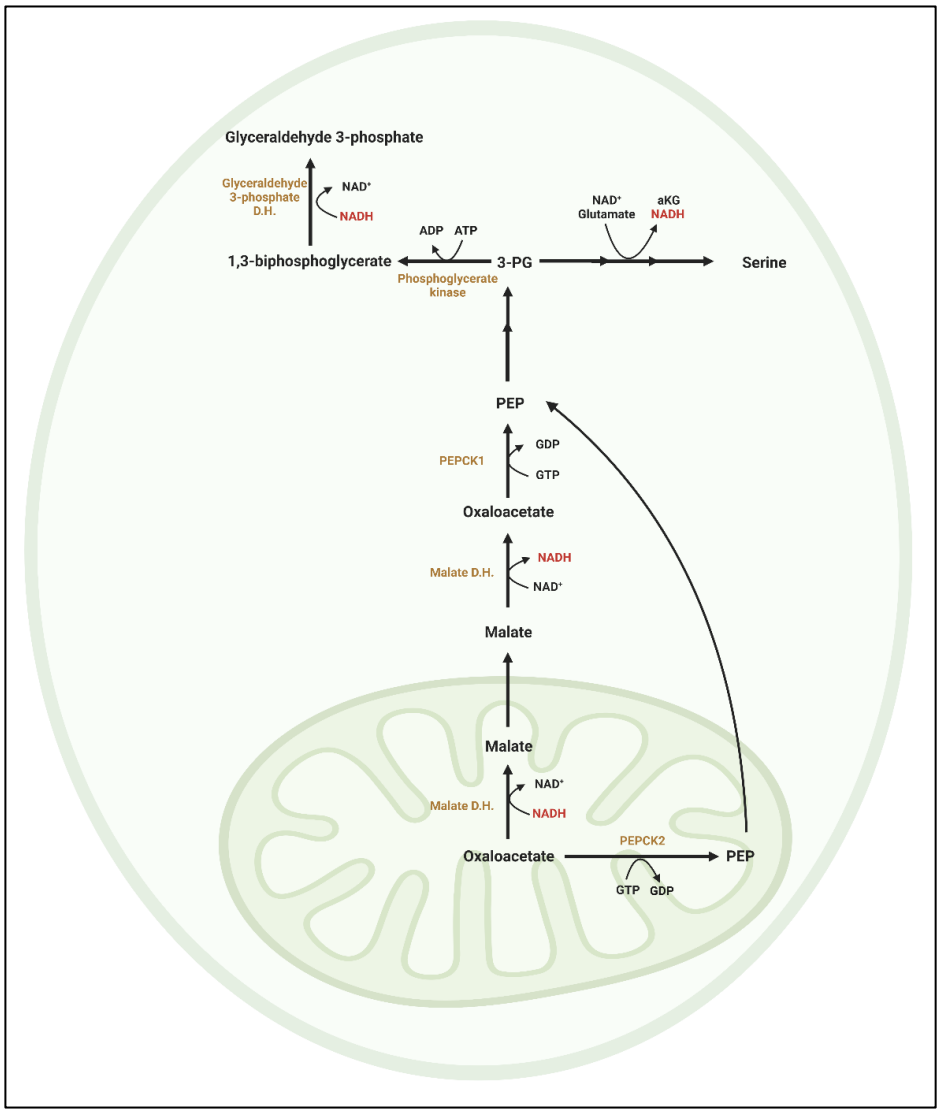


Illustration 10. Cytoplasmic and mitochondrial route for phosphoenol pyruvate generation in gluconeogenesis.

Under glucose limitation, oxaloacetate is generated from the TCA cycle and acts as a substrate for PEP generation. Two possible pathways exist for the conversion of oxaloacetate into PEP, either via PEPCK1 or PEPCK2. Following the route of PEPCK1, NADH is transported to the cytoplasm and as such generation of glyceraldehyde 3-phosphate is NADH neutral. While using PEPCK2 will not transfer any NADH into the cytoplasm. PEPCK, phosphoenolpyruvate carboxykinase; D.H., dehydrogenase; 3-PG, 3-phosphoglycerate; aKG, alpha-ketoglutarate (Figure created with Biorender.com).

Cells maintain SSP under glycolytic stress to support biosynthesis, bioenergetics and redox balance

Culturing cells in galactose led to clearly reduced proliferation. Based on this observation, we hypothesized that the biosynthetic function of the 1C cycle under these conditions is halted. However, by using [U-^{13}C] serine we show that cells maintain the relative flux from serine to *de novo* nucleotide synthesis. This implies that biosynthesis remains a relevant flux under glucose limitation. Yet, investigating the expression of the 1C cycle enzymes revealed a clear upregulation of the mitochondrial branch of the cycle (SHMT2, MTHFD2 and

ALDH1L2), while the expression of the cytoplasmic enzymes remained the same. This Indicates that while the biosynthetic relative flux is unchanged, mitochondrial 1C cycle-derived ATP and NADPH generation might be upregulated. On the one hand, formate overflow was significantly increased under glycolytic limitation in every cell line we tested (Meiser et al., 2016). The release of formate is indicative of generating net ATP for the cell from running the 1C cycle. Further, the NADH generated from formate overflow is mitochondrial, which matches the increased OXPHOS observed under glycolytic stress. On the other hand, deletion of ALDH1L2 significantly reduced the proliferation of MDA-MB-468 cells under glycolytic limitation, showing that mitochondrial 1C cycle-derived NADPH is important for growth under these conditions. Unfortunately, we were not able to measure the relative nor the absolute flux through ALDH1L2, as this requires measurement of either CO_2 or NADPH. Moreover, in this particular case, we would need to exclusively measure the mitochondrial NADPH flux, which is more challenging than whole cell NADPH measurements. A separation of the mitochondrial NADPH relative flux is required as it was shown recently that ALDH1L2 only affects mitochondrial ROS (Hennequart et al., 2023) and the mitochondrial and cytoplasmic NADPH fluxes are independent (Niu et al., 2023). Nevertheless, ALDH1L2 mRNA and protein expressions were markedly increased. This observation in addition to the proliferation data would suggest an increased rate of NADPH generation via ALDH1L2 under glycolytic limitation.

Increased formate overflow alongside increased ALDH1L2 activity is quite a remarkable observation because both reactions rely on the pool of a single metabolite (10-CHO-THF) and mutually deplete it. This points out that under glycolytic stress, the mitochondrial flux of the 1C cycle is significantly increased. Moreover, the re-activation of PKM2 flux upon deletion of MTHFD2 and MTHFD1L adds more importance to the relevance of the mitochondrial 1C under nutrients stress conditions. We speculate that a product of the mitochondrial 1C cycle like formate is able to regulate the flux through PKM2 post-translationally and this is the subject of active research in our lab.

Uncoupling proliferation from the 1C cycle reveals a growth-independent function:

The isolation of the mitochondrial 1C cycle using methotrexate showcased the superior capacity of cancer cells to overcome treatment (exemplified with the relative ease to generate methotrexate-resistant cell lines) through their flexible biochemical network. Another advantage of using methotrexate is that it completely halted the proliferation of cancer cells, allowing us to identify growth-independent function that are supported by serine catabolism. Cancer cells were able to use their mitochondrial 1C cycle independently of the cytoplasmic part to support their motility *in vitro* and metastasis formation *in vivo*. The mitochondrion is able to localize an independent 1C cycle because MTHFD1L and ALDH1L2 reactions release THF (as opposed

to TS releasing DHF), which then accepts a new 1C unit from SHMT2 reaction. In the cytoplasm, when THF is oxidized to DHF, the folates are trapped in that form and can no longer accept 1C units due to the action of methotrexate (Farber and Diamond, 1948). Thereby, serine catabolism is sustained in the presence of methotrexate.

As mentioned above, ALDH1L2 can contribute in the recycling of mitochondrial THF to continuously allow the SHMT2 reaction to take place. In cells lacking detectable expression of ALDH1L2, ablation of MTHFD1L effectively inhibited the autarkic mitochondrial 1C cycle due to the folates being trapped as 10-CHO-THF. However, cells expressing ALDH1L2 were able to free mitochondrial THF in such conditions and keep the autarkic cycle running. Another possibility to release THF is the generation of formyl-methionine via the action of methionyl-tRNA formyltransferase (Hennequart et al., 2023, Tucker et al., 2011), however, the absolute flux and relevance of this reaction under methotrexate are currently unknown.

Limitation of the study:

The main aim of our work was to model the glycolytic limitation that occur within the TME, however, as with all models our approach is not a perfect imitation of the physiological setting in the TME. Areas with limited glucose supply in the tumor can exist due to poor circulation, yet, the circulation will always replenish these areas maintaining a consistent state of limited supply of glucose. To model such situation *in vitro,* a system where glucose is continuously being replenished will need to be utilized. Nonetheless, the best model to study tumor glycolytic limitation would be investigating the spatial metabolome of cross-sectional tumor slides (please see future perspective section).

We have used multiple cell lines *in vitro* to investigate the rewiring towards SSP that we observed under glycolytic limitation. These cell lines represent multiple tumor types which *in vivo* differ in their TME composition, metabolic addiction and mutational landscape. This hinders the translational potential of the presented findings, as these tumors will display different metabolic adaptation strategies alongside the rewiring towards serine. The main driver for such strategies would be the nutrient composition of their respective TME. One *in vitro* method to overcome such discrepancies between TMEs would be to use a medium formula that reflects TIF. Indeed, recently a study has shown that metabolic vulnerabilities could be identified when cancer cells were cultured in a medium that is formulated based on their respective TIF metabolite composition (Apiz Saab et al., 2023). However, to use such method, a TIF-based medium would need to be developed for each specific tumor type (Apiz Saab et al., 2023).

We have utilized two *in vivo* models to recapitulate our *in vitro* findings and while these models could partially reiterate our findings, it cannot be conclusively concluded that the observed rewiring occurs *in vivo.* This is because our metabolic measurements of tumor metabolites represent the average metabolite level of areas of the tumor rather than identifying glucose-limited areas. Identifying glucose-limited areas in tumors and the subsequent metabolic profiling of such areas using stable isotope tracers would provide irrefutable evidence on the physiological relevance of our findings.

Conclusion:

To conclude, by using galactose as a tool compound to mimic the limited glucose supply in the TME, we were able to unmask the metabolic potential of cancer cells and uncover their innate metabolic flexibility and plasticity. Both the limited glycolytic flux and glutamine flux were rewired, via a PKM2 block and PEPCK2 activation respectively, to support serine generation (**Illustration 11**). Serine was needed for the 1C cycle and the mitochondrial 1C cycle activity was upregulated to increase the generation of ATP and NADPH, while the cytoplasmic 1C cycle activity remained unchanged. Methotrexate was the other tool compound we utilized to uncouple proliferative demands from the 1C cycle, disclosing an autarkic mitochondrial 1C cycle. The mitochondrial 1C cycle sustained activity was essential to maintain migration and metastasis in *in vivo* models.

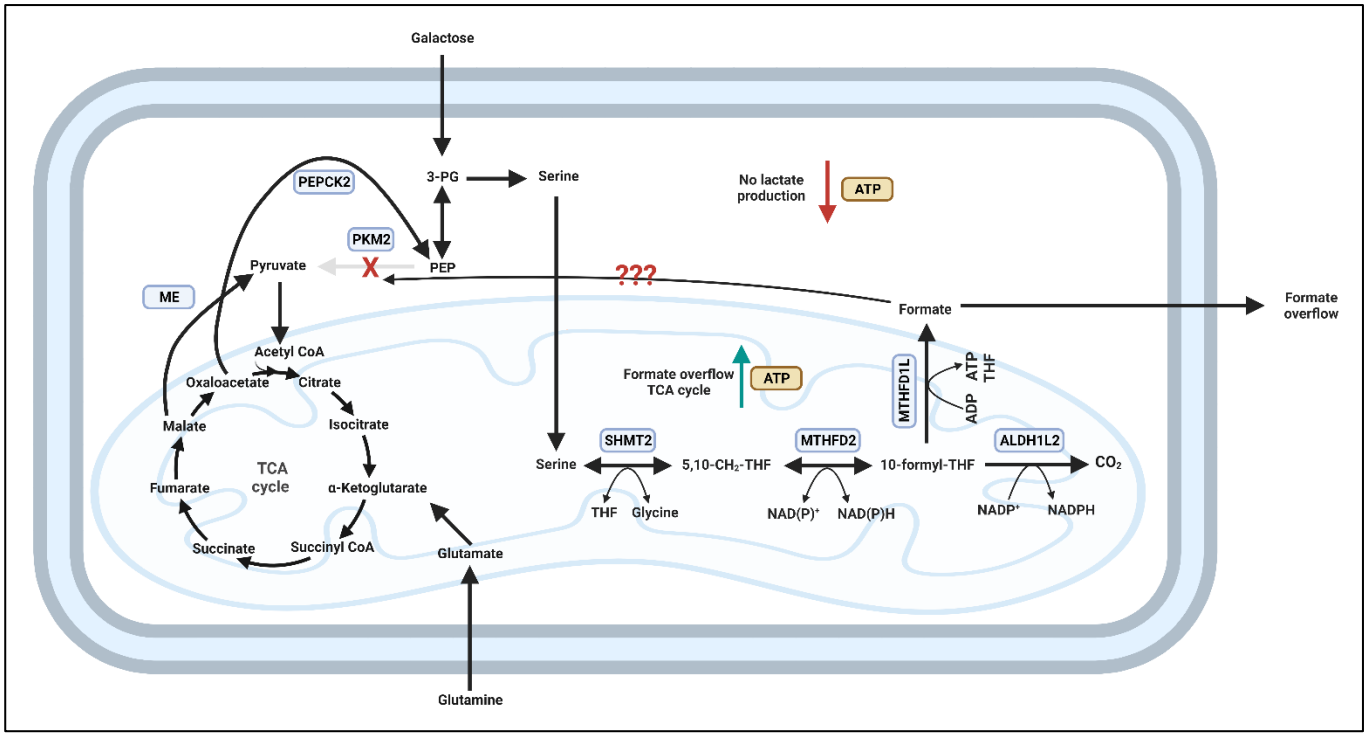


Illustration 11. Summary of the metabolic rewiring in cancer cells under glycolytic stress.

Under glycolytic stress, cancer cells block PKM2 activity to rewire their glycolytic flux towards serine synthesis. Glutamine flux is rewired via malic enzyme to generate glutamine-derived pyruvate and via phosphoenolpyruvate carboxykinase 2 towards serine. Mitochondrial one-carbon cycle activity is increased to generate ATP and NADPH. Lactate production is completely inhibited and therefore only mitochondrial ATP is available for the cell. 3-PG, 3-phosphoglycerate; PEP, phosphoenolpyruvate; PKM2, pyruvate kinase isozyme M2; PEPCK2, phosphoenolpyruvate carboxykinase 2; THF, tetrahydrofolate; SHMT2, serine hydroxyl methyl-transferase 2; MTHFD(L), 5,10-methylene-tetrahydrofolate dehydrogenase/5,10-methenyl-tetrahydrofolate cyclohydrolase (like); ALDH1L2, mitochondrial 10-formyl-tetrahydrofolate dehydrogenase (Figure created with Biorender.com).

Future perspectives:

- Even though ALDH1L2 expression was clearly upregulated, we were not able to measure the output of this reaction due to technical challenges. These challenges did not only pertain to instruments and measurements but also analysis. For example, it was not feasible to reliably distinguish between NADH, NADPH and their labeled isotopologues. This problem was acknowledged and addressed in a recent publication where deuterium labeled glucose tracers are used to distinguish between mitochondrial and cytoplasmic NADPH fluxes (Niu et al., 2023). The methods described here circumvent the difficulties in directly measuring NADPH by assaying its flux via measuring other more stable metabolites (Niu et al., 2023). Establishing and utilizing this method would allow us to measure the relevance of ALDH1L2 in generating mitochondrial NADPH under glucose limitation using knockouts.

- We have now generated a MTHFD1L and ALDH1L2 double knockout in MDA-MB-468 cells. Both of these enzymes are responsible for the main two outputs of the mitochondrial 1C cycle. Therefore, it would be intriguing to study the survival of cancer cells under glycolytic limitation in these knockouts. Another model we have in the lab is SHMT2 knockout in MDA-MB-468 cells, which would be interesting to study and compare to the double knockout cells.

- MTHFD1L is the key enzyme responsible for formate overflow (Meiser et al., 2016). To study the relevance of formate in the rewiring we categorized under glucose limitation, we are in the process of generating cell lines expressing a catalytic-dead mutant of MTHFD1L. These mutants have been designed to lack the ability to hydrolyze formate from 10-CHO-THF. This would be a more appropriate method to study the role of formate, compared to using full MTHFD1L knockouts especially with the potential of moonlighting functions of metabolic enzymes (Rossi et al., 2022).

- PKM2 was identified here as the main rewiring point. We have also identified potential residues on PKM2 that can be formylated (data not shown). It is reasonable to speculate that PKM2 inhibition can be a result of such formylation, since formate release is increased under the same conditions.

Therefore, we currently aim to generate PKM2 mutants that cannot be formylated on the identified residues and study whether we still observe the PKM2 block in these conditions. Moreover, in this dissertation we have used pharmacological activators of PKM2. However, we did not look into the effects of deleting PKM2 and culturing cells in galactose. Many scenarios are possible in this case, as PK can still exist in three different isoforms and their expression can potentially be upregulated. Alternatively, we can force cells to express the constitutively active PK form, PKM1 and study their survival under nutrients stress (Christofk et al., 2008).

- We showed that cells cultured in galactose released almost no lactate. Therefore, the cytoplasmic ATP production is very limited and these cells rely on mitochondrial ATP generation. Consequently, the transfer of energy between the cytoplasm and mitochondria in these conditions is very crucial for survival. Adenylate kinase (AK) is a key regulator of cell energy across subcellular compartments (Dzeja and Terzic, 2009). As such, studying AK role in the energy transfer between the cytoplasm and mitochondria has merits. Many isoforms of AK exist in cells and the main mitochondrial isoform is AK2 (Klepinin et al., 2020, Panayiotou et al., 2014). We are currently generating knockouts of AK2 to profile the importance of cellular energy economy in cells under glycolytic limitation.

- By comparing the core region of tumors to the outer layer, we were hoping to display the difference in the spatial distribution of glucose *in vivo.* Yet, a more reliable and accurate method would be to measure glucose distribution on a cross-sectional slide of tumors. Matrix-assisted laser desorption/ionization (MALDI)-mass spectrometry imaging (MSI) is a technique that allows the direct capture and quantification of metabolites on tissue slides (Fujimura and Miura, 2014). Therefore, MALDI-MSI is the perfect tool to measure the spatial distribution of glucose and other metabolites across the area of a tumor. Visualizing the spatial distribution of glucose is required to determine if areas of very limited glucose supply exist *in vivo* as has been done for other metabolites (Altea-Manzano et al., 2023). Moreover, this technique can be overlaid with an isotopic labeling approach to determine whether low glucose would correlate with increased relative flux of SSP and formate generation.

- Even though the role of PEPCK2 in rewiring the glutamine flux *in vitro* was clear and significant, no effect on proliferation was observed in PEPCK2 KO cells. However, the importance of this flux in our PEPCK2 KOs is yet to be investigated *in vivo.* Previous studies have looked into the effect of deleting PEPCK2 *in vivo* but only in immunocompromised mice which neglect the effects of TME (Hyroššová

et al., 2021, Vincent et al., 2015). As such, we are currently planning to investigate the role of PEPCK2 in the development of breast cancer *in vivo* using our 4T1 PEPCK2 KOs in immunocompetent mice. This system would allow us to account for the TME and investigate the interplay between the deletion of PEPCK2 and immune and stromal component of the TME.

REFERENCES of CHAPTER 1 and 5

ACCORSI, A., PIATTI, E., PIACENTINI, M. P., GINI, S. & FAZI, A. 1989. Isoenzymes of phosphoglucomutase from human red blood cells: isolation and kinetic properties. *Prep Biochem,* 19**,** 251-71.

AHMED, D., EIDE, P. W., EILERTSEN, I. A., DANIELSEN, S. A., EKNÆS, M., HEKTOEN, M., LIND, G. E. & LOTHE, R. A. 2013. Epigenetic and genetic features of 24 colon cancer cell lines. *Oncogenesis,* 2**,** e71.

AL HASHMI, M., SASTRY, K. S., SILCOCK, L., CHOUCHANE, L., MATTEI, V., JAMES, N., MATHEW, R., BEDOGNETTI, D., DE GIORGI, V., MURTAS, D., LIU, W., CHOUCHANE, A., TEMANNI, R., SELIGER, B., WANG, E., MARINCOLA, F. M. & TOMEI, S. 2020. Differential responsiveness to BRAF inhibitors of melanoma cell lines BRAF V600E-mutated. *J Transl Med,* 18**,** 192.

ALTEA-MANZANO, P., DOGLIONI, G., LIU, Y., CUADROS, A. M., NOLAN, E., FERNÁNDEZ-GARCÍA, J., WU, Q., PLANQUE, M., LAUE, K. J., CIDRE-ARANAZ, F., LIU, X. Z., MARIN-BEJAR, O., VAN ELSEN, J., VERMEIRE, I., BROEKAERT, D., DEMEYER, S., SPOTBEEN, X., IDKOWIAK, J., MONTAGNE, A., DEMICCO, M., ALKAN, H. F., RABAS, N., RIERA-DOMINGO, C., RICHARD, F., GEUKENS, T., DE SCHEPPER, M., LEDUC, S., HATSE, S., LAMBRECHTS, Y., KAY, E. J., LILLA, S., ALEKSEENKO, A., GELDHOF, V., BOECKX, B., DE LA CALLE ARREGUI, C., FLORIS, G., SWINNEN, J. V., MARINE, J. C., LAMBRECHTS, D., PELECHANO, V., MAZZONE, M., ZANIVAN, S., COOLS, J., WILDIERS, H., BAUD, V., GRÜNEWALD, T. G. P., BEN-DAVID, U., DESMEDT, C., MALANCHI, I. & FENDT, S. M. 2023. A palmitate-rich metastatic niche enables metastasis growth via p65 acetylation resulting in pro-metastatic NF-κB signaling. *Nat Cancer,* 4**,** 344-364.

AMENDOLA, C. R., MAHAFFEY, J. P., PARKER, S. J., AHEARN, I. M., CHEN, W. C., ZHOU, M., COURT, H., SHI, J., MENDOZA, S. L., MORTEN, M. J., ROTHENBERG, E., GOTTLIEB, E., WADGHIRI, Y. Z., POSSEMATO, R., HUBBARD, S. R., BALMAIN, A., KIMMELMAN, A. C. & PHILIPS, M. R. 2019. KRAS4A directly regulates hexokinase 1. *Nature,* 576**,** 482-486.

APIZ SAAB, J. J., DZIEROZYNSKI, L. N., JONKER, P. B., AMINITABRIZI, R., SHAH, H., MENJIVAR, R. E., SCOTT, A. J., NWOSU, Z. C., ZHU, Z., CHEN, R. N., OH, M., SHEEHAN, C., WAHL, D. R., PASCA DI MAGLIANO, M., LYSSIOTIS, C. A., MACLEOD, K. F., WEBER, C. R. & MUIR, A. 2023. Pancreatic tumors exhibit myeloid-driven amino acid stress and upregulate arginine biosynthesis. *Elife,* 12.

BALSA, E., PERRY, E. A., BENNETT, C. F., JEDRYCHOWSKI, M., GYGI, S. P., DOENCH, J. G. & PUIGSERVER, P. 2020. Defective NADPH production in mitochondrial disease complex I causes inflammation and cell death. *Nature Communications,* 11**,** 2714.

BAO, X. R., ONG, S. E., GOLDBERGER, O., PENG, J., SHARMA, R., THOMPSON, D. A., VAFAI, S. B., COX, A. G., MARUTANI, E., ICHINOSE, F., GOESSLING, W., REGEV, A., CARR, S. A., CLISH, C. B. & MOOTHA, V. K. 2016. Mitochondrial dysfunction remodels one-carbon metabolism in human cells. *Elife,* 5.

BARTMAN, C. R., WEILANDT, D. R., SHEN, Y., LEE, W. D., HAN, Y., TESLAA, T., JANKOWSKI, C. S. R., SAMARAH, L., PARK, N. R., DA SILVA-DIZ, V., ALEKSANDROVA, M., GULTEKIN, Y., MARISHTA, A., WANG, L., YANG, L., ROICHMAN, A., BHATT, V., LAN, T., HU, Z., XING, X., LU, W., DAVIDSON, S., WÜHR, M., VANDER HEIDEN, M. G., HERRANZ, D., GUO, J. Y., KANG, Y. & RABINOWITZ, J. D. 2023. Slow TCA flux and ATP production in primary solid tumours but not metastases. *Nature,* 614**,** 349-357.

BENZARTI, M., DELBROUCK, C., NEISES, L., KIWELER, N. & MEISER, J. 2020. Metabolic Potential of Cancer Cells in Context of the Metastatic Cascade. *Cells,* 9.

BERGERS, G. & FENDT, S. M. 2021. The metabolism of cancer cells during metastasis. *Nat Rev Cancer,* 21**,** 162-180.

BOLUSANI, S., YOUNG, B. A., COLE, N. A., TIBBETTS, A. S., MOMB, J., BRYANT, J. D., SOLMONSON, A. & APPLING, D. R. 2011. Mammalian MTHFD2L encodes a mitochondrial methylenetetrahydrofolate dehydrogenase isozyme expressed in adult tissues. *J Biol Chem,* 286**,** 5166-74.

BUESCHER, J. M., ANTONIEWICZ, M. R., BOROS, L. G., BURGESS, S. C., BRUNENGRABER, H., CLISH, C. B., DEBERARDINIS, R. J., FERON, O., FREZZA, C., GHESQUIERE, B., GOTTLIEB, E., HILLER, K., JONES, R. G., KAMPHORST, J. J., KIBBEY, R. G., KIMMELMAN, A. C., LOCASALE, J. W., LUNT, S. Y., MADDOCKS, O. D., MALLOY, C., METALLO, C. M., MEUILLET, E. J., MUNGER, J., NÖH, K., RABINOWITZ, J. D., RALSER, M., SAUER, U., STEPHANOPOULOS, G., ST-PIERRE, J., TENNANT, D. A., WITTMANN, C., VANDER HEIDEN,

M. G., VAZQUEZ, A., VOUSDEN, K., YOUNG, J. D., ZAMBONI, N. & FENDT, S. M. 2015. A roadmap for interpreting (13)C metabolite labeling patterns from cells. *Curr Opin Biotechnol,* 34**,** 189-201.

BURGOS-BARRAGAN, G., WIT, N., MEISER, J., DINGLER, F. A., PIETZKE, M., MULDERRIG, L., PONTEL, L. B., ROSADO, I. V., BREWER, T. F., CORDELL, R. L., MONKS, P. S., CHANG, C. J., VAZQUEZ, A. & PATEL, K. J. 2017. Mammals divert endogenous genotoxic formaldehyde into one-carbon metabolism. *Nature,* 548**,** 549-554.

CANTOR, J. R. 2019. The Rise of Physiologic Media. *Trends Cell Biol,* 29**,** 854-861.

CANTOR, J. R., ABU-REMAILEH, M., KANAREK, N., FREINKMAN, E., GAO, X., LOUISSAINT, A., JR., LEWIS, C. A. & SABATINI, D. M. 2017. Physiologic Medium Rewires Cellular Metabolism and Reveals Uric Acid as an Endogenous Inhibitor of UMP Synthase. *Cell,* 169**,** 258-272.e17.

CHANDEL, N. S. 2021. Glycolysis. *Cold Spring Harb Perspect Biol,* 13.

CHANETON, B., HILLMANN, P., ZHENG, L., MARTIN, A. C. L., MADDOCKS, O. D. K., CHOKKATHUKALAM, A., COYLE, J. E., JANKEVICS, A., HOLDING, F. P., VOUSDEN, K. H., FREZZA, C., O'REILLY, M. & GOTTLIEB, E. 2012. Serine is a natural ligand and allosteric activator of pyruvate kinase M2. *Nature,* 491**,** 458-462.

CHAVEZ, K. J., GARIMELLA, S. V. & LIPKOWITZ, S. 2010. Triple negative breast cancer cell lines: one tool in the search for better treatment of triple negative breast cancer. *Breast Dis,* 32**,** 35-48.

CHEN, L., ZHANG, Z., HOSHINO, A., ZHENG, H. D., MORLEY, M., ARANY, Z. & RABINOWITZ, J. D. 2019. NADPH production by the oxidative pentose-phosphate pathway supports folate metabolism. *Nat Metab,* 1**,** 404-415.

CHEN, W., HOFFMANN, A. D., LIU, H. & LIU, X. 2018. Organotropism: new insights into molecular mechanisms of breast cancer metastasis. *npj Precision Oncology,* 2**,** 4.

CHEUNG, E. C., DENICOLA, G. M., NIXON, C., BLYTH, K., LABUSCHAGNE, C. F., TUVESON, D. A. & VOUSDEN, K. H. 2020. Dynamic ROS Control by TIGAR Regulates the Initiation and Progression of Pancreatic Cancer. *Cancer Cell,* 37**,** 168-182.e4.

CHRISTOFK, H. R., VANDER HEIDEN, M. G., HARRIS, M. H., RAMANATHAN, A., GERSZTEN, R. E., WEI, R., FLEMING, M. D., SCHREIBER, S. L. & CANTLEY, L. C. 2008. The M2 splice isoform of pyruvate kinase is important for cancer metabolism and tumour growth. *Nature,* 452**,** 230-3.

CLISH, C. B. 2015. Metabolomics: an emerging but powerful tool for precision medicine. *Cold Spring Harb Mol Case Stud,* 1**,** a000588.

CRABTREE, H. G. 1929. Observations on the carbohydrate metabolism of tumours. *Biochem J,* 23**,** 536-45.

DAVIDSON, S. M., PAPAGIANNAKOPOULOS, T., OLENCHOCK, B. A., HEYMAN, J. E., KEIBLER, M. A., LUENGO, A., BAUER, M. R., JHA, A. K., O'BRIEN, J. P., PIERCE, K. A., GUI, D. Y., SULLIVAN, L. B., WASYLENKO, T. M., SUBBARAJ, L., CHIN, C. R., STEPHANOPOLOUS, G., MOTT, B. T., JACKS, T., CLISH, C. B. & VANDER HEIDEN, M. G. 2016. Environment Impacts the Metabolic Dependencies of Ras-Driven Non-Small Cell Lung Cancer. *Cell Metab,* 23**,** 517-28.

DAVIS, S. R., STACPOOLE, P. W., WILLIAMSON, J., KICK, L. S., QUINLIVAN, E. P., COATS, B. S., SHANE, B., BAILEY, L. B. & GREGORY, J. F., 3RD 2004. Tracer-derived total and folate-dependent homocysteine remethylation and synthesis rates in humans indicate that serine is the main one-carbon donor. *Am J Physiol Endocrinol Metab,* 286**,** E272-9.

DAVIT-SPRAUL, A., POURCI, M. L., NG, K. H., SONI, T. & LEMONNIER, A. 1994. Regulatory effects of galactose on galactose-1-phosphate uridyltransferase activity on human hepatoblastoma HepG2 cells. *FEBS Lett,* 354**,** 232-6.

DAYTON, T. L., JACKS, T. & VANDER HEIDEN, M. G. 2016. PKM2, cancer metabolism, and the road ahead. *EMBO Rep,* 17**,** 1721-1730.

DE ALTERIIS, E., CARTENÌ, F., PARASCANDOLA, P., SERPA, J. & MAZZOLENI, S. 2018. Revisiting the Crabtree/Warburg effect in a dynamic perspective: a fitness advantage against sugar-induced cell death. *Cell Cycle,* 17**,** 688-701.

DEBERARDINIS, R. J. & CHANDEL, N. S. 2016. Fundamentals of cancer metabolism. *Sci Adv,* 2**,** e1600200.

DIAZ-RUIZ, R., RIGOULET, M. & DEVIN, A. 2011. The Warburg and Crabtree effects: On the origin of cancer cell energy metabolism and of yeast glucose repression. *Biochim Biophys Acta,* 1807**,** 568-76.

DIEHL, F. F., LEWIS, C. A., FISKE, B. P. & VANDER HEIDEN, M. G. 2019. Cellular redox state constrains serine synthesis and nucleotide production to impact cell proliferation. *Nat Metab,* 1**,** 861-867.

DONG, W., RAWAT, E. S., STEPHANOPOULOS, G. & ABU-REMAILEH, M. 2022. Isotope tracing in health and disease. *Curr Opin Biotechnol,* 76**,** 102739.

DUCKER, G. S., CHEN, L., MORSCHER, R. J., GHERGUROVICH, J. M., ESPOSITO, M., TENG, X., KANG, Y. & RABINOWITZ, J. D. 2016. Reversal of Cytosolic One-Carbon Flux Compensates for Loss of the Mitochondrial Folate Pathway. *Cell Metab,* 23**,** 1140-1153.

DUCKER, G. S. & RABINOWITZ, J. D. 2017. One-Carbon Metabolism in Health and Disease. *Cell Metab,* 25**,** 27-42.

DULBECCO, R. & FREEMAN, G. 1959. Plaque production by the polyoma virus. *Virology,* 8**,** 396-7.

DZEJA, P. & TERZIC, A. 2009. Adenylate kinase and AMP signaling networks: metabolic monitoring, signal communication and body energy sensing. *Int J Mol Sci,* 10**,** 1729-1772.

EAGLE, H. 1955. The specific amino acid requirements of a human carcinoma cell (Stain HeLa) in tissue culture. *J Exp Med,* 102**,** 37-48.

EAGLE, H. 1959. Amino Acid Metabolism in Mammalian Cell Cultures. *Science,* 130**,** 432-437.

EDWARDS-HICKS, J., SU, H., MANGOLINI, M., YONETEN, K. K., WILLS, J., RODRIGUEZ-BLANCO, G., YOUNG, C., CHO, K., BARKER, H., MUIR, M., GUERRIERI, A. N., LI, X.-F., WHITE, R., MANASTERSKI, P., MANDROU, E., WILLS, K., CHEN, J., ABRAHAM, E., SATERI, K., QIAN, B.-Z., BANKHEAD, P., ARENDS, M., GAMMOH, N., VON KRIEGSHEIM, A., PATTI, G. J., SIMS, A. H., ACOSTA, J. C., BRUNTON, V., KRANC, K. R., CHRISTOPHOROU, M., PEARCE, E. L., RINGSHAUSEN, I. & FINCH, A. J. 2022. MYC sensitises cells to apoptosis by driving energetic demand. *Nature Communications,* 13**,** 4674.

FAN, J., YE, J., KAMPHORST, J. J., SHLOMI, T., THOMPSON, C. B. & RABINOWITZ, J. D. 2014. Quantitative flux analysis reveals folate-dependent NADPH production. *Nature,* 510**,** 298-302.

FARBER, S. & DIAMOND, L. K. 1948. Temporary remissions in acute leukemia in children produced by folic acid antagonist, 4-aminopteroyl-glutamic acid. *N Engl J Med,* 238**,** 787-93.

FAUBERT, B., SOLMONSON, A. & DEBERARDINIS, R. J. 2020. Metabolic reprogramming and cancer progression. *Science,* 368**,** eaaw5473.

FENDT, S. M., FREZZA, C. & EREZ, A. 2020. Targeting Metabolic Plasticity and Flexibility Dynamics for Cancer Therapy. *Cancer Discov,* 10**,** 1797-1807.

FERNANDEZ-DE-COSSIO-DIAZ, J. & VAZQUEZ, A. 2017. Limits of aerobic metabolism in cancer cells. *Sci Rep,* 7**,** 13488.

FINLEY, L. W. S. 2023. What is cancer metabolism? *Cell*.

FUJIMURA, Y. & MIURA, D. 2014. MALDI Mass Spectrometry Imaging for Visualizing In Situ Metabolism of Endogenous Metabolites and Dietary Phytochemicals. *Metabolites,* 4**,** 319-46.

GAO, X. & LOCASALE, J. W. 2016. Serine Metabolism Links Tumor Suppression to the Epigenetic Landscape. *Cell Metabolism,* 24**,** 777-779.

GAO, Y., BADO, I., WANG, H., ZHANG, W., ROSEN, J. M. & ZHANG, X. H. 2019. Metastasis Organotropism: Redefining the Congenial Soil. *Dev Cell,* 49**,** 375-391.

GREEN, A. C., MARTTILA, P., KIWELER, N., CHALKIADAKI, C., WIITA, E., COOKSON, V., LESUR, A., EIDEN, K., BERNARDIN, F., VALLIN, K. S. A., BORHADE, S., LONG, M., GHAHE, E. K., JIMÉNEZ-ALONSO, J. J., JEMTH, A. S., LOSEVA, O., MORTUSEWICZ, O., MEYERS, M., VIRY, E., JOHANSSON, A. I., HODEK, O., HOMAN, E., BONAGAS, N., RAMOS, L., SANDBERG, L., FRÖDIN, M., MOUSSAY, E., SLIPICEVIC, A., LETELLIER, E., PAGGETTI, J., SØRENSEN, C. S., HELLEDAY, T., HENRIKSSON, M. & MEISER, J. 2023. Formate overflow drives toxic folate trapping in MTHFD1 inhibited cancer cells. *Nat Metab,* 5**,** 642-659.

GREGORY, J. F., 3RD, CUSKELLY, G. J., SHANE, B., TOTH, J. P., BAUMGARTNER, T. G. & STACPOOLE, P. W. 2000. Primed, constant infusion with [2H3]serine allows in vivo kinetic measurement of serine turnover, homocysteine remethylation, and transsulfuration processes in human one-carbon metabolism. *Am J Clin Nutr,* 72**,** 1535-41.

HANAHAN, D. 2022. Hallmarks of Cancer: New Dimensions. *Cancer Discov,* 12**,** 31-46.

HANAHAN, D. & WEINBERG, R. A. 2000. The hallmarks of cancer. *Cell,* 100**,** 57-70.

HANAHAN, D. & WEINBERG, R. A. 2011. Hallmarks of cancer: the next generation. *Cell,* 144**,** 646-74.

HENNEQUART, M., PILLEY, S. E., LABUSCHAGNE, C. F., COOMES, J., MERVANT, L., DRISCOLL, P. C., LEGRAVE, N. M., LEE, Y., KREUZALER, P., MACINTYRE, B., PANINA, Y., BLAGIH, J., STEVENSON, D., STRATHDEE, D., SCHNEIDER-LUFTMAN, D., GRÖNROOS, E., CHEUNG, E. C., YUNEVA, M., SWANTON, C. & VOUSDEN, K. H. 2023. ALDH1L2 regulation of formate, formyl-methionine, and ROS controls cancer cell migration and metastasis. *Cell Rep,* 42**,** 112562.

HERBIG, K., CHIANG, E. P., LEE, L. R., HILLS, J., SHANE, B. & STOVER, P. J. 2002. Cytoplasmic serine hydroxymethyltransferase mediates competition between folate-dependent deoxyribonucleotide and S-adenosylmethionine biosyntheses. *J Biol Chem,* 277**,** 38381-9.

HILLER, K., HANGEBRAUK, J., JÄGER, C., SPURA, J., SCHREIBER, K. & SCHOMBURG, D. 2009. MetaboliteDetector: comprehensive analysis tool for targeted and nontargeted GC/MS based metabolome analysis. *Anal Chem,* 81**,** 3429-39.

HUFF, S. E., WINTER, J. M. & DEALWIS, C. G. 2022. Inhibitors of the Cancer Target Ribonucleotide Reductase, Past and Present. *Biomolecules,* 12.

HYROŠŠOVÁ, P., ARAGÓ, M., MORENO-FELICI, J., FU, X., MENDEZ-LUCAS, A., GARCÍA-ROVÉS, P. M., BURGESS, S., FIGUERAS, A., VIÑALS, F. & PERALES, J. C. 2021. PEPCK-M recoups tumor cell anabolic potential in a PKC-ζ-dependent manner. *Cancer Metab,* 9**,** 1.

JIANG, L., SHESTOV, A. A., SWAIN, P., YANG, C., PARKER, S. J., WANG, Q. A., TERADA, L. S., ADAMS, N. D., MCCABE, M. T., PIETRAK, B., SCHMIDT, S., METALLO, C. M., DRANKA, B. P., SCHWARTZ, B. & DEBERARDINIS, R. J. 2016. Reductive carboxylation supports redox homeostasis during anchorage-independent growth. *Nature,* 532**,** 255-8.

KANO, A., IWASAKI, T. & SHINDO, M. 2019. Bongkrekic acid facilitates glycolysis in cultured cells and induces cell death under low glucose conditions. *Biochemistry and Biophysics Reports,* 20**,** 100683.

KIWELER, N., DELBROUCK, C., POZDEEV, V. I., NEISES, L., SORIANO-BAGUET, L., EIDEN, K., XIAN, F., BENZARTI, M., HAASE, L., KONCINA, E., SCHMOETTEN, M., JAEGER, C., NOMAN, M. Z., VAZQUEZ, A., JANJI, B., DITTMAR, G., BRENNER, D., LETELLIER, E. & MEISER, J. 2022. Mitochondria preserve an autarkic one-carbon cycle to confer growth-independent cancer cell migration and metastasis. *Nat Commun,* 13**,** 2699.

KLEPININ, A., ZHANG, S., KLEPININA, L., REBANE-KLEMM, E., TERZIC, A., KAAMBRE, T. & DZEJA, P. 2020. Adenylate Kinase and Metabolic Signaling in Cancer Cells. *Front Oncol,* 10**,** 660.

LEE, W. D., PIRONA, A. C., SARVIN, B., STERN, A., NEVO-DINUR, K., BESSER, E., SARVIN, N., LAGZIEL, S., MUKHA, D., RAZ, S., AIZENSHTEIN, E. & SHLOMI, T. 2021. Tumor Reliance on Cytosolic versus Mitochondrial One-Carbon Flux Depends on Folate Availability. *Cell Metabolism,* 33**,** 190-198.e6.

LEITHNER, K., HRZENJAK, A., TRÖTZMÜLLER, M., MOUSTAFA, T., KÖFELER, H. C., WOHLKOENIG, C., STACHER, E., LINDENMANN, J., HARRIS, A. L., OLSCHEWSKI, A. & OLSCHEWSKI, H. 2015. PCK2 activation mediates an adaptive response to glucose depletion in lung cancer. *Oncogene,* 34**,** 1044-50.

LEWIS, C. A., PARKER, S. J., FISKE, B. P., MCCLOSKEY, D., GUI, D. Y., GREEN, C. R., VOKES, N. I., FEIST, A. M., VANDER HEIDEN, M. G. & METALLO, C. M. 2014. Tracing compartmentalized NADPH metabolism in the cytosol and mitochondria of mammalian cells. *Mol Cell,* 55**,** 253-63.

LI, X., DENG, S., LIU, M., JIN, Y., ZHU, S., DENG, S., CHEN, J., HE, C., QIN, Q., WANG, C. & ZHAO, G. 2018. The responsively decreased PKM2 facilitates the survival of pancreatic cancer cells in hypoglucose. *Cell Death Dis,* 9**,** 133.

LOCASALE, J. W. 2013. Serine, glycine and one-carbon units: cancer metabolism in full circle. *Nat Rev Cancer,* 13**,** 572-83.

LONGLEY, D. B., HARKIN, D. P. & JOHNSTON, P. G. 2003. 5-fluorouracil: mechanisms of action and clinical strategies. *Nat Rev Cancer,* 3**,** 330-8.

LUENGO, A., LI, Z., GUI, D. Y., SULLIVAN, L. B., ZAGORULYA, M., DO, B. T., FERREIRA, R., NAAMATI, A., ALI, A., LEWIS, C. A., THOMAS, C. J., SPRANGER, S., MATHESON, N. J. & VANDER HEIDEN, M. G. 2021. Increased demand for NAD(+) relative to ATP drives aerobic glycolysis. *Mol Cell,* 81**,** 691-707.e6.

MADDOCKS, O. D., BERKERS, C. R., MASON, S. M., ZHENG, L., BLYTH, K., GOTTLIEB, E. & VOUSDEN, K. H. 2013. Serine starvation induces stress and p53-dependent metabolic remodelling in cancer cells. *Nature,* 493**,** 542-6.

MADDOCKS, O. D. K., ATHINEOS, D., CHEUNG, E. C., LEE, P., ZHANG, T., VAN DEN BROEK, N. J. F., MACKAY, G. M., LABUSCHAGNE, C. F., GAY, D., KRUISWIJK, F., BLAGIH, J., VINCENT, D. F., CAMPBELL, K. J., CETECI, F., SANSOM, O. J., BLYTH, K. & VOUSDEN, K. H. 2017. Modulating the therapeutic response of tumours to dietary serine and glycine starvation. *Nature,* 544**,** 372-376.

MARROQUIN, L. D., HYNES, J., DYKENS, J. A., JAMIESON, J. D. & WILL, Y. 2007. Circumventing the Crabtree effect: replacing media glucose with galactose increases susceptibility of HepG2 cells to mitochondrial toxicants. *Toxicol Sci,* 97**,** 539-47.

MCCORVIE, T. J., WASILENKO, J., LIU, Y., FRIDOVICH-KEIL, J. L. & TIMSON, D. J. 2011. In vivo and in vitro function of human UDP-galactose 4'-epimerase variants. *Biochimie,* 93**,** 1747-54.

MEISER, J., TUMANOV, S., MADDOCKS, O., LABUSCHAGNE, C. F., ATHINEOS, D., VAN DEN BROEK, N., MACKAY, G. M., GOTTLIEB, E., BLYTH, K., VOUSDEN, K., KAMPHORST, J. J. & VAZQUEZ, A. 2016. Serine one-carbon catabolism with formate overflow. *Sci Adv,* 2**,** e1601273.

MEISER, J. & VAZQUEZ, A. 2016. Give it or take it: the flux of one-carbon in cancer cells. *Febs j,* 283**,** 3695-3704.

MEJIA, N. R. & MACKENZIE, R. E. 1988. NAD-dependent methylenetetrahydrofolate dehydrogenase-methenyltetrahydrofolate cyclohydrolase in transformed cells is a mitochondrial enzyme. *Biochem Biophys Res Commun,* 155**,** 1-6.

MISSELBECK, K., MARCHETTI, L., PRIAMI, C., STOVER, P. J. & FIELD, M. S. 2019. The 5-formyltetrahydrofolate futile cycle reduces pathway stochasticity in an extended hybrid-stochastic model of folate-mediated one-carbon metabolism. *Scientific Reports,* 9**,** 4322.

MOORE, G. E., GERNER, R. E. & FRANKLIN, H. A. 1967. Culture of normal human leukocytes. *Jama,* 199**,** 519-24.

MUKHA, D., FOKRA, M., FELDMAN, A., SARVIN, B., SARVIN, N., NEVO-DINUR, K., BESSER, E., HALLO, E., AIZENSHTEIN, E., SCHUG, Z. T. & SHLOMI, T. 2022. Glycine decarboxylase maintains mitochondrial protein lipoylation to support tumor growth. *Cell Metab,* 34**,** 775-782.e9.

MULLARKY, E., MATTAINI, K. R., VANDER HEIDEN, M. G., CANTLEY, L. C. & LOCASALE, J. W. 2011. PHGDH amplification and altered glucose metabolism in human melanoma. *Pigment Cell Melanoma Res,* 24**,** 1112-5.

NASCENTES MELO, L. M., LESNER, N. P., SABATIER, M., UBELLACKER, J. M. & TASDOGAN, A. 2022. Emerging metabolomic tools to study cancer metastasis. *Trends Cancer,* 8**,** 988-1001.

NELSON, D. L. A. 2017. *Lehninger principles of biochemistry,* New York, NY, USA, W.H. Freeman and Company ; Houndmills, Basingstoke : Macmillan Higher Education.

NIEBEL, B., LEUPOLD, S. & HEINEMANN, M. 2019. An upper limit on Gibbs energy dissipation governs cellular metabolism. *Nature Metabolism,* 1**,** 125-132.

NILSSON, R., JAIN, M., MADHUSUDHAN, N., SHEPPARD, N. G., STRITTMATTER, L., KAMPF, C., HUANG, J., ASPLUND, A. & MOOTHA, V. K. 2014. Metabolic enzyme expression highlights a key role for MTHFD2 and the mitochondrial folate pathway in cancer. *Nat Commun,* 5**,** 3128.

NIU, X., STANCLIFFE, E., GELMAN, S. J., WANG, L., SCHWAIGER-HABER, M., ROWLES, J. L., 3RD, SHRIVER, L. P. & PATTI, G. J. 2023. Cytosolic and mitochondrial NADPH fluxes are independently regulated. *Nat Chem Biol,* 19**,** 837-845.

OSTHUS, R. C., SHIM, H., KIM, S., LI, Q., REDDY, R., MUKHERJEE, M., XU, Y., WONSEY, D., LEE, L. A. & DANG, C. V. 2000. Deregulation of glucose transporter 1 and glycolytic gene expression by c-Myc. *J Biol Chem,* 275**,** 21797-800.

PALM, W. & THOMPSON, C. B. 2017. Nutrient acquisition strategies of mammalian cells. *Nature,* 546**,** 234-242.

PAN, M., REID, M. A., LOWMAN, X. H., KULKARNI, R. P., TRAN, T. Q., LIU, X., YANG, Y., HERNANDEZ-DAVIES, J. E., ROSALES, K. K., LI, H., HUGO, W., SONG, C., XU, X., SCHONES, D. E., ANN, D. K., GRADINARU, V., LO, R. S., LOCASALE, J. W. & KONG, M. 2016. Regional glutamine deficiency in tumours promotes dedifferentiation through inhibition of histone demethylation. *Nat Cell Biol,* 18**,** 1090-101.

PANAYIOTOU, C., SOLAROLI, N. & KARLSSON, A. 2014. The many isoforms of human adenylate kinases. *Int J Biochem Cell Biol,* 49**,** 75-83.

PFEIFFER, T., SCHUSTER, S. & BONHOEFFER, S. 2001. Cooperation and competition in the evolution of ATP-producing pathways. *Science,* 292**,** 504-7.

PIKE, S. T., RAJENDRA, R., ARTZT, K. & APPLING, D. R. 2010. Mitochondrial C1-tetrahydrofolate synthase (MTHFD1L) supports the flow of mitochondrial one-carbon units into the methyl cycle in embryos. *J Biol Chem,* 285**,** 4612-20.

PISKOUNOVA, E., AGATHOCLEOUS, M., MURPHY, M. M., HU, Z., HUDDLESTUN, S. E., ZHAO, Z., LEITCH, A. M., JOHNSON, T. M., DEBERARDINIS, R. J. & MORRISON, S. J. 2015. Oxidative stress inhibits distant metastasis by human melanoma cells. *Nature,* 527**,** 186-191.

POMATTO-WATSON, L. C. D., BODOGAI, M., BOSOMPRA, O., KATO, J., WONG, S., CARPENTER, M., DUREGON, E., CHOWDHURY, D., KRISHNA, P., NG, S., RAGONNAUD, E., SALGADO, R., GONZALEZ ERICSSON, P., DIAZ-RUIZ, A., BERNIER, M., PRICE, N. L., BIRAGYN, A., LONGO, V. D. & DE CABO, R. 2021. Daily caloric restriction limits tumor growth more effectively than caloric cycling regardless of dietary composition. *Nat Commun,* 12**,** 6201.

POSSEMATO, R., MARKS, K. M., SHAUL, Y. D., PACOLD, M. E., KIM, D., BIRSOY, K., SETHUMADHAVAN, S., WOO, H.-K., JANG, H. G., JHA, A. K., CHEN, W. W., BARRETT, F. G., STRANSKY, N., TSUN, Z.-Y., COWLEY, G. S., BARRETINA, J., KALAANY, N. Y., HSU, P. P., OTTINA, K., CHAN, A. M., YUAN, B., GARRAWAY, L. A., ROOT, D. E., MINO-KENUDSON, M., BRACHTEL, E. F., DRIGGERS, E. M. & SABATINI, D. M. 2011. Functional genomics reveal that the serine synthesis pathway is essential in breast cancer. *Nature,* 476**,** 346-350.

PRASANNAN, P., PIKE, S., PENG, K., SHANE, B. & APPLING, D. R. 2003. Human mitochondrial C1-tetrahydrofolate synthase: gene structure, tissue distribution of the mRNA, and immunolocalization in Chinese hamster ovary calls. *J Biol Chem,* 278**,** 43178-43187.

REINFELD, B. I., MADDEN, M. Z., WOLF, M. M., CHYTIL, A., BADER, J. E., PATTERSON, A. R., SUGIURA, A., COHEN, A. S., ALI, A., DO, B. T., MUIR, A., LEWIS, C. A., HONGO, R. A., YOUNG, K. L., BROWN, R. E., TODD, V. M., HUFFSTATER, T., ABRAHAM, A., O'NEIL, R. T., WILSON, M. H., XIN, F., TANTAWY, M. N., MERRYMAN, W. D., JOHNSON, R. W., WILLIAMS, C. S., MASON, E. F., MASON, F. M., BECKERMANN, K. E., VANDER HEIDEN, M. G., MANNING, H. C., RATHMELL, J. C. & RATHMELL, W. K. 2021. Cell-programmed nutrient partitioning in the tumour microenvironment. *Nature,* 593**,** 282-288.

REMPEL, A., MATHUPALA, S. P., GRIFFIN, C. A., HAWKINS, A. L. & PEDERSEN, P. L. 1996. Glucose catabolism in cancer cells: amplification of the gene encoding type II hexokinase. *Cancer Res,* 56**,** 2468-71.

ROBINSON, B. H., PETROVA-BENEDICT, R., BUNCIC, J. R. & WALLACE, D. C. 1992. Nonviability of cells with oxidative defects in galactose medium: a screening test for affected patient fibroblasts. *Biochem Med Metab Biol,* 48**,** 122-6.

ROSSI, M., ALTEA-MANZANO, P., DEMICCO, M., DOGLIONI, G., BORNES, L., FUKANO, M., VANDEKEERE, A., CUADROS, A. M., FERNÁNDEZ-GARCÍA, J., RIERA-DOMINGO, C., JAUSET, C., PLANQUE, M., ALKAN, H. F., NITTNER, D., ZUO, D., BROADFIELD, L. A., PARIK, S., PANE, A. A., RIZZOLLO, F., RINALDI, G., ZHANG, T., TEOH, S. T., AURORA, A. B., KARRAS, P., VERMEIRE, I., BROEKAERT, D., ELSEN, J. V., KNOTT, M. M. L., ORTH, M. F., DEMEYER, S., EELEN, G., DOBROLECKI, L. E., BASSEZ, A., BRUSSEL, T. V., SOTLAR, K., LEWIS, M. T., BARTSCH, H., WUHRER, M., VEELEN, P. V., CARMELIET, P., COOLS, J., MORRISON, S. J., MARINE, J.-C., LAMBRECHTS, D., MAZZONE, M., HANNON, G. J., LUNT, S. Y., GRÜNEWALD, T. G. P., PARK, M., RHEENEN, J. V. & FENDT, S.-M. 2022. PHGDH heterogeneity potentiates cancer cell dissemination and metastasis. *Nature,* 605**,** 747-753.

SCOTT, J. M. & WEIR, D. G. 1981. The methyl folate trap. A physiological response in man to prevent methyl group deficiency in kwashiorkor (methionine deficiency) and an explanation for folic-acid induced exacerbation of subacute combined degeneration in pernicious anaemia. *Lancet,* 2**,** 337-40.

SHIM, H., DOLDE, C., LEWIS, B. C., WU, C. S., DANG, G., JUNGMANN, R. A., DALLA-FAVERA, R. & DANG, C. V. 1997. c-Myc transactivation of LDH-A: implications for tumor metabolism and growth. *Proc Natl Acad Sci U S A,* 94**,** 6658-63.

SHIN, M., MOMB, J. & APPLING, D. R. 2017. Human mitochondrial MTHFD2 is a dual redox cofactor-specific methylenetetrahydrofolate dehydrogenase/methenyltetrahydrofolate cyclohydrolase. *Cancer & metabolism,* 5**,** 11-11.

SMITH, G. K., BANKS, S. D., MONACO, T. J., RIGUAL, R., DUCH, D. S., MULLIN, R. J. & HUBER, B. E. 1990. Activity of an NAD-dependent 5,10-methylenetetrahydrofolate dehydrogenase in normal tissue, neoplastic cells, and oncogene-transformed cells. *Arch Biochem Biophys,* 283**,** 367-71.

SODERBERG, K., NISSINEN, E., BAKAY, B. & SCHEFFLER, I. E. 1980. The energy charge in wild-type and respiration-deficient Chinese hamster cell mutants. *J Cell Physiol,* 103**,** 169-72.

SOUSA, C. M., BIANCUR, D. E., WANG, X., HALBROOK, C. J., SHERMAN, M. H., ZHANG, L., KREMER, D., HWANG, R. F., WITKIEWICZ, A. K., YING, H., ASARA, J. M., EVANS, R. M., CANTLEY, L. C., LYSSIOTIS, C. A. & KIMMELMAN, A. C. 2016. Pancreatic stellate cells support tumour metabolism through autophagic alanine secretion. *Nature,* 536**,** 479-483.

STINE, Z. E., SCHUG, Z. T., SALVINO, J. M. & DANG, C. V. 2022. Targeting cancer metabolism in the era of precision oncology. *Nat Rev Drug Discov,* 21**,** 141-162.

SULLIVAN, M. R., DANAI, L. V., LEWIS, C. A., CHAN, S. H., GUI, D. Y., KUNCHOK, T., DENNSTEDT, E. A., VANDER HEIDEN, M. G. & MUIR, A. 2019. Quantification of microenvironmental metabolites in murine cancers reveals determinants of tumor nutrient availability. *eLife,* 8**,** e44235.

SUNG, H., FERLAY, J., SIEGEL, R. L., LAVERSANNE, M., SOERJOMATARAM, I., JEMAL, A. & BRAY, F. 2021. Global Cancer Statistics 2020: GLOBOCAN Estimates of Incidence and Mortality Worldwide for 36 Cancers in 185 Countries. *CA Cancer J Clin,* 71**,** 209-249.

TEDESCHI, P. M., JOHNSON-FARLEY, N., LIN, H., SHELTON, L. M., OOGA, T., MACKAY, G., VAN DEN BROEK, N., BERTINO, J. R. & VAZQUEZ, A. 2015. Quantification of folate metabolism using transient metabolic flux analysis. *Cancer Metab,* 3**,** 6.

TIBBETTS, A. S. & APPLING, D. R. 2010. Compartmentalization of Mammalian folate-mediated one-carbon metabolism. *Annu Rev Nutr,* 30**,** 57-81.

TIMSON, D. J. & REECE, R. J. 2003. Functional analysis of disease-causing mutations in human galactokinase. *Eur J Biochem,* 270**,** 1767-74.

TRENT, D. F., SEITHER, R. L. & GOLDMAN, I. D. 1991. Compartmentation of intracellular folates. Failure to interconvert tetrahydrofolate cofactors to dihydrofolate in mitochondria of L1210 leukemia cells treated with trimetrexate. *Biochem Pharmacol,* 42**,** 1015-9.

TUCKER, E. J., HERSHMAN, S. G., KÖHRER, C., BELCHER-TIMME, C. A., PATEL, J., GOLDBERGER, O. A., CHRISTODOULOU, J., SILBERSTEIN, J. M., MCKENZIE, M., RYAN, M. T., COMPTON, A. G., JAFFE, J. D., CARR, S. A., CALVO, S. E., RAJBHANDARY, U. L., THORBURN, D. R. & MOOTHA, V. K. 2011. Mutations

in MTFMT underlie a human disorder of formylation causing impaired mitochondrial translation. *Cell Metab,* 14**,** 428-34.

VANDE VOORDE, J., ACKERMANN, T., PFETZER, N., SUMPTON, D., MACKAY, G., KALNA, G., NIXON, C., BLYTH, K., GOTTLIEB, E. & TARDITO, S. 2019. Improving the metabolic fidelity of cancer models with a physiological cell culture medium. *Sci Adv,* 5**,** eaau7314.

VAZQUEZ, A., LIU, J., ZHOU, Y. & OLTVAI, Z. N. 2010. Catabolic efficiency of aerobic glycolysis: The Warburg effect revisited. *BMC Systems Biology,* 4**,** 58.

VENDRAMIN, R., LITCHFIELD, K. & SWANTON, C. 2021. Cancer evolution: Darwin and beyond. *Embo j,* 40**,** e108389.

VINCENT, E. E., SERGUSHICHEV, A., GRISS, T., GINGRAS, M. C., SAMBORSKA, B., NTIMBANE, T., COELHO, P. P., BLAGIH, J., RAISSI, T. C., CHOINIÈRE, L., BRIDON, G., LOGINICHEVA, E., FLYNN, B. R., THOMAS, E. C., TAVARÉ, J. M., AVIZONIS, D., PAUSE, A., ELDER, D. J., ARTYOMOV, M. N. & JONES, R. G. 2015. Mitochondrial Phosphoenolpyruvate Carboxykinase Regulates Metabolic Adaptation and Enables Glucose-Independent Tumor Growth. *Mol Cell,* 60**,** 195-207.

WANG, Y. & PATTI, G. J. 2023. The Warburg effect: a signature of mitochondrial overload. *Trends in Cell Biology*.

WANG, Y., STANCLIFFE, E., FOWLE-GRIDER, R., WANG, R., WANG, C., SCHWAIGER-HABER, M., SHRIVER, L. P. & PATTI, G. J. 2022. Saturation of the mitochondrial NADH shuttles drives aerobic glycolysis in proliferating cells. *Molecular Cell,* 82**,** 3270-3283.e9.

WARBURG, O. 1925. The Metabolism of Carcinoma Cells1. *The Journal of Cancer Research,* 9**,** 148-163.

WIESE, E. K., HITOSUGI, S., LOA, S. T., SREEDHAR, A., ANDRES-BECK, L. G., KURMI, K., PANG, Y. P., KARNITZ, L. M., GONSALVES, W. I. & HITOSUGI, T. 2021. Enzymatic activation of pyruvate kinase increases cytosolic oxaloacetate to inhibit the Warburg effect. *Nat Metab,* 3**,** 954-968.

WILSON, J. E. 2003. Isozymes of mammalian hexokinase: structure, subcellular localization and metabolic function. *J Exp Biol,* 206**,** 2049-57.

WISE, D. R., DEBERARDINIS, R. J., MANCUSO, A., SAYED, N., ZHANG, X.-Y., PFEIFFER, H. K., NISSIM, I., DAIKHIN, E., YUDKOFF, M., MCMAHON, S. B. & THOMPSON, C. B. 2008. Myc regulates a transcriptional program that stimulates mitochondrial glutaminolysis and leads to glutamine addiction. *Proceedings of the National Academy of Sciences,* 105**,** 18782-18787.

XIAO, Y., YU, T. J., XU, Y., DING, R., WANG, Y. P., JIANG, Y. Z. & SHAO, Z. M. 2023. Emerging therapies in cancer metabolism. *Cell Metab,* 35**,** 1283-1303.

YANG, C., KO, B., HENSLEY, C. T., JIANG, L., WASTI, A. T., KIM, J., SUDDERTH, J., CALVARUSO, M. A., LUMATA, L., MITSCHE, M., RUTTER, J., MERRITT, M. E. & DEBERARDINIS, R. J. 2014. Glutamine oxidation maintains the TCA cycle and cell survival during impaired mitochondrial pyruvate transport. *Mol Cell,* 56**,** 414-424.

YANG, L., GARCIA CANAVERAS, J. C., CHEN, Z., WANG, L., LIANG, L., JANG, C., MAYR, J. A., ZHANG, Z., GHERGUROVICH, J. M., ZHAN, L., JOSHI, S., HU, Z., MCREYNOLDS, M. R., SU, X., WHITE, E., MORSCHER, R. J. & RABINOWITZ, J. D. 2020. Serine Catabolism Feeds NADH when Respiration Is Impaired. *Cell Metab,* 31**,** 809-821.e6.

YANG, M. & VOUSDEN, K. H. 2016. Serine and one-carbon metabolism in cancer. *Nat Rev Cancer,* 16**,** 650-62.

YING, H., KIMMELMAN, A. C., LYSSIOTIS, C. A., HUA, S., CHU, G. C., FLETCHER-SANANIKONE, E., LOCASALE, J. W., SON, J., ZHANG, H., COLOFF, J. L., YAN, H., WANG, W., CHEN, S., VIALE, A., ZHENG, H., PAIK, J. H., LIM, C., GUIMARAES, A. R., MARTIN, E. S., CHANG, J., HEZEL, A. F., PERRY, S. R., HU, J., GAN, B., XIAO, Y., ASARA, J. M., WEISSLEDER, R., WANG, Y. A., CHIN, L., CANTLEY, L. C. & DEPINHO, R. A. 2012. Oncogenic Kras maintains pancreatic tumors through regulation of anabolic glucose metabolism. *Cell,* 149**,** 656-70.

YING, M., YOU, D., ZHU, X., CAI, L., ZENG, S. & HU, X. 2021. Lactate and glutamine support NADPH generation in cancer cells under glucose deprived conditions. *Redox Biol,* 46**,** 102065.

ZHANG, B., ZHENG, A., HYDBRING, P., AMBROISE, G., OUCHIDA, A. T., GOINY, M., VAKIFAHMETOGLU-NORBERG, H. & NORBERG, E. 2017. PHGDH Defines a Metabolic Subtype in Lung Adenocarcinomas with Poor Prognosis. *Cell Reports,* 19**,** 2289-2303.

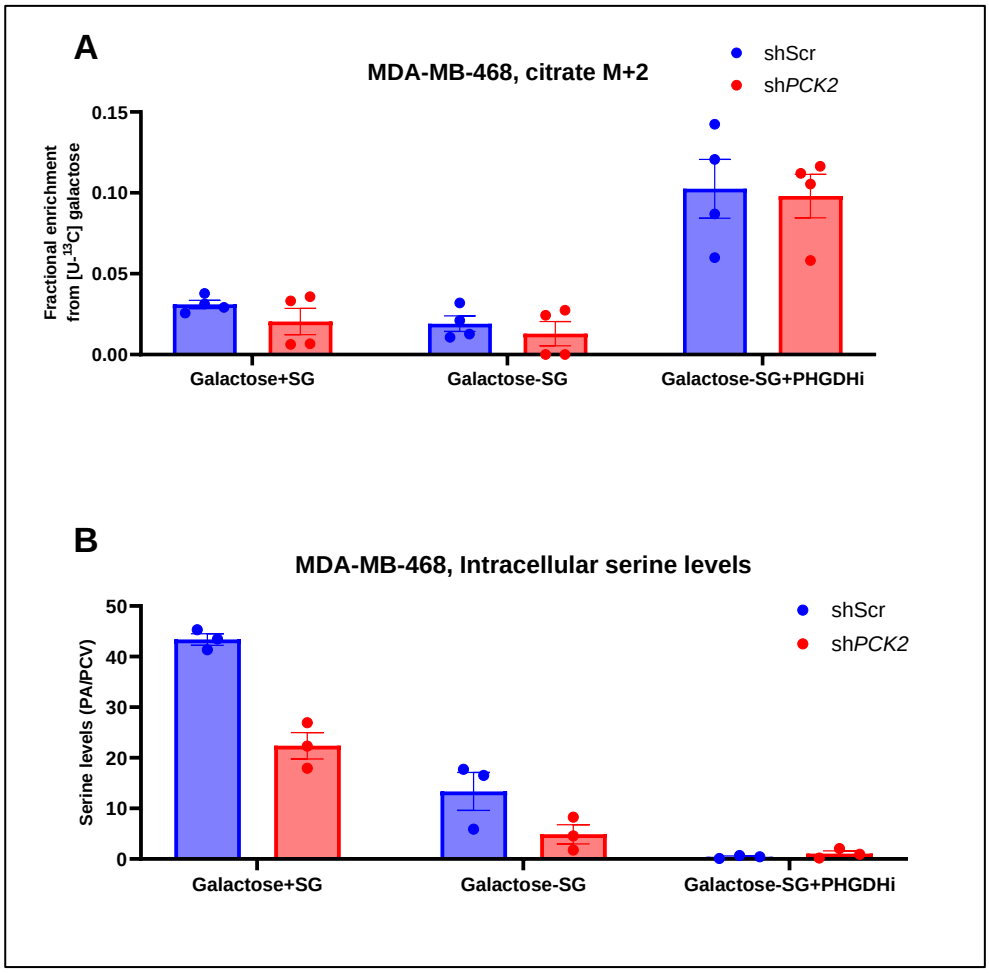
ZHENG, Y., LIN, T. Y., LEE, G., PADDOCK, M. N., MOMB, J., CHENG, Z., LI, Q., FEI, D. L., STEIN, B. D., RAMSAMOOJ, S., ZHANG, G., BLENIS, J. & CANTLEY, L. C. 2018. Mitochondrial One-Carbon Pathway Supports Cytosolic Folate Integrity in Cancer Cells. *Cell,* 175**,** 1546-1560.e17.

ZHU, H., BI, D., ZHANG, Y., KONG, C., DU, J., WU, X., WEI, Q. & QIN, H. 2022. Ketogenic diet for human diseases: the underlying mechanisms and potential for clinical implementations. *Signal Transduct Target Ther,* 7**,** 11.

ZHU, J., MA, J., WANG, X., MA, T., ZHANG, S., WANG, W., ZHOU, X. & SHI, J. 2016. High Expression of PHGDH Predicts Poor Prognosis in Non–Small Cell Lung Cancer. *Translational Oncology,* 9**,** 592-599.

APPENDICES

Appendix 1: Extended data related to chapter 3.



Supplementary Figure 1. A. Fractional enrichment from [U-^{13}C] galactose into M+2 citrate as measured with LC-MS in MDA-MB-468 cells sh*Scr* and sh*PCK2* when cultured in galactose media ± serine/glycine and treated with 15µM PHGDHi. **B.** Intracellular levels of serine presented as peak areas and normalised to packed cell volume (PCV) in MDA-MB-468 cells. **A-B** each dot represent an independent experiment from at least 3 replicate wells.

Appendix 2: PARK7/DJ-1 promotes pyruvate dehydrogenase activity and maintains Treg homeostasis during ageing

DANILEVICIUTE, E., ZENG, N., CAPELLE, C. M., PACZIA, N., GILLESPIE, M. A., KURNIAWAN, H., **BENZARTI, M**., MERZ, M. P., COOWAR, D., FRITAH, S., VOGT WEISENHORN, D. M., GOMEZ GIRO, G., GRUSDAT, M., BARON, A., GUERIN, C., FRANCHINA, D. G., LÉONARD, C., DOMINGUES, O., DELHALLE, S., WURST, W., TURNER, J. D., SCHWAMBORN, J. C., MEISER, J., KRÜGER, R., RANISH, J., BRENNER, D., LINSTER, C. L., BALLING, R., OLLERT, M. & HEFENG, F. Q. 2022. PARK7/DJ-1 promotes pyruvate dehydrogenase activity and maintains Treg homeostasis during ageing. ***Nature Metabolism***, 4, 589-607.

DOI: https://doi.org/10.1038/s42255-022-00576-y

Personal contribution: The key finding in this research article was to show the regulatory function DJ-1 has on pyruvate dehydrogenase (PDH) in regulatory T cells (Tregs). I contributed to this research with the data presented in **Fig. 5G** where I helped plan the experiments to perform targeted metabolomics on Tregs isolated from *DJ-1*$^{+/+}$ *DJ-1*$^{-/-}$mice using [U-^{13}C] glucose and then analysed the data to showcase the reduction in the relative flux to M+2 citrate in DJ-1 KOs and therefore confirming the regulation of PDH by DJ-1. I also reviewed the manuscript prior to submission.

nature metabolism

ARTICLES

https://doi.org/10.1038/s42255-022-00576-y

Check for updates

PARK7/DJ-1 promotes pyruvate dehydrogenase activity and maintains T_{reg} homeostasis during ageing

Egle Danileviciute[1,2,3,16], Ni Zeng[1,3,16], Christophe M. Capelle[1,3], Nicole Paczia[2], Mark A. Gillespie[4], Henry Kurniawan[1], Mohaned Benzarti[3,5], Myriam P. Merz[1,3], Djalil Coowar[2], Sabrina Fritah[6], Daniela Maria Vogt Weisenhorn[7,8], Gemma Gomez Giro[2], Melanie Grusdat[1], Alexandre Baron[1], Coralie Guerin[1], Davide G. Franchina[1,3], Cathy Léonard[1], Olivia Domingues[1], Sylvie Delhalle[1], Wolfgang Wurst[7,8,9,10], Jonathan D. Turner[1], Jens Christian Schwamborn[2], Johannes Meiser[5], Rejko Krüger[2,11,12], Jeff Ranish[4], Dirk Brenner[1,2,13], Carole L. Linster[2], Rudi Balling[2,14], Markus Ollert[1,13] and Feng Q. Hefeng[1,2,15] ✉

Pyruvate dehydrogenase (PDH) is the gatekeeper enzyme of the tricarboxylic acid (TCA) cycle. Here we show that the deglycase DJ-1 (encoded by *PARK7*, a key familial Parkinson's disease gene) is a pacemaker regulating PDH activity in CD4$^+$ regulatory T cells (T_{reg} cells). DJ-1 binds to PDHE1-β (PDHB), inhibiting phosphorylation of PDHE1-α (PDHA), thus promoting PDH activity and oxidative phosphorylation (OXPHOS). *Park7* (*Dj-1*) deletion impairs T_{reg} survival starting in young mice and reduces T_{reg} homeostatic proliferation and cellularity only in aged mice. This leads to increased severity in aged mice during the remission of experimental autoimmune encephalomyelitis (EAE). *Dj-1* deletion also compromises differentiation of inducible T_{reg} cells especially in aged mice, and the impairment occurs via regulation of PDHB. These findings provide unforeseen insight into the complicated regulatory machinery of the PDH complex. As T_{reg} homeostasis is dysregulated in many complex diseases, the DJ-1–PDHB axis represents a potential target to maintain or re-establish T_{reg} homeostasis.

Mitochondria are the organelle providing cellular bioenergy through TCA, OXPHOS and fatty acid oxidation[1,2]. Compelling evidence shows that mitochondrial dysfunction contributes to several major neurological diseases including Parkinson's disease (PD)[3]. In patients with PD, a particular deficiency in mitochondrial complex I (MCI) activity or general mitochondrial functions is described[4,5], and disruption of MCI leads to progressive Parkinsonism in an animal model[6]. The activity and maintenance of MCI is regulated by DJ-1 (encoded by *PARK7*, a key risk gene for early-onset familial PD[7]) via binding to its subunits[8]. As a consequence, murine or human cells that are devoid of DJ-1 showed mitochondrial defects affecting either mitochondrial respiration or integrity[9,10]. Our current understanding of the functions of DJ-1 in mitochondria is essentially based on data from flies[11], immortalised neurectodermal lines and primary or derived neurons[12,13]. However, these studies do not allow extrapolation of whether DJ-1 is also involved in the regulation of mitochondrial functions in the immune system, in which mitochondrial dysfunction has been linked to autoimmune diseases[14]. Meanwhile, a potential contribution of the peripheral immune system to PD pathogenesis has been postulated[15]. We therefore hypothesized that assessing the functions of DJ-1 in immune cells could be valuable for better understanding PD pathogenesis.

As DJ-1 protects dopaminergic neurons from oxidative stress-induced cell death, the influence of DJ-1 on resident glia in the central nervous system has also been investigated[16]. Deletion of *Dj-1* enhances activation of astrocytes and microglia, possibly through a signal transducer and activator of transcription (STAT) signalling pathway[17]. In macrophages, DJ-1 interacts with $p47^{phox}$, a subunit of NADPH oxidase[18,19]. Thus far, it still remains elusive whether and how DJ-1 is involved in the regulation of mitochondrial energetic metabolism on a molecular level and whether this could be potentially important for the physiological role of adaptive immune cells, for example, subsets of CD4$^+$ T cells. While *Dj-1* deletion impairs differentiation of inducible T_{reg} cells (iT_{reg} cells), it enhances the frequency of natural T_{reg} cells (nT_{reg} cells)[20]. T_{reg} cells

[1]Department of Infection and Immunity, Luxembourg Institute of Health (LIH), Esch-sur-Alzette, Luxembourg. [2]Luxembourg Centre for Systems Biomedicine, University of Luxembourg, Belvaux, Luxembourg. [3]Faculty of Science, Technology and Medicine, University of Luxembourg, Esch-sur-Alzette, Luxembourg. [4]Institute for Systems Biology, Seattle, WA, USA. [5]Cancer Metabolism Group, Department of Cancer Research, LIH, Luxembourg, Luxembourg. [6]NORLUX Neuro-Oncology Laboratory, Department of Cancer Research, LIH, Luxembourg, Luxembourg. [7]Helmholtz Zentrum München—German Research Center for Environmental Health, Institute of Developmental Genetics, Neuherberg, Germany. [8]Technische Universität München-Weihenstephan, Neuherberg/Munich, Germany. [9]German Center for Neurodegenerative Diseases (DZNE), Site Munich, Munich, Germany. [10]Munich Cluster for Systems Neurology (SyNergy), Munich, Germany. [11]Centre Hospitalier de Luxembourg, Luxembourg, Luxembourg. [12]Transversal Translational Medicine, Strassen, Luxembourg. [13]Department of Dermatology and Allergy Center, Odense Research Center for Anaphylaxis, University of Southern Denmark, Odense, Denmark. [14]Institute of Molecular Psychiatry, University of Bonn, Bonn, Germany. [15]Institute of Medical Microbiology, University Hospital Essen, University of Duisburg-Essen, Essen, Germany. [16]These authors contributed equally: Egle Danileviciute, Ni Zeng. ✉e-mail: feng.he@lih.lu

are critical to maintain immune homeostasis and self-tolerance in both physiological and pathological conditions[21]. A previous study of DJ-1 functions in T_{reg} cells was performed in young adult mice only[20]. Ageing, however, is the biggest risk factor for PD[22]. We therefore undertook this study to examine the role of DJ-1 in T_{reg} suppressive function (TSF) and/or cellularity, especially during ageing.

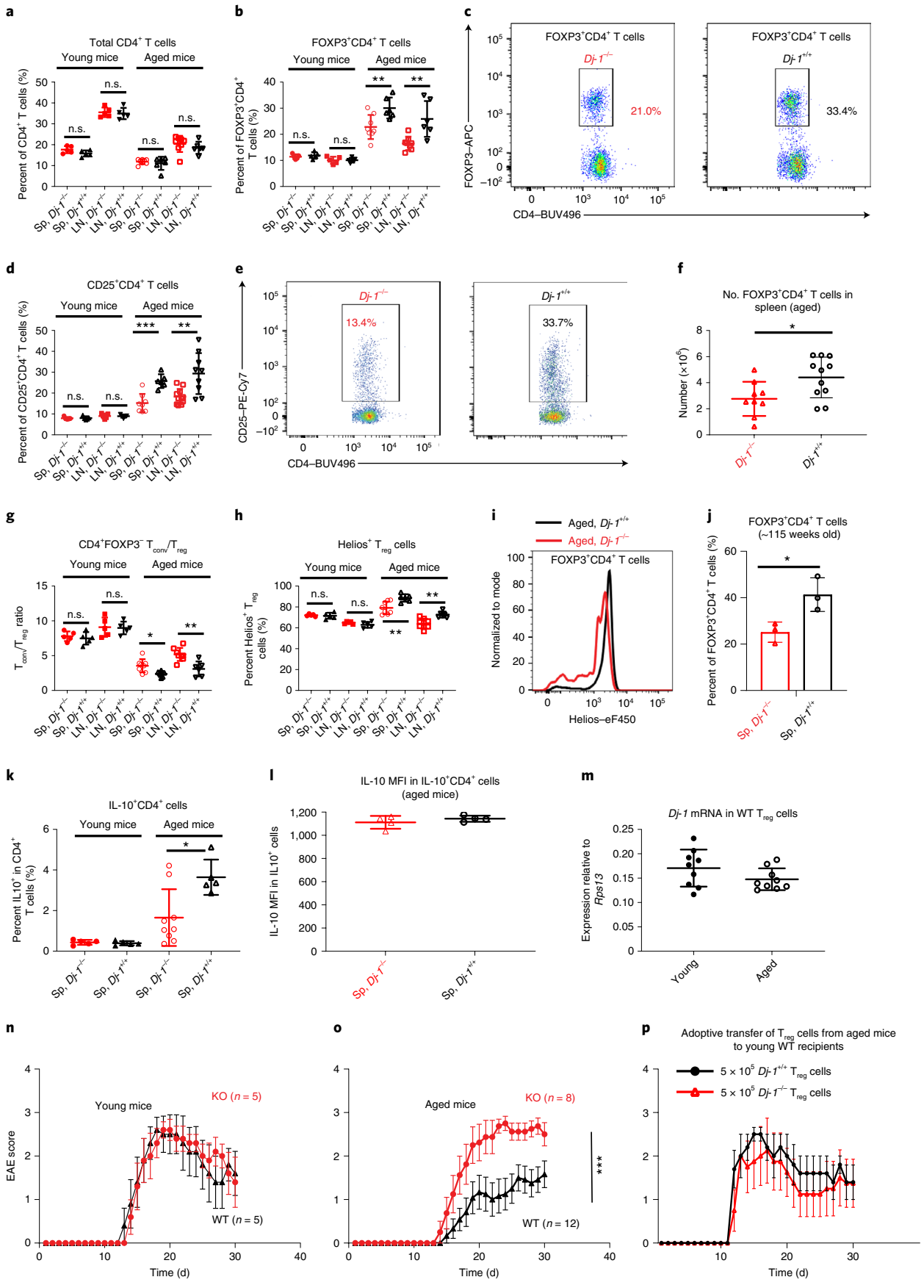
Results

Prediction of *DJ-1* as a potential key gene in T_{reg} cells. In our published time series transcriptome dataset during the first 6 h of T cell receptor (TCR) stimulation[23], *DJ-1* was the most highly expressed gene among 20 reported PD-related genes[24] in both unstimulated and stimulated human T_{reg} cells and $CD4^+CD25^-$ effector T cells (T_{eff} cells) (for isolation and culture details, refer to the Methods and Extended Data Fig. 1a; for T_{reg} characterisation, refer to Extended Data Fig. 2a–c). Furthermore, by using the so-called 'queen bee-surrounding principle' network analysis strategy, derived from the 'guilt-by-association' concept[25], we analysed the *DJ-1* subnetwork from the T_{reg}-specific correlation network[23]. Although the first-degree neighbours of *DJ-1* were not significantly enriched in the genes potentially related to T cell function[23], the second-degree neighbours[25] were highly enriched for well-known T_{reg}-relevant genes (Extended Data Fig. 1b, $P = 4.3 \times 10^{-12}$, cumulative binomial distribution), such as *FOXP3*, *CTLA4*, *ICOS*, *GATA3* and *CD44* (ref. [21]). None of the other known PD genes were highly expressed in T_{reg} and T_{eff} cells and significantly surrounded by potential T cell-related genes in the T_{reg}-specific network (Supplementary Table 1). Together, this network analysis predicts that DJ-1 might play a role in regulating T_{reg} function and/or cellularity.

***Dj-1* deletion impairs T_{reg} cellularity in aged mice.** To test whether DJ-1 affects T_{reg} cellularity, we analysed the T_{reg} compartment in *Dj-1*$^{-/-}$ (knockout (KO)) mice as described elsewhere[26]. As DJ-1 is one of the key PD familial genes and ageing is the major risk factor of PD[22], we investigated both young adult mice (in short, 'young mice', 8–12 weeks of age) and older mice (in short, 'aged mice', ~45 weeks of age unless otherwise specified). For both young and aged mice, the frequency of total $CD4^+$ T cells in the spleen and peripheral lymph nodes (LNs) was not significantly altered between *Dj-1*-KO mice and *Dj-1*$^{+/+}$ littermate controls (wild type (WT); Fig. 1a). The frequency of T_{reg} cells ($CD4^+FOXP3^+$ T cells) among $CD4^+$ T cells was also unchanged between young *Dj-1*-KO and WT mice. Consistent with other reports[27], the frequency of T_{reg} cells among $CD4^+$ cells increased with age in WT mice (Fig. 1b). Notably, the frequency of T_{reg} cells was significantly lower in aged *Dj-1*-KO mice than in age- and sex-matched WT mice (Fig. 1b,c). The percentages of $CD4^+CD25^+$ T cells among $CD4^+$ T cells showed similar changes as those of T_{reg} cells (Fig. 1d,e). The number of splenic T_{reg} cells was also reduced in aged *Dj-1*-KO mice (Fig. 1f). The ratio between $CD4^+FOXP3^-$ (T_{conv}) and T_{reg} cells increased in aged mice but not in young *Dj-1*-KO versus WT mice (Fig. 1g). As Helios is a marker of nT_{reg} cells, we also analysed the expression of Helios. Interestingly, the percentages of Helios$^+$ cells among T_{reg} cells also declined in aged mice but not in young *Dj-1*-KO versus WT mice (Fig. 1h,i). The frequency of T_{reg} cells was still lower in ~115-week-old (~26-month-old) *Dj-1*-KO versus WT mice (Fig. 1j). The frequency of splenic interleukin (IL)-10-producing $CD4^+$ cells following in vitro stimulation was also lower in aged *DJ-1*-KO mice than in aged WT mice (Fig. 1k). Interestingly, the mean fluorescence intensity (MFI) of IL-10 in IL-10-producing $CD4^+$ T cells did not decline in aged *Dj-1*-KO mice compared to aged WT mice (Fig. 1l), indicating that the suppressive function of individual T_{reg} cells was uncompromised. Furthermore, the age-dependent effect of *Dj-1* deletion on T_{reg} cellularity was not simply caused by the differential expression of *Dj-1* between young and aged WT mice (Fig. 1m). Despite reduced T_{reg} cellularity, aged *Dj-1*-KO mice did not develop spontaneous autoimmunity, possibly due to compensation by imbalanced ratios between naive and memory T cell subsets[28].

Functional T_{reg} cells are critical for the remission phase of EAE[29], a murine model of multiple sclerosis. We therefore evaluated the in vivo effects of reduced T_{reg} accumulation in *Dj-1*-KO mice by using the myelin oligodendrocyte glycoprotein (MOG_{35-55})-induced EAE model[30]. In agreement with T_{reg} cellularity phenotypes in young mice, no obvious difference in clinical scores was observed between young *Dj-1*-KO and WT mice (Fig. 1n). Notably, aged *Dj-1*-KO mice exhibited deteriorated EAE symptoms during T_{reg}-dependent remission compared to aged WT mice (Fig. 1o). To assess whether the worsened symptoms were attributable to reduced T_{reg} number or compromised TSF, we performed adoptive transfer of the same number of T_{reg} cells isolated from aged *Dj-1*-KO mice versus aged WT mice into young WT recipients before inducing EAE. Interestingly, no significant difference in the EAE course was observed following the injection of *Dj-1*-KO or WT T_{reg} cells (Fig. 1p), indicating that the worsened symptoms observed in the whole body of aged *Dj-1*-KO mice were not caused by a declined TSF of individual *Dj-1*-KO cells. In agreement with the in vivo data, our in vitro suppressive assay showed that TSF was undamaged in individual *Dj-1*-KO T_{reg} cells regardless of age (Extended Data Fig. 3a,b). The lack of effect on TSF was consistent with results from a previous study[20] in which the authors also investigated TSF of *Dj-1*-KO cells but only analysed young mice. To further characterize T_{reg} cells, we investigated the protein expression of known key T_{reg} effector molecules, such as FOXP3, CTLA4 and IL-2RA (CD25), in T_{reg} cells. Although the fraction of CTLA4$^+$ cells among *Dj-1*-KO versus WT T_{reg} cells of aged mice was similar (Extended Data Fig. 3c), the MFI of CTLA4, FOXP3 and CD25 was modestly but significantly

Fig. 1 | *Dj-1* deletion compromises T_{reg} cellularity in aged mice. a, Percentages of $CD4^+$ T cells among living lymphocyte singlets from the spleen (Sp) or peripheral LNs (young KO mice, $n = 5$; young WT mice, $n = 5$; aged KO mice, $n = 8$; aged WT mice, $n = 6$; for aged mice, data were pooled from two independent experiments). **b**,**d**, Percentages of $FOXP3^+$ (**b**) or $CD25^+$ (**d**) cells among $CD4^+$ T cells (for CD25 results, *n* of young mice is the same as that in **a**, but, for aged mice: spleen (KO, $n = 8$; WT, $n = 6$), LN (KO, $n = 11$; WT, $n = 9$); data were pooled from two independent experiments). Individual significant *P* values are provided as the same order of comparisons (left to right, applicable to all panels): $^{**}P = 0.00955$ and $^{**}P = 0.00388$ (**b**); $^{***}P = 0.000369$ and $^{**}P = 0.00911$ (**d**). **c**,**e**, Representative flow cytometry (FCM) plots of $FOXP3^+$ (**c**) or $CD25^+$ (**e**) cells among $CD4^+$ T cells in the spleen of aged mice. **f**, Number of T_{reg} cells in the spleen (estimated from splenocytes; KO, $n = 11$; WT, $n = 9$; pooled data). $^{*}P = 0.0218$. **g**, Ratios between $CD4^+FOXP3^-$ and $CD4^+FOXP3^+$ cells. $^{*}P = 0.0155$ and $^{**}P = 0.00225$. **h**, Percentages of Helios$^+$ cells among T_{reg} cells. $^{**}P = 0.00477$ and $^{**}P = 0.0021$. **i**, Representative histogram overlay of Helios expression among T_{reg} cells. **j**, Percentages of $FOXP3^+$ cells among splenic $CD4^+$ T cells from very old mice ($n = 3$ per group). $^{*}P = 0.0296$. **k**, Percentages of IL-10-expressing cells in $CD4^+$ T cells after in vitro stimulation for 5 h (young, KO, $n = 5$; young, WT, $n = 5$; aged, KO, $n = 9$; aged, WT, $n = 5$). $^{*}P = 0.0143$. **l**, IL-10 MFI of IL-10-positive $CD4^+$ T cells after in vitro stimulation (of note, we only displayed MFI from the same experiment for comparability; $n = 4$ per group). **m**, Quantification of *Dj-1* expression ($n = 3$ mice per group and three technical replicates per mouse). **n**,**o**, EAE scores of young (**n**) or aged (**o**) mice. $n = 5$ for the young group, $n = 8$ or 12 for aged *Dj-1*-KO or WT mice, respectively. $^{***}P = 5.053 \times 10^{-6}$. **p**, EAE scores following adoptive transfer of 5×10^5 T_{reg} cells from aged KO or WT mice (~74 weeks old) into young WT recipients ($n = 4$ or 5). Results represent at least four (**a**–**i**), two (**k**–**o**) and one (**j**,**p**) independent experiments. Data are mean ± s.d. *P* values were determined by two-tailed Student's *t*-test. n.s. or unlabelled, not significant; $^{*}P \leq 0.05$, $^{**}P \leq 0.01$ and $^{***}P \leq 0.001$.


a
Total CD4+ T cells
Young mice
Aged mice
Percent of CD4+ T cells (%)
n.s.
Sp, Dj-1−/−
Sp, Dj-1+/+
LN, Dj-1−/−
LN, Dj-1+/+
b
FOXP3+CD4+ T cells
Percent of FOXP3+CD4+ T cells (%)
**
c
FOXP3+CD4+ T cells
Dj-1−/−
21.0%
Dj-1+/+
33.4%
FOXP3–APC
CD4–BUV496
d
CD25+CD4+ T cells
Percent of CD25+CD4+ T cells (%)
***
e
Dj-1−/−
13.4%
Dj-1+/+
33.7%
CD25–PE-Cy7
CD4–BUV496
f
No. FOXP3+CD4+ T cells in spleen (aged)
Number (×10^6)
*
g
CD4+FOXP3− Tconv/Treg
Tconv/Treg ratio
h
Helios+ Treg cells
Percent Helios+ Treg cells (%)
i
Aged, Dj-1+/+
Aged, Dj-1−/−
FOXP3+CD4+ T cells
Normalized to mode
Helios–eF450
j
FOXP3+CD4+ T cells (~115 weeks old)
Percent of FOXP3+CD4+ T cells (%)
k
IL-10+CD4+ cells
Percent IL10+ in CD4+ T cells (%)
l
IL-10 MFI in IL-10+CD4+ cells (aged mice)
IL-10 MFI in IL10+ cells
m
Dj-1 mRNA in WT Treg cells
Expression relative to Rps13
Young
Aged
n
Young mice
KO (n = 5)
WT (n = 5)
EAE score
Time (d)
o
Aged mice
KO (n = 8)
WT (n = 12)
p
Adoptive transfer of Treg cells from aged mice to young WT recipients
5 × 10^5 Dj-1+/+ Treg cells
5 × 10^5 Dj-1−/− Treg cells

increased in *Dj-1*-KO splenic T_{reg} cells (Extended Data Fig. 3c–e). Together, these data suggested that *Dj-1* deletion impairs T_{reg} cellularity in aged mice.

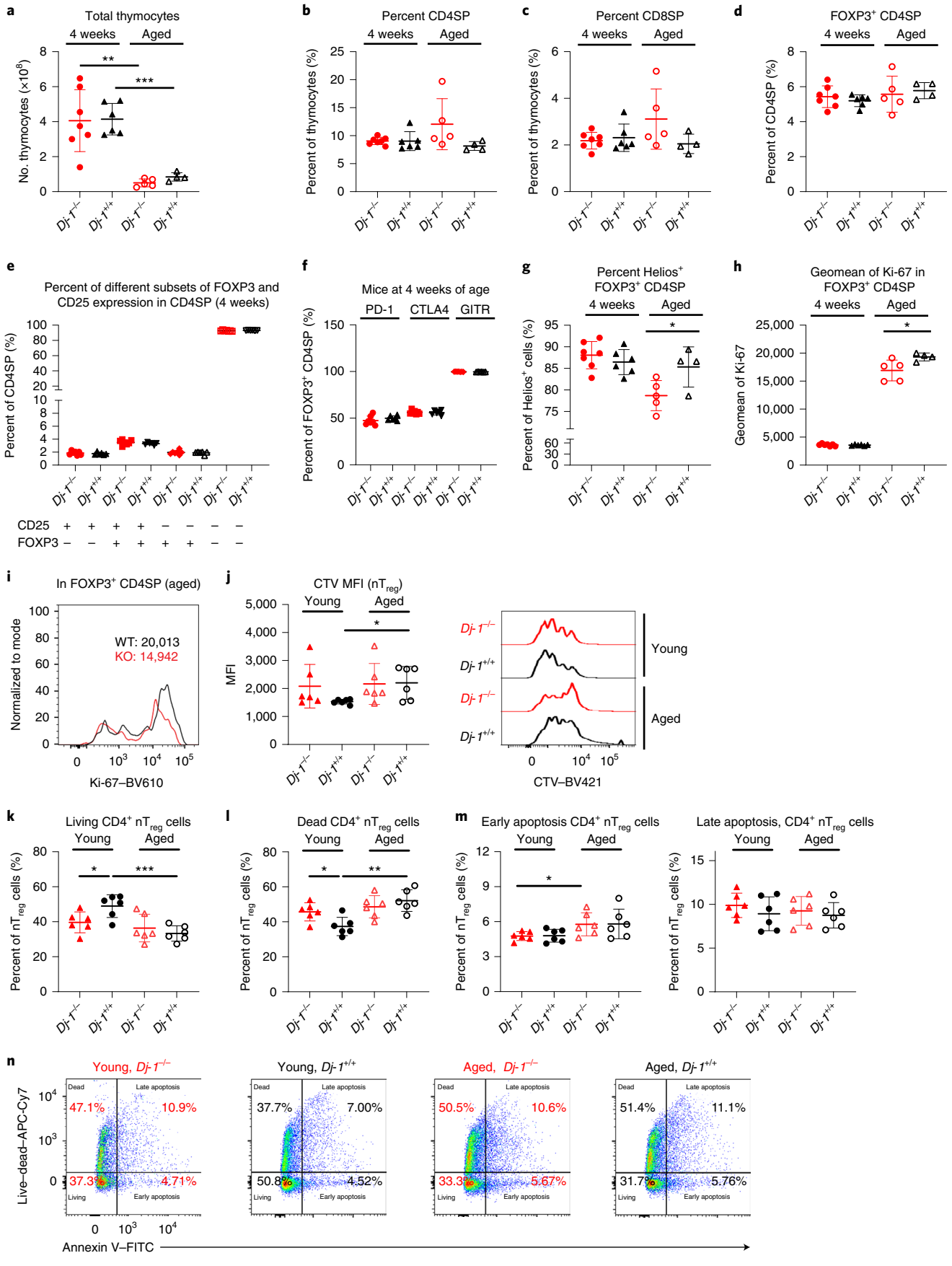
***Dj-1* deletion compromises nT_{reg} survival but not development.** Decreased T_{reg} accumulation in aged mice could be caused by an impairment either in T_{reg} development, homeostatic proliferation or survival maintenance. To test these possibilities, we assessed thymic T_{reg} cells in 4-week-old mice, as thymocyte numbers peak in mice aged 4–6 weeks and gradually involute afterward[31]. In 4-week-old mice, we did not observe any difference between *Dj-1*-KO and WT mice in numbers of total thymocytes, single-positive $CD4^+$ T cells (CD4SP), single-positive $CD8^+$ T cells (CD8SP) or the percentages of T_{reg} cells among CD4SP (Fig. 2a–d). We also did not find any difference in the four subsets determined by the combination of positive or negative expression of CD25 and FOXP3 (Fig. 2e). Neither key T_{reg} markers nor proliferation or functional markers, such as Helios, Ki-67 or PD-1, CTLA4 and GITR, exhibited any difference between 4-week-old *Dj-1*-KO and WT mice (Fig. 2f–h). These data suggest that *Dj-1* deletion does not influence T_{reg} development in juvenile mice before thymic involution. As decreased T_{reg} accumulation only appeared in aged *Dj-1*-KO mice, we also analysed thymocyte composition in aged mice. As the thymus is already atrophied in 45-week-old mice[31], total thymocyte numbers were dramatically lower in aged WT mice than in 4-week-old WT mice (Fig. 2a). However, the number of thymocytes was comparable between aged *Dj-1*-KO mice and aged WT mice (Fig. 2a). No difference was observed between aged KO and WT mice regarding the frequency of CD4SP, CD8SP and T_{reg} cells among CD4SP (Fig. 2b–d). Notably, *Dj-1* ablation selectively decreased the frequency of Helios-expressing T_{reg} cells (Fig. 2g) and modestly but significantly reduced homeostatic proliferation (Ki-67) of T_{reg} cells (Fig. 2h,i). Interestingly, the effect on proliferation disappeared when isolated T_{reg} cells were stimulated in vitro (Fig. 2j). To further delineate our observation on T_{reg} cellularity, we analysed apoptosis and survival of stimulated T_{reg} cells. As expected, the survival rate of nT_{reg} cells decreased during ageing (Fig. 2k–n). Surprisingly, the survival of *Dj-1*-KO versus WT nT_{reg} cells was compromised in young mice and remained quite constant in older mice (Fig. 2k–n). Reduced survival was accompanied by enhanced death of nT_{reg} cells from young *Dj-1*-KO versus WT mice (Fig. 2k–n). The frequency of early apoptotic cells was higher in nT_{reg} cells isolated from aged mice than in those from young mice, but no genotype-dependent effect was observed (Fig. 2m,n).

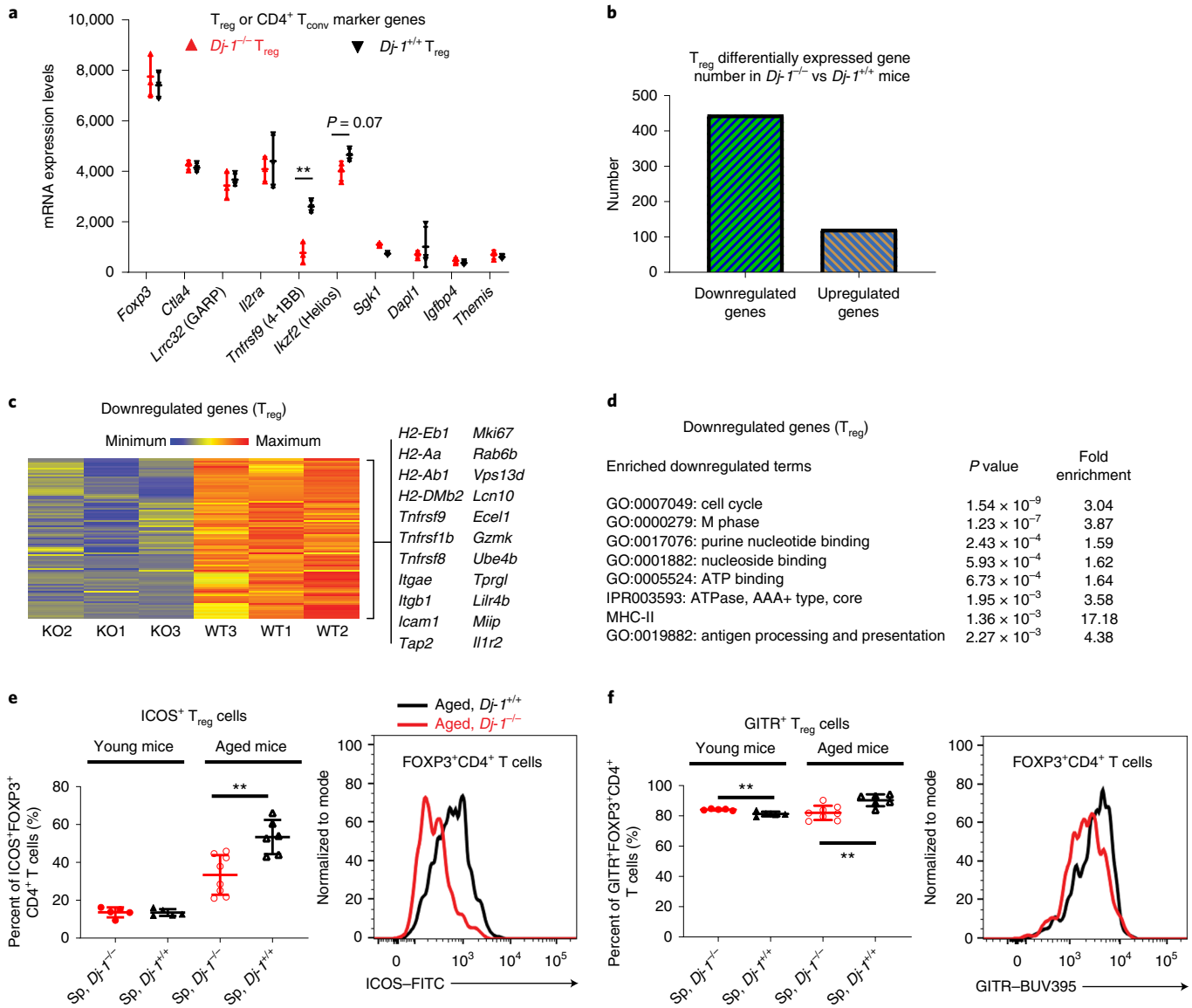
To further investigate whether the reduced T_{reg} cellularity in aged mice is regulated in a haematopoietic-intrinsic manner, we analysed T_{reg} cells in several bone marrow (BM) chimeras developed as described elsewhere by us[28]. The first BM chimeras were generated by transferring BM cells mixed from young $CD45.1^+$ *Dj-1*-WT and $CD45.2^+$ *Dj-1*-KO donors at a ratio of 1:1 into lethally irradiated young WT recipients. Unexpectedly, the frequency of T_{reg} cells among $CD4^+$ T cells was higher in *Dj-1*-KO-derived cells than that from cells of WT origin (Extended Data Fig. 4a,b). Next, we analysed other BM chimeras by transferring BM cells mixed from aged $CD45.2^+$ *Dj-1*-KO and $CD45.1^+$ *Dj-1*-WT donors into lethally irradiated young WT or KO recipients. Considering the ethic restriction (introducing lethal irradiation), we did not use aged recipients. Again, the frequency of T_{reg} cells was higher in *Dj-1*-KO-derived cells than that from cells of WT origin regardless of the type of recipient (Extended Data Fig. 4c). In short, these data indicate that the reduced T_{reg} cellularity in whole bodies of aged *Dj-1*-KO mice was also dependent on an ageing host microenvironment.

***Dj-1* deletion impairs nT_{reg} proliferation and activation.** The existence of a haematopoietic-extrinsic role of DJ-1 in regulating T_{reg} cellularity does not exclude other potential in-parallel nT_{reg}-intrinsic mechanisms. To explore these pathways, we performed transcriptomic analysis of sorted T_{reg} cells from aged *Dj-1*-KO and WT mice. As expected, T_{reg} signature genes were expressed much higher than T_{conv} signature genes[32] (Fig. 3a). Consistent with the view of DJ-1 as a transcriptional coactivator[33], *Dj-1*-deficient T_{reg} cells exhibited a much larger fraction of downregulated genes than of upregulated genes (Fig. 3b). In aged *Dj-1*-KO T_{reg} cells, genes involved in the cell cycle, especially the M phase, and proliferation were significantly enriched in the downregulated list (Fig. 3c,d). Moreover, *Dj-1* deletion reduced the transcription of many key T_{reg} genes[32] and major histocompatibility (MHC)-II-related genes (Fig. 3c). MHC-II genes are reported to be expressed in activated T cells of many species but not in mice[34]; possibly this has never been analysed thoroughly in aged mice. Concordantly, the homeostatic expression of activation markers in T_{reg} cells (Fig. 3e,f), such as that of GITR and ICOS, declined in aged *Dj-1*-KO mice versus aged WT mice. Transcript expression of one well-known costimulatory receptor, 4-1BB, also decreased (Fig. 3a). This unbiased transcriptome analysis demonstrates that *Dj-1* deficiency downregulates the pathways mediating T_{reg} homeostatic proliferation and activation. The reduced activation and proliferation of peripheral nT_{reg} cells from aged *Dj-1*-KO mice was in line with the reduced expression of proliferation and activation markers (for example, Ki-67 and Helios) in thymic T_{reg} cells. In conclusion, DJ-1 is critical for maintaining nT_{reg} cellularity by regulating nT_{reg} homeostatic activation and proliferation, evidently only in aged mice.

DJ-1 promotes PDH activity preferentially in resting T_{reg} cells. To further identify the detailed molecular mechanisms through which DJ-1 maintains T_{reg} cellularity, we examined the binding partners of DJ-1 in resting and activated human primary nT_{reg} cells by co-immunoprecipitation (co-IP)–mass spectrometry (MS) analysis. We found around 20 previously unidentified binding partners of DJ-1 in human nT_{reg} cells by employing a combination of five strict filtering criteria (Fig. 4a and Supplementary Table 2). Interestingly, five proteins regulating RNA splicing bound to DJ-1

Fig. 2 | *Dj-1* ablation compromises nT_{reg} survival in young mice but does not affect thymic T_{reg} development. a, Total thymocyte numbers of 4-week-old or aged *Dj-1*-KO and WT mice (young, KO, $n=7$; young, WT, $n=6$; aged, KO, $n=5$; aged, WT, $n=4$). $^{**}P=0.00133$ and $^{***}P=0.000108$. **b**,**c**, Percentages of CD4SP (**b**) and CD8SP (**c**) among thymocytes. **d**, Percentages of $FOXP3^+$ CD4SP. **e**, Percentages of the four subsets defined by the presence or absence of FOXP3 and CD25 in CD4SP from 4-week-old mice. **f**, Percentages of PD-1-, CTLA4- or GITR-expressing cells in $FOXP3^+$ CD4SP from 4-week-old mice. **g**, Percentages of $Helios^+$ $FOXP3^+$ CD4SP from 4-week-old or aged mice. $^{*}P=0.0437$. **h**, Geometric mean (geomean) (MFI) of Ki-67 in $FOXP3^+$ CD4SP from 4-week-old or aged mice. $^{*}P=0.0452$. **i**, Representative histogram overlay of Ki-67 expression in $FOXP3^+$ CD4SP between aged WT or *Dj-1*-KO mice. **j**, Geometric mean (MFI) of CellTrace Violet (CTV) in isolated peripheral $CD4^+CD25^+$ (nT_{reg}) cells stimulated with anti-CD3 antibody, anti-CD28 antibody and IL-2 for 3 d. Statistical plot (left) and representative FCM plot of CTV (right) (young, KO, $n=6$; young, WT, $n=6$; aged, KO, $n=6$; aged, WT, $n=6$). $^{*}P=0.0198$. **k**,**l**, Percentages of living (**k**) or dead (**l**) cells among isolated nT_{reg} cells stimulated with anti-CD3 antibody, anti-CD28 antibody and IL-2 for 3 d. $^{*}P=0.0274$ and $^{***}P=0.000638$ (**k**); $^{*}P=0.0198$ and $^{**}P=0.00120$ (**l**). **m**, Percentages of early (left) or late (right) apoptotic cells among isolated nT_{reg} cells stimulated with anti-CD3 antibody, anti-CD28 antibody and IL-2 for 3 d. $^{*}P=0.0422$. **n**, Representative FCM plots of live-dead and Annexin V staining of isolated nT_{reg} cells stimulated with anti-CD3 antibody, anti-CD28 antibody and IL-2 for 3 d. Results represent three (**a**–**i**) and two (**j**–**n**) independent experiments. Data are mean ± s.d. *P* values were determined by two-tailed Student's *t*-test. $^{*}P\leq0.05$, $^{**}P\leq0.01$ and $^{***}P\leq0.001$.


a
Total thymocytes
4 weeks
Aged
No. thymocytes (×10^8)
b
Percent CD4SP
Percent of thymocytes (%)
c
Percent CD8SP
d
FOXP3+ CD4SP
Percent of CD4SP (%)
e
Percent of different subsets of FOXP3 and CD25 expression in CD4SP (4 weeks)
CD25
FOXP3
f
Mice at 4 weeks of age
PD-1
CTLA4
GITR
Percent of FOXP3+ CD4SP (%)
g
Percent Helios+ FOXP3+ CD4SP
Percent of Helios+ cells (%)
h
Geomean of Ki-67 in FOXP3+ CD4SP
Geomean of Ki-67
i
In FOXP3+ CD4SP (aged)
Normalized to mode
WT: 20,013
KO: 14,942
Ki-67–BV610
j
CTV MFI (nTreg)
Young
Aged
MFI
CTV–BV421
k
Living CD4+ nTreg cells
Percent of nTreg cells (%)
l
Dead CD4+ nTreg cells
m
Early apoptosis CD4+ nTreg cells
Late apoptosis, CD4+ nTreg cells
n
Young, Dj-1−/−
Young, Dj-1+/+
Aged, Dj-1−/−
Aged, Dj-1+/+
Dead
Late apoptosis
Living
Early apoptosis
47.1%
10.9%
37.3%
4.71%
37.7%
7.00%
50.8%
4.52%
50.5%
10.6%
33.3%
5.67%
51.4%
11.1%
31.7%
5.76%
Live–dead–APC-Cy7
Annexin V–FITC



Enriched downregulated terms	*P* value	Fold enrichment
GO:0007049: cell cycle	1.54×10^{-9}	3.04
GO:0000279: M phase	1.23×10^{-7}	3.87
GO:0017076: purine nucleotide binding	2.43×10^{-4}	1.59
GO:0001882: nucleoside binding	5.93×10^{-4}	1.62
GO:0005524: ATP binding	6.73×10^{-4}	1.64
IPR003593: ATPase, AAA+ type, core	1.95×10^{-3}	3.58
MHC-II	1.36×10^{-3}	17.18
GO:0019882: antigen processing and presentation	2.27×10^{-3}	4.38

Fig. 3 | *Dj-1* deletion impairs T$_{reg}$ homeostatic proliferation and activation pathways in aged mice. a, mRNA expression of T$_{reg}$ signature genes and T$_{conv}$ signature genes in T$_{reg}$ cells freshly isolated from aged *Dj-1*-KO mice and age- and sex-matched WT littermates ($n = 3$ mice per group). Results are the summary of our microarray datasets. $^{**}P = 0.00272$. **b**, Numbers of differentially expressed upregulated and downregulated genes in *Dj-1*-KO versus WT T$_{reg}$ cells from aged mice. **c**, Heatmap showing relative abundance of selected differentially downregulated genes in T$_{reg}$ cells from aged *Dj-1*-KO versus WT littermates. Lilr4b also known as Lilrb4b. **d**, Selected significantly enriched gene ontology (GO) terms of downregulated genes in T$_{reg}$ cells from aged *Dj-1*-KO versus WT littermates. IPR, InterPro. **e**,**f**, Percentages of ICOS$^+$ (**e**) or GITR$^+$ (**f**) subsets of T$_{reg}$ cells (left) and representative histogram overlay of ICOS or GITR expression in T$_{reg}$ cells from aged WT or *Dj-1*-KO mice (right) (young, KO, $n = 5$; young, WT, $n = 5$; aged, KO, $n = 8$; aged, WT, $n = 6$). $^{**}P = 0.00282$ (**e**); $^{**}P = 0.00458$ and $^{**}P = 0.00426$ (**f**). Results represent three (**d**–**f**) independent experiments. Data are mean ± s.d. *P* values were determined by one-tailed modified Fisher's exact test without adjustment for multiple comparisons (from DAVID, **d**) or two-tailed Student's *t*-test (**a**–**c**,**e**,**f**). $^{*}P \leq 0.05$, $^{**}P \leq 0.01$ and $^{***}P \leq 0.001$.

preferentially in stimulated T$_{reg}$ cells compared to unstimulated T$_{reg}$ and T$_{eff}$ cells ($P = 2.8 \times 10^{-4}$, Fig. 4a and Supplementary Table 2). This is consistent with the dynamic binding behaviour of DJ-1 to RNA[35]: the binding occurs in a resting state and then dissociates following activation as shown in a neuroblastoma line. Our results confirmed 11 known DJ-1-binding partners identified from other cell types (Supplementary Table 3), demonstrating the reliability of the technique.

To prioritize the most promising candidates, we ranked the top 20 previously unidentified binding partners based on their preferential binding to DJ-1 relative to the immunoglobulin (Ig)G control (Fig. 4a). Unexpectedly, the top-ranked candidate was PDHB. Furthermore, PDHB also showed the highest fold change in binding affinity between unstimulated and stimulated T$_{reg}$ cells in the MS analysis (Supplementary Table 2). Following the DJ-1 co-IP–MS/MS identification of PDHB (Fig. 4a,b), we confirmed that DJ-1 bound to PDHB by co-IP–immunoblotting analysis and observed that the binding was predominant in T$_{reg}$ cells rather than in T$_{eff}$ cells (Fig. 4c). Moreover, using ImageStream analysis, we demonstrated that DJ-1 preferentially colocalized with PDHB more in T$_{reg}$ cells than in T$_{eff}$ cells, with or without anti-CD3 and anti-CD28 bead stimulation (Fig. 4d,e). Successful T cell stimulation, although only for 5 h, was confirmed by decreased expression of CD4 (Fig. 4f), as established by others[36]. Coincidently, transcript expression of *Dj-1*

and *Pdhb* was significantly correlated only in murine T_{reg} cells but not in other CD4$^+$ subsets[37] (Extended Data Fig. 5a,b). In sum, our data from cobinding, colocalization and coexpression strongly support the concept that DJ-1 binds to PDHB preferentially in T_{reg} cells relative to T_{eff} cells.

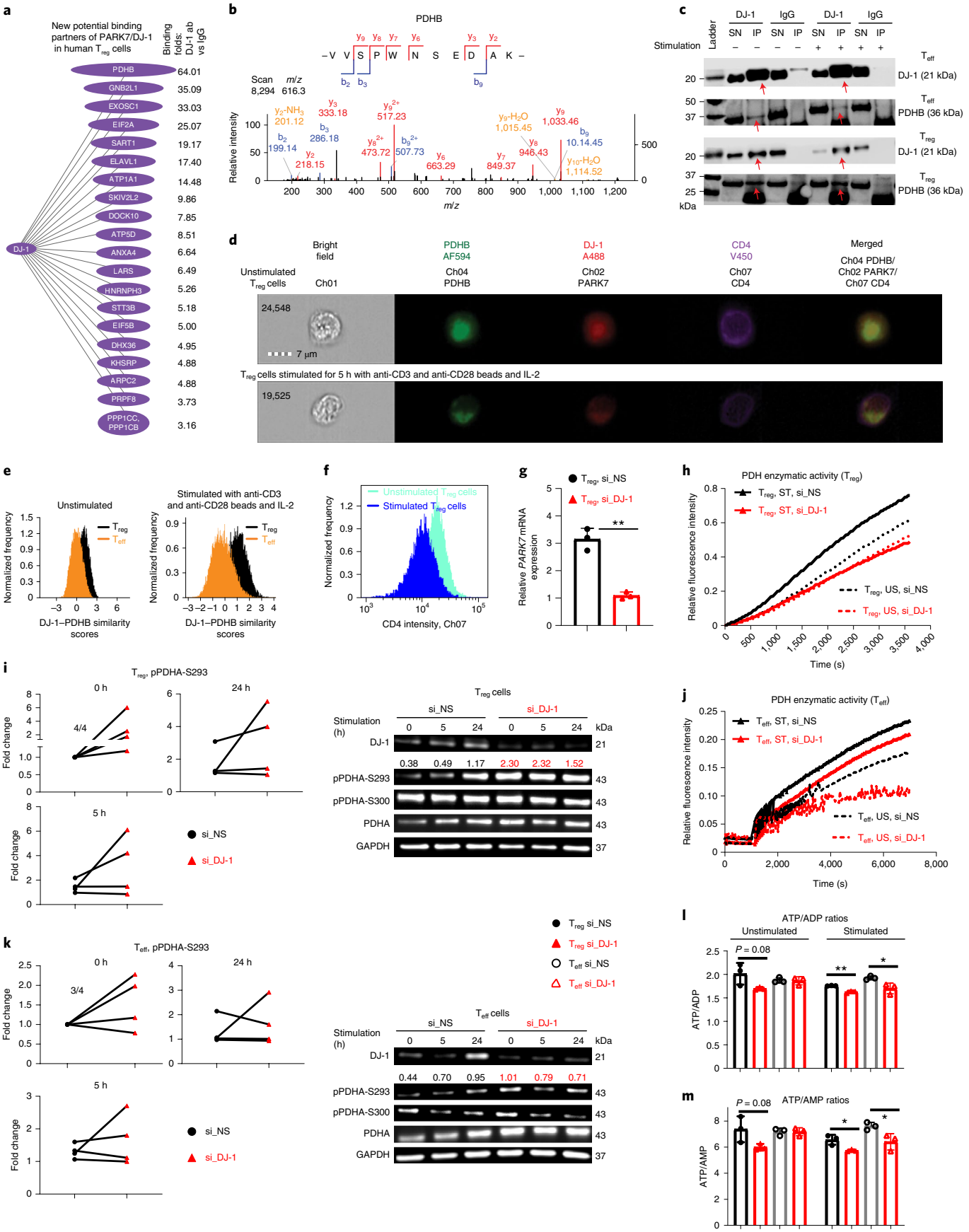
To further investigate whether the physical binding between DJ-1 and PDHB might have any functional consequences, we assessed PDH enzymatic activity. Interestingly, partial knockdown (KD) of *DJ-1* (Fig. 4g) already compromised PDH enzymatic activity in both resting and stimulated states of human T_{reg} cells (Fig. 4h). While stimulation increased PDH enzymatic activity in control (si_NS) T_{reg} cells, enhancement of PDH activity was not observed in stimulated versus unstimulated T_{reg} cells treated with small interfering (si)RNA against *DJ-1* (si_DJ-1) (Fig. 4h). As the PDH enzyme is mainly activated through site-specific dephosphorylation of three sites (Ser232, Ser293 and Ser300) on PDHA1 (also known as PDHA) and phosphorylation at any of the three sites can inhibit PDH activity[38], we measured site-specific phosphorylation in T_{reg} cells. Consistent with PDH enzymatic activity data, *DJ-1* KD in T_{reg} cells consistently increased the phosphorylation of Ser293 but not that of another tested site (Ser300) (as shown in all four tested healthy donors although with varying magnitude; Fig. 4i). In line with the weaker but detectable binding between DJ-1 and PDHB in T_{eff} versus T_{reg} cells (Fig. 4c), *DJ-1* KD in T_{eff} cells only modestly dampened PDH activity (Fig. 4j) and enhanced Ser293 phosphorylation on PDHA (as shown in three of four tested donors; Fig. 4k). A weaker effect of DJ-1 on PDH activity in T_{eff} cells than that in T_{reg} cells might be related to lower expression of *TFAM* (encoding mitochondrial transcription factor A[39]) in T_{eff} cells (Extended Data Fig. 1a). Notably, a more consistent effect of DJ-1 on Ser293 phosphorylation was observed in unstimulated T_{reg} and T_{eff} cells than in stimulated T_{reg} and T_{eff} cells (Fig. 4i,k). This finding is consistent with the quantification in the MS analysis (Supplementary Table 2). A clearer effect on PDH activity in resting T cells is also in agreement with the fact that, following stimulation, T cells switch their energetic model from mainly OXPHOS to glycolysis[40]. As PDH is crucial for ATP generation, partial *DJ-1* KD in T_{reg} cells indeed decreased both ATP/ADP and ATP/AMP ratios, with or without TCR stimulation (Fig. 4l,m).

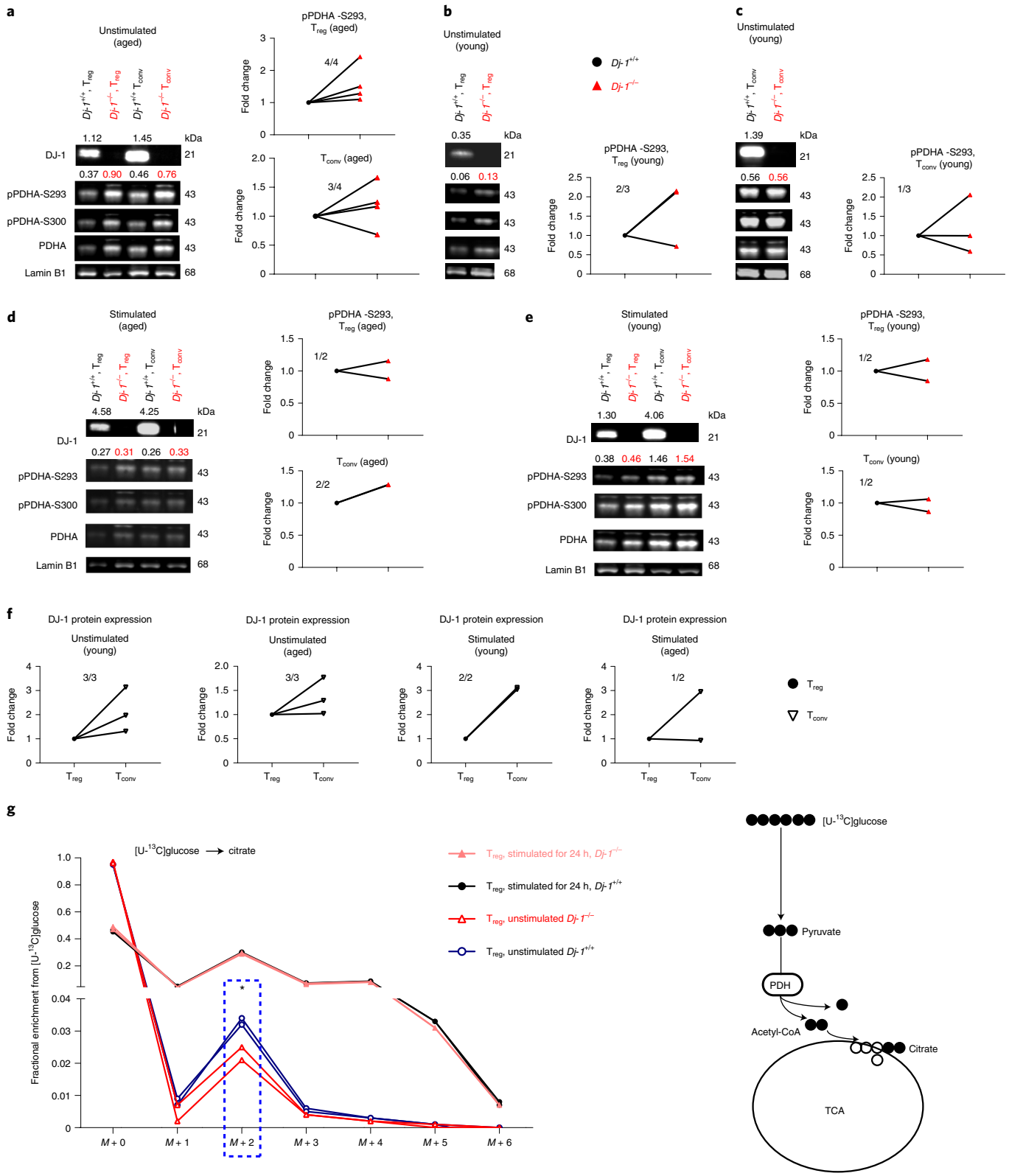
To further evaluate whether DJ-1 regulation of PDH activity is conserved in murine T cells, we analysed site-specific phosphorylation in T_{reg} cells or in CD4$^+$CD25$^-$ (T_{conv}) cells isolated from young and aged *Dj-1*-KO versus WT mice. Similar to human data, Ser293 phosphorylation of PDHA also consistently increased in resting *Dj-1*-KO T_{reg} and T_{conv} cells from most of the analysed aged mice (Fig. 5a). This still held true for resting *Dj-1*-KO T_{reg} cells isolated from most of the analysed young mice (Fig. 5b) but was only partially true for resting *Dj-1*-KO T_{conv} cells from young mice (Fig. 5c). Again, similar to human results, following stimulation, the pattern was not consistent anymore (except for a mild increase in PDHA-Ser293 phosphorylation in T_{conv} cells from aged mice) (Fig. 5d,e). A more consistent effect on PDHA-Ser293 phosphorylation in resting T_{reg} cells than that in T_{conv} cells was not simply due to greater DJ-1 protein expression in T_{reg} cells regardless of age (Fig. 5f). Although Ser300 was unaffected in human T_{reg} cells, Ser300 showed a similar pattern as Ser293 in murine T_{reg} cells. To further consolidate our observations, we employed [U-^{13}C]glucose to quantify the fraction of ^{13}C-labelled citrate in the TCA, the metabolite immediately downstream of the PDH-catalysing reaction. In this setting, the fraction of $M+2$ isotopologues of citrate represents the relative flux of glucose-derived carbon through PDH, thus indicating PDH activity. Remarkably, the fraction of $M+2$ citrate was clearly reduced in resting *Dj-1*-KO versus WT T_{reg} cells, while it was not reduced in TCR-stimulated counterparts (Fig. 5g). Collectively, these findings firmly support the concept that binding of DJ-1 to PDHB promotes PDH enzymatic activity by inhibiting Ser293 phosphorylation levels of PDHA in resting T_{reg} cells conserved in both humans and mice.

We next sought to evaluate whether DJ-1 has any functional consequence on OXPHOS of T_{reg} cells[2]. An impaired spare respiratory capability/maximum respiration was observed in T_{reg} cells from aged *Dj-1*-KO mice compared to those from aged WT mice (Fig. 6a), resulting in lower bioenergetic production and consequently reduced proliferation and activation (Fig. 2h,i). Interestingly, the baseline OXPHOS was only reduced in *Dj-1*-KO T_{reg} cells from aged mice but not in those from young mice (Fig. 6a,b). However, the maximum respiration was already lower in young *Dj-1*-KO T_{reg} cells than in WT T_{reg} cells (Fig. 6b). As OXPHOS is important for long-term survival of quiescent cells such as T_{reg} cells[2], this observation fitted well with an already reduced survival of *Dj-1*-KO nT_{reg} cells from young mice (Fig. 2k,l). T_{conv} cells from young or aged *Dj-1*-KO versus WT mice exhibited no difference in baseline and maximum respiration (Fig. 6c,d). Interestingly, both glycolysis and glycolytic capability were only reduced in *Dj-1*-KO versus WT T_{reg} cells from aged mice but not in those from young mice (Fig. 6e). No effect of *Dj-1* deletion was observed in T_{conv} cells regardless of age (Fig. 6f). Furthermore, a reduction in mitochondrial mass and membrane potential was observed in WT T_{reg} and T_{conv} cells with age, although *Dj-1* deletion did not have an effect (Fig. 6g,h).

As DJ-1 is also known as a transcription coactivator[33], we analysed the expression of genes that might affect PDH activity. We analysed the expression of genes encoding PDH kinases (PDKs), phosphatases (PDPs) and PDH subunits[41] using T_{reg} transcriptomic data from aged mice, but none of the genes encoding PDPs and PDH complexes showed significant differences at the transcriptional level between *Dj-1*-KO and WT mice (Extended Data Fig. 6a,b). Interestingly, the gene encoding PDK1 was upregulated, while the other two genes encoding PDK2 and PDK3 were downregulated

Fig. 4 | DJ-1 promotes PDH activity selectively in human resting nT_{reg} cells. a, Previously unidentified binding partners of DJ-1 as discovered by co-IP–MS analysis. The width of the oval is relatively proportional to the binding specificity relative to IgG. ab, antibody. **b**, Representative MS/MS spectrum for a peptide used to identify PDHB. **c**, Validation of DJ-1 binding to PDHB preferentially in human T_{reg} cells relative to T_{eff} cells by co-IP–immunoblotting analysis. Red arrows indicate the DJ-1 or PDHB band from the anti-DJ-1 immunoprecipitation (IP) elution. SN, supernatant; IP, eluted complexes pulled out by anti-DJ-1 antibody or the IgG control antibody ($n=4$ healthy donors). **d**, Representative single-cell images obtained using ImageStream. White scale bar, 7 µm (numbers in the image refer to cell IDs); original magnification, 60×. Ch02/04/07, channel 02/04/07. **e**, DJ-1 and PDHB are preferentially colocalized in T_{reg} cells relative to in T_{eff} cells ($n=3$). **f**, Representative histogram overlay of CD4 intensity from unstimulated and stimulated human T_{reg} cells. **g**, *DJ-1*-KD efficiency as quantified by *DJ-1* mRNA levels relative to those of *RPS9*. $^{**}P=0.00103$. **h**, Representative data of PDH enzymatic activity from human T_{reg} cells that were unstimulated (US) or stimulated for 5 h (ST) and treated with specific siRNA against *DJ-1* (si_DJ-1) or nonspecific scrambled siRNA (si_NS) ($n=3$). **i**,**k**, Site-specific phosphorylation and expression of PDHA in T_{reg} cells (**i**) and T_{eff} cells (**k**). Representative western blot images and quantification of S293 in the given blot are displayed on the right (the number of samples showing increased S293 levels out of the total number of tested donors ($n=4$) is directly indicated). **j**, PDH enzymatic activities of unstimulated or stimulated T_{eff} cells with or without *DJ-1* KD ($n=3$). **l**,**m**, Ratios between intracellular ATP and ADP (**l**) or between intracellular ATP and AMP (**m**) in T_{reg} cells or T_{eff} cells with or without *DJ-1* KD and with or without stimulation ($n=3$). $^{**}P=0.00125$ and $^{*}P=0.0314$ (**l**); $^{*}P=0.0212$ and $^{*}P=0.0405$ (**m**). Results represent four (**c**,**g**,**h**) and three (**d**–**f**,**i**–**m**) independent experiments. Data are mean ± s.d. *P* values were determined by two-tailed Student's *t*-test. $^{*}P\leq0.05$, $^{**}P\leq0.01$ and $^{***}P\leq0.001$.


a
New potential binding partners of PARK7/DJ-1 in human Treg cells
Binding folds: DJ-1 ab vs IgG
PDHB 64.01
GNB2L1 35.09
EXOSC1 33.03
EIF2A 25.07
SART1 19.17
ELAVL1 17.40
ATP1A1 14.48
SKIV2L2 9.86
DOCK10 7.85
ATP5D 8.51
ANXA4 6.64
LARS 6.49
HNRNPH3 5.26
STT3B 5.18
EIF5B 5.00
DHX36 4.95
KHSRP 4.88
ARPC2 4.88
PRPF8 3.73
PPP1CC, PPP1CB 3.16
DJ-1
b
PDHB
Scan 8,294 m/z 616.3
Relative intensity
m/z
c
Ladder
DJ-1 IgG DJ-1 IgG
SN IP SN IP SN IP SN IP
Stimulation
Teff DJ-1 (21 kDa)
Teff PDHB (36 kDa)
Treg DJ-1 (21 kDa)
Treg PDHB (36 kDa)
kDa
d
Bright field
PDHB AF594 Ch04 PDHB
DJ-1 A488 Ch02 PARK7
CD4 V450 Ch07 CD4
Merged Ch04 PDHB/ Ch02 PARK7/ Ch07 CD4
Unstimulated Treg cells Ch01
24,548
7 μm
Treg cells stimulated for 5 h with anti-CD3 and anti-CD28 beads and IL-2
19,525
e
Unstimulated
Stimulated with anti-CD3 and anti-CD28 beads and IL-2
Normalized frequency
Treg
Teff
DJ-1–PDHB similarity scores
f
Unstimulated Treg cells
Stimulated Treg cells
Normalized frequency
CD4 intensity, Ch07
g
Treg, si_NS
Treg, si_DJ-1
Relative PARK7 mRNA expression
**
h
PDH enzymatic activity (Treg)
Treg, ST, si_NS
Treg, ST, si_DJ-1
Treg, US, si_NS
Treg, US, si_DJ-1
Relative fluorescence intensity
Time (s)
i
Treg, pPDHA-S293
0 h
24 h
5 h
4/4
Fold change
si_NS
si_DJ-1
Treg cells
Stimulation (h)
si_NS si_DJ-1
0 5 24 0 5 24 kDa
DJ-1 21
0.38 0.49 1.17 2.30 2.32 1.52
pPDHA-S293 43
pPDHA-S300 43
PDHA 43
GAPDH 37
j
PDH enzymatic activity (Teff)
Teff, ST, si_NS
Teff, ST, si_DJ-1
Teff, US, si_NS
Teff, US, si_DJ-1
Relative fluorescence intensity
Time (s)
k
Teff, pPDHA-S293
0 h
24 h
5 h
3/4
Fold change
si_NS
si_DJ-1
Treg si_NS
Treg si_DJ-1
Teff si_NS
Teff si_DJ-1
Teff cells
Stimulation (h)
si_NS si_DJ-1
0 5 24 0 5 24 kDa
DJ-1 21
0.44 0.70 0.95 1.01 0.79 0.71
pPDHA-S293 43
pPDHA-S300 43
PDHA 43
GAPDH 37
l
ATP/ADP ratios
Unstimulated Stimulated
P = 0.08
ATP/ADP
m
ATP/AMP ratios
P = 0.08
ATP/AMP



in aged *Dj-1*-KO mice, three of which might compensate each other and contribute to PDH activity in T_{reg} cells (Extended Data Fig. 6a). Thus, DJ-1 might regulate PDH activity in T_{reg} cells at several stages, not only via physical interaction with PDHB but also possibly via transcription of PDH kinase genes. Nevertheless, distinguishing the contribution of each mechanism requires further investigation.

DJ-1 regulates iT_{reg} differentiation via PDHB. We further asked whether there is any causal link between the detected DJ-1–PDHB interaction and the T_{reg} phenotypes. We inhibited PDH activity to measure any potential effect on the proliferation and cell survival of WT nT_{reg} cells sorted from young mice. The use of a PDH inhibitor (CPI-613, the half maximal effective concentration (EC_{50}) being

Fig. 5 | *Dj-1* deletion compromises PDH activity in murine resting nT$_{reg}$ cells. a, Site-specific phosphorylation and expression of PDHA in T$_{reg}$ or T$_{conv}$ cells freshly isolated from aged *Dj-1*-KO or WT mice ($n=3$ per young group, $n=4$ per aged group; of note, not all mice were used for stimulation experiments). Relative quantification (normalized to lamin B1 data) from different mice (paired if the two samples were loaded in the same gel for comparability) is displayed on the right (the number of samples showing increased S293 levels (ratios were normalized to WT samples) out of the total number of analysed pairs is indicated in the corresponding plot). **b**,**c**, Site-specific phosphorylation and expression of PDHA in T$_{reg}$ (**b**) or T$_{conv}$ cells (**c**) freshly isolated from young *Dj-1*-KO or WT mice. **d**,**e**, Site-specific phosphorylation and expression of PDHA in stimulated T$_{reg}$ or T$_{conv}$ cells isolated from aged (**d**) or young (**e**) *Dj-1*-KO or WT mice. The cells were stimulated with anti-CD3 antibody, anti-CD28 antibody and IL-2 for 24 h. **f**, DJ-1 protein expression relative to lamin B1 expression from resting or stimulated young or aged WT mice (the number of samples showing increased DJ-1 levels (ratios were normalized to data from T$_{reg}$ cells) out of the total number of analysed mice is indicated in the corresponding plot). **g**, Representative data of citrate mass isotopomer distribution following [U-^{13}C]glucose tracing ($n=4$ for WT or KO young mice; two mice were grouped into one sample to obtain enough cells for both unstimulated and stimulated conditions) in stimulated (for 24 h) and unstimulated murine T$_{reg}$ cells. $^{*}P=0.0465$. Results represent four (**a**), three (**b**,**c**) and two (**d**,**e**,**g**) independent experiments. *P* values were determined by two-tailed Student's *t*-test without adjustment for multiple comparisons. $^{*}P\leq0.05$, $^{**}P\leq0.01$ and $^{***}P\leq0.001$.

~200 μM in tested tumour cell lines[42]) essentially impaired proliferation and slightly compromised cell survival of nT$_{reg}$ cells following stimulation with anti-CD3 antibody, anti-CD28 antibody and IL-2 for 3 d (Extended Data Fig. 7a,b). But the in vitro lineage stability of T$_{reg}$ cells was unimpaired (Extended Data Fig. 7c). Furthermore, both DJ-1 deficiency and inhibiting PDH decreased maximum respiration in nT$_{reg}$ cells (Fig. 6b), indicating that DJ-1 regulates OXPHOS via PDH.

As *Dj-1*-KO-mediated impairment of iT$_{reg}$ differentiation was demonstrated only using young mice[20], we wondered whether this also held true for aged mice. As *DJ-1* is linked with *TGFB* (*TGFB1*) in the human T$_{reg}$ correlation network (Extended Data Fig. 1b), we analysed whether DJ-1 regulates iT$_{reg}$ differentiation in a manner dependent on the dose of transforming growth factor (TGF)-β in mice. Encouragingly, *Dj-1* deletion impaired iT$_{reg}$ differentiation in a TGF-β-dependent manner (Fig. 7a,b), which was independent from cell survival (Fig. 7c). But the impairment of iT$_{reg}$ differentiation became more obvious in aged mice (Fig. 7d,e). Meanwhile, as the microenvironment of naive CD4^{+} T cell (CD4 Tn) development was different between *Dj-1*-KO and WT mice, it might affect iT$_{reg}$ differentiation. To assess whether DJ-1-mediated iT$_{reg}$ differentiation is realized in a haematopoietic-intrinsic manner, we performed iT$_{reg}$ differentiation from CD4 Tn mixtures developed in our BM chimeras, in which BM cells from aged CD45.2^{+} *Dj-1*-KO and CD45.1^{+} WT donors were transplanted into lethally irradiated young WT recipients (Fig. 7f). Notably, iT$_{reg}$ differentiated from CD4 Tn of *Dj-1*-KO origin was again compromised in a TGF-β-dependent manner (Fig. 7g). Interestingly, no impairment in cell survival was observed during iT$_{reg}$ differentiation even though the cells were isolated or derived from aged mice (Fig. 7h,i). As an ageing-dependent observation indicates a potential role of epigenetic regulation, we asked whether *Dj-1* deletion affected DNA methylation in the *Foxp3* promoter region and the T$_{reg}$-specific demethylated region (TSDR)[43]. The methylation level significantly decreased in the *Foxp3* TSDR of CD4 Tn with age (Extended Data Fig. 8a,b), in line with ageing-related hypomethylation[44]. However, *Dj-1* deletion significantly affected neither *Foxp3* promoter regions nor the TSDR, independent of age (Extended Data Fig. 8a,b). These results indicate that *Dj-1* deletion compromises iT$_{reg}$ differentiation in a TGF-β-dependent and haematopoietic-intrinsic manner.

After ruling out DJ-1 regulation of epigenetic modification, we assessed whether the DJ-1-mediated effects on iT$_{reg}$ differentiation occur via PDH. Inhibiting PDH activity in CD4 Tn with CPI-613 weakened the differentiation toward iT$_{reg}$ cells (Fig. 8a), proliferation and cell survival, although the concentration of CPI-613 (ranging from 50 μM to 100 μM) was lower than the EC$_{50}$ value (Fig. 8b,c). The effect on proliferation was already noticeable at 50 μM (Fig. 8b). As PDH activity is inhibited by PDH kinases, we assessed the effect of a PDH kinase inhibitor (dichloroacetate, DCA). Similar to other reports[45], treating CD4 Tn with 10 mM DCA enhanced iT$_{reg}$ differentiation (Fig. 8d). We further confirmed a similar effect of CPI-613 on cells isolated from aged mice (Extended Data Fig. 9a,b). Notably, the impact on the frequency of FOXP3^{+} cells already appeared after treatment with 50 μM CPI-613, which was, however, independent from cell survival and proliferation (Extended Data Fig. 9b).

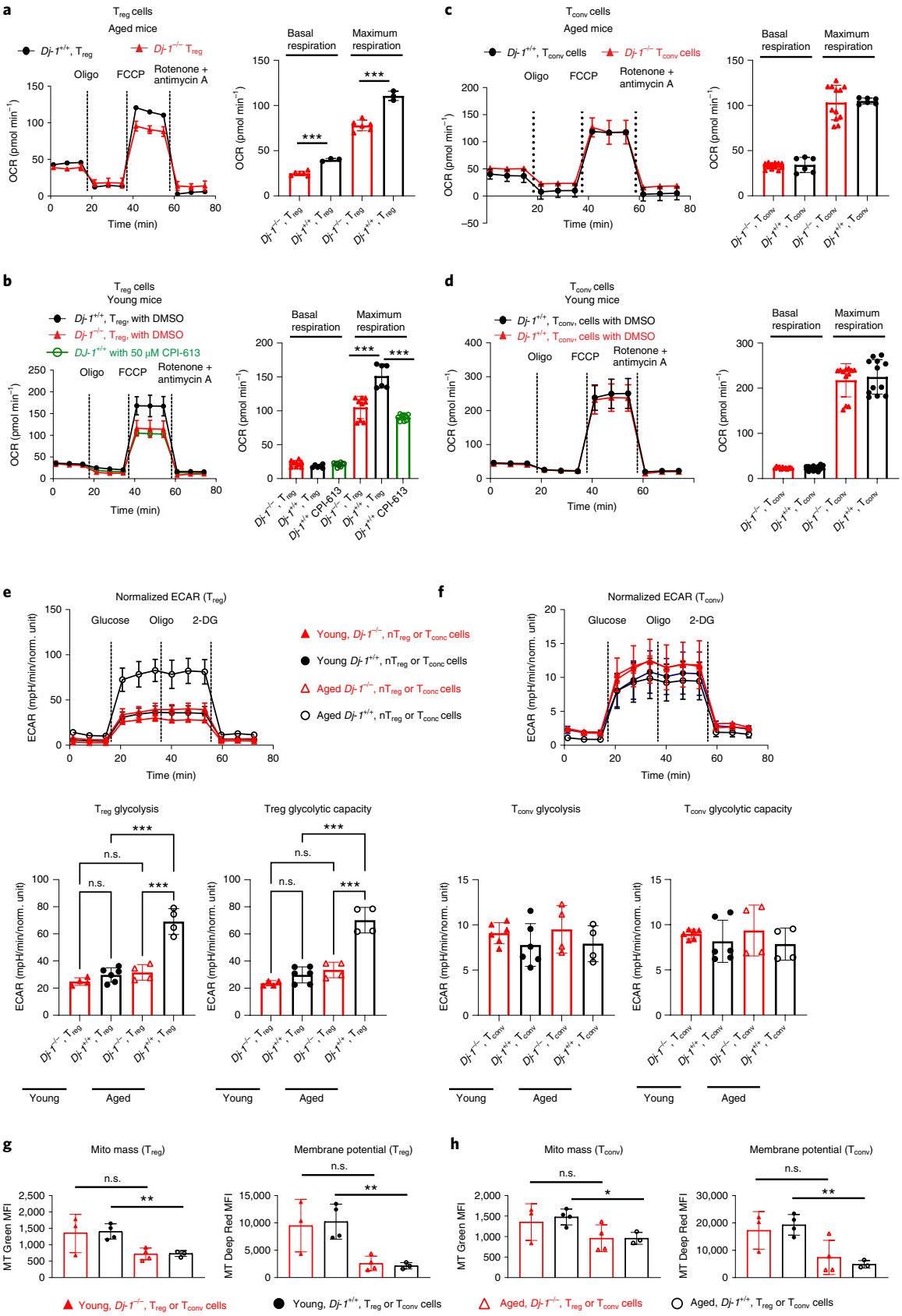
Considering that potential off targets of small molecules are often present, we used a genetic modification approach by using specific siRNA against *Pdhb* (si_PDHB) to KD *Pdhb* in CD4 Tn, followed by iT$_{reg}$ differentiation (Fig. 8e). In line with the PDH inhibitor data, even partial *Pdhb* KD (Fig. 8f) resulted in a significant decrease in FOXP3^{+} iT$_{reg}$ cells generated from CD4 Tn (Fig. 8g,h), while only modestly impeding cell survival (Fig. 8i). As *Dj-1* deletion can only partially inhibit PDH activity, it is foreseeable that partial *Pdhb* KD already generated effects similar to those of *Dj-1* deletion. Unexpectedly, *Pdhb* KD showed an effect only without but not with recombinant IL-2 (even at a low dose of 10 U ml^{-1}) (Fig. 8g,h). This indicates that IL-2 alone can rescue the si_PDHB-mediated defect in iT$_{reg}$ differentiation. Therefore, we further analysed the IL-2 signalling pathway. Notably, diminished iT$_{reg}$ differentiation in *Pdhb*-KD samples was accompanied by reduced pSTAT5 and CD25 levels (Fig. 8j,k). As PDH complex subunits interact with phosphorylated STAT5 in adipocytes[46], it is plausible to observe an effect on pSTAT5 following *Pdhb* KD in differentiated T cells. Interestingly, IL-2 production in CD4 T cells isolated from LNs was dramatically

Fig. 6 | *Dj-1* deletion impairs OXPHOS selectively in nT$_{reg}$ cells. a–**d**, Oxygen consumption rate (OCR) of freshly isolated T$_{reg}$ cells (**a**, aged mice, $n=6$ for KO, $n=3$ for WT; **b**, young mice, $n=9$ for KO, $n=6$ for WT) and T$_{conv}$ cells (**c**, aged mice, $n=6$ for KO, $n=3$ for WT with duplicates for each mouse; **d**, young mice, $n=6$ for KO, $n=6$ for WT with duplicates for each mouse). Plots of the Seahorse Mito stress test (left) or quantitation of basal and maximum respiration (right) are shown. $^{***}P=2.36\times10^{-5}$ and $^{***}P=8\times10^{-5}$ (**a**); $^{***}P=0.000176$ and $^{***}P=1.8\times10^{-7}$ (**b**). FCCP, carbonyl cyanide 4-(trifluoromethoxy)phenylhydrazone; oligo, oligomycin. **e**,**f**, Extracellular acidification rate (ECAR) of freshly isolated nT$_{reg}$ (**e**) or T$_{conv}$ (**f**) cells from young or aged *Dj-1*-KO or WT mice following the Seahorse glycolysis stress test (young, KO, $n=4$; young, WT, $n=6$; aged, KO, $n=4$; aged, WT, $n=4$). The results were normalized (norm.) relative to cell DNA. Quantifications of glycolysis and glycolytic capacity are displayed below the corresponding ECAR plots. $^{***}P=0.000524$, $^{***}P=2.86\times10^{-5}$, $^{***}P=0.000553$ and $^{***}P=3.02\times10^{-5}$ (**e**); 2-DG, 2-deoxyglucose. **g**,**h**, Comparison of mitochondrial (Mito) mass (left) and membrane potential (right) of freshly isolated nT$_{reg}$ (**g**) or T$_{conv}$ (**h**) cells (young, KO, $n=3$; young, WT, $n=4$; aged, KO, $n=4$; aged, WT, $n=3$). $^{**}P=0.00540$ and $^{**}P=0.00836$ (**g**); $^{*}P=0.0116$ and $^{**}P=0.00160$ (**h**). MT, MitoTracker. Results represent two (**a**–**f**) and three (**g**,**h**) independent experiments. Data are mean ± s.d. *P* values were determined by two-tailed Student's *t*-test. $^{*}P\leq0.05$, $^{**}P\leq0.01$ and $^{***}P\leq0.001$.

reduced with age (Fig. 8l). *Dj-1* deletion further modestly but significantly decreased IL-2 production from aged mice (Fig. 8l). These data together could well elucidate why the impairment of iT_{reg} differentiation in *Dj-1*-KO mice became more evident in aged mice.

Discussion

Here we uncovered an unrecognised critical link between DJ-1 and PDHB that has a preferential impact on T_{reg} cells relative to non-T_{reg} cells (that is, T_{conv} cells) and found that *Dj-1* deletion impaired T_{reg}



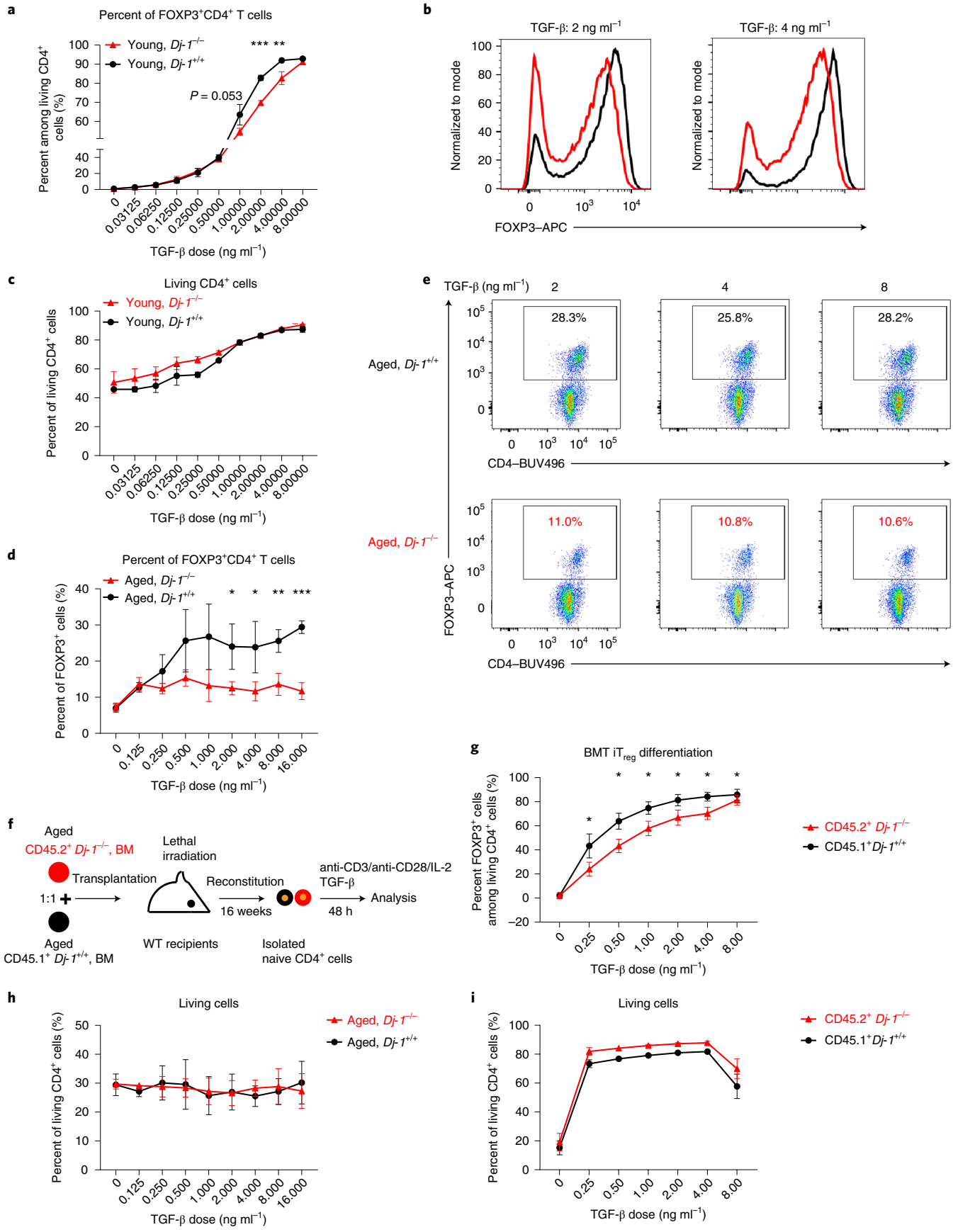

a
Percent of FOXP3+CD4+ T cells
Young, Dj-1−/−
Young, Dj-1+/+
*** **
P = 0.053
Percent among living CD4+ cells (%)
TGF-β dose (ng ml−1)
b
TGF-β: 2 ng ml−1
TGF-β: 4 ng ml−1
Normalized to mode
FOXP3–APC
c
Living CD4+ cells
Percent of living CD4+ cells
d
Percent of FOXP3+CD4+ T cells
Aged, Dj-1−/−
Aged, Dj-1+/+
Percent of FOXP3+ cells (%)
e
TGF-β (ng ml−1)
Aged, Dj-1+/+
Aged, Dj-1−/−
28.3%
25.8%
28.2%
11.0%
10.8%
10.6%
CD4–BUV496
FOXP3–APC
f
Aged
CD45.2+ Dj-1−/−, BM
Transplantation
1:1
Aged
CD45.1+ Dj-1+/+, BM
Lethal irradiation
WT recipients
Reconstitution
16 weeks
Isolated naive CD4+ cells
anti-CD3/anti-CD28/IL-2
TGF-β
48 h
Analysis
g
BMT iTreg differentiation
Percent FOXP3+ cells among living CD4+ cells (%)
CD45.2+ Dj-1−/−
CD45.1+Dj-1+/+
h
Living cells
Aged, Dj-1−/−
Aged, Dj-1+/+
i
Living cells
CD45.2+ Dj-1−/−
CD45.1+Dj-1+/+

Fig. 7 | *Dj-1* deletion impairs iT_{reg} differentiation. a,**d**, Percentages of FOXP3$^+$ cells among gated living CD4$^+$ T cells differentiated from CD4 Tn isolated from young (**a**) or aged (**d**) *Dj-1*-KO or WT mice given different doses of recombinant TGF-β (the concentration per unit was kept constant for anti-CD3 antibody, anti-CD28 antibody and IL-2) ($n=3$ per WT or KO group). ***$P=0.000239$ and **$P=0.00883$ (**a**); *$P=0.0380$, *$P=0.0491$, **$P=0.00897$ and ***$P=0.000458$ (**d**). **b**, Representative histogram overlay of FOXP3 expression of living CD4$^+$ singlets between young *Dj-1*-KO and WT mice following iT_{reg} differentiation. **c**, Living percentages of CD4$^+$ T cells following iT_{reg} differentiation with the indicated doses of TGF-β. **e**, Representative FCM plots of FOXP3$^+$ cells among living CD4$^+$ T cells following iT_{reg} differentiation. **f**, Schematic of iT_{reg} differentiation from CD4 Tn isolated from BM chimeras. **g**, Percentages of FOXP3$^+$ cells among living CD4$^+$ T cells derived from BM of aged CD45.2$^+$ *Dj-1*-KO mice or CD45.1$^+$ WT mice given different doses of TGF-β. BMT, bone marrow transplantation; *$P=0.0432$, *$P=0.0145$, *$P=0.0206$, *$P=0.0321$ and *$P=0.0186$. **h**,**i**, Living percentages of CD4$^+$ T cells following iT_{reg} differentiation for the results presented in **d**,**g**, respectively. Results represent three (**a**–**c**) and two (**d**–**i**) independent experiments. Data are mean ± s.d. *P* values were determined by two-tailed Student's *t*-test. *$P\leq0.05$, **$P\leq0.01$ and ***$P\leq0.001$.

cellularity in aged mice. As OXPHOS is critical for the development and long-term survival[2] of long-lived quiescent cells such as T_{reg} cells, the accelerated cell death in *Dj-1*-KO T_{reg} cells starting at a young age was likely attributable to the compromised spare respiratory capability/maximum respiration of T_{reg} cells already present in young mice. The compromised homeostatic proliferation and activation of *Dj-1*-KO T_{reg} cells in aged mice might be closely linked to the deficit in both OXPHOS and glycolysis and glycolytic capacity in *Dj-1*-KO T_{reg} cells. The effect of *Dj-1* deletion was further exacerbated by a reduction in mitochondrial mass and membrane potential in T cells during ageing. As OXPHOS was reduced in *Dj-1*-KO T_{reg} cells starting from a young age and both OXPHOS and glycolysis were impaired in *Dj-1*-KO T_{reg} cells of aged mice, *Dj-1* deletion most likely impaired ATP production in T_{reg} cells. This notion was further supported by our ATP, ADP and AMP measurements in human T_{reg} cells. In short, we suggest that, as a consequence of various metabolic disturbances, the accelerated cell death in *Dj-1*-KO T_{reg} cells starting at a young age that further accumulates over time and the decreased T_{reg} homeostatic proliferation and activation in aged mice synergistically contributed to the reduction in peripheral homeostatic T_{reg} cellularity at a later stage. Although *Dj-1* deletion impaired maximum respiration, it did not compromise TSF. This again indicates that OXPHOS might be more vital to the long-term survival than to the suppressive function of nT_{reg} cells.

Different from the scenario in resting T_{reg} cells, *Dj-1* deletion did not affect phosphorylation of PDHA in stimulated T_{reg} and T_{conv} cells from young mice. The selective effect on PDH activity in unstimulated or resting T cells might be a result of a metabolic model switching from OXPHOS to glycolysis upon activation[40]. No clear effect on PDH activity in stimulated T_{reg} cells from young mice could partially explain the lack of effect on homeostatic and TCR stimulation-driven proliferation and activation of stimulated T_{reg} cells. Furthermore, intact glycolysis and glycolytic capacity in *Dj-1*-KO nT_{reg} cells from young mice also supported the uncompromised proliferation of nT_{reg} cells. As for iT_{reg} cells, a higher percentage of IL-2-producing CD4$^+$ T cells in young mice could at least partially rescue the deficiency in iT_{reg} differentiation mediated by *Dj-1* KO. These various aspects could explain the lack of difference in the EAE scores between young *Dj-1*-KO and WT mice. Together with other results, our adoptive transfer experiments demonstrate that the number of T_{reg} cells plays a decisive role; that is, a greater number of T_{reg} cells, regardless of *Dj-1* deletion, results in a better outcome in the EAE model.

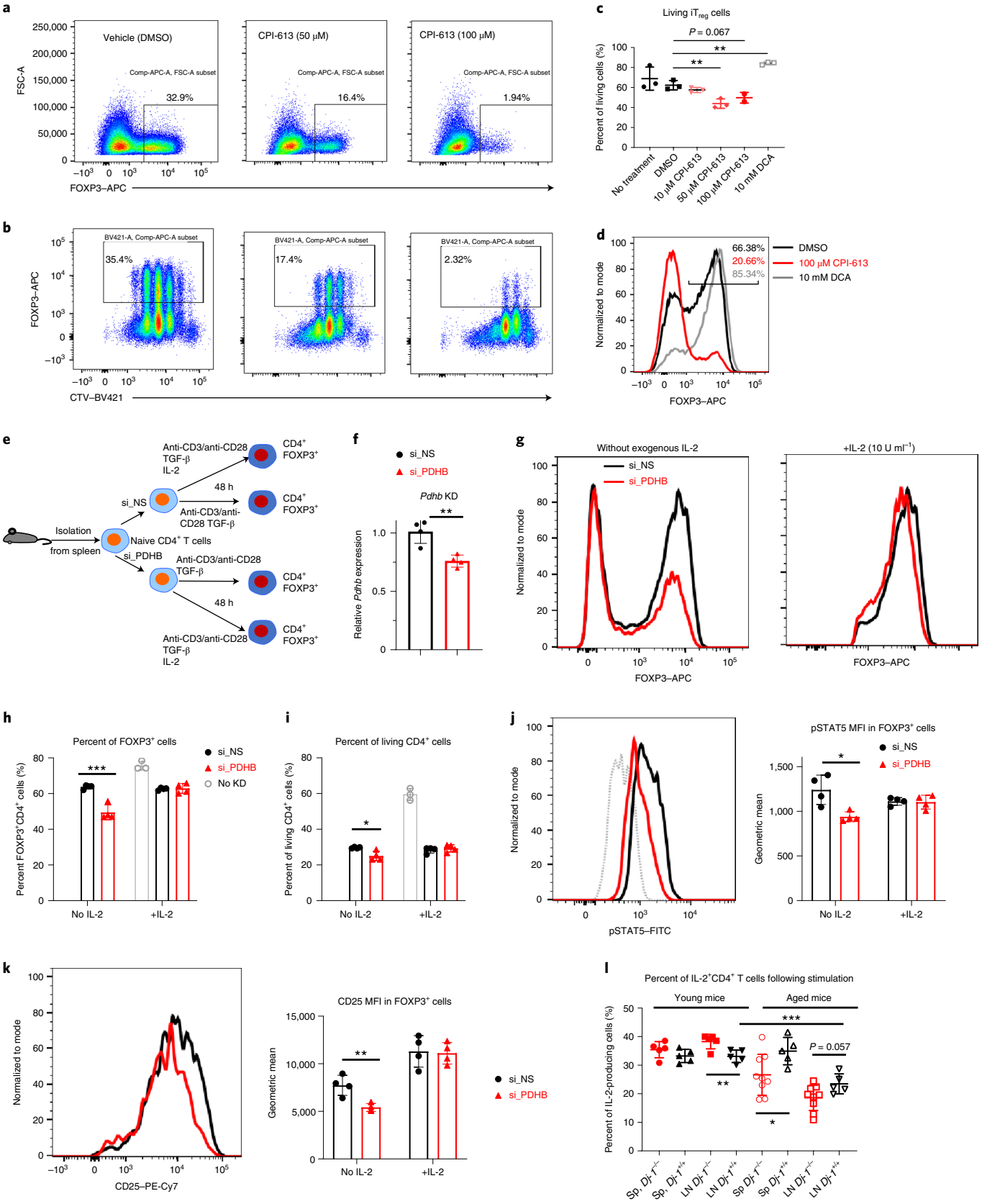
Although both site-specific phosphorylation data and [U-^{13}C] labelling experiments did not show a clear effect of *Dj-1* deletion on murine T_{reg} cells stimulated for 24 h, PDH enzymatic activity was reduced in human T_{reg} cells stimulated for 5 h following *DJ-1* KD. The lack of effect on stimulated murine T_{reg} cells might simply be due to a dose-dependent consequence of the stimulus (e.g., anti-CD3 antibody). As shown in another quiescent cell type, that is, CD8$^+$ naive T cells[28], only very low but not higher doses of anti-CD3 antibody can generate a clear effect of *Dj-1* deletion on TCR sensitivity. Strong TCR stimulation might be able to compensate for the effect of *Dj-1* deletion on PDH activity.

Another interesting observation is the age-dependent regulation of DJ-1. We demonstrate that *Dj-1* deletion impairs nT_{reg} cellularity in aged mice. This is different from another work[20], in which the frequency of thymic T_{reg} cells was higher in 10–12-week-old *Dj-1*-KO mice than that in WT mice. As thymic involution occurs dramatically between the ages of 4 and 12 weeks[31], nT_{reg} development could not be appropriately investigated in 10–12-week-old mice. For this reason, we analysed thymic T_{reg} cells strictly in 4-week-old mice and generated experimental groups only through heterozygous cross-breeding, which was also not specified in their work. Moreover, we investigated both T_{reg} cell-autonomous and T_{reg} cell-extrinsic mechanisms. Unexpectedly, *Dj-1*-KO BM had an advantage over WT BM in maintaining T_{reg} cellularity. As all our BM recipients were young, the ageing host microenvironment might

Fig. 8 | *Dj-1* deletion inhibits iT_{reg} differentiation via PDHB. a, Representative FCM plots of FOXP3 expression among living CD4$^+$ T cells differentiated from *Dj-1*$^{+/+}$ CD4 Tn treated with different doses of CPI-613 or vehicle. Comp., with compensation. **b**, Representative FCM plots of FOXP3 and CTV staining in living CD4$^+$ T cells differentiated from *Dj-1*$^{+/+}$ CD4 Tn. **c**, Percentages of living cells under the iT_{reg} differentiation condition for 3 d ($n=3$; cells were washed away for one mouse in one condition). **$P=0.00862$ and **$P=0.00145$. **d**, Representative histogram overlay of FOXP3 expression in cells differentiated from CD4 Tn. The percentages of FOXP3-expressing cells among gated living CD4$^+$ T cells were enlarged. **e**, Schematic of iT_{reg} differentiation from CD4 Tn following specific *Pdhb* siRNA KD. **f**, *Pdhb*-KD efficiency as quantified by *Pdhb* mRNA expression relative to that of *Rps13* ($n=4$). **$P=0.00427$. **g**, Representative histogram overlay of FOXP3 expression in cells differentiated from CD4 Tn transfected with specific *Pdhb* siRNA (si_PDHB) or control siRNA (si_NS) with or without exogenous IL-2 (but always with the same amount of anti-CD3 antibody, anti-CD28 antibody and TGF-β). **h**, Percentages of FOXP3-expressing cells among differentiated living CD4$^+$ cells transfected with si_PDHB or si_NS or without the electroporation procedure with or without exogenous IL-2 ($n=4$). ***$P=0.000621$. **i**, Percentages of living cells among differentiated CD4$^+$ T cells ($n=4$). *$P=0.0130$. **j**,**k**, Representative histogram overlay of phosphorylated STAT5 (pSTAT5) (Y694) expression (**j**) or CD25 expression (**k**) in cells differentiated from CD4 Tn transfected with si_PDHB or si_NS without exogenous IL-2. Right, quantification for both conditions with and without IL-2 ($n=4$). The dashed grey line in **j** represents the pSTAT5 fluorescence minus one staining control (negative). *$P=0.0131$ (**j**) and **$P=0.00645$ (**k**). **l**, Intracellular IL-2 production in living CD4$^+$ T cells isolated from the spleen or LNs after in vitro stimulation (young, KO, $n=5$; young, WT, $n=5$; aged, KO, $n=9$; aged, WT, $n=5$; of note, LNs were not sampled for each aged mouse). **$P=0.00874$, *$P=0.0404$ and ***$P=0.000788$. Results represent three (**f**–**k**) and two (**a**–**d**,**l**) independent experiments. Data are mean ± s.d. *P* values were determined by two-tailed Student's *t*-test. *$P\leq0.05$, **$P\leq0.01$ and ***$P\leq0.001$.

also be important for DJ-1-mediated T_{reg} cellularity. Future efforts are required to investigate the role of DJ-1 in non-immune cells. Notably, our ageing-dependent observations in mice are consistent with the notion that patients with *DJ-1* loss-of-function mutations develop PD only in their thirties but not during childhood[7]. Although a person at that age is not considered old, the age factor obviously contributes to disease onset mediated by DJ-1 deficiency.

The observed effect of *Dj-1* deletion on PDH activity is only a moderate decrease (~30%), rather than a complete loss, which could well explain the difference in symptoms of patients with *DJ-1*



loss-of-function mutations and genetic PDH complex deficiency[47]. Our discovery that moderate perturbations in central cellular functions of key immune cells early on in life can have a pathophysiological impact only later in the life course might represent a general guiding principle in understanding the pathogenesis of complex age-related diseases. Besides the observed effects on PDH activity, DJ-1 might also regulate other relevant enzymes, for example, ATP5D (another binding candidate in our data), a critical component of complex V in OXPHOS[48].

Methods

Our research complies with all relevant ethical regulations. For human samples, the ethical committee of the Luxembourg Red Cross has approved the study protocol (LIH-2018-0009), and we acquired all the buffy coats or leukopaks from the Luxembourg Red Cross and obtained informed consent from all the healthy blood donors before sampling. We did not have any clinical or demographical information from human donors, not even sex or age. All animal experimental procedures were performed following the approval of the Animal Experimentation Ethics Committee of the University of Luxembourg or the Animal Welfare Society of LIH and eventually the Luxembourg Ministry of Agriculture before the related experiment was started (LUPA2019/04 and LUPA2019/73).

Human T cell-related experiments. *Human T cell isolation.* Human primary natural $CD4^+$ T_{reg} and T_{eff} cells were derived respectively from $CD4^+CD25^{hi}CD127^{lo}$ and $CD4^+CD25^-$ T cells sorted on the BD FACSAria III cell sorter from peripheral blood mononuclear cells. Peripheral blood mononuclear cells were isolated by using Ficoll-Paque PLUS or Lymphoprep followed by magnetic separation with anti-human CD4 microbeads following the manufacturer's recommendations before being stained with anti-human CD4–FITC, anti-human CD25–APC and anti-human CD127–V450 antibodies and sorted with the BD FACSAria III. For sorting gating strategies of various cell types, please refer to Supplementary Fig. 1.

Human T cell culture. We followed the same protocol as descried in our previous work[23]. Sorted T cells were cultured in IMDM complete medium supplemented with 10% heat-inactivated (56 °C, 45 min) Gibco FBS, 1× penicillin–streptomycin, 1× MEM non-essential amino acids and 50 µM β-mercaptoethanol. While information for the antibodies used in this work is provided in Supplementary Table 4, please refer to Supplementary Table 5 for other reagents and materials. All the human T cells were cultured in incubators at 37 °C with 7.5% CO_2. Recombinant human IL-2 at 100 U ml^{-1} (unless otherwise specified; known as Proleukin in medication terminology) was added daily to human T_{reg} (but not T_{eff}) culture medium in different experiments. Every 7 d, all T cells were restimulated with irradiated Epstein–Barr virus-transformed B cells (EBV-B cells), at a 1:1 ratio of T cells and EBV-B cells, to expand and maintain T cells. EBV-B cells were irradiated in an RS 2000 X-Ray Biological Irradiator (Rad Source Technologies) for 30 min at a rate of 2.80 Gy min^{-1}. T cells were regularly characterized by co-staining for CD4, CD25, FOXP3 and Helios protein or GARP[49] by FCM or GZMB by ImageStream (Extended Data Fig. 2a,b). When primary T_{reg} cells were older than 6 weeks or the expression of FOXP3 or Helios or cellular viability decreased, the cells were discarded.

Flow cytometry and ImageStream for human cells. Once T cells were collected and the medium was removed, cell surface markers were stained in human FCM buffer (Ca^{2+}- and Mg^{2+}-free DPBS containing 2% heat-inactivated FBS) with antibodies for 30 min at 4 °C in the dark. Intracellular staining was performed using the FOXP3 staining kit following the manufacturer's instructions. Stained cells were analysed with the BD LSRFortessa. We excluded dead cells from further analysis by using the LIVE/DEAD Fixable Near-IR Dead Cell Stain. The .FCS files from human-related experiments were analysed with FlowJo version 7.6.5 or 10 (Tree Star–BD).

For ImageStream experiments, T_{reg} and T_{eff} cells were stained as described above but using staining panels other than those for the FCM analysis (Supplementary Table 4). Samples were acquired on an ImageStream X Mark II Imaging Flow Cytometer (Amnis, EMD Millipore) at 60× magnification. The results were analysed using IDEAS 6.2 software (Amnis), and the similarity score between PDHB and DJ-1 was determined by means of a similarity dilate algorithm that was often used for quantification of the nuclear translocation of a transcription factor. We used the PDHB-positive area as the targeted location and quantified the degree to which DJ-1 translocated to PDHB-positive areas. Only cells gated as living focused singlets were included in further analysis.

Gene knockdown in human T cells. The expression of targeted genes was knocked down by using the P3 Primary Cell 4D-Nucleofector X kit with 100 µl P3 primary cell solution and 100 pmol of the corresponding siRNA species (resuspended in 10 µl RNase-free water): si_Non-Specific (si_NS or si_CTL) (sc-37007, Santa Cruz) or si_DJ-1 (SI00301091, Qiagen). The Amaxa 4D-Nucleofector X System (Lonza) was used for the experiments with the manufacturer's recommended programme (E0-115) for human primary T cells. Following siRNA transfection, T cells were immediately transferred into 12-well plates with prewarmed complete IMDM medium with 100 U ml^{-1} IL-2 for T_{reg} cells and kept at 37 °C for 1 d. They were then stimulated with Dynabeads Human T-Activator CD3/CD28 (the ratio of cells to beads was 1:1; this ratio was always used) or with ImmunoCult Human T Cell Activator (25 µl per ml; this amount was always used) in 24-well plates for the specified period.

RNA extraction, cDNA synthesis and real-time quantitative PCR. RNA samples were prepared using the RNeasy Mini kit, starting with cell lysis with RLT buffer supplemented with 1% β-mercaptoethanol, following the manufacturer's instructions, and including genomic DNA digestion with DNAse I. For RNA integrity number assessment, the Agilent RNA 6000 Nano kit was used with the Agilent 2100 Bioanalyzer Automated Analysis System. A maximum of 500 ng RNA was used for cDNA synthesis. cDNA synthesis was performed using SuperScript III Reverse Transcriptase. Real-time quantitative (qPCR) was performed using the LightCycler 480 SYBR Green I Master Mix, supplemented with cDNA and primers in a reaction volume of 10 µl. The reaction took place on a LightCycler 480 (384) platform (Roche). The results were analysed with LightCycler 480 SW1.5 software. An annealing temperature of 55 °C was used for the various genes unless otherwise stated.

Human T_{reg} suppression assay. T_{eff} cells were stained with 1 µM CFSE dye in PBS for 2 min and 45 s in the dark at room temperature (RT). The reaction was stopped with cold FBS (2 min, dark, 4 °C) before the cells were washed and recultured in complete IMDM medium. T_{reg} cells were transfected with siRNA species for 1 d before being co-cultured with T_{eff} and EBV-B cells. A total of 6×10^4 CFSE-stained T_{eff} cells were distributed to each well with various amounts of T_{reg} cells and stimulated with 6×10^4 irradiated EBV-B cells. The cell mixtures were cultured at 37 °C for 3–5 d, and FCM analysis was carried out to determine the proliferation capacity of T_{eff} cells.

Co-immunoprecipitation. The same number (around 1×10^7) of expanded T_{reg} and T_{eff} cells were either left unstimulated or stimulated for 5 h with Dynabeads Human T-Activator CD3/CD28 for cell expansion and activation. After 5 h, cell pellets were collected and lysed in homogenisation buffer with 0.2% Triton X-100, 100 mM NaCl, 2 mM EDTA and 50 mM Tris (pH 8.0). Total protein in each sample was quantified by the standard Bradford assay in a microplate Cytation 5 Cell Imaging Multi Mode reader (BioTek). The lysates were diluted to a protein concentration of 3 µg $µl^{-1}$ (ideally a total amount of around 3,000 µg) with protease-inhibitor cocktail at a dilution of 1:100. Lysates were precleared with 10 µl washed Dynabeads Protein G in 100 µl lysis buffer for 1 h at RT, and the beads were then removed. The samples were then evenly distributed into two parts. One part of the sample was immunoprecipitated with rabbit monoclonal (EP2815Y) anti-human PARK7/DJ-1 antibody, and another part of the sample was immunoprecipitated with normal rabbit IgG as a negative control for 1 h at RT (the dilution was 1:10 for both target and control antibodies) before the addition of Dynabeads (20 µl beads for 7 µl antibody) and incubation overnight at 4 °C with gentle rocking. The beads were washed 3× with lysis buffer and sequentially 2× with lysis buffer without detergent. The anti-DJ-1 antibody pull-out complexes were then eluted from the beads by using 0.1% RapiGest in 50 mM ammonium bicarbonate with 5 mM dithiothreitol at 60 °C for 1 h, dried in a SpeedVac Concentrator at 4 °C (Thermo Fisher Scientific, hereafter abbreviated as 'Thermo') and resuspended in a small volume of lysis buffer for western blot or in ultra-pure water with 1% acetonitrile for MS.

Western blotting. Protein samples were mixed with Laemmli sample buffer containing 50 mM dithiothreitol, heated for 5 min at 95 °C, cooled on ice and loaded on gradient PAGEr Gold Precast Gels. ProSieve EX Running and Transfer buffers were used for the assay. Proteins were transferred to a methanol-activated (5 min, RT) Immun-Blot PVDF membrane and then blocked with 5% milk in DPBS with 0.2% Tween-20 for 1 h at RT with gentle shaking. All primary antibodies were diluted in blocking solution and incubated overnight at 4 °C. The membrane was washed (3× for 10 min) with PBS–Tween-20 (0.2%) before and after incubation with secondary antibodies. The chemiluminescence-based Amersham ECL Prime Western Blotting Detection Reagent was employed to detect the bands, which were visualized with the Westburg Odyssey FC Imaging System (LI-COR). If needed, the membrane was stripped with Restore Western Blot Stripping Buffer for 30 min at RT, washed, blocked and blotted with other antibodies again. For assessment of PDHA phosphorylation, *DJ-1* was knocked down in 5×10^6 T_{reg} or T_{eff} cells. Detection was carried out with an ECL Chemocam Imager (Intas). If needed, the contrast and brightness of the whole image was adjusted using ImageJ (https://imagej.nih.gov/ij/index.html) software. S293 phosphorylation levels (first normalized to GAPDH values and then normalized to the values at 0 h in the same blots) were quantified in human T_{reg} and T_{eff} cells that were isolated from different healthy donors and stimulated for different time periods.

Mass spectrometry. The quality of the samples prepared for MS analysis was checked by western blot by loading a small amount of the resuspended IP elution

products onto an acrylamide gel. The IP was only considered successful if the bait protein (DJ-1) was detected on the blotted membrane, and only these samples were analysed by MS in the proteomic facility (Institute for Systems Biology). Eluted proteins were digested with Lys-C and trypsin and purified using C18 reversed-phase chromatography. Purified peptides were separated by online reversed-phase HPLC over an increasing 90-min gradient of 3–35% acetonitrile and analysed with an Orbitrap Elite mass spectrometer operating in Top15 data-dependent mode. Raw output data files were analysed using MaxQuant (version 1.5.2.8) (https://www.maxquant.org/). Peptides were searched against the UniProt human database (02-2015 release). A reverse sequence database was used to impose a strict cutoff of 1% FDR. Label-free quantification was performed using the maxLFQ algorithm. Data processing was performed in Microsoft Excel and Perseus (version 1.5.0.15)[50]. We removed contaminants, decoys and single-peptide identifications for further analysis. Zero values in the remaining data were substituted by imputation. We selected potential previously unidentified binding partners by using a combination of the following criteria: (1) the average mRNA levels of the corresponding transcripts in T_{reg} cells over the first 6 h following TCR stimulation should be >250 (the average expression of FOXP3 in human natural T_{reg} cells from the time series transcriptomic datasets is around 250); (2) the LFQ value of MS-identified proteins bound to the anti-DJ-1 antibody should be at least 2.5-fold higher than that from the IgG control in human primary T cells; (3) the fold changes in the LFQ value of the bound proteins between stimulated and unstimulated T cells for all three analysed conditions (T_{eff} cells and T_{reg} cells with or without IL-2 addition) should be ≥2; (4) a similar trend (increase or decrease) in binding affinity between stimulated and unstimulated samples should be consistent for all the three analysed conditions; (5) the LFQ value of the bound proteins in the eluates of T_{reg} cells, with or without IL-2, should be higher than the 25th percentile of all the detected binding proteins in the given sample.

The known DJ-1-binding partners in human cells were downloaded from the NCBI database. Independent of mRNA expression levels, the binding partners were considered confirmed when the following two criteria were met: (1) the LFQ value of the eluted protein was at least twofold higher than that in the corresponding IgG controls of either human T cells or the Jurkat cell line; (2) the fold enrichment (stimulated versus unstimulated) from at least two of the four measured conditions (T_{eff} cells, Jurkat cells and T_{reg} cells with or without IL-2 addition) was similar.

Nucleotide analysis. Following KD for 24 h, half of the samples were stimulated with Dynabeads Human T-Activator for 1 d with (T_{reg} cells) or without (T_{eff} cells) IL-2. A 0.5-ml cell suspension were transferred to 1.5 ml 60% methanol, 0.85% AMBIC, pH 7.4, at −60 °C. The cells were separated by centrifugation (3 min, 13,000*g*, −10 °C). Intracellular metabolites were extracted by adding equal volumes (0.5 ml per 3×10^6 cells) of extraction fluid (50% methanol TE buffer, pH 7.0) and chloroform at −20 °C. After incubation, cell debris was separated by centrifugation (10 min, 13,000*g*, −10 °C), and the extract was filtered (0.22 µm, CA). Determination of nucleotides was performed using a Dionex UltiMate 3000 UHPLC System coupled to a Q Exactive mass spectrometer (Thermo). Chromatographic separation was performed on a ZIC-pHILIC column (SeQuant, 150×2.1 mm, 3.5 µm, Merck) at a constant flow rate of 0.4 ml min^{-1} at 25 °C with eluent A being water and eluent B being 90% acetonitrile, both containing 20 mM ammonium acetate adjusted to pH 7.5. The elution profile consisted of the following steps: 0–10 min from 90% to 50% B; 10–11 min from 50% to 20% B; 11–12 min from 20% to 90% B; 12–20 min, constant at 90% B. Full scan measurements were conducted by applying a mass resolution of 70,000.

PDH enzymatic assay. The same number (~1×10^6) of T_{reg} or T_{eff} cells were either left unstimulated or stimulated for 5 h with Dynabeads Human T-Activator CD3/CD28 with (T_{reg} cells) or without IL-2 (T_{eff} cells). Protein concentrations were determined by using the Bradford assay, and the same amount of protein was used for different samples within one experiment. PDH activity was determined using the colorimetric PDH Activity Assay kit following the manufacturer's recommendations in Nunc MicroWell 96-well microplates using an Infinite 200 PRO plate reader (Tecan) to measure the absorbance at 450 nm every 10–30 s over a time course of 1–5 h. Of note, multichannel pipettes should be used to avoid time delay between samples.

Mouse-related experiments. *Mice and in vivo experiments.* B6.129P2-*Park7*$^{Gt(XE726)Byg}$/Mmucd mice were developed and characterized elsewhere[26]. The *Dj-1* line used in our laboratory had already been backcrossed with B6N mice for at least ten generations. The *Dj-1*$^{-/-}$ (KO), *Dj-1*$^{+/-}$ and *Dj-1*$^{+/+}$ (WT) mice used in our experiments were sex- and age-matched siblings generated from heterozygous *Dj-1*$^{+/-}$ breeding pairs. Aged mice used in this work were around 45 weeks old unless otherwise mentioned. CD45.1$^+$ mice (also known as Ly5.1 mice) were imported from Charles River (strain code 494). All mice were maintained in our specific pathogen-free animal facility (also refer to the Reporting Summary). Specific pathogen-free mice were housed in IVC cages at a maximum of five mice per cage and maintained at a temperature of 22 °C and a relative humidity of 55%. They were given autoclaved corn cob bedding enriched with a sizzle nest, paper, a wooden block and a tunnel. They were fed with SAFE Maintenance Diets irradiated at a minimum of 25 kGy. The watering system consisted of reverse osmosis water supplied with 2 p.p.m. chlorine. The EAE model was performed as previously described[30]. In brief, each mouse was injected subcutaneously with 115 µg MOG35-55 peptide (Washington Biotech) emulsified in CFA and intraperitoneally with 300 ng pertussis toxin on days 0 and 2. For adoptive transfer experiments, we resuspended 5×10^5 *Dj-1*-KO or WT T_{reg} cells isolated from ~70-week-old mice in 100 µl PBS (Ca^{2+} and Mg^{2+} free) and performed intravenous injections into each young WT recipient 1 d before EAE induction. We also injected the same volume of PBS alone into control mice. Of note, we always used Ca^{2+}- and Mg^{2+}-free PBS unless otherwise specified. For BM transplantation experiments, 1×10^7 BM cells mixed from age- and sex-matched CD45.2$^+$ *Dj-1*-KO mice and CD45.1$^+$ mice at a ratio of 1:1 were injected into different sex-matched young recipients (WT or KO, refer to the figures). Young recipients aged 8–12 weeks received two doses of 450 rad in an RS 2000 X-Ray Biological Irradiator at an interval of 3 h and received BM cells resuspended in 100 µl cold PBS via intravenous injection 6 h following the second irradiation. We analysed T_{reg} cells or induced iT_{reg} cells from the CD4 Tn mixture in splenocytes (refer to the iT_{reg} differentiation section) following 16 or 8 weeks of reconstitution for BM transplantation from aged or young donors, respectively. No randomisation was applied to our experiments. The investigators were blind to the genotype groups in the EAE experiments using whole bodies of KO or WT mice but not in the adoptive transfer and BM experiments.

Murine T cell-isolation procedures and cell culture. Spleens and peripheral LNs (cervical, axillary or inguinal LNs were sampled) were minced through a strainer with 70-µM pores. The cell suspension was centrifuged at 300*g* for 5 min at 4 °C. The supernatant was discarded, and 3 ml 1× red blood lysis buffer for splenocytes was added per mouse. Samples were incubated at RT for 7 min. Next, 10 ml ice-cold murine FCM (mFCM) buffer (2% heat-inactivated FBS, 2 mM EDTA in PBS; of note, compared with human FCM buffer, mFCM buffer contains EDTA) was added, the cells were centrifuged (300*g*, 4 °C for 5 min), and the supernatant was discarded. The cell pellet was resuspended with cold FCM buffer. The cell suspension was passed through a 40-µM cell strainer again. When the microbeads were available in the lab, CD4$^+$ T cells were first enriched with anti-mouse CD4 (L3T4) microbeads following the manufacturer's instructions with the QuadroMACS Separator (for magnetic isolation procedures, we always used this type of separator). Otherwise, no CD4 T-cell pre-enrichment was performed before staining and sorting.

For T_{reg} isolation, CD4-enriched cells were stained with anti-mouse CD4–FITC and anti-mouse CD25–APC antibodies at 4 °C for 20 min. After staining, T_{reg} (CD4$^+$CD25^{hi}) cells and conventional CD4$^+$CD25$^-$ (T_{conv}) T cells were sorted using the BD FACSAria III sorter. Alternatively, we isolated CD25$^+$CD4$^+$ (T_{reg}) and CD25$^-$CD4$^+$ (T_{conv}) cells using the mouse CD4$^+$CD25$^+$ isolation kit with LD and MS columns following the manufacturer's protocols. For each column, we loaded at most 1×10^8 splenocytes.

For naive T cell isolation, CD4$^+$ T cells were stained with anti-mouse CD4–FITC, anti-mouse CD25–APC, anti-mouse CD44–PE-Cy7 and anti-CD62L–PerCP-Cy5.5 surface antibodies. If no CD4 enrichment was applied, we also added anti-CD8–eFluor450 antibody. After staining, naive CD4$^+$ T cells (CD4 Tn) (CD4$^+$CD25$^-$CD62L^{hi}CD44^{lo}) were sorted on the BD FACSAria III sorter (Supplementary Fig. 1). Alternatively, untouched CD4 Tn were isolated via magnetic separation using the Naive CD4$^+$ T Cell Isolation kit with an LS column following the manufacturer's recommendation.

Mouse T cell culture medium is composed of complete RPMI medium, including RPMI 1640 medium supplemented with 10% heat-inactivated FBS, 50 U ml^{-1} penicillin, 50 µg streptomycin, 1 mM sodium pyruvate, 2 mM GlutaMAX, 1× non-essential amino acids, 50 µM β-mercaptoethanol and 10 mM HEPES. All murine cells were cultured in incubators at 37 °C with 5% CO_2.

FCM for murine T cells. The same number (~1×10^6) of cells from the spleen or peripheral LNs were first incubated with anti-mouse CD16/CD32 Fc blocker and then stained with various surface and intracellular antibodies (Supplementary Table 4). Cell numbers were determined by CASY (Innovatis). Of note, all these antibodies might not necessarily be used in the same staining panel. For intracellular cytokine measurement, cells (2×10^5) from the spleen and pLNs of young or aged mice were restimulated with 50 ng ml^{-1} PMA and 750 ng ml^{-1} ionomycin in the presence of GolgiPlug and GolgiStop for 5 h in 96-well plates. Following cell surface staining, cells were fixed and permeabilized with the Cytofix/Cytoperm buffer. Other intracellular staining was performed using the Foxp3 staining kit following the manufacturer's recommendations. Following staining, murine cells were acquired in a BD LSRFortessa and analysed with FlowJo version 10 software.

Murine T_{reg} suppression assay. Isolated T_{conv} (1×10^5) cells from WT C57BL/6 mice were first labelled with 1 µM CFSE. Splenocytes depleted of T cells by using anti-CD90.2 beads were irradiated with a total dose of 30 Gy using the RS 2000 X-Ray Biological Irradiator (Rad Source Technologies) and used as feeder cells (2×10^5 cells). Labelled T_{conv} cells were co-cultured with irradiated feeder cells and various amounts of T_{reg} cells from various genotypes in the presence of 1 µg ml^{-1} soluble anti-CD3 antibody (no azide, low endotoxin levels).

Microarray analysis. RNA samples of CD25^{hi}CD4$^+$ T cells (T_{reg} cells) sorted from ~45-week-old *Dj-1*$^{-/-}$ mice and *Dj-1*$^{+/+}$ littermates were analysed with the

Affymetrix Mouse Gene 2.0 ST Array at the EMBL Genomics Core Facility. Samples were first checked with an Agilent Bioanalyzer 2100 using the RNA 6000 Pico kit, and only RNA samples with an RNA integrity number greater than 8.5 were processed further. The expression signal at the exon level was summarized with the Affymetrix PLIER algorithm (https://tools.thermofisher.com/content/sfs/brochures/plier_technote.pdf) with 'DABG' and 'PM-GCBG' options by means of the sketch-quantile normalisation approach (Affymetrix Expression Console version 1.4). The corresponding probesets were considered differentially expressed if they passed the following combinatory filters: (1) whether the fold changes were ≥2 between the mean values of *Dj-1*-KO and -WT T_{reg} cells, (2) whether the *P* value resulting from a two-tailed Student's *t*-test was ≤0.05, (3) whether the cross-hybridisation type of the probeset was 1, (4) whether the probeset with the highest expression level was >100 (with a median value of ~90 for each of our samples), (5) for a given group (for example, WT) with the higher mean intensity of the probeset, whether the probeset in all replicates of the given group was detected as 'present' according to the default setting of the Affymetrix Expression Console. DAVID version 6.7 (https://david.ncifcrf.gov/) was used to perform functional enrichment analysis for the lists of differentially upregulated or downregulated genes. To simplify analysis of the DAVID enrichment results, we mainly selected representative GO terms and KEGG pathways with *P* value <0.05 and fold enrichment ≥1.5 from each enrichment cluster. Heatmaps were generated using the R heatmap.2 function (gplots package) with scaled row values (with a mean of 0 and a standard deviation of 1).

Seahorse metabolic assay. Freshly sorted cells (4×10^5 cells) were rested for 3 h in complete RPMI medium before being plated in wells using Cell-Tak. T_{reg} cells were pooled together from different mice of the same group to reach 4×10^5 cells per well due to a limited number of sorted T_{reg} cells from each individual mouse. The oxygen consumption rate was measured in XF base medium, containing 1 mM pyruvate, 2 mM L-glutamine and 25 mM glucose, under basal conditions and in response to 1 µM oligomycin, 1.5 µM carbonyl cyanide 4-(trifluoromethoxy) phenylhydrazone and 1 µM rotenone and antimycin A sequentially by the Seahorse XF96 Analyzer (Agilent). The concentration of the stressor compounds refers to the final concentration in the plate. For the glycolysis stress test, assay medium (Seahorse XF base medium with 2 mM L-glutamine) was used. The measurement was performed in response to glucose (10 mM), oligomycin (1 µM) and 2-deoxyglucose (50 mM) in sequence. For the glycolysis test, we normalized the results to cell counts. Cell numbers in each well of the plate were quantified with the CyQUANT Cell Proliferation Assay (C7026, Thermo) using the microplate Cytation 5M Cell Imaging Multi Mode reader (BioTek). The results were analysed with Wave 2.6.0 (Agilent).

Mitochondrial mass and membrane-potential analysis. Splenocyte suspensions were stained for 30 min in complete supplemented RPMI medium with anti-CD4–PE antibody, anti-CD25–BUV395 antibody, DAPI (1:2,000), MitoTracker Green FM (1:100,000) and MitoTracker Deep Red (1:10,000) in an incubator at 37 °C. Before acquisition in a BD LSRFortessa, the cells were first washed with ice-cold mFCM buffer. Of note, considering the high technical variability, to ensure that the mitochondrial results were fully comparable, we sacrificed and analysed the groups of young and aged *Dj-1*-KO and WT mice on the same day.

PDH inhibitor-mediated iT_{reg} differentiation and nT_{reg} cell proliferation. CD4 Tn were sorted from the spleen and pLNs of *Dj-1*$^{+/+}$ WT B6 mice aged 8–12 weeks old. First, 1 µl 5 mM CTV dye was added into 1 ml PBS, which was used to suspend naive CD4$^+$ T cells. The cell mixture was incubated at 37 °C for 7 min, and then the cells were washed with RPMI complete medium three times. A total of 1.5×10^5 CD4 Tn were seeded in one well of a 96-well flat-bottom plate coated with 2 µg ml^{-1} anti-mouse CD3 and 2 µg ml^{-1} anti-mouse CD28 antibodies. Next, 2 ng ml^{-1} recombinant human TGF-β and 20 U ml^{-1} mouse IL-2 were added for iT_{reg} differentiation. Cells were treated with PDH inhibitor (CPI-613) at different concentrations or the vehicle (DMSO) or DCA sodium. Cells were kept in the incubator for 3 d. On day 2, half of the medium was exchanged to apply cytokines and treatments. On day 3, the cells were collected, and staining was performed.

For the proliferation assay, CD4$^+$CD25^{hi} nT_{reg} cells were sorted from the spleen and pLNs of WT B6 mice aged 8–12 weeks old and labelled with 5 µM CTV dye. A total of 1×10^5 nT_{reg} cells were seeded into a 96-well round-bottom plate coated with 1 µg ml^{-1} anti-CD3 and 1 µg ml^{-1} anti-CD28 antibodies and 50 U ml^{-1} IL-2 with the indicated amount of the PDH inhibitor or DMSO. On day 3, cells were collected, and staining was performed.

TGF-β-dose-dependent iT_{reg} differentiation. We used different doses of TGF-β as indicated in the figures. At the same time, we stimulated 1.5×10^5 CD4 Tn isolated with beads using 2 µg ml^{-1} coated anti-CD3 antibody (coating, 4 h, 37 °C), 1 µg ml^{-1} soluble anti-CD28 antibody and 10 U ml^{-1} IL-2 in a 96-well flat-bottom plate for 72 h before the analysis.

Pdhb siRNA-mediated iT_{reg} differentiation. Following transfection using *Pdhb* siRNA (SI01373953, Qiagen, as described above for human cells except for the programme used for murine T cells (DN-100)), CD4 Tn were transferred into a 1.5-ml tube containing 900 µl prewarmed complete RPMI medium and incubated at 37 °C with 5% CO_2 for 4 h with the lid open. Next, iT_{reg} differentiation was induced using 2 µg ml^{-1} coated anti-CD3 antibody and 1 µg ml^{-1} soluble anti-CD28 antibody in the presence of 2 ng ml^{-1} TGF-β with or without 10 U ml^{-1} IL-2 for 48 h in a 96-well flat-bottom plate. The starting number of CD4 Tn was in the range from 1.5×10^5 to 1.75×10^5 cells, dependent on availability, but the number was identical between different conditions within the same experiment.

T_{reg} survival and apoptosis assay. Isolated T_{reg} cells were first labelled with 5 µM CTV following the manufacturer's recommendations. A total of 2×10^5 cells per well were seeded in complete RPMI medium in a 96-well flat-bottom plate coated with 2 µg ml^{-1} anti-CD3 antibody plus 1 µg ml^{-1} soluble anti-CD28 antibody and 50 U ml^{-1} IL-2 and incubated for 72 h in the incubator at 37 °C. Following stimulation, the cells were stained with Annexin V Apoptosis Detection kit FITC and LIVE/DEAD Fixable Near-IR staining following the manufacturer's recommendations to simultaneously analyse cell survival and death and early and late apoptosis.

Stable isotope tracing and metabolite extraction. A total of 8×10^5 sorted T_{reg} cells were seeded in a 48-well plate and incubated in Gibco SILAC RPMI 1640 Flex medium (no glucose, no phenol red), supplemented with [U-^{13}C6] glucose (2 mg ml^{-1}), glutamine (0.29 mg ml^{-1}), arginine (0.2 mg ml^{-1}) and lysine (0.036 mg ml^{-1}), for 24 h with or without stimulation. Stimulation was performed with coated 2 µg ml^{-1} anti-CD3 and anti-CD28 antibodies plus 50 U ml^{-1} IL-2. After 24 h of incubation, cells were pelleted and then washed with a cold 0.9% NaCl solution. Ice-cold methanol:Milli-Q water (400 µl (ratio, 1:1), containing the internal standards pentanedioc-d_6 acid and [U-^{13}C]ribitol at a concentration of 1 µg ml^{-1}) was added to each sample, followed by 200 µl $CHCl_3$. Samples were incubated on a thermomixer for 20 min (4 °C, maximum speed), followed by a 10-min centrifugation (13,000*g* at 4 °C). The upper polar phase was collected and stored at −80 °C for MS analysis.

Determination of mass isotopomer distributions of intracellular metabolites using gas chromatography–mass spectrometry. Polar metabolites were derivatized for 90 min at 45 °C with 20 µl methoxyamine (20 mg ml^{-1}) in pyridine with continuous shaking and subsequently for 90 min at 45 °C with 20 µl MTBSTFA with 1% TBDMCS. Gas chromatography–MS analysis was performed using an Agilent 7890B Gas Chromatograph coupled to an Agilent 5977A Mass Selective Detector (Agilent Technologies). A sample volume of 1 µl was injected into a split/splitless inlet, operating in splitless mode at 270 °C. The gas chromatograph was equipped with a 30-m (I.D., 250 µm; film, 0.25 µm) ZB-35MS capillary column with a 5-m guard column (Phenomenex). Helium was used as the carrier gas with a constant flow rate of 1.2 ml min^{-1}. Gas chromatograph oven temperature was held at 100 °C for 2 min and increased to 300 °C at 10 °C min^{-1} and held for 4 min. The total run time was 26 min. The transfer line temperature was set to 280 °C. The mass selective detector was operating under electron ionisation at 70 eV. The MS source was held at 230 °C, and the quadrupole was held at 150 °C. For precise quantification of mass isotopomer distribution, measurements were performed in the selected ion monitoring mode. Our target ions (*m*/*z*) was citric acid 4TBDMS (591.3–600.3 *m*/*z*) (dwell time, 10 ms). MetaboliteDetector software (version 3.220180913, https://md.tu-bs.de/) was used for analyses.

DNA-methylation analysis of Foxp3. Genomic DNA was extracted from isolated CD4 Tn using the Monarch Genomic DNA purification kit following the manufacturer's instructions. DNA was bisulfite modified using the EpiTect Fast Bisulfite Conversion kit following the manufacturer's low input protocol. PCR amplification was performed using a standard PyroMark PCR kit as described in Supplementary Table 6. PCR amplicon intensity was verified by agarose gel electrophoresis relative to the intensity of the marker (10787026, Thermo). Multiple PCR replicates were pooled when necessary. Pyrosequencing was performed on a PyroMark Q96 ID using PyroMark Gold Q96 reagents and buffer sets (Supplementary Table 5) and sequencing primers (Supplementary Table 6). The PyroMark Control Oligo was included in each run. Data were analysed with PyroMark 2.5 software (9022198, Qiagen). 'Passed' or 'checked' quality reads were exported, and statistical analyses were performed in R (version 4.0.2; packages, tidyverse 1.3.0, ggpubr 0.4.0, multcomp 1.4-15).

Quantitative PCR of sorted murine T_{reg} cells or differentiated iT_{reg} cells. Total T_{reg} cells used in qPCR analysis were sorted from the spleen of young adult (8–12-week-old) and very old (~75-week-old) WT *Dj-1*$^{+/+}$ mice. qPCR was performed as described above. The housekeeping gene for normalizing *Dj-1* and *Pdhb* mRNA expression was *Rps13*.

Western blotting for murine T_{reg} and T_{conv} cells. Unstimulated cells were collected and lysed in RIPA buffer directly following isolation. For activation, 2×10^5 cells resuspended in 200 µl complete RPMI medium were stimulated in 96-well (flat) plates (2 µg ml^{-1} plate-coated anti-CD3 antibody and 1 µg ml^{-1} soluble anti-CD28 antibody with 20 U ml^{-1} recombinant mouse IL-2) for 24 h. The cells were lysed in RIPA buffer with Protease Inhibitor Cocktail (1:50) and Phosphatase Inhibitor Cocktail II (1:100)

before being frozen at −80 °C. We performed western blotting to analyse murine T cells as described above for human cells except that we used lamin B1 instead of GAPDH as the loading control. To analyse murine cells, we used Ladder Precision Plus Dual Color Standards. The relative quantification of Ser293 (normalized to lamin B1 values) from different mice (paired if the two samples were loaded in the same gel for comparability) is displayed on the right (the number of samples showing increased S293 levels (ratios were normalized to WT samples) out of the total number of analysed pairs is directly indicated in the plots) in Fig. 5.

Statistical analysis. *P* values were calculated with unpaired or paired two-tailed Student's *t*-test (GraphPad Prism version 7 or 9.0 or Excel) as specified in the corresponding figure legend. Of note, the EAE clinical scores between WT and KO groups were compared by paired two-tailed Student's *t*-test (GraphPad). All error bars represent the standard deviation. *P* values associated with Pearson correlation analysis were from two-tailed tests generated in GraphPad Prism. *P* values for microarray enrichment analysis were determined by one-tailed modified Fisher's exact test (from DAVID). The exact significant *P* values are provided in the legends for the corresponding plots, following the same order of comparisons from left to right.

Reporting summary. Further information on research design is available in the Nature Research Reporting Summary linked to this article.

Data availability

The microarray data have been deposited in the NCBI Gene Expression Omnibus under the accession number GSE115269. The proteomic mass spectrometry data (https://doi.org/doi:10.25345/C5437F) of the co-IP analysis have been deposited in ProteomeXchange via MassIVE under the identifier PXD016610. Source data are provided with this paper.

Received: 20 December 2019; Accepted: 20 April 2022;
Published online: 26 May 2022

References

1. Smeitink, J., van den Heuvel, L. & DiMauro, S. The genetics and pathology of oxidative phosphorylation. *Nat. Rev. Genet.* **2**, 342–352 (2001).
2. O'Neill, L. A., Kishton, R. J. & Rathmell, J. A guide to immunometabolism for immunologists. *Nat. Rev. Immunol.* **16**, 553–565 (2016).
3. Abou-Sleiman, P. M., Muqit, M. M. & Wood, N. W. Expanding insights of mitochondrial dysfunction in Parkinson's disease. *Nat. Rev. Neurosci.* **7**, 207–219 (2006).
4. Mizuno, Y. et al. Deficiencies in complex I subunits of the respiratory chain in Parkinson's disease. *Biochem. Biophys. Res. Commun.* **163**, 1450–1455 (1989).
5. Schapira, A. H. et al. Mitochondrial complex I deficiency in Parkinson's disease. *J. Neurochem.* **54**, 823–827 (1990).
6. González-Rodríguez, P. et al. Disruption of mitochondrial complex I induces progressive parkinsonism. *Nature* **599**, 650–656 (2021).
7. Bonifati, V. et al. Mutations in the *DJ-1* gene associated with autosomal recessive early-onset parkinsonism. *Science* **299**, 256–259 (2003).
8. Hayashi, T. et al. DJ-1 binds to mitochondrial complex I and maintains its activity. *Biochem. Biophys. Res. Commun.* **390**, 667–672 (2009).
9. Irrcher, I. et al. Loss of the Parkinson's disease-linked gene *DJ-1* perturbs mitochondrial dynamics. *Hum. Mol. Genet.* **19**, 3734–3746 (2010).
10. Krebiehl, G. et al. Reduced basal autophagy and impaired mitochondrial dynamics due to loss of Parkinson's disease-associated protein DJ-1. *PLoS ONE* **5**, e9367 (2010).
11. Hao, L. Y., Giasson, B. I. & Bonini, N. M. DJ-1 is critical for mitochondrial function and rescues PINK1 loss of function. *Proc. Natl Acad. Sci. USA* **107**, 9747–9752 (2010).
12. Burbulla, L. F. et al. Dopamine oxidation mediates mitochondrial and lysosomal dysfunction in Parkinson's disease. *Science* **357**, 1255–1261 (2017).
13. Ariga, H. et al. Neuroprotective function of DJ-1 in Parkinson's disease. *Oxid. Med. Cell. Longev.* **2013**, 683920 (2013).
14. Pisetsky, D. S. The role of mitochondria in immune-mediated disease: the dangers of a split personality. *Arthritis Res. Ther.* **18**, 169 (2016).
15. Mosley, R. L., Hutter-Saunders, J. A., Stone, D. K. & Gendelman, H. E. Inflammation and adaptive immunity in Parkinson's disease. *Cold Spring Harb. Perspect. Med.* **2**, a009381 (2012).
16. Waak, J. et al. Regulation of astrocyte inflammatory responses by the Parkinson's disease-associated gene *DJ-1*. *FASEB J.* **23**, 2478–2489 (2009).
17. Kim, J. H. et al. DJ-1 facilitates the interaction between STAT1 and its phosphatase, SHP-1, in brain microglia and astrocytes: a novel anti-inflammatory function of DJ-1. *Neurobiol. Dis.* **60**, 1–10 (2013).
18. Amatullah, H. et al. DJ-1/PARK7 impairs bacterial clearance in sepsis. *Am. J. Respir. Crit. Care Med.* **195**, 889–905 (2017).
19. Liu, W. et al. Park7 interacts with $p47^{phox}$ to direct NADPH oxidase-dependent ROS production and protect against sepsis. *Cell Res.* **25**, 691–706 (2015).
20. Singh, Y. et al. Differential effect of DJ-1/PARK7 on development of natural and induced regulatory T cells. *Sci. Rep.* **5**, 17723 (2015).
21. Sakaguchi, S., Miyara, M., Costantino, C. M. & Hafler, D. A. $FOXP3^+$ regulatory T cells in the human immune system. *Nat. Rev. Immunol.* **10**, 490–500 (2010).
22. Reeve, A., Simcox, E. & Turnbull, D. Ageing and Parkinson's disease: why is advancing age the biggest risk factor? *Ageing Res. Rev.* **14**, 19–30 (2014).
23. He, F. et al. PLAU inferred from a correlation network is critical for suppressor function of regulatory T cells. *Mol. Syst. Biol.* **8**, 624 (2012).
24. Bras, J., Guerreiro, R. & Hardy, J. SnapShot: genetics of Parkinson's disease. *Cell* **160**, 570 (2015).
25. Gillis, J. & Pavlidis, P. The role of indirect connections in gene networks in predicting function. *Bioinformatics* **27**, 1860–1866 (2011).
26. Pham, T. T. et al. DJ-1-deficient mice show less TH-positive neurons in the ventral tegmental area and exhibit non-motoric behavioural impairments. *Genes Brain Behav.* **9**, 305–317 (2010).
27. Jagger, A., Shimojima, Y., Goronzy, J. J. & Weyand, C. M. Regulatory T cells and the immune aging process: a mini-review. *Gerontology* **60**, 130–137 (2014).
28. Zeng, N. et al. DJ-1 depletion prevents immunoaging in T-cell compartments. *EMBO Rep.* **23**, e53302 (2022).
29. Kohm, A. P., Carpentier, P. A., Anger, H. A. & Miller, S. D. Cutting edge: $CD4^+CD25^+$ regulatory T cells suppress antigen-specific autoreactive immune responses and central nervous system inflammation during active experimental autoimmune encephalomyelitis. *J. Immunol.* **169**, 4712–4716 (2002).
30. Mak, T. W. et al. Glutathione primes T cell metabolism for inflammation. *Immunity* **46**, 675–689 (2017).
31. Gray, D. H. et al. Developmental kinetics, turnover, and stimulatory capacity of thymic epithelial cells. *Blood* **108**, 3777–3785 (2006).
32. Zemmour, D. et al. Single-cell gene expression reveals a landscape of regulatory T cell phenotypes shaped by the TCR. *Nat. Immunol.* **19**, 291–301 (2018).
33. Xu, J. et al. The Parkinson's disease-associated DJ-1 protein is a transcriptional co-activator that protects against neuronal apoptosis. *Hum. Mol. Genet.* **14**, 1231–1241 (2005).
34. Holling, T. M., Schooten, E. & van Den Elsen, P. J. Function and regulation of MHC class II molecules in T-lymphocytes: of mice and men. *Hum. Immunol.* **65**, 282–290 (2004).
35. van der Brug, M. P. et al. RNA binding activity of the recessive parkinsonism protein DJ-1 supports involvement in multiple cellular pathways. *Proc. Natl Acad. Sci. USA* **105**, 10244–10249 (2008).
36. Weyand, C. M., Goronzy, J. & Fathman, C. G. Modulation of CD4 by antigenic activation. *J. Immunol.* **138**, 1351–1354 (1987).
37. Vandenbon, A. et al. Immuno-Navigator, a batch-corrected coexpression database, reveals cell type-specific gene networks in the immune system. *Proc. Natl Acad. Sci. USA* **113**, E2393–E2402 (2016).
38. Patel, M. S. & Roche, T. E. Molecular biology and biochemistry of pyruvate dehydrogenase complexes. *FASEB J.* **4**, 3224–3233 (1990).
39. Desdin-Mico, G. et al. T cells with dysfunctional mitochondria induce multimorbidity and premature senescence. *Science* **368**, 1371–1376 (2020).
40. Wang, R. & Green, D. R. Metabolic checkpoints in activated T cells. *Nat. Immunol.* **13**, 907–915 (2012).
41. Zhou, Z. H., McCarthy, D. B., O'Connor, C. M., Reed, L. J. & Stoops, J. K. The remarkable structural and functional organization of the eukaryotic pyruvate dehydrogenase complexes. *Proc. Natl Acad. Sci. USA* **98**, 14802–14807 (2001).
42. Zachar, Z. et al. Non-redox-active lipoate derivates disrupt cancer cell mitochondrial metabolism and are potent anticancer agents in vivo. *J. Mol. Med.* **89**, 1137–1148 (2011).
43. Polansky, J. K. et al. DNA methylation controls *Foxp3* gene expression. *Eur. J. Immunol.* **38**, 1654–1663 (2008).
44. Benayoun, B. A., Pollina, E. A. & Brunet, A. Epigenetic regulation of ageing: linking environmental inputs to genomic stability. *Nat. Rev. Mol. Cell Biol.* **16**, 593–610 (2015).
45. Gerriets, V. A. et al. Metabolic programming and PDHK1 control $CD4^+$ T cell subsets and inflammation. *J. Clin. Invest.* **125**, 194–207 (2015).
46. Richard, A. J., Hang, H. & Stephens, J. M. Pyruvate dehydrogenase complex (PDC) subunits moonlight as interaction partners of phosphorylated STAT5 in adipocytes and adipose tissue. *J. Biol. Chem.* **292**, 19733–19742 (2017).
47. Patel, K. P., O'Brien, T. W., Subramony, S. H., Shuster, J. & Stacpoole, P. W. The spectrum of pyruvate dehydrogenase complex deficiency: clinical, biochemical and genetic features in 371 patients. *Mol. Genet. Metab.* **106**, 385–394 (2012).
48. Olahova, M. et al. Biallelic mutations in *ATP5F1D*, which encodes a subunit of ATP synthase, cause a metabolic disorder. *Am. J. Hum. Genet.* **102**, 494–504 (2018).
49. Probst-Kepper, M. et al. GARP: a key receptor controlling FOXP3 in human regulatory T cells. *J. Cell. Mol. Med.* **13**, 3343–3357 (2009).

50. Tyanova, S. et al. The Perseus computational platform for comprehensive analysis of (prote)omics data. *Nat. Methods* **13**, 731–740 (2016).

Acknowledgements

This work was supported by the Luxembourg National Research Fund (FNR) CORE programme (CORE/14/BM/8231540/GeDES), the Luxembourg–RIKEN bilateral programme 'TregBar', 'NEXTIMMUNE' (PRIDE/11012546) and 'CRiTiCS' DTU (to F.Q.H.); individual Aide à la Formation Recherche grants to E.D. (PHD-2014-1/7603621) and N.Z. (PHD-2015-1/9989160); and other PhD position grants to C.M.C. (PRIDE/2015/10907093) and D.G.F. (through the Luxembourg–RIKEN bilateral programme (2015/11228353, 'TregBar')) through the group of F.Q.H. The work was also supported by the DFG (grant WU 164/5-1) to W.W. and by the German Federal Ministry of Education and Research (BMBF) through the Integrated Network MitoPD (grant 031A430E to W.W. and D.M.V.W.). J.M. is supported by FNR ATTRACT (A18/BM/11809970). D.B. is supported by FNR ATTRACT (A14/BM/7632103) and FNR CORE grants (C21/BM/15796788 and C18/BM/12691266). R.K. is supported by the FNR NCER-PD and PEARL programme (FNR/P13/6682797). We also thank the Luxembourg Centre for Systems Biomedicine Metabolomics Platform for providing technical and analytical support and acknowledge the EMBL Genomics Core Facility (Heidelberg, V. Benes) for their microarray analysis. We thank A. Daujeumont, N. Ouzren, T. Li, O. Boyd, N. Bonjean, C. Davril, S. Köglsberger, J. Walter, X. Dong, S. Badeke and F. Fack for their expert technical support. We acknowledge M.P. Dufresne (Liege, Belgium) for allowing us to access their irradiator and N. Malvaus from the Luxembourg Red Cross for providing buffy coats and leukopaks.

Author contributions

E.D. and N.Z. designed and performed major parts of the human- and mouse-related experiments, respectively. N.Z. analysed mouse-related data. C.M.C. performed and analysed human-, patient- and mouse-related experiments. N.P. and C.L.L. performed and analysed metabolome-related experiments. J.M. and M.B. performed and supervised ^{13}C tracing experiments and data analysis. D.G.F. and S.D. performed parts of primary human T cell-related experiments. G.G.G. and J.C.S. contributed to Seahorse assays. M.P.M. and J.D.T. contributed to epigenetic analysis. M.A.G. and J.R. performed and analysed proteomic experiments. H.K., M.G. and D.B. performed EAE-related experiments. C.G. supervised FCM-related experiments. A.B., S.F., O.D., D.C. and C.L. performed and/or supervised parts of mouse-related experiments. D.M.V.W. performed part of the EAE experiments. W.W., R.K., R.B. and M.O. provided insights and supervised parts of the experiments. R.B. and M.O. revised the manuscript. F.Q.H. conceived and directed the project and wrote the manuscript.

Competing interests

F.Q.H., R.B. and E.D. once filed a patent on some of the related data.

Additional information

Extended data is available for this paper at https://doi.org/10.1038/s42255-022-00576-y.

Supplementary information The online version contains supplementary material available at https://doi.org/10.1038/s42255-022-00576-y.

Correspondence and requests for materials should be addressed to Feng Q. Hefeng.

Peer review information *Nature Metabolism* thanks Ulf Beier, Alexander Eggel and the other, anonymous, reviewers for their contribution to the peer review of this work. Primary handling editors: Alfredo Gimenez-Cassina and George Caputa, in collaboration with the *Nature Metabolism* team.

Reprints and permissions information is available at www.nature.com/reprints.

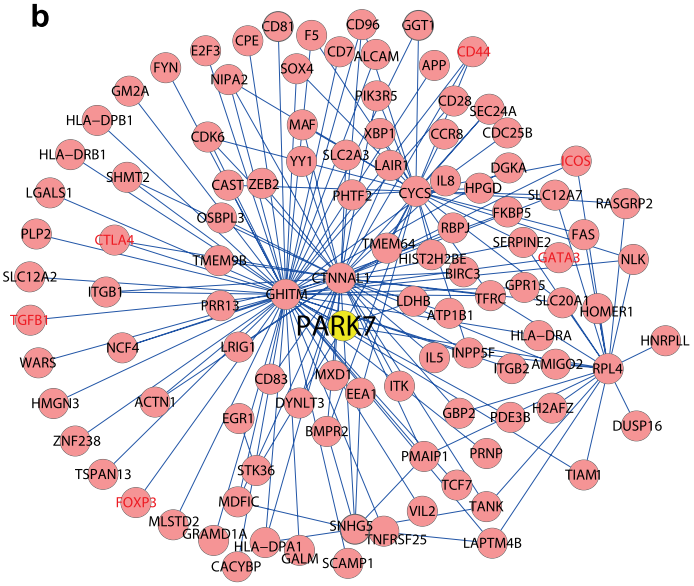
Publisher's note Springer Nature remains neutral with regard to jurisdictional claims in published maps and institutional affiliations.

© The Author(s), under exclusive licence to Springer Nature Limited 2022

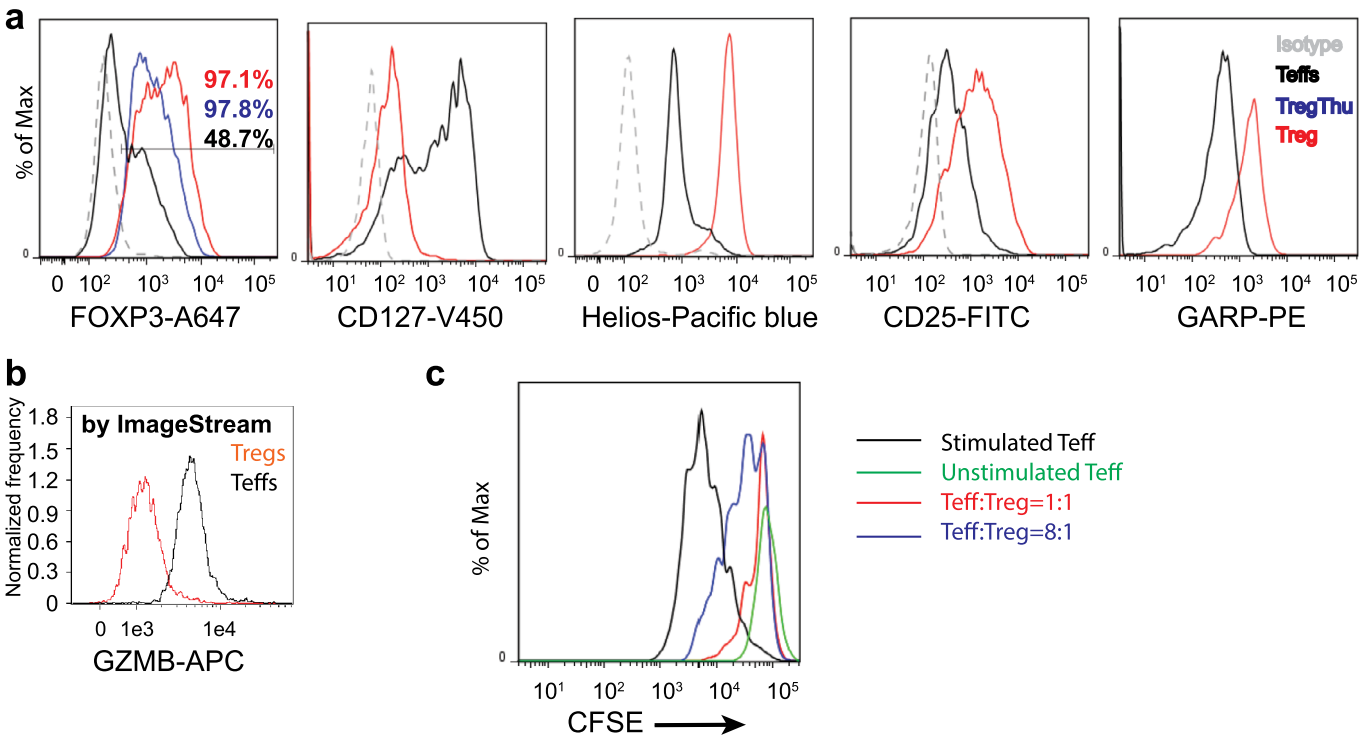
a

Gene symbol	Mean Teff1	Mean Teff2	Mean Treg1	Mean Treg2
SLC18A2	16.71	16.11	20.09	15.52
PARK2	19.72	17.05	21.93	20.76
PARK7/DJ-1	6830.89	8011.65	9783.31	8266.40
UCHL1	33.73	21.37	33.14	45.84
STK39	868.74	1036.97	744.92	567.04
HTRA2	199.75	346.14	307.10	248.92
SNCA	10.72	10.97	110.39	248.24
LAMP3	24.06	100.21	74.69	164.72
PINK1	89.99	105.74	143.04	111.72
SYT11	325.62	235.47	291.42	347.74
HIP1R	10.67	7.74	7.28	5.98
PLA2G6	120.08	136.30	141.53	149.91
MCCC1	279.89	210.59	293.56	255.56
ATP13A2	37.09	49.15	58.06	27.87
MAPT	48.81	39.95	56.77	57.12
LRRK2	11.39	9.22	7.11	8.27
ACMSD	12.19	9.75	11.66	17.98
CCDC62	36.84	24.69	34.38	37.92
TFAM	423.13	521.16	494.28	618.08
FBXO7	1012.48	974.32	1065.89	992.16

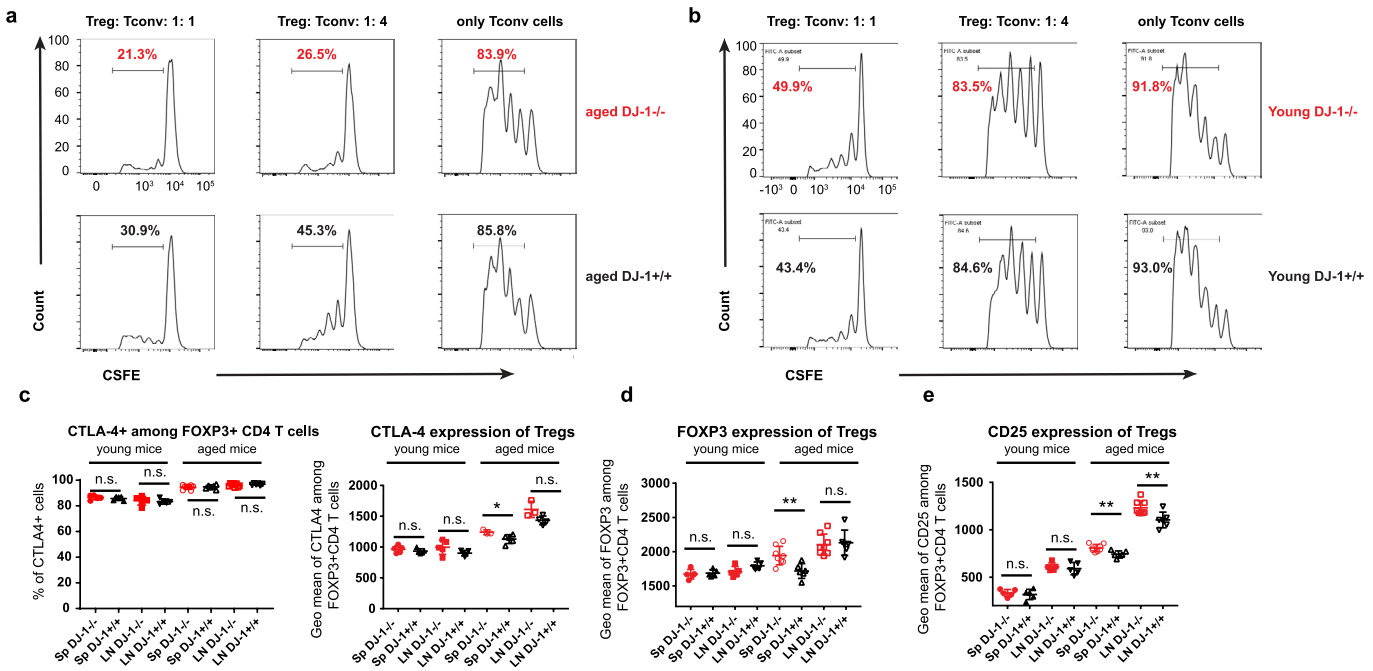
b



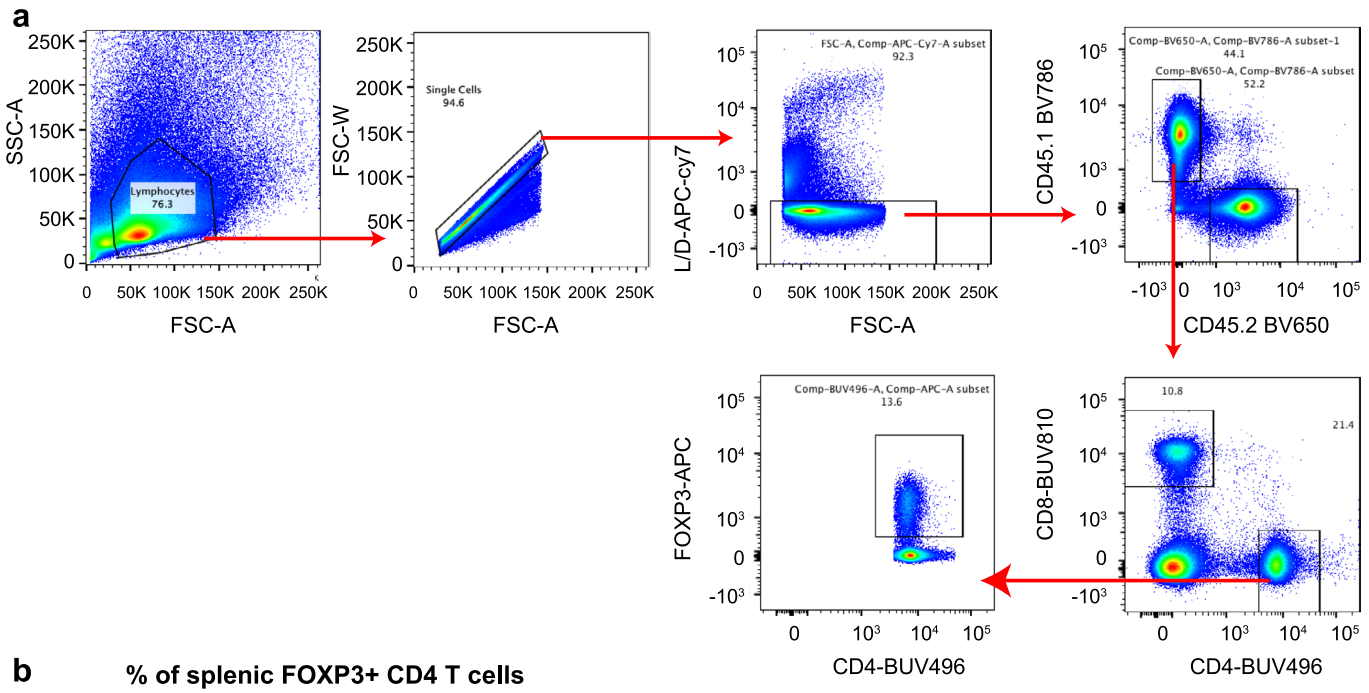
Extended Data Fig. 1 | DJ-1 is highly expressed in human Tregs and connected with well-known Treg genes in Treg specific-correlation network. a, Mean transcription expression of the known PD genes measured in the first 6hrs of anti-CD3-/-CD28/IL-2 stimulation assessed by our published high-time-resolution (an interval of 20min) time-series transcriptome (with 19 time points)[23]. Treg1 and Treg2 (or Teff1 and Teff2) represent two independently repeated HTR time-series experiments for Tregs (or Teffs). DJ-1 is highlighted by red rectangle. b, PARK7/DJ-1 subnetwork extracted from the constructed human Treg-specific correlation network. Each oval represents one gene. A selection of known key Treg genes were highlighted in red. Each line between DJ-1 and the other genes represents a correlation-based functional linkage.

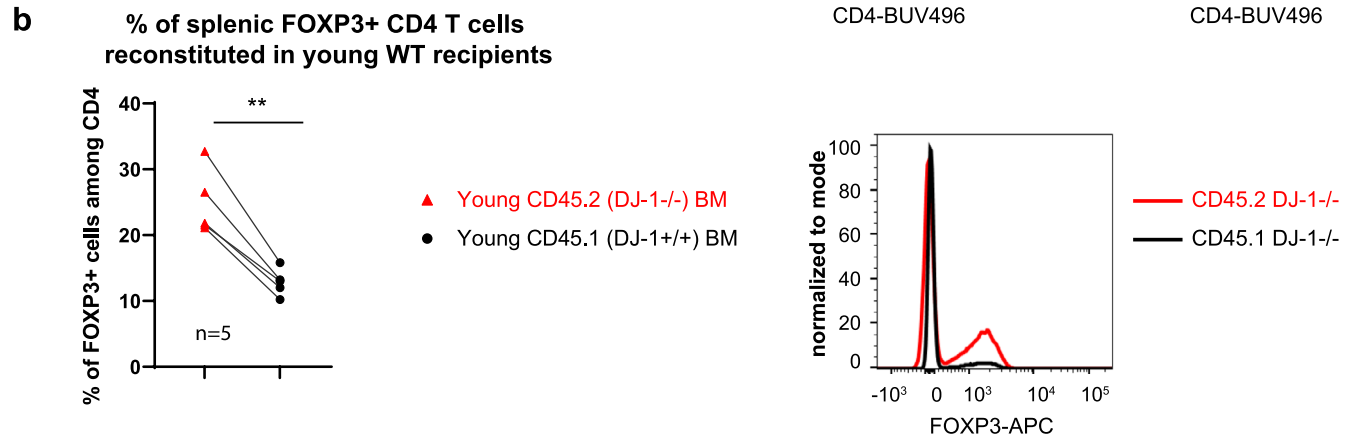


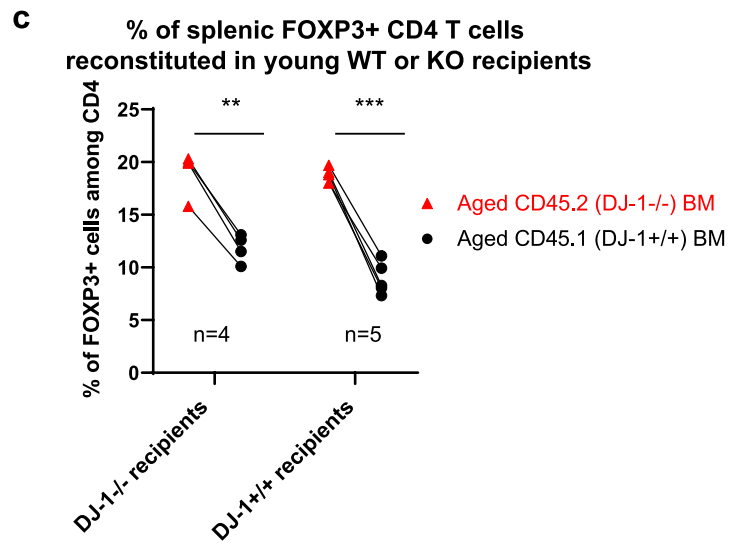
Extended Data Fig. 2 | Characterization of highly purified human nTregs. a, Characterization of highly purified human nTregs ($CD4^{+}CD25^{high}CD127^{low}$). Representative FCM plots of FOXP3, CD127, Helios, and CD25 on human Tregs relative Teffs (all the markers were not stained in the same panel). 'TregThu' is a golden standard of isolated human Tregs[50]. The protein expression of *LRRC32* (GARP) was measured after 3-day stimulation by irradiated EBV-transformed B cells. **b**, Representative *ImageStream* plot of GZMB expression in unstimulated Tregs or Teffs. **c**, Representative *In-vitro* proliferation assay of human Teffs suppressed by human Tregs at different ratios, in co-culture with irradiated EBV-B cells for 5 days. Only living CD4 T cells were gated for analysis. Results represent 7-10 (**a-c**) independent experiments (from different heathy donors).



Extended Data Fig. 3 | Dj-1 deletion does not compromise suppressor function of individual Tregs. a, **b**, *In-vitro* suppression assay of *Dj-1*$^{-/-}$ or *Dj-1*$^{+/+}$ Tregs isolated from aged (**a**) or young (**b**) mice in co-culture with Tconv and irradiated feeder cells in the presence of anti-CD3 for 3.5 days. Percentages of dividing cells from the total population (the total population indicates the gated DAPI-negative and CD4^{+}, CFSE-labelled Tconv) are presented on the plots. **c**, Frequency of CTLA4-expressing cells among CD4^{+}FOXP3^{+} Treg cells (left) and Geometric mean (Geo mean, MFI) of CTLA4 among CD4+FOXP3+ Tregs from spleen (Sp) and lymph nodes (LN) from *Dj-1*$^{-/-}$ and *Dj-1*$^{+/+}$ WT littermates [for the frequency, n=that in d and e; for CTLA4 MFI measurement in aged mice (aged KO, n=3; WT, n=5 sp; KO, n=3 LN; WT, n=4 LN; of note, for comparability, the CTLA4 MFI results were not pooled from different batches; for CTLA4 MFI measurement in young mice, n=that in d and e]. *P=0.0500. **d, e**, Geometric mean (MFI) of FOXP3 (**d**) or CD25 (**e**) expression among CD4+FOXP3+ Tregs. Young or aged murine results are marked in each panel (young KO, n=5; young WT, n=5; aged KO, n=8; aged WT, n=6; aged data pooled from 2 independent experiments). **P=0.00581 (**d**); **P=0.00654 and **P=0.00946 (**e**). Results represent three (**a, b**) and four (**c, d, e**) independent experiments. Data are mean ± s.d. P values are determined by two-tailed Student's *t*-test. ns, not significant, *P<=0.05, **P<=0.01 and ***P<=0.001.

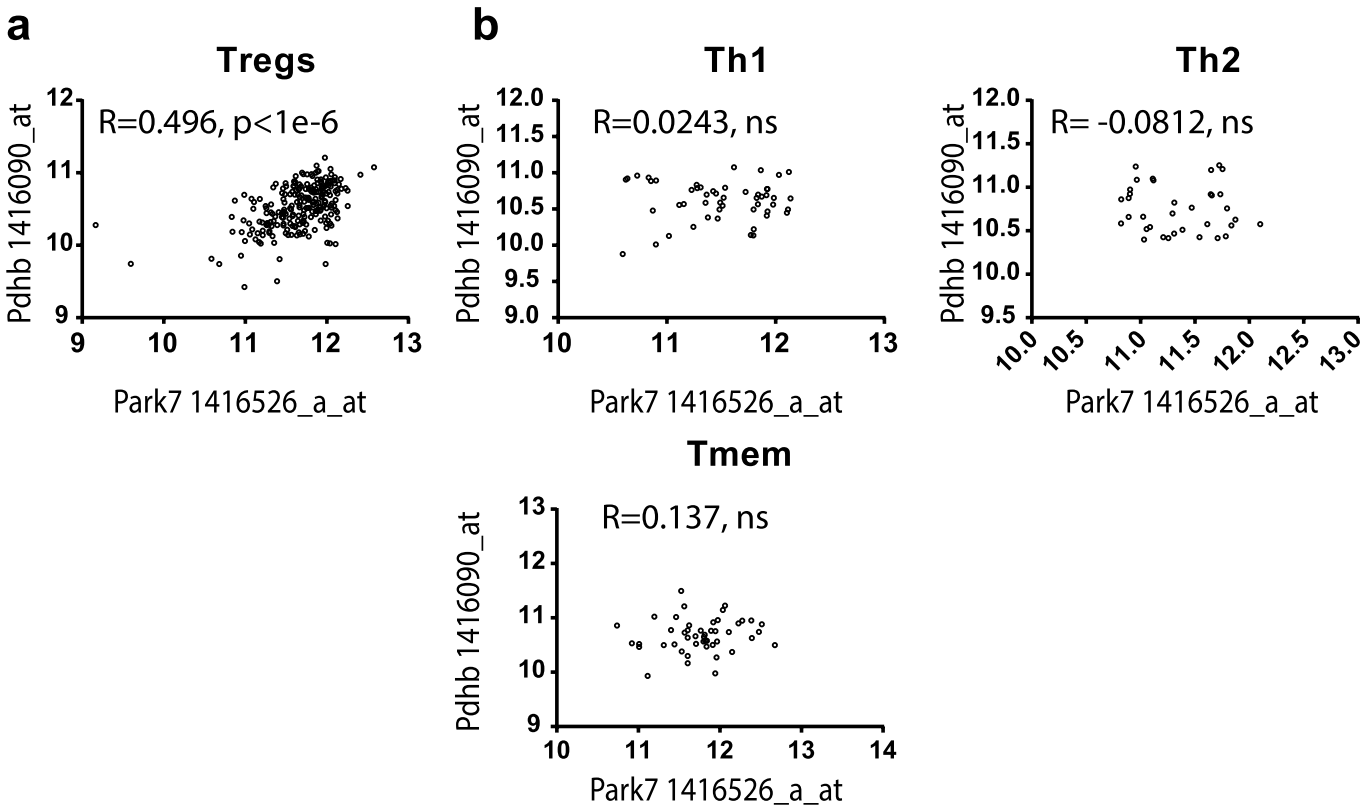




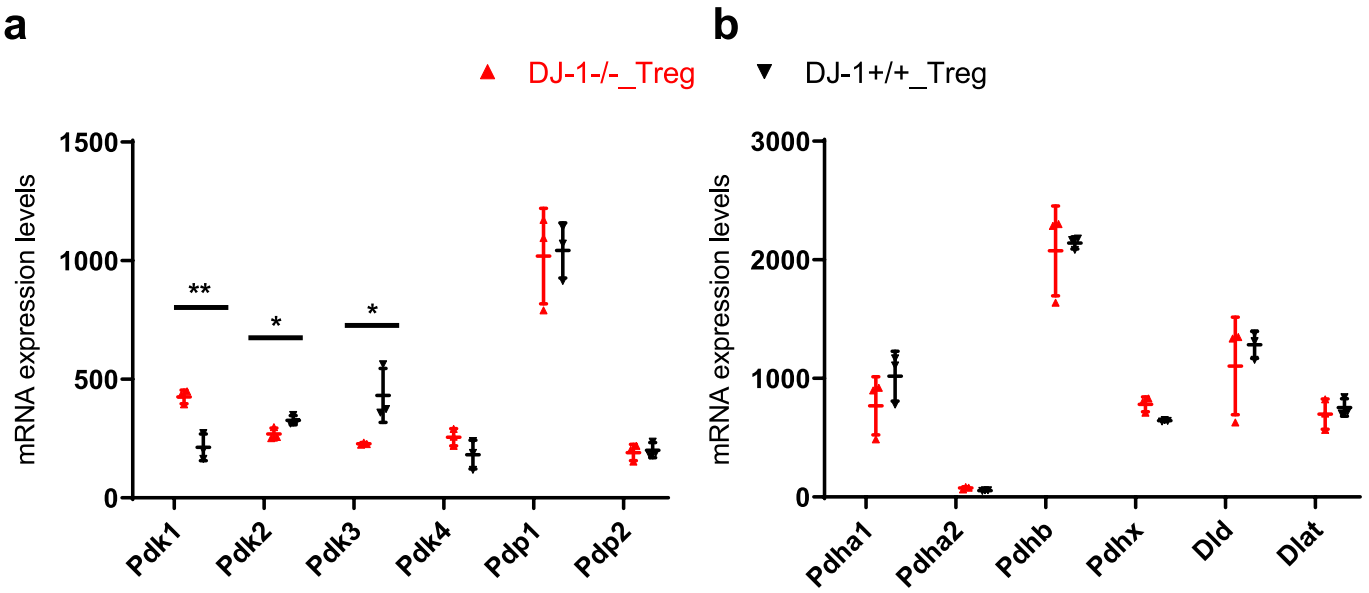


Extended Data Fig. 4 | See next page for caption.

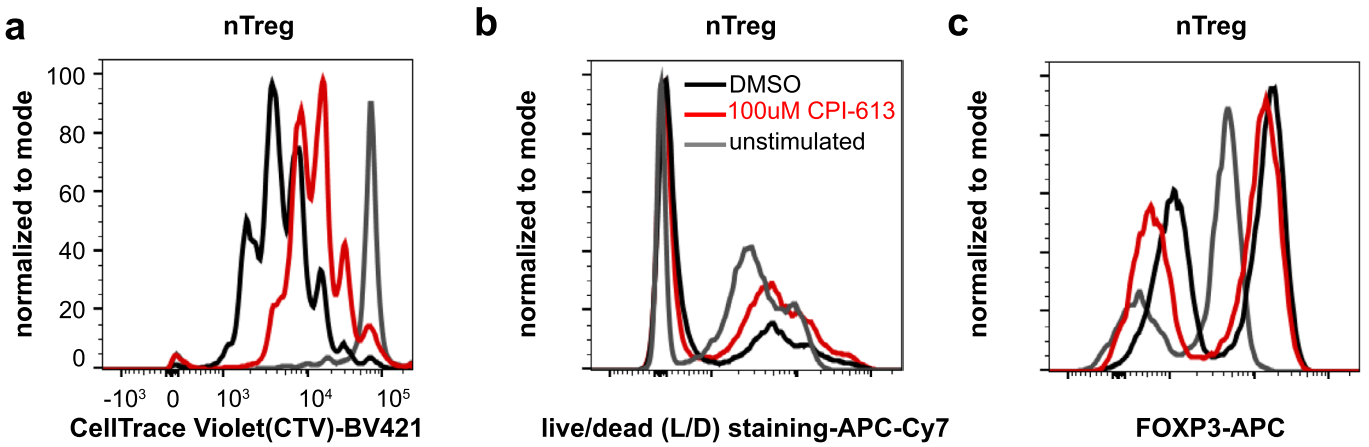
Extended Data Fig. 4 | BM models show that Treg cellularity is also regulated in a hematopoietic-extrinsic and host micro-environmental aging-dependent manner. a, Gating strategy used to identify FOXP3+ cells among CD4 T cells developed from CD45.1 *Dj-1* WT- and CD45.2 *Dj-1* KO-origin cells in bone marrow (BM) chimeras. **b**, Percentages of FOXP3+ cells among living CD4+ cells originated from CD45.1 or CD45.2 BM cells transplanted from young donors (left panel, n=5). Representative histogram overlay of FOXP3 expression among living CD4 T cells derived from CD45.2 *Dj-1* KO or CD45.1 *Dj-1* WT BM cells (right panel). **P=0.00131. **c**, Percentages of FOXP3+ cells among living CD4+ cells originated from CD45.1 *Dj-1* WT or CD45.2 *Dj-1* KO BM cells transplanted from aged donors and reconstituted in young *Dj-1* KO (n=4) or WT recipients (n=5). **P=0.00113 and ***P=0.000106. Results represent two (**b, c**) independent experiments. Data are mean ± s.d. P values are determined by paired two-tailed Student's *t*-test. ns, not significant, *P<=0.05, **P<=0.01 and ***P<=0.001.



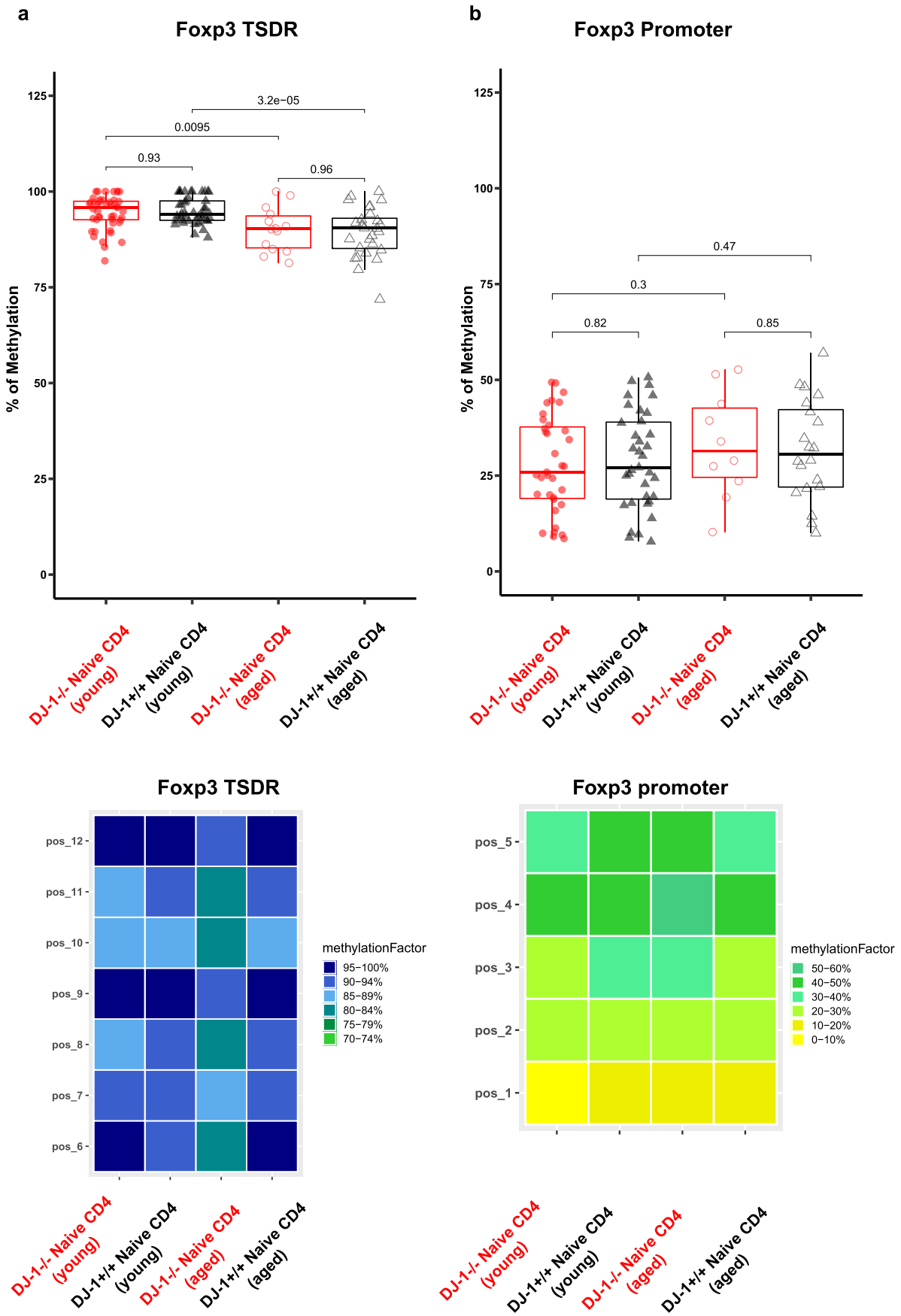
Extended Data Fig. 5 | Treg-specific correlation between Dj-1 and Pdhb. a, mRNA expression of *Park7/Dj-1* is highly correlated with *Pdhb* only in murine Tregs but not in other analyzed CD4 T-cell subsets. 1416526_a_at and 1416090_at are the probeset IDs measuring *Park7* and *Pdhb* in Affymetric microarrays, respectively. The number (n) of microarray samples used for correlation analysis is 240, 51, 35 and 47 from CD4 Tregs, Th1, Th2 and Tmem (memory CD4 T cells), respectively. The R value corresponds to Pearson correlation coefficient and the associated P-value is from two-tailed test (Prism). Ns, non-significant and otherwise, P value is provided for the corresponding cell type. For the details, refer to the database (from *Sakaguchi's lab*): https://sysimm.ifrec.osaka-u.ac.jp/immuno-navigator/?o=10090&probe1=1416526_a_at&probe2=1416090_at&cell=5.



Extended Data Fig. 6 | Expression analysis of the genes encoding PDH complex and the PDH regulatory machinery in nTregs of aged mice. a, mRNA expression of the genes (*Pdks*) encoding PDH kinases and the genes (*Pdps*) encoding pyruvate dehydrogenase phosphatases in Tregs freshly isolated from aged *Dj-1* KO and age- and gender-matched WT littermates (n=3/group). **P=0.00420, *P=0.0348, and *P=0.0362. b, mRNA expression of the genes encoding several PDH complex subunits in Tregs freshly isolated from aged *Dj-1 KO* and WT littermates. Results are the summary of the microarray datasets (from 3 mice each group). Data are mean± s.d. P values are determined by two-tailed Student's *t*-test. ns or unlabeled, not significant, *P<=0.05, **P<=0.01 and ***P<=0.001.

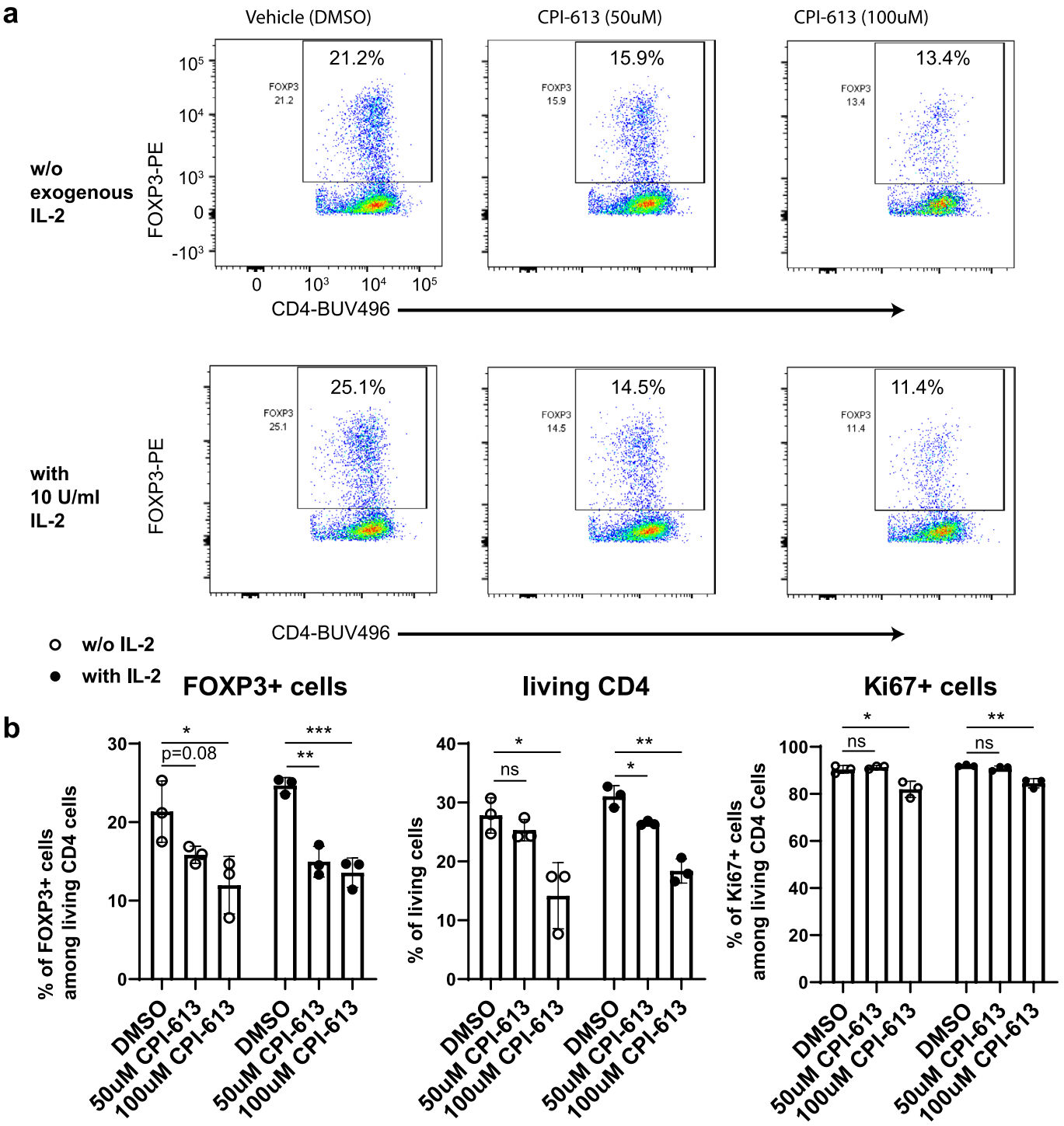


Extended Data Fig. 7 | PDH inhibition compromises nTreg proliferation but not lineage stability. a, b, c, Cell proliferation [as labelled by CTV] (**a**), cell survival as measured by live/dead staining among CD4+ cells (**b**) or histogram overlay of FOXP3 expression (**c**) in isolated nTregs stimulated for three days treated with the indicated concentration of a PDH inhibitor (CPI-613) or control vehicle or without stimulation (gray). Results represent at least three independent experiments.



Extended Data Fig. 8 | See next page for caption.

Extended Data Fig. 8 | Age-dependent loss of methylation in Foxp3 TSDR in naïve CD4 cells. a, upper panel: Methylation analysis of isolated naïve CD4+ T cells (CD4 Tn) from *DJ-1 KO* or WT mice for *Foxp3* TSDR (Regulatory T-Cell-Specific Demethylated Region). Individual values for CpG positions 6-12 are shown as individual data points. lower panel: Heatmap displays mean methylation per CpG position in 5% intervals. **P=0.0095 and ***P=3.2E-05. **b**, upper panel: Methylation analysis of isolated CD4 Tn from *DJ-1 KO* or WT mice for the *Foxp3* promoter region. Individual values for CpG positions 1-5 are shown as individual data points. Lower panel: Heatmap displays mean methylation per CpG position in 10% intervals. Results represent 2-4 independent experiments (young KO n= 7; young WT n= 7; aged KO n= 2; aged WT n= 4; all males). Boxplots show 25th and 75th percentiles around the median. Whiskers correspond to 1.5× IQR (interquantile range). Horizontal bars show Holm-adjusted P values after two-sided Wilcox test. Of note, since *Foxp3* is an X-linked gene, to avoid observing x-inactivation-related methylation alteration, we focused on males here.



Extended Data Fig. 9 | PDH inhibition also compromises iTreg differentiation in naïve CD4 T cells isolated from aged mice. a, Representative FCM plots of FOXP3 expression among living CD4 T cells differentiated from naïve CD4 T cells (CD4 Tn) treated with different doses of CPI-613 or control vehicle without (upper panel) or with 10U/ml of recombinant IL-2 (lower panel). The CD4 Tn were isolated from very old DJ-1 WT mice (~105-wk-old). **b**, Percentages of FOXP3+ cells (left panel) or Ki67+ cells (right panel) among living CD4 T cells following iTreg differentiation with different doses of CPI-613 or control vehicles with or without exogenous IL-2 for three days (n=3 mice). Middle panel, Percentages of living cells among total CD4 T cells following iTreg differentiation. Of note, a PE instead of APC fluorochrome (the latter was used in other experiments) was used to analyze FOXP3 expression in the experiments of this figure. *P=0.0387, **P=0.00157 and ***P=0.000845 (left panel); *P=0.0206, *P=0.0130 and **P=0.00130 (middle panel); *P=0.0183 and **P=0.00312 (right panel). Results represent two (**a, b**) independent experiments. Data are mean ± s.d. P values are determined by two-tailed Student's *t*-test. ns, not significant, *P<=0.05, **P<=0.01 and ***P<=0.001.

nature portfolio

Corresponding author(s): Feng Q. Hefeng

Last updated by author(s): Apr 19, 2022

Reporting Summary

Nature Portfolio wishes to improve the reproducibility of the work that we publish. This form provides structure for consistency and transparency in reporting. For further information on Nature Portfolio policies, see our Editorial Policies and the Editorial Policy Checklist.

Statistics

For all statistical analyses, confirm that the following items are present in the figure legend, table legend, main text, or Methods section.

n/a	Confirmed	
☐	☒	The exact sample size (*n*) for each experimental group/condition, given as a discrete number and unit of measurement
☐	☒	A statement on whether measurements were taken from distinct samples or whether the same sample was measured repeatedly
☐	☒	The statistical test(s) used AND whether they are one- or two-sided *Only common tests should be described solely by name; describe more complex techniques in the Methods section.*
☐	☒	A description of all covariates tested
☒	☐	A description of any assumptions or corrections, such as tests of normality and adjustment for multiple comparisons
☐	☒	A full description of the statistical parameters including central tendency (e.g. means) or other basic estimates (e.g. regression coefficient) AND variation (e.g. standard deviation) or associated estimates of uncertainty (e.g. confidence intervals)
☐	☒	For null hypothesis testing, the test statistic (e.g. *F*, *t*, *r*) with confidence intervals, effect sizes, degrees of freedom and *P* value noted *Give P values as exact values whenever suitable.*
☒	☐	For Bayesian analysis, information on the choice of priors and Markov chain Monte Carlo settings
☒	☐	For hierarchical and complex designs, identification of the appropriate level for tests and full reporting of outcomes
☐	☒	Estimates of effect sizes (e.g. Cohen's *d*, Pearson's *r*), indicating how they were calculated

Our web collection on statistics for biologists contains articles on many of the points above.

Software and code

Policy information about availability of computer code

Data collection	No software was used for data collection.
Data analysis	All the flow cytometry data have been analyzed by the Flowjo software v7.6.5 or v10 . The ImageStream data were analyzed by IDEAS 6.2 software (Amnis). All the statistical figures were visualized and analyzed in GraphPad Prism v7 or v9 . The expression signal at the exon level was summarized by the Affymetrix PLIER algorithm with DABG and PM-GCBG options by means of the sketch-quantile normalization approach (Affymetrix Expression Console v1.4). DAVID v6.7 (https://david.ncifcrf.gov/) was used to perform functional enrichment analysis for the lists of differentially up- or down-regulated genes. The heatmap of microarray data was visualized using the R Heatmap.2 (gplots package). The seahorse data were analyzed by Wave 2.6.0 (Agilent Technologies). Realtime PCR data were analyzed by with LightCycler 480 SW 1.5 software. Raw output data files of mass spectometry analysis were analysed by using Maxquant (v1.5.2.8). Peptides were compared with the UniProt human database (02-2015 release). A reverse sequence database was used to impose a strict 1% FDR cut-off. Label-free quantification was performed by using the MaxLFQ algorithm. Data processing was performed in Microsoft Excel and Perseus (v1.5.0.15)5. Contaminants, decoys and single peptide identifications were removed. If needed, the contrast and brightness of the whole Western Blotting image was adjusted by using the ImageJ software. The MetaboliteDetector software (v3.220180913) was used for mass spectrometric data post processing, quantification, MID calculations, correction of natural isotope abundance, and determinations of fractional carbon contributions. For the DNA methylation analysis, pyrosequencing runs were analyzed with PyroMark 2.5 software (9022198, QIAGEN) and only passed or checked quality reads were exported for further analysis. Subsequent statistics were done in R (version 4.0.2) using the following packages (tidyverse 1.3.0, ggpubr 0.4.0, multcomp 1.4-15).

For manuscripts utilizing custom algorithms or software that are central to the research but not yet described in published literature, software must be made available to editors and reviewers. We strongly encourage code deposition in a community repository (e.g. GitHub). See the Nature Portfolio guidelines for submitting code & software for further information.

Data

Policy information about availability of data

All manuscripts must include a data availability statement. This statement should provide the following information, where applicable:

- Accession codes, unique identifiers, or web links for publicly available datasets
- A description of any restrictions on data availability
- For clinical datasets or third party data, please ensure that the statement adheres to our policy

The microarray data have been deposited in the NCBI Gene Expression Omnibus (GEO) under the access number of GSE115269. The proteomic mass spectrometry data [doi:10.25345/C5437F] of the Co-IP analysis have been deposited in ProteomeXchange via MassIVE under the identifier PXD016610.

Field-specific reporting

Please select the one below that is the best fit for your research. If you are not sure, read the appropriate sections before making your selection.

☒ Life sciences ☐ Behavioural & social sciences ☐ Ecological, evolutionary & environmental sciences

For a reference copy of the document with all sections, see nature.com/documents/nr-reporting-summary-flat.pdf

Life sciences study design

All studies must disclose on these points even when the disclosure is negative.

Sample size	Sample size was chosen according to standard practices in the field (Zeng et al. Nature, 2013) or our recent own publication (Zeng et al., EMBO Reports, 2022). All experiments were performed several times and conclusions were considered valid if results were reproducible between experiments.
Data exclusions	No data was excluded from analysis
Replication	All of reported data were successfully independently reproduced at least twice (often more than twice, the exact number of replications has been specified in the corresponding Figure legends).
Randomization	No randomization is applied in our experiments. In our work, we essentially compared and analysed DJ-1 WT and KO mice during the natural aging process. The group (WT or KO) has already been determined in advance by the genotype itself and therefore it is not possible to randomly re-assign/change the murine groups again.
Blinding	For the normal EAE experiments, the investigators are blind to the genotype during injection and EAE symptom scoring to avoid bias in scoring. To perform EAE adoptive transfer experiments, in order to get enough Tregs, we had to pool different mice from the same genotype together. Therefore, blinding is not possible for the EAE adoptive transfer experiments. For the same rationale, it also not possible keep the investigators blind to donor mouse genotype for bone marrow model experiments. For the flow cytometry phenotypic analysis or other machine-based (e.g., qPCR, WB) quantitative measurement, blinding is not relevant because knowing the genotypes or not in advance has no impact on data analysis.

Reporting for specific materials, systems and methods

We require information from authors about some types of materials, experimental systems and methods used in many studies. Here, indicate whether each material, system or method listed is relevant to your study. If you are not sure if a list item applies to your research, read the appropriate section before selecting a response.

Materials & experimental systems

n/a	Involved in the study
☐	☒ Antibodies
☐	☒ Eukaryotic cell lines
☒	☐ Palaeontology and archaeology
☐	☒ Animals and other organisms
☐	☒ Human research participants
☒	☐ Clinical data
☒	☐ Dual use research of concern

Methods

n/a	Involved in the study
☒	☐ ChIP-seq
☐	☒ Flow cytometry
☒	☐ MRI-based neuroimaging

Antibodies

Antibodies used	All the antibodies we used in this work including dilution factors (specified for human and murine cells) have been listed in Supplementary Table 4 in the Supplementary Information. We provided them here again.

Part 1, List of human-related antibodies used in the study (IS: ImageStream; CQA: Control quality assessment by conventional FACS; WB: Western blotting; Of note, different fluoresces of the same antiboies might be used in different staining panels).
For each item, the information is provided in the following order: Antibody name, Clone, Company/provider, Catalogue number, Dilution and application (if different applications were used separated by ";").
rabbit anti-human PARK7/DJ-1, EP2815Y, Abcam ab76008, 1:2000 WB; 1:10 IP
normal rabbit IgG, NA, Santa Cruz sc-2027, 1:10 IP
rabbit Anti-Pyruvate Dehydrogenase E1-alpha subunit, EPR11098, Abcam ab168379, 1:3000 WB
rabbit anti-human Pyruvate Dehydrogenase E1 beta subunit polyclonal, Thermo Fisher Scientific PA5-31519, 1:1000 WB
rabbit anti-human GAPDH, 6C5, Santa Cruz sc-32233, 1:1000 WB
goat anti-rabbit IgG (H+L)-HRP, NA, Bio-Rad 172-1019, 1:5000 WB
goat anti-mouse IgG-HRP, NA, Santa Cruz sc-2005, 1:2000 WB
LIVE/DEAD® Fixable Near-IR Dead Cell Stain, NA, Thermo Fisher Scientific L10119, 1:500 FACS/IS/CQA
mouse anti-human CD4 V450, RPA-T4, BD Biosciences 560346, 1:100 FACS; 1:100 IS
rabbit anti-human PARK7/DJ-1 Alexa Fluor 488, EP2815Y, Abcam ab203989, 1:100 FACS;1:50 IS
rabbit anti-human PDHB Alexa Fluor 594, EPR11097(B), Abcam ab211838, 1:100 FACS;1:100 IS
rabbit IgG Alexa Fluor 488, EPR25A, Abcam ab199091, 1:100 FACS;1:50 IS
rabbit IgG Alexa Fluor 594, EPR25A, Abcam ab208568, 1:100 FACS;1:100 IS
goat anti-rabbit IgG (H+L) Alexa Fluor 647, NA, Thermo Fisher Scientific A21245, 1:200 FACS
rabbit anti-human Pyruvate Dehydrogenase E1-alpha subunit (pSer293), polyclonal, Abcam ab92696, 1:300 WB
rabbit anti-human phospho PHE1-A type I (pSer300), polyclonal, Merck Millipore ABS194, 1:1000 WB
Anti-Lamin B1, polyclonal, Abcam ab16048, 1 :10000 WB
mouse anti-human CD4 APC, RPA-T4, BD Biosciences 561840, 1:200 FACS
mouse anti-human CD4 FITC, RPA-T4, BD Biosciences 555346, 1:200 FACS;1:20 sorting
mouse anti-human CD4 V450, G44-26, BD Biosciences 561292, 1:200 FACS
mouse anti-human CD4 BUV395, RPA-T4, BD Biosciences 564724, 1:200 FACS;1:100 CQA
mouse anti-human CD4 PE-Cy7, L200, BD Biosciences 560644, 1:200 FACS
mouse anti-human CD25 APC, M-A251, BD Biosciences 555434, 1:200 FACS;1:20 sorting
mouse anti-human CD25 FITC, M-A251, BD Biosciences 555431, 1:200 FACS;1:100 CQA
mouse anti-human CD25 V450, M-A251, BD Biosciences 560356, 1:200 FACS
mouse anti-human CD127 V450, HIL-7R-M21 BD Biosciences 560823, 1:200 FACS;1:20 sorting
mouse anti-human GARP, 50G10, Synaptic Systems GmbH 221 011, 1:100 FACS
mouse anti-human FOXP3 Alexa Fluor 647, 206D, BioLegend 320119, 1:10 FACS;1:10 CQA
mouse IgG1 Alexa Fluor 647, NA, BioLegend 50-167-013, 1:10 FACS
mouse anti-human Helios Pacific blue, 22F6, BioLegend 137210, 1:100 FACS;1:100 CQA
mouse anti-human GZMB APC, GB12, Thermo Fisher Scientific MHGB05, 1:200 FACS;1:200 IS
CellTrace CFSE Cell Proliferation Kit FITC, NA, Thermo Fisher Scientific C34554, 1:5000 FACS

Part 2, List of mouse-related antibodies used in this work (if the application is not specified, the application is conventional FACS analysis; Specified application is mentioned in the bracket.).
For each item, the information is provided in the following order: Antibody name, Clone, Company/provider, Catalogue number, Dilution and application.
Annexin V Apoptosis Detection Kit FITC, N.A., Thermo Fisher Scientific 88-8005-74, 1:20
CD16/CD32, 2.4G2, BD Biosciences 553141, 1:50
CD25-APC, PC61, BD Biosciences 557192,1:100 (Sorting)
CD25-BUV395, PC61, BD Biosciences 564022, 1:200 (additional very old mice Treg analysis)
CD25-PE-Cy7, PC61.5, eBioscience 25-0251-82, 1:200
CD44-PE-Cy7, IM7, BD Biosciences 560569, 1:200 (Sorting)
CD3 BV421, 145-2C11, BD Biosciences 562600, 1:200 (additional very old mice Treg analysis)
CD4-APC, RM4-5, eBioscience 17-0042-83, 1:200 (suppressive assay)
CD4-BUV496, GK1.5, BD Biosciences 564667, 1:200
CD4-BUV496, GK1.5, BD Biosciences 612952, 1:200 (additional very old mice Treg analysis)
CD4-FITC, RM4-5, eBioscience 11-0042-82, 1:100 (Sorting)
CD45.1-BV785, A20, Biolegend 110743,1:200
CD45.2-BV650, 104, Biolegend 109835, 1:200
CD62L-PerCP-Cy5.5, MEL-14, BD Biosciences 560513, 1:200 (Sorting)
CD8-BUV805, 53-6.7, BD Biosciences 564920, 1:200
CD8-eFluor450, 53-6.7, eBioscience 48-0081-82, 1:100 (Sorting)
CTLA4/CD152-PE, UC10-4B9, eBioscience 12-1522-83, 1:100
FOXP3-APC, FJK-16s, eBioscience 17-5773-82, 1:100
FOXP3-PE, 150D, Biolegend 320008 , 1:100
GITR/CD357-BUV395, DTA-1 , BD Biosciences 740322, 1:100
HELIOS-Pacific Blue (PB), 22F6, Biolegend 137220, 1:100
ICOS/CD278-FITC, 7E.17G9, Thermo Fisher Scientific 11-9942-82, 1:100
IL-10-PerCP-Cy5.5, JES5-16E3, Biolegend 505028, 1:100
IL-2-PE-Cy7, JES6-5H4, eBioscience 25-7021-82, 1:200
Ki-67-BV605, 16A8, BioLegend 652413, 1:100 (Thymus FACS staining)
Ki-67-EF450, SolA15, eBioscience 48-5698-82, 1:100
PD-1-BV711, J43, BD Biosciences 744547, 1:100

pSTAT5 Y694 FITC, Stat5Y694-G11, Abcam ab278791, 1:100
Purified NA/LE hamster anti-mouse CD3e (without azide), 145-2C11, BD Biosciences 553057, 1 or 2 µg/ml
Purified NA/LE Hamster Anti-Mouse CD28 (without azide), 37.51, BD Biosciences 553294, 1 or 2ug/ml
LIVE/DEAD® Fixable Near-IR, NA, Thermo Fisher Scientific L10119, 1:500

Validation

We used primary antibodies mainly from leading providers, such as BD, Biolegend, eBioscience/Thermo Fisher Scientific and Abcam. For example, anti-FOXP3 ab (the essential ab for this project) was obtained from eBioscience (now part of Thermo Fisher Scientific) and has been tested by flow cytometry analysis and already cited by more than 300 papers (https://www.thermofisher.com/antibody/product/FOXP3-Antibody-clone-FJK-16s-Monoclonal/17-5773-82). Anti-PDHB used in WB has been tested for the application of WB by Thermo Fisher Scientific (https://www.thermofisher.com/antibody/product/PDHB-Antibody-Polyclonal/PA5-31519). Anti-PDHA Ser293 ab has been tested for WB by Abcam as indicated in their website (https://www.abcam.com/pdha1-phospho-s293-antibody-ab92696.html). Anti-PARK7 used in this work has been tested for the application of WB and IP (https://www.abcam.com/park7dj1-antibody-ep2815y-ab76008.html) and has been cited by 33 different references. All the BD antibodies we used in this work often include the following statement "Application: Flow cytometry (Routinely Tested)" in their website, see the example in anti-CD4 ab (https://www.bdbiosciences.com/en-lu/products/reagents/flow-cytometry-reagents/research-reagents/single-color-antibodies-ruo/v450-mouse-anti-human-cd4.560346). All the Biolegend antibodies we used in this work often include the following statement "Application ICFC - Quality tested (ICFC: Flow cytometric analysis of intracellularly-stained cells.) ". For instance, anti-FOXP3 ab has been cited by at least 9 papers as shown in the webpage (https://www.biolegend.com/fr-lu/products/alexa-fluor-647-anti-human-foxp3-antibody-2945). For Thermo Fisher Scientific (or eBioscience) abs, the flow-cytometry abs are also often tested for the given applications listed in their websites. For instance, anti-ICOS ab we used in this work has been tested for flow cytometry analysis and has been cited by at least nine references (https://www.thermofisher.com/antibody/product/CD278-ICOS-Antibody-clone-7E-17G9-Monoclonal/11-9942-82). The only primary ab from Santa Cruz we used was for the loading control of human protein samples (anti-GAPDH), which has been cited by more than 3700 papers (https://www.scbt.com/p/gapdh-antibody-6c5).

Eukaryotic cell lines

Policy information about cell lines

Cell line source(s)

All the relevant results are from either isolated primary human T cells or mice T cells. We have only used Jurkat cells (DSMZ : ACC 282) for the control purpose.

Authentication

Our Jurkat cells were bought from the leading cell line provider DSMZ, who have performed authentication tests themselves and we did not perform additional authentication tests.

Mycoplasma contamination

The used Jurkat cells were regularly tested for mycoplasma contamination in the lab and found negative .

Commonly misidentified lines
(See ICLAC register)

No commonly misidentified cell lines were used in the study.

Animals and other organisms

Policy information about studies involving animals; ARRIVE guidelines recommended for reporting animal research

Laboratory animals

B6.129P2-Park7Gt (XE726) Byg/Mmucd mice were developed and characterized as described elsewhere. Of note, the Dj-1 line used in our laboratory have already been crossed with B6N mice for at least 10 generations. The Dj-1-/- (KO), Dj-1+/-, Dj-1+/+ (WT) mice used in our experiments were gender- and age-matched siblings generated from heterozygous Dj-1+/- breeding pairs. CD45.1 mice (also known as Ly5.1 mice) were imported from Charles River (strain code 494, Italy). Old Dj-1 mice used in this week were around 45-week-old ones otherwise unless specified. The young mice were aged between 8-12 weeks. We used both genders of mice in our experiments depending which gender of mice with a sufficient number per group were availability at the given time and did not notice any gender-biased effects so far, but for comparability, we only used the same gender of mice between different groups within the same experiments. All mice were maintained in our SPF animal facility and all animal experimental procedures were performed following the approval of the Animal Welfare Society (AWS) of University of Luxembourg or Luxembourg Institute of Health. The SPF mice are housed in IVC cages at a maximum of 5 per cage and maintained at a temperature of 22°C and a relative humidity of 55%. They are kept on autoclaved corn cob bedding enriched with sizzle nest, paper, wooden block and a tunnel. They are fed with SAFE Maintenance Diets irradiated at a minimum of 25 kGy. The watering system consists of Reverse Osmosis water supplied with 2ppm of Chlorine.

Wild animals

This study did not use any wild animals.

Field-collected samples

This study did not collect samples from the field.

Ethics oversight

All animal experimental procedures were performed following the approval of the Animal Experimentation Ethics Committee or Animal Welfare Society of University of Luxembourg or Luxembourg Institute of Health and eventually by Luxembourg Ministry of Agriculture before the related experiment was started (LUPA2019/04 and LUPA2019/73).

Note that full information on the approval of the study protocol must also be provided in the manuscript.

Human research participants

Policy information about studies involving human research participants

Population characteristics

We always asked to get buffy coats or leukopaks from the same blood group and young male if possible. However, there is no

	guarantee for this request as we isolated and analyzed T cells based on what we could get from Luxembourg Red Cross. We also could not get any clinical information from those healthy blood donors. The number of participants have been specified in each of the figures.
Recruitment	The buffy coats or leukopaks from healthy donors used for primary T cell culture and analysis were obtained via the Luxembourg Red Cross.
Ethics oversight	Our research complies with all relevant ethical regulations. For the human samples, the ethical committee of Luxembourg Red Cross has approved the study protocol (LIH-2018-0009) and we got all the buffy coats or leukopaks through Luxembourg Red Cross and obtained informed consent from all the healthy blood donors before sampling. We did not know any clinical information from human donors, even not sex and age of them.

Note that full information on the approval of the study protocol must also be provided in the manuscript.

Flow Cytometry

Plots

Confirm that:

☒ The axis labels state the marker and fluorochrome used (e.g. CD4-FITC).

☒ The axis scales are clearly visible. Include numbers along axes only for bottom left plot of group (a 'group' is an analysis of identical markers).

☒ All plots are contour plots with outliers or pseudocolor plots.

☒ A numerical value for number of cells or percentage (with statistics) is provided.

Methodology

Sample preparation	Mice spleen and peripheral lymph nodes were collected in FACS buffer (PBS (pH 7.2) supplemented with 2% FBS and 2 mM EDTA). Single cells suspension were harvested by mashing the organs using the plunger from a sterile 5 ml syringe in a 40 µm cell strainer over a 50 ml conical tube. Red blood cells were removed using the Lysis buffer(BD Biosciences). Cells were incubated at 4 degree for 10 minutes with 1 µg/mL of anti-CD16/32 antibody (BD Biosciences) and then stained for cell surface markers (Supplementary Table 6) at 4 °C for 30 min followed by intracellular staining if needed . For sorting, Tregs and Tconv were identified as CD4+CD25high and CD4+CD25-, respectively. CD4 Naïve and effector memory T cells were identified as CD4+CD44lowCD62Lhigh and CD4+CD44highCD62Llow, respectively. CD8 Naïve, central memory and effector memory T cells were identified as CD8+CD44lowCD62Lhigh, CD8+CD44highCD62Lhigh and CD8 +CD44highCD62Llow, respectively. Many activation, exhaustion and proliferation markers were co-stained and described in the manuscript. For iTreg differentiation, spleens and peripheral lymph nodes were minced through a 70 µM-pore strainer. Centrifuge the cell suspension at 350xg for 5 min at 4°C. Discard the supernatant and add 3 ml of 1x Red blood lysis buffer for spleen per mouse and incubate at room temperature for 7 min. Add 10 ml of ice-cold FCM buffer [2% heat-inactivated FBS+2 mM EDTA in Ca2+ and Mg2+ free PBS (BE17-516F, Lonza)] to stop the reaction and centrifuge the cells (200xg, 4°C for 5 min) and discard the supernatant. Resuspend the cell pellet with cold FCM buffer. Pass the cell suspension through 40 uM cell strainer again. Untouched naive CD4 T cells were isolated via magnetic separation using the Naive CD4+ T Cell Isolation Kit, mouse (130-104-453, Miltenyi Biotec) with LS column (130-042-401, Miltenyi Biotec) following manufacture's recommendation. For assasy requiring nTregs and Tconv, Tregs were isolated using CD25+CD4+ isolation kit (130-091-041, Miltenyi Biotec). Humans: Tregs and Teffs were isolated from the blood as CD4+ CD25highCD127low and CD4+ CD25-, respectively.
Instrument	BD LSRFortessa (Analysis) or BD FACSAria III (Sorting).
Software	Samples were acquired using Diva software (BD Biosciences) and analyzed by Flowjo.
Cell population abundance	The abundance of the relevant cell population in the post-sort fraction was not directly assessed in the samples from aged mice due to the limited number of cells from isolated T-cell subsets. But the purity of the sorted human Treg and Teffs cells from PBMC of healthy donors using the same sorter with a similar setting was reassessed and was found higher than >99%.
Gating strategy	Based on the pattern of FSC-A/SSC-A, cells in the lymphocyte gate were used for analysis of T cell subsets. Singlets were gated according to the pattern of FSC-H vs. FSC-A. All the following detailed subset analysis was based on viable cells identified by using the LIVE/DEAD® Fixable Near-IR Dead Cell Stain kit. For ImageStream analysis, we selected only living focused singlets for further analysis. Positive populations were determined by the specific antibodies.

☒ Tick this box to confirm that a figure exemplifying the gating strategy is provided in the Supplementary Information.

Appendix 3: Extracellular Vesicle Secretion by Leukemia Cells In Vivo Promotes CLL Progression by Hampering Antitumor T-cell Responses

GARGIULO, E., VIRY, E., MORANDE, P. E., LARGEOT, A., GONDER, S., XIAN, F., IOANNOU, N., **BENZARTI, M**., KLEINE BORGMANN, F. B., MITTELBRONN, M., DITTMAR, G., NAZAROV, P. V., MEISER, J., STAMATOPOULOS, B., RAMSAY, A. G., MOUSSAY, E. & PAGGETTI, J. 2023. Extracellular Vesicle Secretion by Leukemia Cells In Vivo Promotes CLL Progression by Hampering Antitumor T-cell Responses. ***Blood Cancer Discovery***, 4, 54-77.

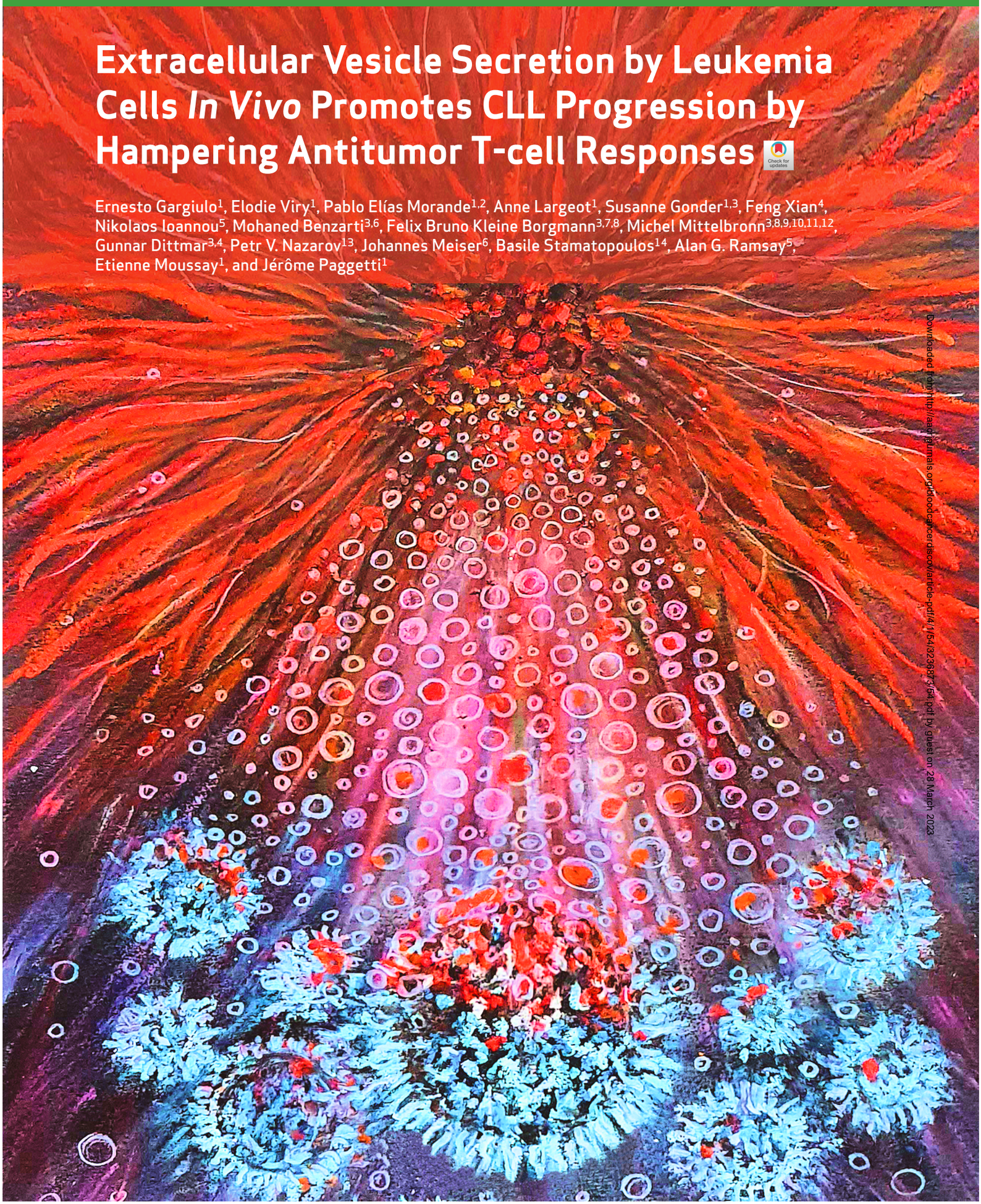
DOI: https://doi.org/10.1158/2643-3230.BCD-22-0029

Personal contribution: The major finding of this publication is how leukemic extracellular vesicle weaken the anti-tumour response by $CD8^+$ T cells in chronic lymphocytic leukemia (CLL). This effect is achieved by changing the transcriptome, proteome and metabolome of $CD8^+$ T cells. I contributed to this research with the data presented in figure panels: **4I, 4K, 4L, S4F, S4G, S4H and S4I**. Here I helped plan and perform targeted metabolomics using [U-^{13}C] glucose and glutamine on $CD8^+$ T cells treated with leukemic EVs, I then processed and analyzed the metabolomics data which showed the metabolic exhaustion of the treated $CD8^+$ T cells. Moreover, I performed extracellular oxygen consumption assay using Seahorse bioanalyser to show the reduction in oxidative phosphorylation in treated $CD8^+$ T cells. I also reviewed the manuscript prior to submission.

RESEARCH ARTICLE

Extracellular Vesicle Secretion by Leukemia Cells *In Vivo* Promotes CLL Progression by Hampering Antitumor T-cell Responses

Ernesto Gargiulo[1], Elodie Viry[1], Pablo Elías Morande[1,2], Anne Largeot[1], Susanne Gonder[1,3], Feng Xian[4], Nikolaos Ioannou[5], Mohaned Benzarti[3,6], Felix Bruno Kleine Borgmann[3,7,8], Michel Mittelbronn[3,8,9,10,11,12], Gunnar Dittmar[3,4], Petr V. Nazarov[13], Johannes Meiser[6], Basile Stamatopoulos[14], Alan G. Ramsay[5], Etienne Moussay[1], and Jérôme Paggetti[1]



Downloaded from http://aacrjournals.org/bloodcancerdiscov/article-pdf/4/1/54/3236877/54.pdf by guest on 28 March 2023

ABSTRACT Small extracellular vesicle (sEV, or exosome) communication among cells in the tumor microenvironment has been modeled mainly in cell culture, whereas their relevance in cancer pathogenesis and progression *in vivo* is less characterized. Here we investigated cancer–microenvironment interactions *in vivo* using mouse models of chronic lymphocytic leukemia (CLL). sEVs isolated directly from CLL tissue were enriched in specific miRNA and immune-checkpoint ligands. Distinct molecular components of tumor-derived sEVs altered CD8$^+$ T-cell transcriptome, proteome, and metabolome, leading to decreased functions and cell exhaustion *ex vivo* and *in vivo*. Using antagomiRs and blocking antibodies, we defined specific cargo-mediated alterations on CD8$^+$ T cells. Abrogating sEV biogenesis by *Rab27a/b* knockout dramatically delayed CLL pathogenesis. This phenotype was rescued by exogenous leukemic sEV or CD8$^+$ T-cell depletion. Finally, high expression of sEV-related genes correlated with poor outcomes in CLL patients, suggesting sEV profiling as a prognostic tool. In conclusion, sEVs shape the immune microenvironment during CLL progression.

SIGNIFICANCE: sEVs produced in the leukemia microenvironment impair CD8$^+$ T-cell mediated antitumor immune response and are indispensable for leukemia progression *in vivo* in murine preclinical models. In addition, high expression of sEV-related genes correlated with poor survival and unfavorable clinical parameters in CLL patients.

See related commentary by Zhong and Guo, p. 5.

INTRODUCTION

Small extracellular vesicles (sEV), or exosomes, are small-size particles (30–150 nm) released by every cell and found in any body fluid. They are involved in cell-to-cell communication through the transfer of genetic material and proteins (1), and ligands/receptors interactions, affecting biological functions of target cells (2). Release of sEVs and their cargo depends on the cellular and physiologic context (3). Tumor-derived sEVs are involved in the reeducation of microenvironment cells promoting tumor proliferation, immune escape, and metastasis (4–7).

The survival and proliferation of chronic lymphocytic leukemia (CLL) cells depend strictly on interactions with the microenvironment (8, 9). CLL cells evolve in a highly immunosuppressive environment (10) where sEVs affect progression, invasion, and resistance to treatment (7). We and others previously demonstrated that CLL-derived sEVs reeducate surrounding cells and enhance immune-escape mechanisms (11–13), such as stromal cell conversion into cancer-associated fibroblasts and modulation of PD-L1 expression on monocytes, among others (14, 15).

However, these studies are mostly based on *in vitro*–generated sEVs. In light of the complex leukemia microenvironment (LME) composition, the role of sEVs in CLL pathogenesis *in vivo* still needs to be evaluated. Herein, we developed a protocol to isolate sEVs directly from the LME of Eμ-*TCL1* mice with the aim to uncover their complexity and their role in CLL development and progression *in vivo*. We show that sEVs isolated from the LME contain specific miRNA and proteins and display on their surface multiple immune-checkpoints (ICP), which play a key role in CLL development, by hampering the antitumor CD8$^+$ T cell–mediated immune response. LME-sEVs reprogrammed the CD8$^+$ T-cell transcriptome, proteome, and metabolome, leading to cell exhaustion, decreased granzyme B production, cytokine secretion, and tumor cell lysis. Decrease of sEV secretion by *Rab27* KO led to the impairment

[1]Tumor–Stroma Interactions Group, Department of Cancer Research, Luxembourg Institute of Health, Luxembourg City, Luxembourg. [2]Instituto de Medicina Experimental (IMEX)-CONICET-Academia Nacional de Medicina, Buenos Aires, Argentina. [3]Faculty of Science, Technology and Medicine, University of Luxembourg, Esch-sur-Alzette, Luxembourg. [4]Proteomics of Cellular Signaling, Department of Infection and Immunity, Luxembourg Institute of Health, Strassen, Luxembourg. [5]School of Cancer and Pharmaceutical Sciences, Faculty of Life Sciences and Medicine, King's College London, London, United Kingdom. [6]Cancer Metabolism Group, Department of Cancer Research, Luxembourg Institute of Health, Luxembourg City, Luxembourg. [7]Department of Neurosurgery, Centre Hospitalier de Luxembourg, Luxembourg City, Luxembourg. [8]Luxembourg Centre of Neuropathology, Department of Cancer Research, Luxembourg Institute of Health, Luxembourg City, Luxembourg. [9]Luxembourg Centre of Neuropathology, University of Luxembourg, Esch-sur-Alzette, Luxembourg. [10]Department of Life Sciences and Medicine, University of Luxembourg, Esch-sur-Alzette, Luxembourg. [11]National Center of Pathology, Laboratoire National de Santé (LNS), Dudelange, Luxembourg. [12]Luxembourg Centre for Systems Biomedicine, University of Luxembourg, Esch-sur-Alzette, Luxembourg. [13]Multiomics Data Science Group, Department of Cancer Research, Luxembourg Institute of Health, Strassen, Luxembourg. [14]Laboratory of Clinical Cell Therapy, Jules Bordet Institute, Université Libre de Bruxelles, Brussels, Belgium.

E. Moussay and J. Paggetti are the co–senior authors of this article.

Current address for F. Xian: Division of Pharmacology and Toxicology, Department of Pharmaceutical Science, University of Vienna, Austria.

Corresponding Authors: Jérôme Paggetti, Department of Cancer Research, Luxembourg Institute of Health, 6, Rue Nicolas-Ernest Barblé, Luxembourg, L-1210, Luxembourg. Phone: 352-26970-344; E-mail: jerome.paggetti@lih.lu; and Etienne Moussay. Phone: 352-26970-232; E-mail: etienne.moussay@lih.lu

Blood Cancer Discov 2023;4:54–77

doi: 10.1158/2643-3230.BCD-22-0029

This open access article is distributed under the Creative Commons Attribution 4.0 International (CC BY 4.0) license.

©2022 The Authors; Published by the American Association for Cancer Research

Downloaded from http://aacrjournals.org/bloodcancerdiscov/article-pdf/4/1/54/3236873/54.pdf by guest on 28 March 2023

of CLL growth *in vivo*. Finally, we showed in a cohort of CLL patients that the expression of genes involved in sEV biogenesis and secretion differs between groups defined by the classic prognosis markers and correlates with survival. Overall, our findings highlight the importance of sEVs in the microenvironment for leukemia development and progression.

RESULTS

sEVs Are Enriched in Leukemia Microenvironment

To assess the relevance of sEV biogenesis in CLL, we performed gene-expression analysis using a public data set (16) comparing CLL patient cells with normal B cells. We observed higher expression of genes associated with sEV biogenesis in CLL cells (Fig. 1A), whereas regulators of retrograde transport and lysosomal degradation were less expressed, resulting in higher computed sEV scores (Fig. 1B). Furthermore, we observed a higher expression of typical sEV markers, such as the RAB family members and the programmed cell death 6-interacting protein (PDCD6IP, also known as ALIX), associated with increased sEV production (Fig. 1C; Supplementary Fig. S1A; refs. 17–19). This is in accordance with increased levels of CLL-derived sEVs ($CD20^+$) in the plasma of CLL patients compared with healthy controls, as we previously reported (15, 20). Interestingly, individual or combined gene expression of major sEV biogenesis regulators, such as *Rab10*, *Rab35*, and *Rab40c*, was higher in cells from patients with unfavorable UM-IGHV than from patients with M-IGHV (Fig. 1D and E; Supplementary Fig. S1B). Similar results were obtained with the Eμ-*TCL1* (TCL1) CLL murine model (GSE175564, ref. 21; vs. WT B cells from C57BL/6 mouse; Fig. 1F and G) as *Cd9*, *Rab3b*, and *Rab31* were upregulated (Fig. 1H; Supplementary Fig. S1C) in leukemic cells, suggesting an important role of sEVs in CLL pathology (18, 22, 23).

Commonly, sEVs are isolated from cell line culture supernatants, allowing to conveniently isolate tumor-derived sEVs in large amounts and study their functional impact on accessory cells. However, this method does not fully reflect the complexity of a whole organism. As sEV biogenesis and release are dynamic processes, we aimed to obtain a closer biological representation of sEVs from the CLL microenvironment (24). Therefore, we established a protocol to isolate sEV directly from the spleen of murine models (Fig. 1I), preserving at the same time cell integrity (Supplementary Fig. S1D). First, we detected a 10-fold enrichment in LME-sEVs compared with healthy controls (HCME-sEV; Fig. 1J). Similarly, we found greater levels of circulating sEVs in the peripheral blood (PB) of TCL1 mice compared with healthy controls (Supplementary Fig. S1E), further highlighting sEV potential impact in leukemogenesis.

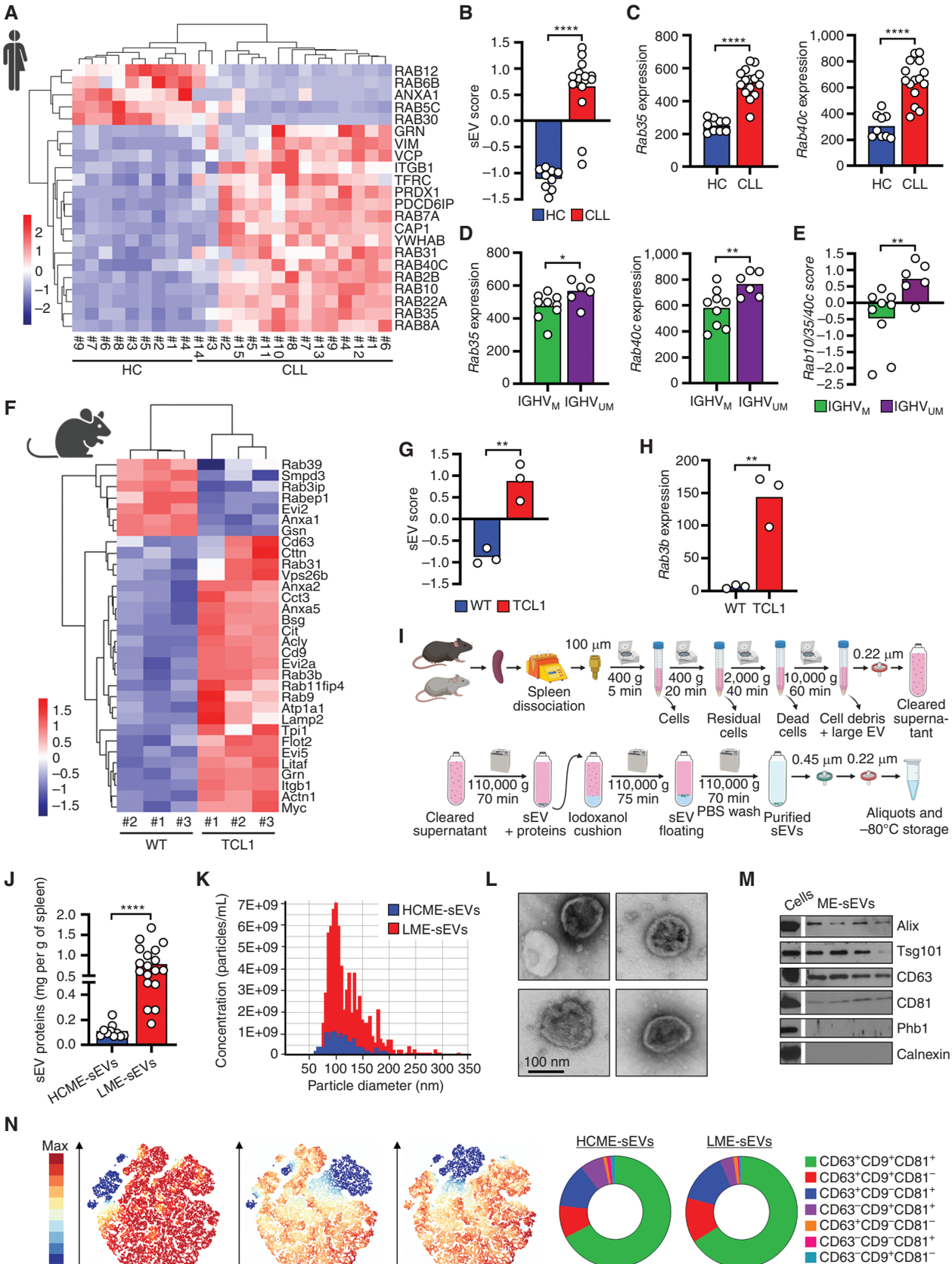
Overall, isolated ME-sEVs showed expected size and morphology (80–120 nm; Fig. 1K and L), presence of typical sEV markers (Fig. 1M; Supplementary Fig. S1F), and the absence of major contaminants for both conditions, validating their use for further downstream analysis. In order to analyze more in-depth the tetraspanin distribution on ME-sEVs from both sources, we performed single sEV FC analysis of CD63, CD81, and CD9 (Fig. 1N). Phenotyping of single sEV suggests alteration of tetraspanins distribution between LME- and HCME-sEVs. Hierarchical clustering further highlighted the heterogeneity of the tetraspanin distribution on single sEV, showing different combinations of CD63, CD9, and CD81 within ME-sEVs subsets (Supplementary Fig. S1G). Interestingly, tetraspanin distribution analysis reveals the expansion of distinct LME-sEVs subpopulations compared with the healthy counterpart (clusters C1–C10; Supplementary Fig. S1H). These observations, beyond emphasizing the risk of introducing a bias when isolating sEVs with single marker-directed beads, highlight the heterogeneity of tumor sEVs even on such widely distributed markers.

LME-sEVs Present a Specific Proteome and miRNA Fingerprint

Although we observed a 10-fold enrichment in sEVs in the LME compared with HCME, as well as an alteration of the tetraspanins distribution, we investigated whether their protein and miRNA cargo composition differed. First, a label-free proteomic analysis of equal amounts of proteins derived from LME-sEVs and HCME-sEVs identified 1,865 proteins with 527 proteins differentially present between groups (Fig. 2A–C; Supplementary Table S1). Proteins more abundant in LME-sEVs (n = 281) were involved in translation, RNA splicing, and binding, and in the regulation of gene expression and cellular metabolic processes (Fig. 2D), whereas proteins depleted (n = 246) were associated with intracellular transport and with the positive regulation of immune processes, more specifically in lymphocyte activation, migration, and cytokine production (Fig. 2E), suggesting that LME-sEVs may not optimally sustain immune responses but rather stimulate leukemic growth. Given that our proteomic analysis suggested the presence of some conventional (LGALS1 and LGALS9) and metabolic (IL4I1) ICP in LME-sEV (Fig. 2B), we analyzed the presence of further immune regulatory proteins on the ME-sEV surface. Interestingly, LME-sEVs carried several ICP ligands, including PD-L1, GAL9, B7-H2, VISTA, and MHC I/II (Fig. 2F; Supplementary Fig. S2A and S2B). Furthermore, imaging FC highlighted the coexpression of multiple ICP ligands on $CD20^+$ CLL-derived sEVs (Fig. 2G). The latter was confirmed with single-sEV analysis combined with hierarchical stochastic neighbor

Figure 1. sEV are enriched in the human and murine leukemic microenvironments. **A,** Relative mRNA expression of selected genes involved in sEV biogenesis and secretion in B cells from PB of healthy donors (HC, n = 9) and CLL patients (CLL, n = 15; from GSE67640). **B,** Score based on sEV-related mRNA levels from **A**. **C,** mRNA levels of selected genes extracted from **A**. **D,** mRNA expression of selected genes according to IGHV mutational status. **E,** Score combining the expression of *Rab10*, *Rab35*, and *Rab40C* according to IGHV mutational status. **F,** Relative mRNA expression of selected genes involved in sEV biogenesis and secretion in B cells from C57BL/6 (WT) and Eμ-TCL1 mice (TCL1; from GSE175564). **G,** Score based on sEV-related RNA levels from **F**. **H,** *Rab3b* mRNA level extracted from **F**. **I,** Detailed protocol to isolate and purify sEVs from the murine spleen. **J,** Amount of proteins (in mg) recovered from LME- (n = 18) or HCME-sEVs (n = 10), normalized per gram of spleen. **K,** Representative TRPS analysis of ME-sEVs for size and concentration. **L,** Electron microscopy images of ME-sEVs. **M,** Western blot analysis of ME-sEVs. **N,** HSNE clustering analysis of $MB488^+$ LME-sEVs based on CD63, CD81, and CD9 expression measured by bead-free FC (left) and relative percentages of combined expression (right). *, $P < 0.05$; **, $P < 0.01$; ****, $P < 0.0001$ (unpaired Student t test). Data are mean.

Downloaded from http://aacrjournals.org/bloodcancerdiscov/article-pdf/4/1/54/3236873/54.pdf by guest on 28 March 2023



Downloaded from http://aacrjournals.org/bloodcancerdiscov/article-pdf/4/1/54/3236873/54.pdf by guest on 28 March 2023

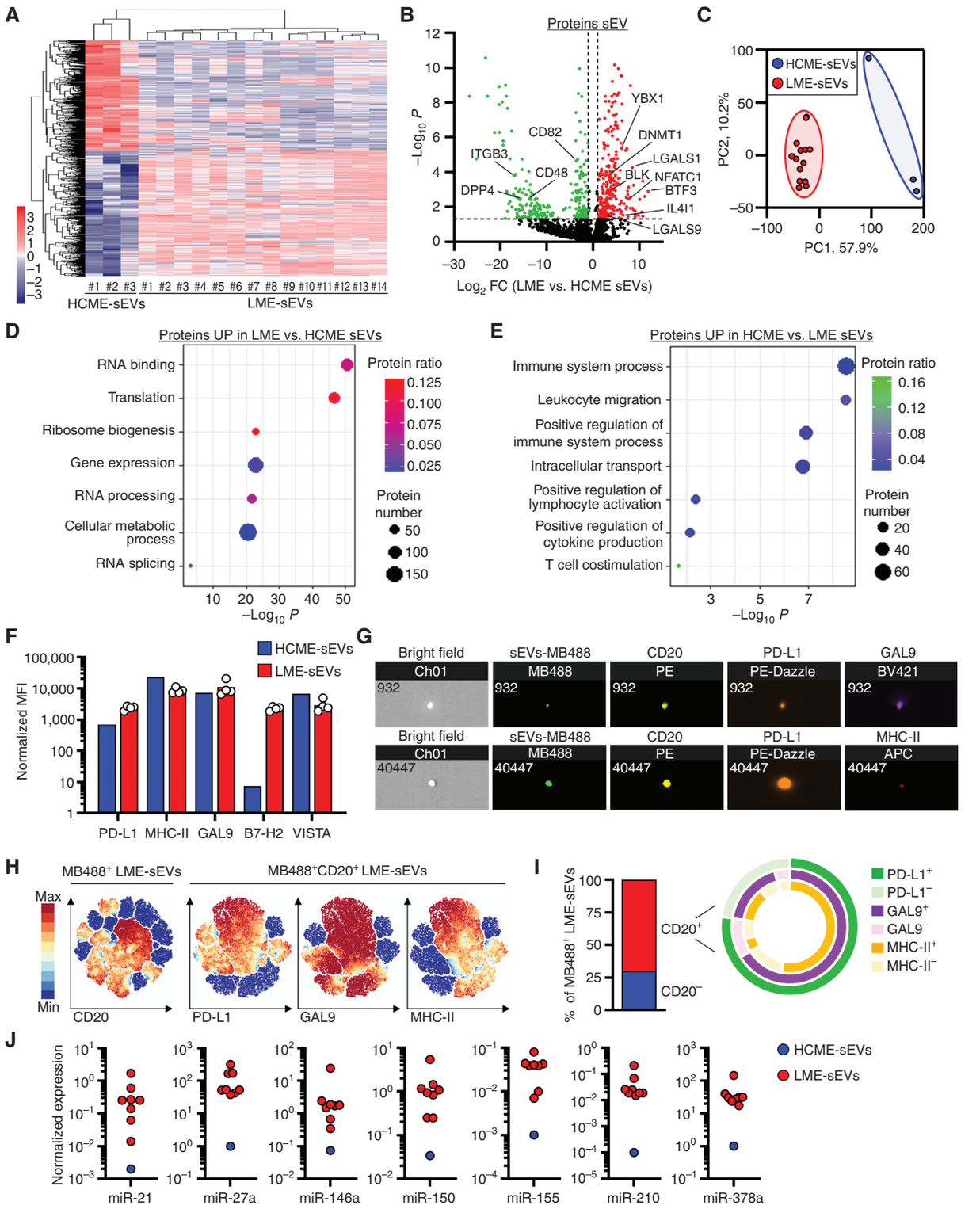


Figure 2. LME-sEVs present a specific proteome and miRNA fingerprint. **A,** Hierarchical clustering of sEVs differentially expressed proteins (DEP with $q < 0.05$) identified by mass spectrometry between HCME-sEVs ($n = 3$, isolated from independent pools of 5 C57BL/6 spleens) and LME-sEVs ($n = 14$). **B,** Volcano plot showing DEP between LME- and HCME-sEVs with FDR <0.05 and $\log_2$FC >1. **C,** PCA based on DEP. **D** and **E,** Ontology analysis of DEP between LME-sEVs and HCME-sEVs. **F,** Expression of ICP ligands on HCME- or LME-sEVs quantified by bead-based FC. **G,** Representative pictures of ICP ligand expression on single MB488+CD20+ LME-sEVs visualized by imaging FC. **H** and **I,** HSNE clustering of MB488+ LME-sEVs based on CD20, PD-L1, GAL9, and MHC-II expression analyzed by FC and related combinations of markers on CD20+ LME-sEVs. **J,** miRNA levels measured using RT-qPCR from HCME- (isolated from a pool of 5 C57BL/6 mice spleens) and LME-sEVs ($n = 8$). Data are mean.

Downloaded from http://aacrjournals.org/bloodcancerdiscov/article-pdf/4/1/54/3236873/54.pdf by guest on 28 March 2023

embedding (HSNE) clustering, showing PD-L1 and GAL9 often coexpressed on CD20$^+$MHC-II$^+$ vesicles (Fig. 2H–I), suggesting LME-sEV immunosuppressive capabilities toward immune cells expressing corresponding receptors. We also observed surface expression of the ectonucleotidases CD39 and CD73, capable to hydrolyze surrounding ATP into adenosine, on LME-sEVs (Supplementary Fig. S2C).

We previously reported several miRNA enriched in the plasma of CLL patients (e.g., miR-150 and -155) that correlated with unfavorable clinical parameters (24), and also showed their transfer and functional activity into target cells (14, 25). Therefore, we screened a shortlist of miRNA known to be abundant in CLL and other cancers. Our data showed that murine LME-sEVs abundantly carry several miRNA, such as miR-150, -155, -21, -146a, -378a, and -27a (Fig. 2J), typically found in sEVs isolated from MEC-1 culture supernatant and patient plasma (Supplementary Fig. S2D; ref. 15). Although not previously reported in CLL-derived sEVs, miR-210, a miRNA associated with hypoxia, was found highly abundant and enriched in LME-sEVs, highlighting the dependency of sEV cargo on microenvironment conditions, which are not reflected in cell culture *in vitro*.

LME-sEVs Enter Different Lymphocyte Subsets and Modify CD8$^+$ T Cells in the Microenvironment

As we isolated sEVs produced in the spleen, we sought to validate the interaction between these LME-sEVs and splenic immune cells. Splenocytes treated *ex vivo* with fluorescent-LME-sEVs displayed a rapid and time-dependent internalization that was inhibited by heparin (Fig. 3A and B), a known inhibitor of sEV uptake (14). Around 90% of each lymphocyte subsets internalized sEVs after 24 hours (Fig. 3C). To rule out a possible indirect transfer between splenocytes, we presorted different T-cell subsets. Both FC and confocal microscopy confirmed that CD4$^+$ T_{conv} cells, regulatory T cells (Treg), and CD8$^+$ T cells actively internalized LME-sEVs *ex vivo*. A total inhibition was observed in the presence of heparin, highlighting the specificity of the internalization process (Fig. 3D and E). Injection of fluorescent-ME-sEVs in mice led to increased fluorescence in total splenocytes, confirming ME-sEV uptake *in vivo* (Fig. 3F). In particular, 5% to 10% of T cells and 40% of B cells internalized sEVs 24 hours after a single injection (Fig. 3G and H). Our observations on T-cell subsets contrast with previous studies using *in vitro*–secreted sEVs and reporting low internalization (26, 27), highlighting the importance of using sEVs produced *in vivo* and to study their uptake in a whole organism.

In light of these results, we aimed to evaluate LME-sEV activity on immune surveillance *in vivo*. We injected LME-sEVs in Foxp3$^{YFP/Cre}$ mice daily for 7 days, then sorted YFP$^+$-Treg, CD4$^+$ T_{conv}, CD8$^+$ T, and CD19$^+$ B lymphocytes and analyzed gene expression (Fig. 3I–L; Supplementary Fig. S3; Supplementary Table S2). Surprisingly, exclusively CD8$^+$ T cells showed different expression profiles (Fig. 3I–K; Supplementary Fig. S3A) with downregulation of genes involved in immune response (*Cd27*, *Cd226*, and *Ms4a4b*) and amino acid transport (*Slc7a5*), whereas genes associated with inhibition of immune response (*Itpkc*) and T-cell differentiation (*Fgr*) were upregulated (Fig. 3I and 3L). K-means clustering confirmed the repression of genes regulating immune response and lymphocyte activation (Supplementary Fig. S3B). Ontology analysis also revealed significant changes in crucial biological functions, such as actin cytoskeleton organization (Fig. 3L; Supplementary Fig. S3C). Similarly, our data showed significant changes in genes associated with oxidoreductase activity, and kinase and phosphatase activities (Supplementary Fig. S3C). Importantly, we could confirm, in a separate *ex vivo* experiment, the rapid decrease in the amino acid transporter *Slc7a5*, and of the costimulatory molecules CD27, CD96, and CD226, crucial for T-cell activation. We also observed the increase in the kinases *Itpkc* and *Fgr* (Fig. 3M and N), pointing to the negative regulation of cell activation, migration, and adhesion. Despite the changes detected in CD8$^+$ T cells, no significant effect was detected in Tregs, CD4$^+$ T_{conv}, and CD19$^+$ B cells after treating mice *in vivo* (Supplementary Fig. S3D–S3F). This indicates the selective immunomodulation of CD8$^+$ T-cell compartment, making LME-sEV influence cell-selective rather than systemic. In our experimental setup, CD8$^+$ T cells appear the principal targets of LME-sEVs *in vivo*.

LME-sEVs Affect the CD8$^+$ T-cell Transcriptome, Proteome, and Metabolome

As LME-sEVs alter preferentially CD8$^+$ T cells *in vivo*, we focused on these essential antitumor cytotoxic cells. We profiled gene expression and protein content of sorted CD8$^+$ T lymphocytes treated *ex vivo* with ME-sEVs. Only a slight modulation of genes and proteins was observed after 24 hours (77 genes and 43 proteins; Supplementary Fig. S4A–S4C; Supplementary Tables S1 and S2), all of them involved in lymphocyte activation and immune response (*Itgb1*, *Card6*, *Tnfrsf4/Ox40*). After 48 hours, striking changes were observed (331 genes modulated) with the repression of genes involved with CD8$^+$ T-cell activation (*Tlr7* and *Icosl*), survival and proliferation (*Il2* and *Il2ra*), and immune activity (*Il17a*, *Lta*, *Gzmm*, and *Map6*: Fig. 4A–C; Supplementary Table S2). In contrast, genes associated with decreased activation and functionality (*Gzmk*), proliferation and survival (*Rora*, *Il10ra*), and the generation of memory CD8$^+$ T cells (*Bcl6*) were increased in these cells. The differential transcription factor usage following treatment with LME-sEVs suggested an increased differentiation to effector-memory T (T_{em}) cells (Zfp281), hyporesponsiveness (Stat1/3 and Myc), and a reduced T-cell activation (Snai1/Zeb and Tbr1; Supplementary Fig. S4D).

In addition, proteomic analysis of LME-sEV–treated CD8$^+$ T cells showed time-dependent changes in key proteins involved in immune response and metabolism (96 hours, 422 proteins modulated, Fig. 4D; Supplementary Table S1). Downregulated proteins included the activation marker CD69, and the serine protease granzyme B (GzmB), both crucial for CD8$^+$ T-cell effector functions. Repression of both cytolytic effector molecules GzmB and perforin was also independently confirmed (Fig. 4E and F). Analysis of proteomics data with a miRNA-target prediction algorithm indicated that a significant fraction of proteins repressed by LME-sEVs are putative targets of at least a specific miRNA found enriched in LME-sEVs (Fig. 2J; Supplementary Fig. S4E). This suggests an active protein downregulation mediated by miRNA transferred by LME-sEVs into CD8$^+$ T cells.

Functionally, proteins increased were involved in gene expression, RNA processing, and translation, whereas proteins

Downloaded from http://aacrjournals.org/bloodcancerdiscov/article-pdf/4/1/54/3236873/54.pdf by guest on 28 March 2023

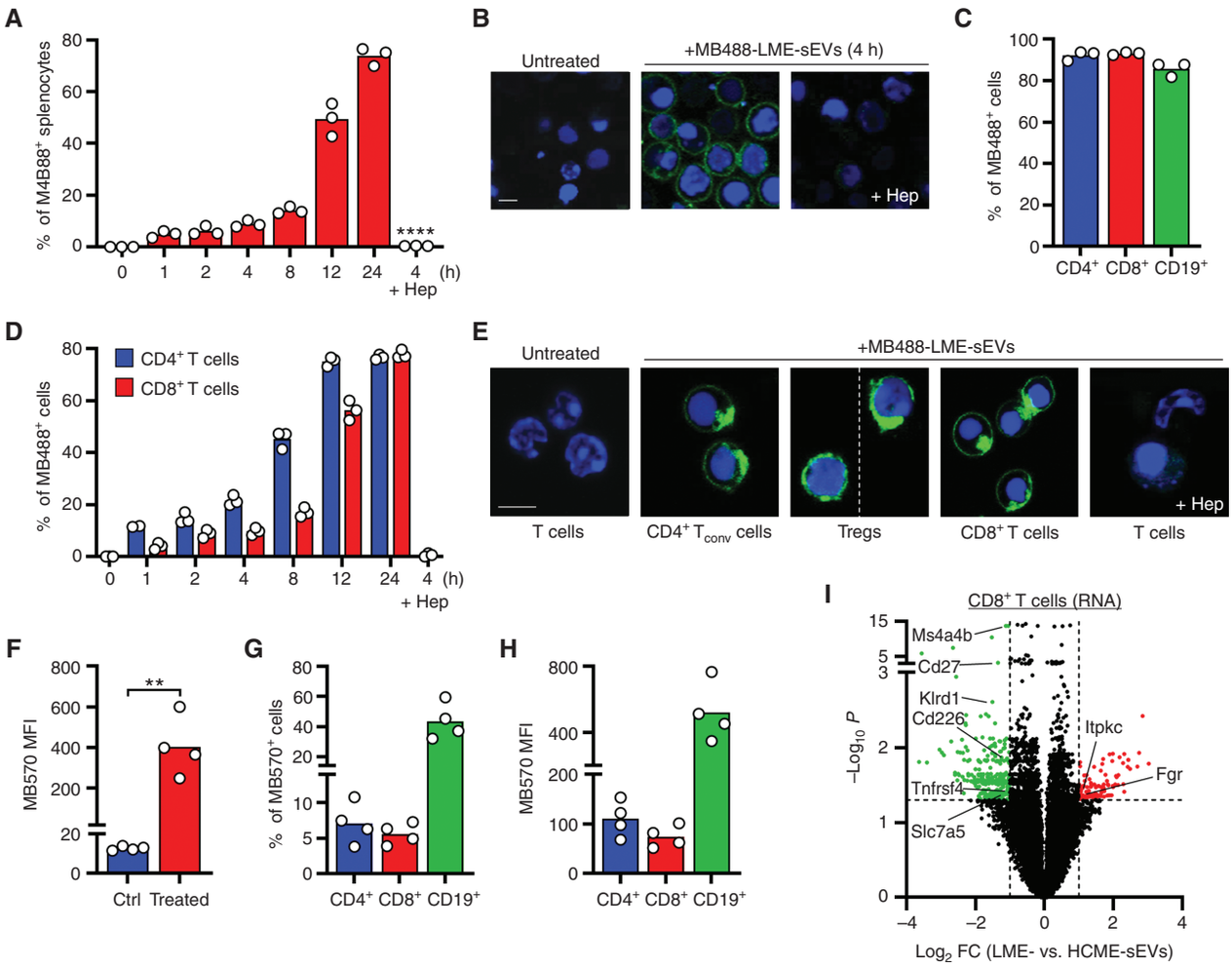


Figure 3. LME-sEVs enter different lymphocyte subsets and modify CD8+ T cells in the microenvironment. **A,** Percentage of splenocytes internalizing MB488+ sEVs. Splenocytes from C57BL/6 mice were incubated for increasing periods of time with MB488+ LME-sEVs and analyzed by FC. sEV preincubation with heparin sulfate (Hep) was performed for 4 hours. **B,** Representative confocal microscopy pictures of total splenocytes after 4 hours of treatment with LME-sEVs, in the absence or presence of heparin (scale bar, 5 μm). **C,** Splenocytes from C57BL/6 mice were incubated for 24 hours with MB488+ LME-sEVs and then analyzed by FC with lymphocyte-lineage markers. **D,** FACS-sorted CD4+ and CD8+ T cells were incubated for increasing periods of time with MB488+ LME-sEVs and analyzed by FC. **E,** Representative confocal microscopy pictures of FACS-sorted CD4+ T_{conv} cells, CD8+ T cells, and Tregs after treatment with LME-sEVs (24 hours; scale bar, 5 μm). **F–H,** MB570+-LME-sEVs were i.v. injected in C57BL/6 mice. Total splenocytes were harvested 24 hours later and analyzed by FC directly (**F**) or after staining for specific immune subsets (CD19+ B cells, CD4+ and CD8+ T cells, **G**–**H**). **I,** Volcano plot showing differential expression of genes (DEG) with FDR <0.05 and log_2FC >1 in CD8+ T cells isolated from spleens of mice treated with LME- or HCME-sEVs for 1 week. (*continued on following page*)

repressed were linked to metabolism (Fig. 4G and H). Interestingly, the amino acid transporter Slc1a5 and the glutamate cysteine ligase (Gclc) were affected, the latter being essential for fueling CD8+ lymphocytes after activation (28). Conversely, we observed accumulation of the inhibitory pyruvate dehydrogenase phosphatase regulatory subunit (Fig. 4D). To validate these observations, we performed metabolic profiling on ME-sEV–treated CD8+ T cells. By analyzing the uptake/release rates from the cell culture medium, an increased consumption of glucose and glutamine, as well as increased lactate release rate, suggested a rewiring of central carbon metabolism (Fig. 4I; Supplementary Fig. S4F). Enhanced glycolysis was also highlighted by the increase of glycolysis-related proteins, including glucose transporter 1 (GLUT1) and D-3-phosphoglycerate dehydrogenase (PHGDH; Fig. 4J). However, isotopologue tracing demonstrated that the contribution of glucose to nucleotide *de novo* synthesis, via the pentose phosphate pathway, was considerably reduced (Fig. 4K; Supplementary S4G), indicating a decreased proliferative potential. Based on the results derived from ^{13}C-Glucose tracing, we hypothesized that an increased consumption of glutamine would lead to an increased usage in the tricarboxylic acid (TCA) cycle. Interestingly, the relative flux of glutamine toward TCA metabolites, proline, and glutathione (GSH) was not different after LME-sEV treatment (Supplementary Fig. S4H). Throughout the TCA cycle, molecules of NADH (nicotinamide adenine dinucleotide (NAD) + hydrogen (H)) are generated. Oxygen is particularly important to oxidize NADH to NAD+ used to generate ATP and perform multiple biological processes. However, using SeaHorse analysis, we

Downloaded from http://aacrjournals.org/bloodcancerdiscov/article-pdf/4/1/54/3236873/54.pdf by guest on 28 March 2023

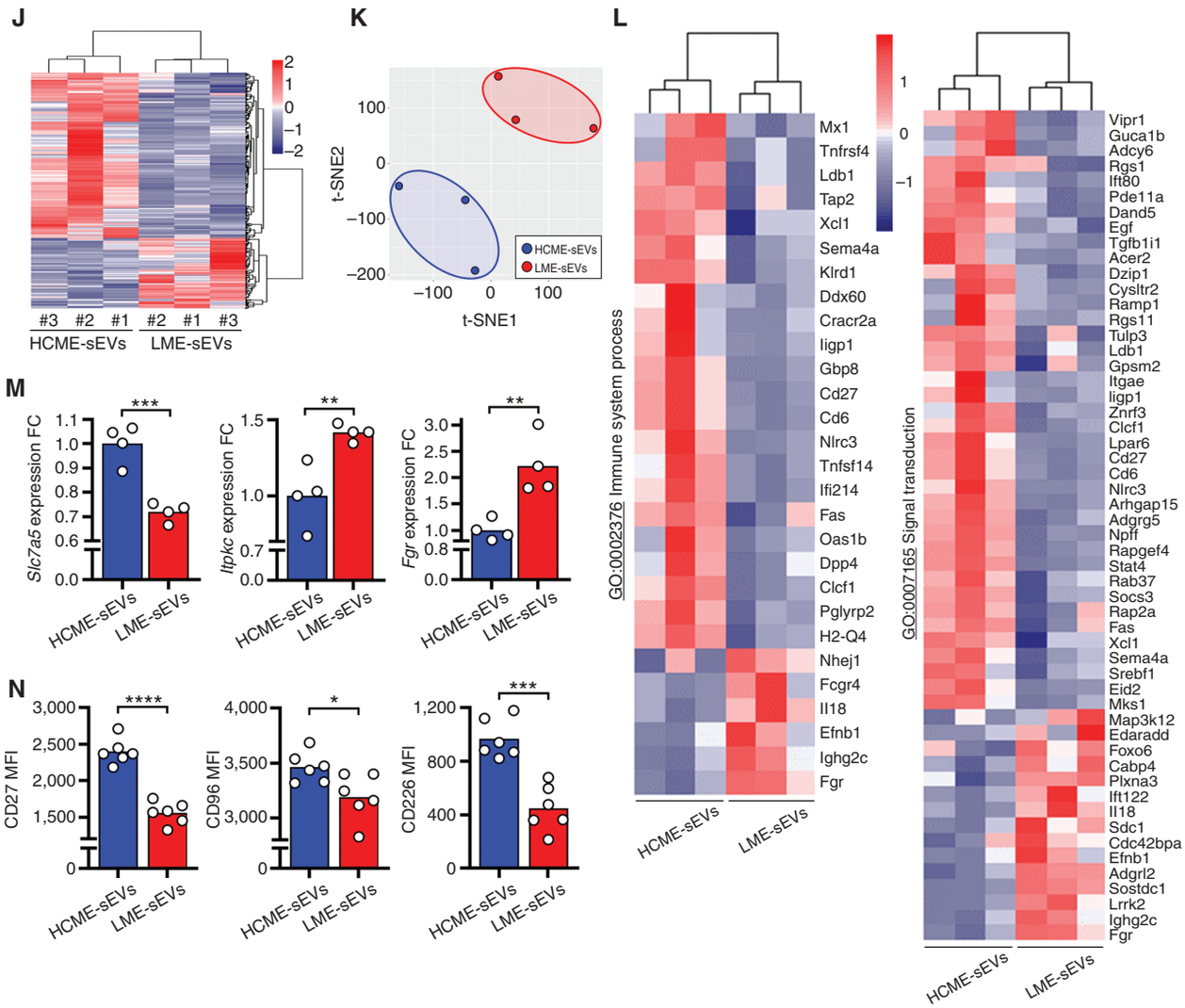
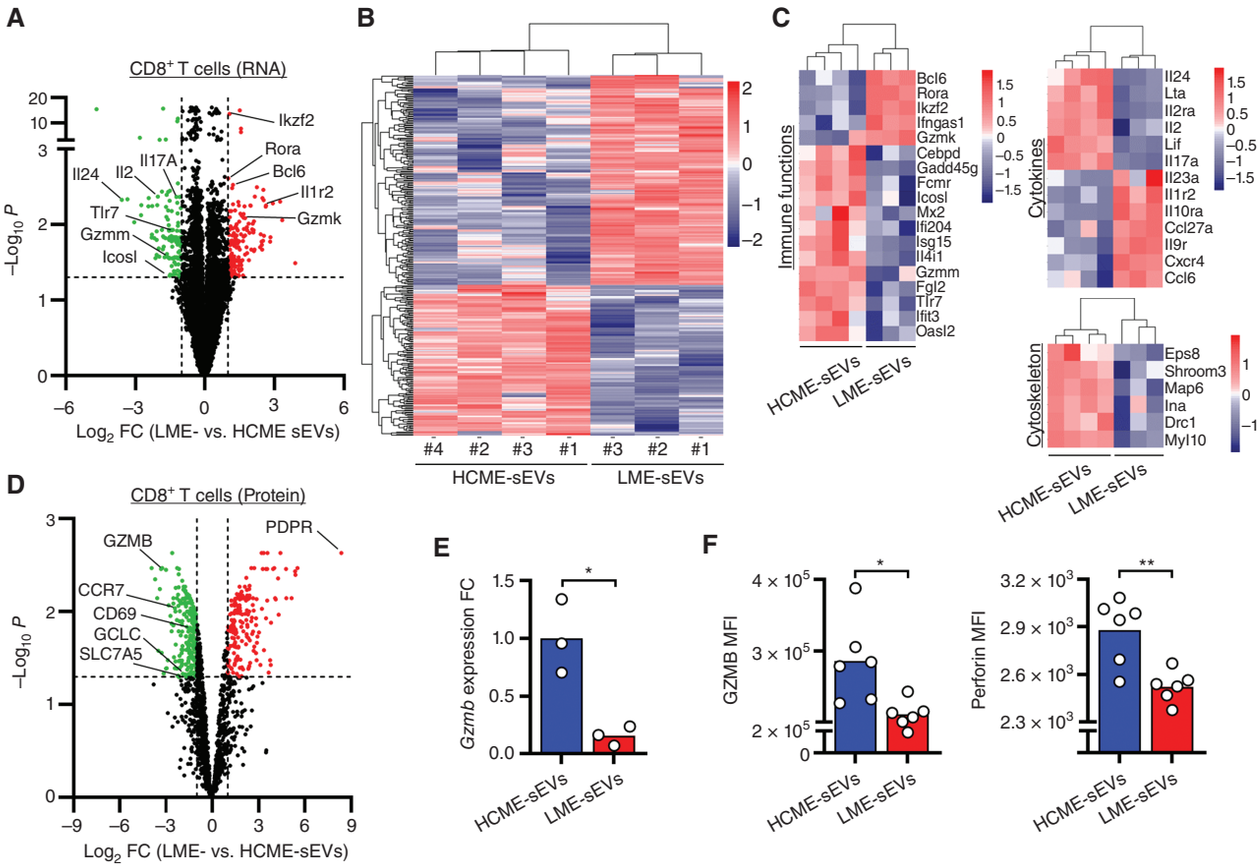


Figure 3. ***(Continued)*** **J,** Hierarchical clustering of DEG from **I**. **K,** t-distributed stochastic neighbor embedding (t-SNE) of samples from **I**. **L,** Hierarchical clustering of selected genes from **J**, grouped by enriched gene ontologies. **M** and **N,** mRNA (**M**) or protein levels (**N**) of 3 selected DEG from **I**, quantified by RT-qPCR or FC, in CD8$^+$ T cells treated *in vitro* for 48 hours with HCME- or LME-sEVs. *, $P < 0.05$; **, $P < 0.01$; ***, $P < 0.001$; ****, $P < 0.0001$ (unpaired Student *t* test). Data are mean.

observed a decreased oxygen consumption rate (OCR) in the presence of LME-sEVs (Fig. 4L). These data demonstrated that CD8$^+$ T cells have decreased oxidative phosphorylation potential when treated with LME-sEVs. Finally, the use of glutamine for protein synthesis is in accordance with our observation that translation is highly increased in CD8$^+$ T cells treated with LME-sEVs (Fig. 4H). Glutamine is also used for purine and pyrimidine bases synthesis. Indeed, higher levels of metabolites, including ADP and ATP, were found in CD8$^+$ T cells treated with LME-sEVs (Supplementary Fig. S4I). Altogether, our data suggest LME-sEV–mediated profound perturbations in CD8$^+$ T cells, leading to metabolic blockade (Supplementary Fig. S4J). Accordingly, increased glycolysis was recently linked with CD8$^+$ T-cell exhaustion (29).

Finally, CD8$^+$ T-cell functions are tightly regulated by other immune cells, in particular other lymphocyte subsets. Despite the injection of LME-sEVs *in vivo* did not show a considerable effect on other lymphocytes than CD8$^+$ T cells (Supplementary Fig. S3D–S3F), we cannot rule out that a direct exposure to sEVs in the LME could lead to a substantial impact on these cells. Thus, we exposed Tregs, CD4$^+$ T_{conv} cells, and CD19$^+$ B cells to purified ME-sEVs *ex vivo* and inspected gene expression. We identified 378 genes regulated in Treg pointing to an activated phenotype (ref. 30; TNFRSF9$^+$; Supplementary Fig. S5A–C; Supplementary Table S2). Effector molecules (*GzmB* and *GzmK*), signaling molecules (*Stat1*, *Irf4*, and *Irak3*), and activation markers (*Pdcd1*, *Cd27*, and *Tigit*) were increased. We also confirmed an increase of GzmB at the protein level (Supplementary Fig. S5D). Interestingly, the majority of differential expression of genes (DEG) were repressed by LME-sEVs in CD4$^+$ T_{conv} cells (211 out of 227, *Cd27*, *Il7r*, *Il17ra*, *Tcf7*, and *Tox*), indicating a strong suppression of T-cell activation and proliferation (Supplementary Fig. S5E–S5G; Supplementary Table S2). CD19$^+$ B cells were

Downloaded from http://aacrjournals.org/bloodcancerdiscov/article-pdf/4/1/54/3236873/54.pdf by guest on 28 March 2023



Downloaded from http://aacrjournals.org/bloodcancerdiscov/article-pdf/4/1/54/3236873/54.pdf by guest on 28 March 2023

the least affected (77 DEGs and no enriched ontology; Supplementary Fig. S5H and S5I; Supplementary Table S2).

Altogether, these data indicate that CD8$^+$ T cells are major targets of LME-sEVs *in vivo* and *ex vivo* as transcriptomic, proteomic, and metabolic evaluations pointed to profound perturbations of cell activation, proliferation, and immune functions. Worth of notice, *ex vivo* LME-sEV–treated Tregs showed a highly suppressive phenotype that could contribute to CD8$^+$ T-cell repression in the tumor microenvironment.

LME-sEVs Decrease CD8$^+$ T-cell Functions

First, we screened splenic CD3$^+$ versus CD3$^-$ cells from leukemic mice for the expression of ICP receptors and found an enrichment of a variety of ICP receptors in CD3$^+$ T cells (Supplementary Fig. S6A), confirming the highly exhausted and immunosuppressive microenvironment we previously reported in TCL1 mice (10). Next, we evaluated the phenotype and activity of CD8$^+$ T cells treated with LME-sEVs. First, LME-sEVs stimulated the generation of CD8$^+$ lymphocyte subpopulations, as visible by the expansion of T_{em} cells (Fig. 5A and B). We performed a clustering of CD8$^+$ T cells based on ICP surface expression, using the HSNE algorithm. Eleven clusters were identified based on ICOS, LAG3, PD1, TIGIT, and TIM3 expression among T_{em} cells (Fig. 5C and D). Clusters C1 and C8 coexpressing the 5 ICP were significantly enriched (Fig. 5E), suggesting an exhausted phenotype. Concerning sEV immuno-modulatory effects, IL2 and IFNγ synthesis was particularly decreased by LME-sEVs, demonstrating their impact on CD8$^+$ lymphocyte cytokine polyfunctionality (Supplementary Fig. S6B–S6D). In addition, adenosine, converted by CD39/CD73 starting from ATP, significantly reduces CD8$^+$ T-cell proliferative capacity (31). Indeed, the proliferation of CD8$^+$ T cells is markedly reduced by LME-sEV (expressing CD39; Supplementary Fig. S2C) treatment in the presence of ATP (Supplementary Fig. S6E). This, together with the decrease in perforin and GzmB (Fig. 4F), strongly suggests a robust LME-sEV–mediated deregulation of CD8$^+$ T-cell signaling and production of cytokines and cytotoxic molecules.

Therefore, we aimed to confirm the functional impact of LME-sEVs on CD8$^+$ T cells using an *ex vivo* quantitative cytotoxicity assay against TCL1 CLL cells. LME-sEV treatment led to reduced cytotoxic activity of CD8$^+$ T cells against CLL cells (Fig. 5F), without altering the ability of CD8$^+$ lymphocytes to interact with target cells (Fig. 5G). Importantly, LME-sEVs decreased the ability of CD8$^+$ T cells to form F actin–enriched immune synapses, a key signaling structure required to drive the secretion of cytolytic granules to lytic synapses (Fig. 5H). Consistent with decreased RNA and protein levels (Fig. 4E and F), the level of GzmB expression at the synapse was markedly reduced in CD8$^+$ T cells treated with LME-sEVs (Fig. 5I). In accordance with the enrichment of LME-sEVs in several miRNAs (Fig. 2J), we observed a significant increase in miRNA levels in CD8$^+$ T cells treated with LME-sEVs (Fig. 5J; Supplementary Fig. S6F). Interestingly, these miRNAs (miR-150, -155, and -378a) were previously described as negative regulators of GmzB in CD8$^+$ T and NK cells (32–35), two markers that we found recurrently downregulated in CD8$^+$ lymphocytes treated with LME-sEVs (Fig. 4D–F; Supplementary Fig. S5I).

To identify particular cargoes responsible for the effects observed on CD8$^+$ T cells, we focused on these miRNAs as they are transferred to target cells as well as on ICP as highly important regulators of T-cell functions.

Treated CD8$^+$ T cells with LME-sEVs previously transfected with antagomiRs targeting miR-150, -155, and -378a, showed a rescue in GzmB and CD226 protein levels, comparable to CD8$^+$ T cells treated with HCME-sEVs or LME-sEVs precoated with heparin (Fig. 5K), whereas Prf1 and Itpkc levels remained unaffected (Supplementary Fig. S6G). In addition, the transfection of LME-sEVs with single antagomiRs did not restore the levels of target genes in treated CD8$^+$ T cells (Supplementary Fig. S6H), demonstrating that multiple miRNAs are needed to target these molecules. Interestingly, treatment with HCME-sEVs transfected with miRNA mimics for miR-150, -155, and -378a had a similar effect on GzmB level than LME-sEVs, confirming that the repression of GzmB we observed was due to these miRNAs (Supplementary Fig. S6I).

Next, we focused on ICP ligands present on LME-sEV surface and used blocking antibodies to neutralize their immunosuppressive functions on CD8$^+$ T cells. Although LME-sEVs (+ isotype Ab) stimulated ICP expression and decreased GzmB and perforin levels as we previously showed, preincubation with anti–PD-L1, GAL9, VISTA, and MHC-II blocking Ab decreased ICP expression, restored perforin level, but had no effect on the GzmB level in treated CD8$^+$ T cells (Fig. 5L), suggesting that different molecules present in LME-sEVs affect multiple pathways in target cells leading to their overall effect.

Altogether, through multiple molecules, LME-sEVs decreased CD8$^+$ T-cell functional potential, impacting cytokine production and engaging ICP receptors, thus decreasing cytotoxic effect toward tumor cells.

sEVs Are Crucial for CLL Development by Impairing the Antitumor Immune Response *In Vivo*

Considering the enrichment of sEVs in the LME, their specific cargo and surface molecules, and impact on CD8$^+$ T cells, we investigated their role during CLL development *in vivo*, by genetically impairing sEV release in a novel preclinical

Figure 4. LME-sEVs impact CD8$^+$ T-cell transcriptome, proteome, and metabolome. **A,** Volcano plot showing DEG identified by RNA-seq from CD8$^+$ T cells treated for 48 hours with LME- ($n = 4$) or HCME-sEVs ($n = 3$) with FDR <0.05 and $\log_2$FC >1. **B** and **C,** Hierarchical clustering of all DEG (**B**) and of selected genes from relevant cell functions (**C**). **D,** Volcano plot showing differentially expressed proteins (DEP) identified by mass spectrometry from CD8$^+$ T cells treated for 96 hours with LME- ($n = 3$) and HCME-sEVs ($n = 3$) with FDR <0.05 and $\log_2$FC >1. **E** and **F,** GzmB mRNA expression and GzmB and perforin levels in CD8$^+$ T cells treated for 48 hours with HCME- or LME-sEVs. **G** and **H,** Ontology analysis of enriched (**G**) or diminished (**H**) DEP in CD8$^+$ T cells treated with LME- or HCME-sEVs (from **D**). **I,** Levels of glucose measured by mass spectrometry in culture medium in CD8$^+$ T-cell treated with LME- or HCME-sEVs for 96 hours. Negative value represents consumption. **J,** Immunoblot analysis of glycolysis-related proteins from CD8$^+$ T cells treated for 96 hours with LME- or HCME-sEVs. **K,** Levels of ADP and ATP generated from ^{13}C-glucose measured by mass spectrometry in CD8$^+$ T cells treated with LME- ($n = 5$) or HCME-sEVs ($n = 6$) for 96 hours. **L,** Oxygen consumption measured by SeaHorse assay from CD8$^+$ T cells treated with LME- or HCME-sEVs for 96h. *, $P < 0.05$; **, $P < 0.01$; ****, $P < 0.0001$ (unpaired Student *t* test). Data are mean and SEM.

Downloaded from http://aacrjournals.org/bloodcancerdiscov/article-pdf/4/1/54/3236873/54.pdf by guest on 28 March 2023

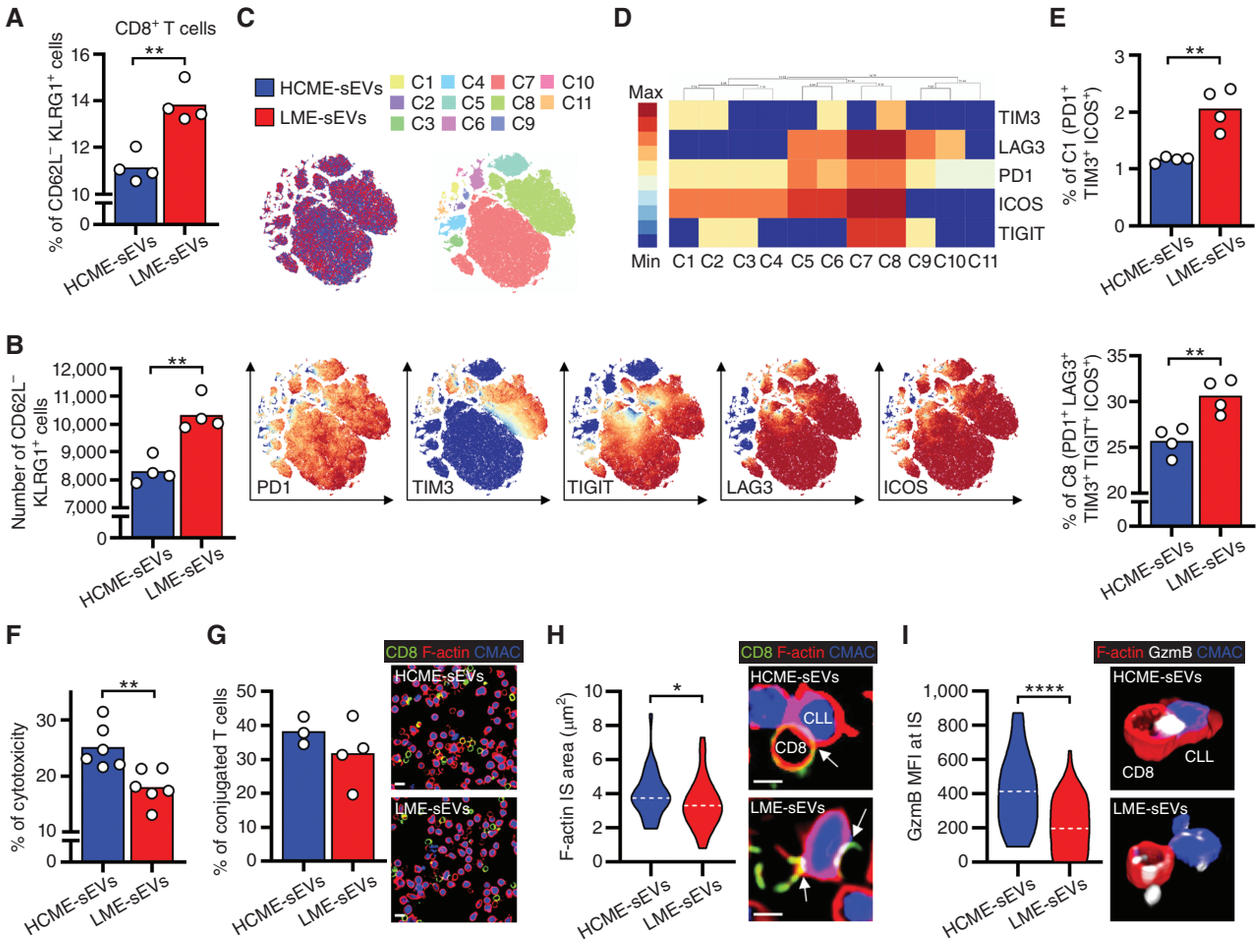


Figure 5. LME-sEVs decrease CD8+ T-cell functions. **A** and **B,** Percentages (**A**) and numbers (**B**) of CD62L−KLRG1+ CD8+ T cells after 48 hours of treatment with LME- and HCME-sEVs assessed by FC. **C,** Expression of ICP on CD62L−KLRG1+ CD8+ T cells from **B**. HSNE clustering depicting treatments, cluster identity, and marker expression. **D,** Hierarchical clustering based on ICP expression. **E,** Percentages of PD1+TIM3+ICOS+ CD8+ T cells from cluster C1 (top) and of PD1+LAG3+TIM3+TIGIT+ICOS+ CD8+ T cells from cluster C8 (bottom). **F–I,** CD8+ T cells were isolated from C57BL/6 and CLL cells from TCL1 mice. **F,** Percentage of T cell–mediated killing of TCL1 cells (cytotoxic assay) in the presence of HCME-sEVs or LME-sEVs ($N = 6$). **G,** Quantification of CD8+ T-cell:TCL1 cell conjugates upon treatment with LME- or HCME-sEVs ($N = 3$–4) and representative images (scale bar, 10 μm). **H,** Quantification of immune synapse formation (F-actin area in μm2, HCME-, $n = 31$ and LME-sEVs, $n = 39$, dashed line representing median) and representative medial optical sections (scale bar, 5 μm) with arrows indicating the synapse. **I,** Mean Fluorescence intensity (MFI) of GzmB at the synapse between CD8+ T and CLL cells (HCME-, $n = 31$ and LME-sEVs, $n = 51$) and representative 3D volume-rendered images. (*continued on following page*)

CLL murine model, TCL1-RAB27DKO (Fig. 6A). RAB27A and B are two proteins essential for sEV release, being majorly involved in the docking of vesicles at the cellular membrane (36–38). Validation of the model showed the presence of the human *TCL1* transgene together with the *Rab27b* genomic deletion, and lack of both RAB27A and B proteins (Fig. 6B and C). TCL1-RAB27DKO showed a striking delay in CLL progression, noticeable by the slower accumulation of CD5+CD19+ CLL cells in the PB, and consequently increased mouse survival (Fig. 6D and E), further confirmed with histologic analyses of the spleens (Supplementary Fig. S7A). TCL1-RAB27DKO ultimately developed the disease and required euthanasia. Despite TCL1-RAB27DKO spleens being of comparable size as TCL1, the quantity of LME-sEVs was dramatically decreased (Fig. 6F; Supplementary Fig. S7B). In addition, LME-sEV$_{TCL1\text{-}RAB27DKO}$ protein content is largely different (546 proteins modulated; Fig. 6G–H; Supplementary Fig. S7C; Supplementary Table S1). Indeed, LME-sEVs$_{TCL1\text{-}RAB27DKO}$ contained a lower quantity of several proteins involved in the suppression and control of lymphocyte activation, signaling, and proliferation (LGASL1, LGASL9, CXCR5, IL4I1, BLK, and SYK), whereas proteins enriched were involved in gene expression, RNA processing, and translation (Fig. 6H; Supplementary Fig. S7D and S7E). Based on the differentially present proteins, sEV preparations clustered in principal component analysis (PCA) according to mouse genotypes (Supplementary Fig. S7F).

Next, we compared gene expression from TCL1-RAB27DKO and TCL1 leukemic cells (Supplementary Fig. S7G–S7H; Supplementary Table S2). GSEA confirmed the decrease, at the mRNA level, of protein secretion in TCL1-RAB27DKO cells (Supplementary Fig. S7I). Rab27 inactivation led to decreased expression of genes involved in vesicle trafficking (*Bet1*, *Lamp2*, *Rab7*, *Scamp1*, and *Vamp1*), whereas *Snx31* responsible for

Downloaded from http://aacrjournals.org/bloodcancerdiscov/article-pdf/4/1/54/3236873/54.pdf by guest on 28 March 2023

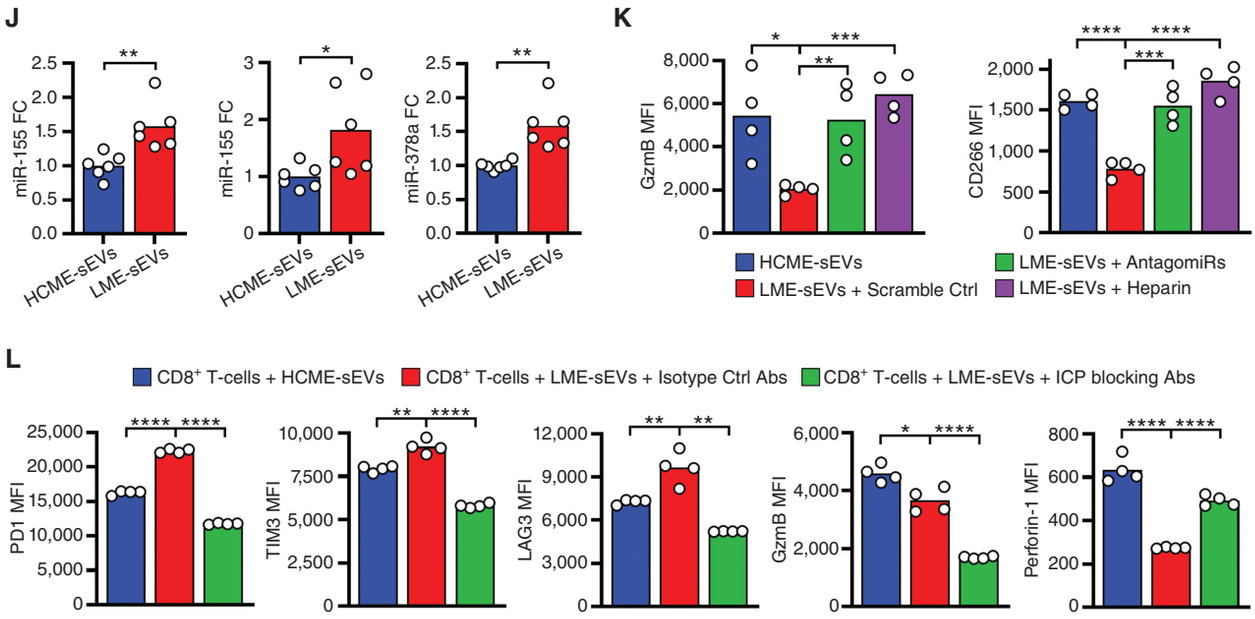


Figure 5. ***(Continued)*** **J,** miRNA levels quantified by RT-qPCR in CD8+ T cells treated with HCME- or LME-sEVs for 24 hours. **K,** Protein levels of miRNA targets determined by FC in CD8+ T cells treated for 48 hours with HCME-sEVs or LME-sEVs transfected with scramble or antagomiRs (miR-150, -155, and -378a). Preincubation of LME-sEVs with heparin was used as an inhibitor of sEV internalization. **L,** ICP levels determined by FC in CD8+ T cells treated for 48 hours with HCME-sEVs or LME-sEVs preincubated with blocking Abs (PD-L1, GAL9, VISTA, and MHC-II) or corresponding isotypes. *, $P < 0.05$; **, $P < 0.01$; ***, $P < 0.001$; ****, $P < 0.0001$ (unpaired Student *t* test). Data are mean.

vesicles formation in the MVB was upregulated (Supplementary Fig. S7G). Interestingly, an enrichment in gene sets driven by NF-κB, Myc, and Wnt/β-catenin was observed, suggesting the induction of oncogenic programs as a compensatory mechanism (Supplementary Fig. S7I).

To confirm that the delay in CLL development was due to CLL cell inability to release sEVs, rather than to a general lack of sEVs in the LME, we transferred CLL cells isolated from spleens of TCL1 or TCL1-RAB27DKO mice into WT C57BL/6 recipient mice. Contrary to TCL1 cells, TCL1-RAB27DKO cells failed to recapitulate CLL development (Fig. 6I and J; Supplementary Fig. S8A). Importantly, injection of LME-sEVs rescued leukemia development to levels comparable to TCL1 transfer, demonstrating the impact of LME-sEVs on CLL development (Fig. 6I–J; Supplementary Fig. S8A). To evaluate a potential autocrine effect, we treated *ex vivo* TCL1-RAB27DKO leukemic cells with LME-sEVs or LME-$sEVs_{TCL1\text{-}RAB27DKO}$ (Supplementary Fig. S8B–S8D; Supplementary Table S2). The effect was moderate and pointed to B-cell functions (*Bach2* and *Maf*) and increased immunosuppressive capabilities (*Cx3cr1*).

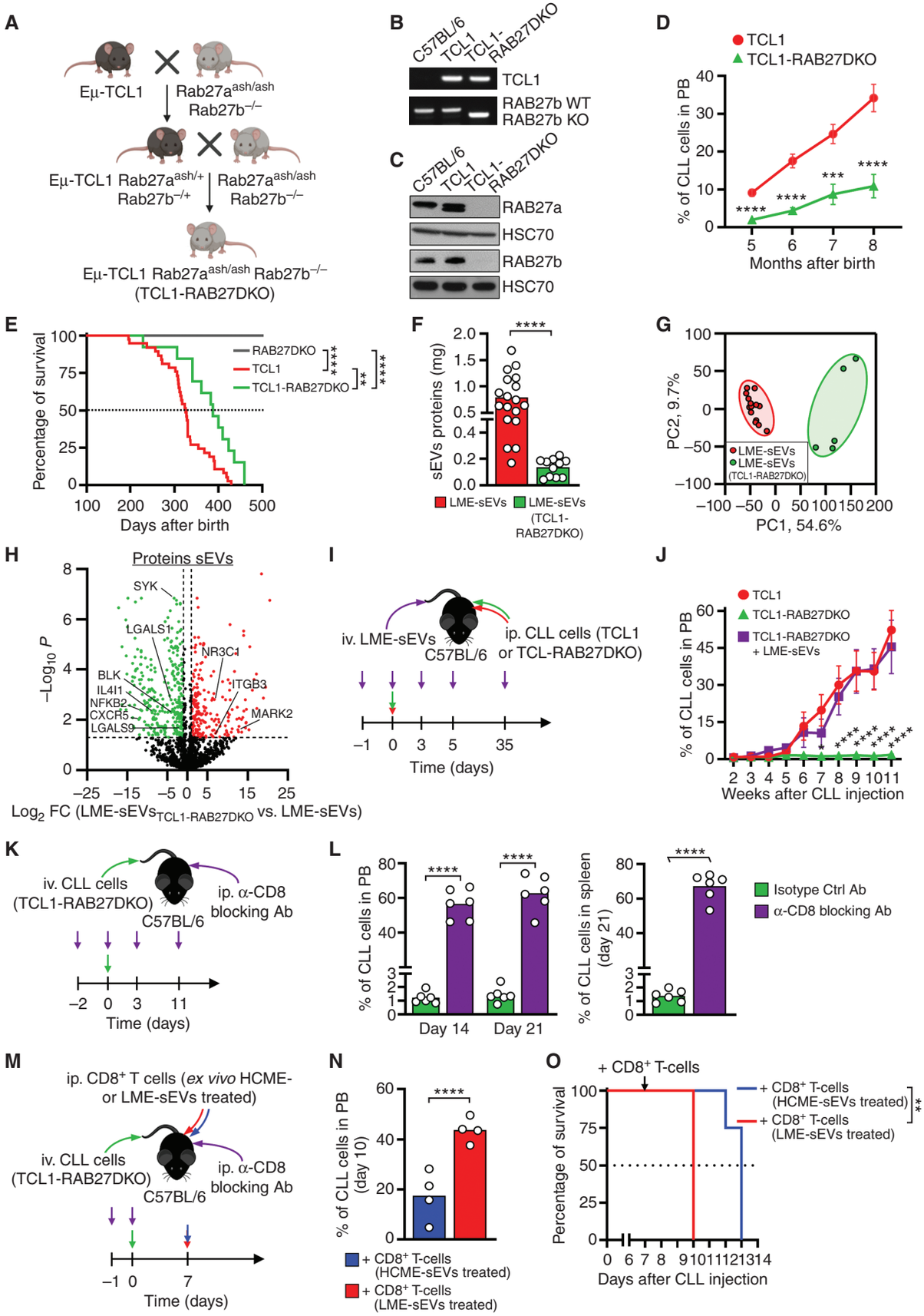
Despite being unable to recapitulate the disease in immunocompetent C57BL/6 mice, TCL1-RAB27DKO CLL cells successfully induced leukemia development in immunodeficient NSG mice (Supplementary Fig. S8E–S8H), highlighting the proficiency of TCL1-RAB27DKO CLL cells to engraft when the immune system is not intact. To confirm that CD8+ T cells are key in the control of CLL development, we selectively depleted CD8+ T cells in C57BL/6 mice before injecting TCL1-RAB27DKO CLL cells (Fig. 6K; Supplementary Fig. S8I). We observed a rapid increase of percentage and number of leukemic cells in the blood and spleen of CD8+-depleted mice (Fig. 6L; Supplementary Fig. S8J and S8K), endorsing the role of CD8+ T cell–mediated immune surveillance of TCL1-RAB27DKO CLL cells. In a final experiment, we sought to evaluate *in vivo* the ability of ME-sEVs to affect CD8+ T cells and therefore to influence disease outcome (Fig. 6M). Mice depleted in endogenous CD8+ T cells and injected with TCL1-RAB27DKO CLL cells, had significantly more CLL cells in the PB and shorter survival when injected with CD8+ T cells previously treated with LME-sEVs compared with HCME-sEVs (Fig. 6N and O). We also observed that LME-sEV–treated CD8+ T cells did neither persist nor proliferate in recipient mice, possibly explaining the different outcomes (Supplementary Fig. S8L and S8M).

Altogether, we demonstrated here that TCL1-RAB27DKO CLL cells fail to induce CLL in C57BL/6 due to their inability to release sEV and impact the microenvironment. LME-sEVs inhibit CD8+ T cell–mediated antitumor immunity and are sufficient to restore the leukemic potential of TCL1-RAB27DKO CLL cells.

Expression of sEV-Related Genes Correlates with Disease Progression and Poor Survival in CLL Patients

To validate the importance of sEVs in CLL patients, we quantified the expression of *RAB7a*, *RAB10*, *RAB27a*, *RAB31*, *RAB35*, *RAB40C*, and *PDCD6IP*, involved in vesicle biogenesis and secretion by RT-qPCR in a cohort of 144 CLL patients. We identified *RAB27a* and *RAB31* as predictors of overall survival (OS), as higher expression correlated with poor OS (Fig. 7A and B; Supplementary Fig. S9A). Similarly, when combining *RAB27a* and *RAB31* with other sEV-related genes, the signature correlated with OS (Fig. 7C) and a higher

Downloaded from http://aacrjournals.org/bloodcancerdiscov/article-pdf/4/1/54/3236873/54.pdf by guest on 28 March 2023



Downloaded from http://aacrjournals.org/bloodcancerdiscov/article-pdf/4/1/54/3236873/54.pdf by guest on 28 March 2023

hazard ratio (HR; Fig. 7D). Similar results were obtained for treatment-free survival (TFS; Fig. 7E and F; Supplementary Fig. S9B–S9D). Single-gene analysis confirmed the differential expression of *RAB7a*, *RAB27a*, *RAB31*, and *RAB35* between CLL groups (e.g., ZAP70$^+$ vs. ZAP70$^-$) and subgroups (e.g., $IGHV_M$ LPL$^+$ vs. $IGHV_{UM}$ LPL$^-$; Fig. 7G; Supplementary Fig. S9E) characterized by the expression of markers classifiers of prognosis. Similarly, we identified signatures differentially expressed between clinical groups (Fig. 7H). Altogether, our data confirmed the relevance of sEVs in CLL pathology.

DISCUSSION

Recent studies focused on understanding how the microenvironment sustains tumor growth and protects cancer cells. In this regard, sEVs are important for cell-to-cell communication, and thus represent possible targets for antitumor therapies. The complexity behind sEV-based communication during cancer development relies on their ability to alter the microenvironment cellular composition and functions. Previous works by us and others partially elucidated sEV involvement in CLL progression and remodeling of the TME (5, 13–15). Interestingly, we found here a sEV signature linked with the biogenesis and release of sEVs by CLL cells in humans and mice. However, the relevance of such studies using cell line– or plasma-derived sEVs and *in vitro* cultures points to the need of more physiologic conditions to study sEV (24). This confirmed the relevance of designing a robust protocol to isolate sEVs from the murine LME. We focused our attention on the functional effect of LME-sEVs on lymphocyte subsets as they internalized LME-sEVs, highlighting the possibility of cargo-mediated effects in addition to surface molecule interactions. T lymphocytes are known to poorly internalize sEV (26, 27). This discrepancy suggests the presence of surface molecules on sEVs produced in a whole organism that could lack when produced *in vitro*. Importantly, we noted that exclusively CD8$^+$ T cells were affected after seven days of treatment *in vivo*. This unforeseen observation indicated a certain specificity of sEV rather than a broad effect, as LME-sEVs could enter multiple lymphocyte subsets *in vitro*. Again, this highlights the need for a whole microenvironment to fully understand the role of sEVs in cancer (24).

We characterized LME-sEVs to decipher their impact on the TME. Surface molecules screening highlighted the enrichment in CD20 on LME-sEVs, confirming the B-cell origin of the vesicles and our previous observation (14). PD-L1, CTLA-4, and TIM-3 were already reported as crucial effectors of sEV function on immune cells (39). Given the complexity of sEV content, we believe that sEVs convey molecules of multiple natures (ICP, miRNA, enzymes) having complementary functions. First, we found multiple ICP ligands on LME-sEVs, and the corresponding receptors on matched spleens CD3$^+$ T cells. This supports our previous report of multiple ICP receptors on T cells in murine CLL (10), the possible engagement of ligands carried by sEV inducing T-cell exhaustion and immune escape (7). Moreover, the presence of multiple miRNAs enriched in CLL-sEVs (15, 25, 40, 41), transferred to CD8$^+$ T cells, and known to disrupt effector cell cytotoxic properties (32–35) pointed to GzmB and perforin, consistently inhibited by LME-sEVs in CD8$^+$ T cells. miRNA neutralization and ICP blockade both partially reversed the effects observed on CD8$^+$ T cells. As a functional readout, we also focused on immune synapse formation between CD8$^+$ T cells and TCL1 leukemic B cells and confirmed reduced expression of GzmB at lytic synapses in CD8$^+$ T cells previously exposed to LME-sEVs *in vitro*, ultimately leading to decreased functional cytotoxicity. Interestingly, LME-sEVs had an opposite effect on Tregs, stimulating the expression of GzmB, and thus their immunosuppressive functions (42). We confirmed that treatment of CD8$^+$ T cells with ATP and CD39$^+$LME-sEVs decreased proliferation, cytotoxicity, and IL2/GzmB production (31, 43). Overall, the combinatory activity of ICP, miRNAs, and hydrolytic enzymes leads to a decrease in T-cell functionalities, ultimately suppressing the antitumor immune response. In accordance with this, gene-expression profiling from *in vitro* and *in vivo* LME-sEV–treated CD8$^+$ T cells further showed a consistent impact on immune functions, cytokine release, cytoskeleton organization, and metabolic changes. Metabolic adaptation and manipulation by the tumor is recognized as a hallmark of cancer. Recently, tumor-derived EVs were shown to reprogram the metabolism of macrophages, thereby preparing an immunosuppressive niche characterized by increased glycolysis and lactate release (44). These metabolic adaptations—increased glucose consumption and lactate release—are known markers of exhaustion (29) that we also observed in LME-sEV–treated CD8$^+$ T cells. The TCA cycle produces energy to feed the oxidative phosphorylation (OXPHOS). Recently, a high OXPHOS in CD8$^+$ T cells was described to be deleterious for immunotherapy in melanoma (45). In addition, we identified inside LME-sEV proteins

Downloaded from http://aacrjournals.org/bloodcancerdiscov/article-pdf/4/1/54/3236873/54.pdf by guest on 28 March 2023

Figure 6. sEVs are crucial for CLL development by impairing the antitumor immune response *in vivo*. **A,** Generation of a new TCL1-RAB27DKO mouse model. **B,** Detection of the human *TCL1* transgene and Rab27b excision in gDNA of C57BL/6, TCL1, and TCL1-RAB27DKO mice. **C,** Immunoblot analysis of RAB27A and RAB27B proteins in the same mice. **D,** Percentage of CD5$^+$CD19$^+$ CLL cells in the PB of TCL1 ($n = 35$) or TCL1-RAB27DKO ($n = 12$) mice over time. **E,** Survival of mice from **D** and RAB27DKO mice ($n = 10$). **F,** Quantity of proteins recovered from LME-sEVs ($n = 18$) or LME-$sEVs_{TCL1\text{-}RAB27DKO}$ ($n = 11$) normalized per gram of spleen. **G,** PCA based on differentially expressed proteins (DEP) between LME-$sEVs_{TCL1\text{-}RAB27DKO}$ and LME-sEVs with FDR <0.05 and $\log_2$FC >1. **H,** Volcano plot showing DEP. **I,** Injection scheme of CLL cells competent (TCL1, red arrows) or deficient in sEV release (TCL1-RAB27DKO, green arrows) into C57BL/6 mice, with or without LME-sEVs (violet arrows). **J,** Percentage of CD5$^+$CD19$^+$ CLL cells in the blood of C57BL/6 mice injected according to **I** ($n = 16$ per condition). Four different clones for each genotype were injected into 4 mice each. **K,** Injection scheme of CLL cells deficient in sEV release (TCL1-RAB27DKO, green arrows) into C57BL/6 mice, treated with α-CD8 blocking or isotype-control Abs (violet arrows). **L,** Percentage of CD5$^+$CD19$^+$ CLL cells in the PB of mice injected according to **K** ($n = 6$ per group) at days 14 and 21 (left) and in the spleen of the same mice at day 21. **M,** Injection scheme of CLL cells deficient in sEV release (TCL1-RAB27DKO, green arrows) into C57BL/6 mice, together with α-CD8 blocking Ab (violet arrows) and followed by injection of activated CD8$^+$ T cells treated *ex vivo* with HCME- (blue arrows) or LME-sEVs (red arrows). **N,** Percentage of CD5$^+$CD19$^+$ CLL cells at day 10 in the PB of mice injected according to panel **M** ($n = 4$ per group). **O,** Survival of mice from **M** ($n = 4$ per group). *, $P < 0.05$; **, $P < 0.01$; ***, $P < 0.001$; ****, $P < 0.0001$ (unpaired Student *t* test for **F**, **L**, and **N** two-way ANOVA followed by the Bonferroni multiple comparison test for **D** and **J**, log-rank test for **E** and **O**). Data are mean with SEM.

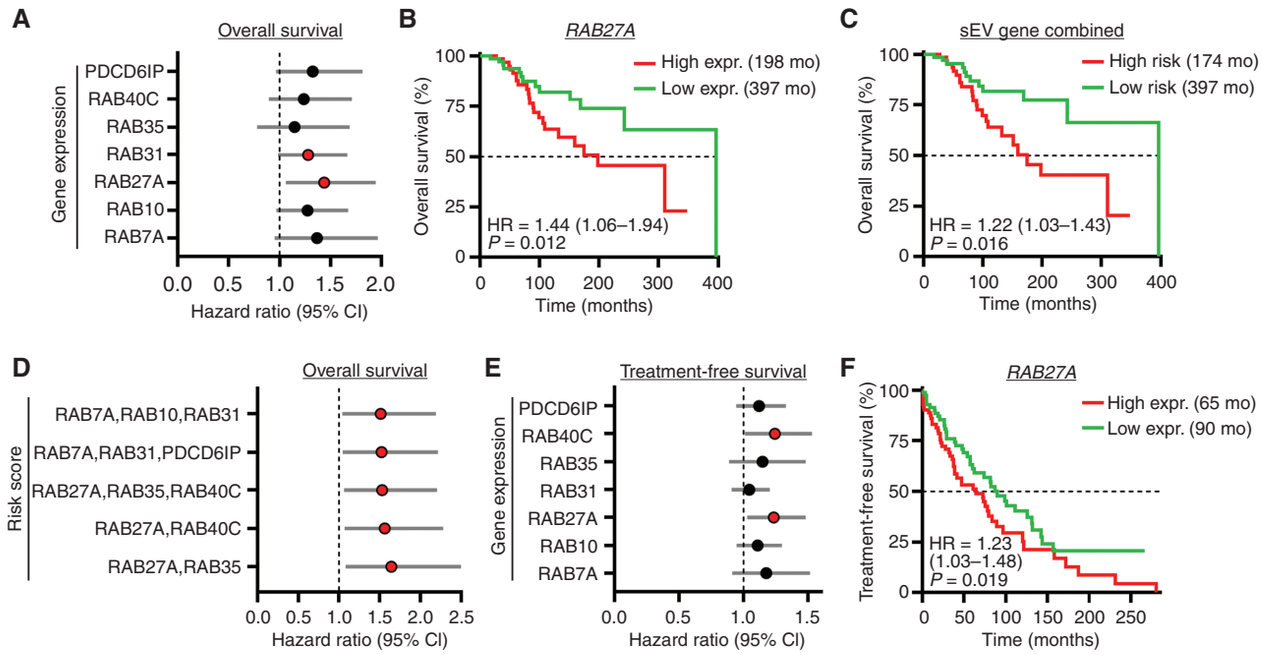


Figure 7. Expression of sEV-related genes correlates with disease progression and poor survival in CLL patients. Gene-expression analysis was performed by RT-qPCR for 7 genes involved in sEV biogenesis and secretion in a cohort of 144 CLL patients. The correlation between gene expression and survival was evaluated by Cox univariate regression analysis. Gene expression in clinical groups was evaluated by differential expression analysis for single genes or by logistic regression (LR) analysis for multiple genes. **A,** Calculated hazard ratios >1 (red dots, $P < 0.05$) indicate an increased risk for patients with high single-gene expression in terms of OS. **B,** Correlation between high or low gene expression and OS. Low and high groups are of identical size ($n = 72$) Median OS is indicated in months (mo). **C,** Correlation between high or low combined 7-gene expression and OS. **D,** Calculated hazard ratios >1 (red dots, $P < 0.05$) indicate an increased risk for patients with high multiple gene expression in terms of OS. **E,** Calculated hazard ratios >1 (red dots, $P < 0.05$) indicate an increased risk for patients with high single-gene expression in terms of TFS. **F,** Correlation between high or low gene expression and TFS. (*continued on following page*)

involved in metabolism, including IL4I1, a metabolic ICP recently described in CLL (46), also pointing to the possible delivery of the enzyme to immune cells, thus influencing their activation status. Finally, although no striking effect of LME-sEVs on Tregs was observed *in vivo*, the vesicles rapidly modified Tregs *in vitro* toward a more immunosuppressive phenotype similar to the one observed in TCL1 mice. Their activation and GzmB increase *in vitro* confirmed their potential to respond to LME-sEVs and suggested their involvement in the long-term hindered T-cell response *in vivo*.

To confirm the crucial role of sEVs *in vivo*, we generated a TCL1-RAB27DKO model in which sEVs release is inhibited (47). Although Rab27DKO mice are partially immunodeficient (48), secretion of cytokines by Rab27DKO immune cells remains unaffected (49). TCL1-RAB27DKO CLL cells showed strong NFκB- and Myc-driven oncogenic transcriptional programs and grew in immunodeficient mice. However, we noted a striking delay of disease onset in mice deprived of sEVs, and TCL1-RAB27DKO CLL cells transfer into immunocompetent mice failed to recapitulate the disease. Importantly, the reintroduction of LME-sEVs rescued leukemia development. We also showed, by a depletion experiment, that $CD8^+$ T cells are crucial for controlling CLL development in the absence of sEVs. Finally, we confirmed that LME-sEVs are impairing T-cell functions as leukemic mice adoptively transferred with $CD8^+$ T cells activated in the presence of LME-sEVs had a shorter survival than with HCME-sEVs. Altogether, despite sEV-deficient CLL cells were fit to grow *in vivo*, sEVs are indispensable to escape the antitumor immune response in immunocompetent animals.

Finally, using a cohort of CLL patients, we found a correlation between sEV-related gene expression, prognostic markers, and survival. Enhanced expression of the *RAB27A* gene by breast cancer cells promotes invasiveness and metastasis potential (50), suggesting a crucial role for sEVs in aggressive malignancies. In conclusion, we stressed on the importance to focus and characterize more complex sources of sEVs, and not limiting our evaluations to sEVs produced *in vitro*. Current therapies using ICP blockers showed a limited effect against CLL, with benefits for patients with Richter transformation (51). Having a broader overview of the TME, including sEV composition, could be key to better understand cancer progression and resistance to establish effective therapeutic strategies for patients (52).

METHODS

Patient Samples

All experiments involving human samples were conducted in accordance with the declaration of Helsinki, approved by the institutional review board (Jules Bordet Institute Ethics Committee), and PB samples were collected from treatment-naïve CLL patients after written informed consent. Patient cohort demographic characteristics (age and gender) and clinical parameters [Binet stage,

Downloaded from http://aacrjournals.org/bloodcancerdiscov/article-pdf/4/1/54/3236873/54.pdf by guest on 28 March 2023

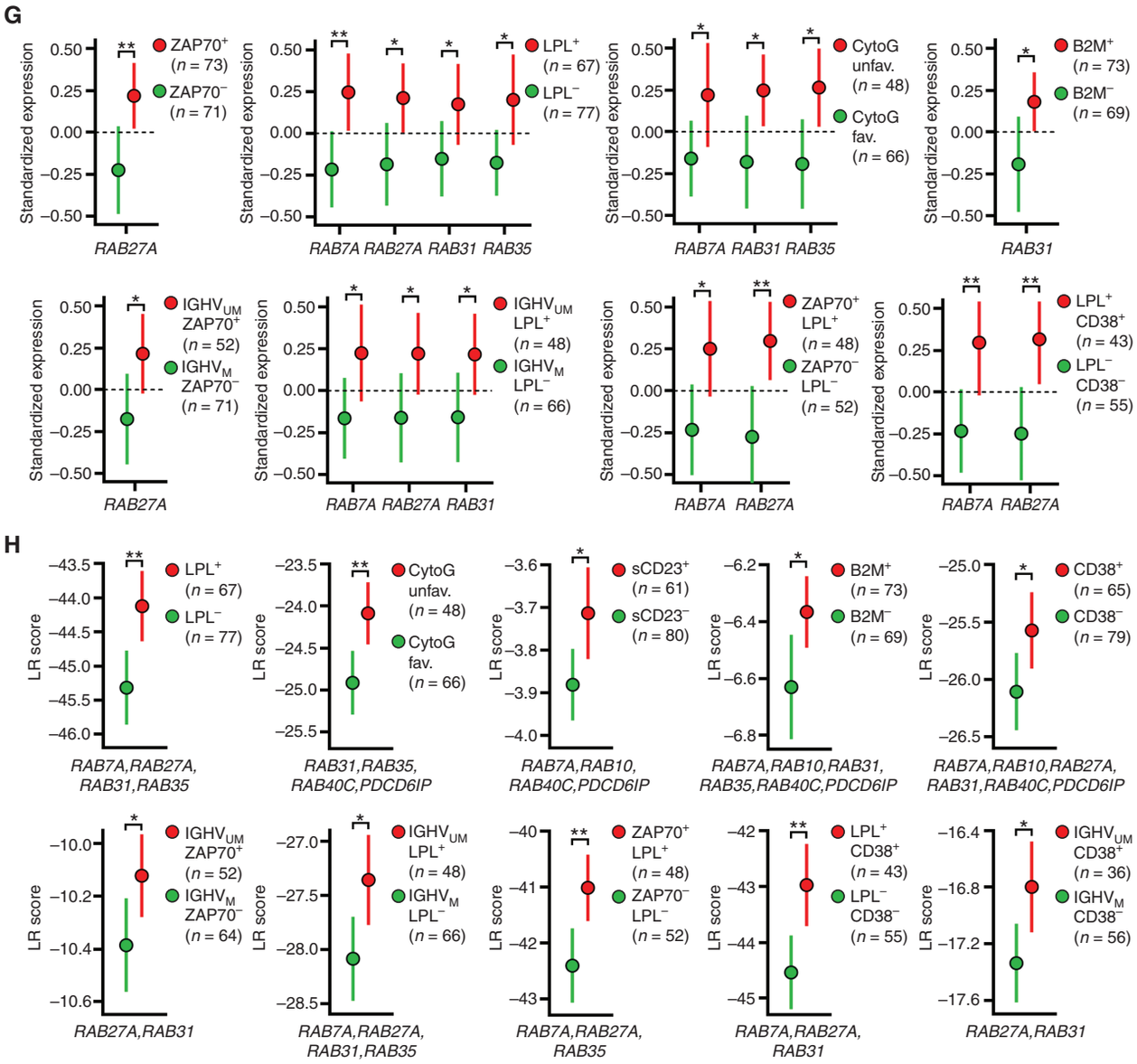


Figure 7. ***(Continued)*** **G** and **H,** Standardized expression of single genes (**G**) or LR scores for multiple genes (**H**) in groups of patients according to prognostic markers (CytoG, cytogenetics, group size indicated in each panel). *, $P < 0.05$; **, $P < 0.01$. Data are mean with 95% confidence intervals.

IgHV status, zeta-associated protein 70 (ZAP70), lipoprotein lipase (LPL), CD38 molecule (CD38) expression, cytogenetic abnormalities, lymphocyte doubling time, and soluble CD23 (sCD23] are derived from our previous reports (53, 54) and reported in Supplementary Table S3. All patients had a $CD19^+CD5^+CD23^+$ phenotype and a Catovsky score of 4/5 or 5/5. All tested prognostic factors were proven to be significant predictors of TFS and OS, indicating that our cohort is representative of a CLL population.

Animal Experiments

All experiments involving laboratory animals were conducted in a pathogen-free animal facility with the approval of the Luxembourg Ministry for Agriculture (#LECR-2016-03, #LECR-2018-02, and #LECR-2018-03). Mice were treated in accordance with the European Union guidelines. C57BL/6 mice (MGI:3028467, RRID:IMSR_JAX:000664) were purchased from Janvier Labs (France) and NSG (MGI:3577020, RRID:IMSR_JAX:005557) mice and $Foxp3^{YFP/Cre}$ (MGI:3790499, RRID:IMSR_JAX:016959) from Jackson Laboratories (USA). Eμ-*TCL1* mice (on C57BL/6 background; MGI:3527221) were a kind gift from Pr. Carlo Croce and Pr. John Byrd (OSU, OH) and provided by Dr. Martina Seiffert (DKFZ Heidelberg, Germany). The *Rab27a*$^{ash/ash}$ (MGI:1856656) *Rab27b*$^{-/-}$ (MGI:3834149; RAB27DKO) were previously described (47). Eμ-*TCL1 Rab27a*$^{ash/ash}$ *Rab27b*$^{-/-}$ (called TCL1-RAB27DKO) mice were generated in-house as depicted in Fig. 6A, by crossing the RAB27DKO with TCL1, to introduce the TCL1 oncogene, generating the Eμ-*TCL1 Rab27a*$^{ash/+}$ *Rab27b*$^{-/+}$. Further breeding with the RAB27DKO mice established the Eμ-*TCL1 Rab27a*$^{ash/ash}$ *Rab27b*$^{-/-}$. CLL progression was monitored over several months in TCL1 and TCL1-RAB27DKO by determining the percentage of $CD5^+CD19^+$ CLL cells in PBMC by flow cytometry on a CytoFLEX (Beckman Coulter) using CD19-APC and CD5-PE

Downloaded from http://aacrjournals.org/bloodcancerdiscov/article-pdf/4/1/54/3236873/54.pdf by guest on 28 March 2023

(BioLegend). Mice reaching the humane endpoint were euthanized by cervical dislocation. All deaths unrelated to leukemia were excluded from this study. To perform the adoptive transfer (AT) in C57BL/6 and NSG control mice, CLL cells were isolated from either TCL1 or TCL1-RAB27DKO diseased spleens. Then, 10×10^6 CLL cells were injected intravenously in 100 μL of DMEM without phenol red, and CLL progression was followed by weekly bleeding, as described previously. Otherwise stated, mice used for experiments were eight to ten weeks old. Both male and female mice were used (age and gender were matched within the same experiment), no variation or impact on the results due to the different sex was detected.

Validation of the TCL1-RAB27DKO Mouse Model

Genomic DNA was extracted from a tail biopsy using Mouse Direct PCR Kit (#B40015, Biotool) following the manufacturer's instructions. The specific primer sequences were: for *Tcl1* F: 5′-GCCGAGTGCC CGACACTC-3′ and R: 5′-CATCTGGCAGCAGCTCGA-3′, for *Rab27b* F: 5′-CTGCTGCAGGATCTCACATCAGTG-3′, R_1: 5′-AGCATCTG TAACCTAGACATTGGC-3′ and R_2: 5′-GAAATGGGACATTGGGAC AGGAGG-3′. Both amplifications were performed with the following program: 94°C for 5 minutes, 35 cycles of 94°C for 20 seconds, 59°C for 30 seconds, and 72°C for 60 seconds. After amplification, the product was run on a 1% agarose gel with SYBR Safe DNA Gel Stain (Thermo Fisher) and visualized by Image Quant Las 4000 (GE Healthcare).

Proteins from freshly isolated cells (total blood) were extracted using RIPA buffer including the cOmplete Protease Inhibitor Cocktail (Roche) and the Phosphatase Inhibitor Cocktail 2 and 3 (Sigma-Aldrich). Then, 10 μg of cell lysates were resolved on 10% SDS-PAGE and transferred to a nitrocellulose membrane. To confirm equivalent loading between lanes, a Ponceau red staining was performed. Membranes were incubated in 1× PBS-0.1%Tween and fat-free dry milk (5%, Roth) blocking buffer for 1 hour at room temperature (RT). Membranes were then incubated with primary antibodies against RAB27a (#sc-81914, RRID:AB_1128884, Santa Cruz), RAB27b (#NBP1–79631, RRID:AB_11014614, Novus), and HSC70 (#sc-7298, RRID:AB_627761, Santa Cruz) in blocking buffer at 4°C overnight. Membranes were washed three times in 1× PBS-0.1%Tween for 10 minutes each time. Secondary antibodies coupled to HRP were from Jackson ImmunoResearch. For detection, the ECL western blot detection kit was purchased from Amersham and the radiographic films from Santa Cruz Biotechnology.

In Vivo *Depletion of CD8⁺ T cells*

TCL1-RAB27DKO cells (20×10^6/mouse) were injected (i.v.) in C57BL/6 mice treated with 200 μg (days –2, 0, and 3) and 100 μg (weekly) of either blocking ab against CD8 (InVivoMAb anti-mouse CD8α, #BE0061, RRID:AB_1125541, Bio X Cell) or isotype control (InVivoMAb polyclonal Armenian hamster IgG, #BE0091, RRID:AB_1107773, Bio X Cell) as shown in Fig. 6K.

For the $CD8^+$ T-cell transfer experiment, TCL1-RAB27DKO cells (5×10^6/mouse) were injected i.v. (tail vein) in C57BL/6 mice treated with 100 μg (days –1 and 0) of anti-CD8 blocking Ab as shown in Fig. 6M. On day 7, 2×10^6 *ex vivo* ME-sEV–treated $CD8^+$ T cells were injected i.p. in each mouse.

ME-sEV Isolation

To isolate LME-sEVs, we used spleens from animals with over 70% $CD5^+CD19^+$ cells in PB. Dissociation was performed using GentleMACS™ (Miltenyi). The protocol derives from previous publications with modifications (14, 55) and is depicted in Fig. 1I. Dissociated spleens were centrifuged for 5 minutes at 400 g, allowing to collect cells for downstream analysis and supernatant, called spleen plasma. Spleen plasma was centrifuged for 20 minutes at 400 × *g* to remove remaining cells, 40 minutes at 2,000 × *g* to remove dead cells, and 60 minutes at 10,000 × *g* to remove cellular debris and large EVs. Before ultracentrifugation (UC), the spleen plasma was filtered (0.22 μm) to remove any impurity. sEVs were isolated by UC (70 minutes, 110,000 × *g*, 4°C) followed by flotation on 17% iodixanol cushion (Optiprep, Axis-Shield, 75 minutes, 100,000 × *g*, 4°C) to remove protein complexes. Finally, sEVs were washed in PBS (70 minutes, 110,000 × *g*, 4°C). To remove aggregates, we filtered sEVs at 0.45 μm followed by 0.22 μm. To prepare fluorescent sEVs, vesicles were incubated with MemBright (now called MemGlow) 488 or 570 dyes (200 nmol/L; ref. 56) for 15 minutes at 4°C before being loaded on 17% iodixanol cushion and further processed with standard protocol. To preserve sEV integrity, each preparation was divided into aliquots and kept at –80°C until further use. Quantification of sEV-associated proteins was performed as previously described (55). Briefly, 4.5 μL of fresh isolated sEVs was lysed in 0.5 μL of 10× RIPA buffer, and 2 μL of the mix was measured via spectrophotometer (595 nm) using 1 mL of Bradford reagent (Bio-Rad). Protein concentration was determined using a BSA standard curve.

ME-sEV Size Analysis

Tunable resisting pulse sensing (TRPS) was performed with Exoid (Izon Science) using an NP100 nanopore (100 nm) and PBS buffer as electrolyte. Data were analyzed using the provided Izon Control Suite software (RRID:SCR_021922).

Detection of sEV Markers by Western Blot

Details for sEV western blot were previously described (55). To assess sEV purity, the presence of the following markers was assessed: Alix (i.e., PDCD6IP, #2171, RRID:AB_2299455, Cell Signaling Technology), TSG101 (#GTX70255, RRID:AB_373239, GeneTex), CD63 (#556019, RRID:AB_396297, BD Biosciences), and CD81 (#sc-7637, RRID:AB_627190, Santa Cruz Biotechnology). Furthermore, the absence of two common contaminating proteins, Calnexin (#2433, RRID:AB_2243887, Cell Signaling Technology) and PHB (#sc-377037, RRID:AB_2714190, Santa Cruz Biotechnology), was also evaluated.

Electron Microscopy

sEV analysis was performed using formvar- and carbon-coated (ultra-thin, 200 mesh, EMS 215–412–8400) copper grids in a Cressington 208 glow-discharge unit before applying 1 μL of the sample (diluted in different concentrations in H_2O) per grid. The grids were then washed in H_2O three times and stained with uranylacetate for negative contrast. Imaging was taken with a Gemini SEM 300 (Zeiss) at 30 kV acceleration voltage using the sTEM detector.

Flow Cytometry Analysis of sEVs

Conventional Flow Cytometry (Bead-based Strategy). sEVs were coated on beads as previously published (57). Briefly, 4-μm aldehyde/sulfate latex beads were coated with 5 μg of ME-sEVs by incubating them overnight at 4°C. Saturation of remaining free binding sites was done using 1M glycine. Beads were then washed 4 times in PBS/0.5% BSA (3 minutes 4,000 × *g* RT). Finally, 10 μL of ME-sEV–coated beads were incubated with 50 μL of antibody diluted in PBS/0.5% BSA (30 minutes at 4°C). After two washes, sEV-coated beads were analyzed with the CytoFLEX flow cytometer (Beckman Coulter; RRID:SCR_019627). The full list of antibodies used for sEV staining can be found in Supplementary Table S4.

Conventional Flow Cytometry (Bead-free Single-EV Strategy). Prior to the staining, antibodies and PBS were filtered through a 0.22-μm filter. $MB488^+$ sEVs were then stained with antibodies for 30 minutes at 4°C. Acquisition was performed with a NovoCyte Quanteon Flow Cytometer (Agilent) equipped with a 0.22-μm filter for the sheath

Downloaded from http://aacrjournals.org/bloodcancerdiscov/article-pdf/4/1/54/3236873/54.pdf by guest on 28 March 2023

fluid to reduce electronic noise. Furthermore, the instrument was set to a minimum flow rate (5 μL/minute).

Imaging Flow Cytometry (Bead-free Single-EV Strategy). MB488$^+$ sEVs were stained with antibodies for 30 minutes at RT, resuspended in PBS up to 200 μL, filtered (0.22 μm), and incubated at 4°C overnight before acquisition with the ImageStreamX Mark II imaging flow cytometer (EMD Millipore). Stained MB488$^+$ sEVs were acquired by setting the imaging flow cytometer as previously published (57). Briefly, the instrument was set to low-speed/high-sensitivity mode (60× magnification), and the power for the used lasers was set to the maximum.

In Vitro *Uptake of sEVs*

Cells were seeded on glass coverslips in μ-slides (Ibidi). Then, MB488 fluorescently labeled LME-sEVs were used to treat the cells for the desired time points. Heparin (Hep) was used as an uptake inhibitor; in this case, the labeled sEVs were incubated 30 minutes at 37°C with 10 ng/mL heparin (Sigma-Aldrich) prior to treating the cells (14).

Flow Cytometry Analysis. At the time of collection, cells were washed in MACS buffer (Miltenyi Biotec). Cell-surface staining was performed in 100 μL of MACS buffer (Miltenyi Biotec) for 30 minutes on ice in the dark prior analysis on the CytoFLEX (Beckman Coulter).

Confocal Microscopy Analysis. At the time of collection, cells were washed in PBS, resuspended in DAPI solution (1 μg/mL) to counterstain nuclei and transferred on a new glass coverslips in μ-slides (Ibidi), letting them naturally settle at the bottom. Images were acquired on a confocal laser scanning microscope (LSM510; RRID:SCR_018062, Zeiss).

Transfection of miRNA Inhibitors into LME-sEVs

Transfection of miRCURY LNA miRNA inhibitors against miR-150 (MMU-MIR-150-5P, #339121 YI04101206-ADA, Qiagen), -155 (MMU-MIR-155-5P, #339121 YI04101319-ADA, Qiagen), and -378a (MMU-MIR-378A-5P, #339121 YI04101421-ADA, Qiagen) or scramble control (negative control A, #339126 YI00199006-ADA, Qiagen) into LME-sEV was performed using HiPerFect Transfection Reagent (#301704, Qiagen) following a published protocol (58). Briefly, 20 pmol/L of each miRCURY LNA miRNA Inhibitors were diluted in a medium without serum, 2 μL transfection reagent was added and mixed by vortexing. The formation of molecular complexes was allowed for 10 minutes at RT. Next, the complexes were added dropwise onto LME-sEVs and incubated at 37°C for 6 hours. sEVs were washed once in PBS before adding them to CD8$^+$ T cells for 48 hours.

In Vivo *Injection of sEVs*

sEVs* In Vivo *Uptake. In order to define the uptake of sEVs *in vivo*, 100 μL of MB570$^+$ LME-sEVs (1 mg/mL) were injected i.v. in 8-week-old C57BL/6 mice, which were euthanized 24 hours later. Total splenocytes were stained for different cell-surface markers (CD4, CD8, and CD19) and analyzed using NovoCyte Quanteon Flow Cytometer (Agilent).

In Vivo *Treatment with sEVs.* Serial injections of LME-sEVs during the rescue experiment were performed as shown in Fig. 6I. Briefly, 100 μL of LME-sEVs (1 mg/mL) were injected i.v. the day before the experiment (day −1), together with the cells (d0), and then again on days 3, 5, and 35.

Culture Conditions and In Vitro *sEV Treatment*

Spleens were collected from C57BL/6 or Foxp3$^{YFP/Cre}$ mice (for Treg isolation) and rapidly transferred in a tube containing PBS (without Ca^{2+}/Mg^{2+}). Splenocytes isolation was performed by mechanical spleen dissociation through a 100-μm strainer (BD Biosciences), and cells were recovered by centrifugation (400 × *g*, 4°C, 10 minutes). The cell pellet was resuspended in ACK lysing solution (Lonza) to lyse red blood cells. Finally, splenocytes were washed in MACS buffer (Miltenyi Biotec), filtered through a 50-μm strainer (Celltrics, Sysmex), and counted. CD3$^+$ T cells were isolated by negative selection using the MojoSort Mouse CD3 T-Cell Isolation Kit (BioLegend) following the manufacturer's instructions. The isolated T-cell population contained at least 95% of CD3$^+$ T cells. CD8$^+$ T cells were isolated by negative selection using the MojoSort Mouse CD8 T-Cell Isolation Kit (BioLegend) following the manufacturer's instructions. The isolated T-cell population contained at least 95% of CD8$^+$ T cells. CD8$^+$ T cells were cultured in anti-CD3–coated wells (10 μg/mL; #100302, RRID:AB_312667, BioLegend) in RPMI-1640 medium supplemented with 10% fetal bovine serum (FBS), 1% penicillin/streptomycin (P/S), IL2 (10 ng/mL; #589104), CD28 (3 μg/mL; #102102, RRID:AB_312867, BioLegend) and β-Mercaptoethanol (50 μmol/L). Depending on experiment duration, cells were fed with fresh medium every 48 hours. For intracellular cytokine production, cultured CD8$^+$ T cells were stimulated overnight with PMA/ionomycin (100 nmol/L/1 μmol/L) and incubated for a maximum of 4 hours with Brefeldin A (BFA, 1×). CD4$^+$ T cells were isolated by negative selection using the MojoSort Mouse CD4 T-Cell Isolation Kit (BioLegend) following the manufacturer's instructions. The isolated T-cell population contained at least 95% of CD4$^+$ T cells (comprising CD4$^+$ T_{conv} cells and Tregs). CD4$^+$ T cells were cultured in anti-CD3–coated wells (10 μg/mL) with RPMI-1640 medium supplemented with 10% FBS, 1% P/S, IL2 (10 ng/mL), and β-Mercaptoethanol (50 μmol/L). For immune-checkpoint blockade, CD8$^+$ T cells were treated for 48 hours using ME-sEVs previously coated with 5 μg/mL of antibodies directed against PD-L1 (#124302, RRID:AB_961228, BioLegend), MHC-II (#107601, RRID:AB_313316, BioLegend), GAL9 (#136115, RRID:AB_2860679, BioLegend), and VISTA (#BE0310, RRID:AB_2736990, Bio X Cell) for 6 hours at 4°C.

Depending on experiment duration, cells were fed with a fresh medium every 48 hours. B/CLL cells were isolated by negative selection using the MojoSort Mouse Pan B-Cell Isolation Kit II (BioLegend) following the manufacturer's instructions. The isolated B and CLL cell populations contained at least 90% of CD19$^+$ or CD19$^+$CD5$^+$ double-positive cells, respectively.

Human PBMC were isolated by density-gradient centrifugation over Linfosep (Biomedics). B cells were purified with a CD19$^+$ magnetic-bead system (MidiMACS, Miltenyi Biotech) according to the manufacturers' instructions. Mean B-cell purity was >99% and the mean percentage of CD5$^+$/CD19$^+$ cells after purification was >98%, as measured by flow cytometry.

Cells used for microarray analysis were cultured for 24 hours with RPMI-1640 medium supplemented with 10% FBS, 1% P/S, and IL2 (10 ng/mL) with either LME-sEVs or HCME-sEVs.

Cells were incubated with LME-sEVs or HCME-sEVs based on the physiologic amount found in the respective spleen microenvironment (Fig. 1J). Depending on experiment duration, additional sEVs were added every 48 hours. TCL1-RAB27DKO cells were cultured for 24 hours with RPMI-1640 medium supplemented with 10% FBS, 1% P/S with either LME-sEVs$_{TCL1}$ or LME-sEVs$_{TCL1\text{-}RAB27DKO}$ based on the physiologic amount found in the respective spleen microenvironment (Fig. 6F).

Flow Cytometry Sorting of Cells

Cells used for microarray analysis were sorted directly from Foxp3$^{YFP/Cre}$ derived purified splenocytes using BD FACSAria III Cell Sorter (RRID:SCR_018934). CD4$^+$Foxp3$^+$ were isolated based on YFP expression, antibodies for CD8$^+$ and CD4$^+$Foxp3$^-$ staining can be found in Supplementary Table S4.

For the experiment requiring to separate CD4$^+$Foxp3$^+$ from CD4$^+$ T_{conv}, cells were sorted directly from LME-sEV–treated Foxp3$^{YFP/Cre}$-derived purified splenocytes using BD FACSAria III Cell Sorter

Downloaded from http://aacrjournals.org/bloodcancerdiscov/article-pdf/4/1/54/3236873/54.pdf by guest on 28 March 2023

(RRID:SCR_018934). Tregs were isolated based on YFP expression, and antibodies for $CD8^+$, $CD4^+$, and $CD19^+$ staining can be found in Supplementary Table S4.

Flow Cytometry Analysis of Cells

Surface Staining. Cell-surface staining was performed in 100 μL of MACS buffer (Miltenyi Biotec) for 30 minutes on ice in the dark prior to analysis on NovoCyte Quanteon Flow Cytometer (Agilent).

PB was directly stained for 30 minutes on ice in the dark, and then red blood cells were lysed using RBC Lysis/Fixation Solution (BioLegend), according to the manufacturer's instructions. After washing twice, samples were ready for acquisition on a CytoFLEX analyzer (Beckman Coulter).

Intracellular Staining. Previously surface stained cells were permeabilized using the eBioscience Foxp3/Transcription Factor Staining Buffer Set (Thermo Fisher Scientific) following the manufacturer's instructions before intracellular staining. The list of antibodies used for cell-surface and intracellular staining can be found in Supplementary Table S4.

Flow Cytometry Clustering

Clustering analysis of live lymphocytes was performed with Cytosplore software. Briefly, 50,000 events per sample were subjected to HSNE to generate clusters based on intracellular and transmembrane markers expression. Clusters were generated using the Gaussian mean shift algorithm using the density estimate as input.

T cell–Mediated Cytotoxicity Assay

The definition of cytotoxicity of ME-sEV–treated T cells on CLL cells was performed as previously published (59). Briefly, C57BL/6 $CD3^+$ T cells were cultured in a 48-well plate on anti-CD3–coated wells (1 μg/mL) with RPMI-1640 medium supplemented with 10% FBS, 1% P/S, and 1 μg/mL anti-CD28 antibody for 48 hours at 37°C, in the presence of LME-sEVs or HCME-sEVs. Treatment with ME-sEV was repeated every 24 hours. CLL cells ($CD5^+CD19^+$) isolated from the TCL1 mouse model were stained with CellTrace CFSE (200 nmol/L, Thermo Fisher). On the day of the assay, CLL target cells were pulsed with 2 μg/mL of super antigen (sAg; SEA and SEB; Sigma-Aldrich) for 30 minutes at 37°C. Target primary CLL cells (2.5×10^4) loaded with sAg were added to the ME-sEV–pretreated $CD3^+$ T cells at a 1:20 (target:effector). Cell mixtures were centrifuged, and the cell pellet was incubated for 4 hours at 37°C. Cells were stained with TO-PRO-3 viability dye (Thermo Fisher) according to the manufacturer's instructions, and T cell–mediated cytotoxicity against CLL target cells was determined by flow cytometry. Cytotoxicity was calculated as: % target cell death = (% $CFSE^+$ TO-PRO-3^+ target cells incubated with effector T cells – % of $CFSE^+$ TO-PRO-3^+ target cells incubated alone) × 100/(100 – % of $CFSE^+$ TO-PRO-3^+ target cells incubated alone).

T-cell:CLL (Tumor) Cell Conjugation and Immunologic Synapse Assays

Immune synapse assays and quantitative analysis were performed as previously described (59). Briefly, purified murine $CD3^+$ T cells and purified $CD5^+CD19^+$ CLL cells from the TCL1 mouse model were incubated for 48 hours at 37°C or in the presence of LME-sEVs or HCME-sEVs. Treatment with ME-sEVs was repeated every 24 hours. Next, the same CLL cells were stained with CellTracker Blue CMAC according to the manufacturer's instructions and pulsed with 2 μg/mL of super antigen (sAg; SEA and SEB; Sigma-Aldrich) for 30 minutes at 37°C before washing. Tumor cells were then pooled with an equal number of T cells (1×10^6; to ensure identical cell numbers per sample and allow accurate evaluation of changes in the percentage of conjugated T cells and F-actin immune synapse formation with treatment), centrifuged at $260 \times g$ (5 minutes) and incubated at 37°C for 10 minutes ($CD8^+$ T cells). Cells were then transferred onto microscope slides (Polysine slides; Thermo Scientific) using a cell concentrator (Cytofuge 2) and fixed for 15 minutes at RT with 3% formaldehyde (Thermo Scientific) in PBS.

Immunofluorescence (IF) labeling was done using Cytofuge2 cell concentrator units. After fixing, cells were permeabilized with 0.3% Triton X-100 (Sigma-Aldrich) in PBS for 5 minutes and treated for 10 minutes with 5% goat serum (Sigma-Aldrich) in PBS-blocking solution. Primary and secondary antibodies (Alexa Fluor 488 or 647, Thermo Fisher Scientific) were applied sequentially for 45 minutes at 4°C in 5% goat serum (Sigma-Aldrich) in PBS blocking solution. F-actin was stained with rhodamine phalloidin (Thermo Fisher) following the manufacturer's instructions and applied alone or with the secondary antibody. After washing, cell specimens were sealed with coverslips using mounting solution FluorSave reagent (Merck Millipore). The specificity of staining was optimized and controlled by using appropriate dilutions of isotype control, primary Abs, and subsequent fluorescent secondary Abs. Background staining using Abs alone was compared with positively stained cells and was not visible when using identical acquisition settings. Medial optical section (or Z-stacks for 3D volume images) images were captured with a high-sensitivity A1R confocal microscope (with gallium arsenide phosphide, GaAsP detector) using a 63×/1.40 oil objective with NIS-elements imaging software (Nikon). Detectors were set to detect an optimal signal below saturation limits. Fluorescence was acquired sequentially to prevent the passage of fluorescence from other channels (DU4 sequential acquisition). Image sets to be compared were acquired during the same session using identical acquisition settings.

Real-time PCR

RNA Isolation. Cellular and sEV RNA were isolated using NucleoZOL, one phase RNA purification reagent and columns from the NucleoSpin RNA Set for NucleoZOL Mini kit, according to the manufacturer's instructions (Macherey-Nagel). For transcriptomics analysis using microarrays or RNA sequencing, RNA was quantified with Qubit (Thermo Scientific), and the quality was assessed with the Fragment Analyzer 5200 using RNA kits (Agilent). For purified human CLL cells, total RNA was extracted in a single step using TriPure Isolation Reagent (Roche Applied Science).

MicroRNA Detection in sEV and sEV-treated $CD8^\pm$ T Cells. MicroRNA were quantified by RT-qPCR performed using TaqMan MicroRNA assays, TaqMan MicroRNA Reverse Transcription Kit (Thermo Scientific) and the Takyon Low ROX Probe 2X MasterMix dTTP blue (Eurogentec) (15, 20). The following probes were used: miR-21 (#002438), miR-146a (#000468), miR-378a (#000567), miR-210 (#000512), miR-27a (#000408), miR-150 (#000473), miR-155 (#002623), and U6 (#001973).

Gene Expression in Cells. Reverse transcription of mRNA was performed in a SimpliAmp Thermal Cycler (Thermo Fisher) using FastGene Scriptase II cDNA 5× ReadyMix (Nippon genetics). Real-time PCR was performed in the QuantStudio 5 Real-Time PCR System (Thermo Fisher) using the SYBR Green detection system. The primers were for *GzmB* F: 5′-CAGGAGAAGACCCAGCAAGTCA-3′ and R: 5′-CTCACAGCTCTAGTCCTCTTGG-3′, *Prf1* F: 5′-TGGTGGGACTTCAGCTTTCC-3′ and R: 5′-TGCTTGCATTCTGACCGAGT-3′, *Slc7a5* F: 5′-CATCAACGACTCTGTTGTAGACC-3′ and R: 5′-CGCTGGATACAGGATTGCGG-3′, *Itpkc* F: 5′-CATCACCCCAGAGACTCCTGA-3′ and R: 5′-TTCTTCCAGGGCTTGCTTCCAG-3′ and *Fgr* F: 5′-GAGGCGGGTAGCACCTCAC-3′ and R: 5′-CCCATTCCAGATGCCCCCAC-3′ were from Eurogentec. For RNA isolated from purified human CLL cells, cDNA was generated by a retrostranscription using the qScript cDNA Synthesis Kits (Quanta Biosciences/VWR International).

Downloaded from http://aacrjournals.org/bloodcancerdiscov/article-pdf/4/1/54/3236873/54.pdf by guest on 28 March 2023

Real-time PCR was performed in the QuantStudio 5 Real-Time PCR System (Thermo Fisher) using the SYBR Green detection system. The primers used were *28S* F: 5′-GGGTGGTAAACTCCATCTAAGG-3′ and R: 5′-GCCCTCTTGAACTCTCTCTTC-3′, *RAB27a* F: 5′-TGG GAGACTCTGGTGTAGGG-3′ and R: 5′-ACTGGCTCTGTACACCA CTC-3′, *RAB10* F: 5′-TCCCAATGGCGAAGAAGAC-3′ and R: 5′-TG ATCTTGAAGTCTATTCCTATGGT-3′, *RAB35* F: 5′-GCACCATCAC CTCCACGTAT-3′ and R: 5′-CCGCTTGACGTTGACAAAGG-3′, *RAB40c* F: 5′-CGTACGCCTACAGTAACGGGAT-3′ and R: 5′-GTAGGACCTG AAGATGGTGCAG-3′, *RAB31* F: 5′-TGTGCCTTCTCGGGGACAC-3′ and R: 5′-GCCCCAATAGTAGGGCTGAT-3′, *PDCD6IP* F: 5′-TCGAG ACGCTCCTGAGATATT-3′ and R: 5′-AGCCAGTTTTACAGAGCCT CC-3′, *RAB7A* F: 5′-ATGCACTTAAGCAGGAAACGG-3′ and R: 5′-TG GCCCGGTCATTCTTGTC-3′.

Transcriptomics

RNA Sequencing. Librairies were prepared with the QuantSeq 3′ mRNA-Seq Library Prep Kit FWD for Illumina (Lexogen), according to the manufacturer's instructions, with the addition of UMI. Barcoded samples were pooled, diluted, and loaded onto a NextSeq 500/500 Mid Output flowcell (130M reads, Illumina), and single-end sequencing was performed on a NextSeq 550 (Illumina). After initial QCs using FastQC (https://www.bioinformatics.babraham.ac.uk/projects/fastqc/; RRID:SCR_014583) and FastQ Screen (https://www.bioinformatics.babraham.ac.uk/projects/fastq_screen/; RRID:SCR_000141), fastq files were processed using a local Snakemake workflow including the following main steps. First, raw reads were trimmed from their UMI index, poly A and adapter sequences using a combination of dedicated scripts and cutadapt (v2.10). Next, filtered reads were submitted for mapping (STAR v2.5.3a; RRID:SCR_004463) on the Mouse Reference genome (GRCm38). Collapsing of reads originating from the same fragment was achieved with umi_tools (v1.0.0) and counting was performed with featureCounts (subread v2.0.0; RRID:SCR_012919).

Gene-Expression Analysis. Differential expression analysis was performed using the *limma*-based R/Bioconductor EdgeR package (RRID:SCR_012802; ref. 60) for *in vitro*–treated samples or using the nonparametric NOISeq (RRID:SCR_003002) package (61) for *in vivo*–treated samples presenting lower sequencing depth and more intrinsic variability. Genes with less than 5 counts were filtered out and counts were processed for a trimmed mean of M values (TMM) normalization. DEG was assessed by imposing an FDR <0.05 and a $\log_2$ fold change cutoff of 1. The pheatmap function was used for data visualization. For k-means clustering, the 2,500 most variable genes were included and six clusters were defined according to the elbow method with the iDEP9.2 online tool, followed by Gene Ontology analysis for Biological Process (http://bioinformatics.sdstate.edu/idep/).

Gene Ontology Analysis. Ontology analyses of differentially expressed genes were performed with the g:Profiler web server (RRID:SCR_006809) for functional profiling (https://biit.cs.ut.ee/gprofiler/gost).

sEV Score. We used public data sets to compare gene-expression profiles of normal B cells and CLL cells in human (GSE67640) and mouse (GSE175564; refs. 16, 21). GSE67640 was analyzed with GEO2R online tool [RRID:SCR_016569; *limma* (RRID:SCR_010943), Benjamini and Hochberg (false discovery rate) adjusted $P < 0.05$, and $\log_2$FC >1). The DEG lists were compared with a list of 143 genes (combining genes involved in sEV biology based on literature review and Top100 proteins found in sEVs according to http://microvesicles.org, listed in Supplementary Table S2). The expression values of genes present in both lists (shown in the heat maps) were used to compute sEV scores for human and mouse B and CLL cells, corresponding to a z-scored-geometric mean of expression values.

Proteomics

Sample Preparation of sEV Proteome. Starting from the same amount of sEV proteins between conditions, each sEV sample was split into triplicates. Proteins were extracted with sodium deoxycholate (SDC, 3% final concentration) following a 30-minute incubation at 4°C in the presence of protease inhibitors (cOmplete EDTA-free Protease Inhibitor Cocktail, Roche). Following centrifugation at 16,000 × *g* for 10 minutes, supernatants were subjected to protein reduction (5 mmol/L DTT, 1-hour incubation at 37°C) and alkylation (10 mmol/L IAA, 45 minutes at RT in the dark). Samples were then acidified with formic acid (FA, 1% final concentration), and SDC was precipitated after centrifugation at 16,000 × *g* for 15 minutes. The supernatants were transferred into clean tubes and supplied with preprepared SP3 beads (Fisher Scientific, #09-981-121, #09-981-123). One volume of acetonitrile (ACN, 100% v/v) was added immediately followed by incubation at RT for 10 minutes. The supernatants were removed using a magnetic rack, and the beads were rinsed first with 200 μL of 70% ethanol, and then further rinsed with 180 μL of 100% ACN. Rinsed beads were reconstituted in 30 μL digestion buffer (50 mmol/L ammonium bicarbonate, pH 8). Protein digestion was performed with 1 μg of sequencing grade trypsin (Promega, V5111) for 4 hours at 37°C, then incubated overnight at 37°C with additional 1 μg trypsin. After digestion, ACN was added to each sample to a final concentration of 95%. Mixtures were incubated for 10 minutes at RT and then placed on a magnetic rack for 2 minutes. The supernatants were discarded, and the beads were rinsed with 180 μL of 100% ACN. Rinsed beads were reconstituted in 30 μL LC-MS grade water and incubated for 5 minutes at RT to elute the digested peptides. The eluted peptide samples were acidified with formic acid to a final concentration of 0.1%.

Proteomic Sample Preparation of sEV-treated Cells. $CD8^+$ T cells treated with sEVs were collected in triplicate after 24 hours and 4 days of treatment. After being harvested, cells were washed twice with cold PBS. Next, pellets were resuspended in lysis buffer (6 mol/L urea, 2 mol/L thiourea, 50 mmol/L ammonium bicarbonate, pH 8) supplemented with fresh prepared cOmplete EDTA-free Protease Inhibitor Cocktail (Roche). After incubation at 22°C for 30 minutes, samples were sonicated (3-second sonication and 2-second pause for a total of 30 seconds). The supernatants were taken into new tubes following centrifugation at 16,000 × *g* for 15 minutes. Protein quantification assay of the cell extracts was performed with Bradford assay (Sigma-Aldrich, B6916) to estimate the concentrations. A total of 30 μg of each sample were taken for protein reduction and alkylation and digested with Lys-C (FUJIFILM Wako, 125-05061) at 1:30 ratio (enzyme/protein substances) for 4 hours at 37°C, and then samples were diluted 4 times with 50 mmol/L ammonium bicarbonate and digested overnight with 1 μg of trypsin at 37°C. The protein digestion was terminated with the addition of formic acid (1% final concentration). The digested peptides were cleaned up with reverse phase Sep-Pak C18 1 cc Vac Cartridge (Waters, WAT054955) and eluted with 1 mL 50% ACN. Eluted peptides were dried by Speedvac (Thermo Fisher Scientific) and resuspended in 0.1% formic acid. Nanodrop was used to estimate the peptide concentration.

LC-MS/MS Data Acquisition. Digested peptides were measured by LC-MS/MS on either Q-Exactive Plus or Q-Exactive HF mass spectrometer (Thermo Fisher) connected to a Dionex Ultimate 3000 (Thermo Fisher). A total of 400 ng of peptides were loaded onto a trap column (Acclaim PepMap 75 μm × 2 cm, C18, 3 μm) and separated on a 25-cm Acclaim PepMap RSLC column (75 μm × 25 cm, C18, 2 μm) using a 150-minute gradient with a flow rate of 0.3 μL/minute. MS data were acquired in data-dependent mode (DDA). Survey scans of peptide precursors from 375 to 1500 m/z were performed at 70,000 resolution with a 3×10^6 ion count target and the top 12 abundant

Downloaded from http://aacrjournals.org/bloodcancerdiscov/article-pdf/4/1/54/3236873/54.pdf by guest on 28 March 2023

peaks from the survey scan were selected for fragmentation. Tandem MS was performed by isolation at 1.4 m/z with the quadrupole, HCD fragmentation with a normalized collision energy of 28. The MS2 ion count target was set to 1×10^5, and the max injection time was 45 ms. Only precursors with a charge state of 2 to 7 were sampled for MS2. The dynamic exclusion duration was set to 20 s with a 10 ppm tolerance around the selected precursor and its isotopes.

Database Searching and Protein Identification. All raw data were analyzed with MaxQuant (version 1.6.7.0; RRID:SCR_014485) and searched with Andromeda against the mus musculus database from Uniprot. The minimal peptide length was set to 7 amino acids, and a maximum of 3 missed cleavages were allowed. The search included variable modifications of methionine oxidation and N-terminal acetylation, deamidation (N and Q) and fixed modification of carbamidomethyl cysteine. The "Match between run" was checked within a 1-minute retention time window. Mass tolerance for peptide precursor and fragments were set as 10 ppm and 20 ppm, respectively. The FDR was set to 0.01 for peptide and protein identifications. Label-free quantification was used for quantitative data of identified protein based on its razor and unique peptides. Proteus, an R-package, was used for the downstream analysis of MaxQuant (RRID:SCR_014485) output. The input for Proteus is the evidence file. Evidence data are aggregated into peptides and then into proteins.

Proteomic Data Analysis. For sEV proteome, LFQ intensities of proteins identified in HCME-sEVs, LME-sEVs, and LME-sEV TCL1-RAB27DKOs were processed as follows. We first removed zero intensities across all samples, and then we performed $\log_2$ transformation and quantile normalization. As samples were acquired in two batches, we performed batch correction using the combat algorithm. Values were then imported in the MaxQuant Perseus software (version 1.6.15.0). Two-sample tests were performed and proteins with a q-value < 0.05 (Benjamini–Hochberg FDR) were considered statistically enriched in a condition. Coordinates from PCA were exported and plotted with GraphPad Prism (version 9.1.2; RRID:SCR_002798). Heat maps were generated with the R pheatmap function.

Gene and Protein Ontology Analysis. Ontology analyses of differentially expressed proteins were performed with the g:Profiler (RRID:SCR_006809) web server for functional profiling (https://biit.cs.ut.ee/gprofiler/gost).

Metabolomics Analysis

Detection of Metabolic Protein by Western Blot. To assess alterations of metabolic protein expression induced by ME-sEV treatment, total proteins isolated from treated $CD8^+$ T cells were subjected to western blot: PFKP (#ab204131, RRID:AB_2828009, Abcam), PHGDH (#HPA021241, RRID:AB_1855299, Sigma-Aldrich), PCK2 (#6924S, RRID:AB_10836185, Cell Signaling Technology), MCT4 (#sc-50329, RRID:AB_2189333, Santa Cruz) and GLUT1 (#PA1-46152, RRID:AB_2302087, Thermo Fisher).

Stable Isotope Tracing and Metabolite Extraction. Stable isotope tracing experiments with [U-^{13}C]-glucose tracer (Cambridge Isotope Laboratories, CLM-1396) were performed in RPMI-1640 medium supplemented with 11.1 mmol/L [U-^{13}C]-glucose, 2 mmol/L glutamine, 10% FBS, 1% P/S, IL2 (10 ng/mL), CD28 (3 μg/mL). For [U-^{13}C]-glutamine tracing (Cambridge isotope Laboratories, CLM-1822), RPMI-1640 medium for SILAC (#A24942-01) was used and supplemented as above with the addition of 1.15 mmol/L arginine and 0.219 mmol/L lysine. A total of 1×10^6 cells were seeded in triplicates in 24-well plates precoated with anti-CD3 antibody (10 μg/mL), already in the [U-^{13}C]-glucose or glutamine medium. At the time point of metabolite extraction, cell number and volume were determined to calculate packed cell volume. For metabolite extraction, cells were collected and pelleted at $350 \times g$ for 5 minutes at 4°C and the medium was stored at –80°C to determine metabolites exchange rates. To determine the basal medium composition for the subsequent calculation of exchange rates, an identical medium was incubated in empty 24 wells throughout the experiment and analyzed in parallel to the medium samples. The cell pellet was then washed with ice-cold 1× PBS solution. 400-μL ice-cold extraction fluid [acetonitrile/H2OMQ/methanol (ratio, 3:2:5); LC-MS grade solvents)] was added to each cell pellet. Cells were mixed for 10 minutes on a thermomixer at 4°C at maximum speed, then the tubes were centrifuged for 10 minutes at $16{,}100 \times g$ at 4°C. 100 μL of the supernatant was collected and transferred to an already-cooled LC-MS glass vial with inserts and stored at –80°C until measurement.

YSI Measurements and Medium Exchange Rates. Medium samples were filtered (PVDF, 0.22 μm) prior to measurement to remove particles. Absolute quantitative values for lactic acid, glutamine, glutamic acid, and glucose were acquired using a YSI 2950D Biochemistry Analyzer (Kreienbaum KWM). For a precise and reliable quantification, external concentration curves of each target compound were prepared and measured in triplicates. Absolute uptake and release rates were calculated as previously described (62).

LC-MS Measurements. The following analytical conditions are based on a previously published protocol (62). Metabolite analyses were performed using a Thermo Vanquish Flex Quaternary LC coupled to a Thermo Q-Exactive HF mass spectrometer. Chromatography was carried out with a SeQuant ZIC-pHILIC 5-μm polymer (150 × 2.1 mm) column connected to the corresponding SeQuant ZIC-pHILIC Guard (20 × 2.1 mm) precolumn. Column temperature was maintained at 45°C. The flow rate was set to 0.2 mL/minute and the mobile phases consisted of 20 mmol/L ammonium carbonate in water, pH 9.2 (Eluent A), and Acetonitrile (Eluent B). The gradient was: 0 minutes, 80% B; 2 minutes, 80% B; 17 minutes, 20% B; 18 minutes 20% B; 19 minutes 80% B; 20 minutes 80% B (0.4 mL/minute); 24 minutes 80% B (0.4 mL/minute); 24.5 minutes 80% B. The injection volume was 5 μL. All MS experiments were performed using electrospray ionization with polarity switching enabled (+ESI/–ESI). The source parameters were applied as follows: sheath gas flow rate, 25; aux gas flow rate, 15; sweep gas flow rate, 0; spray voltage, 4.5 kV (+)/3.5 kV (–); capillary temperature, 325°C; S-lense RF level, 50; aux gas heater temperature, 50°C. The Orbitrap mass analyzer was operated at a resolving power of 30,000 in full-scan mode (scan range, m/z 75…1,000; automatic gain control target: 1e6; maximum injection time: 250 ms). Data were acquired with Thermo Xcalibur software (Version 4.3.73.11; RRID:SCR_014593) and analyzed with TraceFinder (Version 4.1). Subsequent data analysis for normalization and natural isotope subtraction was performed using in-house scripts as previously described (62).

OCR Using SeaHorse. A Seahorse XFe96 Bioanalyser (RRID:SCR_019545, Agilent) was used to determine the basal OCR of $CD8^+$ T cells after *ex vivo* treatment with ME-sEVs (96h), following the manufacturer's instructions using WAVE software (RRID:SCR_014526). Treated cells were washed in assay media (XF Base media (Agilent) with glucose (10 mmol/L), sodium pyruvate (1 mmol/L), and L-glutamine (2 mmol/L; Gibco), pH 7.4 at 37°C) before being plated onto Seahorse cell culture plates coated with Cell-Tak (Corning) at 3.5×10^5 cells/well followed by a gentle centrifugation (5 minutes, $300 \times g$, RT, 0 break).

Statistical Analysis of sEV Gene Expression in CLL Patient Cohort

Differential Expression Analysis and Predictive Power. CT values obtained from real-time PCR were normalized using CTs of

Downloaded from http://aacrjournals.org/bloodcancerdiscov/article-pdf/4/1/54/3236873/54.pdf by guest on 28 March 2023

ribosomal RNA 28S as a housekeeping gene. Differential expression analysis was performed to check which genes were associated with patient groups by the "limma" package of R/Bioconductor (RRID:SCR_010943; ref. 63).

Survival Analysis and Risk Score. Univariate Cox regression models independently for TFSOS were built. R-package "survival" was used for the analysis and visualization of the data. Normalized log expression of the considered genes was used for the regression model. Individual genes were combined to a risk score with better prognostic properties based on previous publications (64, 65). However, in the current study, we weighted the contribution of each gene by its *P* value: the risk score (RS) for *i*th patient was calculated as

$$RS_i = -\sum_j \log(P_j) \cdot H_j \cdot X_{i,j}$$

where P_j and H_j—a *P* value of likelihood ratio test and a log HR from a univariate Cox model of the *j*th gene accordingly, $X_{i,j}$ is the log expression of the *j*th gene in the *i*th patient. Here we run an exhaustive search of all gene combinations and selected the Cox model with the minimal *P*-value. Kaplan–Meier plots were built to visualize the linkage between genes or RS and patient survival. The median level was used to dichotomize patients into two groups. Significance of the variation in RS regarding mutational status and prognosis markers for each patient was assessed by ANOVA.

Analysis Using Logistic Regression. We tried to link gene expression and binary outcomes using logistic regression ("glm" from R/Bioconductor). In order to avoid uncertainty resulting from gene–gene correlation, we used a similar approach as for Cox regression. First, coefficients or log odds ratios and *P* values were determined from univariable logistic models for each gene independently and then combined into a score using the same formula as for the RS in Cox regression, with log odds ratios instead of log-hazard ratios.

Statistical Analysis

Statistical analysis was performed using GraphPad Prism software (version 9.1.2; RRID:SCR_002798). Data are presented as mean ± standard error of the mean (SEM). The log-rank test was used for the survival curves. For the percentage of CLL cells in mice over time, we performed two-way ANOVA followed by Bonferroni's multiple comparison test. The unpaired t test was used for the rest of the figures. A *P*-value lower than 0.05 was considered statistically significant. Significance displayed in each figure is explained in figure legends.

Data Availability Statement

The data sets presented in this study are openly available in the Gene-Expression Omnibus with the accession numbers GSE188898, GSE189391, GSE190789, GSE190790, and GSE191186.

Authors' Disclosures

G. Dittmar reports grants from Luxembourg National Research Fund (FNR) during the conduct of the study. J. Meiser reports grants from Luxembourg Research Foundation during the conduct of the study; grants from FNR-ATTRACT outside the submitted work. No disclosures were reported by the other authors.

Authors' Contributions

E. Gargiulo: Conceptualization, formal analysis, investigation, visualization, methodology, writing–original draft, writing–review and editing. **E. Viry:** Formal analysis, investigation, writing–review and editing. **P.E. Morande:** Formal analysis, investigation, writing–review and editing. **A. Largeot:** Formal analysis, investigation, writing–review and editing. **S. Gonder:** Investigation, writing–review and editing. **F. Xian:** Formal analysis, investigation, methodology, writing–review and editing. **N. Ioannou:** Formal analysis, investigation, writing–review and editing. **M. Benzarti:** Formal analysis, investigation, methodology, writing–review and editing. **F.B. Kleine Borgmann:** Formal analysis, investigation, methodology, writing–review and editing. **M. Mittelbronn:** Formal analysis, writing–review and editing. **G. Dittmar:** Formal analysis, writing–review and editing. **P.V. Nazarov:** Software, formal analysis, writing–review and editing. **J. Meiser:** Formal analysis, methodology, writing–review and editing. **B. Stamatopoulos:** Resources, formal analysis, investigation, writing–review and editing. **A.G. Ramsay:** Formal analysis, writing–review and editing. **E. Moussay:** Conceptualization, software, formal analysis, supervision, funding acquisition, visualization, methodology, writing–original draft, project administration, writing–review and editing. **J. Paggetti:** Conceptualization, formal analysis, supervision, funding acquisition, investigation, visualization, methodology, writing–original draft, project administration, writing–review and editing.

Acknowledgments

We thank Pr. Carlo Croce and Pr. John Byrd (Ohio State University) for the kind gift of Eμ-*TCL1* mouse, and Pr. Miguel Seabra and Dr Tanya Tolmachova (Imperial College London, UK) for the RAB27DKO mouse. We thank Dr Javier Alves Ferreira (JAF, Laboratoire National de Santé, Luxembourg) for the histopathology expertise. We thank the National Cytometry Platform (LIH; Dr Antonio Cosma, Dr Céline Hoffmann, Thomas Cerutti, Fanny Hedin, and Maria Konstantinou) for assistance in flow cytometry, imaging flow cytometry, confocal microscopy and FACS experiments, the LUXGEN platform (LIH/LNS; Nathalie Nicot, Elise Mommaerts, Arnaud Muller and Dr Daniel Stieber) for RNA sequencing, the bioinformatics platform (LIH; Tony Kaoma and Kim Sang Yoon) for assistance, and the Animal Facility (LIH) staff. We thank the Metabolomics Platform (University of Luxembourg, Christian Jäger) for GC-MS measurements and Xiangyi Dong and Floriane Vanhalle for providing technical and analytical support. Furthermore, we thank the Metabolomics core facility (LIH, Antoine Lesur and François Bernardin) for technical and analytical support. Special thanks to Dr Martina Seiffert (DKFZ, Germany) for the useful scientific discussions and for providing the Eμ-*TCL1* animals. Finally, we thank Dr Marina Wierz, Bilgee Bayanaa, and Sandrine Pierson (LIH) for technical support. This work was supported by grants from the Luxembourg National Research Fund (FNR) to E. Gargiulo, E. Moussay, and J. Paggetti (PRIDE15/10675146/CANBIO, INTER/DFG/16/11509946, C20/BM/14582635, and C20/BM/14592342), to J. Meiser (ATTRACT grant A18/BM/11809970), and to M. Mittelbronn (PEARL grant P16/BM/11192868), from FNRS-Télévie to E. Viry, P.E. Morande, A. Largeot, and S. Gonder (7.4509.20, 7.8506.19, 7.4503.19, and 7.6604.21), from the European Commission to P.E. Morande (H2020-MSCA-IF-2020: 101029602).

The publication costs of this article were defrayed in part by the payment of publication fees. Therefore, and solely to indicate this fact, this article is hereby marked "advertisement" in accordance with 18 USC section 1734.

Note

Supplementary data for this article are available at Blood Cancer Discovery Online (https://bloodcancerdiscov.aacrjournals.org/).

Received February 24, 2022; revised July 4, 2022; accepted September 7, 2022; published first September 14, 2022.

REFERENCES

1. Beach A, Zhang HG, Ratajczak MZ, Kakar SS. Exosomes: an overview of biogenesis, composition and role in ovarian cancer. J Ovarian Res 2014;7:14.
2. Raposo G, Stoorvogel W. Extracellular vesicles: exosomes, microvesicles, and friends. J Cell Biol 2013;200:373–83.

Downloaded from http://aacrjournals.org/bloodcancerdiscov/article-pdf/4/1/54/3236873/54.pdf by guest on 28 March 2023

3. Colombo M, Moita C, van Niel G, Kowal J, Vigneron J, Benaroch P, et al. Analysis of ESCRT functions in exosome biogenesis, composition and secretion highlights the heterogeneity of extracellular vesicles. J Cell Sci 2013;126:5553–65.
4. Kumar B, Garcia M, Weng L, Jung X, Murakami JL, Hu X, et al. Acute myeloid leukemia transforms the bone marrow niche into a leukemia-permissive microenvironment through exosome secretion. Leukemia 2018;32:575–87.
5. Prieto D, Sotelo N, Seija N, Sernbo S, Abreu C, Durán R, et al. S100-A9 protein in exosomes from chronic lymphocytic leukemia cells promotes NF-kappaB activity during disease progression. Blood 2017;130: 777–88.
6. Mannavola F, Tucci M, Felici C, Passarelli A, D'Oronzo S, Silvestris F. Tumor-derived exosomes promote the in vitro osteotropism of melanoma cells by activating the SDF-1/CXCR4/CXCR7 axis. J Transl Med 2019;17:230.
7. Gargiulo E, Paggetti J, Moussay E. Hematological malignancy-derived small extracellular vesicles and tumor microenvironment: the art of turning foes into friends. Cells 2019;8:511.
8. Tsukada N, Burger JA, Zvaifler NJ, Kipps TJ. Distinctive features of "nurselike" cells that differentiate in the context of chronic lymphocytic leukemia. Blood 2002;99:1030–7.
9. Burger JA, Ghia P, Rosenwald A, Caligaris-Cappio F. The microenvironment in mature B-cell malignancies: a target for new treatment strategies. Blood 2009;114:3367–75.
10. Wierz M, Pierson S, Guyonnet L, Viry E, Lequeux A, Oudin A, et al. Dual PD1/LAG3 immune checkpoint blockade limits tumor development in a murine model of chronic lymphocytic leukemia. Blood 2018;131:1617–21.
11. Radulovic K, Rossini V, Manta C, Holzmann K, Kestler HA, Niess JH. The early activation marker CD69 regulates the expression of chemokines and CD4 T cell accumulation in intestine. PLoS One 2013;8: e65413.
12. Shiow LR, Rosen DB, Brdicková N, Xu Y, An J, Lanier LL, et al. CD69 acts downstream of interferon-alpha/beta to inhibit S1P1 and lymphocyte egress from lymphoid organs. Nature 2006;440:540–4.
13. Smallwood DT, Apollonio B, Willimott S, Lezina L, Alharthi A, Ambrose AR, et al. Extracellular vesicles released by CD40/IL-4-stimulated CLL cells confer altered functional properties to CD4+ T cells. Blood 2016;128:542–52.
14. Paggetti J, Haderk F, Seiffert M, Janji B, Distler U, Ammerlaan W, et al. Exosomes released by chronic lymphocytic leukemia cells induce the transition of stromal cells into cancer-associated fibroblasts. Blood 2015;126:1106–17.
15. Haderk F, Schulz R, Iskar M, Cid LL, Worst T, Willmund KV, et al. Tumor-derived exosomes modulate PD-L1 expression in monocytes. Sci Immunol 2017;2:eaah5509.
16. Filarsky K, Garding A, Becker N, Wolf C, Zucknick M, Claus R, et al. Kruppel-like factor 4 (KLF4) inactivation in chronic lymphocytic leukemia correlates with promoter DNA-methylation and can be reversed by inhibition of NOTCH signaling. Haematologica 2016;101: e249–253.
17. Hsu C, Morohashi Y, Yoshimura S-I, Manrique-Hoyos N, Jung S, Lauterbach MA, et al. Regulation of exosome secretion by Rab35 and its GTPase-activating proteins TBC1D10A-C. J Cell Biol 2010;189: 223–32.
18. Stenmark H. Rab GTPases as coordinators of vesicle traffic. Nat Rev Mol Cell Biol 2009;10:513–25.
19. Matsui T, Osaki F, Hiragi S, Sakamaki Y, Fukuda M. ALIX and ceramide differentially control polarized small extracellular vesicle release from epithelial cells. EMBO Rep 2021;22:e51475.
20. Paggetti J, Berchem G, Moussay E. Stromal cell-induced miRNA alteration in chronic lymphocytic leukemia: how a minute and unavoidable cell contamination impairs miRNA profiling. Leukemia 2013; 27:1773–6.
21. Gonder S, Largeot A, Gargiulo E, Pierson S, Fernandez Botana I, Pagano G, et al. The tumor microenvironment-dependent transcription factors AHR and HIF-1α Are dispensable for leukemogenesis in the Eμ-TCL1 mouse model of chronic lymphocytic leukemia. Cancers 2021;13:4518.
22. Schiller LT, Lemus-Diaz N, Ferreira RR, Boker KO, Gruber J. Enhanced production of Exosome-associated AAV by overexpression of the tetraspanin CD9. Mol Ther Methods Clin Dev 2018;9:278–87.
23. Wei D, Zhan W, Gao Y, Huang L, Gong R, Wang W, et al. RAB31 marks and controls an ESCRT-independent exosome pathway. Cell Res 2021;31:157–77.
24. Kalluri R, LeBleu VS. The biology, function, and biomedical applications of exosomes. Science 2020;367:eaau6977.
25. Moussay E, Wang K, Cho J-H, van Moer K, Pierson S, Paggetti J, et al. MicroRNA as biomarkers and regulators in B-cell chronic lymphocytic leukemia. Proc Natl Acad Sci U S A 2011;108:6573–8.
26. Andreola G, Rivoltini L, Castelli C, Huber V, Perego P, Deho P, et al. Induction of lymphocyte apoptosis by tumor cell secretion of FasL-bearing microvesicles. J Exp Med 2002;195:1303–16.
27. Chen Z, You L, Wang L, Huang X, Liu H, Wei JY, et al. Dual effect of DLBCL-derived EXOs in lymphoma to improve DC vaccine efficacy in vitro while favor tumorgenesis in vivo. J Exp Clin Cancer Res 2018; 37:190.
28. Mak TW, Grusdat M, Duncan GS, Dostert C, Nonnenmacher Y, Cox M, et al. Glutathione primes T cell metabolism for inflammation. Immunity 2017;46:1089–90.
29. Schurich A, Pallett LJ, Jajbhay D, Wijngaarden J, Otano I, Gill US, et al. Distinct metabolic requirements of exhausted and functional virus-specific CD8 T cells in the same host. Cell Rep 2016;16:1243–52.
30. Zheng L, Qin S, Si W, Wang A, Xing B, Gao R, et al. Pan-cancer single-cell landscape of tumor-infiltrating T cells. Science 2021;374:abe6474.
31. Zhang F, Li R, Yang Y, Shi C, Shen Y, Lu C, et al. Specific decrease in B-cell-derived extracellular vesicles enhances post-chemotherapeutic CD8(+) T cell responses. Immunity 2019;50:738–50.
32. Kim T-D, Lee SU, Yun S, Sun H-N, Lee SH, Kim JW, et al. Human microRNA-27a* targets Prf1 and GzmB expression to regulate NK-cell cytotoxicity. Blood 2011;118:5476–86.
33. Wang P, Gu Y, Zhang Q, Han Y, Hou J, Lin L., et al. Identification of resting and type I IFN-activated human NK cell miRNomes reveals microRNA-378 and microRNA-30e as negative regulators of NK cell cytotoxicity. J Immunol 2012;189:211.
34. Trotta R, Chen L, Costinean S, Josyula S, Mundy-Bosse BL, Ciarlariello D, et al. Overexpression of miR-155 causes expansion, arrest in terminal differentiation and functional activation of mouse natural killer cells. Blood 2013;121:3126–34.
35. Kim N, Kim M, Yun S, Doh J, Greenberg PD, Kim T-D, et al. MicroRNA-150 regulates the cytotoxicity of natural killers by targeting perforin-1. J Allergy Clin Immunol 2014;134:195–203.
36. Bobrie A, Krumeich S, Reyal F, Recchi C, Moita LF, Seabra MC, et al. Rab27a supports exosome-dependent and -independent mechanisms that modify the tumor microenvironment and can promote tumor progression. Cancer Res 2012;72:4920–30.
37. Jae N, McEwan DG, Manavski Y, Boon RA, Dimmeler S. Rab7a and Rab27b control secretion of endothelial microRNA through extracellular vesicles. FEBS Lett 2015;589(20 Pt B):3182–8.
38. Ostrowski M, Carmo NB, Krumeich S, Fanget I, Raposo G, Savina A, et al. Rab27a and Rab27b control different steps of the exosome secretion pathway. Nat Cell Biol 2010;12:19–30; sup 11–13.
39. Xing C, Li H, Li RJ, He H, Wu Z, Song B, et al. The roles of exosomal immune checkpoint proteins in tumors. Mil Med Res 2021;8:56.
40. Moussay E, Palissot V, Vallar L, Poirel HA, Wenner T, El Khoury V, et al. Determination of genes and microRNAs involved in the resistance to fludarabine in vivo in chronic lymphocytic leukemia. Mol Cancer 2010;9:115.
41. Yeh Y-Y, Ozer HG, Lehman AM, Maddocks K, Yu L, Johnson AJ, et al. Characterization of CLL exosomes reveals a distinct microRNA signature and enhanced secretion by activation of BCR signaling. Blood 2015;125:3297–305.
42. Szajnik M, Czystowska M, Szczepanski MJ, Mandapathil M, Whiteside TL. Tumor-derived microvesicles induce, expand and up-regulate biological activities of human regulatory T cells (Treg). PLoS One 2010;5:e11469.
43. Clayton A, Al-Taei S, Webber J, Mason MD, Tabi Z. Cancer exosomes express CD39 and CD73, which suppress T cells through adenosine production. J Immunol 2011;187:676–83.

Downloaded from http://aacrjournals.org/bloodcancerdiscov/article-pdf/4/1/54/3236873/54.pdf by guest on 28 March 2023

44. Morrissey SM, Zhang F, Ding C, Montoya-Durango DE, Hu X, Yang C, et al. Tumor-derived exosomes drive immunosuppressive macrophages in a pre-metastatic niche through glycolytic dominant metabolic reprogramming. Cell Metab 2021;33:2040–58.
45. Li C, Phoon YP, Karlinsey K, Tian YF, Thapaliya S, Thongkum A, et al. A high OXPHOS CD8 T cell subset is predictive of immunotherapy resistance in melanoma patients. J Exp Med 2022;219:e20202084.
46. Sadik A, Somarribas Patterson LF, Öztürk S, Mohapatra SR, Panitz V, Secker PF, et al. IL4I1 is a metabolic immune checkpoint that activates the AHR and promotes tumor progression. Cell 2020;182:1252–70.
47. Tolmachova T, Abrink M, Futter CE, Authi KS, Seabra MC. Rab27b regulates number and secretion of platelet dense granules. Proc Natl Acad Sci U S A 2007;104:5872–7.
48. Stinchcombe JC, Barral DC, Mules EH, Booth S, Hume AN, Machesky LM, et al. Rab27a is required for regulated secretion in cytotoxic T lymphocytes. J Cell Biol 2001;152:825–34.
49. Okoye IS, Coomes SM, Pelly VS, Czieso S, Papayannopoulos V, Tolmachova T, et al. MicroRNA-containing T-regulatory-cell-derived exosomes suppress pathogenic T helper 1 cells. Immunity 2014;41:503.
50. Wang JS, Wang FB, Zhang QG, Shen ZZ, Shao ZM. Enhanced expression of Rab27A gene by breast cancer cells promoting invasiveness and the metastasis potential by secretion of insulin-like growth factor-II. Mol Cancer Res 2008;6:372–82.
51. Ding W, LaPlant BR, Call TG, Parikh SA, Leis JF, He R, et al. Pembrolizumab in patients with CLL and Richter transformation or with relapsed CLL. Blood 2017;129:3419–27.
52. Gargiulo E, Morande PE, Largeot A, Moussay E, Paggetti J. Diagnostic and therapeutic potential of extracellular vesicles in B-Cell malignancies. Front Oncol 2020;10:580874.
53. Stamatopoulos B, Van Damme M, Crompot E, Dessars B, El Housni H, Mineur P, et al. Opposite prognostic significance of cellular and serum circulating microRNA-150 in patients with chronic lymphocytic leukemia. Mol Med 2015;21:123–33.
54. Stamatopoulos B, Smith T, Crompot E, Pieters K, Clifford R, Mraz M, et al. The light chain IgLV3–21 defines a new poor prognostic subgroup in chronic lymphocytic leukemia: results of a multicenter study. Clin Cancer Res 2018;24:5048–57.
55. Wierz M, Pierson S, Gargiulo E, Guerin C, Moussay E, Paggetti J. Purification of leukemia-derived exosomes to study microenvironment modulation. Methods Mol Biol 2019;1884:231–45.
56. Collot M, Ashokkumar P, Anton H, Boutant E, Faklaris O, Galli T, et al. MemBright: a family of fluorescent membrane probes for advanced cellular imaging and neuroscience. Cell Chem Biol 2019; 26:600–14.
57. Théry C, Amigorena S, Raposo G, Clayton A. Isolation and characterization of exosomes from cell culture supernatants and biological fluids. Curr Protoc Cell Biol 2006;30:3.22.1–3.22.29.
58. Wang F, Li L, Piontek K, Sakaguchi M, Selaru FM. Exosome miR-335 as a novel therapeutic strategy in hepatocellular carcinoma. Hepatology 2018;67:940–54.
59. Ioannou N, Hagner PR, Stokes M, Gandhi AK, Apollonio B, Fanous M, et al. Triggering interferon signaling in T cells with avadomide sensitizes CLL to anti-PD-L1/PD-1 immunotherapy. Blood 2021;137:216–31.
60. Robinson MD, McCarthy DJ, Smyth GK. edgeR: a Bioconductor package for differential expression analysis of digital gene expression data. Bioinformatics 2010;26:139–40.
61. Tarazona S, Garcia-Alcalde F, Dopazo J, Ferrer A, Conesa A. Differential expression in RNA-seq: a matter of depth. Genome Res 2011;21: 2213–23.
62. Meiser J, Schuster A, Pietzke M, Vande Voorde J, Athineos D, Oizel K, et al. Increased formate overflow is a hallmark of oxidative cancer. Nat Commun 2018;9:1368.
63. Ritchie ME, Phipson B, Wu D, Hu Y, Law CW, Shi W, et al. limma powers differential expression analyses for RNA-sequencing and microarray studies. Nucleic Acids Res 2015;43:e47.
64. Nazarov PV, Wienecke-Baldacchino AK, Zinovyev A, Czerwińska U, Muller A, Nashan D, et al. Deconvolution of transcriptomes and miRNomes by independent component analysis provides insights into biological processes and clinical outcomes of melanoma patients. BMC Med Genomics 2019;12:132.
65. Coll-de la Rubia E, Martinez-Garcia E, Dittmar G, Nazarov PV, Bebia V, Cabrera S, et al. In silico approach for validating and unveiling new applications for prognostic biomarkers of endometrial cancer. Cancers (Basel) 2021;13:5052.

Downloaded from http://aacrjournals.org/bloodcancerdiscov/article-pdf/4/1/54/3236873/54.pdf by guest on 28 March 2023

Appendix 4: Inhibition of MYC translation through targeting of the newly identified PHB-eIF4F complex as therapeutic strategy in CLL

LARGEOT, A., KLAPP, V., VIRY*, E., GONDER*, S., FERNANDEZ BOTANA,* I., BLOMME, A*., **BENZARTI, M***., PIERSON, S., DUCULTY, C., MARTTILA, P., WIERZ, M., GARGIULO, E., PAGANO, G., AN, N., EL HACHEM, N., PEREZ HERMANDEZ, D., CHAKRABORTY, S., YSEBAERT, L., FRANÇOIS, J. H., CORTEZ CLEMENTE, S. D., BERCHEM, G., EFREMOV, D. G., DITTMAR, G., SZPAKOWSKA, M., CHEVIGNE, A., NAZAROV, P. V., HELLEDAY, T., CLOSE, P., MEISER, J., STAMATOPOULOS, B., DÉSAUBRY, L., PAGGETTI, J. & MOUSSAY, E. 2023. Inhibition of MYC translation through targeting of the newly identified PHB-eIF4F complex as therapeutic strategy in CLL. ***Blood***.

* Authors have contributed equally to this work.

DOI: https://doi.org/10.1182/blood.2022017839

Personal contribution: This paper demonstrate that the therapeutic effects of inhibiting translation machinery in CLL, and how these effects are specifically achieved via MYC inhibition. MYC is a well-known metabolic regulator of cancer cells, therefore, I contributed to this research with the metabolomics data presented in figure panels**: 3G, 5G, S3H, S3I, S3L, S3M and S5H**. Here I helped in performing targeted metabolomics using [U-^{13}C] glucose and [U-^{13}C] glutamine on FL3 treated and PHB-KD CLL cells, I then processed and analyzed the data generated from these experiments. I also reviewed the manuscript prior to submission.

blood®
Regular Article

Check for updates

LYMPHOID NEOPLASIA

Inhibition of MYC translation through targeting of the newly identified PHB-eIF4F complex as a therapeutic strategy in CLL

Anne Largeot,[1] Vanessa Klapp,[1,2] Elodie Viry,[1,*] Susanne Gonder,[1,2,*] Iria Fernandez Botana,[1,2,*] Arnaud Blomme,[3,*] Mohaned Benzarti,[2,4,*] Sandrine Pierson,[1] Chloé Duculty,[1,2] Petra Marttila,[5] Marina Wierz,[1] Ernesto Gargiulo,[1] Giulia Pagano,[1,2] Ning An,[3] Najla El Hachem,[3] Daniel Perez Hernandez,[6] Supriya Chakraborty,[7] Loïc Ysebaert,[8] Jean-Hugues François,[9] Susan Cortez Clemente,[10] Guy Berchem,[10,11] Dimitar G. Efremov,[7] Gunnar Dittmar,[6,12] Martyna Szpakowska,[13] Andy Chevigné,[13] Petr V. Nazarov,[14] Thomas Helleday,[5,15] Pierre Close,[3,16] Johannes Meiser,[4] Basile Stamatopoulos,[17] Laurent Désaubry,[18] Jérôme Paggetti,[1,†] and Etienne Moussay[1,†]

[1]Department of Cancer Research, Tumor Stroma Interactions, Luxembourg Institute of Health, Luxembourg, Luxembourg; [2]Faculty of Science, Technology and Medicine, University of Luxembourg, Esch-sur-Alzette, Luxembourg; [3]Laboratory of Cancer Signaling, GIGA Stem Cells, University of Liège, Liège, Belgium; [4]Department of Cancer Research, Cancer Metabolism Group, Luxembourg Institute of Health, Luxembourg, Luxembourg; [5]Department of Oncology-Pathology, Science for Life Laboratory, Karolinska Institutet, Solna, Sweden; [6]Department of Infection and Immunity, Proteomics of Cellular Signaling, Luxembourg Institute of Health, Esch-sur-Alzette, Luxembourg; [7]Molecular Hematology, International Centre for Genetic Engineering and Biotechnology, Trieste, Italy; [8]Haematology Department, Institut Universitaire du Cancer Toulouse Oncopole, Toulouse, France; [9]Laboratoire d'hématologie and [10]Département d'hémato-oncologie, Centre Hospitalier de Luxembourg, Luxembourg, Luxembourg; [11]Luxembourg Institute of Health, Luxembourg, Luxembourg; [12]Department of Life Sciences and Medicine, University of Luxembourg, Belvaux, Luxembourg; [13]Department of Infection and Immunity, Immuno-Pharmacology and Interactomics, Luxembourg Institute of Health, Esch-sur-Alzette, Luxembourg; [14]Department of Cancer Research, Multiomics Data Science, Luxembourg Institute of Health, Luxembourg, Luxembourg; [15]Department of Oncology and Metabolism, Weston Park Cancer Centre, The Medical School, University of Sheffield, Sheffield, United Kingdom; [16]WELBIO Department, WEL Research Institute, Wavre, Belgium; [17]Laboratory of Clinical Cell Therapy, ULB-Research Cancer Center, Jules Bordet Institute, Université Libre de Bruxelles, Brussels, Belgium; and [18]Regenerative Nanomedicine Laboratory (UMR1260), Faculty of Medicine, Fédération de Médecine Translationnelle de Strasbourg, INSERM-University of Strasbourg, Strasbourg, France

KEY POINTS

- **Inhibition of translation initiation prevents CLL growth in vitro and in vivo, through targeting the MYC oncogene.**
- **PHBs directly interact with the translation initiation machinery, filling a gap in the understanding of the crucial roles of these proteins.**

Dysregulation of messenger RNA (mRNA) translation, including preferential translation of mRNA with complex 5′ untranslated regions such as the MYC oncogene, is recognized as an important mechanism in cancer. Here, we show that both human and murine chronic lymphocytic leukemia (CLL) cells display a high translation rate, which is inhibited by the synthetic flavagline FL3, a prohibitin (PHB)-binding drug. A multiomics analysis performed in samples from patients with CLL and cell lines treated with FL3 revealed the decreased translation of the MYC oncogene and of proteins involved in cell cycle and metabolism. Furthermore, inhibiting translation induced a proliferation arrest and a rewiring of MYC-driven metabolism. Interestingly, contrary to other models, the RAS-RAF-(PHBs)-MAPK pathway is neither impaired by FL3 nor implicated in translation regulation in CLL cells. Here, we rather show that PHBs are directly associated with the eukaryotic initiation factor (eIF)4F translation complex and are targeted by FL3. Knockdown of PHBs resembled FL3 treatment. Importantly, inhibition of translation controlled CLL development in vivo, either alone or combined with immunotherapy. Finally, high expression of translation initiation–related genes and PHBs genes correlated with poor survival and unfavorable clinical parameters in patients with CLL. Overall, we demonstrated that translation inhibition is a valuable strategy to control CLL development by blocking the translation of several oncogenic pathways including MYC. We also unraveled a new and direct role of PHBs in translation initiation, thus creating new therapeutic opportunities for patients with CLL.

Introduction

In human chronic lymphocytic leukemia (CLL), the lymph node microenvironment sustains the proliferation of leukemic cells through different stimuli, such as the activation of B-cell receptor (BCR),[1] or Toll-like receptors (TLRs).[2] Targeting their downstream signaling led to a major breakthrough in the standard of care in CLL.[3] The oncogene MYC represents another interesting target in CLL, because MYC aberrations are detected in CLL cells and associated with Richter transformation, a rare but aggressive complication of CLL.[4-6] In addition, its expression is upregulated in the lymph

Downloaded from http://ashpublications.org/blood/article-pdf/141/26/3166/2060573/blood_bld-2022-017839-main.pdf by guest on 10 October 2023

node microenvironment,[7-9] especially at the translational level.[10]

Recently, translation initiation was recognized as an Achilles' heel of cancer cells. Indeed, increase in global translation rate and aberrant translation of specific oncogenic transcripts seems to be a common feature for a large variety of tumors.[11,12] Interestingly, translation is also a nexus of resistance to several kinase inhibitors.[13] Particularly in CLL, several reports demonstrated a dysregulation of translation, either through mutations in ribosomal proteins[14-17] or through activation of translation by microenvironment-mediated stimuli.[10,18] In addition, ZAP-70 expression also contributes to aberrant translation through direct interaction with ribosomal proteins.[19] The pathways and mechanisms leading to increased translation are not fully understood yet. Some studies demonstrated the efficacy of inhibiting translation in CLL, using different types of translation inhibitors.[20-22] However, there is still a debate on the mechanisms of action of the different molecules used, and only little evidence of their efficacy in vivo.

Here, we investigated translation in CLL and its inhibition. We used the translation inhibitor FL3, which has previously shown antitumor activity both in vitro and in vivo.[13,23,24] This molecule, from the flavagline family, was shown to bind prohibitins (PHBs).[25] These scaffold proteins are found in several cellular sublocalizations that dictate their activity.[26] At the membrane, they are required for the RAF activation by RAS in a large variety of cancers,[27] leading to the phosphorylation of eukaryotic initiation factor 4E (eIF4E) through the MAPK pathway, and ultimately resulting in increased translation. By binding to PHBs, FL3 was shown to prevent the activation of RAF and therefore decreases translation.[28]

In the present paper, we showed that aberrant translation is indeed a feature of human and murine CLL. We demonstrated that inhibition of translation in CLL targets the MYC oncogene, leading to decreased proliferative capacities and reversion of metabolic rewiring. Finally, we identified PHBs as direct interactors of the eIF4F machinery and as crucial factors for translation in CLL cells.

Methods

Animal experiments

All experiments involving laboratory animals were conducted in a pathogen-free animal facility with the approval of the Luxembourg Ministry for Agriculture. Mice were treated in accordance with European guidelines. C57BL/6 mice were purchased from Janvier Labs. Eμ-TCL1 mice (called TCL1) were kindly given by Carlo Croce and John Byrd.[29] CLL progression was monitored by determining the percentage of $CD5^+CD19^+$ CLL cells in the peripheral blood using flow cytometry.

Patient samples

All experiments involving human samples were conducted in accordance with the declaration of Helsinki, approved by the institutional review board (Jules Bordet Institute Ethics Committee) or the Luxembourg Comité National d'Ethique et de Recherche. Samples were collected from patients with CLL after written informed consent. For the cohort of 144 patients used, all patients had a $CD19^+CD5^+CD23^+$ phenotype and a Catovsky score of 4/5 or 5/5. All tested prognostic factors were proven to be significant predictors of treatment-free survival (TFS) and overall survival (OS), indicating that our cohort is representative of a CLL population (supplemental Table 1, available on the *Blood* website).

OPP protein synthesis assay

O-propargyl-puromycin (OPP, Bioconnect) was added into cell culture at a final concentration of 20 μM for 30 minutes. The viability staining was performed at 4°C for 30 minutes with a Zombie Fixable Viability kit (BioLegend). The cells were fixed for 15 minutes at room temperature with 3.7% paraformaldehyde, and permeabilized with 0.5% Triton X-100 in phosphate-buffered saline for 15 minutes at room temperature. The detection of the OPP was performed per the manufacturer's protocol, using the Click-iT technology (Life Technologies). The cells were further subjected to antibody staining and analyzed by flow cytometry.

Pulsed SILAC assay

The stable isotope labeling by amino acids in cell culture (SILAC) labeling medium used was the following: RPMI 1640 for SILAC (Thermofisher) containing 10% of dialyzed serum, 1% of penicillin/streptomycin, unlabeled leucine, and either "heavy" amino acids [0.398 mM L-($^{13}C_6$,$^{15}N_4$)-arginine and 0.798 mM L-($^{13}C_6$,$^{15}N_2$)-lysine] or "medium-heavy" amino acids [0.398 mM L-($^{13}C_6$)-arginine and 0.798 mM L-(D_4)-lysine]. MEC-1 or OSU-CLL cells (10×10^6) were resuspended at a concentration of 0.6×10^6 cells per mL, and treated as indicated for 8 hours. Cells (20×10^6) from patients with CLL were resuspended at a concentration of 10×10^6 cells per mL, and treated as indicated for 16 hours. At the end of the labeling, the cells were washed 3 times in cold phosphate-buffered saline and snap frozen, before proceeding to protein extraction and to mass spectrometry analysis.

The detailed material and methods can be found as supplemental Information.

Results

Translation is increased in CLL cells and can be inhibited by FL3

First, using publicly available gene expression data sets, we showed that translation-related genes are upregulated in leukemic B cells compared with healthy B cells, in both human and mice, resulting in a functional enrichment in translation (Figure 1A). We also observed increased levels of proteins responsible for translation initiation in CLL cells from patients (Figure 1B). Therefore, we quantified translation by OPP incorporation (Figure 1C) and confirmed that protein translation is increased in CLL cells compared with B cells from healthy donors and from patients with CLL (Figure 1D-E). To investigate whether an increased translation is also a feature observed in a murine model of CLL, we analyzed the translation rate in different cell populations from the spleen of mice with leukemia. We observed a higher translation rate in CLL cells ($CD19^+CD5^+$) compared with normal B cells ($CD19^+CD5^-$) and with both $CD8^+$ and $CD4^+$ T lymphocytes. Interestingly, $FOXP3^+$ regulatory T cells (Tregs) also showed a higher

Downloaded from http://ashpublications.org/blood/article-pdf/141/26/3166/2060573/blood_bld-2022-017839-main.pdf by guest on 10 October 2023

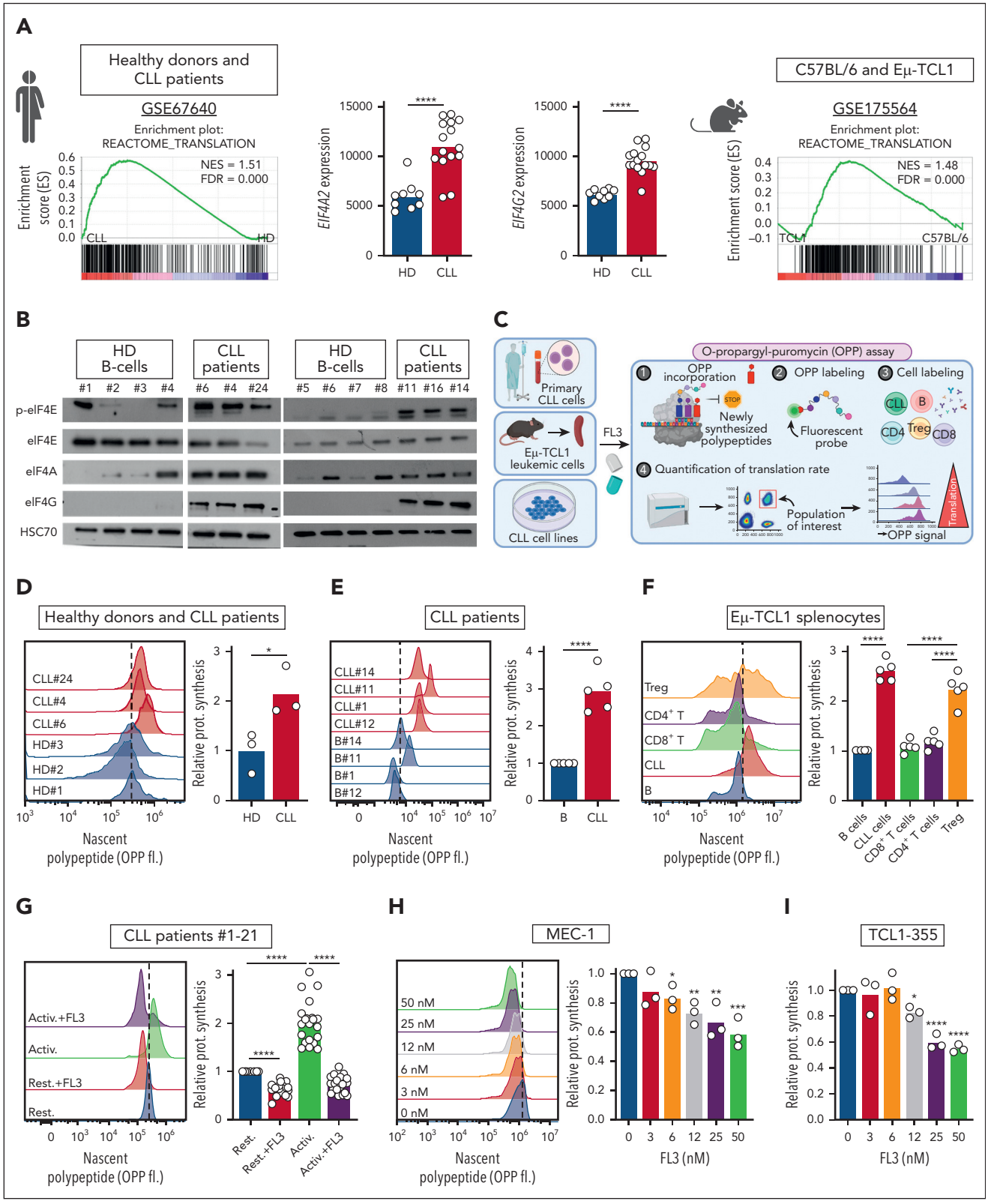


Figure 1. Translation is increased in CLL cells and can be inhibited by FL3. (A) Preranked gene set enrichment analysis (GSEA) from public data sets indicating an enrichment in translation in CLL cells compared with healthy B cells in human (NCBI Gene Expression Omnibus, GSE67640, GSEA, left panel; and EIF4A2 and EIF4G2 gene expression in healthy donor [HD] B cells vs CLL cells, middle panels), and in mouse (GSE175564, TCL1 cells compared with C57BL/6 B cells, right panel). (B) Western-blot analysis of phospho-eIF4E, eIF4E, eIF4A, eIF4G, and HSC70 proteins in B cells from HDs and patients with CLL. (C) Schematic representation of the OPP incorporation assay to evaluate translation rate. (D-F) Determination of translation rate by OPP assay in B cells from HDs and patients with CLL (D, n = 3), in normal B cells and CLL cells from patients with CLL (E, n = 5) and in T- and B-cell subsets from the spleen of sick recipient mice, after transfer of Eμ-TCL1 splenocytes (F, n = 5). Left panel: representative plots; right panel: quantification. (G-I) Determination of translation rate by OPP assay in patients' CLL cells activated (Activ.) or not (Rest.) with CpG ODN-2006, and treated with

Downloaded from http://ashpublications.org/blood/article-pdf/141/26/3166/2060573/blood_bld-2022-017839-main.pdf by guest on 10 October 2023

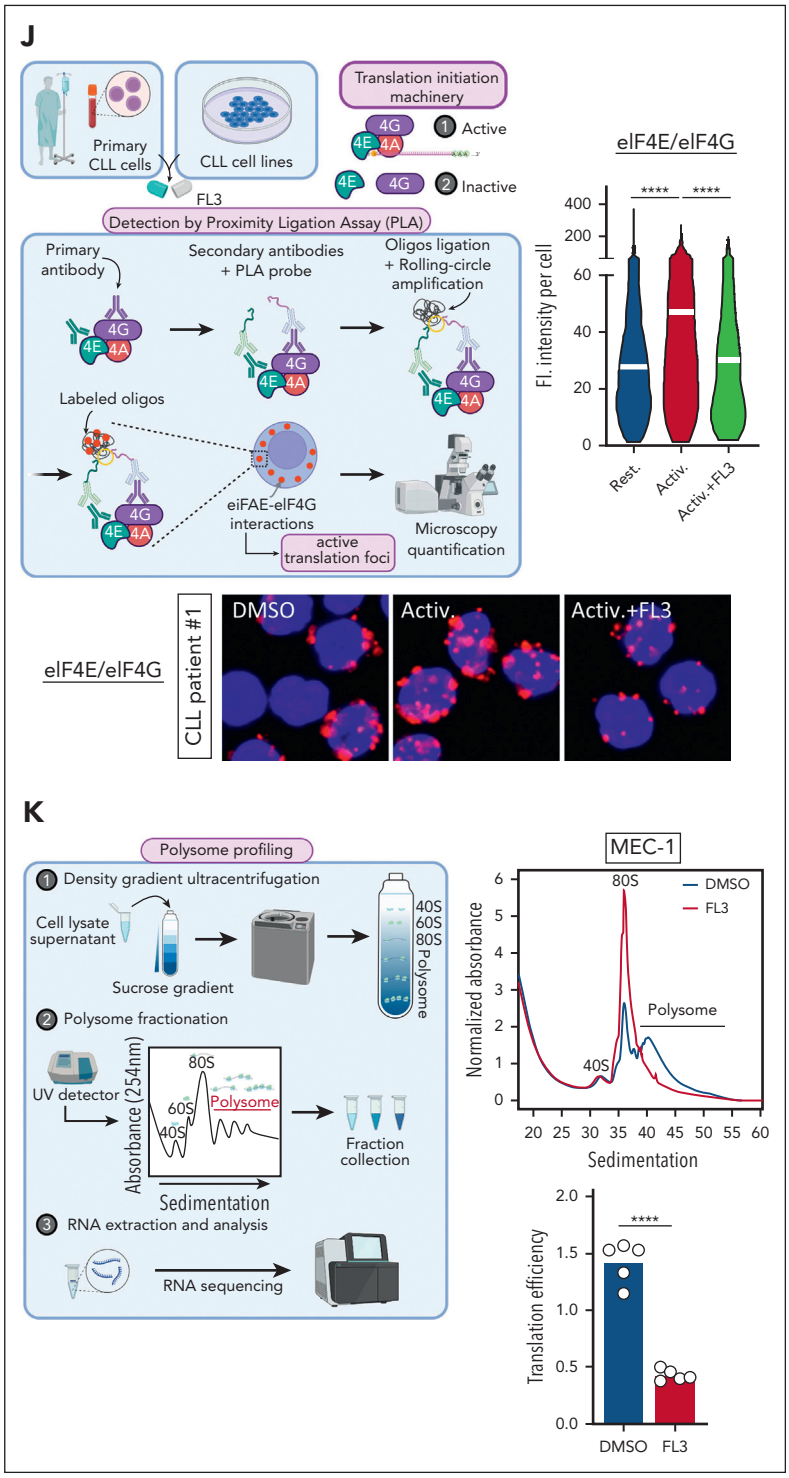


Figure 1 (continued) dimethyl sulfoxide (DMSO) or 100 nM FL3 for 16 hours (left panel: representative plots; right panel: quantification; n = 21) (G), and in MEC-1 (H) or TCL1-355 (I) cells treated with DMSO or FL3 for 3 hours (0-50 nM) (left panel: representative plots; right panel: quantification; n = 3). (J) Schematic representation of proximity ligation assay (PLA) and determination of translation rate, based on PLA detection of eIF4E/eIF4G interaction, in patient CLL cells activated or not with CpG ODN-2006 and treated with DMSO or 100 nM FL3 for 3 hours (Rest.:858 cells, Activ.: 695 cells, and Activ.+FL3: 357 cells). (K) Schematic representation of polysome profiling, representative plot, and translation efficiency in MEC-1 cells treated with DMSO or 50 nM FL3 for 24 hours.

translation rate compared with other T cells (Figure 1F). Next, to verify that TLR and BCR activation induce translation, we treated CLL cells with the TLR9-agonist Class B CpG ODN-2006 or with an anti-immunoglobulin M antibody. Indeed, the cellular activation increased translation, as attested by increased OPP incorporation (Figure 1G; supplemental Figure 1A). In addition, we showed that treatment of patient samples with the synthetic flavagline FL3 decreased translation (Figure 1G; supplemental Figure 1A). Accordingly, in human (MEC-1, OSU-CLL, HG-3, WA-OSEL, and PGA-1) and murine (TCL1-355)[30] CLL cell lines,

Downloaded from http://ashpublications.org/blood/article-pdf/141/26/3166/2060573/blood_bld-2022-017839-main.pdf by guest on 10 October 2023

incubation with FL3 led to a significant decrease in translation, starting from 6 nM FL3, after only 3 hours of treatment (Figure 1H-I; supplemental Figure 1B-F). The reduction in translation after FL3 treatment was also confirmed by measuring the incorporation of the methionine analog L-propargylglycine (supplemental Figure 1G). Active translation is characterized by the interaction between the translation initiation factors eIF4E and eIF4G, which can be detected by proximity ligation assay (Figure 1J). Indeed, we observed an increased interaction between eIF4E and eIF4G in activated CLL cells from patients and CLL cell lines, which was decreased upon FL3 treatment (Figure 1J; supplemental Figure 1H-I). Finally, the effect of FL3 on translation was analyzed by polysome profiling. We observed a decreased polysome peak amplitude and an accumulation of RNA in subpolysome fractions, demonstrating a significant reduction in translation efficiency (Figure 1K; supplemental Figure 1J). Altogether, these results confirm the relevance of studying translation in CLL, and demonstrates that FL3 can efficiently inhibit translation in human and murine CLL cells.

Multiomics analysis revealed that inhibition of translation affects proteins involved in translation, cell cycle regulation, MYC, and other oncogenic pathways

Because flavaglines were shown to reprogram the translational landscape rather than completely inhibit protein translation,[31] we wanted to understand more precisely the effect of FL3 in CLL cells. For this purpose, we performed pulsed SILAC assay on 5 patient samples and CLL cell lines (Figure 2A). First, we confirmed the increase in protein synthesis after activation in CLL cells from patients, representing 16% of the detected proteins (supplemental Figure 2A-B; supplemental Table 2). This includes proteins involved in translation and activating signaling pathways (supplemental Figure 2C). In resting samples, FL3 treatment led to decreased protein synthesis for 17% of the detected proteins (supplemental Figure 2B-D; supplemental Table 2). However, the effect was more striking when CLL cells were activated and treated with FL3, with 31% of the detected proteins showing a decrease in their translation rate (Figure 2B; supplemental Figure 2B-E; supplemental Table 2). Treatment of MEC-1 and OSU-CLL cell lines led to a similar effect (51% and 30%, respectively, of the detected proteins) (Figure 2C; supplemental Figure 2B-F; supplemental Table 3). The ontology analysis revealed that FL3 treatment affected common pathways in patient samples and cell lines, including proteins involved in translation and cell cycle regulation (Figure 2D; supplemental Figure 2G). In addition, proteins regulated by several known oncogenes in CLL, such as the targets of MYC and NFκB, displayed a decreased synthesis (Figure 2E-F). Thus, our pulsed SILAC experiments suggest a decreased MYC activity in FL3-treated cells. Translation of MYC is reportedly increased upon CLL stimulation, contributing to leukemia development and proggression.[18] RNA sequencing followed by gene set enrichment analysis confirmed the repression of translation-related genes and MYC target genes in FL3-treated cells (Figure 2G-H; supplemental Figure 2H; supplemental Table 4). Furthermore, transcription factor enrichment analysis confirmed the involvement of MYC/MAX in the regulation of these repressed genes by FL3 (Figure 2I). Ontology analysis indicated that deregulated MYC target genes were mainly involved in metabolism-related biological processes (supplemental Figure 2I-J). We thus hypothesized that FL3 could directly inhibit MYC translation (undetectable in pulsed SILAC assay). Indeed, treatment with FL3 resulted in a rapid loss of the MYC protein (Figure 2J; supplemental Figure 2K), whereas its messenger RNA (mRNA) level was increased (Figure 2K). In addition, FL3 led to decreased levels of other oncogenes, such as ETS-1 (supplemental Figure 2L-M). Finally, polysome profiling confirmed the lower abundance of *Myc* transcripts in the polysome fraction of both human and murine cells treated with FL3 (Figure 2L; supplemental Table 4), confirming the reduction in MYC translation. Preranked gene set enrichment analysis indicated that FL3 predominantly repressed translation of genes involved in metabolism (glycolysis, fatty acid metabolism, and oxidative phosphorylation; Figure 2M).

Altogether, these data show that FL3 specifically inhibits the translation of proteins involved in translation, cell cycle regulation, and MYC oncogenic pathways.

Targeting of MYC translation is associated with decreased proliferative capacities, and reversion of metabolic rewiring

Based on the aforementioned results, we decided to investigate the biological consequences of inhibiting translation. First, we measured cell viability of CLL cells, healthy peripheral blood mononuclear cells, MEC-1 and Eμ-TCL1 primary murine cells (Figure 3A; supplemental Figure 3A). Interestingly, healthy peripheral blood mononuclear cells were less sensitive to FL3 compared with patient leukemic cells (50% inhibitory concentration at 72 hours: 118.2 and 11.7 nM, respectively). In addition, FL3 induced more cell death in CLL cells from patients than in B cells from healthy donors at the same dose (Figure 3B), confirming the therapeutic window for treating CLL with inhibitors of translation. Cell growth of human and murine CLL cell lines was strongly impaired by very low doses of FL3 (from 6 nM, Figure 3C; supplemental Figure 3B). Drug withdrawal experiments indicated that 4 days of treatment were necessary for total impairment of cell recovery (Figure 3D; supplemental Figure 3C). We also showed a limited effect of FL3 on apoptosis at an early time point, appearing only for higher doses and after 48 hours of treatment (Figure 3E; supplemental Figure 3D). On the contrary, carboxyfluorescein succinimidyl ester assay revealed a block of proliferation even with low FL3 doses (Figure 3F; supplemental Figure 3E). However, no difference in cell cycle phase distribution was observed, indicating a complete block of the cell cycle rather than the inhibition of a specific phase (supplemental Figure 3F). The decreased expression of several targets involved in cell proliferation (CDK4, BIRC5, and MCL1) in cells treated with FL3 was validated at protein level (supplemental Figure 3G).

Data in Figure 2 strongly suggest impairment of cell metabolism as majority of the MYC target genes, which show decreased transcription/translation, are associated with metabolic pathways. We performed stable isotope tracing using [U-^{13}C]-glucose and [U-^{13}C]-glutamine (Figure 3G). After [U-^{13}C]-glucose tracing (depicted in orange), we observed a reduction in glycolytic flux and pyruvate dehydrogenase (PDH) flux (Figure 3G; supplemental Figure 3H). The pentose phosphate pathway and purine/pyrimidine synthesis were also affected by FL3

Downloaded from http://ashpublications.org/blood/article-pdf/141/26/3166/2060573/blood_bld-2022-017839-main.pdf by guest on 10 October 2023

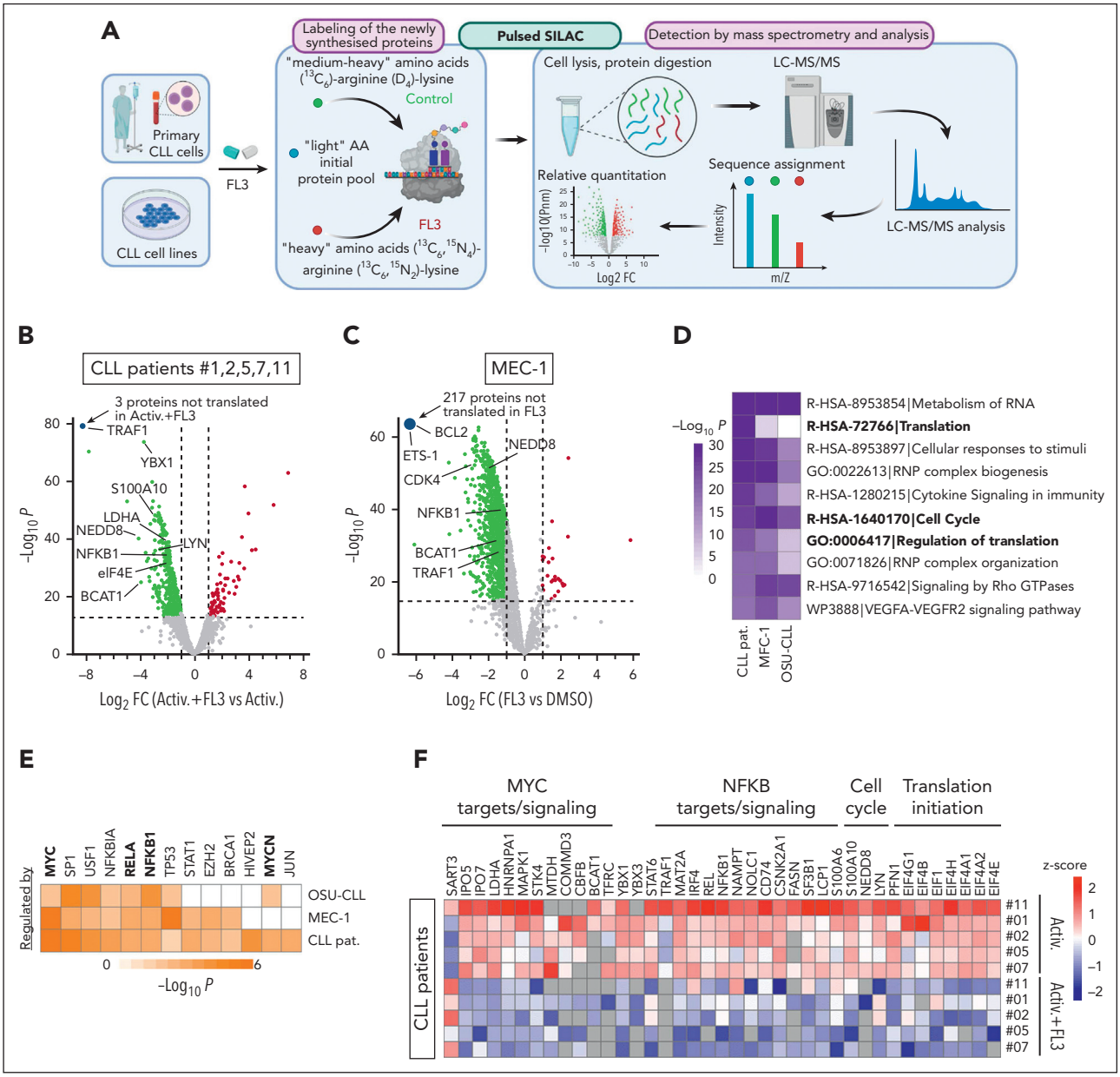


Figure 2. Multiomics analysis revealed that inhibition of translation affects proteins involved in translation, cell cycle regulation, MYC and other oncogenic pathways. (A) Schematic representation of pulsed SILAC assay. (B) Volcano plot showing differentially translated proteins (DTP) in CpG ODN-2006–activated cells from patients with CLL treated with DMSO or 100 nM of FL3 for 16 hours, with false discovery rate of <0.2 and log_2–fold change of >1 (n = 5). (C) Volcano plot showing DTP between MEC-1 treated with DMSO or 50 nM of FL3 for 8 hours, with false discovery rate of <0.05 and log_2–fold change of >1. (n = 3). (D) Heatmap depicting the ontology terms enriched in proteins with decreased translation in CpG ODN-2006–activated patient CLL cells, MEC-1 cells, and OSU-CLL cells treated with FL3. (E) Heatmap depicting the upstream factors that regulate the expression of proteins with decreased translation in CpG ODN-2006–activated patient CLL cells, MEC-1 cells, and OSU-CLL cells treated with FL3. (F) Heatmap showing the expression of DTP from selected pathways (identified in panels D-E) in samples from patients with CLL. (G-H) GSEA plots obtained from gene expression data generated from MEC-1 (G) and TCL1-355 cells (H) treated with DMSO or 50 nM FL3 for 24 hours. (I) Transcription factor enrichment analysis (top10) for differentially expressed genes downregulated by FL3. (J) Western-blot analysis of MYC proteins in patient CLL cells activated (Activ.) or not (Rest.) with CpG ODN-2006 and treated with DMSO or FL3 for 24 hours, and in MEC-1 and OSU-CLL cell lines treated for 3h. (K) *Myc* mRNA levels in cell lines treated with DMSO or 50 nM FL3 for 3 hours by quantitative reverse transcription polymerase chain reaction (qRT-PCR) (n = 3). (L) *Myc* mRNA ratio of expression in polysome vs subpolysome fractions of cells treated with DMSO or 50 nM FL3 for 24 hours. (M) Heatmap showing GSEA normalized enrichment scores (NES) from polysome profiling RNA sequencing. *P < .05, **P < .01, ***P < .001.

(Figure 3G), contributing to the block in proliferation observed in previous experiments. In addition, the production of lactate from pyruvate is decreased in FL3-treated cells (Figure 3G), because lactate dehydrogenase-A, the enzyme catalyzing this reaction and target of MYC, was also decreased (supplemental Figure 3G). [U-^{13}C]-glutamine tracing (in green), revealed that FL3 inhibits glutaminolysis, in line with the role of MYC in this context.[32,33] In addition, the tricarboxylic acid cycle activity was markedly reduced (Figure 3G; supplemental Figure 3I). As expected, after translation inhibition, we observed an accumulation of proteinogenic amino acids after FL3 treatment (supplemental Figure 3J). To confirm the involvement of MYC in the metabolic reprogramming observed upon FL3 treatment, we used specific inhibitors (10058-F4 and 10074-G5) that block MYC

Downloaded from http://ashpublications.org/blood/article-pdf/141/26/3166/2060573/blood_bld-2022-017839-main.pdf by guest on 10 October 2023

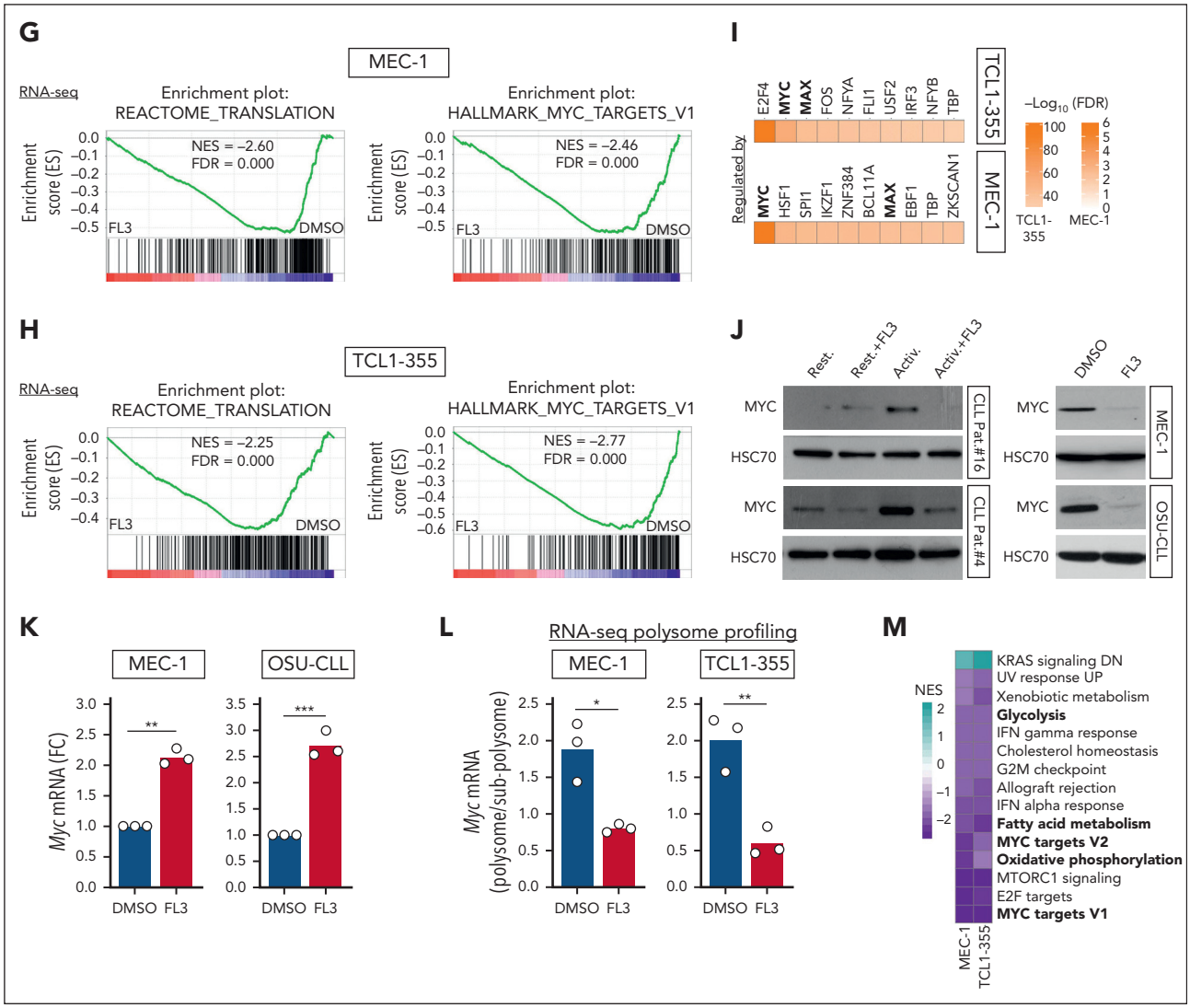


Figure 2 (continued)

transcriptional activity. We validated their efficacy in our cells (supplemental Figure 3K) and repeated the metabolic tracing. MYC inhibition led to similar metabolic changes to those after FL3 treatment, except for glycolysis (supplemental Figure 3L-M). This suggests that FL3-mediated metabolism rewiring is mainly owing to MYC inhibition but other proteins may also contribute partially to this effect.

In conclusion, through the targeting of MYC and other factors, FL3 treatment leads to the arrest of the proliferative capacities of CLL cells and results in major changes in cellular metabolism.

PHBs interact directly with the eIF4F translation initiation machinery, and FL3 binding disrupts this complex

Next, we investigated FL3's mechanism of action in CLL cells. Through its binding to PHBs, FL3 was shown to block RAS-RAF-MAPK pathway activation.[27,34] In CLL cells from patients, activation led to increased phosphorylation of RAF1, extracellular signal-regulated kinase (ERK)1/2, and eIF4E (Figure 4A; supplemental Figure 4A). Surprisingly, the phosphorylation of RAF1 and ERK1/2 was further increased upon FL3 treatment, whereas eIF4E phosphorylation was decreased (Figure 4A; supplemental Figure 4A-B), demonstrating that translation inhibition was not caused by the impairment of RAF1-ERK1/2 signaling. To understand whether the decrease in eIF4E phosphorylation is responsible for the phenotype observed in FL3-treated cells, we used the MAP kinase–interacting kinases (MNK) inhibitors eFT-508 (Tomivosertib) and CGP57380, because MNK1/2 are the main kinases that phosphorylate eIF4E.[35] Treatment with inhibitors completely abolished eIF4E phosphorylation without affecting cell growth and translation rate (Figure 4B-D; supplemental Figure 4C-H), showing that eIF4E phosphorylation status is not responsible for the decreased translation observed upon FL3 treatment. In addition, phosphorylation of MNK is not affected by FL3 treatment (supplemental Figure 4I). 4E-BP1 is a major repressor of translation by complexing with eIF4E.[36] Phosphorylation of 4E-BP1 upon activation of the mTORC1 pathway leads to decreased interaction with eIF4E, promoting translation initiation.[37] We observed that p-4E-BP1 and 4E-BP1 protein levels were

Downloaded from http://ashpublications.org/blood/article-pdf/141/26/3166/2060573/blood_bld-2022-017839-main.pdf by guest on 10 October 2023

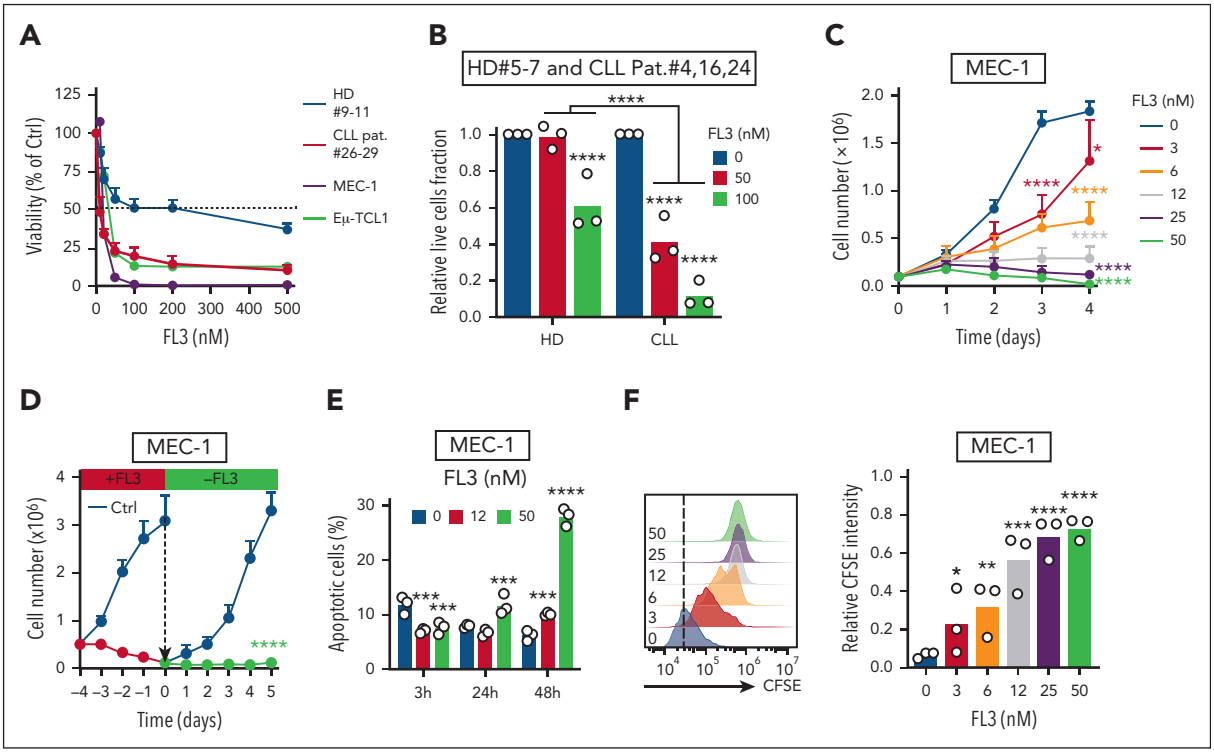


Figure 3. Targeting of MYC translation is associated with decreased proliferative capacities, and reversion of metabolic rewiring. (A) Viability of peripheral blood mononuclear cells from HDs, cells from patients with CLL, MEC-1 cells, and primary Eμ-TCL1 splenocytes treated for 72 hours with FL3 (0-500 nM) assessed by CCK8 assay. (B) Viability of sorted CD19$^+$ B cells from HDs and patients with CLL, treated with FL3 (0-100 nM) for 48 hours (n = 3, Apotracker green and 7AAD staining). (C) Growth of MEC-1 cells treated with FL3 (0-50 nM) for 4 days (n = 3). (D) Growth of MEC-1 cells after drug withdrawal. The cells were treated (red, then green after withdrawal) with 50 nM FL3 or DMSO (blue) for 96 hours, before being washed and resuspended at 0.1 × 10^6 cells per mL without the drug at day 0. The growth was assessed for 5 days after drug withdrawal. (E) Percentage of apoptotic cells after 3, 24, or 48 hours of treatment with FL3 (0-50 nM) in MEC-1 cells determined by Apotracker green and propidium iodide (PI) staining. (F) Determination of the proliferation of MEC-1 cells based on carboxyfluorescein succinimidyl ester assay (left panel: representative plot, right panel: quantification, n = 3). (G) Metabolomic isotopologue analysis of MEC-1 and TCL1-355 cells treated with DMSO or 50 nM FL3 for 24 hours in the presence of [U-^{13}C]-glucose (orange) and [U-^{13}C]-glutamine (green). Relative metabolic fluxes are indicated with gray for the unlabeled fraction, in orange or green for the labeled fractions (n = 3). *P < .05, **P < .01, ***P < .001, ****P < .0001.

unaffected by FL3, and the interaction between eIF4E and 4E-BP1 was even slightly decreased upon FL3 treatment (Figure 4E-F; supplemental Figure 4J-K). Cap-binding assay indicated that FL3 does not impair eIF4E binding to the cap but strongly reduces the ability of eIF4G to interact with cap-bound eIF4E, with no effect on 4E-BP1 (supplemental Figure 4L). These data suggest a direct targeting of the eIF4F translation initiation complex by FL3, rather than deregulation of upstream signaling pathways.

Using drug affinity responsive target stability (DARTS) assay, we confirmed that FL3 binds to PHBs in CLL cells (Figure 4G), but not to eIF4A (supplemental Figure 4M), which was shown to be the target of other flavaglines such as rocaglamide A (RocA) or silvestrol.[23,26,38] In addition, we tested whether other molecules targeting PHBs, not related to flavaglines, such as IN44 and fluorizoline, were associated with a defect in translation. Indeed, treatment of CLL cells with IN44 and fluorizoline at sublethal doses was associated with a decreased translation rate (supplemental Figure 4N-O). Altogether, these data point to a direct role of PHBs in the translation initiation machinery. In addition, we quantified PHB levels in patient cells and observed that PHBs are more abundant in CLL cells than in healthy donor B cells, both at mRNA and protein levels (Figure 4H-I).

Considering all these results, we hypothesized that PHBs interact with the translation initiation machinery. By immunoprecipitation of the endogenous eIF4E protein in MEC-1 cells, and of the tagged version of eIF4E and eIF4G in transfected HEK-293T cells, we showed their interaction with PHB (Figure 4J-K). Using a proximity ligation assay, we demonstrated the cytoplasmic interaction of PHB and PHB2 with eIF4E, eIF4G, and eIF4A in CLL cells from patients and MEC-1 cells (Figure 4L-M; supplemental Figure 4P-T). Interestingly, these interactions increased upon activation, and decreased upon treatment with FL3. To understand the stoichiometry of these interactions, we performed NanoBRET experiments (Figure 4N). Bioluminescence resonance energy transfer (BRET) ratios were measured in HEK-293T cells transfected with plasmids encoding PHB fused with the nanoluciferase and either eIF4E or HaloTag (HT, control) fused with the NeonGreen (NG), in N- or C-terminal. The higher ratio observed when using PHB(nanoluciferase) and eIF4E(NG), compared with HT(NG), indicates that PHB and eIF4E indeed interact (supplemental Figure 4U). The plateau reached when using increasing amounts of NG-eIF4E, and the linear curve when using the NG-HT control, confirmed the specificity of the observed interaction (Figure 4N). These experiments proved the interaction of PHB with the eIF4F complex.

Downloaded from http://ashpublications.org/blood/article-pdf/141/26/3166/2060573/blood_bld-2022-017839-main.pdf by guest on 10 October 2023

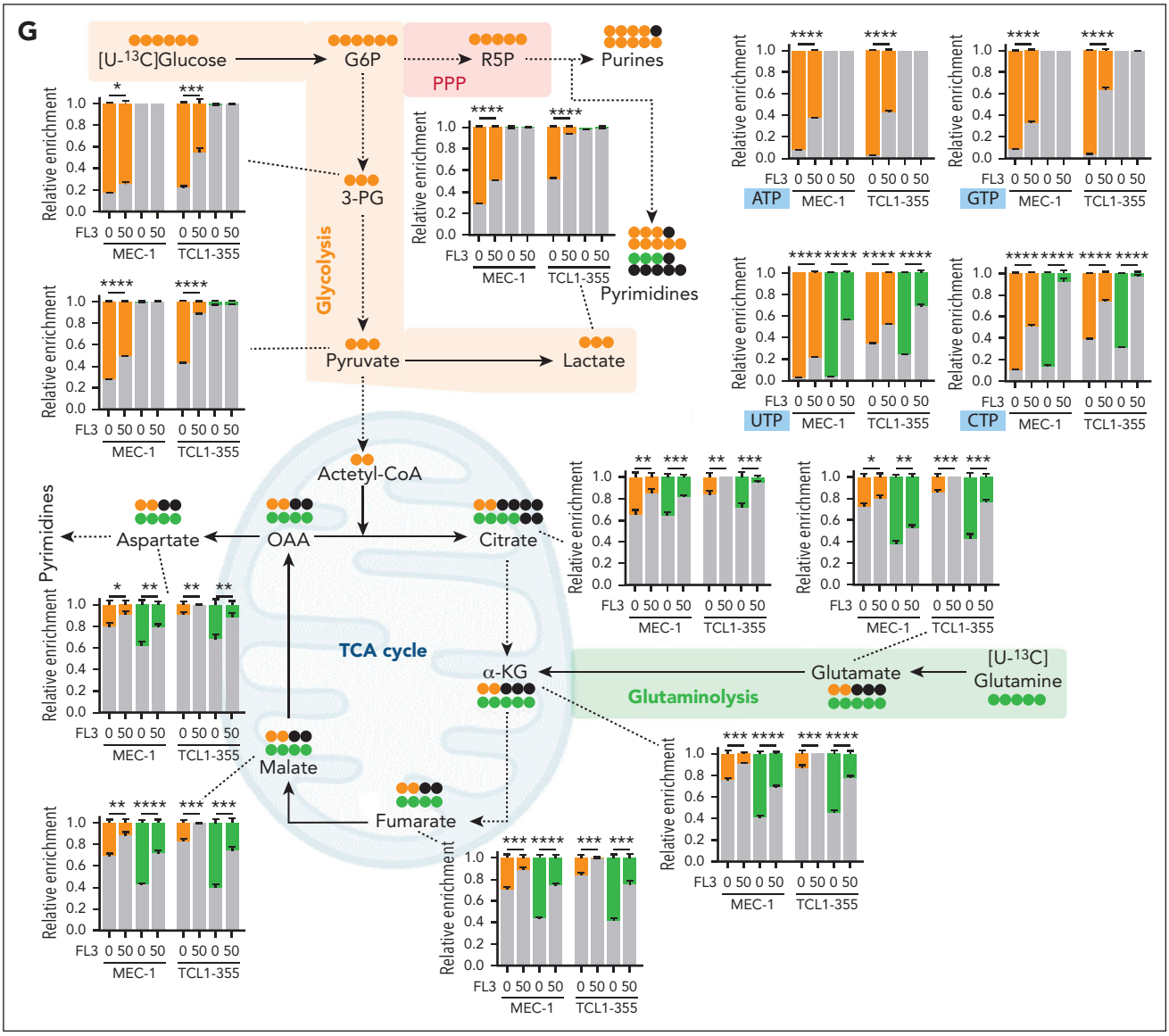


Figure 3 (continued)

Finally, we used the other flavaglines RocA and silvestrol, known to destabilize the eIF4F complex by binding to eIF4A. Both molecules decreased translation rate and cell proliferation, similar to FL3 treatment; however, they induced much higher rates of apoptosis (supplemental Figure 4V-X). In addition, they led to decreased phosphorylation of eIF4E, without affecting the RAF/ERK pathway (supplemental Figure 4Y), which is comparable with FL3 treatment. The similarity between FL3 and RocA/silvestrol confirms that FL3 also destabilizes the eIF4F complex but through binding to PHBs instead of eIF4A.

Silencing of PHBs inhibits translation and replicates the effects of FL3 treatment

The interaction of PHBs with the members of the translation initiation machinery strongly suggests a direct role of PHBs in translation. To validate this hypothesis, we knocked down (KD) PHBs using short hairpin RNA against either PHB or PHB2, as validated at the mRNA and protein levels (Figure 5A; supplemental Figure 5A-C). First, we investigated translation and protein interactions and we could confirm that PHBs KD decreased translation rate in CLL cells, reduced the formation of the eIF4E/eIF4G complex, and inhibited eIF4E phosphorylation (Figure 5B-C; supplemental Figure 5D-E). In addition, PHBs KD was associated with a decrease in cell growth and proliferation (Figure 5D-E), but not inducing cell death (supplemental Figure 5F). KD of PHBs was also associated with a decrease in MYC expression and activity (Figure 5F; supplemental Figure 5G). Finally, we repeated the targeted metabolomics analysis with glucose or glutamine tracing in PHBs KD cells. We observed an impact of the KD similar to treatment with FL3, as exemplified by a reduction in glycolysis and the tricarboxylic acid cycle, a decreased synthesis of purines and pyrimidines (Figure 5G), and an accumulation of proteinogenic amino acid (supplemental Figure 5H). In conclusion, KD of PHBs replicated all the effects observed with FL3. Altogether, using different experimental strategies, we demonstrated, to the best of our kowledge, for the first time, a direct role for PHBs in translation.

Downloaded from http://ashpublications.org/blood/article-pdf/141/26/3166/2060573/blood_bld-2022-017839-main.pdf by guest on 10 October 2023

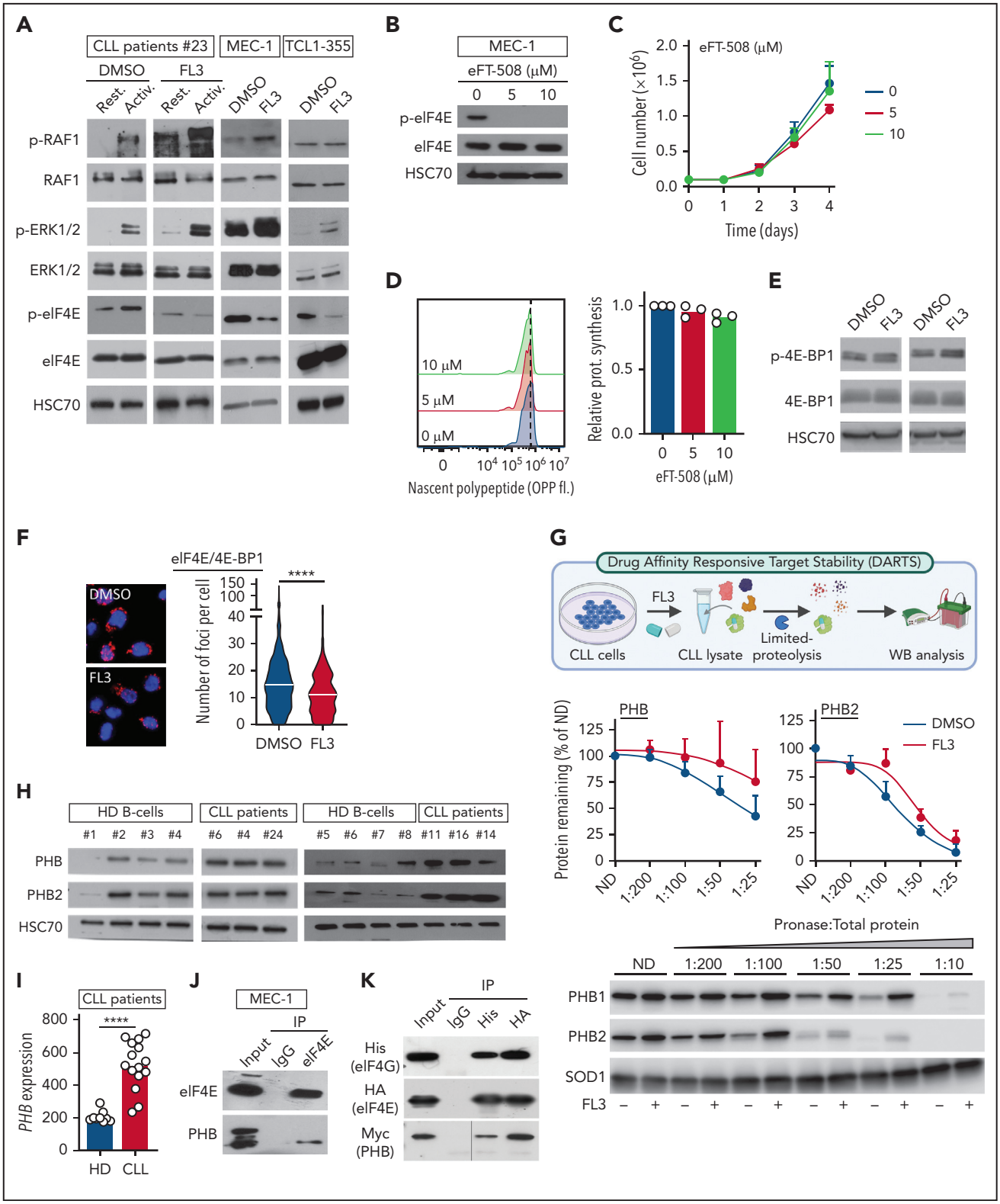


Figure 4. PHBs interact directly with the eIF4F translation initiation machinery, and FL3 binding disrupts this complex. (A) Western-blot analysis of p-RAF1, RAF1, p-ERK1/2, ERK1/2, p-eIF4E, and eIF4E proteins in patient CLL cells activated or not (resting) with anti-immunoglobulin M, and treated with DMSO or 100 nM FL3 for 3 hours, and MEC-1 and TCL1-355 cells treated with 50 nM FL3 for 3 hours. (B-D) MEC-1 cells treated with MNK1/2 inhibitor eFT-508 (0-10 μM) for 24 hours were analyzed by western blot for p-eIF4E and eIF4E levels (B), for proliferation (C), and protein synthesis (D, OPP assay), n = 3. (E-F) Western-blot analysis of p-4E-BP1 and 4E-BP1 (E) and PLA detection of eIF4E/4E-BP1 interaction (DMSO: 583 cells; FL3: 612 cells; n = 3) (F) in MEC-1 cells treated with DMSO or 50 nM FL3 for 3 hours. (G) Schematic representation of DARTS assay (upper panel). PHB and PHB2 stability in presence of pronase in MEC-1 cells treated with DMSO or 100 nM FL3 for 3 hours. Middle panels: % of PHB or PHB2 remaining at different concentrations of pronase, n = 3; lower panel: representative western blot. (H) Western-blot analysis of PHB and PHB2 proteins in HDs and patient CLL cells. (I) PHB gene expression in HD B cells vs CLL cells from patients with CLL (GSE67640 data set). (J) Western-blot analysis of eIF4E and PHB proteins after immunoprecipitation of eIF4E

Downloaded from http://ashpublications.org/blood/article-pdf/141/26/3166/2060573/blood_bld-2022-017839-main.pdf by guest on 10 October 2023

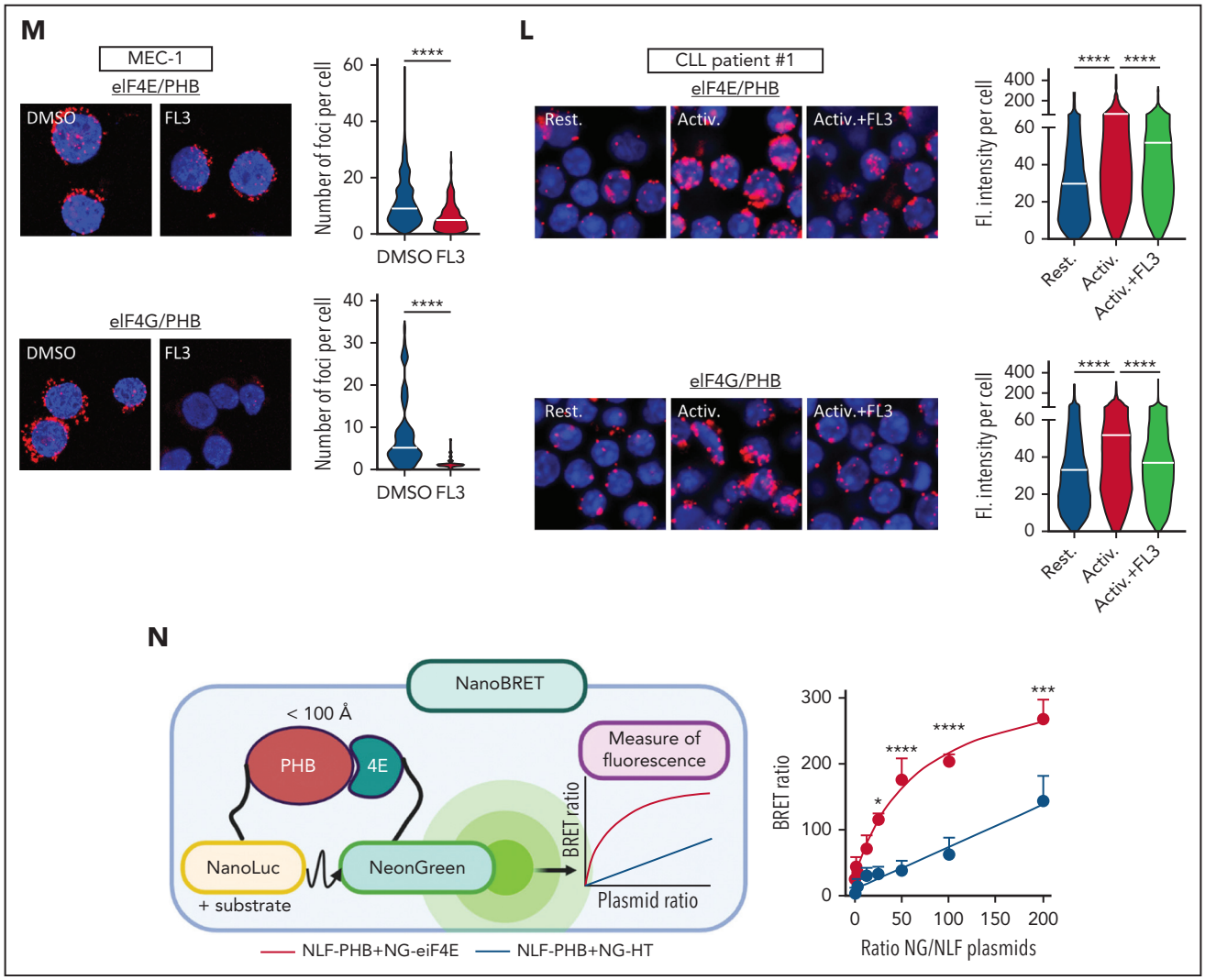


Figure 4 (continued) in MEC-1 cells. (K) Western-blot analysis of His-tag, HA-tag, and Myc-tag after immunoprecipitation of His-tag and HA-tag in HEK-293T cells over-expressing His-eIF4G, HA-eIF4E, and Myc-PHB. (L-M) PLA detection of eIF4E/PHB or eIF4G/PHB interactions in cells from patients with CLL that were activated or not with CpG ODN-2006 and treated with DMSO or 100 nM FL3 for 16 hours (K), and MEC-1 cells treated with 50 nM FL3 for 3 hours (left panel: representative image; right panel: quantification; L, upper: Rest.: 1147 cells, Activ.: 1223 cells, Activ+FL3: 1097 cells; L, lower: Rest.: 1297 cells, Activ.: 1195 cells, Activ+FL3: 1155 cells; M, upper: DMSO: 419 cells, FL3: 411; M, lower: DMSO: 53, FL3: 52; n = 3). (N) Schematic representation of NanoBRET assay and BRET ratio measured in HEK-293T cells transfected with increasing amounts of plasmids encoding PHBs fused with the nanoluciferase (NLF) and either eIF4E or HT fused with the NG. *P < .05, ***P < .001, ****P < .0001. ND, not digested.

FL3 alone, or in combination with immunotherapy, controls CLL development in vivo

Next, we tested the efficiency of translation inhibition to control CLL development in vivo. For this, we performed adoptive transfer of Eμ-TCL1 splenocytes into C57BL/6 mice and treated recipient mice with FL3 or vehicle. The analysis of $CD19^+CD5^+$ CLL cells in the peripheral blood indicated that FL3 treatment significantly controlled the development of the disease (Figure 6A-B). This correlated with an increased survival of the mice (median survival of 62 days in FL3-treated mice vs 48 days in vehicle-treated mice, Figure 6C). In a second independent cohort, we analyzed the splenocytes after 15 days of treatment. The percentage of CLL cells in the spleen was again significantly decreased (Figure 5D), confirming the efficiency of FL3 to control CLL progression in vivo. FL3 treatment inhibited the translation rate in the CLL cells in vivo but had no effect on nonleukemic B cells ($CD19^+CD5^-$, Figure 6E). Interestingly, the high translation rate of Tregs was inhibited by FL3 treatment in vivo, whereas their percentage was significantly reduced (Figure 6D-E). In addition, CLL cells expressing high levels of the inhibitory immune checkpoint PD-L1 displayed a higher translation rate (Figure 6F). Finally, we observed that combining FL3 with anti–programmed cell death protein 1 (PD1) therapy resulted in a better outcome in vivo (Figure 6G-H). Altogether, these data indicate that FL3 is effective in vivo by targeting the malignant cells, but also probably by removing the brakes on cell-mediated antitumor immunity.

Expression of translation-related genes correlates with disease progression and poor survival in patients with CLL

To validate the importance of translation in CLL, we quantified the expression of 6 genes from the translation-initiation machinery (*eIF4E1*, *eIF4E2*, *eIF4G1*, *eIF4G2*, *eIF4A1*, and *eIF4A2*) along with *PHB* and *PHB2* by reverse transcription quantitative polymerase chain reaction in a cohort of patients

Downloaded from http://ashpublications.org/blood/article-pdf/141/26/3166/2060573/blood_bld-2022-017839-main.pdf by guest on 10 October 2023

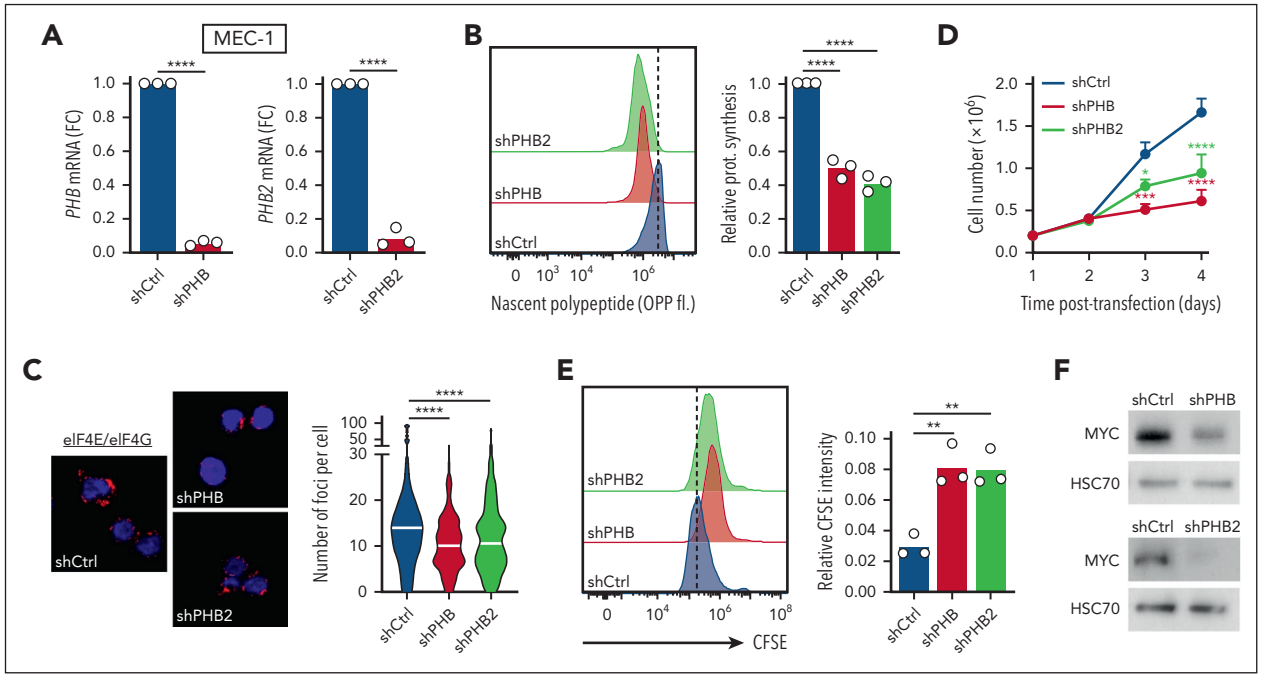


Figure 5. Silencing of PHBs inhibits translation and replicates the effects of FL3 treatment. MEC-1 cells were transfected with plasmids encoding short hairpin RNA (shRNA) against Scramble (shCtrl), PHB (shPHB), and PHB2 (shPHB2) and analyzed 72 to 96 hours after transfection. (A) Gene expression measured by qRT-PCR (72 hours, n = 3). (B) Determination of translation rate (OPP assay, 72 hours, n = 3). (C) PLA detection of eIF4E/eIF4G interaction (72 hours; shCtrl: 117 cells; shPHB: 127 cells; and shPHB2: 92 cells; n = 3). (D) Growth of cells up to 96 hours after transfection (n = 4). (E) Determination of proliferation (carboxyfluorescein succinimidyl ester assay, 96 hours, n = 3). (F) Western-blot analysis of MYC protein (72 hours). (G) Metabolomic isotopologue analysis of cells (72 hours, tracers incubated after 48 hours) in the presence of [U-^{13}C]-glucose (orange) and [U-^{13}C]-glutamine (green). Relative metabolic fluxes are indicated with gray for the unlabeled fraction, in orange or green for the labeled fractions. *P < .05, **P < .01, ***P < .001, ****P < .0001.

with CLL (N = 144). First, using Cox regression analysis, we identified *eIF4E2* and *eIF4G2* expression as predictors of OS (hazard ratio [HR] >1 and P value <.05), a high expression was related with poor OS (Figure 7A-B, median survival of 174 vs 397 months, supplemental Figure 6A). When combining these genes, the 8-gene translation signature was also linked to OS (Figure 7C) and higher HRs were obtained when combining 2 genes (Figure 7D, HR >1.5). We made similar observations when analyzing the TFS. We identified that *eIF4G2, eIF4E2, eIF4A1*, and *PHB2* transcript expression, as well as the translation gene signature and multiple gene combinations, was related with TFS in these patients (Figure 7E-F; supplemental Figure 6B-D). We then analyzed the expression of single or multiple genes in groups of patients segregated by the classical prognostic parameters. Single-gene analysis confirmed the increased expression of *eIF4E1, eIF4E2, eIF4G1, eIF4G2, PHB*, and *PHB2* in unfavorable groups (eg, ZAP70$^+$ vs ZAP70$^-$) and subgroups (eg, IGHV$_M$ LPL$^+$ vs IGHV$_{UM}$ LPL$^-$) (Figure 7G; supplemental Figure 6E), whereas logistic regression identified differentially expressed gene signatures (supplemental Figure 6F). Within groups of patients, the level of expression of *eIF4E2* was linked to OS and TFS (Figure 7H-I; supplemental Figure 6G). Altogether, our data confirmed the relevance of translation in CLL because the expression of selected genes is related to survival and clinical parameters.

Discussion

Although often overlooked in favor of transcriptional alterations, the relevance of translation defects in cancer has been long established. Such importance can be illustrated by the tight association between ribosomopathies and cancer susceptibility.[39] In addition, increased expression of several translation initiation factors has been described in a large variety of neoplasms.[11] This overexpression can be associated with either overall increase in translation or with alteration of specific mRNA translation. Here, we showed through gene expression analysis, that translation-related genes are upregulated in leukemic B cells compared with healthy B cells, in both humans and mice, which correlate with a higher translation rate observed in CLL cells. In addition to patient samples, Epstein-Barr virus–infected human cell lines[40] were used in this study for functional and gene expression studies. Being aware that they might not fully represent CLL cells, we validated all key experiments with patient samples and with the new murine cell line TCL1-355. This corroborates the interest of targeting translation in this neoplasm. Activation signals converge to upregulation of translation, and inhibiting this common end point appears to be more promising compared with targeting different pathways independently. In addition, oncogenes are more susceptible to dysregulation of translation, owing to the complex 5′ structure found in the mRNAs of these genes. Our multiomics analysis demonstrated that translation inhibition affects the translation of the oncogene MYC, which is associated with decreased proliferation capacity and a switch in metabolism. Thus, inhibiting translation allows targeting the leukemic process at different levels. MYC translation is highly regulated at the translational level[10,41] and previous studies demonstrated that eIF4A inhibition targets MYC translation in CLL.[22,42] Here, we show that targeting translation through PHB leads to a similar effect. In addition, we demonstrated that MYC inhibition is responsible for major metabolism reprogramming.

Downloaded from http://ashpublications.org/blood/article-pdf/141/26/3166/2060573/blood_bld-2022-017839-main.pdf by guest on 10 October 2023

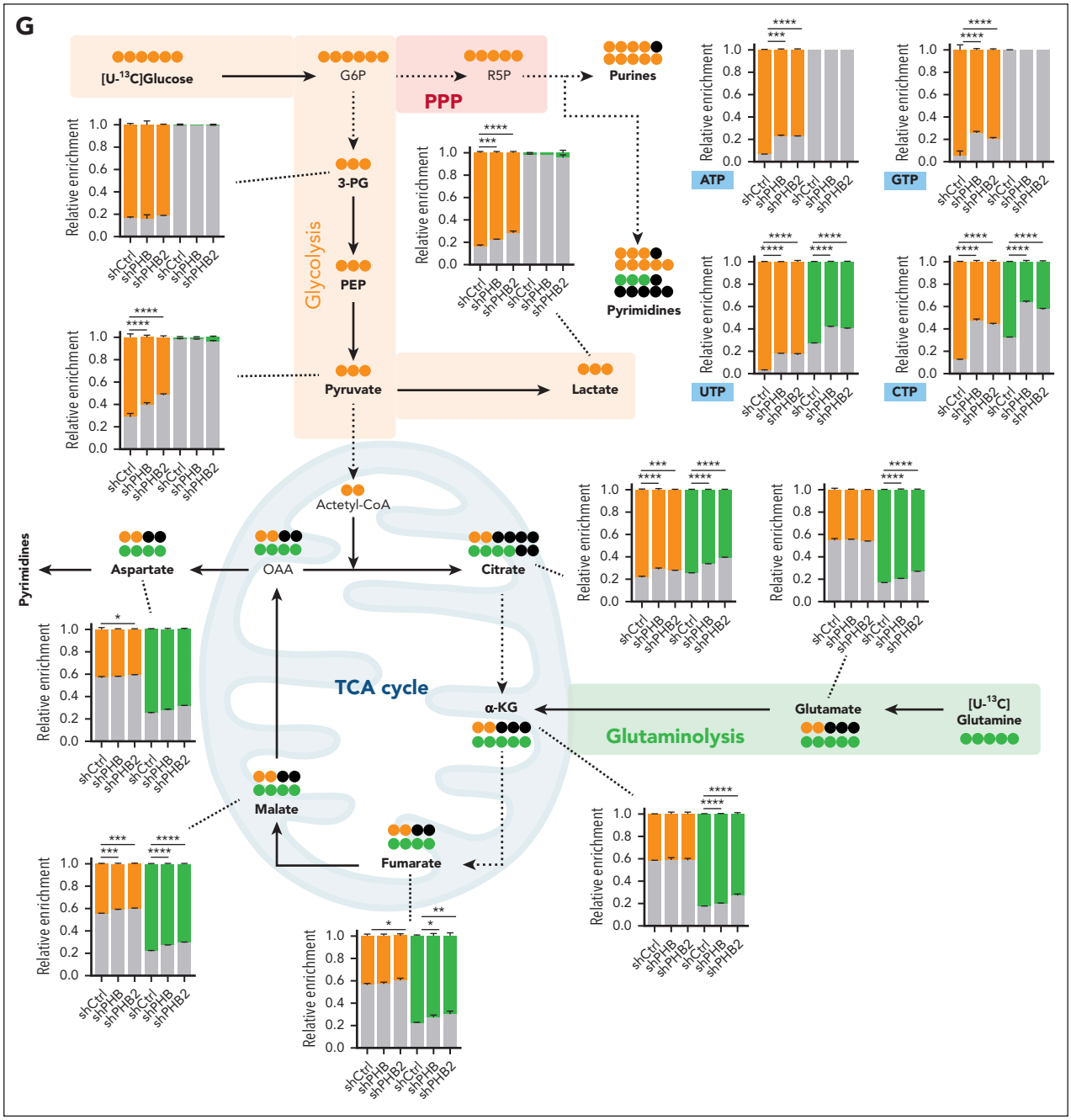


Figure 5 (continued)

The exact mechanism of action of flavaglines is still under debate. Surprisingly, despite having biological effects in the nanomolar concentration range, the mechanistic studies on flavagline molecules are often conducted in the micromolar concentration range, thus one must be careful when interpreting the data, because increased doses of the drug often lead to off-target effects. The known targets of flavaglines are PHBs,[26,43] eIF4A,[26,44] and DDX3.[19] By binding to eIF4A, flavaglines stimulate the RNA-binding function of eIF4A, which prevents RNA/eIF4A dissociation, and therefore incorporation of free eIF4A in a new eIF4F complex.[23,45] Through targeting of PHBs, FL3 was believed to act on translation indirectly, through the inhibition of the RAS-RAF-MAPK pathway, ultimately leading to decrease eIF4E phosphorylation.[27,34,43,46,47] By using DARTS analysis, we proved that FL3 targets PHBs in CLL cells. In addition, this study demonstrates that FL3 treatment is not associated with decreased phosphorylation of RAF1 and ERK1/2 in CLL cells. We also showed that in any case the level of eIF4E phosphorylation (downstream of RAF1/ERK signaling) does not account for translation rate or cell proliferation. This might be seen as a contradiction to some reports on the role of eIF4E phosphorylation in cancer[48-50]; nevertheless, elegant work has demonstrated that defects in eIF4E phosphorylation are not associated with impaired translation nor cell growth.[51] The decreased eIF4E phosphorylation rather reflects the dissociation of the translation initiation machinery. Indeed,

Downloaded from http://ashpublications.org/blood/article-pdf/141/26/3166/2060573/blood_bld-2022-017839-main.pdf by guest on 10 October 2023

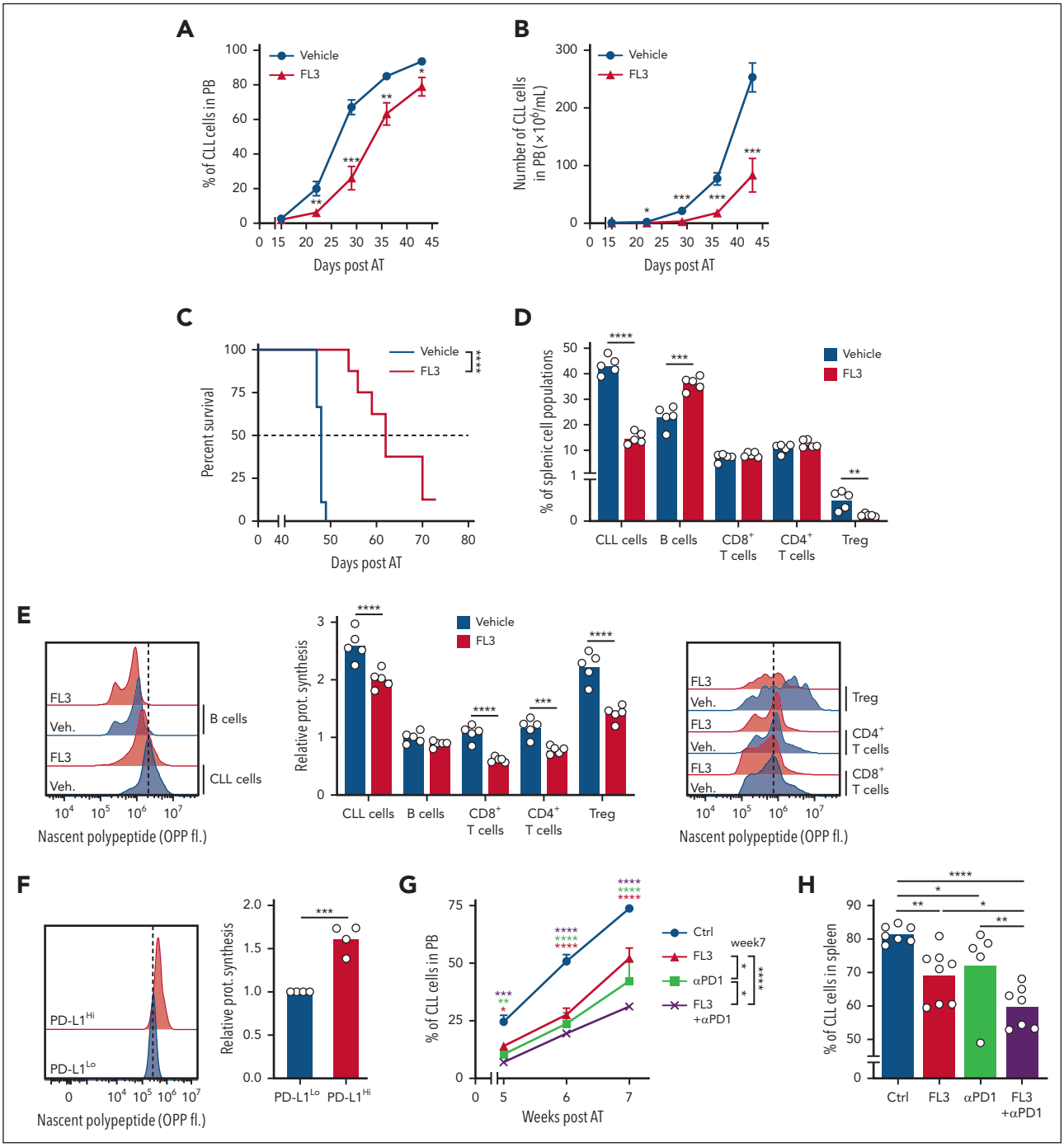


Figure 6. FL3 alone, or in combination with immunotherapy, controls CLL development in vivo. (A-B) Percentage (A) and number (B) of $CD19^+CD5^+$ CLL cells in the peripheral blood (PB) of C57BL/6 mice after adoptive transfer of splenocytes from a sick Eμ-TCL1 mouse, and treated with vehicle (n = 9) or FL3 (n = 8). (C) Survival of mice from panels A-B. (D) Percentage of CLL cells ($CD19^+CD5^+$), B cells ($CD19^+CD5^-$), $CD8^+$ T cells ($CD3^+CD8^+$), $CD4^+$ T cells ($CD3^+CD4^+$), and Tregs ($CD4^+FOXP3^+$) in the spleen of mice treated with vehicle or FL3, 17 days after adoptive transfer of splenocytes from a sick Eμ-TCL1 mouse (n = 5). (E) Determination of the translation rate in cells from panel D. (F) Determination of the translation rate in PD-$L1^{high}$ or PD-$L1^{low}$ $CD19^+CD5^+$ CLL cells from the spleen of C57BL/6 mice after TCL1 adoptive transfer (n = 4). (G-H) Percentage of CLL cells in the blood at the indicated time points (G) and the spleen at euthanasia (H) of C57BL/6 mice after adoptive transfer of splenocytes from a sick Eμ-TCL1 mouse, and treated with vehicle, FL3, anti-PD1 antibody, or the combination FL3/anti-PD1. *P < .05, **P < .01, ***P < .001, ****P < .0001.

eIF4E-eIF4G interaction is crucial for MNKs-driven eIF4E phosphorylation.[52] Furthermore, we showed that 4E-BP1 is also not affected in FL3-treated cells, demonstrating that the effect of FL3 on translation does not involve upstream pathways.

Therefore, we hypothesized that PHBs are directly involved in translation. We used different approaches to demonstrate the interaction of PHBs with the eIF4F complex. Then, by using short hairpin RNA, we showed that KD of PHBs mirror FL3 treatment. This discovery represents an important breakthrough that provides key

Downloaded from http://ashpublications.org/blood/article-pdf/141/26/3166/2060573/blood_bld-2022-017839-main.pdf by guest on 10 October 2023

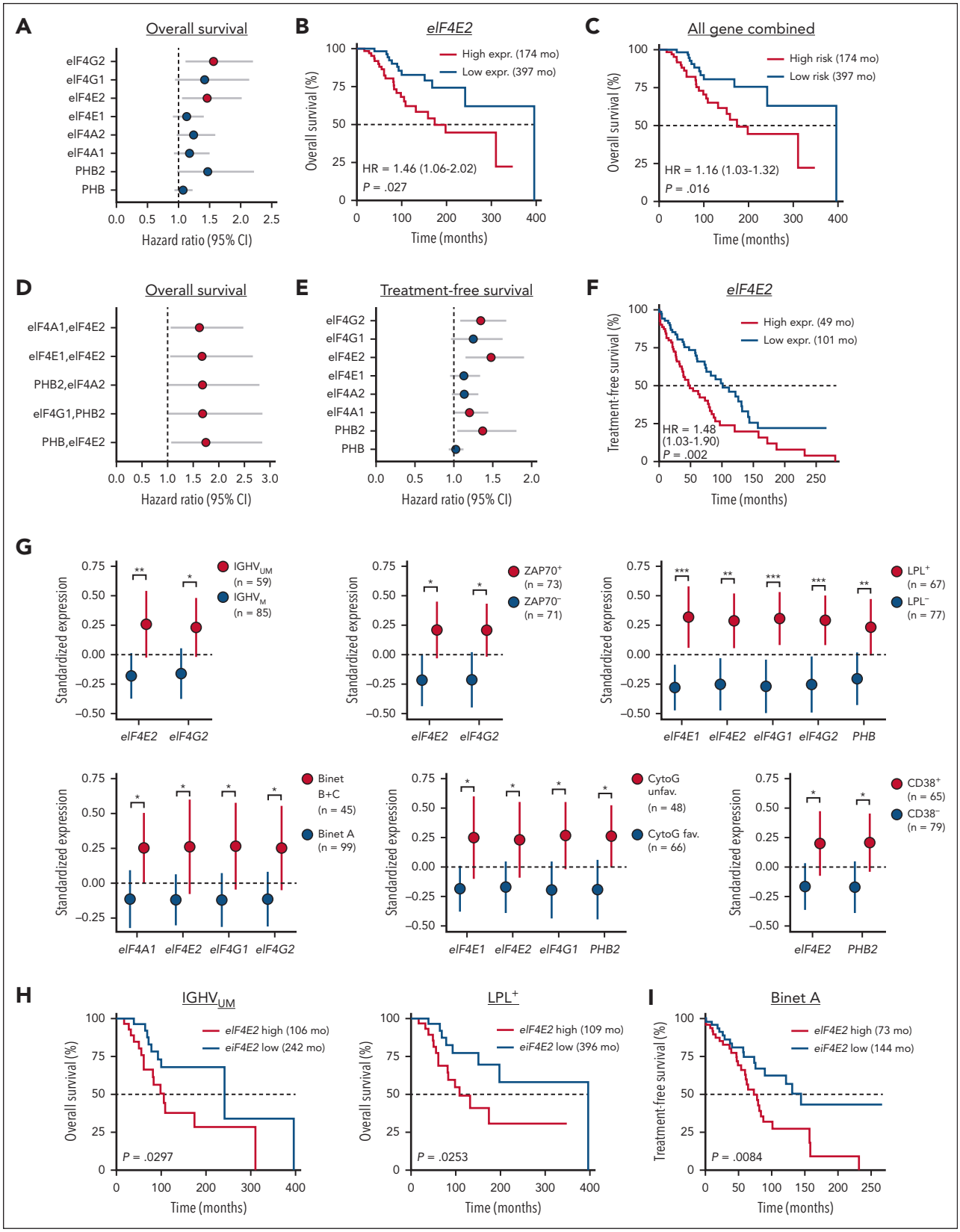


Figure 7. Expression of translation-related genes correlates with disease progression and poor survival in patients with CLL. Gene expression analysis was performed by qRT-PCR for 8 genes involved in translation in a cohort of 144 patients with CLL. The relationship between gene expression and survival was evaluated by Cox univariate regression analysis. Gene expression in clinical groups was evaluated by differential expression analysis for single genes or by logistic regression (LR) analysis for multiple genes. (A,E) Calculated HRs >1 (red dots, *P* value <.05) indicate an increased risk for patients with high single-gene expression in term of OS (A) and TFS (E). (B,F) Relation between high or low *eIF4E2* gene expression and OS (B) or TFS (F). Low and high groups are of identical size (n = 72). (C) Relationship between high or low combined 8-gene expression and OS. (D) Calculated HRs >1 (red dots, *P* value <.05) indicate an increased risk for patients with high multiple gene expression in term of OS. (G) Standardized expression of single genes in groups of patients based on prognostic markers (CytoG unfav.: cytogenetics unfavorable; group size indicated in each panel). (H-I) Relation between high or low *eIF4E2* gene expression and OS in patients with $IGHV_{UM}$ or LPL^+ CLL (H), and TFS in patients with Binet A CLL (I). **P* < .05, ***P* < .01, ****P* < .001.

Downloaded from http://ashpublications.org/blood/article-pdf/141/26/3166/2060573/blood_bld-2022-017839-main.pdf by guest on 10 October 2023

biological insights necessary to understand both PHB biology and PHB-targeting drugs. However, many questions remain open. Future work must determine whether the interaction between PHBs and the eIF4F machinery is limited to CLL cells, what factors govern this interaction, and how FL3 impairs it. Finally, whether PHBs are general players in translation or limited to certain circumstances (eg, oncogenic process or hypoxia) remains to be elucidated.

We showed that CLL cells and Tregs have a higher translation rate in vivo compared with normal B cells and conventional $CD4^+$ T cells, respectively. Moreover, inhibition of translation led to an efficient control of the disease after adoptive transfer of Eμ-TCL1 diseased splenocytes. In FL3-treated mice, we observed a decrease in translation rate in the leukemic cells and in $CD8^+$ and $CD4^+$ T lymphocytes and Tregs. Interestingly, the translation rate in nonleukemic B cells was not decreased by FL3 treatment. In addition, only CLL cells and Tregs were negatively affected by translation inhibition, indicating a specific effect of the drug. We recently demonstrated the crucial role of Tregs in the development of CLL,[53,54] thus the possibility to target both CLL cells and Tregs appears promising for the therapeutic potential of translation inhibition in CLL. Interestingly, Tregs rely on a noncanonical translation initiation machinery[55] and on the ribosome biogenesis factor Nocl4,[56] suggesting that FL3 might also be able to target specific translation mechanisms that do not use the canonical factors. In addition, we demonstrated that FL3 treatment in combination with immunotherapies targeting PD1 is more efficient than single therapies. Future studies should compare the advantage of inhibiting translation relative to current treatments. As translation is the nexus of resistance to several therapies,[13] the possibility to combine inhibition of translation with standard of care in CLL represents a promising approach, particularly in a malignancy characterized by relapse and refractory disease.

In conclusion, we have highlighted the importance of the deregulation of translation in CLL, unveiled a direct role of PHBs in translation, and demonstrated that translation inhibition is efficient in controlling CLL development in a preclinical model. We also found a correlation between translation-related/PHB gene expression, prognostic markers, and survival in a cohort of patients with CLL. Current therapies targeting downstream of the BCR constituted a major advance in the standard of care in CLL. However, resistance to these therapies remains an important pitfall. The identification of translation as a novel therapeutic target could be key to establishing effective therapeutic strategies for patients with CLL who are at high risk.

Acknowledgments

The authors thank Carlo Croce and John Byrd (Ohio State University, US) for the kind gift of Eμ-TCL1 mouse and the OSU-CLL cell line. The authors also thank the National Cytometry Platform (LIH; Antonio Cosma, Céline Hoffmann, Thomas Cerutti, Fanny Hedin, Mario Gomez) for assistance in flow cytometry and confocal microscopy, the bioinformatics platform (LIH; Reka Toth) for assistance, and the animal facility (LIH) staff, particularly Anais Oudin and Coralie Pulido; the Metabolomics Platform (LIH, Antoine Lesur, François Bernardin) for liquid chromatography mass spectrometry measurements and for providing technical and analytical support; the LUXGEN platform (LIH/LNS; Nathalie Nicot, Pol Hoffmann, Arnaud Muller and Daniel Stieber) for RNA sequencing; and the GIGA genomics facility. The authors also thank Nadia Beaupain, Jean-Marc Plesseria, and Manuel Counson from the Immuno-Pharmacology and Interactomics group (LIH) for their help in the NanoBRET experiments; Vincent Schlesser, Sigrid De Wilde, Laurent Plawny, and Sebastien Rinaldetti from the Centre Hospitalier du Luxembourg for their help in sample collection; and Titiksha Basu, Jil Delmarque, Olinda Pinto, Carmen Lahr, and Audrey Kopp for technical support. Finally, the authors thank Maxmilan Jeyakumar (LIH) for proofreading the manuscript.

This work was supported by grants from the Luxembourg National Research Fund (FNR) and Fondation Cancer to V.K., E.G., C.D., E.M., and J.P. (PRIDE19/14254520/i2TRON, PRIDE15/10675146/CANBIO, PRIDE21/16763386, C20/BM/14582635, and C20/BM/14592342); to A.C. and M.S. (INTER/FNRS/20/15084569); and to J.M. (ATTRACT grant A18/BM/11809970); from FNRS-Télévie to A.L. (7.4502.17, 7.4503.19), E.V. (7.4509.20, 7.4572.22), S.G. (7.4502.19, 7.6604.21), G.P. (7.4501.18, 7.6518.20), I.F.B. (7.4529.19, 7.6603.21), M.W. (7.4508.16, 7.6504.18), A.C. and M.S. (7.8508.22, 7.8504.20 and 7.4593.19); from the Plooschter Projet to J.P. and E.M.; from the Belgian Foundation for Cancer Research to P.C. (No 2020-068); and from the Swedish Children's Cancer Foundation (PR2021-003), the Swedish Research Council (2015-00162), and Swedish Cancer Society (21 1490) to T.H.

Authorship

Contribution: A.L. designed and performed experiments, analyzed results, and wrote the manuscript; V.K., E.V., S.G., I.F.B., S.P., C.D., M.W., E.G., and G.P. performed experiments and analyzed data; A.B., N.A., N.E.H., and P.C. performed L-propargylglycine assay, polysome profiling and analysis, and provided expertise on translation; P.M. and T.H. performed DARTS assay and analysis; D.P.H. and G.D. performed pulsed SILAC experiments and analysis; S.C. and D.G.E. provided materials and expertise; P.V.N. performed statistical analysis of gene expression data in patients with CLL; M.B. and J.M. performed metabolomics experiments and analyzed data; M.S. and A.C. performed BRET experiments and analyzed data; B.S. provided sample from patients with CLL, complementary DNA from cohort of patients with CLL, patients' data, and expertise for analyses; L.D. synthetized FL3 and provided his expertise on the molecule; L.Y., J.-H.F., S.C.C., and G.B., provided samples from patients with CLL, and expertise on hemato-oncology; E.M. and J.P. designed and supervised the study, performed bioinformatics analyses, analyzed results, and wrote the final version of the manuscript; and all authors revised the manuscript.

Conflict-of-interest disclosure: The authors declare no competing financial interests.

ORCID profiles: A.L., 0000-0002-9388-8461; V.K., 0000-0001-5507-1963; E.V., 0000-0002-1226-1473; A.B., 0000-0003-4183-8726; M.B., 0000-0002-6413-3983; C.D., 0000-0001-7643-0515; P.M., 0000-0002-0115-8067; E.G., 0000-0002-4485-4599; N.A., 0000-0001-9512-6869; N.E.H., 0000-0002-4180-3016; D.P.H., 0000-0003-0266-9050; G.B., 0000-0003-0157-2257; G.D., 0000-0003-3647-8623; M.S., 0000-0002-5659-8377; A.C., 0000-0003-4768-6743; P.V.N., 0000-0003-3443-0298; P.C., 0000-0002-8844-9616; J.M., 0000-0002-9093-6210; L.D., 0000-0002-1192-2970; J.P., 0000-0001-9460-5876; E.M., 0000-0002-0879-8067.

Correspondence: Etienne Moussay, Luxembourg Institute of Health, 6 rue Nicolas-Ernest Barblé, L-1210 Luxembourg, Luxembourg; email: etienne.moussay@lih.lu; and Jérôme Paggetti, Luxembourg Institute of Health, 6 rue Nicolas-Ernest Barblé, L-1210 Luxembourg, Luxembourg; email: jerome.paggetti@lih.lu.

Footnotes

Submitted 18 July 2022; accepted 5 March 2023; prepublished online on *Blood* First Edition 21 April 2023. https://doi.org/10.1182/blood.2022017839.

*E.V., S.G., I.F.B., A.B., and M.B. contributed equally to this study.

†J.P. and E.M. are joint senior authors.

RNA sequencing data may be found at the NCBI Gene Expression Omnibus database under the accession number GSE221880.

Downloaded from http://ashpublications.org/blood/article-pdf/141/26/3166/2060573/blood_bld-2022-017839-main.pdf by guest on 10 October 2023

Data are available on request from the corresponding authors, Etienne Moussay (etienne.moussay@lih.lu) and Jérôme Paggetti (jerome.paggetti@lih.lu).

The online version of this article contains a data supplement.

There is a *Blood* Commentary on this article in this issue.

The publication costs of this article were defrayed in part by page charge payment. Therefore, and solely to indicate this fact, this article is hereby marked "advertisement" in accordance with 18 USC section 1734.

REFERENCES

1. Burger JA, Chiorazzi N. B cell receptor signaling in chronic lymphocytic leukemia. *Trends Immunol*. 2013;34(12):592-601.
2. Dadashian EL, McAuley EM, Liu D, et al. TLR signaling is activated in lymph node-resident CLL cells and is only partially inhibited by ibrutinib. *Cancer Res*. 2019;79(2):360-371.
3. Brown JR. How I treat CLL patients with ibrutinib. *Blood*. 2018;131(4):379-386.
4. Filip D, Mraz M. The role of MYC in the transformation and aggressiveness of 'indolent' B-cell malignancies. *Leuk Lymphoma*. 2020;61(3):510-524.
5. Moussay E, Palissot V, Vallar L, et al. Determination of genes and microRNAs involved in the resistance to fludarabine in vivo in chronic lymphocytic leukemia. *Mol Cancer*. 2010;9:115.
6. Nguyen-Khac F. "Double-hit" chronic lymphocytic leukemia, involving the TP53 and MYC genes. *Front Oncol*. 2021;11:826245.
7. Chen Z, Simon-Molas H, Cretenet G, et al. Characterization of metabolic alterations of chronic lymphocytic leukemia in the lymph node microenvironment. *Blood*. 2022;140(6):630-643.
8. Herishanu Y, Perez-Galan P, Liu D, et al. The lymph node microenvironment promotes B-cell receptor signaling, NF-kappaB activation, and tumor proliferation in chronic lymphocytic leukemia. *Blood*. 2011;117(2):563-574.
9. Krysov S, Dias S, Paterson A, et al. Surface IgM stimulation induces MEK1/2-dependent MYC expression in chronic lymphocytic leukemia cells. *Blood*. 2012;119(1):170-179.
10. Yeomans A, Thirdborough SM, Valle-Argos B, et al. Engagement of the B-cell receptor of chronic lymphocytic leukemia cells drives global and MYC-specific mRNA translation. *Blood*. 2016;127(4):449-457.
11. Ruggero D. Translational control in cancer etiology. *Cold Spring Harb Perspect Biol*. 2013;5(2):a012336.
12. Silvera D, Formenti SC, Schneider RJ. Translational control in cancer. *Nat Rev Cancer*. 2010;10(4):254-266.
13. Boussemart L, Malka-Mahieu H, Girault I, et al. eIF4F is a nexus of resistance to anti-BRAF and anti-MEK cancer therapies. *Nature*. 2014;513(7516):105-109.
14. Bretones G, Alvarez MG, Arango JR, et al. Altered patterns of global protein synthesis and translational fidelity in RPS15-mutated chronic lymphocytic leukemia. *Blood*. 2018;132(22):2375-2388.
15. Ljungstrom V, Cortese D, Young E, et al. Whole-exome sequencing in relapsing chronic lymphocytic leukemia: clinical impact of recurrent RPS15 mutations. *Blood*. 2016;127(8):1007-1016.
16. Ntoufa S, Gerousi M, Laidou S, et al. RPS15 mutations rewire RNA translation in chronic lymphocytic leukemia. *Blood Adv*. 2021;5(13):2788-2792.
17. Sbarrato T, Horvilleur E, Poyry T, et al. A ribosome-related signature in peripheral blood CLL B cells is linked to reduced survival following treatment. *Cell Death Dis*. 2016;7(6):e2249.
18. Paggetti J, Moussay E. BCR engagement in CLL: when translation goes wrong. *Blood*. 2016;127(4):378-380.
19. Chen M, Asanuma M, Takahashi M, et al. Dual targeting of DDX3 and eIF4A by the translation inhibitor rocaglamide A. *Cell Chem Biol*. 2021;28(4):475-486.e8.
20. Chen J, Sathiaseelan V, Moore A, et al. ZAP-70 constitutively regulates gene expression and protein synthesis in chronic lymphocytic leukemia. *Blood*. 2021;137(26):3629-3640.
21. Willimott S, Beck D, Ahearne MJ, Adams VC, Wagner SD. Cap-translation inhibitor, 4EGI-1, restores sensitivity to ABT-737 apoptosis through cap-dependent and -independent mechanisms in chronic lymphocytic leukemia. *Clin Cancer Res*. 2013;19(12):3212-3223.
22. Wilmore S, Rogers-Broadway KR, Taylor J, et al. Targeted inhibition of eIF4A suppresses B-cell receptor-induced translation and expression of MYC and MCL1 in chronic lymphocytic leukemia cells. *Cell Mol Life Sci*. 2021;78(17-18):6337-6349.
23. Cencic R, Carrier M, Galicia-Vazquez G, et al. Antitumor activity and mechanism of action of the cyclopenta[b]benzofuran, silvestrol. *PLoS One*. 2009;4(4):e5223.
24. Jackson DN, Alula KM, Delgado-Deida Y, et al. The synthetic small molecule FL3 combats intestinal tumorigenesis via Axin1-mediated inhibition of Wnt/beta-catenin signaling. *Cancer Res*. 2020;80(17):3519-3529.
25. Basmadjian C, Thuaud F, Ribeiro N, Desaubry L. Flavaglines: potent anticancer drugs that target prohibitins and the helicase eIF4A. *Future Med Chem*. 2013;5(18):2185-2197.
26. Nebigil CG, Moog C, Vagner S, Benkirane-Jessel N, Smith DR, Desaubry L. Flavaglines as natural products targeting eIF4A and prohibitins: from traditional Chinese medicine to antiviral activity against coronaviruses. *Eur J Med Chem*. 2020;203:112653.
27. Rajalingam K, Rudel T. Ras-Raf signaling needs prohibitin. *Cell Cycle*. 2005;4(11):1503-1505.
28. Thuaud F, Ribeiro N, Nebigil CG, Desaubry L. Prohibitin ligands in cell death and survival: mode of action and therapeutic potential. *Chem Biol*. 2013;20(3):316-331.
29. Bichi R, Shinton SA, Martin ES, et al. Human chronic lymphocytic leukemia modeled in mouse by targeted TCL1 expression. *Proc Natl Acad Sci U S A*. 2002;99(10):6955-6960.
30. Chakraborty S, Martines C, Porro F, et al. B-cell receptor signaling and genetic lesions in TP53 and CDKN2A/CDKN2B cooperate in Richter transformation. *Blood*. 2021;138(12):1053-1066.
31. Ho JJD, Cunningham TA, Manara P, et al. Proteomics reveal cap-dependent translation inhibitors remodel the translation machinery and translatome. *Cell Rep*. 2021;37(2):109806.
32. Tambay V, Raymond VA, Bilodeau M. MYC rules: leading glutamine metabolism toward a distinct cancer cell phenotype. *Cancers*. 2021;13(17):4484.
33. Wise DR, DeBerardinis RJ, Mancuso A, et al. Myc regulates a transcriptional program that stimulates mitochondrial glutaminolysis and leads to glutamine addiction. *Proc Natl Acad Sci U S A*. 2008;105(48):18782-18787.
34. Rajalingam K, Wunder C, Brinkmann V, et al. Prohibitin is required for Ras-induced Raf-MEK-ERK activation and epithelial cell migration. *Nat Cell Biol*. 2005;7(8):837-843.
35. Waskiewicz AJ, Flynn A, Proud CG, Cooper JA. Mitogen-activated protein kinases activate the serine/threonine kinases Mnk1 and Mnk2. *EMBO J*. 1997;16(8):1909-1920.
36. Avdulov S, Li S, Michalek V, et al. Activation of translation complex eIF4F is essential for the genesis and maintenance of the malignant phenotype in human mammary epithelial cells. *Cancer Cell*. 2004;5(6):553-563.
37. Yang M, Yao B, Lin R, Jin H. The translational regulation in mTOR pathway. *Biomolecules*. 2022;12(12):1790.
38. Iwasaki S, Iwasaki W, Takahashi M, et al. The translation inhibitor rocaglamide targets a bimolecular cavity between eIF4A and polypurine RNA. *Mol Cell*. 2019;73(4):738-748.e9.

Downloaded from http://ashpublications.org/blood/article-pdf/141/26/3166/2060573/blood_bld-2022-017839-main.pdf by guest on 10 October 2023

39. Kampen KR, Sulima SO, Vereecke S, De Keersmaecker K. Hallmarks of ribosomopathies. *Nucleic Acids Res*. 2020; 48(3):1013-1028.

40. Rasul E, Salamon D, Nagy N, et al. The MEC1 and MEC2 lines represent two CLL subclones in different stages of progression towards prolymphocytic leukemia. *PLoS One*. 2014; 9(8):e106008.

41. Wolfe AL, Singh K, Zhong Y, et al. RNA G-quadruplexes cause eIF4A-dependent oncogene translation in cancer. *Nature*. 2014; 513(7516):65-70.

42. Taylor J, Yeomans AM, Packham G. Targeted inhibition of mRNA translation initiation factors as a novel therapeutic strategy for mature B-cell neoplasms. *Explor Target Antitumor Ther*. 2020;1(1):3-25.

43. Polier G, Neumann J, Thuaud F, et al. The natural anticancer compounds rocaglamides inhibit the Raf-MEK-ERK pathway by targeting prohibitin 1 and 2. *Chem Biol*. 2012;19(9):1093-1104.

44. Sadlish H, Galicia-Vazquez G, Paris CG, et al. Evidence for a functionally relevant rocaglamide binding site on the eIF4A-RNA complex. *ACS Chem Biol*. 2013;8(7): 1519-1527.

45. Bordeleau ME, Robert F, Gerard B, et al. Therapeutic suppression of translation initiation modulates chemosensitivity in a mouse lymphoma model. *J Clin Invest*. 2008; 118(7):2651-2660.

46. Chiu CF, Ho MY, Peng JM, et al. Raf activation by Ras and promotion of cellular metastasis require phosphorylation of prohibitin in the raft domain of the plasma membrane. *Oncogene*. 2013;32(6): 777-787.

47. Mishra S, Ande SR, Nyomba BL. The role of prohibitin in cell signaling. *FEBS J*. 2010; 277(19):3937-3946.

48. Furic L, Rong L, Larsson O, et al. eIF4E phosphorylation promotes tumorigenesis and is associated with prostate cancer progression. *Proc Natl Acad Sci U S A*. 2010; 107(32):14134-14139.

49. Ueda T, Sasaki M, Elia AJ, et al. Combined deficiency for MAP kinase-interacting kinase 1 and 2 (Mnk1 and Mnk2) delays tumor development. *Proc Natl Acad Sci U S A*. 2010;107(32):13984-13990.

50. Wendel HG, Silva RL, Malina A, et al. Dissecting eIF4E action in tumorigenesis. *Genes Dev*. 2007;21(24):3232-3237.

51. Ueda T, Watanabe-Fukunaga R, Fukuyama H, Nagata S, Fukunaga R. Mnk2 and Mnk1 are essential for constitutive and inducible phosphorylation of eukaryotic initiation factor 4E but not for cell growth or development. *Mol Cell Biol*. 2004;24(15):6539-6549.

52. Shveygert M, Kaiser C, Bradrick SS, Gromeier M. Regulation of eukaryotic initiation factor 4E (eIF4E) phosphorylation by mitogen-activated protein kinase occurs through modulation of Mnk1-eIF4G interaction. *Mol Cell Biol*. 2010;30(21):5160-5167.

53. Wierz M, Janji B, Berchem G, Moussay E, Paggetti J. High-dimensional mass cytometry analysis revealed microenvironment complexity in chronic lymphocytic leukemia. *Oncoimmunology*. 2018;7(8):e1465167.

54. Wierz M, Pierson S, Guyonnet L, et al. Dual PD1/LAG3 immune checkpoint blockade limits tumor development in a murine model of chronic lymphocytic leukemia. *Blood*. 2018;131(14):1617-1621.

55. Volta V, Perez-Baos S, de la Parra C, et al. A DAP5/eIF3d alternate mRNA translation mechanism promotes differentiation and immune suppression by human regulatory T cells. *Nat Commun*. 2021;12(1):6979.

56. Zhu X, Zhang W, Guo J, et al. Noc4L-mediated ribosome biogenesis controls activation of regulatory and conventional T cells. *Cell Rep*. 2019;27(4):1205-1220.e4.

© 2023 by The American Society of Hematology. Licensed under Creative Commons Attribution-NonCommercial-NoDerivatives 4.0 International (CC BY-NC-ND 4.0), permitting only noncommercial, nonderivative use with attribution. All other rights reserved.

Downloaded from http://ashpublications.org/blood/article-pdf/141/26/3166/2060573/blood_bld-2022-017839-main.pdf by guest on 10 October 2023

Appendix 5: Pyruvate dehydrogenase fuels a critical citrate pool that is essential for Th17 cell effector functions

SORIANO-BAGUET, L., GRUSDAT, M., KURNIAWAN, H., **BENZARTI, M.**, BINSFELD, C., EWEN, A., LONGWORTH, J., BONETTI, L., GUERRA, L., FRANCHINA, D. G., KOBAYASHI, T., HORKOVA, V., VERSCHUEREN, C., HELGUETA, S., GÉRARD, D., MORE, T. H., HENNE, A., DOSTERT, C., FARINELLE, S., LESUR, A., GÉRARDY, J. J., JÄGER, C., MITTELBRONN, M., SINKKONEN, L., HILLER, K., MEISER, J. & BRENNER, D. 2023. Pyruvate dehydrogenase fuels a critical citrate pool that is essential for Th17 cell effector functions. ***Cell Reports***, 42, 112153.

DOI: https://doi.org/10.1016/j.celrep.2023.112153

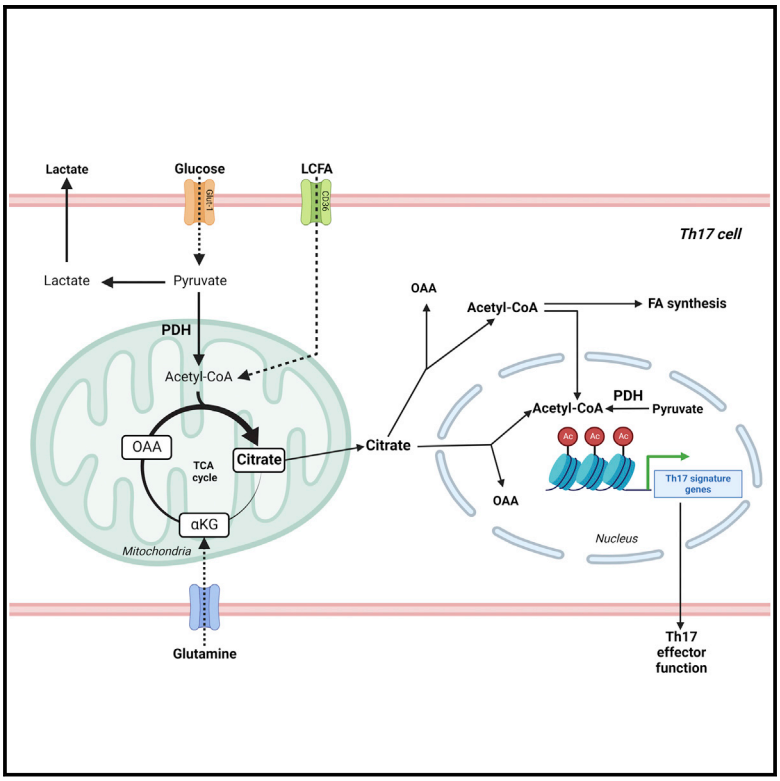
Personal contribution: The key finding of this paper is the importance of PDH in generating a specific pool of citrate which is crucial for the immune effector function of Th17 cells *in vitro* and immune regulatory function of $CD4^+$ T cell *in vivo*. I contributed to this research with the data presented in the following panels: **2C, 2H, 2J, 2K, 2L, 2M, 2N, 2O, 2P, 3A, 3B, 3C, 3D, 3E, 3K, 3L, 3M, 3N, 4A, 4B, 6A, 6B, 6C, 7C, 7D, 7F, 7G, 7L, S3A, S3B and S6C.** Here I helped in performing targeted metabolomics using several stable isotopic tracers and then I processed and analyzed the data generated from these experiments. The data generated served to metabolically profile the Th17 cells harboring the PDH deletion and mechanistically understand PDH importance in the function of Th17 cells. I also reviewed the manuscript prior to submission.

Cell Reports

Article

Pyruvate dehydrogenase fuels a critical citrate pool that is essential for Th17 cell effector functions

Graphical abstract



Highlights

- PDH-ablation in T cells lowers Th17 cell-mediated autoimmunity
- PDH is essential for the pathogenic function of Th17 cells and IL-17 production
- PDH fuels a citrate pool controlling glycolysis, glutaminolysis, and lipids
- PDH controls histone acetylation and Th17 cell gene transcription

Authors

Leticia Soriano-Baguet, Melanie Grusdat, Henry Kurniawan, ..., Karsten Hiller, Johannes Meiser, Dirk Brenner

Correspondence

dirk.brenner@lih.lu

In brief

Pyruvate dehydrogenase (PDH) connects glycolysis with the mitochondrial tricarboxylic acid (TCA) cycle. Soriano-Baguet et al. show that PDH directs a glucose-derived citrate pool that coordinates the central carbon metabolism and histone acetylation and is essential for Th17 cell function.

Soriano-Baguet et al., 2023, Cell Reports *42*, 112153
March 28, 2023 © 2023 The Author(s).
https://doi.org/10.1016/j.celrep.2023.112153

CellPress

Cell Reports

CellPress
OPEN ACCESS

Article

Pyruvate dehydrogenase fuels a critical citrate pool that is essential for Th17 cell effector functions

Leticia Soriano-Baguet,[1,2] Melanie Grusdat,[1,2] Henry Kurniawan,[1,2] Mohaned Benzarti,[3,4] Carole Binsfeld,[1,2] Anouk Ewen,[1,2] Joseph Longworth,[1,2] Lynn Bonetti,[1,2] Luana Guerra,[1,2] Davide G. Franchina,[1,2] Takumi Kobayashi,[1,2] Veronika Horkova,[1,2] Charlène Verschueren,[1,2] Sergio Helgueta,[5,6] Deborah Gérard,[6] Tushar H. More,[7] Antonia Henne,[7] Catherine Dostert,[1,2] Sophie Farinelle,[1,2] Antoine Lesur,[8] Jean-Jacques Gérardy,[5,9] Christian Jäger,[10] Michel Mittelbronn,[4,5,9,10,11,12] Lasse Sinkkonen,[6] Karsten Hiller,[7] Johannes Meiser,[3,8] and Dirk Brenner[1,2,13,14,*]

[1]Experimental and Molecular Immunology, Department of Infection and Immunity, Luxembourg Institute of Health, Esch-sur-Alzette, Luxembourg

[2]Immunology and Genetics, Luxembourg Centre for Systems Biomedicine, University of Luxembourg, 7, Avenue des Hauts Fourneaux, Esch-sur-Alzette, Luxembourg

[3]Cancer Metabolism Group, Department of Cancer Research, Luxembourg Institute of Health, Luxembourg, Luxembourg

[4]Faculty of Science, Technology, and Medicine, University of Luxembourg, Esch-sur-Alzette, Luxembourg

[5]Luxembourg Center of Neuropathology, 3555 Dudelange, Luxembourg

[6]Epigenetics Team, Systems Biology Group, Department of Life Sciences and Medicine, University of Luxembourg, Belvaux, Luxembourg

[7]Department of Bioinformatics and Biochemistry, Braunschweig Integrated Center of Systems Biology, Technische Universität Braunschweig, Rebenring 56, 38106 Braunschweig, Germany

[8]Metabolomics Platform, Department of Cancer Research, Luxembourg Institute of Health, Luxembourg, Luxembourg

[9]National Center of Pathology, Laboratoire National de Santé (LNS), Dudelange, Luxembourg

[10]Luxembourg Center for Systems Biomedicine, University of Luxembourg, 4362 Esch-sur-Alzette, Luxembourg

[11]Department of Life Sciences and Medicine, University of Luxembourg, Esch-sur-Alzette, Luxembourg

[12]Department of Cancer Research, Luxembourg Institute of Health, 1526 Luxembourg, Luxembourg

[13]Odense Research Center for Anaphylaxis, Department of Dermatology and Allergy Center, Odense University Hospital, University of Southern Denmark, Odense, Denmark

[14]Lead contact

*Correspondence: dirk.brenner@lih.lu

https://doi.org/10.1016/j.celrep.2023.112153

SUMMARY

Pyruvate dehydrogenase (PDH) is the central enzyme connecting glycolysis and the tricarboxylic acid (TCA) cycle. The importance of PDH function in T helper 17 (Th17) cells still remains to be studied. Here, we show that PDH is essential for the generation of a glucose-derived citrate pool needed for Th17 cell proliferation, survival, and effector function. *In vivo*, mice harboring a T cell-specific deletion of PDH are less susceptible to developing experimental autoimmune encephalomyelitis. Mechanistically, the absence of PDH in Th17 cells increases glutaminolysis, glycolysis, and lipid uptake in a mammalian target of rapamycin (mTOR)-dependent manner. However, cellular citrate remains critically low in mutant Th17 cells, which interferes with oxidative phosphorylation (OXPHOS), lipid synthesis, and histone acetylation, crucial for transcription of Th17 signature genes. Increasing cellular citrate in PDH-deficient Th17 cells restores their metabolism and function, identifying a metabolic feedback loop within the central carbon metabolism that may offer possibilities for therapeutically targeting Th17 cell-driven autoimmunity.

INTRODUCTION

T cells are essential for adaptive immune responses, and T helper 17 (Th17) cells are the $CD4^+$ subset that protects the host against extracellular bacteria and fungi.[1] However, Th17 cells are also linked to autoimmune diseases such as multiple sclerosis and rheumatoid arthritis.[2,3] Th17 cells are defined by their expression of RORγT and the ability to produce interleukin-17 (IL-17).[3,4]

All T cells adapt their metabolism according to their energy demands.[5,6] Upon activation, $CD4^+$ T cells switch from mitochondrial metabolism (i.e., the tricarboxylic acid [TCA] cycle, oxidative phosphorylation [OXPHOS], and fatty acid β-oxidation) to glycolysis and glutaminolysis to generate ATP and biosynthetic precursors, a process dubbed "metabolic reprogramming." This metabolic rewiring then supports the molecular signaling needed for T cell proliferation and effector functions.[7–10] However, each Th cell subset shows features during

This is an open access article under the CC BY license (http://creativecommons.org/licenses/by/4.0/).

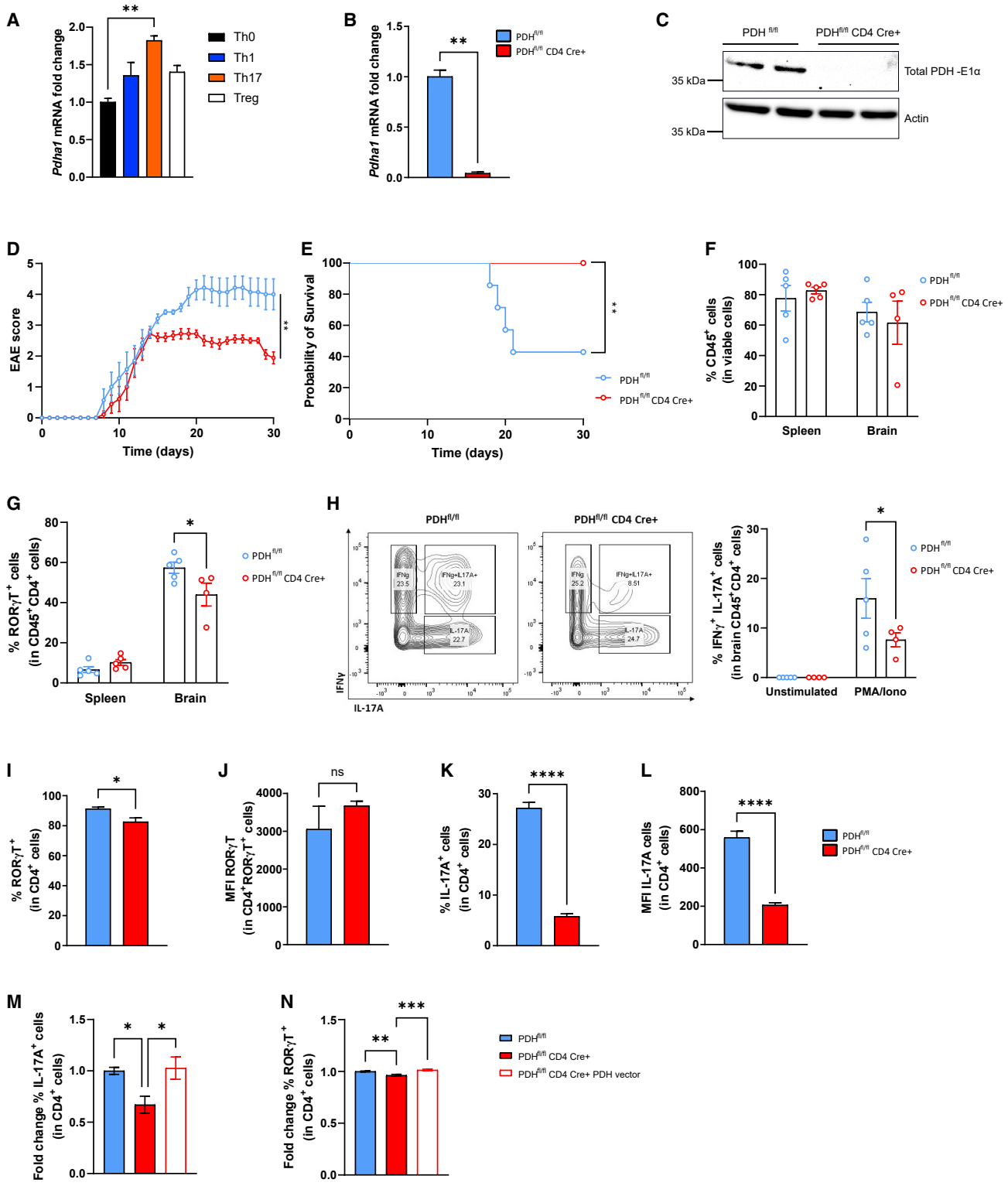


Figure 1. *Pdh* ablation in T cells protects mice from severe EAE and impairs IL-17 production

(A) qPCR determination of fold change in *Pdha1* mRNA levels in the indicated wild-type (WT) T cell subsets that were induced to differentiate *in vitro* as described in STAR Methods. ΔΔCt values were normalized to Tbp expression. Data are mean ± SEM (n = 3) and representative of 2 trials.

(B) qPCR determination as in (A) of *Pdha1* mRNA levels in total CD4$^+$ T cells that were isolated from spleen and lymph nodes of control (PDH$^{fl/fl}$) and PDH-deficient (PDH$^{fl/fl}$CD4 Cre+) mice and activated *in vitro* for 24 h with anti-CD3/anti-CD28 antibodies. Data are mean ± SEM (n = 3) and representative of 2 trials.

(legend continued on next page)

metabolic reprogramming that are specific to that subset,[11] and the details of this process in Th17 cells are not fully understood.

The mitochondrial pyruvate dehydrogenase (PDH) complex regulates the flux of cytoplasmic glucose into the TCA cycle.[12] PDH catalyzes the conversion of glucose-derived pyruvate into acetyl coenzyme A (CoA), which then condenses with oxaloacetate (OAA) to generate citrate.[1,13] Citrate enters the TCA cycle to produce the reducing equivalents necessary for ATP production via OXPHOS. In addition, citrate is transported out of the mitochondria into the cytoplasm and can even enter the nucleus, where it is converted back into acetyl-CoA and OAA by ATP-citrate lyase (ACLY).[11,14–17] Cytoplasmic acetyl-CoA drives lipid synthesis, whereas nuclear acetyl-CoA participates in histone acetylation regulating cell-type-specific gene expression.[18–20]

In this study, we show in mice that PDH plays a crucial role in metabolic adaptation and functions of Th17 cells. Mechanistically, genetic ablation of PDH reduces cellular citrate below a threshold level, which triggers metabolic alterations such as increased glycolysis, glutaminolysis, and fatty acid uptake. These changes can sustain the survival and proliferation of Th17 cells but not their effector functions, either *in vitro* or *in vivo*. PDH-synthesized citrate was found to be essential for histone acetylation and subset-specific gene expression in Th17 cells. Consequently, replenishing the citrate pool by exogenous addition of acetate reinstated normal Th17 cell metabolism and function. Our results demonstrate the importance of PDH in the generation of a critical citrate pool that is indispensable for maintaining Th17 cell function.

RESULTS

Loss of *Pdh* in T cells protects mice from severe experimental autoimmune encephalomyelitis (EAE)

The PDH complex is composed of the PDH-E1α subunit, which is encoded by the *Pdha1* gene, and the PDH-E1β subunit, encoded by *Pdhb*. The PDH-E1α subunit catalyzes the rate-limiting step of pyruvate conversion into acetyl-CoA, whereas the PDH-E1β subunit has no catalytic activity in the absence of PDH-E1α.[21] To investigate PDH's importance in T cell metabolic adaptation, we analyzed *Pdha1* mRNA levels in various $CD4^+$ Th subsets induced to differentiate *in vitro*. Th17 cells showed greater *Pdha1* expression than Th0, Th1, or regulatory T (Treg) cells (Figure 1A). We then crossed CD4 Cre+ mice with $Pdha1^{flox8}$ mice to generate a mutant mouse strain ($PDH^{fl/fl}$ CD4 Cre+) in which T cells did not express *Pdha1* mRNA or protein (Figures 1B and 1C) but continued to express *Pdhb1* mRNA encoding the inactive PDH-E1β subunit (Figure S1A).

Next, we induced EAE, a mouse model of multiple sclerosis known to depend on Th17 cells,[2] in control ($PDH^{fl/fl}$) and $PDH^{fl/fl}$ CD4 Cre+ mice. $PDH^{fl/fl}$ CD4 Cre+ mice showed significant reductions in disease burden and mortality compared with littermate controls (Figures 1D and 1E). T cells isolated from brains and spleens of control and $PDH^{fl/fl}$ CD4 Cre+ mice on day 14 post EAE induction showed comparable percentages and numbers of $CD45^+$ infiltrating cells (Figures 1F and S1B). However, while brains of $PDH^{fl/fl}$ CD4 Cre+ mice showed normal infiltration of $Tbet^+$ Th1 cells, the percentages of infiltrating $ROR\gamma T^+$ Th17 cells and $CD25^+Foxp3^+$ Treg cells were reduced (Figures 1G, S1C, and S1D). We then analyzed Th17 cell function by measuring interferon γ (IFNγ) and IL-17A production by $CD45^+CD4^+$ cells that were isolated from mouse brains and stimulated *in vitro* with phorbol 12-myristate 13-acetate (PMA)/ionomycin. The $IFN\gamma^+IL\text{-}17A^+$ Th17 cell subset deemed to be pathogenic was significantly decreased in proportion in $PDH^{fl/fl}$ CD4 Cre+ brains (Figure 1H), whereas the frequencies of $IFN\gamma^+IL\text{-}17A^-$ and $IFN\gamma^-IL\text{-}17A^+$ $CD4^+$ T cells were unaffected (Figures S1E and S1F). Thus, PDH is critical for Th17 cell function *in vivo*.

To gain mechanistic insight into PDH's role in Th17 cells, we induced naive $CD4^+$ T cells isolated from spleens and lymph nodes of control and $PDH^{fl/fl}$ CD4 Cre+ mice to differentiate into Th17 cells *in vitro* by exposing them to anti-CD3/CD28 antibodies plus IL-6 and transforming growth factor β (TGF-β).[4,22] PDH-deficient Th17 cells showed only marginally decreased $ROR\gamma T$ expression but markedly impaired IL-17 production

(C) Representative immunoblot to detect total PDH-E1α protein in total $CD4^+$ T cells that were isolated from spleen and lymph nodes of two $PDH^{fl/fl}$ and two $PDH^{fl/fl}$ CD4 Cre+ mice and activated *in vitro* as in (B). Actin, loading control. Data are representative of 4 mice/genotype.
(D and E) EAE clinical scores (D) and survival (E) of $PDH^{fl/fl}$ (n = 7) and $PDH^{fl/fl}$ CD4 Cre+ (n = 9) mice 30 days post induction. Data in (D) are mean ± SEM.
(F) Flow cytometry analysis (FCA) of frequencies of $CD45^+$ cells among viable cells isolated from spleens and brains of $PDH^{fl/fl}$ and $PDH^{fl/fl}$ CD4 Cre+ mice on day 14 post EAE induction. Data are mean ± SEM (n = 4–5/group).
(G) Intracellular FCA of frequencies of $ROR\gamma T^+$ cells among viable $CD45^+CD4^+$ cells isolated from spleens and brains of the mice in (F). Data are mean ± SEM (n = 4–5/group).
(H) Left: representative contour plots of intracellular staining of IL-17A and IFNγ among viable $CD45^+CD4^+$ cells isolated from the brains of the mice in (F) (n = 4/genotype). Cells were stimulated *in vitro* with PMA/calcium ionophore/Brefeldin A (PMA/Iono) for 5 h before staining. Right: quantification of frequencies of the $IFN\gamma^+IL\text{-}17A^+$ cells in the left panel. Data are mean ± SEM (n = 4–5/group).
(I and J) Naive T cells were isolated from spleen and lymph nodes of $PDH^{fl/fl}$ and $PDH^{fl/fl}$ CD4 Cre+ mice and differentiated *in vitro* into Th17 cells for 3 days. Results shown are intracellular FCA of frequencies of $ROR\gamma T^+$ cells (I) and quantification of $ROR\gamma T$ mean fluorescence intensity (MFI) (J), gated on viable $CD4^+ROR\gamma T^+$ cells. Data are mean ± SEM (n = 3) and representative of 4 trials.
(K and L) Naive T cells were isolated from spleen and lymph nodes of $PDH^{fl/fl}$ and $PDH^{fl/fl}$ CD4 Cre+ mice and differentiated *in vitro* into Th17 cells for 3 days. Results shown are intracellular FCA of frequencies of $IL\text{-}17A^+$ cells after 5-h stimulation with PMA/Iono (K) and quantification of IL-17A MFI (L), gated on viable $CD4^+$ cells. Data are mean ± SEM (n = 3) and representative of 4 trials.
(M and N) Naive T cells were isolated from spleen and lymph nodes of $PDH^{fl/fl}$ and $PDH^{fl/fl}$ CD4 Cre+ mice and differentiated *in vitro* into Th17 cells for 3 days. On day 1, Th17 cells were infected with a control- or PDH-expressing retroviral vector. Results shown are intracellular FCA of frequencies of $IL\text{-}17A^+$ cells after 5-h stimulation with PMA/Iono (M) and intracellular FCA of frequencies of $ROR\gamma T^+$ cells gated on viable $CD4^+$ cells (N). Data are mean ± SEM (n = 9) and pooled from 3 trials.
The p values are determined by unpaired two-tailed Student's t test or one- or two-way ANOVA where appropriate. Correction for multiple comparisons was performed using the Tukey test. *$p < 0.05$, **$p < 0.01$, ***$p < 0.001$, ****$p < 0.0001$).

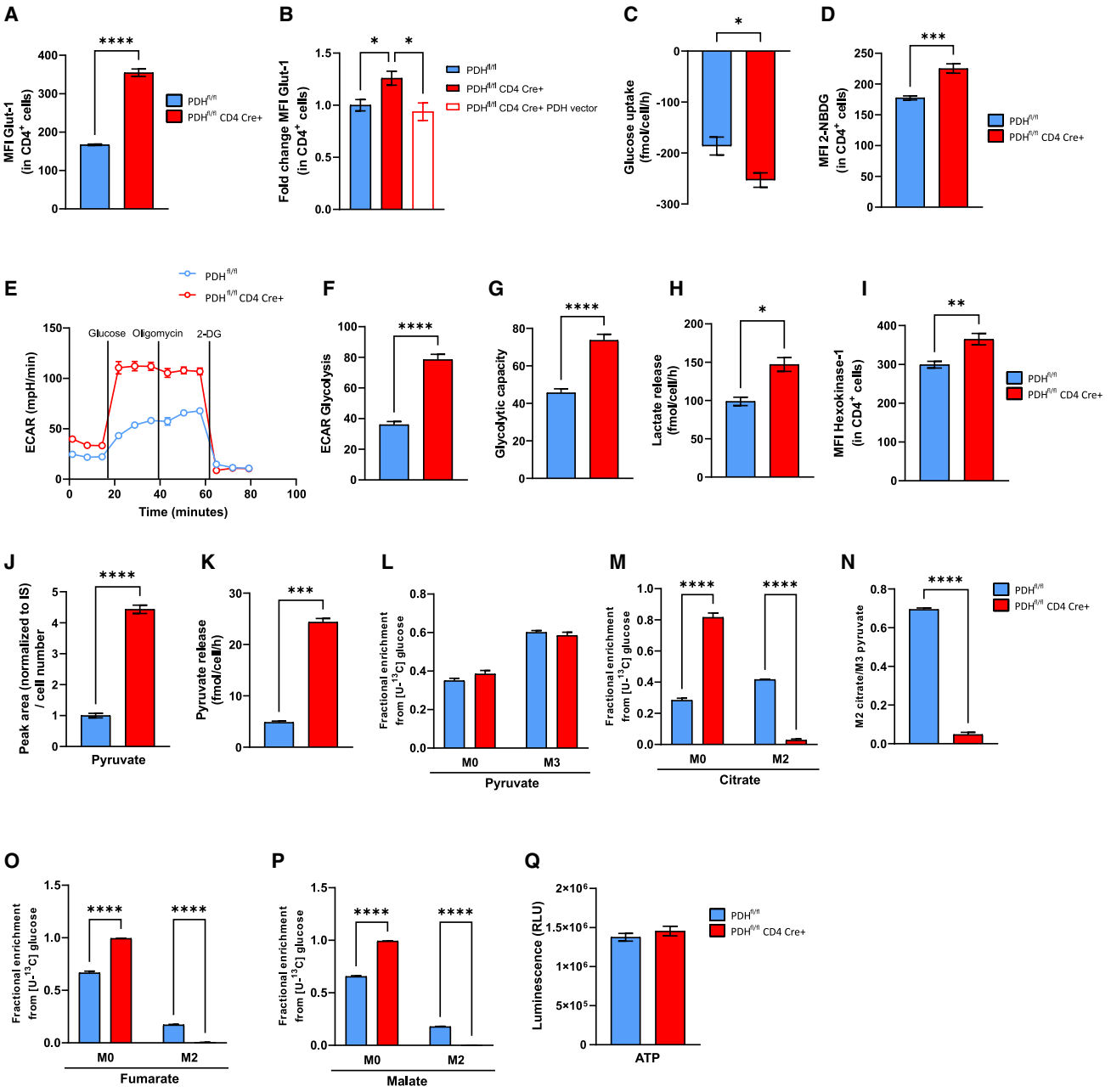


Figure 2. PDH in T cells is essential for glucose metabolism

(A) Quantification of Glut-1 MFI in PDH$^{fl/fl}$ and PDH$^{fl/fl}$ CD4 Cre+ Th17 cells, gated on viable CD4$^+$ cells. Data are mean ± SEM (n = 3) and representative of 3 trials.

(B) Naive T cells were isolated from spleen and lymph nodes of PDH$^{fl/fl}$ and PDH$^{fl/fl}$ CD4 Cre+ mice and differentiated *in vitro* into Th17 cells for 3 days. On day 1, Th17 cells were infected with a control or PDH-expressing retroviral vector as in Figure 1M. Results shown are quantification of Glut-1 MFI, gated on viable CD4$^+$ cells. Data are mean ± SEM (n = 6) and representative of 3 trials.

(C) YSI quantification of glucose uptake from the culture medium of PDH$^{fl/fl}$ and PDH$^{fl/fl}$ CD4 Cre+ Th17 cells. Data are mean ± SEM (n = 3) and representative of 2 trials.

(D) Quantification of 2-NBDG MFI in PDH$^{fl/fl}$ and PDH$^{fl/fl}$ CD4 Cre+ Th17 cells, gated on viable CD4$^+$ cells. Data are mean ± SEM (n = 3) and representative of 3 trials.

(E) Representative Seahorse ECAR plot for PDH$^{fl/fl}$ and PDH$^{fl/fl}$ CD4 Cre + Th17 cells. Data are mean ± SEM (n = 3) and representative of 3 trials.

(F and G) Quantification of Seahorse determinations of glycolytic capacity (F) and glycolysis (G) in PDH$^{fl/fl}$ and PDH$^{fl/fl}$ CD4 Cre+ Th17 cells. Data are mean ± SEM (n = 3) and representative of 3 trials.

(H) YSI quantification of lactate released into the culture medium of PDH$^{fl/fl}$ and PDH$^{fl/fl}$ CD4 Cre+ Th17 cells. Data are mean ± SEM (n = 3) and representative of 2 trials.

(legend continued on next page)

(Figures 1I–1L and S1G). Importantly, upon PDH re-expression via retroviral transduction of a PDH-expressing vector (Figure S1H), IL-17A production was restored to control levels in PDH-deficient Th17 cells (Figure 1M). The slight reduction in RORγT expression in PDH-deficient Th17 cells could also be restored by PDH re-expression (Figure 1N). In contrast, Th1 cell differentiation, effector function, or Treg induction were not affected by PDH ablation (Figures S1I–S1K). Thus, Th17 cell effector functions, but not differentiation per se, depend on PDH.

PDH is essential for regulation of glucose metabolism in Th17 cells

We hypothesized that PDH loss in Th17 cells would trigger a metabolic shift impeding their function. Flow cytometry analysis (FCA) revealed that expression of Glut-1, the major glucose transporter in T cells,[23] was increased in PDH-deficient Th17 cells compared with controls and restored to wild-type levels upon PDH re-expression (Figures 2A and 2B). This result aligned with the PDH-deficient cells' elevated glucose uptake as determined by mass spectrometry (MS) and enhanced uptake of the fluorescent glucose analog 2-(N-(7-nitrobenz-2-oxa-1,3-diazol-4-yl) amino)-2-deoxyglucose (2-NBDG)[24] (Figures 2C and 2D). Extracellular flux analyses confirmed significantly increased glycolysis and glycolytic capacity in PDH-deficient Th17 cells that were associated with heightened lactate release (Figures 2E–2H). Furthermore, the mutant cells exhibited increased expression of hexokinase-1, which catalyzes the irreversible conversion of glucose to glucose-6-phosphate,[25] as well as enhanced intracellular concentrations and release of pyruvate, the end product of glycolysis (Figures 2I–2K). These data pointed to increased flux through glycolysis that, because PDH-deficient Th17 cells cannot further metabolize pyruvate, resulted in pyruvate release into the culture medium.

Despite the above, glycolytic flux analysis using an exogenous ^{13}C-glucose tracer[26] revealed no difference in the contribution of ^{13}C-glucose to pyruvate (M3 label) between control and PDH-deficient Th17 cells (Figure 2L). This result further substantiated our findings that glycolytic activity was increased but that glucose flux through glycolysis itself remained unchanged in the absence of PDH. In contrast, there was minimal ^{13}C-glucose incorporation into citrate (M2 label) (Figure 2M). We then calculated the ratio of M2 citrate/M3 pyruvate as a proxy for measuring PDH activity and observed that this ratio was drastically reduced in PDH-deficient Th17 cells (Figure 2N). ^{13}C-glucose incorporation into other TCA metabolites, such as fumarate and malate (M2 label), was also minimal in PDH-deficient Th17 cells (Figures 2O and 2P). Nonetheless, despite this lack of glucose entering the TCA cycle, PDH-deficient Th17 cells generated normal amounts of energy in the form of ATP (Figure 2Q). These data suggested that these mutant cells used an alternative source of carbon for energy production.

PDH-derived acetyl-CoA is essential for a functioning TCA cycle in Th17 cells

Glutamine can replenish the TCA cycle at the stage of α-ketoglutarate (αKG),[27] and we observed that glutamine uptake was increased in PDH-deficient Th17 cells (Figure 3A). In accordance, ^{13}C-glutamine incorporation into TCA metabolites such as fumarate and malate (M4 label) was elevated in PDH-deficient Th17 cells (Figures 3B and 3C). However, we did not detect an increased flux to citrate, either by oxidative (M4 label) or reductive (M5 label) glutamine metabolism (Figures 3D and 3E). These results bolstered our hypothesis that citrate synthesis in Th17 cells requires PDH-generated acetyl-CoA.

RNA sequencing (RNA-seq) analysis revealed a significant sample distance between the transcriptomes of wild-type and PDH-deficient Th17 cells (Figure S2A). Moreover, in line with their decreased glucose flux into the TCA cycle, we observed an overall reduction in expression of TCA cycle enzymes in mutant Th17 cells compared with controls (Figure S2B). Thus, without PDH-E1α, Th17 cells cannot convert pyruvate into acetyl-CoA to feed into the TCA cycle, and this deficit compromises Th17 cell effector functions. Indeed, in accordance with their reduced expression of TCA enzymes, PDH-deficient Th17 cells showed deficits in basal oxygen consumption rate (OCR), OCR-dependent ATP production, and spare respiratory capacity (Figures 3F–3J).

Because the contributions of glucose- and glutamine-derived carbons to the TCA cycle were altered, we used MS to measure total intracellular levels of TCA metabolites in control and PDH-deficient Th17 cells. In line with our previous results, we observed that absolute levels of αKG, fumarate, and malate were reduced and citrate levels were minimal in PDH-deficient Th17 cells (Figures 3K–3N). Thus, an absence of PDH in Th17 cells drastically alters the central oxidative metabolism, prevents glucose flux into the TCA cycle, and impairs citrate formation so that it cannot be replenished by glutamine.

PDH ablation induces fatty acid uptake by Th17 cells

Citrate is an essential metabolite for several processes, including *de novo* lipid synthesis. In this context, citrate exits the

(I) Quantification of hexokinase-1 MFI in PDH$^{fl/fl}$ and PDH$^{fl/fl}$ CD4 Cre+ Th17 cells, gated on viable CD4$^+$ cells. Data are mean ± SEM (n = 3) and representative of 2 trials.
(J) Quantification of intracellular pyruvate in PDH$^{fl/fl}$ and PDH$^{fl/fl}$ CD4 Cre+ Th17 cells. Data are mean ± SEM (n = 3) and representative of 2 trials.
(K) Gas chromatography (GC)-MS quantification of pyruvate release into the culture medium of PDH$^{fl/fl}$ and PDH$^{fl/fl}$ CD4 Cre + Th17 cells. Data are mean ± SEM (n = 3) and representative of 2 trials.
(L and M) Mass isotopomer distribution (MID) of M0 and M3 pyruvate (L) and M0 and M2 citrate (M) in PDH$^{fl/fl}$ and PDH$^{fl/fl}$ CD4 Cre+ Th17 cells incubated for 24 h with [U-$^{13}C_6$]-glucose. Data are mean ± SEM (n = 3) and representative of 2 trials.
(N) PDH activity ratio (M2 citrate/M3 pyruvate) in the cells in (L) and (M). Data are mean ± SEM (n = 3) and representative of 2 trials.
(O and P) MID of M0 and M2 fumarate (O) and M0 and M2 malate (P) in PDH$^{fl/fl}$ and PDH$^{fl/fl}$ CD4 Cre+ Th17 cells incubated for 24 h with [U-$^{13}C_6$]-glucose. Data are mean ± SEM (n = 3) and representative of 2 trials.
(Q) Luminescence determination of ATP in PDH$^{fl/fl}$ and PDH$^{fl/fl}$ CD4 Cre+ Th17 cells. Data are mean ± SEM (n = 3) and representative of 2 trials.
The p values are determined by unpaired two-tailed Student's t test or one- or two-way ANOVA where appropriate. Correction for multiple comparisons was performed using the Tukey test. *p < 0.05, **p < 0.01, ***p < 0.001, ****p < 0.0001.

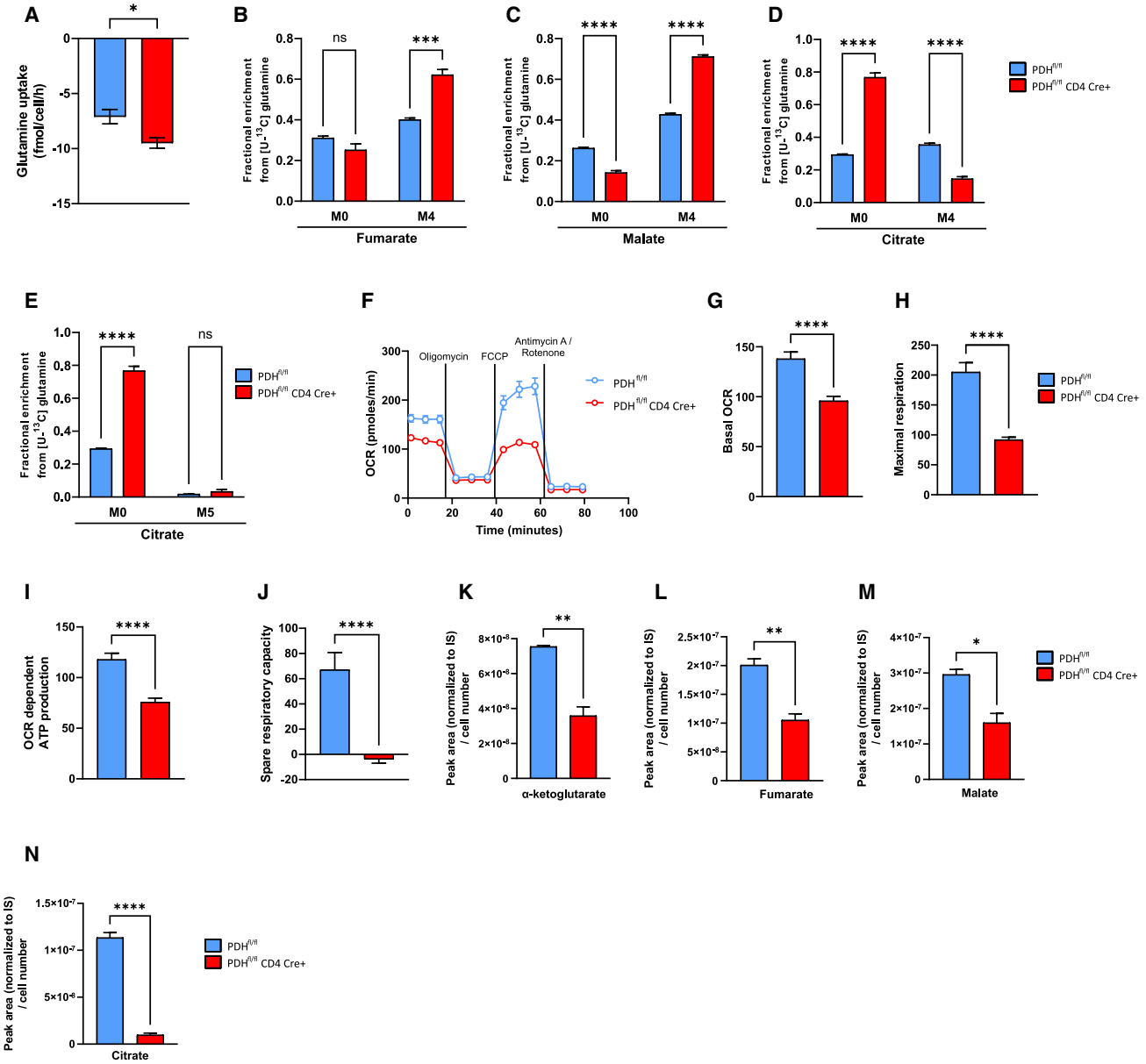


Figure 3. Glutamine metabolism is altered upon PDH ablation

(A) YSI quantification of glutamine uptake from the culture medium of $PDH^{fl/fl}$ and $PDH^{fl/fl}$CD4Cre+ Th17 cells. Data are mean ± SEM (n = 3) and representative of 2 trials.

(B–E) MID of M0 and M4 fumarate (B), M0 and M4 malate (C), M0 and M4 citrate (D), and M0 and M5 citrate (E) in $PDH^{fl/fl}$ and $PDH^{fl/fl}$ CD4 Cre+ Th17 cells incubated for 24 h with [U-$^{13}C_5$]-glutamine. Data are mean ± SEM (n = 3) and representative of 2 trials.

(F) Representative Seahorse OCR plot of $PDH^{fl/fl}$ and $PDH^{fl/fl}$ CD4 Cre+ Th17 cells. Data are mean ± SEM (n = 3) and representative of 3 trials.

(G–J) Quantification of Seahorse determinations of basal OCR (G), maximal respiration (H), OCR-dependent ATP (I), and spare respiratory capacity (J) in $PDH^{fl/fl}$ and $PDH^{fl/fl}$ CD4 Cre+ Th17 cells. Data are mean ± SEM (n = 3) and representative of 3 trials.

(K–N) Quantification of intracellular αKG (K), fumarate (L), malate (M), and citrate (N) in $PDH^{fl/fl}$ and $PDH^{fl/fl}$ CD4 Cre+ Th17 cells. Data are mean ± SEM (n = 3) and representative of 2 trials.

The p values are determined by unpaired two-tailed Student's t test or two-way ANOVA where appropriate. Correction for multiple comparisons was performed using the Tukey test. *p < 0.05, **p < 0.01, ***p < 0.001, ****p < 0.0001.

mitochondria and enters the cytoplasm, where it is converted by ACLY into OAA and acetyl-CoA, which is used for fatty acid synthesis.[14,16,19] We first measured total levels of fatty acid octadecenoic acid in control and PDH-deficient Th17 cells and observed them to be similar (Figure 4A). However, ^{13}C-glucose and ^{13}C-glutamine tracing revealed almost no contribution of these carbon sources to octodecenoic acid synthesis in PDH-deficient Th17 cells (Figures 4B, S3A, and S3B). Thus, the

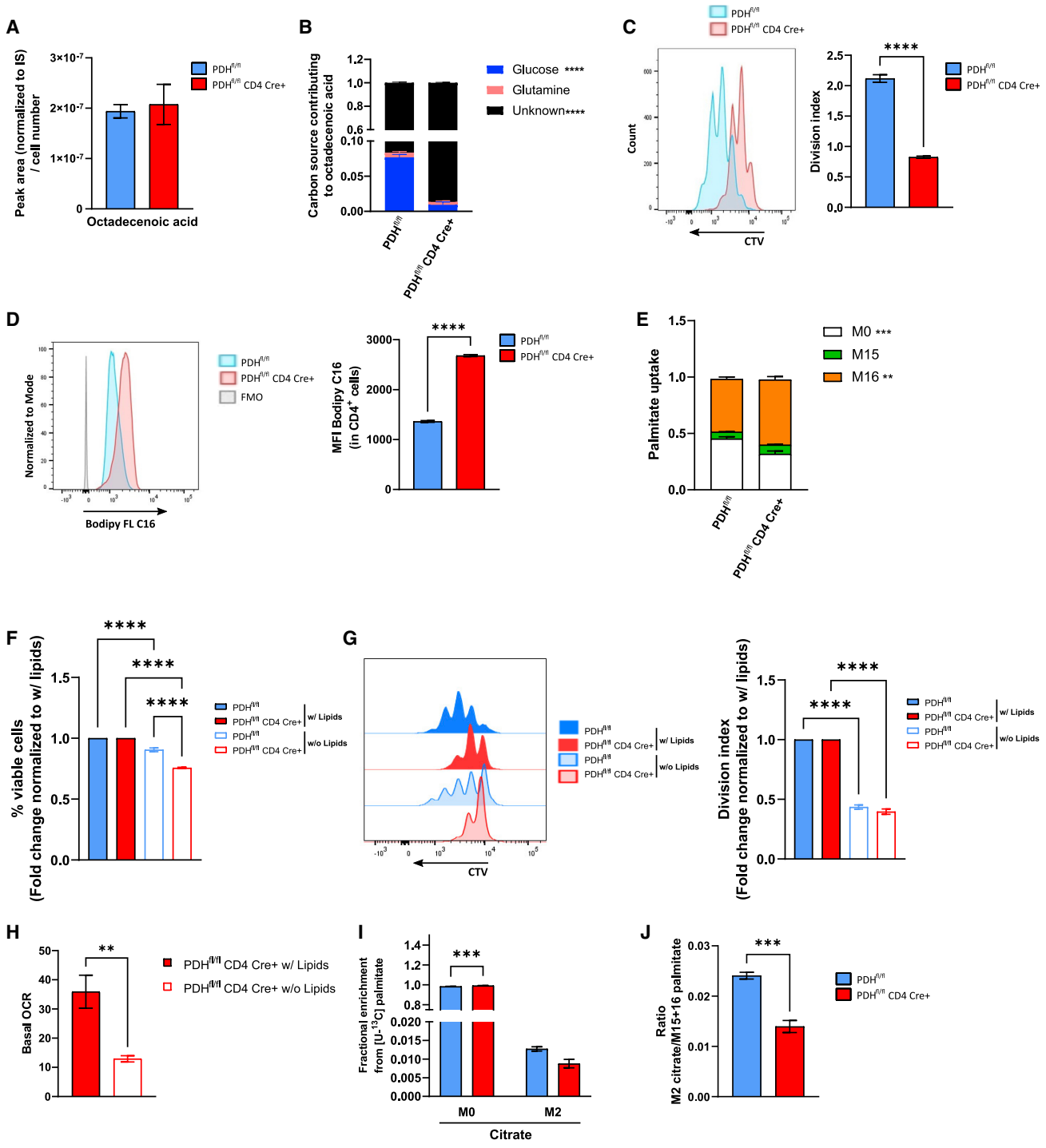


Figure 4. Ablation of PDH in Th17 cells induces fatty acid metabolism

(A) GC-MS quantification of intracellular octadecenoic acid in PDH$^{fl/fl}$ and PDH$^{fl/fl}$ CD4 Cre+ Th17 cells. Data are mean ± SEM (n = 3) and representative of 2 trials.

(B) Distribution of carbon sources contributing to octadecenoic acid in PDH$^{fl/fl}$ and PDH$^{fl/fl}$ CD4 Cre+ Th17 cells. Data are mean ± SEM (n = 3) and representative of 2 trials.

(C) Left: representative FCA of the proliferation of CellTrace Violet (CTV)-labeled PDH$^{fl/fl}$ and PDH$^{fl/fl}$ CD4 Cre+ Th17 cells. Right: fold change of the division index of the Th17 cells in the left panel. Data are mean ± SEM (n = 3) and representative of 3 trials.

(D) Left: representative FCA of BODIPY FL C16-labeled PDH$^{fl/fl}$ and PDH$^{fl/fl}$ CD4 Cre+ Th17 cells and fluorescence minus one (FMO) of unlabeled Th17 cells. Right: Quantification of BODIPY FL C16 MFI in the Th17 cells in the left panel, gated on viable CD4$^+$ cells. Data are mean ± SEM (n = 3) and representative of 3 trials.

(legend continued on next page)

absence of citrate in PDH-deficient Th17 cells affects the biosynthesis of critical metabolites such as lipids.

Because lipids are essential for proliferation,[19,28] we used CellTrace Violet (CTV) to monitor the proliferation of PDH-deficient Th17 cells in culture. Although $PDH^{fl/fl}$ CD4 Cre+ Th17 cells showed significantly decreased proliferation compared with controls, proliferation was still substantial (Figure 4C), suggesting that the necessary lipids were derived from a citrate-independent source. This result prompted us to measure the uptake of extracellular lipids using fluorescently labeled palmitate (BODIPY FL C16). We observed a marked increase in uptake of this agent by the mutant cells (Figure 4D) and confirmed that ^{13}C-palmitate uptake (M16 label) was increased in PDH-deficient Th17 cells (Figure 4E). Furthermore, when cultured in medium lacking extracellular lipids, although mutant and control Th17 cells showed impaired survival and proliferation, the survival of PDH-deficient Th17 cells was more markedly impaired (Figures 4F and 4G). Moreover, lipids were essential for maintenance of the basal OCR in $PDH^{fl/fl}$ CD4 Cre+ Th17 cells (Figure 4H). These results supported our contention that the mutant cells rely on the import of extracellular lipids for proliferation and survival. However, when measuring the contribution of ^{13}C-palmitate to the generation of citrate, we detected no differences between control and PDH-deficient Th17 cells (Figure 4I). Thus, despite their increased uptake of lipids, mutant Th17 cells do not replenish the TCA cycle with carbons from lipids (Figure 4J). Taken together, these data suggest that PDH-deficient Th17 cells use extracellular fatty acids from the culture medium to directly generate the new lipids and membranes required for survival and proliferation, independent of citrate.

PDH restricts upregulation of the glutamine-mTOR-CD36 axis in Th17 cells

Long-chain fatty acids (LCFAs) require transporters such as CD36 to enter cells.[17] We observed increased CD36 expression in $PDH^{fl/fl}$ CD4 Cre+ Th17 cells, which could be partially reversed by restoring PDH expression in the mutant cells (Figures 5A and S4A). CD36 expression is controlled by mammalian target of rapamycin (mTOR),[29–31] and we detected increased phosphorylation of mTOR (p-mTOR) and its downstream target ribosomal protein S6 (p-S6) in the mutant cells (Figures 5B and 5C). CD36 induction and the observed increase in lipid uptake by PDH-deficient Th17 cells could be partially reversed by two chemical inhibitors of mTOR, Torin 1 and rapamycin (Figures 5D, 5E, S4B, and S4C).

mTOR is activated by amino acids, particularly glutamine,[32] and we had already established that PDH-deficient Th17 cells showed increased glutamine uptake and glutaminolysis (Figures 3A–3C). In line with these results, glutamine deprivation decreased p-mTOR and CD36 expression as well as lipid uptake in PDH-deficient Th17 cells to control levels (Figures 5F–5H), exposing a metabolic feedback loop regulating central carbon metabolism. Thus, it seems that PDH-deficient Th17 cells increase their mTOR activity to promote extracellular lipid uptake through CD36 and thereby maintain the survival and functionality of these cells.

PDH-derived citrate is crucial for histone acetylation and gene transcription in Th17 cells

Citrate-derived acetyl-CoA is required for post-translational histone acetylation,[19] an important epigenetic modification that opens up condensed chromatin and fosters transcriptional activity.[18] Intriguingly, when measuring total acetyl-CoA levels, we observed no differences between wild-type and PDH-deficient Th17 cells (Figure 6A). However, the contribution of ^{13}C-glucose to the acetyl-CoA pool was reduced in the mutant Th17 cells, whereas the contribution of ^{13}C-palmitate was increased (Figures 6B and 6C). Despite having normal acetyl-CoA levels, PDH-deficient Th17 cells showed reduced histone-3 lysine-27 acetylation (H3K27Ac) as well as a decrease in the contribution of glucose to the acetyl groups of histone-3 (Figures 6D, 6E, and S5A). This indicated an exclusive role of glucose-derived acetyl-CoA for histone acetylation in Th17 cells. Taken together, these data suggest that there are different pools of acetyl-CoA in Th17 cells that are derived from different carbon sources. Not all of these acetyl-CoA pools are used for histone acetylation; such a diversification has been recently documented in cancer cell lines.[33]

To analyze the effects of this decreased histone acetylation, we performed assay for transposase-accessible chromatin using sequencing (ATAC-seq) analysis[34,35] of *in vitro*-differentiated control and PDH-deficient Th17 cells. This technique revealed 39,647 significant regions with differentially opened areas in PDH-deficient Th17 cells compared with control Th17 cells with dramatically reduced open areas in the mutant cells (Figure 6F). The *Il17a*, *Il17f*, *Il23r*, *Smad3*, *Hif1a*, and *Stat3* loci showed decreases in chromatin accessibility and mRNA expression (Figures 6G and S5B). Although the accessibility of the *Rorc* locus encoding RORγT was reduced, levels of RORγT mRNA were not affected (Figure 6G), in line with the near-normal RORγT expression levels in mutant Th17 cells (Figures 1I and 1J). Similarly, the accessibility of the *Il17ra* locus was affected, whereas the mRNA levels remained unchanged (Figure S5B). Therefore, we hypothesized that the PDH-mediated synthesis

(E) GC-MS measurements of relative levels of fully labeled (M16 or M15) and unlabeled (M0) palmitate in $PDH^{fl/fl}$ and $PDH^{fl/fl}$ CD4 Cre+ Th17 cells incubated for 24 h with [U-$^{13}C_{16}$]-palmitate. Data are mean ± SEM (n = 4).
(F) Fold change in frequencies of viable $PDH^{fl/fl}$ and $PDH^{fl/fl}$ CD4 Cre+ *in vitro*-differentiated Th17 cells cultured in complete IMDM with or without lipids, gated on viable cells. Data are mean ± SEM (n = 3) and representative of 3 trials.
(G) Left: representative FCA of the proliferation of CTV-labeled $PDH^{fl/fl}$ and $PDH^{fl/fl}$ CD4 Cre+ Th17 cells cultured in complete IMDM with or without lipids. Right: fold change in division index of the Th17 cells in the left panel. Data are mean ± SEM (n = 3) and representative of 3 trials.
(H) Quantification of Seahorse determination of basal OCR in $PDH^{fl/fl}$ CD4 Cre+ *in vitro*-differentiated Th17 cells cultured in complete IMDM with or without lipids. Data are mean ± SEM (n = 3) and representative of 3 trials.
(I) MID of M0 and M2 citrate in $PDH^{fl/fl}$ and $PDH^{fl/fl}$ CD4 Cre+ Th17 cells incubated for 24 h with [U-$^{13}C_{16}$]-palmitate. Data are mean ± SEM (n = 4).
(J) Contribution to M2 citrate of labeled M15+16 palmitate in the cells in (I), expressed as a ratio. Data are mean ± SEM (n = 4).
The p values are determined by unpaired two-tailed Student's t test or one- or two-way ANOVA where appropriate. Correction for multiple comparisons was performed using the Tukey test. **p < 0.01, ***p < 0.001, ****p < 0.0001.

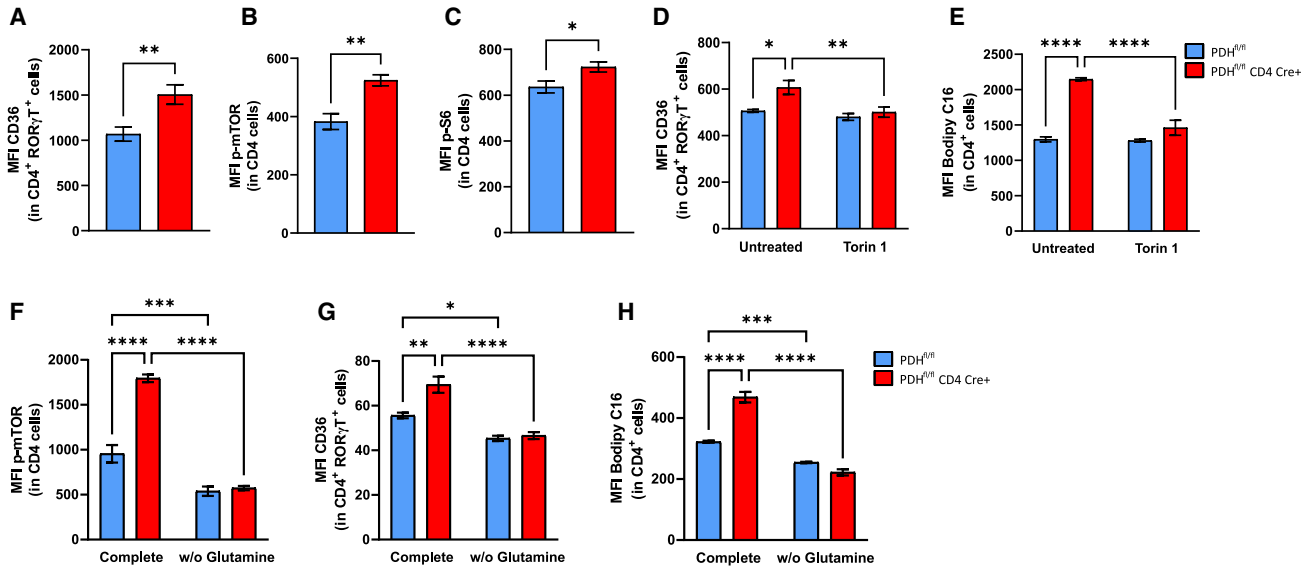


Figure 5. PDH restricts induction of the glutamine-mTOR-CD36 axis in Th17 cells

(A–C) Quantification of CD36 MFI (A), intracellular p-mTOR MFI (B), and intracellular p-S6 MFI (C) in $PDH^{fl/fl}$ and $PDH^{fl/fl}$ CD4 Cre+ Th17 cells, gated on viable $CD4^+ROR\gamma T^+$ cells. Data are mean ± SEM (n = 3) and representative of 3 trials.

(D and E) Quantification of CD36 MFI (D) and BODIPY FL C16 MFI (E) in $PDH^{fl/fl}$ and $PDH^{fl/fl}$ CD4 Cre+ *in vitro*-differentiated Th17 cells cultured with or without Torin 1 (100 nM), gated on viable $CD4^+ROR\gamma T^+$ cells. Data are mean ± SEM (n = 3) and representative of 3 trials.

(F–H) Quantification of intracellular p-mTOR MFI (F), CD36 MFI (G), and BODIPY FL C16 MFI (H) in $PDH^{fl/fl}$ and $PDH^{fl/fl}$ CD4 Cre+ *in vitro*-differentiated Th17 cells cultured in either RPMI medium containing 1% L-glutamine (complete) or RPMI medium without glutamine, gated on viable $CD4^+$ (F and H) or $CD4^+ROR\gamma T^+$ (G) cells. Data are mean ± SEM (n = 3) and representative of 2 trials.

The p values are determined by unpaired two-tailed Student's t test or two-way ANOVA where appropriate. Correction for multiple comparisons was performed using the Tukey test. *p < 0.05, **p < 0.01, ***p < 0.001, ****p < 0.0001.

of glucose-derived acetyl-CoA produces citrate that regulates Th17 cells' function via histone acetylation.

Acetate treatment restores the metabolic, epigenetic, and effector alterations caused by PDH deficiency in Th17 cells

To confirm the effects of acetylation on Th17 cells, we bypassed the PDH deficiency in $PDH^{fl/fl}$ CD4 Cre+ T cells by treating them (and control Th17 cells) with the short-chain fatty acid (SCFA) acetate,[36,37] which is converted by acetyl-CoA synthetases into acetyl-CoA.[38] Indeed, upon acetate supplementation, PDH-deficient Th17 cells increased H3K27 acetylation to wild-type levels (Figure 7A). Furthermore, to test whether acetate was incorporated into the acetyl groups on histone-3 molecules, we treated PDH-deficient and control Th17 cells with ^{13}C-labeled acetate and observed that it contributed much more intensely to histone-3 acetylation in the mutant cells (Figures 7B and S6A). Moreover, acetate treatment increased chromatin accessibility in PDH-deficient Th17 cells, as measured by ATAC-seq (Figure S6B). We also detected the contribution of ^{13}C-acetate to TCA metabolites such as citrate, fumarate, and malate in mutant Th17 cells (Figures 7C, 7D, and S6C). As expected, these contributions were increased over those in control Th17 cells because of the lack of glucose flux into the TCA cycle in the mutant cells. In addition, RNA-seq revealed that the transcriptome of acetate-treated PDH-deficient Th17 cells was similar to the transcriptomes of acetate-treated or untreated control Th17 cells (Figure 7E). Acetate treatment also restored the expression of TCA cycle enzymes to mutant Th17 cells (Figure S6D) so that the citrate pool recovered (Figure 7F). As a result, acetate-treated PDH-deficient Th17 cells were able to re-establish their *de novo* lipid synthesis, regain their proliferative potential, and normalize their basal OCR and extracellular acidification rate (ECAR) glycolysis (Figures 7G–7I and S6E). Indeed, Glut-1 expression and 2-NBDG uptake also returned to control levels in acetate-treated PDH-deficient Th17 cells (Figures 7J and 7K), as did glutamine and lipid uptake and levels of p-mTOR and CD36 (Figures 7L–7O). Finally, acetate-treated PDH-deficient Th17 cells regained the capacity to produce IL-17A (Figure 7P).

These data indicate that PDH-generated acetyl-CoA contributes to a critical citrate pool that cannot be derived from any other carbon source except exogenous acetate. This citrate pool is crucial for maintaining the correct chromatin state that allows Th17 signature gene transcription and thereby coordinates the metabolism, proliferation, and functionality of these cells.

DISCUSSION

Previous work has shown that the metabolism and functions of effector T cells are closely connected.[8,10,11,39] In our study, we genetically targeted the PDH-E1α subunit specifically in T cells, disconnecting glycolysis from the TCA cycle. Th17 cells are known to rely on glycolytic ATP and regulators such as myc, HIF-1α, and mTOR for their differentiation and function,[40–45]

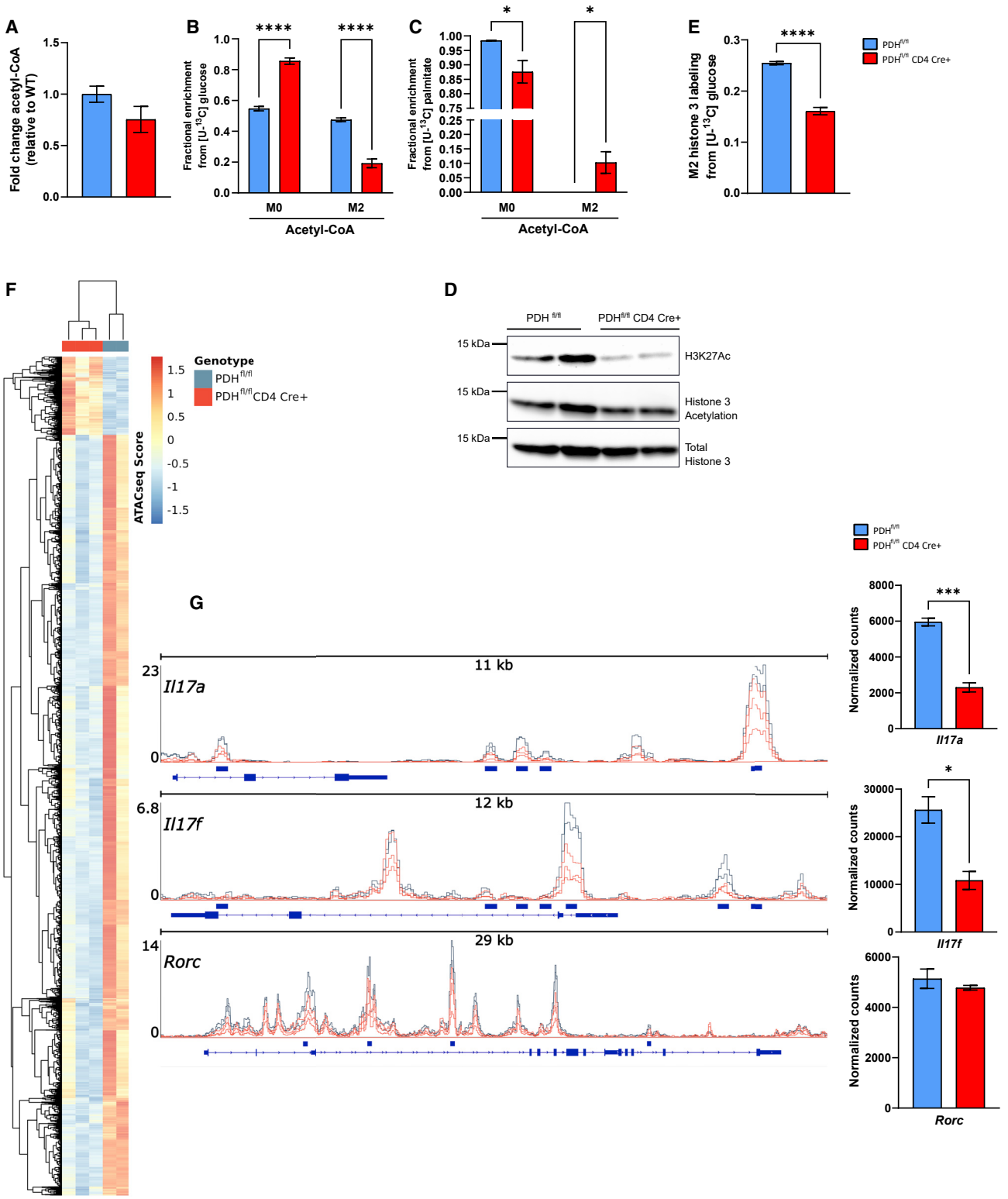


Figure 6. PDH is crucial for histone acetylation and epigenetic modifications in Th17 cells

(A) LC-MS quantification of fold change in intracellular acetyl-CoA levels in PDH$^{fl/fl}$ CD4 Cre+ Th17 cells relative to PDH$^{fl/fl}$ Th17 cells. Data are mean ± SEM (n = 3) and representative of 2 trials.

(legend continued on next page)

and we have now added PDH to this list. Without PDH, Th17 cells rewire their metabolism to increase uptake of glucose, glutamine, and fatty acids to ensure their survival and proliferation. However, our mutant Th17 cells lacked a critical citrate pool that could not be generated in a PDH-independent manner and was essential for the functionality of Th17 cells *in vivo* and *in vitro*.

The mitochondrial pyruvate carrier (MPC) imports pyruvate into the mitochondria, where it is converted into acetyl-CoA.[46–48] MPC1$^{fl/fl}$ Vav Cre mutant mice, which do not express *Mpc1* in any hematopoietic cells, suffer from more severe EAE than control littermates,[49] a finding that contrasts with the effects of T cell-specific PDH deletion we observed. However, pyruvate in the mitochondria can also be generated from glutamine in Th17 cells, as shown previously,[50] which could provide a substrate for PDH while bypassing the need for MPC-mediated pyruvate import. We surmise that PDH-dependent conversion of pyruvate to acetyl-CoA, and not its transport into the mitochondria, might be essential for Th17 cell effector function during EAE. In another study, Wenes et al.[51] showed that MPC deletion in CD8$^+$ T cells induced increased uptake of fatty acids and glutamine, similar to our findings. However, in this context, acetyl-CoA production was induced in the mutant cells.[51] As a result, histone acetylation of genes supporting memory T cell development was increased, promoting CD8$^+$ memory T cell differentiation. In addition, a different study showed that PDH could be localized in the nucleus in a constitutively active form.[52] The generation of acetyl-CoA in the nucleus could explain the discrepancies between the Ramstead et al.[49] article and our data because PDH is deleted in both, mitochondria and nucleus, in our study, while MPC is only expressed in the mitochondria. These results stand in clear contrast to our findings but strengthen our theory that a PDH-dependent acetyl-CoA pool is necessary for histone acetylation.

It is also possible that the developmental stage at which pyruvate metabolism is disrupted defines its effects. VavCre-mediated MPC1 deletion occurs very early during hematopoiesis and so affects T cell development, which favors the establishment of a more activated T cell pool.[49] Similarly, when Mx1Cre is employed to delete PDH in bone marrow and hematopoietic stem cells, T cell development in the thymus is impaired, which is not the case when CD4 Cre is used.[53] However, it was surprising that, during EAE progression, we found decreased amounts of Treg cells in the brains of mice bearing PDH-deficient T cells, whereas the differentiation of this cell subset *in vitro* was not affected. This result is puzzling because it has been shown previously that Treg cells rely heavily on mitochondrial oxidation for their suppressive abilities.[9] These data suggest that how PDH operates during T cell development, and PDH's effects on Treg function, are worthy of further investigation.

Tight regulation of metabolism is important for maintaining Th cell functionality,[54] and too much or too little glycolysis and/or OXPHOS impairs T cell functions.[55,56] Our data show that abrogation of PDH activity affects Th17 cell functionality. Conversely, sustained PDH activation achieved by pharmacological inhibition of PDK1 (an inhibitor of PDH) also has a negative effect on Th17 cells.[57] Thus, PDH is a vital regulator of Th17 cell functions, consistent with the idea that too little or too much flux through this metabolic gatekeeper is detrimental to Th17 cells.

Glutamine contributes to the energy produced via the TCA cycle,[27] and ablation of glutaminase impairs Th17 cell differentiation and function so that Th17-driven inflammatory diseases are mitigated *in vivo*.[50] Glutamine is also required for the synthesis of glutathione (GSH), an important antioxidant in T cells that is essential for effector T cell reprogramming and Treg cell suppressive capacity.[55,56] However, we showed that increased glutamine uptake did not relieve the functional defects of PDH-deficient Th17 cells because glutamine could not replenish the critical PDH-dependent citrate pool in these cells. Thus, only stringent control of a specific metabolic program in a given Th subset can ensure cell functionality. Fortunately, this restriction offers the possibility of subset-specific therapeutic interference at key regulatory points.

Upon PDH deletion, Th17 cells were unable to generate fatty acids *de novo*. Instead, they increased their uptake of extracellular fatty acids through mTOR-dependent upregulation of CD36. Although CD36 is a target of mTOR signaling, mTOR is also crucial for Th17 cell differentiation and metabolic rewiring.[58–60] A major activator of mTOR is glutamine,[32] and the increased mTOR activation in our PDH-deficient Th17 cells was causally linked to their heightened glutamine uptake. These data reveal a metabolic feedback loop between glycolysis and glutaminolysis in Th17 cells that can respond to exogenous acetyl-CoA in the form of acetate. Acetate treatment of PDH-deficient Th17 cells reversed the metabolic dysregulation in these cells and restored their functionality. Similarly, other studies have shown that acetate can serve as a source of acetyl-CoA to regulate effector T cell functions.[37,45,61] These

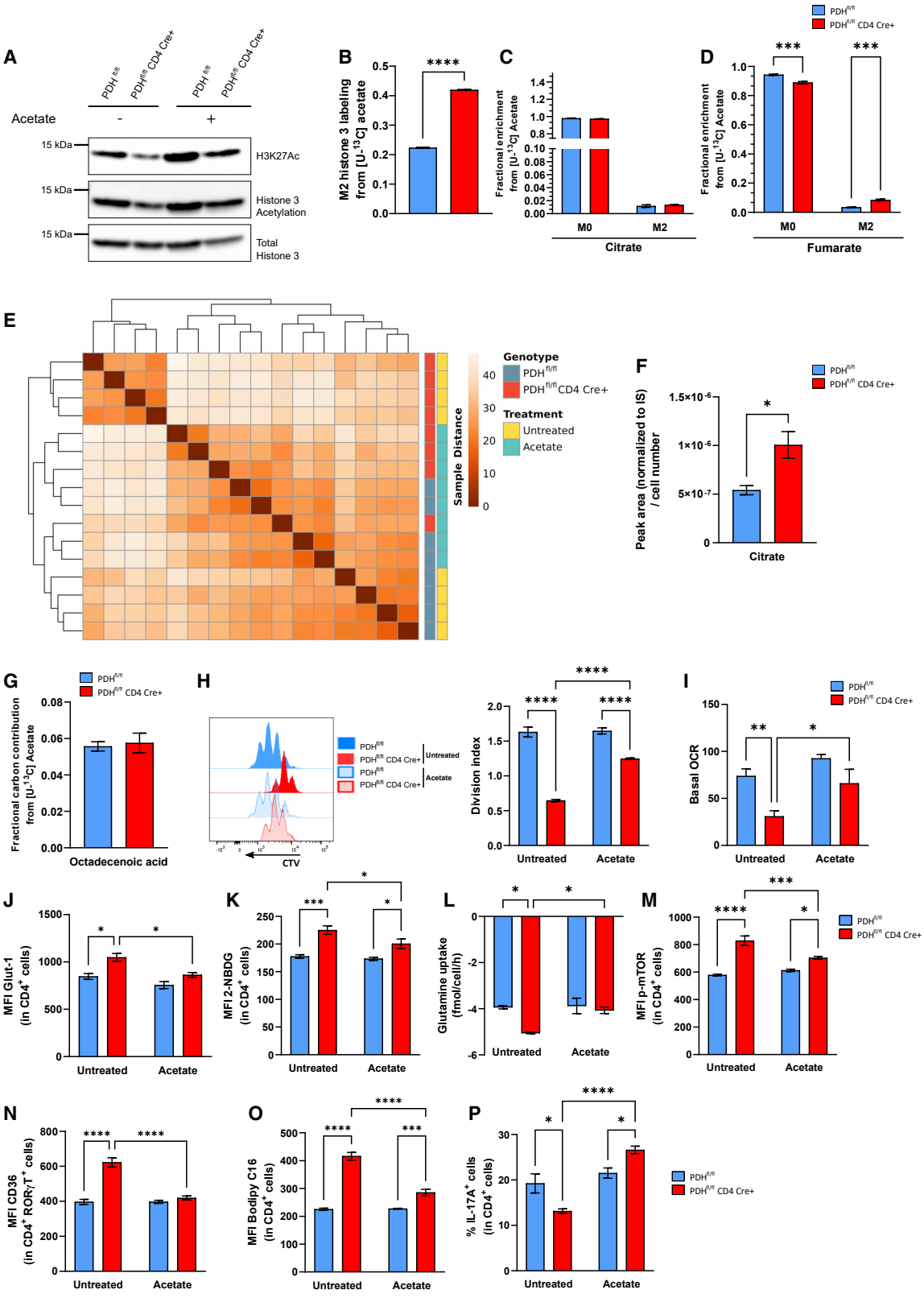
(B and C) MID of M0 and M2 acetyl-CoA in PDH$^{fl/fl}$ and PDH$^{fl/fl}$ CD4 Cre+ Th17 cells incubated for 24 h with [U-$^{13}C_5$]-glucose (B) or [U-$^{13}C_{16}$]-palmitate (C). Data are mean ± SEM (n = 3) and representative of 2 trials.

(D) Representative immunoblot to detect histone-3 lysine-27 acetylation (H3K27Ac) and histone-3 acetylation in Th17 cells from two PDH$^{fl/fl}$ and two PDH$^{fl/fl}$ CD4 Cre+ mice. Total histone-3, loading control. Data are representative of 3 mice/genotype.

(E) MID of M2 histone-3 labeling in PDH$^{fl/fl}$ and PDH$^{fl/fl}$ CD4 Cre+ Th17 cells incubated for 24 h with [U-$^{13}C_5$]-glucose. Data are mean ± SEM (n = 4) and representative of 2 trials.

(F) Heatmap of ATAC-seq showing significantly differentially accessible regions (DBSs) in PDH$^{fl/fl}$ vs. PDH$^{fl/fl}$ CD4 Cre+ Th17 cells as identified by DiffBind. The ATAC-seq score is the *Z* score for the normalized count of each DBS.

(G) Left: plot of chromatin accessibility at the *Il17a*, *Il17f*, and *Rorc* loci in PDH$^{fl/fl}$ (blue lines) and PDH$^{fl/fl}$ CD4 Cre+ (red lines) Th17 cells. Dark blue bars depict significant DBSs as identified by DiffBind. Above each ATAC trace, a scale bar indicates the size of the genomics sequence covered in the graph. For each gene, the local sequence coverage observed in the ATAC experiment is shown as normalized counts (left x axis) obtained by scaling to normalization factors observed with DiffBind. Right: quantitation of *Il17a*, *Il17f*, and *Rorc* mRNA levels (normalized counts) in PDH$^{fl/fl}$ and PDH$^{fl/fl}$ CD4 Cre+ Th17 cells as measured by RNA-seq. The p values are determined by unpaired two-tailed Student's t test or two-way ANOVA where appropriate. Correction for multiple comparisons was performed using the Tukey test. *p < 0.05, ***p < 0.001, ****p < 0.0001.



(legend on next page)

aspects of cellular metabolism are closely linked to epigenetic modifications. However, in contrast to our findings, Peng et al.[61] showed that LDH ablation in Th1 cells leads to reduced acetyl-CoA levels and, thus, histone acetylation, impairing IFNγ production. We demonstrated that our PDH-deficient T cells are perfectly capable of Th1 cell differentiation and IFNγ production. This discrepancy could be due to the fact that Th17 cells rely on glucose-derived acetyl-CoA for histone acetylation, whereas Th1 cells are able to use other acetyl-CoA pools for that purpose. When PDH localizes in the nucleus in a constitutively active form, it generates a mitochondrion-independent pool of acetyl-CoA for histone acetylation.[52] We demonstrated that an absence of PDH impairs histone H3K27Ac in a manner that can be restored by acetate treatment, emphasizing the importance of PDH for maintaining normal epigenetic control in Th17 cells. However, we would like to mention that chromatin accessibility can be regulated by non-classical histone modifications that are distinct from acetylation.[62]

Our results are bolstered by a recent study showing that ablation of Glut-3 in murine T cells also impairs Th17 effector function.[63] These mutant mice were protected against developing EAE because Glut-3-derived acetyl-CoA production and epigenetic modifications were defective. Our study highlights the importance of regulating metabolism and defining the connections between metabolic disruptions and epigenetic modulations in Th17 cells.

In conclusion, our study uncovered an unexpected role of PDH as a central regulator of the effector functions of Th17 cells *in vivo* and *in vitro*. In particular, Th17 cells use PDH for establishment of a glucose-derived citrate pool that controls the chromatin accessibility of Th17-specific loci and, thus, the survival, proliferation, and effector functions of these cells. Furthermore, this work uncovered potential targets for the therapy of Th17 cell-driven autoimmune diseases.

Limitations of the study

(1) Our study deciphers the role of the catalytic subunit of PDH in Th17 cell differentiation and function in mice *in vitro* and *in vivo*. While we show an impact during EAE, a mouse model of multiple sclerosis, the role of PDH in human subjects of this particular subset and Th17 cell-driven diseases was not analyzed. (2) This study uses cells harboring a T cell-specific deletion of the catalytic subunit of PDH and focuses on its function (i.e., conversion of pyruvate into acetyl-CoA). However, we cannot exclude potential structural effects of ablation of PDH E1α that might contribute to our results. (3) Here, we focus on the role of a glucose-derived pool of citrate and its importance in Th17 cell function. However, we describe that there are no significant differences in cellular acetyl-CoA concentrations between control and PDH-deficient Th17 cells. This points to an alternative source and an alternative acetyl-CoA pool with distinct functionality, which we have not been able to identify in this study.

STAR★METHODS

Detailed methods are provided in the online version of this paper and include the following:

- KEY RESOURCES TABLE
- RESOURCE AVAILABILITY
  - Lead contact
  - Materials availability
  - Data and code availability
- EXPERIMENTAL MODEL AND SUBJECT DETAILS
  - Mice

Figure 7. Acetate treatment reverses the effects caused by PDH ablation in Th17 cells

(A) Representative immunoblot to detect H3K27Ac and histone-3 acetylation in $PDH^{fl/fl}$ and $PDH^{fl/fl}$ CD4 Cre+ Th17 cells treated with (+) or without (−) acetate (10 mM). Total histone-3, loading control. Data are representative of 3 mice/genotype.

(B) MID of M2 histone-3 labeling in $PDH^{fl/fl}$ and $PDH^{fl/fl}$ CD4 Cre+ Th17 cells incubated for 72 h with [U-$^{13}C_2$]-acetate. Data are mean ± SEM (n = 4) and representative of 2 trials.

(C and D) MID of M0 and M2 citrate (C) and M0 and M2 fumarate (D) in $PDH^{fl/fl}$ and $PDH^{fl/fl}$ CD4 Cre+ Th17 cells incubated for 72 h with [U-$^{13}C_2$]-acetate. Data are mean ± SEM (n = 3) and representative of 2 trials.

(E) Sample distance matrix between the RNA-seq normalized counts of $PDH^{fl/fl}$ and $PDH^{fl/fl}$ CD4 Cre+ Th17 cells cultured in complete IMDM and treated or not with acetate (10 mM). Results shown are after conversion to homoskedastic data by variance stabilizing transformation.

(F) Quantification of intracellular citrate in $PDH^{fl/fl}$ and $PDH^{fl/fl}$ CD4 Cre+ Th17 cells incubated for 72 h with acetate (10 mM). Data are mean ± SEM (n = 3) and representative of 2 trials.

(G) Fractional carbon contribution of ^{13}C-acetate to octadecenoic acid in $PDH^{fl/fl}$ and $PDH^{fl/fl}$ CD4 Cre+ Th17 cells. Data are mean ± SEM (n = 3) and representative of 2 trials.

(H) Left: representative FCA of the proliferation of CTV-labeled $PDH^{fl/fl}$ and $PDH^{fl/fl}$ CD4 Cre+ Th17 cells cultured in complete IMDM and treated or not with acetate (10 mM). Right: division index of the Th17 cells in the left panel. Data are mean ± SEM (n = 3) and representative of 3 trials.

(I) Quantification of Seahorse determination of basal OCR in $PDH^{fl/fl}$ and $PDH^{fl/fl}$ CD4 Cre+ *in vitro*-differentiated Th17 cells treated or not with acetate (10 mM). Data are mean ± SEM (n = 3) and representative of 3 trials.

(J and K) Quantification of Glut-1 MFI (J) and 2-NBDG MFI (K) in $PDH^{fl/fl}$ and $PDH^{fl/fl}$ CD4 Cre+ *in vitro*-differentiated Th17 cells treated or not with acetate (10 mM), gated on viable $CD4^+$ cells. Data are mean ± SEM (n = 3) and representative of 3 trials.

(L) YSI quantification of glutamine uptake from the culture medium of $PDH^{fl/fl}$ and $PDH^{fl/fl}$CD4 Cre+ Th17 cells treated or not with acetate (10 mM). Data are mean ± SEM (n = 3) and representative of 2 trials.

(M–O) Quantification of intracellular p-mTOR MFI (M), CD36 MFI (N), and BODIPY FL C16 MFI (O) in $PDH^{fl/fl}$ and $PDH^{fl/fl}$ CD4 Cre+ *in vitro*-differentiated Th17 cells treated or not with acetate (10 mM), gated on viable $CD4^+$ cells. Data are mean ± SEM (n = 3) and representative of 3 trials.

(P) Intracellular FCA of frequencies of IL-$17A^+$ cells among $PDH^{fl/fl}$ and $PDH^{fl/fl}$ CD4 Cre+ Th17 cells treated or not with acetate (10 mM) and stimulated for 5 h with PMA/Iono, gated on viable $CD4^+$ cells. Data are mean ± SEM (n = 3) and representative of 4 trials.

The p values are determined by unpaired two-tailed Student's t test or two-way ANOVA where appropriate. Correction for multiple comparisons was performed using the Tukey test. *p < 0.05, **p < 0.01, ***p < 0.001, ****p < 0.0001.

- EAE mouse model
- Study approval

- METHOD DETAILS
  - Naive T cell isolation from spleen and lymph nodes
  - Isolation of lymphocytes from mouse brain
  - *In vitro* differentiation of Th cell subsets
  - Immunoblotting
  - Flow cytometry
  - Expression plasmids and retroviral transduction
  - Cytokine quantification
  - ATP quantification
  - Metabolic flux measurements and analysis
  - Isotopic labeling
  - GC-MS measurement of non-polar fractions, data processing and normalization
  - LC-MS analysis of histones
  - GC-MS of samples labeled by ^{13}C-palmitate
  - Acetyl-CoA measurement by LC-MS
  - Proliferation
  - RNA extraction and quantitative RT-PCR
  - RNA-seq sample preparation
  - RNA-seq data analysis
  - ATAC-seq sample preparation
  - ATAC-seq data analysis
- QUANTIFICATION AND STATISTICAL ANALYSIS

SUPPLEMENTAL INFORMATION

Supplemental information can be found online at https://doi.org/10.1016/j.celrep.2023.112153.

ACKNOWLEDGMENTS

We are grateful to Max Löhning (Charité University Berlin) and Alexander Skupin (University of Luxembourg) for helpful discussions, Dr. Aurelien Ginolhac (University of Luxembourg) for bioinformatic analysis, the Metabolomics Platform of the Luxembourg Center for Systems Biomedicine (LCSB; University of Luxembourg) for metabolomics data, Dr. Rashi Halder of the Sequencing Platform of the LCSB for sequencing data (RRID: SCR_021931), the High-Performance Computing (HPC) platform (University of Luxembourg), and the National Cytometry Platform (LIH; Luxembourg) for support with flow cytometry. We also thank Samantha Storn, Anaïs Oudin, all Animal Facility staff, and LIH's Animal Welfare Structure for animal services at LIH, Luxembourg, and Djalil Coowar, Jennifer Behm, Marthe Schmit and all Animal Facility staff for animal services at the University of Luxembourg.

D.B. is supported by FNR-ATTRACT (A14/BM/7632103) and FNR-CORE grants (C21/BM/15796788 and C18/BM/12691266). D.B., T.K., and C.D. are supported by FNRS-Televie grants 7.4587.20 and/or 7.497.19; D.B., L.B., L.G., and L.S.-B. by FNR-PRIDE (PRIDE/11012546/NEXTIMMUNE); D.B. and A.E. by PRIDE17/11823097/MicrOH; D.B. and D.G.F. by FNR-RIKEN (TregBar/11228353); S.H. by FNR-PRIDE (PRIDE17/12244779/PARK-Q); D.G. by a postdoctoral fellowship from the Fondation du Pélican de Mie et Pierre Hippert-Faber; J.M. by FNR-ATTRACT (A18/BM/11809970); and M.M. by FNR PEARL (P16/BM/11192868).

AUTHOR CONTRIBUTIONS

L.S.-B. performed most experiments, assisted by M.G., H.K., L.B., A.E., L.G., D.G.F., C.B., C.V., and S.F. L.S.-B., M.G., and C.B. isolated brains and spleens from EAE mice. L.S.-B., H.K., A.E., and D.G.F. performed Seahorse flux assays. Isotopic and metabolic tracing experiments were performed by L.S.-B., M.G., and H.K. and analyzed by M.B. and J.M. Histone and palmitate tracing experiments were performed and analyzed by T.H.M. and A.H. Analysis of RNA-seq data was performed by J.L. and S.H. ATAC-seq and data analysis were performed by S.H., D.G., and L.S. T.K., C.D., J.-J.G., C.J., M.M., L.S., K.H., and J.M. provided reagents and expert comments. D.B. supervised the project. L.S.-B. and D.B. conceptualized the work, designed all experiments, analyzed data, and wrote the manuscript. All authors reviewed and edited the final manuscript.

DECLARATION OF INTERESTS

The authors declare no competing interests.

INCLUSION AND DIVERSITY

We support inclusive, diverse, and equitable conduct of research.

Received: April 5, 2022
Revised: December 5, 2022
Accepted: February 7, 2023

REFERENCES

1. Pearce, E.L., Poffenberger, M.C., Chang, C.-H., and Jones, R.G. (2013). Fueling immunity: insights into metabolism and lymphocyte function. Science *342*, 1242454. https://doi.org/10.1126/science.1242454.
2. Aranami, T., and Yamamura, T. (2008). Th17 cells and autoimmune encephalomyelitis (EAE/MS). Allergol. Int. *57*, 115–120. https://doi.org/10.2332/allergolint.R-07-159.
3. Basu, R., Hatton, R.D., and Weaver, C.T. (2013). The Th17 family: flexibility follows function. Immunol. Rev. *252*, 89–103. https://doi.org/10.1111/imr.12035.
4. Wu, B., and Wan, Y. (2020). Molecular control of pathogenic Th17 cells in autoimmune diseases. Int. Immunopharm. *80*, 106187. https://doi.org/10.1016/j.intimp.2020.106187.
5. Franchina, D.G., Dostert, C., and Brenner, D. (2018). Reactive oxygen species: involvement in T cell signaling and metabolism. Trends Immunol. *39*, 489–502. https://doi.org/10.1016/j.it.2018.01.005.
6. Guerra, L., Bonetti, L., and Brenner, D. (2020). Metabolic modulation of immunity: a new concept in cancer immunotherapy. Cell Rep. *32*, 107848. https://doi.org/10.1016/j.celrep.2020.107848.
7. Pearce, E.L., and Pearce, E.J. (2013). Metabolic pathways in immune cell activation and quiescence. Immunity *38*, 633–643. https://doi.org/10.1016/j.immuni.2013.04.005.
8. Buck, M.D., O'Sullivan, D., and Pearce, E.L. (2015). T cell metabolism drives immunity. J. Exp. Med. *212*, 1345–1360. https://doi.org/10.1084/jem.20151159.
9. Kurniawan, H., Soriano-Baguet, L., and Brenner, D. (2020). Regulatory T cell metabolism at the intersection between autoimmune diseases and cancer. Eur. J. Immunol. *50*, 1626–1642. https://doi.org/10.1002/eji.201948470.
10. Rangel Rivera, G.O., Knochelmann, H.M., Dwyer, C.J., Smith, A.S., Wyatt, M.M., Rivera-Reyes, A.M., Thaxton, J.E., and Paulos, C.M. (2021). Fundamentals of T Cell metabolism and strategies to enhance cancer immunotherapy. Front. Immunol. *12*, 645242. https://doi.org/10.3389/fimmu.2021.645242.
11. Chapman, N.M., and Chi, H. (2022). Metabolic adaptation of lymphocytes in immunity and disease. Immunity *55*, 14–30. https://doi.org/10.1016/j.immuni.2021.12.012.
12. DeBrosse, S.D., and Kerr, D.S. (2016). Pyruvate dehydrogenase complex deficiency. In Mitochondrial Case Studies (Elsevier), pp. 93–101. https://doi.org/10.1016/B978-0-12-800877-5.00012-7.
13. O'Neill, L.A.J., Kishton, R.J., and Rathmell, J. (2016). A guide to immunometabolism for immunologists. Nat. Rev. Immunol. *16*, 553–565. https://doi.org/10.1038/nri.2016.70.

14. Wellen, K.E., Hatzivassiliou, G., Sachdeva, U.M., Bui, T.V., Cross, J.R., and Thompson, C.B. (2009). ATP-citrate lyase links cellular metabolism to histone acetylation. Science *324*, 1076–1080. https://doi.org/10.1126/science.1164097.

15. Wang, R., and Green, D.R. (2012). Metabolic reprogramming and metabolic dependency in T cells. Immunol. Rev. *249*, 14–26. https://doi.org/10.1111/j.1600-065X.2012.01155.x.

16. Zhao, S., Torres, A., Henry, R.A., Trefely, S., Wallace, M., Lee, J.V., Carrer, A., Sengupta, A., Campbell, S.L., Kuo, Y.-M., et al. (2016). ATP-citrate lyase controls a glucose-to-acetate metabolic switch. Cell Rep. *17*, 1037–1052. https://doi.org/10.1016/j.celrep.2016.09.069.

17. Koundouros, N., and Poulogiannis, G. (2020). Reprogramming of fatty acid metabolism in cancer. Br. J. Cancer *122*, 4–22. https://doi.org/10.1038/s41416-019-0650-z.

18. Li, B., Carey, M., and Workman, J.L. (2007). The role of chromatin during transcription. Cell *128*, 707–719. https://doi.org/10.1016/j.cell.2007.01.015.

19. Pietrocola, F., Galluzzi, L., Bravo-San Pedro, J.M., Madeo, F., and Kroemer, G. (2015). Acetyl coenzyme A: a central metabolite and second messenger. Cell Metabol. *21*, 805–821. https://doi.org/10.1016/j.cmet.2015.05.014.

20. Sivanand, S., Viney, I., and Wellen, K.E. (2018). Spatiotemporal control of acetyl-CoA metabolism in chromatin regulation. Trends Biochem. Sci. *43*, 61–74. https://doi.org/10.1016/j.tibs.2017.11.004.

21. Yang, W., Pang, D., Chen, M., Du, C., Jia, L., Wang, L., He, Y., Jiang, W., Luo, L., Yu, Z., et al. (2021). Rheb mediates neuronal-activity-induced mitochondrial energetics through mTORC1-independent PDH activation. Dev. Cell *56*, 811–825.e6. https://doi.org/10.1016/j.devcel.2021.02.022.

22. Baricza, E., Marton, N., Királyhidi, P., Kovács, O.T., Kovácsné Székely, I., Lajkó, E., Kőhidai, L., Rojkovich, B., Érsek, B., Buzás, E.I., and Nagy, G. (2018). Distinct in vitro T-helper 17 differentiation capacity of peripheral naive T cells in rheumatoid and psoriatic arthritis. Front. Immunol. *9*, 606. https://doi.org/10.3389/fimmu.2018.00606.

23. Macintyre, A.N., Gerriets, V.A., Nichols, A.G., Michalek, R.D., Rudolph, M.C., Deoliveira, D., Anderson, S.M., Abel, E.D., Chen, B.J., Hale, L.P., and Rathmell, J.C. (2014). The glucose transporter Glut1 is selectively essential for CD4 T cell activation and effector function. Cell Metabol. *20*, 61–72. https://doi.org/10.1016/j.cmet.2014.05.004.

24. Zou, C., Wang, Y., and Shen, Z. (2005). 2-NBDG as a fluorescent indicator for direct glucose uptake measurement. J. Biochem. Biophys. Methods *64*, 207–215. https://doi.org/10.1016/j.jbbm.2005.08.001.

25. Katsen, M., Soderman, D., and Nitowsky, M. (1965). Kinetic and electrophoretic evidence for multiple forms of glucose-ATP phosphotransferase activity from human cell cultures and rat liver. Biochem. Biophys. Res. Commun. *19*, 6.

26. Buescher, J.M., Antoniewicz, M.R., Boros, L.G., Burgess, S.C., Brunengraber, H., Clish, C.B., DeBerardinis, R.J., Feron, O., Frezza, C., Ghesquiere, B., et al. (2015). A roadmap for interpreting 13 C metabolite labeling patterns from cells. Curr. Opin. Biotechnol. *34*, 189–201. https://doi.org/10.1016/j.copbio.2015.02.003.

27. Yoo, H.C., Yu, Y.C., Sung, Y., and Han, J.M. (2020). Glutamine reliance in cell metabolism. Exp. Mol. Med. *52*, 1496–1516. https://doi.org/10.1038/s12276-020-00504-8.

28. de Jong, A.J., Kloppenburg, M., Toes, R.E.M., and Ioan-Facsinay, A. (2014). Fatty acids, lipid mediators, and T-cell function. Front. Immunol. *5*, 483. https://doi.org/10.3389/fimmu.2014.00483.

29. Wang, C., Yan, Y., Hu, L., Zhao, L., Yang, P., Moorhead, J.F., Varghese, Z., Chen, Y., and Ruan, X.Z. (2014). Rapamycin-mediated CD36 translational suppression contributes to alleviation of hepatic steatosis. Biochem. Biophys. Res. Commun. *447*, 57–63. https://doi.org/10.1016/j.bbrc.2014.03.103.

30. Angela, M., Endo, Y., Asou, H.K., Yamamoto, T., Tumes, D.J., Tokuyama, H., Yokote, K., and Nakayama, T. (2016). Fatty acid metabolic reprogramming via mTOR-mediated inductions of PPARγ directs early activation of T cells. Nat. Commun. *7*, 13683. https://doi.org/10.1038/ncomms13683.

31. Wipperman, M.F., Montrose, D.C., Gotto, A.M., and Hajjar, D.P. (2019). Mammalian target of rapamycin. Am. J. Pathol. *189*, 492–501. https://doi.org/10.1016/j.ajpath.2018.11.013.

32. Takahara, T., Amemiya, Y., Sugiyama, R., Maki, M., and Shibata, H. (2020). Amino acid-dependent control of mTORC1 signaling: a variety of regulatory modes. J. Biomed. Sci. *27*, 87. https://doi.org/10.1186/s12929-020-00679-2.

33. Izzo, L., Trefely, S., Demetriadou, C., Drummond, J., Mizukami, T., Kuprasertkul, N., Farria, A., Nguyen, P., Reich, L., Shaffer, J., et al. (2022). The carnitine shuttle links mitochondrial metabolism to histone acetylation and lipogenesis. Cell Biol. https://doi.org/10.1101/2022.09.24.509197.

34. Buenrostro, J.D., Giresi, P.G., Zaba, L.C., Chang, H.Y., and Greenleaf, W.J. (2013). Transposition of native chromatin for fast and sensitive epigenomic profiling of open chromatin, DNA-binding proteins and nucleosome position. Nat. Methods *10*, 1213–1218. https://doi.org/10.1038/nmeth.2688.

35. Buenrostro, J.D., Wu, B., Chang, H.Y., and Greenleaf, W.J. (2015). ATAC-seq: a method for assaying chromatin accessibility genome-wide. Curr. Protoc. Mol. Biol. *109*, 21.29.1–21.29.9. https://doi.org/10.1002/0471142727.mb2129s109.

36. Bulusu, V., Tumanov, S., Michalopoulou, E., van den Broek, N.J., MacKay, G., Nixon, C., Dhayade, S., Schug, Z.T., Vande Voorde, J., Blyth, K., et al. (2017). Acetate recapturing by nuclear acetyl-CoA synthetase 2 prevents loss of histone acetylation during oxygen and serum limitation. Cell Rep. *18*, 647–658. https://doi.org/10.1016/j.celrep.2016.12.055.

37. Qiu, J., Villa, M., Sanin, D.E., Buck, M.D., O'Sullivan, D., Ching, R., Matsushita, M., Grzes, K.M., Winkler, F., Chang, C.-H., et al. (2019). Acetate promotes T cell effector function during glucose restriction. Cell Rep. *27*, 2063–2074.e5. https://doi.org/10.1016/j.celrep.2019.04.022.

38. Comerford, S.A., Huang, Z., Du, X., Wang, Y., Cai, L., Witkiewicz, A.K., Walters, H., Tantawy, M.N., Fu, A., Manning, H.C., et al. (2014). Acetate dependence of tumors. Cell *159*, 1591–1602. https://doi.org/10.1016/j.cell.2014.11.020.

39. Chapman, N.M., Boothby, M.R., and Chi, H. (2020). Metabolic coordination of T cell quiescence and activation. Nat. Rev. Immunol. *20*, 55–70. https://doi.org/10.1038/s41577-019-0203-y.

40. Dang, E.V., Barbi, J., Yang, H.-Y., Jinasena, D., Yu, H., Zheng, Y., Bordman, Z., Fu, J., Kim, Y., Yen, H.-R., et al. (2011). Control of TH17/treg balance by hypoxia-inducible factor 1. Cell *146*, 772–784. https://doi.org/10.1016/j.cell.2011.07.033.

41. Michalek, R.D., Gerriets, V.A., Jacobs, S.R., Macintyre, A.N., MacIver, N.J., Mason, E.F., Sullivan, S.A., Nichols, A.G., and Rathmell, J.C. (2011). Cutting edge: distinct glycolytic and lipid oxidative metabolic programs are essential for effector and regulatory CD4 $^{+}$ T cell subsets. J. Immunol. *186*, 3299–3303. https://doi.org/10.4049/jimmunol.1003613.

42. Shi, L.Z., Wang, R., Huang, G., Vogel, P., Neale, G., Green, D.R., and Chi, H. (2011). HIF1α–dependent glycolytic pathway orchestrates a metabolic checkpoint for the differentiation of TH17 and Treg cells. J. Exp. Med. *208*, 1367–1376. https://doi.org/10.1084/jem.20110278.

43. Wang, R., Dillon, C.P., Shi, L.Z., Milasta, S., Carter, R., Finkelstein, D., McCormick, L.L., Fitzgerald, P., Chi, H., Munger, J., and Green, D.R. (2011). The transcription factor myc controls metabolic reprogramming upon T lymphocyte activation. Immunity *35*, 871–882. https://doi.org/10.1016/j.immuni.2011.09.021.

44. Zhang, D., Jin, W., Wu, R., Li, J., Park, S.-A., Tu, E., Zanvit, P., Xu, J., Liu, O., Cain, A., and Chen, W. (2019). High glucose intake exacerbates autoimmunity through reactive-oxygen-species-mediated TGF-β cytokine activation. Immunity *51*, 671–681.e5. https://doi.org/10.1016/j.immuni.2019.08.001.

45. Xu, K., Yin, N., Peng, M., Stamatiades, E.G., Chhangawala, S., Shyu, A., Li, P., Zhang, X., Do, M.H., Capistrano, K.J., et al. (2021). Glycolytic ATP fuels phosphoinositide 3-kinase signaling to support effector T helper 17 cell

responses. Immunity *54*, 976–987.e7. https://doi.org/10.1016/j.immuni.2021.04.008.

46. Bricker, D.K., Taylor, E.B., Schell, J.C., Orsak, T., Boutron, A., Chen, Y.-C., Cox, J.E., Cardon, C.M., Van Vranken, J.G., Dephoure, N., et al. (2012). A mitochondrial pyruvate carrier required for pyruvate uptake in yeast, *Drosophila* , and humans. Science *337*, 96–100. https://doi.org/10.1126/science.1218099.
47. Herzig, S., Raemy, E., Montessuit, S., Veuthey, J.-L., Zamboni, N., Westermann, B., Kunji, E.R.S., and Martinou, J.-C. (2012). Identification and functional expression of the mitochondrial pyruvate carrier. Science *337*, 93–96. https://doi.org/10.1126/science.1218530.
48. Zangari, J., Petrelli, F., Maillot, B., and Martinou, J.-C. (2020). The multifaceted pyruvate metabolism: role of the mitochondrial pyruvate carrier. Biomolecules *10*, 1068. https://doi.org/10.3390/biom10071068.
49. Ramstead, A.G., Wallace, J.A., Lee, S.-H., Bauer, K.M., Tang, W.W., Ekiz, H.A., Lane, T.E., Cluntun, A.A., Bettini, M.L., Round, J.L., et al. (2020). Mitochondrial pyruvate carrier 1 promotes peripheral T cell homeostasis through metabolic regulation of thymic development. Cell Rep. *30*, 2889–2899.e6. https://doi.org/10.1016/j.celrep.2020.02.042.
50. Johnson, M.O., Wolf, M.M., Madden, M.Z., Andrejeva, G., Sugiura, A., Contreras, D.C., Maseda, D., Liberti, M.V., Paz, K., Kishton, R.J., et al. (2018). Distinct regulation of Th17 and Th1 cell differentiation by glutaminase-dependent metabolism. Cell *175*, 1780–1795.e19. https://doi.org/10.1016/j.cell.2018.10.001.
51. Wenes, M., Jaccard, A., Wyss, T., Maldonado-Pérez, N., Teoh, S.T., Lepez, A., Renaud, F., Franco, F., Waridel, P., Yacoub Maroun, C., et al. (2022). The mitochondrial pyruvate carrier regulates memory T cell differentiation and antitumor function. Cell Metabol. *34*, 731–746.e9. https://doi.org/10.1016/j.cmet.2022.03.013.
52. Sutendra, G., Kinnaird, A., Dromparis, P., Paulin, R., Stenson, T.H., Haromy, A., Hashimoto, K., Zhang, N., Flaim, E., and Michelakis, E.D. (2014). A nuclear pyruvate dehydrogenase complex is important for the generation of acetyl-CoA and histone acetylation. Cell *158*, 84–97. https://doi.org/10.1016/j.cell.2014.04.046.
53. Jun, S., Mahesula, S., Mathews, T.P., Martin-Sandoval, M.S., Zhao, Z., Piskounova, E., and Agathocleous, M. (2021). The requirement for pyruvate dehydrogenase in leukemogenesis depends on cell lineage. Cell Metabol. *33*, 1777–1792.e8. https://doi.org/10.1016/j.cmet.2021.07.016.
54. Marelli-Berg, F.M., Fu, H., and Mauro, C. (2012). Molecular mechanisms of metabolic reprogramming in proliferating cells: implications for T-cell-mediated immunity: the metabolic control of T-cell immunity. Immunology *136*, 363–369. https://doi.org/10.1111/j.1365-2567.2012.03583.x.
55. Mak, T.W., Grusdat, M., Duncan, G.S., Dostert, C., Nonnenmacher, Y., Cox, M., Binsfeld, C., Hao, Z., Brüstle, A., Itsumi, M., et al. (2017). Glutathione primes T cell metabolism for inflammation. Immunity *46*, 675–689. https://doi.org/10.1016/j.immuni.2017.03.019.
56. Kurniawan, H., Franchina, D.G., Guerra, L., Bonetti, L., - Baguet, L.S., Grusdat, M., Schlicker, L., Hunewald, O., Dostert, C., Merz, M.P., et al. (2020). Glutathione restricts serine metabolism to preserve regulatory T cell function. Cell Metabol. *31*, 920–936.e7. https://doi.org/10.1016/j.cmet.2020.03.004.
57. Gerriets, V.A., Kishton, R.J., Nichols, A.G., Macintyre, A.N., Inoue, M., Ilkayeva, O., Winter, P.S., Liu, X., Priyadharshini, B., Slawinska, M.E., et al. (2015). Metabolic programming and PDHK1 control CD4+ T cell subsets and inflammation. J. Clin. Invest. *125*, 194–207. https://doi.org/10.1172/JCI76012.
58. Delgoffe, G.M., Kole, T.P., Zheng, Y., Zarek, P.E., Matthews, K.L., Xiao, B., Worley, P.F., Kozma, S.C., and Powell, J.D. (2009). mTOR differentially regulates effector and regulatory T cell lineage commitment. Immunity *30*, 832–844. https://doi.org/10.1016/j.immuni.2009.04.014.
59. Nagai, S., Kurebayashi, Y., and Koyasu, S. (2013). Role of PI3K/Akt and mTOR complexes in Th17 cell differentiation: Th17 cells and PI3K-Akt-mTOR complexes. Ann. N. Y. Acad. Sci. *1280*, 30–34. https://doi.org/10.1111/nyas.12059.
60. Salmond, R.J. (2018). mTOR regulation of glycolytic metabolism in T cells. Front. Cell Dev. Biol. *6*, 122. https://doi.org/10.3389/fcell.2018.00122.
61. Peng, M., Yin, N., Chhangawala, S., Xu, K., Leslie, C.S., and Li, M.O. (2016). Aerobic glycolysis promotes T helper 1 cell differentiation through an epigenetic mechanism. Science *354*, 481–484. https://doi.org/10.1126/science.aaf6284.
62. Soriano-Baguet, L., and Brenner, D. (2023). Metabolism and epigenetics at the heart of T cell function. Trends Immunol.
63. Hochrein, S.M., Wu, H., Eckstein, M., Arrigoni, L., Herman, J.S., Schumacher, F., Gerecke, C., Rosenfeldt, M., Grün, D., Kleuser, B., et al. (2022). The glucose transporter GLUT3 controls T helper 17 cell responses through glycolytic-epigenetic reprogramming. Cell Metabol. *34*, 516–532.e11. https://doi.org/10.1016/j.cmet.2022.02.015.
64. Brüstle, A., Brenner, D., Knobbe, C.B., Lang, P.A., Virtanen, C., Hershenfield, B.M., Reardon, C., Lacher, S.M., Ruland, J., Ohashi, P.S., and Mak, T.W. (2012). The NF-κB regulator MALT1 determines the encephalitogenic potential of Th17 cells. J. Clin. Invest. *122*, 4698–4709. https://doi.org/10.1172/JCI63528.
65. Cossarizza, A., Chang, H., Radbruch, A., Acs, A., Adam, D., Adam-Klages, S., Agace, W.W., Aghaeepour, N., Akdis, M., Allez, M., et al. (2019). Guidelines for the use of flow cytometry and cell sorting in immunological studies (second edition). Eur. J. Immunol. *49*, 1457–1973. https://doi.org/10.1002/eji.201970107.
66. Battello, N., Zimmer, A.D., Goebel, C., Dong, X., Behrmann, I., Haan, C., Hiller, K., and Wegner, A. (2016). The role of HIF-1 in oncostatin M-dependent metabolic reprogramming of hepatic cells. Cancer Metabol. *4*, 3. https://doi.org/10.1186/s40170-016-0141-0.
67. Hiller, K., Hangebrauk, J., Jäger, C., Spura, J., Schreiber, K., and Schomburg, D. (2009). MetaboliteDetector: comprehensive analysis tool for targeted and nontargeted GC/MS based metabolome analysis. Anal. Chem. *81*, 3429–3439. https://doi.org/10.1021/ac802689c.
68. Lauterbach, M.A., Hanke, J.E., Serefidou, M., Mangan, M.S.J., Kolbe, C.-C., Hess, T., Rothe, M., Kaiser, R., Hoss, F., Gehlen, J., et al. (2019). Toll-like receptor signaling rewires macrophage metabolism and promotes histone acetylation via ATP-citrate lyase. Immunity *51*, 997–1011.e7. https://doi.org/10.1016/j.immuni.2019.11.009.
69. Meiser, J., Tumanov, S., Maddocks, O., Labuschagne, C.F., Athineos, D., Van Den Broek, N., Mackay, G.M., Gottlieb, E., Blyth, K., Vousden, K., et al. (2016). Serine one-carbon catabolism with formate overflow. Sci. Adv. *2*, e1601273. https://doi.org/10.1126/sciadv.1601273.
70. Seim, G.L., Britt, E.C., John, S.V., Yeo, F.J., Johnson, A.R., Eisenstein, R.S., Pagliarini, D.J., and Fan, J. (2019). Two-stage metabolic remodelling in macrophages in response to lipopolysaccharide and interferon-γ stimulation. Nat. Metab. *1*, 731–742. https://doi.org/10.1038/s42255-019-0083-2.
71. Andrews, S. (2010). FastQC: A Quality Control Tool for High Throughput Sequence Data.
72. Schubert, M., Ermini, L., Der Sarkissian, C., Jónsson, H., Ginolhac, A., Schaefer, R., Martin, M.D., Fernández, R., Kircher, M., McCue, M., et al. (2014). Characterization of ancient and modern genomes by SNP detection and phylogenomic and metagenomic analysis using PALEOMIX. Nat. Protoc. *9*, 1056–1082. https://doi.org/10.1038/nprot.2014.063.
73. Kopylova, E., Noé, L., and Touzet, H. (2012). SortMeRNA: fast and accurate filtering of ribosomal RNAs in metatranscriptomic data. Bioinformatics *28*, 3211–3217. https://doi.org/10.1093/bioinformatics/bts611.
74. Dobin, A., Davis, C.A., Schlesinger, F., Drenkow, J., Zaleski, C., Jha, S., Batut, P., Chaisson, M., and Gingeras, T.R. (2013). STAR: ultrafast universal RNA-seq aligner. Bioinformatics *29*, 15–21. https://doi.org/10.1093/bioinformatics/bts635.
75. Patro, R., Duggal, G., Love, M.I., Irizarry, R.A., and Kingsford, C. (2017). Salmon provides fast and bias-aware quantification of transcript expression. Nat. Methods *14*, 417–419. https://doi.org/10.1038/nmeth.4197.
76. Frankish, A., Diekhans, M., Ferreira, A.-M., Johnson, R., Jungreis, I., Loveland, J., Mudge, J.M., Sisu, C., Wright, J., Armstrong, J., et al. (2019).

GENCODE reference annotation for the human and mouse genomes. Nucleic Acids Res. *47*, D766–D773. https://doi.org/10.1093/nar/gky955.

77. Love, M.I., Soneson, C., Hickey, P.F., Johnson, L.K., Pierce, N.T., Shepherd, L., Morgan, M., and Patro, R. (2020). Tximeta: reference sequence checksums for provenance identification in RNA-seq. PLoS Comput. Biol. *16*, e1007664. https://doi.org/10.1371/journal.pcbi.1007664.
78. Love, M.I., Huber, W., and Anders, S. (2014). Moderated estimation of fold change and dispersion for RNA-seq data with DESeq2. Genome Biol. *15*, 550. https://doi.org/10.1186/s13059-014-0550-8.
79. Yu, G., Wang, L.-G., Han, Y., and He, Q.-Y. (2012). clusterProfiler: an R Package for comparing biological themes among gene clusters. OMICS A J. Integr. Biol. *16*, 284–287. https://doi.org/10.1089/omi.2011.0118.
80. Luo, W., and Brouwer, C. (2013). Pathview: an R/Bioconductor package for pathway-based data integration and visualization. Bioinformatics *29*, 1830–1831. https://doi.org/10.1093/bioinformatics/btt285.
81. Corces, M.R., Trevino, A.E., Hamilton, E.G., Greenside, P.G., Sinnott-Armstrong, N.A., Vesuna, S., Satpathy, A.T., Rubin, A.J., Montine, K.S., Wu, B., et al. (2017). An improved ATAC-seq protocol reduces background and enables interrogation of frozen tissues. Nat. Methods *14*, 959–962. https://doi.org/10.1038/nmeth.4396.
82. Adams, M.D., Celniker, S.E., Holt, R.A., Evans, C.A., Gocayne, J.D., Amanatides, P.G., Scherer, S.E., Li, P.W., Hoskins, R.A., Galle, R.F., et al. (2000). The genome sequence of *Drosophila melanogaster*. Science *287*, 2185–2195. https://doi.org/10.1126/science.287.5461.2185.
83. Li, H., Handsaker, B., Wysoker, A., Fennell, T., Ruan, J., Homer, N., Marth, G., Abecasis, G., and Durbin, R.; 1000 Genome Project Data Processing Subgroup (2009). The sequence alignment/map format and SAMtools. Bioinformatics *25*, 2078–2079. https://doi.org/10.1093/bioinformatics/btp352.
84. Stark, R., and Brown, G. (2022). DiffBind: differential binding analysis of ChIP-Seq peak data. Bioconductor *75*. https://doi.org/10.18129/B9.bioc.DiffBind.
85. Amemiya, H.M., Kundaje, A., and Boyle, A.P. (2019). The ENCODE blacklist: identification of problematic regions of the genome. Sci. Rep. *9*, 9354. https://doi.org/10.1038/s41598-019-45839-z.
86. Ramírez, F., Ryan, D.P., Grüning, B., Bhardwaj, V., Kilpert, F., Richter, A.S., Heyne, S., Dündar, F., and Manke, T. (2016). deepTools2: a next generation web server for deep-sequencing data analysis. Nucleic Acids Res. *44*, W160–W165. https://doi.org/10.1093/nar/gkw257.

STAR★METHODS

KEY RESOURCES TABLE

REAGENT or RESOURCE	SOURCE	IDENTIFIER
Antibodies		
Anti-mouse CD4-APC Clone GK1.5	BioLegend	Cat# 100412, RRID:AB_312697
Anti-mouse CD3ε-PE-Cy7 Clone 145-2C11	BioLegend	Cat# 100320, RRID:AB_312685
Anti-mouse CD4-PE Clone GK1.5	BioLegend	Cat# 100408, RRID:AB_312693
Anti-mouse CD4-BV785 Clone GK1.5	BioLegend	Cat# 100453, RRID:AB_2565843
Anti-mouse CD4-BUV737 Clone GK1.5 (RUO)	BD Biosciences	Cat# 612761, RRID:AB_2870092
Anti-mouse IL17A-BV605 Clone TC11-18H10	BD Biosciences	Cat# 564169, RRID:AB_2738640
Anti-mouse IFN-γ-APC Clone XMG1.2	BioLegend	Cat# 505810, RRID:AB_315404
Anti-mouse RORγT-BV421 Clone Q31-378	BD Biosciences	Cat# 562894, RRID:AB_2687545
Anti-mouse Tbet-PE/Cy7 Clone 4B10	BioLegend	Cat# 644824, RRID:AB_2561761
Anti-mouse FoxP3-APC Clone FJK-16	Thermo Fisher Scientific	Cat# 17-5773-82, RRID:AB_469457
Anti-mouse CD25-PE Clone PC61	BioLegend	Cat# 102008, RRID:AB_312857
Anti-mouse pmTOR-PE Clone MRRBY	Thermo Fisher Scientific	Cat# 12-9718-42, RRID:AB_2572724
Anti-mouse pS6-APC Clone cupk43k	Thermo Fisher Scientific	Cat# 17-9007-42, RRID:AB_2573270
Anti-mouse CD45-PerCP/Cyanine5.5 Clone 30-F11	BioLegend	Cat# 103132, RRID:AB_893340
Anti-mouse Glut-1 – Alexa Fluor® 647 Clone EPR3915	Abcam	Cat# ab195020, RRID:AB_2783877
Anti-mouse Hexokinase-1 - Alexa Fluor® 488 Clone EPR10134(B)	Abcam	Cat# ab184818
Anti-mouse CD36-PerCP/Cyanine5.5 Clone HM36	BioLegend	Cat# 102620, RRID:AB_2750188
Ultra-LEAF™ Purified anti-mouse CD3ε Clone 145-2C11	BioLegend	Cat# 100340, RRID:AB_11149115
Ultra-LEAF™ Purified anti-mouse CD28 Clone 37.51	BioLegend	Cat# 102116, RRID:AB_11147170
Purified NA/LE Rat Anti-Mouse IFN-γ Clone XMG1.2	BD Biosciences	Cat# 554408, RRID:AB_395373
Anti-mouse pyruvate dehydrogenase E1-alpha subunit antibody	Abcam	Cat# ab168379
Anti-mouse acetyl-histone H3 antibody	Millipore	Cat# 06–599, RRID:AB_2115283
Anti-mouse actin antibody produced in rabbit	Sigma-Aldrich	Cat# A2066, RRID:AB_476693
Anti-mouse histone H3	Cell Signaling Technology	Cat# 9715S
Anti-mouse acetyl-histone H3 Lys27	Cell Signaling Technology	Cat# 8173S
Mouse anti-rabbit IgG-HRP	Santa Cruz Biotechnology	Cat# sc-2357, RRID:AB_628497
Chemicals, peptides, and recombinant proteins		
PBS (1X) without Ca^{2+}, Mg++, 500mL	Lonza	#BE17-516F
FBS Superior Lot: 0193F	Biochrom GmbH	#S0615
Penicillin-Streptomycin (10,000 U/mL)	Gibco	#11548876
L-Glutamine	Lonza	#BE17-605E
2-Mercaptoethanol	Gibco	#11508916
Methanol	Sigma-Aldrich	#1060351000
Chloroform	Sigma-Aldrich	#34854-1L-M
Ethanol absolute	VWR	#20821.330
Ethanol eurodenatured	VWR	#85823.440
Sodium acetate trihydrate	Sigma-Aldrich	#71188-250MG

(*Continued on next page*)

Continued

REAGENT or RESOURCE	SOURCE	IDENTIFIER
HEPES	Sigma-Aldrich	#H4034-100G
EDTA	Sigma-Aldrich	#EDS-100G
DL-Dithiothreitol solution (DTT)	Sigma-Aldrich	#43816-10ML
BSA	Sigma-Aldrich	#A9647-500G
RPMI 1640 (without L-Glutamine)	Lonza	#BE12-167F
IMDM with HEPES and L-Glutamine	Lonza	#BE12-722F
Collagenase D from *Clostridium histolyticum*	Roche	#11088866001
DNAseI	Sigma-Aldrich	#D4513-1VL
Percoll®	Sigma-Aldrich	#GE17-0891-01
Recombinant human TGF-β	R&D Biosystems	#240-B-002
Mouse IL-6, research grade	Miltenyi Biotec	#130-094-065
Mouse IL-2, research grade	Miltenyi Biotec	#130-098-221
Mouse IL-12, research grade	Miltenyi Biotec	#130-096-707
Cell Trace Violet	Invitrogen	#C34557
Molecular Probes™ 2-NBDG	Invitrogen	#N13195
SYBR™ Fast Green Master Mix	Applied Biosystems™	#4385612
Luna Universal One-Step RT-qPCR Kit	New England BioLabs Inc.	#E3005E
Formaldehyde	Sigma-Aldrich	#252549-1L
Saponin	Sigma-Aldrich	#S4521-25G
DAPI (1:2000)	Invitrogen	#D1306
Zombie NIR™ Fixable Viability Kit	Biolegend	#423106
Zombie Green™ Fixable Viability Kit	Biolegend	#423112
7-AAD	Invitrogen	#A1310
Bodipy™ FL C16	Invitrogen	#D3821
Corning™ Cell-Tak Cell and Tissue Adhesive	Corning™	#354240
Oligomycin A	Sigma-Aldrich	#75351-5MG
FCCP	Sigma-Aldrich	#C2920-10MG
Antimycin A	Sigma-Aldrich	#A8674-25MG
Rotenone	Sigma-Aldrich	#R8875-1G
2-Deoxy-D-glucose	Sigma-Aldrich	#D6134-1G
Sodium pyruvate	Gibco	#12539059
Phorbol 12-myristate 13-acetate (PMA)	Sigma-Aldrich	#P8139-1MG
Calcium ionophore A23187	Sigma-Aldrich	#C7522-1MG
Rapamycin	Invivogen	#tlrl-rap
Torin 1	Sigma-Aldrich	#475991-10MG
SILAC RPMI 1640 Flex Medium	Gibco	#15347143
$^{13}C_6$-glucose	Cambridge Isotope Lab	#CLM-1396
$^{13}C_5$-L-Glutamine	Cambridge Isotope Lab	#CLM-1822-H
$^{13}C_2$-Acetate	Sigma-Aldrich	#282014-250MG
D-(+)-Glucose solution	Sigma-Aldrich	#G8769-100ML
GolgiPlug™ (Protein Transport Inhibitor)	BD Biosciences	#555029
Tween 20	Sigma-Aldrich	#P7949-500ML
NaCl	Sigma-Aldrich	#S9888-5KG
Sodium bicarbonate solution	Sigma-Aldrich	#S8761-100ML
Protease/Phosphatase Inhibitor Cocktail (100x)	Cell Signaling Technology	#5872
Powdered milk	Carl Roth	#T145.2
Luminata™ Crescendo Western HRP substrate	Merck Millipore	#WBLUR0100
Seahorse XF DMEM medium	Agilent Technologies	#103575-100
Critical commercial assays		
$CD4^+$ T cell Isolation Kit	Miltenyi Biotec	#130-104-454

(*Continued on next page*)

Continued

REAGENT or RESOURCE	SOURCE	IDENTIFIER
Naive CD4$^+$ T cell Isolation Kit, mouse	Miltenyi Biotec	#130-104-453
NucleoSpin RNA 250	Macherey-Nagel	#740955.250
Foxp3/Transcription Factor Staining Buffer Set	Invitrogen	#00-5521-00
BD Cytofix/Cytoperm Fixation/Permeabilization kit	BD Biosciences	#554714
Mouse IL17 DuoSet ELISA	R&D Systems	#DY421
Seahorse XFe96 Fluxpak	Agilent Technologies	#102416-100
EAE induction kit: MOG35-55/CFA Emulsion PTX	Hooke Laboratories, Inc	#EK-2110
Deposited data		
RNA-seq	This manuscript	GEO: GSE222882
ATAC-seq	This manuscript	GEO: GSE222882
Experimental models: Organisms/strains		
Mouse: B6.129P2-Pdha1^{tm1Ptl}/J	Jackson Laboratory	JAX: 17,443, RRID:IMSR_JAX:017,443
Mouse: B6.Cg-Tg(Cd4-cre)1Cwi/BfluJ	Jackson Laboratory	JAX: 022,071, RRID:IMSR_JAX:022,071
Oligonucleotides		
Tbp Forward: GAAGAACAATCCAGACTAGCAGCA	Kurniawan et al., 2020[56]	N/A
Tbp Reverse: CCTTATAGGGAACTTCACATCACAG	Kurniawan et al., 2020[56]	N/A
Pdha1 Forward: CGT CTG TTG AGA GAG CAG CA	This manuscript	N/A
Pdha1 Reverse: CGC ACA AGA TAT CCA TTC CA	This manuscript	N/A
Pdhb Forward: AGGAGGGAATTGAATGTGAGGT	This manuscript	N/A
Pdhb Reverse: ACTGGCTTCTATGGCTTCGAT	This manuscript	N/A
Recombinant DNA		
Plasmid: pMIT-Pdha1-CD90.1	This manuscript	N/A
Plasmid: pMIT-CD90.1	This manuscript	N/A
Software and algorithms		
FlowJo Software	Tree Star	RRID:SCR_008520
Graphpad Prism	GraphPad Software, Inc	RRID:SCR_002798
Wave Software	Agilent	RRID:SCR_014526
Inkscape	Inkscape	RRID:SCR_014479

RESOURCE AVAILABILITY

Lead contact

Further information and requests for resources or reagents should be directed to and will be made available upon reasonable request by the Lead Contact, Dirk Brenner (dirk.brenner@lih.lu).

Materials availability

All unique/stable reagents generated in this study are available from the lead contact without restriction.

Data and code availability

- RNA-seq and ATAC-seq data have been deposited at GEO and are publicly available as of the date of publication. Accession number is listed in the key resource table. All other data reported in this paper will be shared by the lead contact upon request.
- This paper does not report original code.
- Any additional information required to reanalyze the data reported in this paper is available from the lead contact upon request.

EXPERIMENTAL MODEL AND SUBJECT DETAILS

Mice

PDH$^{fl/fl}$ mice [B6.129P2-Pdha1tm1Ptl/J] were purchased from The Jackson Laboratory and crossed with CD4 Cre-expressing mice, also obtained from The Jackson Laboratory. All experiments used sex- and age-matched mice (8–12 weeks old) with corresponding littermate controls. Male and female mice were used in all *in vitro* experiments.

EAE mouse model

Induction of EAE was performed and clinical scores determined based on the neurological signs described in Table S1.[64] Briefly, $PDH^{fl/fl}$ and $PDH^{fl/fl}$ CD4 Cre + male mice were injected subcutaneously with MOG_{35-55}/CFA emulsion, followed by two intraperitoneal injections of pertussis toxin (Hooke Labs). Mouse brains and spleens were analyzed at day 14 post-induction.

Study approval

All animal experimentation protocols were approved and conducted according to the LIH Animal Welfare Structure guidelines.

METHOD DETAILS

Naive T cell isolation from spleen and lymph nodes

Naive $CD4^+$ T cells were isolated from $PDH^{fl/fl}$ and $PDH^{fl/fl}$ CD4 Cre + mouse spleen and lymph nodes by magnetic bead sorting (MACS) using the Naive $CD4^+$ T cell isolation kit (Miltenyi Biotec) according to the manufacturer's protocol. Sorting was performed using an autoMACS pro-Separator (Miltenyi Biotec). Cell number calculations were performed using a CASY cell counter (Omni Life Science).

Isolation of lymphocytes from mouse brain

Isolation of lymphocytes from the brains of EAE-affected mice at day 14 post-induction was performed.[64] Mice were sacrificed and brains were perfused with 20 mL cold PBS through the left ventricle. Brains were digested in RPMI supplemented with 50 μg/mL collagenase D (Roche) and 10 μg/mL DNAse I (Sigma-Aldrich) for 1 h at 37°C in a mixer (Labortechnik). Lymphocyte enrichment was obtained by centrifugation using a two-layer Percoll gradient (40% and 70%), followed by two washes in RPMI.

In vitro differentiation of Th cell subsets

Naive T cells isolated from $PDH^{fl/fl}$ and $PDH^{fl/fl}$ CD4 Cre + spleen and lymph nodes as described above were seeded at $2x10^6$ cells/mL in complete medium consisting of IMDM (Lonza) supplemented with 10% FBS (Biochrom GmbH), 55μM 2-mercaptoethanol (Gibco) and 1% penicillin/streptomycin (Gibco), and incubated for 3 days in the presence of the appropriate Th subset-specific cytokine mix (cf. Table S2). For acetate-treated cells, *in vitro* Th cell differentiation was performed in the presence of 10 mM sodium acetate (Sigma-Aldrich) diluted in culture medium. For experiments examining the effects of glutamine, cells were cultured in RPMI-1640 medium (Lonza) supplemented with 10% FBS (Biochrom GmbH), 55μM 2-mercaptoethanol (Gibco) and 1% penicillin/streptomycin (Gibco) with 1% L-Glutamine (Lonza) (Complete) or without glutamine (w/o Glutamine).

Immunoblotting

Cells were lysed in lysis buffer (Cell Signaling Technology, 9803S) containing protease and phosphatase inhibitors (Cell Signaling Technology) following manufacturer's instructions. 20 μL of lysates were loaded on 16% polyacrylamide gels (Invitrogen), followed by electrophoresis and transfer to membrane.[56] The antibodies used for protein detection were anti-Pdha1 (Abcam, ab168379), anti-actin (Sigma Aldrich), anti-acetyl-histone H3 Lys27 (Cell Signaling Technology, 8173S), anti-histone H3 (Cell Signaling Technology, 9715S) and anti-acetyl-histone H3 (Millipore, 06–599) all diluted 1:1000 in TBS-T.

Flow cytometry

For the detection of surface markers, cells were stained for 30 min at 4°C in FACS buffer (PBS with 1% fetal bovine serum (FBS; Gibco) and 5 mM EDTA, pH 8.0) containing antibodies (cf. key resources table; 1:200 dilution) and one of four viability dyes: DAPI (Invitrogen), LIVE/DEAD Fixable Near-IR or Green Dye (Biolegend), or 7-AAD (Invitrogen; 1:1000-1:3000 dilution). Cells were washed in FACS buffer before flow cytometry measurements.

For intracellular staining of transcription factors, cells were fixed at 4°C for 1hr using the eBioscience FoxP3/Transcription Factor Fixation kit (Invitrogen) and permeabilized using the buffer provided by the kit. To measure intracellular cytokine expression, cells were restimulated for 5hr *in vitro* with phorbol 12-myristate 13-acetate (PMA; Sigma, 50 ng/mL), calcium ionophore A23187 (Ionomycin, Sigma, 750 ng/mL), and BD GolgiPlug Protein Transport Inhibitor (BD Biosciences, 1:1000 dilution). Cells were washed once with FACS buffer before extracellular staining, then fixed for 20 min at 4°C with BD Cytofix/Cytoperm and permeabilized with BD Perm/Wash buffer (BD Biosciences). To detect hexokinase-1, cells were fixed in 4% formaldehyde (Sigma-Aldrich) for 10 min at room temperature (RT), then permeabilized in PBS containing 0.1% Tween 20. For p-mTOR and p-S6 detection, cells were fixed in 2% formaldehyde (Sigma-Aldrich) for 10 min at RT, then permeabilized in 0.01% saponin (Sigma-Aldrich). Antibodies used for intracellular staining were diluted 1:200 in the appropriate permeabilization buffer prior to incubation with cells for 30 min at 4°C.

To measure 2-NBDG uptake, cells were incubated in glucose-free RPMI for 2 h at 37°C in the presence of 50 μM 2-NBDG (Invitrogen). To measure lipid uptake, cells were incubated in IMDM containing 1 μM BODIPY FL C16 (Invitrogen) for 30 min at 37°C. Cells were washed once with PBS prior to flow cytometric measurements.

Experiments have been done in accordance with the guidelines for flow cytometry and cell sorting.[65] All flow cytometric measurements were obtained using a BD Fortessa instrument (BD Biosciences) and analyses were performed using FlowJo v10.6.2 software (Tree Star).

Expression plasmids and retroviral transduction

Murine full-length *Pdha1* cDNA was cloned into the pMIT-CD90.1 vector at the EcoRI restriction site (GeneCust, France), with empty pMIT-CD90.1 vector serving as the control. Retroviral transduction was performed by adding retroviral supernatants to *in-vitro* differentiated Th17 cells on day 1 by spin infection.[55,56] Infected cells were cultured at 37°C in the appropriate Th subset differentiation medium for 48h, followed by MACS-sorting using the CD90.1 marker.

Cytokine quantification

Measurement of IL-17 in culture supernatants of *in vitro*-differentiated Th17 cells was performed using the Mouse IL-17 DuoSet ELISA kit (R&D Systems) following the manufacturer's instructions.

ATP quantification

ATP levels in $1x10^5$ *in vitro*-differentiated Th17 cells were measured using the CellTiter-Glo assay (Promega) according to the manufacturer's protocol.

Metabolic flux measurements and analysis

In vitro-differentiated Th17 cells were seeded at $3x10^5$ cells/well in a pre-coated XFe96 cell culture plate (Agilent Technologies) using Corning Cell-Tak Cell and Tissue Adhesive (Corning) and 0.1 M sodium bicarbonate (Sigma-Aldrich).

For OCR measurements, plated cells were cultured in XF Seahorse DMEM medium (Agilent Technologies) containing 2 mM glutamine (Lonza), 1 mM sodium pyruvate (Gibco) and 25 mM glucose (Sigma-Aldrich). OCR was measured using the XF Cell Mito Stress Test (Agilent Technologies) following the manufacturer's protocol, which involved sequential injections of oligomycin A (1 μM), carbonyl cyanide 4-(trifluoromethoxy)phenylhydrazone (FCCP; 3 μM) and antimycin A/rotenone (1 μM) (all from Sigma-Aldrich).

For ECAR measurements, plated cells were cultured in XF Seahorse DMEM medium (Agilent Technologies) containing 2 mM glutamine (Lonza), and ECAR was determined by the XF Glycolysis Stress Test Kit (Agilent Technologies). Measurements were taken during sequential injections of glucose (10 mM), oligomycin (1 μM) and 2-deoxy-D-glucose (2-DG; 50 mM) (all from Sigma-Aldrich).

Experiments were performed using an XFe96 Extracellular Flux Analyzer (Agilent), and results were analyzed using Wave 2.6.1 software (Agilent Technologies). All measurements were calculated from raw OCR or ECAR data as described in Table S3.

Isotopic labeling

For glucose and glutamine isotopic tracing, naive T cells were incubated for 3 days with the appropriate cytokine cocktail to induce Th cell differentiation *in vitro*. At day 3, cells were counted, washed and seeded for 24hr in tracing medium consisting of SILAC RPMI 1640 (Gibco) supplemented with 10% FBS (Biochrom GmbH), 55μM 2-mercaptoethanol (Gibco), 1% penicillin/streptomycin (Gibco), L-arginine (Sigma-Aldrich) and L-lysine (Sigma-Aldrich), and containing [U-$^{13}C_6$]-glucose (11.1 mmol/L; Cambridge Isotope Laboratories) or [U-$^{13}C_5$]-glutamine (2 mmol/L; Cambridge Isotope Laboratories).

For acetate isotopic tracing, naive T cells were incubated for 3 days in complete IMDM medium containing the appropriate cytokine cocktail and [U-$^{13}C_2$]-acetate (10 mM; Sigma-Aldrich).

Extraction of intracellular metabolites, MID and carbon contribution determinations, GC and LC-MS measurements, and substractions of natural isotope abundance, were performed using MetaboliteDetector software.[66] Glucose, lactate and glutamine concentrations in medium were measured by a YSI 2950D Biochemistry Analyzer (YSI Incorporated).

GC-MS measurement of non-polar fractions, data processing and normalization

Derivatization was performed using a multi-purpose sample preparation robot (Gerstel). Dried non-polar extracts of ^{13}C-glucose or ^{13}C-glutamine treated Th17 cells were dissolved in 30 μL N-Methyl-N-(tert-butyldimethylsilyl)trifluoroacetamide (MTBSTFA) containing 1% tert-butyldimethylchlorosilane (TBDMCS) and incubated for 60 min at 55°C with continuous shaking.

GC-MS analysis was performed using an Agilent 7890A GC coupled to an Agilent Mass Selective Detector (MSD; Agilent Technologies). A sample volume of 1 μL was injected into a Split/Splitless inlet operating in splitless mode at 280°C. The gas chromatograph was equipped with a 30 m (I.D. 0.25 mm, film 0.25 μm) ZB-5MSplus capillary column (Phenomenex) with a 5 m guard column in front of the analytical column. Helium was used as the carrier gas with a constant flow rate of 1.4 mL/min. GC temperature program was 100°C for 1 min, then increased to 325 °C at 7.5 °C/min, and held for 4 min. The total run time was 35 min. The transfer line temperature was set to 280°C. The MSD was operating under electron ionization at 70 eV. The MS source was held at 230°C and the quadrupole at 150°C. GC-MS measurements were performed in selected ion monitoring mode for precise determination of MIDs.

MetaboliteDetector (v3.2.20190704) was used to process all GC-MS chromatograms.[67] Compounds were annotated by retention time and mass spectrum using an in-house mass spectral library (overall similarity: >0.85). The following deconvolution settings were

applied: Peak threshold of 2; Minimum peak height of 2; 10 Bins per scan; Deconvolution width of 8 scans; No baseline adjustment; Minimum 1 peak per spectrum; No minimum required base peak intensity. MIDs for the following fragments were calculated (cf. Table S4).

LC-MS analysis of histones

Histones were extracted using acid extraction and separated on a 16% polyacrylamide gel.[68] In-gel acylation of histones was performed using propionic anhydride. Subsequently, in-gel digestion of histone proteins was performed to obtain tryptic-digested peptides. Peptides were desalted using C18-Omix tips (Agilent Technologies), vacuum-dried, and reconstituted in 0.1% formic acid in water. Peptide digest (10 μL) was injected into a Vanquish UHPLC System (Thermo Scientific) equipped with Hypersil GOLD and coupled to an Orbitrap ID-X Tribrid Mass Spectrometer (Thermo Scientific). Peptides were separated on Vanquish C18 UHPLC Columns (150*2.1 mm, 1.9 μm) at a flow rate of 300 μL/min using a 50 min gradient program starting from 5% to 50% of mobile phase B, where mobile phase A was water containing 0.1% formic acid and mobile phase B was acetonitrile containing 0.1% formic acid. The MS instrument was operated in full scan mode (m/z 350–1600) with resolution R = 60,000 at m/z 400. Peptide fragmentation was performed using data-dependent acquisition (DDA). The top 10 peptide ions subjected to DDA-based ms/ms fragmentation were selected based on peptide ions' intensity. Typical mass spectrometric conditions were as follows: AGC target, standard; spray voltage, 4000 V; 45; auxiliary gas flow, 10; ion transfer tube temperature, 325°C; vaporizer temperature, 325°C; DDA cycle time, 3; collision energy, 30%. Tracefinder software was used for manual inspection of chromatograms and integration of peak areas. Peptide identification and confirmation were performed using Skyline software.

GC-MS of samples labeled by ^{13}C-palmitate

From the polar phase of ^{13}C-palmitate treated Th17 cells, 250 μL were transferred to a glass vial with a micro insert and lyophilized in a CentriVap (Labconco Corporation). The metabolites in the polar phase were derivatized before injection into the GC-MS system. To this end, 15 μL methoxyamine hydrochloride (20 mg/mL in pyridin) were injected into the glass vials and incubated at 55°C for 30 min, followed by injection of 15 μL MTBSTFA and further derivatization for 90 min. For quantification of labeled palmitate, 500 μL derivatization reagent [2% (v/v) H_2SO_4 in methanol] was added to the dried non-polar phase. The samples were incubated for 2 h at 50°C. Subsequently, 100 μL saturated NaCl solution and 500 μL hexane were added to the reaction tube, followed by vortexing for 2 min. After phase separation, 400 μL of the upper hexane phase was collected in a new reaction tube. An additional 500 μL hexane were added to the first reaction tube and the previous steps were repeated. After evaporating the hexane from the second reaction tube in a CentriVap, the samples were reconstituted in 75 μL hexane and transferred to a glass vial with micro insert and capped immediately.

For analysis of polar metabolites, 1 μL sample was injected into an SSL injector at 270°C in splitless mode. GC-MS analysis was performed using a 7890A GC System from Agilent coupled to a 5975C inert XL MSD. The GC was equipped with a 30 m ZB-35 column from Zebron and helium was used as a carrier gas with a flow rate of 1 mL/min. The initial oven temperature of 100°C was held for 2 min, followed by an increase in temperature to 300 °C at a rate of 10 °C/min, which was held for 4 min. Metabolites were detected in selected ion monitoring (SIM) mode. The MSD was operating under electron ionization at 70 eV.

For fatty acid analysis, 1 μL sample was injected into an SSL injector at 270°C in splitless mode. GC-MS analysis was performed using a 7890A GC System from Agilent coupled to a 5975C inert XL MSD. The GC was equipped with a VF-35 MS column from Agilent and helium was used as a carrier gas with a flow rate of 1 mL/min. The initial oven temperature of 55°C was held for 5 min, followed by an increase in temperature to 325 °C at a rate of 6 °C/min, which was held for 10 min. Metabolites were detected in full scan mode and mass spectra were acquired from *m/z* 70 to 800. The MSD was operating under electron ionization at 70 eV.

Data analysis of relative metabolite levels and analysis of mass isotopomer distribution (MID) were performed using Metabolite Detector software.[67]

Acetyl-CoA measurement by LC-MS

The LC-MS setup consisted of a Vanquish Flex (Thermo Scientific) liquid chromatography system configured in binary gradient coupled to a Q-Exactive Plus mass spectrometer (Thermo Scientific). The analytical column was a SeQuant ZIC-pHILIC (Merck) (2.1 mm × 150 mm, 5 μm) with a guard column (2.1 mm × 20 mm), and was heated at 45°C in the column oven. Solvent A was 20mM ammonium carbonate (pH 9.2) containing 5μM medronic acid. Solvent B was pure acetonitrile. Samples were injected onto the column and eluted using a linear gradient that ranged from 80% Solvent B to 20% Solvent B, and was conducted over 15 min at a constant flow rate of 200 μL/min.

Acetyl-CoA isotopic enrichment was measured by selected ion monitoring (SIM). The quadrupole isolation window was set from 808 to 838 m/z in order to accumulate all the isotopologues of acetyl-CoA, from the M+0 (810.1331 m/z) to the M+23 (833.2102 m/z). The maximum accumulation time was set to 250 ms, with automatic gain control of 1e6 charges. Orbitrap resolution was set to 140,000 at 200 m/z. Data was acquired with Thermo Xcalibur software (Version 4.3.73.11) and analyzed with TraceFinder (Version 4.1). Subsequent data analysis for normalization and natural isotope subtraction were performed using in house script.[69]

For calculations of isotopic distributions of acetyl groups in acetyl-CoA, the formulas described by Seim et al. were applied but, instead of using the MIDs for CoA, the MIDs of ATP were used.[70]

Proliferation

Cells ($1x10^6$) were labeled with 5μM CellTrace Violet (CTV; Invitrogen) for 72hr and analyzed by flow cytometry according to the manufacturer's protocol. Division indexes were calculated using FlowJo software.

RNA extraction and quantitative RT-PCR

RNA was extracted using a NucleoSpin RNA Kit (Macherey-Nagel) according to the manufacturer's protocol. RNA concentrations were measured by a NanoDrop 2000c Spectrophotometer (Thermo Fisher Scientific). RT-qPCR was carried out by mixing 2μL RNA (150 ng) with 5μL Master Mix (Luna Universal One-Step RT-qPCR Kits; New England BioLabs Inc.), 2pmol forward primer, 2pmol reverse primer, 0.3μL reverse transcriptase and 2.7μL RNAse-free water (cf. key resources table). Reactions were run on a CFX384 instrument (Bio-Rad). Data were normalized to *Tbp* gene (housekeeping) and analyzed using the ΔΔCt method.[55]

RNA-seq sample preparation

RNA was extracted as described above. RNA-seq and ATAC-seq were performed on the same pools of $PDH^{fl/fl}$ and $PDH^{fl/fl}$CD4 Cre + naive T cells induced to differentiate into Th17 cells *in vitro* for 72 h mRNA sequencing was performed by the Sequencing Platform of the Luxembourg Center for Systems Biomedicine (LCSB) of the University of Luxembourg. Single-end (RNA-seq samples round 1) or paired-end (RNA-seq samples round 2), stranded sequencing was executed using an Illumina NextSeq 500 machine with a read length of 75 bp. The TruSeq Stranded mRNA Library Prep kit (Illumina) was used for library preparation.

RNA-seq data analysis

FastQC (v0.11.5) was used to assess the quality control of the raw reads.[71] Adapter removal was performed using the PALEOMIX pipeline (v1.2.12),[72] with a minimum length of the remaining reads set to 25 bp. SortMeRNA (v2.1) was used to remove rRNA reads,[73] followed by mapping using STAR (v.2.5.2b).[74] RNA-seq transcript alignment was performed with Salmon[75] against the Mouse Transcriptome from Genecode v.M30.[76] Subsequent analysis was conducted in R, and Tximeta[77] was used to assign transcripts to genes before differential analysis with DESeq2.[78] Gene set enrichment analysis (GSEA) was performed using ClusterProfiler.[79] Colored KEGG view pathways were prepared using Pathview.[80]

ATAC-seq sample preparation

RNA-seq and ATAC-seq were performed on the same pools of $PDH^{fl/fl}$ and $PDH^{fl/fl}$ CD4 Cre + naive T cells induced to differentiate into Th17 cells *in vitro* for 72 h. ATAC-seq was performed using OMNI-ATAC supplementary protocol 1 by Corces et al.[81] with some modifications. Viable cells ($1x10^5$) were resuspended in 50 μL cold ATAC-Resuspension Buffer (RSB) containing 0.1% NP40, 0.1% Tween 20 and 0.01% digitonin, and lysed for 3 min on ice. Lysates were washed with 1 mL cold ATAC-RSB containing 0.1% Tween 20 but no NP40 or digitonin. Samples were centrifuged for 10 min at 500×g at 4°C, the supernatants removed, and the pellets resuspended in 50 μL transposition mix (Tagment DNA buffer from Illumina, #15027866) containing 2.5 μL Tagment DNA TDE1 Enzyme (Illumina #15027865). After 45 min incubation at 37°C and 1000 rpm in an Eppendorf ThermoMixer, chromatin fragments were isolated using the Zymo Research DNA Clean & Concentrator kit (ZymoResearch ZY-D4013). For pre-amplification of transposed fragments, 5 PCR cycles were run using primers Ad1 and Ad2.x.[35] The remaining cycles of library amplification were determined by qPCR.[82] Another clean-up was performed using the Zymo Research DNA Clean & Concentrator kit (21 μL elution volume) followed by size selection using AMPure XP beads (Beckman Coulter #A63880), with samples adjusted to 100 μL plus 55 μL of beads to remove large fragments. Samples were incubated for 5 min before bead separation using a magnetic stand and transfer of the supernatant to a new tube. Another 225 μL of beads were added followed by incubation for 10 min and separation on a magnetic stand. After washing with 80% ethanol, beads were resuspended in 20 μL elution buffer and incubated for 5 min. After separation on a magnetic stand, the eluate was transferred to a new tube. Library quality control was performed using the Agilent DNA High Sensitivity Bioanalyzer chip (Agilent #5067-4626). The sequencing of ATAC-seq libraries was performed by the Sequencing Platform of LCSB. Paired-end, unstranded library sequencing was performed using the Illumina NextSeq 500/550 75 cycles High Output Kit.

ATAC-seq data analysis

FastQC (v0.11.5) was used to assess the quality control of raw reads.[71] Alignment and mapping to generate BAM files were performed with BWA (v.0.7.16a).[83] The mouse reference genome used for mapping was GRCm38 release 102 downloaded from GENCODE (https://www.gencodegenes.org/). The Picard tool (v2.10.9)[82] was used to validate BAM files. Genrich (https://github.com/jsh58/Genrich) was used for peak calling with parameters "-r -m 30 -j -a 200 -g 15 -L 15 -d 50" to remove PCR duplicates and include only reads with mapping quality of at least 30. This approach also achieved a minimum AUC for a peak of 200 bp, a maximum distance between significant sites of 15 bp, a minimum length of a peak of 15 bp, and cut sites to 50 bp.

Samples for ATAC-seq with more than 15 million read were kept for analysis. Differentially accessible regions were detected using DiffBind (3.6.1)[84] in R (4.2.0). Briefly, peaks from all samples have been overlapped and merged resulting into 132,759 unique regions. Then, a blacklist region obtained from the ENCODE[85] project was applied to filter out problematic regions resulting into 116,364 peaks that were identified in at least two samples and constituted the peakset. Then, the number of mapped reads was calculated for each peak included in the peakset and background normalization was performed. Finally, differential analysis was performed using DESeq2 resulting into 39,647 significant regions with differentially opened chromatin between the $PDH^{fl/fl}$ and $PDH^{fl/fl}$ CD4

Cre + untreated conditions using an adjusted p value of 0.05. ATAC-seq tracks were generated using the bamCoverage command from deepTools (3.5.1)[86] with the –scaleFactor setting enabled and being equaled to the normalization factors as calculated by DESeq2 for each sample.

QUANTIFICATION AND STATISTICAL ANALYSIS

Data are presented as the mean ± SEM with a minimum n = 3 per group (for more information, please refer to the Figure Legends). p values were calculated using the unpaired Student's t test, or one or two-way ANOVA using Tukey test correction for multiple comparisons, and Prism 9.3.1 (GraphPad). Statistical significance was set at $p \leq 0.05$, with levels indicated by asterisks as follows: *$p \leq 0.05$; **$p \leq 0.01$; ***$p \leq 0.001$; ****$p \leq 0.0001$; ns, not significant.

Cell Reports, Volume *42*

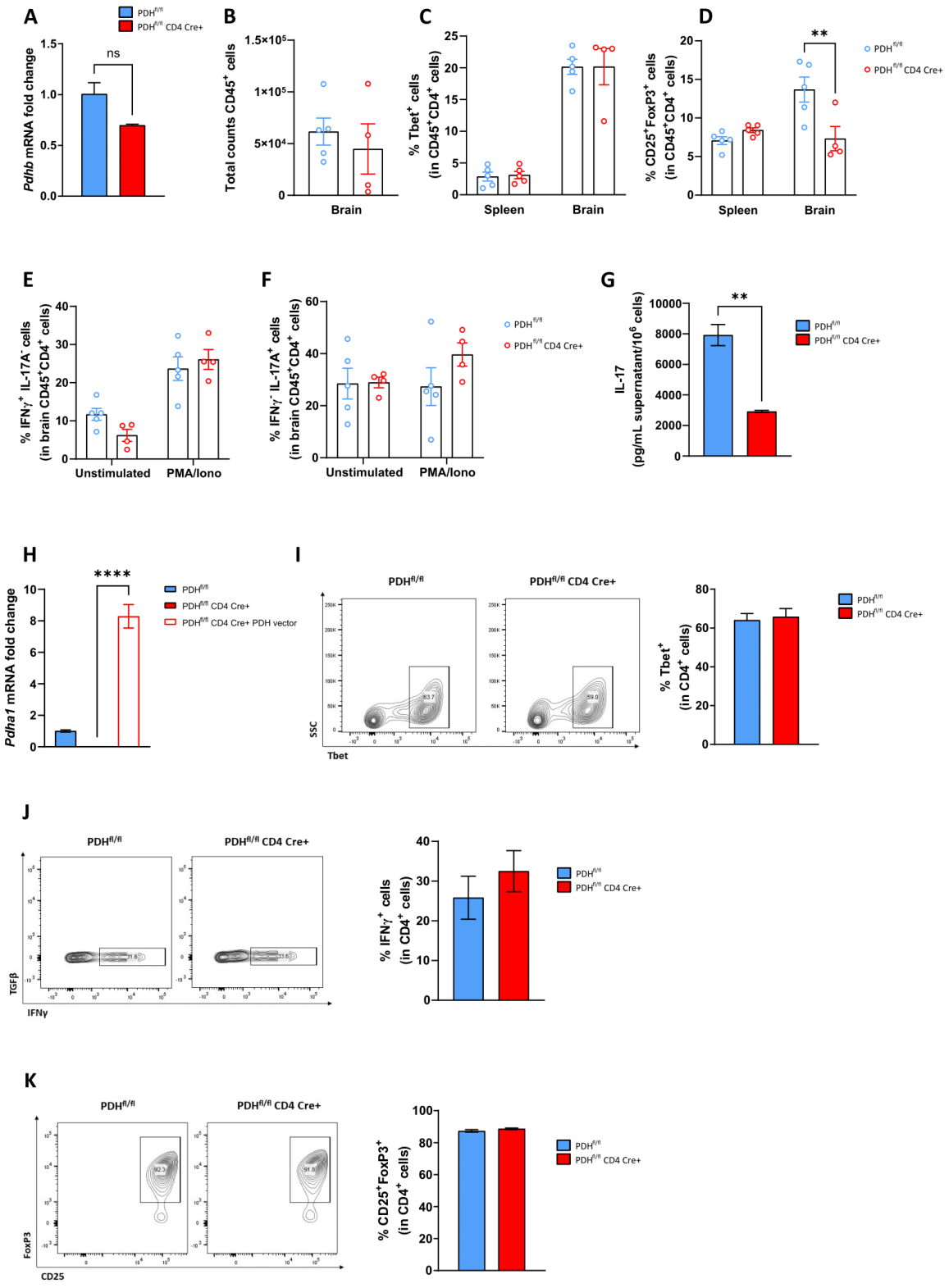
Supplemental information

Pyruvate dehydrogenase fuels a critical citrate pool that is essential for Th17 cell effector functions

Leticia Soriano-Baguet, Melanie Grusdat, Henry Kurniawan, Mohaned Benzarti, Carole Binsfeld, Anouk Ewen, Joseph Longworth, Lynn Bonetti, Luana Guerra, Davide G. Franchina, Takumi Kobayashi, Veronika Horkova, Charlène Verschueren, Sergio Helgueta, Deborah Gérard, Tushar H. More, Antonia Henne, Catherine Dostert, Sophie Farinelle, Antoine Lesur, Jean-Jacques Gérardy, Christian Jäger, Michel Mittelbronn, Lasse Sinkkonen, Karsten Hiller, Johannes Meiser, and Dirk Brenner

SUPPLEMENTARY INFORMATION

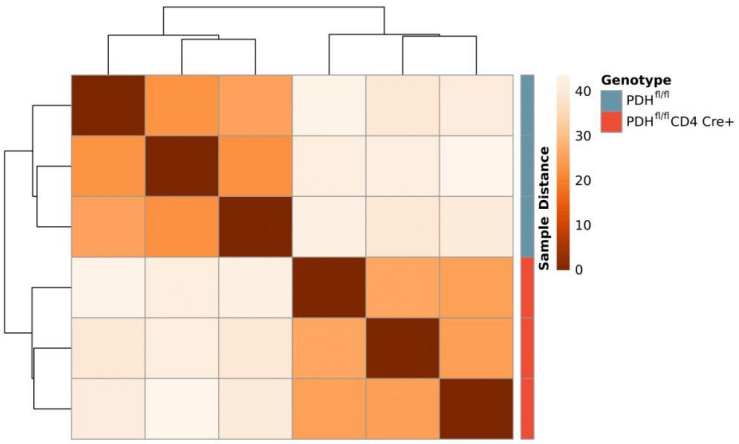
Figure S1



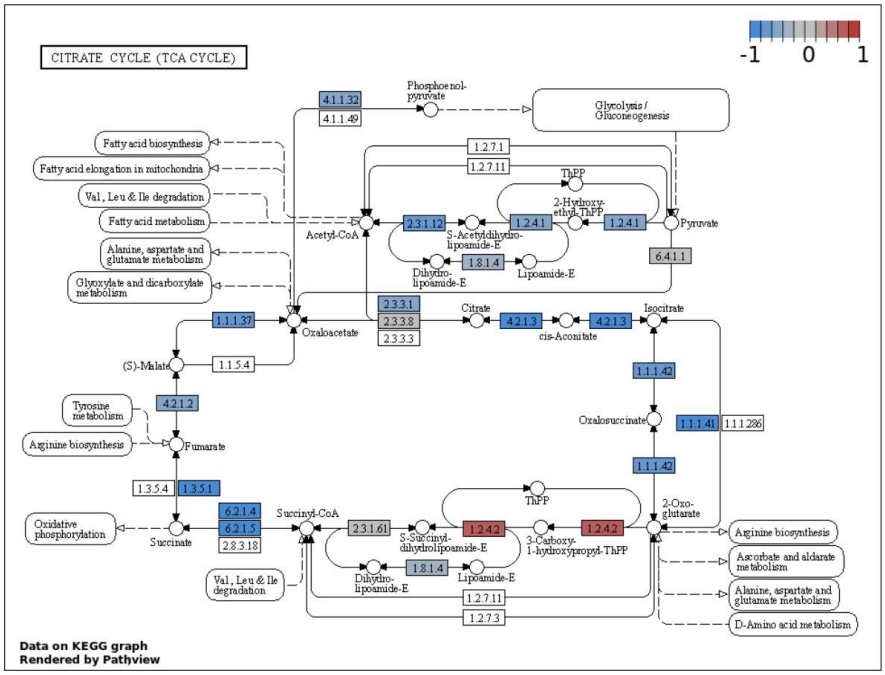
Supplementary Figure 1: PDH-E1α deficiency in T cells does not affect PDH-E1β expression or the frequencies of Th1 cells in EAE-affected mice. Related to Figure 1. (A) qPCR determination of fold change in *Pdhb* mRNA levels in total $CD4^+$ T cells that were isolated from spleen and lymph nodes of control ($PDH^{fl/fl}$) and PDH-deficient ($PDH^{fl/fl}$ CD4 Cre+) mice and activated *in vitro* for 24hr with anti-CD3 and anti-CD28 antibodies. Data are mean±SEM (n=3) and representative of 2 trials. ΔΔCt values were normalized to Tbp expression. **(B)** Flow cytometric analysis (FCA) of total counts of $CD45^+$ cells from the brains of $PDH^{fl/fl}$ and $PDH^{fl/fl}$ CD4 Cre+ mice at day 14 post-EAE induction, gated on viable cells. Data are mean±SEM (n=4-5/group). **(C, D)** Intracellular FCA of frequencies of $Tbet^+$ (Th1) **(C)** and $CD25^+FoxP3^+$ (Treg) **(D)** cells from spleens and brains of the mice in (B), gated on viable $CD45^+CD4^+$ cells. Data are mean±SEM (n=4-5/group). **(E, F)** Intracellular FCA of frequencies of $IFNγ^+IL\text{-}17A^-$ (E) and $IFNγ^-IL\text{-}17A^+$ (F) cells from the brains of the mice in (B), gated on viable $CD45^+CD4^+$ cells. Cells were left unstimulated or stimulated *in vitro* for 5hr with PMA/calcium ionophore/Brefeldin A (PMA/Iono) before staining. Data are mean±SEM (n=4-5/group). **(G)** ELISA determination of IL-17 protein in culture supernatants of *in vitro*-differentiated Th17 cells of the indicated genotypes. Naïve T cells were isolated from spleens and lymph nodes of $PDH^{fl/fl}$ and $PDH^{fl/fl}$ CD4 Cre+ mice and cultured for 3 days with anti-CD3, anti-CD28, IL-6, anti-IFNγ, and TGFβ. Data are mean±SEM (n=3) and representative of 3 trials. **(H)** Naïve T cells were isolated from spleen and lymph nodes of $PDH^{fl/fl}$ and $PDH^{fl/fl}$ CD4 Cre+ mice and *in vitro*-differentiated into Th17 cells for 3 days. On day 1, Th17 cells were infected with control- or PDH-expressing retroviral vector. Results shown are qPCR determination of fold change in *Pdha1* mRNA levels. Data are mean±SEM (n=3). ΔΔCt values were normalized to Tbp expression. **(I-K)** Naïve T cells were isolated from spleen and lymph nodes of $PDH^{fl/fl}$ and $PDH^{fl/fl}$ CD4 Cre+ mice and *in vitro*-differentiated into Th1 (I, J) or Treg (K) cells for 3 days. **(I)** Left: Representative contour plots of intracellular staining of Tbet and SSC among viable $CD4^+$ cells. Right: Intracellular FCA of frequencies of $Tbet^+$ cells, gated on viable $CD4^+$ cells. **(J)** Left: Representative contour plots of intracellular staining of IFNγ and TGFβ among viable $CD4^+$ cells. Cells were stimulated *in vitro* with PMA/calcium ionophore/Brefeldin A (PMA/Iono) for 5hr before staining. Right: Intracellular FCA of frequencies of $IFNγ^+$ cells gated on viable $CD4^+$ cells. **(K)** Left: Representative contour plots of intracellular staining of CD25 and FoxP3 among viable $CD4^+$ cells. Right: Intracellular FCA of frequencies of $CD25^+FoxP3^+$ cells gated on viable $CD4^+$ cells. Data are mean±SEM (n=3) and representative of 3 trials. P values are determined by unpaired two-tailed Student's t-test, one or two-way ANOVA where appropriate. Correction for multiple comparison was performed using the Tukey test. (ns: no significance; **: $p<0.01$; ****:$p<0.0001$).

Figure S2

A

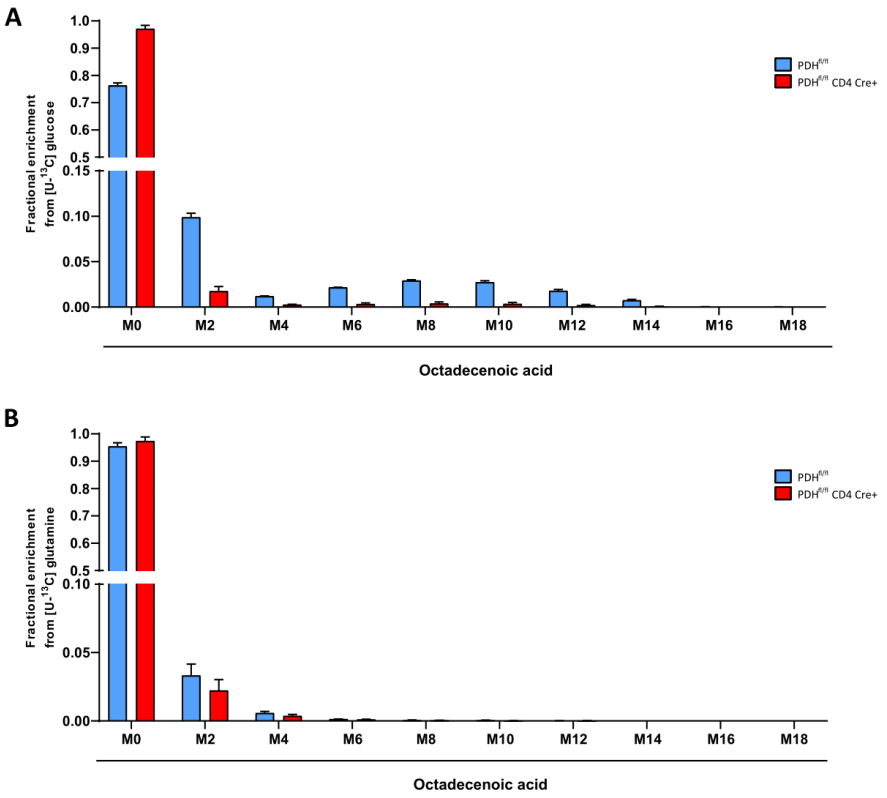


B



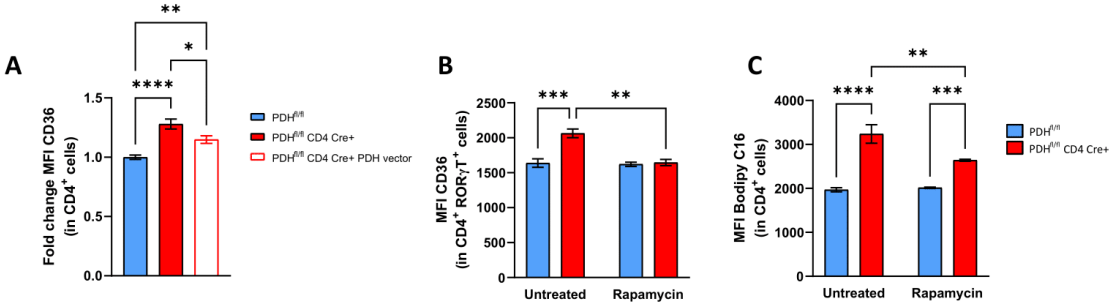
Supplementary Figure 2: PDH ablation impairs TCA cycle enzyme expression in Th17 cells. Related to Figure 3. (A) Sample distance matrix between the RNA-seq normalized counts of $PDH^{fl/fl}$ and $PDH^{fl/fl}$ CD4 Cre+ Th17 cells. Results shown are after conversion to homoskedastic data by variance stabilizing transformation. **(B)** Coloured KEGG map of changes to gene expression levels (log2) in TCA cycle pathways in $PDH^{fl/fl}$ CD4 Cre+ vs. $PDH^{fl/fl}$ Th17 cells.

Figure S3



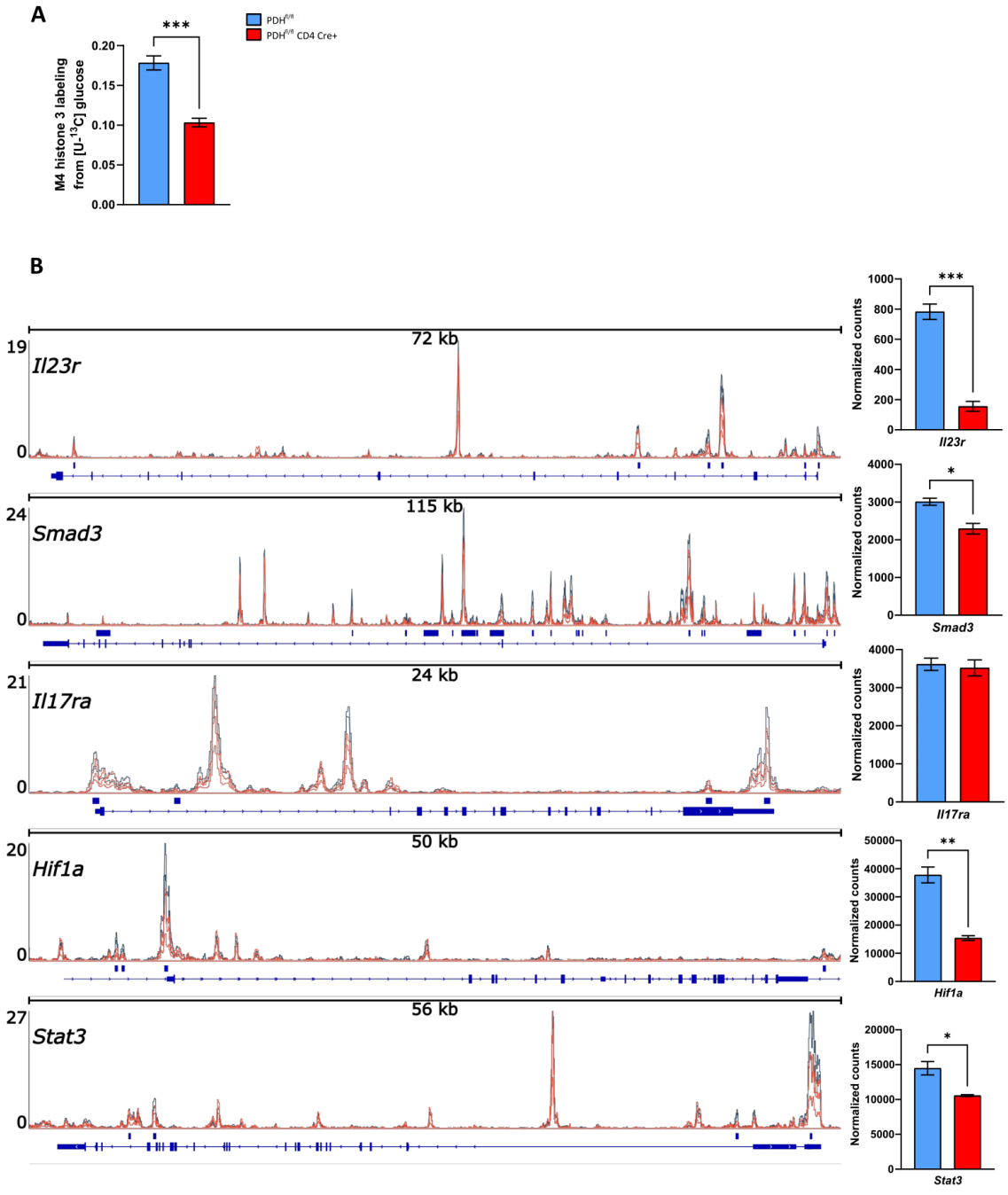
Supplementary Figure 3: PDH deficiency in T cells alters *de novo* lipid synthesis in Th17 cells. Related to Figure 4. (A) MID from M0 to M18 of octadecenoic acid in $PDH^{fl/fl}$ and $PDH^{fl/fl}$ CD4 Cre+ Th17 cells incubated for 24hr with [U-$^{13}C_6$]-glucose. Data are mean±SEM (n=3) and representative of 2 trials. **(B)** MID from M0 to M18 of octadecenoic acid in $PDH^{fl/fl}$ and $PDH^{fl/fl}$ CD4 Cre+ Th17 cells incubated for 24hr with [U-$^{13}C_6$]-glutamine. Data are mean±SEM (n=3) and representative of 2 trials.

Figure S4



Supplementary Figure 4: PDH alters CD36 and mTOR expression in Th17 cells. Related to Figure 5. (A) Naïve T cells were isolated from spleen and lymph nodes of $PDH^{fl/fl}$ and $PDH^{fl/fl}$ CD4 Cre+ mice and *in vitro*-differentiated into Th17 cells for 3 days. On day 1, Th17 cells were infected with control- or PDH-expressing retroviral vector. Results shown are the fold change in CD36 MFI cells relative to $PDH^{fl/fl}$ control and gated on viable $CD4^+RORγT^+$ cells. Data are mean±SEM (n=12) and pooled from 4 trials. **(B, C)** Quantification of CD36 MFI (B) and BODIPY FL C16 MFI (C) in $PDH^{fl/fl}$ and $PDH^{fl/fl}$ CD4 Cre+ *in vitro*-differentiated Th17 cells treated or not with rapamycin (100 nM), gated on viable $CD4^+RORγT^+$ (B) or $CD4^+$ (C) cells. Data are mean±SEM (n=3) and representative of 3 trials. P values are determined by one or two-way ANOVA where appropriate. Correction for multiple comparison was performed using the Tukey test. (*: $p<0.05$; **: $p<0.01$; ***: $p<0.001$; ****:$p<0.0001$).

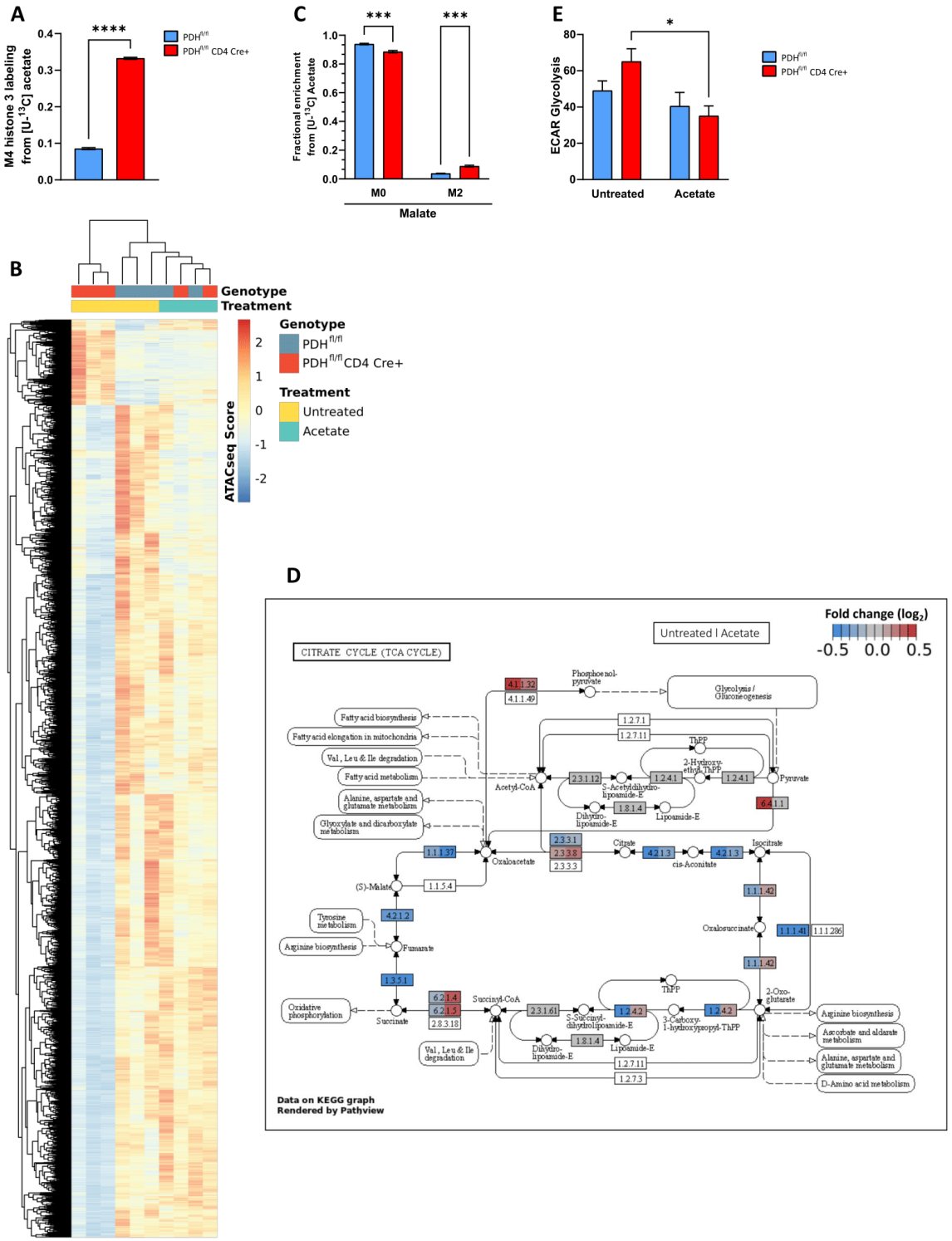
Figure S5



Supplementary Figure 5: PDH deficiency in Th17 cells alters histone acetylation and chromatin accessibility. Related to Figure 6. (A) MID of M4 histone-3 labeling in $PDH^{fl/fl}$ and $PDH^{fl/fl}$ CD4 Cre+ Th17 cells incubated for 24hr with [U-$^{13}C_5$]-glucose. Data are mean±SEM (n=4) and representative of 2 trials. **(B)** Left: Chromatin accessibility of the *Il23r, Smad3, Il17ra, Hif1a* and *Stat3* loci in $PDH^{fl/fl}$ (blue lines) and $PDH^{fl/fl}$ CD4 Cre+ (red lines) Th17 cells. Dark blue bars depict significant DBS as identified by DiffBind. Above each ATAC trace, a scale bar indicates the size of the genomics sequence covered in

the graph. For each gene, the local sequence coverage observed in the ATAC experiment is shown as normalized counts (left x-axis) obtained by scaling to normalization factors observed with DiffBind. Right: Levels of *Il23r, Smad3, Il17ra, Hif1a* and *Stat3* mRNA expression (normalized counts) in $PDH^{fl/fl}$ and $PDH^{fl/fl}$ CD4 Cre+ Th17 cells as measured by RNA-seq. P values are determined by unpaired two-tailed Student's t-test (*: $p<0.05$; **: $p<0.01$; ***: $p<0.001$).

Figure S6



Supplementary Figure 6: Acetate treatment reverses the effects of PDH deficiency in Th17 cells. Related to Figure 7. (A) MID of M4 histone-3 labeling in $PDH^{fl/fl}$ and $PDH^{fl/fl}$ CD4 Cre+ Th17 cells incubated for 72hr with [U-$^{13}C_2$]-acetate. Data are mean±SEM (n=4) and representative of 2 trials. **(B)** Heatmap of ATAC-seq showing significant DBS between $PDH^{fl/fl}$ and $PDH^{fl/fl}$ CD4 Cre+ Th17 cells as

identified by DiffBind. The associated counts for selected regions of acetate-treated samples are also shown. ATAC-seq score is the the Z score for the Normalized Count of each DBS. **(C)** MID of M0 and M2 malate in $PDH^{fl/fl}$ and $PDH^{fl/fl}$ CD4 Cre+ Th17 cells incubated for 72hr with [U-$^{13}C_2$]-acetate. Data are mean±SEM (n=3) and representative of 2 trials. **(D)** Coloured KEGG map of changes to gene expression levels (log2) in TCA cycle pathways in $PDH^{fl/fl}$ CD4 Cre+ vs. $PDH^{fl/fl}$ Th17 cells that were treated or not with acetate (10 mM). **(E)** Quantification of Seahorse determination of ECAR glycolysis in $PDH^{fl/fl}$ and $PDH^{fl/fl}$ CD4 Cre+ *in vitro*-differentiated Th17 cells treated or not with acetate (10 mM). Data are mean±SEM (n=3) and representative of 3 trials. P values are determined by unpaired two-tailed Student's t-test or two-way ANOVA where appropriate. Correction for multiple comparison was performed using the Tukey test. (*: $p<0.05$; ***: $p<0.001$; ****:$p<0.0001$).

Supplementary Table 1. EAE scoring based on neurological signs. Related to EAE mouse model in Experimental model and subject details section in STAR Methods.

Score	**Neurological signs**
0	No neurological signs
1	Loss of tail tonicity
2	Abnormal gait and hind limb weakness
3	Hind limb paralysis
3,5	Hind limb paralysis and falling over
4	Hind limb paralysis and forelimb involvement
5	Moribund or dead

Supplementary Table 2. Th subset-specific cytokine cocktails used for the differentiation of naïve T cells *in vitro*. Related to *In vitro* differentiation of Th cell subsets in Method details section in STAR Methods.

Th subset	**Cytokine**	**Concentration**	**Source**
Th0	anti-CD3 (plate-bound)	5 µg/mL	Biolegend
	anti-CD28	1 µg/mL	Biolegend
	anti-IFNγ	5 µg/mL	BD Biosciences
	IL-2	50 U/mL	Miltenyi Biotec
Th1	anti-CD3 (plate-bound)	5 µg/mL	Biolegend
	anti-CD28	1 µg/mL	Biolegend
	IL-12	2 ng/mL	Miltenyi Biotec
	IL-2	50 U/mL	Miltenyi Biotec
Th17	anti-CD3 (plate-bound)	5 µg/mL	Biolegend
	anti-CD28	1 µg/mL	Biolegend
	IL-6	30 ng/mL	Miltenyi Biotec
	anti-IFNγ	5 µg/mL	BD Biosciences
	TGFβ	2 ng/mL	R&D Systems
Treg	anti-CD3 (plate-bound)	5 µg/mL	Biolegend
	anti-CD28	1 µg/mL	Biolegend
	IL-2	50 U/mL	Miltenyi Biotec
	anti-IFNγ	5 µg/mL	BD Biosciences
	TGFβ	4 ng/mL	R&D Systems

Supplementary Table 3. Calculations of OCR and ECAR measurements. Related to Metabolic flux measurements and analysis in Method details section in STAR Methods.

Parameter	Raw data source	Calculations
Basal OCR	OCR	3rd minus 12th measurement
Maximal respiration	OCR	9th minus 12th measurement
OCR-dependent ATP production	OCR	3rd minus 6th measurement
Spare respiratory capacity	OCR	9th minus 3rd measurement
Glycolytic capacity	ECAR	9th minus 12th measurement
ECAR glycolysis	ECAR	6th minus 3rd measurement

Supplementary Table 4. Fragments calculated for MIDs of the non-polar fraction. Related to GC-MS measurement of non-polar fractions, data processing and normalization in Method details section in STAR Methods.

Derivative	Metabolite	*m/z* - *R*ange	Sum Formula (Fragment)	MID size
Dodecanoic acid 1TBDMS	C12:0	257-272	C14H29O2Si	13
Tetradecanoic acid 1TBDMS	C14:0	285-302	C16H33O2Si	15
Hexadecanoic acid 1TBDMS	C16:0	313-332	C18H37O2Si	17
Hexadecenoic acid 1TBDMS	C16:1	311-330	C18H35O2Si	17
Octadecanoic acid 1TBDMS	C18:0	341-362	C20H41O2Si	19
Octadecenoic acid 1TBDMS	C18:1	339-360	C20H39O2Si	19
Octadecadienoic acid 1TBDMS	C18:2	337-358	C20H37O2Si	19
Cholesterol 1TBDMS	Cholesterol	443-473	C29H51OSi	28